

Larry L Altgilbers • Jason Baird • Bruce L Freeman
Christopher S Lynch • Sergey I Shkuratov

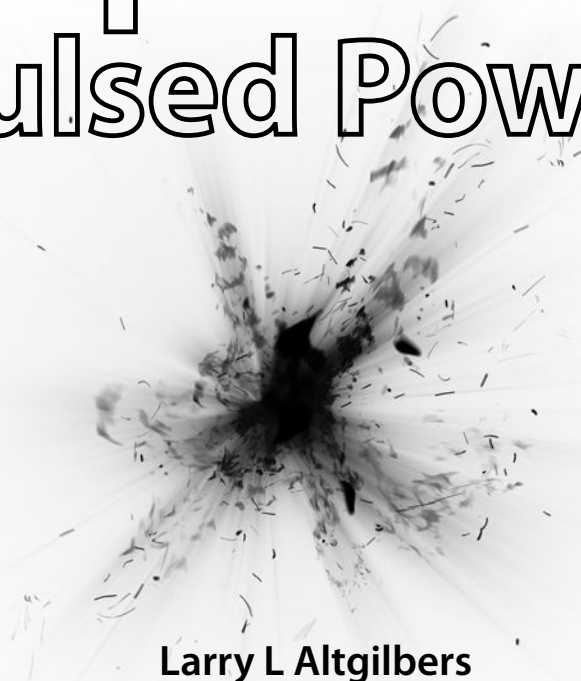
Explosive Pulsed Power

Imperial College Press

**Explosive
Pulsed Power**

This page intentionally left blank

Explosive Pulsed Power



Larry L Altgilbers

US Army Space and Missile Defense Command, USA

Jason Baird

Missouri University of Science and Technology, USA

Bruce L Freeman

KTECH Corporation, USA

Christopher S Lynch

University of California, Los Angeles, USA

Sergey I Shkuratov

Loki Incorporated, USA

Imperial College Press

Published by

Imperial College Press
57 Shelton Street
Covent Garden
London WC2H 9HE

Distributed by

World Scientific Publishing Co. Pte. Ltd.
5 Toh Tuck Link, Singapore 596224
USA office: 27 Warren Street, Suite 401-402, Hackensack, NJ 07601
UK office: 57 Shelton Street, Covent Garden, London WC2H 9HE

British Library Cataloguing-in-Publication Data

A catalogue record for this book is available from the British Library.

EXPLOSIVE PULSED POWER

Copyright © 2011 by Imperial College Press

All rights reserved. This book, or parts thereof, may not be reproduced in any form or by any means, electronic or mechanical, including photocopying, recording or any information storage and retrieval system now known or to be invented, without written permission from the Publisher.

For photocopying of material in this volume, please pay a copying fee through the Copyright Clearance Center, Inc., 222 Rosewood Drive, Danvers, MA 01923, USA. In this case permission to photocopy is not required from the publisher.

ISBN-13 978-1-84816-322-5
ISBN-10 1-84816-322-3

Typeset by Stallion Press
Email: enquiries@stallionpress.com

Printed in Singapore.

This book is dedicated to
C. M. ‘Max’ Fowler,
father of the U.S. Flux Compression Generator program

This page intentionally left blank

Contents

<i>Preface</i>	xvii
1. Introduction	1
1.1 What is Pulsed Power?	1
1.2 Pulsed Power Parameters	4
1.3 Explosive Power Sources	5
1.3.1 Flux Compression Generators	6
1.3.2 Explosive Magnetohydrodynamic Generators	7
1.3.3 Moving Magnet Generators	8
1.3.4 Ferroelectric Generators	9
1.3.5 Ferromagnetic Generators	10
1.4 Book Outline	10
Bibliography	11
2. Fundamentals of Electromagnetic Theory and Electric Circuits	13
2.1 Introduction	13
2.2 Maxwell's Equations	13
2.3 Circuit Elements and Equations	17
2.3.1 Circuit Elements	17
2.3.2 Circuit Equations	27
2.3.3 Transient Circuits	30
2.4 Electromagnetic Phenomena	31
2.4.1 Magnetic Diffusion	31
2.4.2 Magnetic Force	33
2.4.3 Magnetic Pressure	34
2.4.4 Electric Fields	35

2.4.5	Electrical Breakdown	36
2.5	Summary	42
	Bibliography	43
3.	Fundamentals of Shock Waves and High Explosives	45
3.1	Introduction	45
3.2	Shock and Detonation Waves	45
3.2.1	Stress and Strain	45
3.2.2	Sound Velocity	47
3.2.3	Shock Waves	48
3.2.4	Detonation Waves	52
3.2.5	Detonation Jump Equations	55
3.3	Explosives and Explosive Components	57
3.3.1	Explosives	57
3.3.2	Explosive Train	73
3.4	Interaction of Detonation Waves with Materials	81
3.4.1	Impedance	81
3.4.2	Gurney Equations	83
3.4.3	Taylor Angle Approximation	87
3.5	Summary	88
	Bibliography	89
4.	Measurement Techniques	91
4.1	High Power Electrical Measurements	91
4.1.1	Voltage Measurements	92
4.1.2	Current Measurements	99
4.1.3	Power and Energy Measurements	109
4.2	Pulsed Electric and Magnetic Field Measurements	110
4.2.1	B-Dot Probes	110
4.2.2	D-Dot Probes	111
4.2.3	Current Monitor Transformer	111
4.2.4	Antennae	112
4.2.5	Thin Film Sensors	114
4.3	Detonic Measurement Techniques	117
4.3.1	Time of Arrival Detectors	118
4.3.2	Surface Displacement Detectors	120
4.3.3	Stress Versus Time Detectors	122
4.3.4	Cinematographic and Flash X-Ray Techniques	123

4.4	Summary	127
	Bibliography	128
5.	Flux Compression Generators	129
5.1	Classifications of FCGs	130
5.2	Historical Perspectives	132
5.3	Principles of Operation	134
5.3.1	General Principles	134
5.3.2	Some Important Generator Parameters	137
5.3.3	Generator Impedance	137
5.3.4	Example: An Idealised Generator	139
5.3.5	Advantages and Disadvantages	141
5.4	Specific Types of Generator	145
5.4.1	Plate Generators	146
5.4.2	Strip Generators	147
5.4.3	Cylindrical Implosion System	149
5.4.4	Coaxial Generators	151
5.4.5	Disk Generators	153
5.4.6	Loop Generators	155
5.4.7	Helical or Spiral Generators	159
5.4.8	Simultaneous Helical Generators	161
5.4.9	Shock Wave Generators	161
5.4.10	Summary of Generator Classes	166
5.5	Losses and Efficiencies	167
5.5.1	Diffusion Related Losses	167
5.5.2	Mechanical Related Losses	168
5.5.3	Efficiencies	170
5.6	Power Conditioning	172
5.6.1	Switches	172
5.6.2	Transformer Coupling	176
5.6.3	Transformers	191
5.6.4	Generator Flux Sources (Seed Sources)	194
5.7	Summary	199
	Bibliography	201
6.	Helical Flux Compression Generators	217
6.1	Basic Theoretical Treatment	222
6.2	Figures of Merit	224

6.3	Loss Mechanisms	227
6.3.1	Electrical Loss Mechanisms	227
6.3.2	Mechanical Loss Mechanisms	231
6.3.3	Geometrical Loss Mechanisms	235
6.4	Seed Sources for HFCGs	237
6.4.1	Capacitive Energy Stores	239
6.4.2	Batteries	239
6.4.3	Permanent Magnets	240
6.5	HFCGs with Simultaneous Axial Initiation	242
6.6	Cascaded HFCGs	244
6.7	Practical Design and Optimisation of HFCGs	247
6.7.1	Philosophy	247
6.7.2	Preliminary Design	250
6.7.3	Advanced Design	251
6.8	Small versus Large HFCGs	251
6.9	Computer Models	254
6.10	Summary	255
	Bibliography	256
7.	Magnetic Materials and Circuits	261
7.1	Properties of Magnetic Materials	262
7.1.1	Types of Magnetic Materials	262
7.1.2	Properties of Magnetic Materials	264
7.2	Shock Compression of Ferromagnetic Materials	266
7.3	Magnetic Circuits	267
7.3.1	Magnetic Circuit Laws	270
7.3.2	Magnetic Circuit Model for Permanent Magnets .	273
7.4	Magnetic Loss Mechanisms	274
7.4.1	Hysteresis Loss	274
7.4.2	Eddy Current Loss	274
7.5	Summary	275
	Bibliography	275
8.	Ferromagnetic Generators	277
8.1	Explosive Driven Soft Ferromagnetic Generators	277
8.2	Explosive Driven Soft Ferromagnetic Generator Limitations	277

8.3	Pressure Induced Magnetic Phase Transitions in Hard Ferromagnets	280
8.3.1	Longitudinal Shock Wave Demagnetisation of Nd ₂ Fe ₁₄ B	281
8.3.2	Pressure in Shock Compressed Nd ₂ Fe ₁₄ B Ferromagnets	286
8.3.3	High Voltage and High Current Generation by Longitudinally Shock Demagnetising Nd ₂ Fe ₁₄ B	288
8.4	Transverse Shock Wave Demagnetisation of Nd ₂ Fe ₁₄ B Ferromagnets	290
8.4.1	Static Magnetic Flux Initially Stored in Nd ₂ Fe ₁₄ B Ferromagnets	292
8.4.2	Transverse Shock Wave Demagnetisation of Nd ₂ Fe ₁₄ B Ferromagnets	293
8.5	Generation of High Currents by Miniature Transverse FMGs	295
8.5.1	The Physical Principle of Seed Current Generation	295
8.5.2	Magnetic Flux Changes in Transverse FMGs	297
8.5.3	Currents Produced by Transverse FMGs	300
8.6	FMG Analytical Techniques	304
8.6.1	Analytical Equations	304
8.6.2	Current Generated by Longitudinal FMGs	306
8.6.3	Current Generated by Transverse FMGs	307
8.6.4	Summary	308
8.7	Charging Capacitors with High Voltage Transverse FMGs	309
8.7.1	High Voltage Transverse FMG Design	309
8.7.2	Results and Discussion	310
8.7.3	Summary	315
8.8	Miniature High Voltage, Nanosecond FMG System	316
8.8.1	Operating Principles	316
8.8.2	Performance of the FMG-VIG System	317
8.8.3	Summary	319
8.9	Explosive Driven FMG-FCG System	319
8.9.1	FMG-FCG System	320
8.9.2	FMG-FCG Performance	320
8.10	Summary	324
	Bibliography	326

9.	Ferroelectric Materials and Their Properties	331
9.1	Introduction	331
9.2	Historical Perspectives	331
9.3	Electromechanical Effects in Ferroelectric Materials	333
9.4	Piezoelectric Figures of Merit	339
9.4.1	Dielectric Constant/Permittivity	339
9.4.2	Dielectric Strength	340
9.4.3	Remnant Polarisation	340
9.4.4	Coercive Field	341
9.4.5	Compliance	341
9.4.6	Piezoelectric Charge Constant or Piezoelectric Coefficient	341
9.4.7	Piezoelectric Voltage Constant	341
9.4.8	Electromechanical Coupling Factor	342
9.4.9	Acoustic Impedance	342
9.5	Notation	343
9.6	Ferroelectric Materials	345
9.6.1	Single-Crystals	345
9.6.2	Ferroceramics	346
9.6.3	Ferropolymers	346
9.6.4	Ferrocomposites	346
9.6.5	Thin Films	346
9.7	Lead Zirconate Titanate (PZT)	347
9.7.1	PZT Properties	347
9.7.2	Important PZT Parameters	351
9.7.3	Fabrication of PZT	358
9.7.4	Factors that Affect PZT	359
9.7.5	Optimisation of PZT for FEGs	362
9.7.6	PZT Failure Modes	363
9.8	Chapter Summary	364
9.9	Suggested Reading on Ferromagnetic Materials	365
	Bibliography	366
10.	Phase Transformations in Ferroelectric Crystals	369
10.1	Introduction	369
10.2	Perovskite-Type ABO_3 Crystal Structure	370
10.3	The Phase Diagram	375
10.3.1	Cubic	377

10.3.2	Tetragonal	378
10.3.3	Rhombohedral, F	379
10.3.4	Rhombohedral, AF	379
10.3.5	Orthorhombic	380
10.3.6	Monoclinic A, B, C	380
10.4	Single-Crystal Behavior	380
10.4.1	Domains (Crystal Variants)	381
10.4.2	Domain Walls	381
10.5	Driving Forces for Domain Wall Motion (Evolution of Variants, Poling and Depoling)	384
10.5.1	Mechanical Work	384
10.5.2	Electric Work	385
10.5.3	Combined Stress and Electric Field	386
10.5.4	Orientation Effects (Orthogonal Transformations)	387
10.5.5	Stress	388
10.5.6	Electric Field	389
10.5.7	Kinetics of Variant Evolution	389
10.5.8	Volume Average Single Crystal Properties	392
10.6	Phases Transformations in Single Crystal	394
10.6.1	Ceramic Behavior	396
10.7	Properties of Soft, Hard and Phase Transforming PZT	398
10.7.1	PLZT 8/65/35 (Soft Rhombohedral Ferroelectric)	398
10.7.2	PLSnZT (AF-F Double Loop)	401
10.7.3	PZT 95-5	403
10.8	Discussion of the Rh (F) to Rh (AF) Phase Transformation and FEG Design	406
10.9	Summary	408
	Bibliography	408
11.	Ferroelectric Shock Depolarisation Studies	411
11.1	Early Shock Depolarisation Studies	411
11.2	Recent Shock Depolarisation Studies	420
11.2.1	Shock Induced Stress Test Methods	420
11.3	Early FEG Studies	425
11.4	Summary	429
	Bibliography	433

12. Ferroelectric Generators	439
12.1 Introduction	439
12.2 Gas Gun Accelerated Projectiles	440
12.3 Electromagnetic Launcher Accelerated Flyer Plates	440
12.4 Propellant Gun Accelerated Projectiles	441
12.5 Explosive Driven Ferroelectric Generators	444
12.5.1 Design of Explosive Driven FEGs	444
12.5.2 Electrical Breakdown Problems	447
12.6 FEG Pulsed Power Generation: High Resistance Loads . .	449
12.7 Longitudinal Shock Wave Depolarisation of Polycrystalline PZT 54/48	455
12.7.1 Experimental Results	456
12.8 Pulse Charging Capacitor Banks with FEGs	460
12.8.1 FEG-Capacitor Bank System: Oscillatory Mode .	461
12.8.2 Theoretical Description of FEG-Capacitor Bank Systems	465
12.8.3 FEG-Capacitor Bank Energy Transfer	468
12.9 Operation of FEGs with Resistive Loads	473
12.9.1 Experimental Results	474
12.10 Theoretical Models for FEGs	479
12.10.1 Single Element FEGs	479
12.10.2 Multi-Element FEG Model	485
12.10.3 Semi-Empirical Model for PZT Breakdown . .	489
12.11 High-Voltage Nanosecond FEG-VIG Pulsed Power System	490
12.11.1 General Design of a FEG-VIG Pulsed Power System	490
12.11.2 FEG-VIG System Performance	493
12.12 Other Factors That Affect FEG Design	498
12.12.1 Ferroelectric Material and Geometry	498
12.12.2 Potting Materials	499
12.12.3 Shock Wave Profile	500
12.13 Summary	501
Bibliography	502
13. Moving Magnet Generators	507
13.1 Principles of Operation	507
13.2 Moving Magnet Pulsed Power Generators	510

13.3	Principle MMG Designs	512
13.3.1	Open Magnetic Circuit MMGs	512
13.3.2	Closed Magnetic Circuit MMGs	514
13.3.3	MMG Ferromagnetic Projectiles	516
13.4	High-Current Explosive-Driven MMGs	520
13.4.1	Experimental Systems	520
13.4.2	Principles of High Current Generation	522
13.4.3	High Current MMG Seed Sources	524
13.5	High-Voltage Explosive-Driven MMGs	530
13.5.1	High-Voltage Generation	531
13.5.2	Multi-Stage High-Voltage MMGs	532
13.6	Summary	538
	Bibliography	539
14.	Case Studies	543
14.1	Introduction	543
14.2	Case Study 1: Piezoelectric High Voltage Generator	543
14.2.1	Three Ferroelectric Element Module Voltage Tests	545
14.2.2	Summary	547
14.3	Case Study 2: FEG-Driven Antenna	548
14.4	Case Study 3: FCG-Driven Microwave Test Bed	550
14.4.1	Fire Set	551
14.4.2	Compact Seed Source	551
14.4.3	Helical Flux Compression Generator	553
14.4.4	Power Conditioning System	561
14.4.5	Loads	565
14.5	Case Study 4: Birdseed Program	568
14.6	Summary	570
	Bibliography	571
	Index	573

This page intentionally left blank

Preface

Explosive pulsed power (EPP) is an outgrowth of the nuclear weapon programs in the United States, United Kingdom and Soviet Union. Its history can be traced back to the early 1950s and involves several of the great scientists of the time. The development of EPP has been cyclic with the most recent upturn starting in 1998 with a university consortium funded by the US Air Force of Scientific Research and led by Texas Tech University. Since 1998, there have been many advances in this technology in the U.S., which are reported on in this book. This book only reports on advances in the U.S., since these are more familiar to the authors. Advances continue to be made in other countries such as China, Germany, Russia, South Korea, Sweden and others.

As in any endeavor, there are many people who make valuable contributions. First and foremost is the late C.M. ‘Max’ Fowler, who pioneered the work on EPP in the U.S. and served as teacher to two of the authors. Max also co-authored Chapter 5 and provided several historical photos and drawings. Others include Wes Hackenberger and Ed Alberta at TRS Technologies, who provided valuable inputs to the chapters on ferroelectric materials, David Hemmert at HEM Technologies, who provided valuable insights on shock wave sources, and Frank Rose at Radiance Technologies, who provided insights into the history of ferroelectric generators, Yaroslav Tkach at Gomez Research Associates, who helped model the FEGs, Kris Kristiansen, Andreas Neuber, Jim Dickens, Thomas Holt, Andrew Young, Moe Elsayed, and others at Texas Tech University, who helped revive and maintain EPP starting in the late 1990s, and Randy Curry and Kevin O’Connor at the University of Missouri in Columbia, who made advances in EPP power conditioning. We would also like to acknowledge Robert Barker, who, as the Program Manager for Plasma Physics at the Air Force

Office of Scientific Research, supported the basic research into explosive pulsed power for many years. In addition, we would like to thank Rodney Robertson, Michael Lavan, Mark Rader, Dale Perry and John Wachs at the US Army Space and Missile Defense Command for their encouragement and the freedom to pursue our lines of research and to Allen Stults, David Clark and Robert Hartleben at the US Army Aviation and Missile Research, Development, and Engineering Center for their experimental support and contributions to the development of EPP generators.

This page intentionally left blank

Chapter 1

Introduction

The objective of this book is to acquaint the reader with explosive driven pulsed power devices, theory and applications. This includes those devices that convert the chemical energy stored in high explosives into electrical energy and that use shock waves generated by the explosives to release the energy stored in ferromagnetic or ferroelectric materials in the form of electrical energy. The reader might well ask why one should use explosive driven pulsed power for any application, since it is inherently single shot in nature. There are really two very different answers to this question. First, explosives store the greatest amount of energy per unit mass (4 MJ/kg) or per unit volume (8 GJ/m³) of any readily accessible energy source. In the case of high-quality solid explosives, they can convert chemical bond energy into PdV energy at a rate of 10^{10} W/cm² at its detonation front. If this energy is converted into pulses of electrical energy having the proper characteristics, then very compact, lightweight, high power sources may be developed. The requirements of a particular load to be energised is a critical consideration in selecting an explosive pulsed power system. Second, C. Max Fowler often listed four criteria for using explosive driven pulsed power. These criteria are requirements for (1) portability, (2) compactness, (3) a very large quantity of electrical energy and (4) a need for a limited number of events or tests that do not justify the investment in a conventional pulsed power system. In this chapter, a brief introduction to pulsed power and, in particular, to explosive pulsed power devices, is presented.

1.1 What is Pulsed Power?

Pulsed power are those processes by which stored energy is subsequently released or delivered very rapidly to a load. A mechanical variant of pulsed

power is a bull whip. Energy is stored in the angular momentum of the whip as it is rotated, only to be delivered to the tip of the whip in the form of a ‘crack’ as the tip snaps. An electrical variant of pulsed power is the Marx generator. Electrical energy is slowly stored in a capacitive medium and then delivered to a load as a single short pulse or as a train of short pulses with a controllable repetition rate. For the purposes of this book, pulsed power systems can be categorised as being one of two types: explosive driven and non-explosive driven. A detailed description of non-explosive pulsed power technologies is given in [1–3], but there is no single book that addresses all the explosive driven pulsed power technologies. This work intends to do just that.

Non-explosive pulsed power is the generation of short, intense pulses of electrical energy through a process called *pulse compression*. Pulse compression is the process of taking energy from a low voltage, long pulse system and compressing this energy in time and space, increasing both voltage and current, with an accompanying decrease in pulse duration [4]. The development of high voltage pulsed power systems was started in the early 1960s by J.C. Martin at the Atomic Weapons Research Establishment in England [5]. The objective of his research was to develop a technique for using a Marx generator to pulse charge a transmission line to produce short (10–100 ns), high power electrical pulses for X-ray machines, which were needed to resolve fast explosive events. A Marx generator is a specialised capacitor bank that is charged in parallel and subsequently discharged in series. This process enables the production of very high voltages (~ 1 MV) from a relatively low voltage source (40–100 kV). Since then, progress in developing non-explosive pulsed power technologies has been rapid and work still continues in many laboratories around the world today.

As pointed out by Sarjeant and Dollinger [6], there are two main types of energy storage used in non-explosive pulsed power systems: mechanical and electrical. In the case of mechanical energy storage, energy is stored in the rotary motion of a machine such as a flywheel homopolar DC generator or a pulse compensated alternator. This energy can be represented mathematically by the expression $W_r = I_0\omega^2/2$, where I_0 is the moment of inertia of the rotating component and ω is its angular velocity. In the case of electrical energy storage, the energy is stored either electrostatically or magnetostatically. In the case of electrostatic storage, energy is typically stored in capacitors, which is mathematically represented by the formula $CV^2/2$, where C is capacitance with units of farads (F) and V is voltage with units of volts (V). In the case of magnetostatic storage, energy is

typically stored in inductors, which is mathematically represented by the formula $LI^2/2$, where L is inductance with units of henries (H) and I is current with units of amperes (A). While all these energy storage systems can store very large amounts of energy, none of them can match the energy storage per unit volume or mass of explosives.

Initially, *explosively driven pulsed power*, or simply *explosive pulsed power*, was generally defined as the conversion of the chemical energy stored in high explosives into electrical energy. This conversion has usually been accomplished by propelling a conductive medium with the explosive. In turn, this medium is used to compress or do work on a magnetic field. More recently, explosive pulsed power has been generalised to include any use of explosives to produce an electrical pulse. For example, the explosive may be used to induce a shock that initiates the release of energy stored in ferromagnetic, ferroelectric or superconducting materials. It is important to note that these latter examples do not convert the explosive energy into electrical energy in the usual sense. The energy is already stored in the ferromagnetic or ferroelectric materials. In the case of the superconducting system, the pre-stored energy is in the form of a magnetic field supported by the current in a superconductor.

The development of explosive pulsed power was started by W.B. Garn, C.M. Fowler and their colleagues [7] at Los Alamos National Laboratory in the United States and, independently, by A.D. Sahkarov, A.I. Pavlovskii, V.D. Chernyshev, R.Z. Lyudaev and others [8] at the All-Russian Institute of Experimental Physics (VNIIEF), also known as Arzamas-16, in the Soviet Union in the early 1950s. The objective of this research was to support the nuclear weapon programs in the respective countries. In particular, E. Teller and J. Willig in the United States and A.D. Sahkarov in the Soviet Union proposed using magnetic flux compression generators in place of fission bombs to achieve fusion in the hydrogen bomb. Throughout the intervening period to the present, this research has continued in a cyclic manner to support a variety of weapon programs, including the development of directed energy weapons, electromagnetic launchers and so on. However, only recently has there been a systematic investigation of the physics of explosive pulsed power sources by a consortium of universities and by a few companies in the United States in an attempt to improve the performance of explosive pulsed power generators. While nearly all of the findings in these recent studies were known to researchers at the various national laboratories and are considered to be rules of thumb in good design practice, the completion of these studies has provided a fundamental understanding of many cause and effect issues.

Both types of pulsed power systems have their advantages and disadvantages. For example, explosive pulsed power systems generate the highest electrical powers and currents and have the smallest mass and size, but they also generally destroy themselves and, quite usually, the load they are driving. Thus, they are single shot in nature. Non-explosive pulsed power systems are usually not self-destructive and can be repetitively pulsed, but they tend to be massive, large in size and fairly expensive. The advantages and disadvantages of both types of system must be closely examined when selecting the proper pulsed power source for a particular application. In this book, attention is focused on explosive pulsed power sources, since there has been recent progress in our understanding of their performance limitations and how to negate them and since laboratories in several countries are currently developing these power sources for specific applications.

1.2 Pulsed Power Parameters

No matter what method — i.e. explosive or non-explosive driven — is used to generate the electrical pulses produced by pulsed power systems, these pulses all have common characteristics. They include power level, energy content and pulse shape — i.e. rise time, pulse width, fall or decay time and flatness of the top of the pulse.

The electrical power generated by pulsed power systems typically ranges from kilowatts (kW) to terawatts (TW). The energy content of the pulses ranges from a joule (J) to megajoules (MJ), depending on the type and size of the pulsed power source used. Presently, the highest power and energy that have been achieved in a single pulse are a few hundred terawatts and 100 MJ respectively. The corresponding voltages and currents that have been achieved range from 10 kV to 50 MV and from 1 kA to >100 MA respectively [3].

In addition to power and energy, the shape of the pulse is also an important parameter since the input requirements of the load often require certain pulse shapes to operate properly. The parameters that determine the shape of the pulse are depicted in Fig. 1.1. Typically, the overall duration of high power pulses lies between a few nanoseconds to a few tens of microseconds. The rise time of the pulse from a pulsed power system, which is defined to be the time it takes the voltage to rise from 10 to 90% of its peak value typically ranges from a few nanoseconds to a few microseconds. The fall time is similarly defined and typically ranges from a few nanoseconds

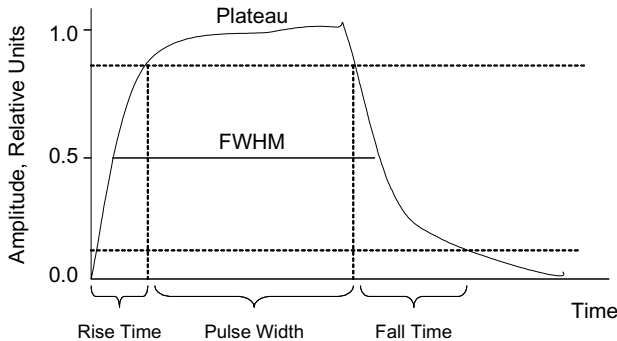


Fig. 1.1 Pulse shape parameters.

to a few microseconds. The pulse length or duration is often taken to be the Full Width of the pulse at Half its Maximum amplitude (Full Width Half Max, FWHM) or, in some cases, the width of the pulse at 90% of its peak amplitude. The flatness of the plateau of the pulse is usually another important parameter when driving certain types of loads, such as high power microwave tubes like virtual cathode oscillators (VIRCATORs) or magnetically insulated line oscillators (MILOs).

The particular pulse characteristics required to optimally power a given load will dictate which type of pulsed power is best suited to drive that load and what power conditioning is needed. In a low-energy example, if high peak voltage is required, the explosive driven ferroelectric generator would be the best choice as the power supply. If high peak current is required, then the explosive driven ferromagnetic generator would be the better choice here.

1.3 Explosive Power Sources

There are five basic types of explosive pulsed power systems. Of these, the one that is the most developed and that generates the highest electrical powers (kilowatts to gigawatts) and currents (kiloamperes to megaamperes) is the magnetic flux compression generator (FCG) [9]. These generators were first developed in the early 1950s. Likewise, the other types of explosive generators have also been investigated since the 1950s, but they have not

received the attention, until recently, dedicated to the FCG. A brief description of each major type of explosive pulsed power source is given in this section.

The operation of three of the generators (FCG, explosive magnetohydrodynamic generator (EMHDG) and moving magnet generator (MMG)) is based on a moving conducting medium interacting with a magnetic field or vice versa. The ferroelectric generator (FEG) and ferromagnetic generator (FMG) are based on phase transitions, i.e. polarised-to-depolarised and magnetised-to-demagnetised states respectively. A variant of the FCG that utilises both a phase transition and a moving conductor in a magnetic field is the semiconductor or solid state FCG, generally referred to as a Shock Wave Source (SWS). Unlike classical FCGs, where compression takes place in air or in a gas such as SF₆, the compression in the semiconductor generator takes place in a solid crystal, such as CsI, or a powder, such as oxidised aluminium. Shock pressures cause the dielectric to transition into a metallic state. The resulting moving conducting shock front takes the place of the metal armature in the conventional FCG. One potential advantage of this approach is that liner instabilities observed in classical FCGs may not occur. However, this optimism should be tempered with the knowledge that there has been little development of the SWS at the very high magnetic fields associated with conventional FCGs. Another variant of the FCG is the superconducting generator, which is also based on a phase transition. In this case, the transition is from a superconducting to a non-superconducting state, where this moving transition forms the armature of the generator.

In summary, there are two general classes of explosive pulsed power generators: *field interaction* generators, which include the FCG, EMHDG, and MMG, and *phase transition* generators, include the FEG and FMG.

1.3.1 Flux Compression Generators

There are several different types of FCGs, depending primarily on their geometrical shape — that is, the shape of their conducting components. In this introduction, attention is focused on the helical FCG (Fig. 1.2), which is further discussed in Chapter 6. The other types of FCG will be discussed in Chapter 5. Helical FCG consist of an outer coil or solenoid, called a *stator*, and an inner coaxial explosive-filled tube, known as a *liner* or *armature*. For an FCG to operate, a magnetic field must be present between the armature and stator. Thus, a seed source of energy is required, either in the form of a current source or an externally imposed magnetic

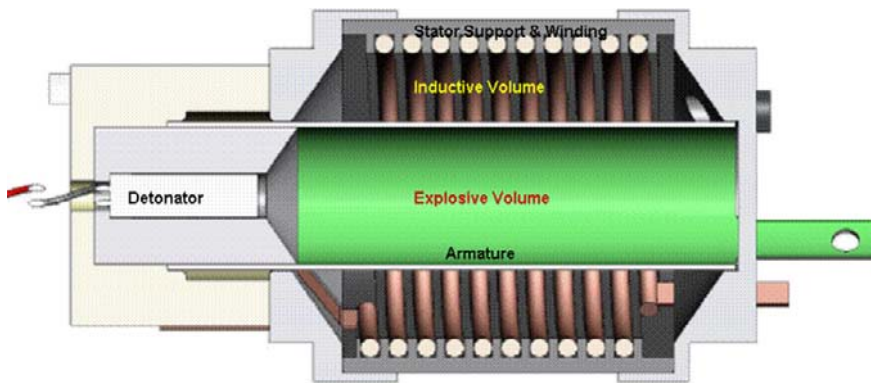


Fig. 1.2 Helical flux compression generator.

field. Given the appropriate conditions for the seed magnetic field, the high explosive in the armature is typically initiated at one end. The detonation releases chemical energy, which causes the armature to expand and form a propagating cone of conducting material that forces the magnetic field down the length of the generator by continually shorting turns of the stator, thus compressing the magnetic field. Initially, the expansion of the armature causes it to make contact with the input block of the FCG, which causes the armature and stator to short together, forming a magnetic flux trap within the annular region between the stator and armature and the FCGs associated load. The armature then propagates outwards along a *glide plane* that must support this shorting action without losing contact between the conductor connected to the stator and the armature. The term ‘glide plane’ is a misnomer in the sense that the armature does not glide along anything in its outward expansion. Rather, this is an input surface that is tapered appropriately to control the collision of the armature in such a way to avoid ‘tent pegging’ the input glide plane or tearing the armature. The explosive process converts the chemical energy of the explosive into the mechanical energy of the armature. In turn, the armature kinetic energy is converted into electrical energy, which is delivered to the load, by performing work against the magnetic field.

1.3.2 Explosive Magnetohydrodynamic Generators

The *explosive magnetohydrodynamic generator* (EMHDG) (Fig. 1.3) consists of an explosive charge, magnets, electrodes and output circuit. When

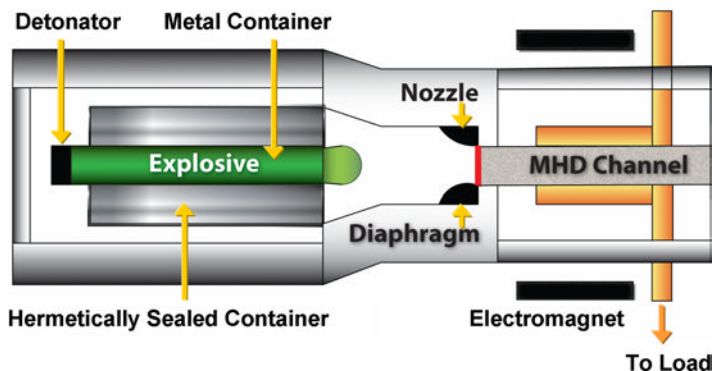


Fig. 1.3 Explosive driven magnetohydrodynamic generator.

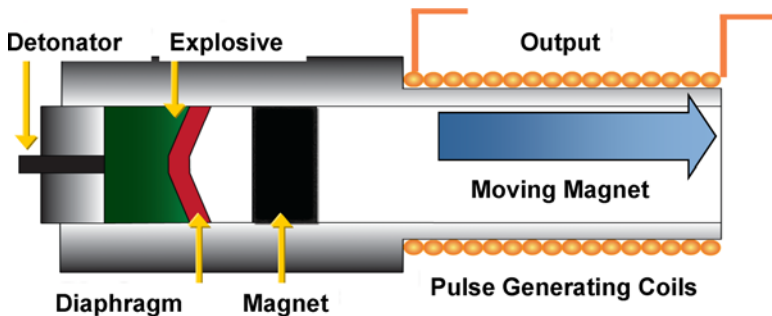


Fig. 1.4 Explosive driven moving magnet generator.

specially seeded explosives are detonated, the explosive products retain sufficient ionisation that their flow between electrodes, immersed in an external magnetic field, induces Hall currents. In other words, the magnetic field causes a charge separation in the plasma as it flows between the electrodes. Positive charge accumulates on one electrode and the negative charge on the other. The accumulated charge then flows through the output circuit to a load. Since these generators are thoroughly discussed in Refs. 1.10 and 1.11, they will not be further discussed in this book.

1.3.3 Moving Magnet Generators

The explosive driven version of the *moving magnet generator* (MMG) (Fig. 1.4) consists of an explosive charge, magnet, solenoid and output

circuit and is discussed in Chapter 13. When the explosive is detonated, the shock wave it produces propels the magnet through the solenoid. The changing magnetic flux inside the solenoid induces a current in the coil, which is delivered to a load. An alternative version of this generator is the so-called Pro-FLUX system. In this case, the coil is first energised, just as in the instance of a conventional helical FCG. The conducting projectile is then fired into the magnetic field, forcing it to perform work on the field. This, in turn, amplifies the initial current in the exterior coil.

1.3.4 Ferroelectric Generators

The *ferroelectric generator* (FEG) (Fig. 1.5) is also sometimes called a *piezoelectric generator* (PEG), though this is not entirely correct, since the ferroelectric process is a nonlinear process, while the piezoelectric process is a linear process. The difference between the two types of generator will be discussed in Chapters 9–12.

The FEG consists of an explosive charge, ferroelectric element, end plates and output circuit, and is discussed in Chapters 9–12. When the explosive is detonated, a shock wave is generated that propagates into the ferroelectric element. The shock wave depolarises the ferroelectric element and the charge that has accumulated on the polarised element's end plates is released to an output circuit and delivered to a load. Thus, the energy delivered to the load in this instance is strictly the energy that was initially stored within the polarised ferroelectric material.

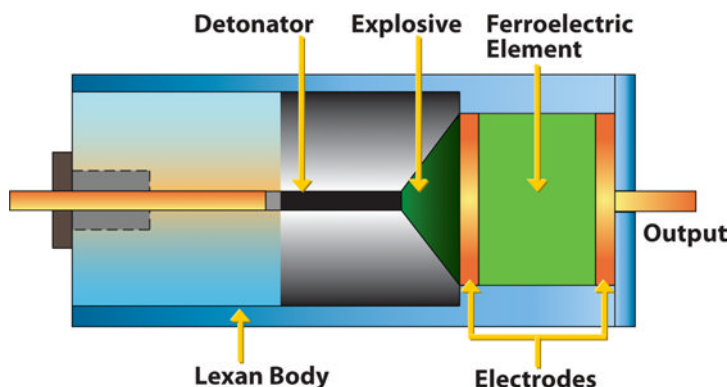


Fig. 1.5 Ferroelectric generator.

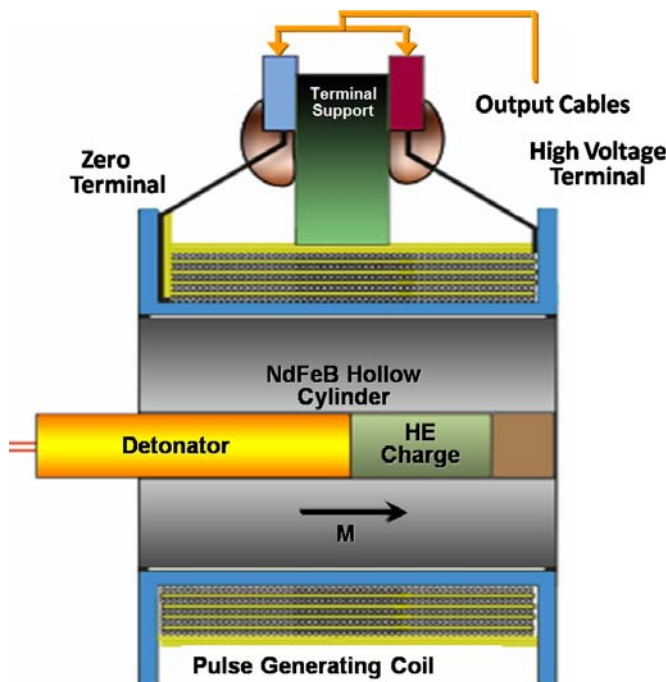


Fig. 1.6 Ferromagnetic Generator.

1.3.5 Ferromagnetic Generators

The *ferromagnetic generator* (FMG) (Fig. 1.6) consists of an explosive charge, a permanent magnet within a solenoid and output circuit, and is discussed in Chapters 7 and 8. When the explosive charge is detonated, a shock wave is generated that propagates into the magnet material. The shock wave demagnetises the permanent magnet material. This changing magnetic field within the coil induces a current in the solenoid coil, which is delivered to the load.

1.4 Book Outline

Explosive pulsed power generators have been around since the early 1950s. They have been used in a number of applications. For example, FCGs have been used to drive high-power lasers [12], high-energy density plasma systems, high-power microwave and ultra-wide band sources [13],

electromagnetic launchers [14], detonator arrays [15] and particle accelerators [16]. The FEG and FMG have been used as seed sources for FCGs and to charge capacitor banks. In this book, we will discuss the design, construction and testing of four of the five types of explosive generators along with some of their applications.

To make this a self-contained book, the basic principles of electromagnetic theory and electric circuits are presented in Chapter 2. Similarly, the basic principles of shock waves, high explosives, detonation trains and explosive interactions with materials are presented in Chapter 3. Since the operation of explosive pulsed power generators requires both mechanical and electrical measurements, methods for making detonic and electrical measurements will be presented in Chapter 4. As the electrical output parameters of explosive pulsed power sources are not usually electrically matched to those of the load, power conditioning is usually required. Since each type of generator has its own unique set of output characteristics, power conditioning for one will be discussed in their respective chapters. Flux compression generators are considered in Chapters 5 and 6. In Chapter 5, all the known versions of FCGs are discussed, while Chapter 6 focuses on one specific type of generator — i.e. the helical FCG, since it is the most widely used of all the FCGs. In Chapter 7, an introduction to magnetic circuits is presented, followed by a detailed discussion of FMGs in Chapter 8. Even though ferroelectric generators have been around since the mid-1950s, not much is known about them outside of a small community of specialists. Therefore, four chapters are devoted to FEGs. Chapter 9 is an introduction to ferroelectric materials, Chapter 10 looks at the phase transitions that occur in ferroelectric materials, Chapter 11 provides a historical review of shock studies involving ferroelectric materials, and Chapter 12 is an in-depth look at FEGs. Chapter 13 is devoted to MMGs. Finally, several examples of how explosive pulsed power generators were used with specific loads are presented in Chapter 14.

Bibliography

- [1] S. T. Pai and Q. Zhang, *High Power Pulse Technology*, World Scientific Publishing Co., Singapore (1995).
- [2] P. W. Smith, *Transient Electronics: Pulsed Circuit Technology*, John Wiley & Sons, LTD., Chichester (2002).
- [3] H. Bluhm, *Pulsed Power Systems: Principles and Applications*, Springer, Berlin (2006).

- [4] J. Benford and J. Swegle, *High Power Microwaves*, Artech House, Boston (1992).
- [5] R. B. Miller, *Introduction to the Physics of Intense Charged Particle Beams*, Plenum Press, New York (1982).
- [6] W. J. Sarjeant and R.E. Dollinger, *High-Power Electronics*, TAB Books, Inc. Blue Ridge Summit, PA (1989).
- [7] C. M. Fowler, W. B. Garn and R. S. Caird, Production of Very High Magnetic Fields by Implosion, *Journal of Applied Physics* **31** (1960) 88–594.
- [8] V. K. Chernyshev, V. D. Selemir and L. N. Plyashhevich (eds.), *Megagauss and Megaampere Pulse Technology and Applications*, Sarov, VNIIEF (1997).
- [9] L. L. Altgilbers, M. D. J. Brown, I. Grishnaev, B. M. Novac, I. R. Smith, I. Tkach and Y. Tkach, *Magnetocumulative Generators*, Springer-Verlag, New York (2000).
- [10] Eh. I. Asinovskij, V. A. Zejgarnik and E. F. Lebedev, *Pulse Magnetohydrodynamic (MHD) Converters of Chemical Energy into Electrical Energy*, Nauka, Moscow (1997).
- [11] V. E. Fortov (ed.), *Explosive Generators of Powerful Pulses of an Electrical Current*, Nauka, Moscow (2002).
- [12] A. I. Pavlovskii, R. Z. Lyudaev, V. N. Plyashkevich, N. B. Romanenko, G. M. Spirov and L. B. Sukhanov, MCG applications for powered channeling neodim laser, *Megagauss Magnetic Field Generation and Pulsed Power Applications*, eds. M. Cowan and R. B. Spielman (Nova Science Publishers, Inc., 1994), pp. 969–976.
- [13] A. B. Prishchepenko and V. P. Zhitnikov, Microwave Ammunitions: SUUM CUIQUE, *Proceedings of AMREM 96*, Albuquerque (1996).
- [14] G. A. Shvetsov, Yu. L. Bashkatov, A. G. Anisov and I. A. Stadnichenko, Flux Compression Generators for Railguns, *Proceedings of the 8th IEEE International Pulsed Power* (1991), pp. 465–471.
- [15] X. Cong, M. Cai, Y. Chen, S. Zhong and C. Sun, A Compact Magnetic Flux Compression Generator Driven by Explosives, *Megagauss Technology and Pulsed Power Applications*, eds. C. M. Fowler, R. S. Caird and D. J. Erickson (Plenum Press, New York, 1987), pp. 417–424.
- [16] B. L. Freeman, D. J. Erickson, C. M. Fowler, R. F. Hoeberling, J. C. King, P. J. Kruse, A. L. Peratt, D. G. Nickel, L. E. Thode, J. W. Toeva and A. H. Williams, Magnetic Flux Compression Generator Power Electron Beam Experiments, *Megagauss Technology and Pulsed Power Applications*, eds. C. M. Fowler, R. S. Caird and D. J. Erickson (Plenum Press, New York, 1987), pp. 729–737.

Chapter 2

Fundamentals of Electromagnetic Theory and Electric Circuits

2.1 Introduction

Since explosive driven generators are designed to generate very high magnetic and/or electric fields or very high electric currents and/or voltages, it is essential that the relationship between electric and magnetic fields and/or forces, as well as such phenomena as magnetic diffusion and electrical breakdown, be understood. Therefore, in this chapter a brief introduction to electromagnetic theory is presented. This will not be an extensive review, but rather an introduction to those electromagnetic phenomena that are important to explosive driven pulsed power sources.

2.2 Maxwell's Equations

In order to understand the relationship between electric fields and magnetic fields, consider Maxwell's equations [1]:

$$\nabla \times \mathbf{H} = \mathbf{j} + \frac{\partial \mathbf{D}}{\partial t} \quad (2.1)$$

$$\nabla \times \mathbf{E} = -\frac{\partial \mathbf{B}}{\partial t} \quad (2.2)$$

$$\nabla \cdot \mathbf{B} = 0 \quad (2.3)$$

$$\nabla \cdot \mathbf{D} = \rho_e, \quad (2.4)$$

where \mathbf{H} is the *magnetic field strength* or *magnetic intensity* (A/m), \mathbf{j} is the *free current density* (A/m^2), \mathbf{D} is the *electric flux density* or *electric displacement* ($\text{coulombs}/\text{m}^2$), \mathbf{E} is the *electric field strength* or *electric intensity* (V/m), \mathbf{B} is the *magnetic flux density* or *magnetic induction* (Webers/m^2)

and ρ_e is the *density of free electric charges* (coulombs/m³). The constitutive relations that specify the properties of materials (or free space) must also be specified. In isotropic media, these are:

$$\mathbf{B} = \mu \mathbf{H} \quad (2.5)$$

$$\mathbf{D} = \epsilon \mathbf{E} \quad (2.6)$$

in which $\mu = \mu_0 \mu_R$ is the *magnetic permeability* with $\mu_0 = 4\pi \times 10^{-7}$ H/m and $\epsilon = \epsilon_0 \cdot \epsilon_R$ is the *dielectric constant* with $\epsilon_0 = 8.854 \times 10^{-12}$ F/m. The relative quantities μ_R and ϵ_R can be complicated functions of space, time, material properties and field variables. An additional constitutive relation is *Ohm's law*:

$$\mathbf{j} = \sigma \mathbf{E}, \quad (2.7)$$

in which the *conductivity*, σ , is a material coefficient that is a complicated function of temperature and magnetic field. The *constitutive parameters* (ϵ, μ, σ) are used to characterise the electrical properties of a material. In general, materials are described as being dielectrics (insulators), magnetics or conductors depending on whether polarisation, magnetisation or conduction, respectively, is the predominant response to electromagnetic stimuli.

Throughout this chapter, it is assumed that the magnetic fields are *quasistationary* so that the displacement term $\partial \mathbf{D} / \partial t$ can be neglected in Eq. (2.1). In *free space*, where $\mathbf{j} = \mathbf{0}$, the magnetic field varies with time, but is independent of position. Therefore, the quasistationary field approximation is valid if $\lambda \gg l$, where λ is the characteristic wavelength of any field variation and l is the characteristic length of a magnetic coil or other spatial configuration under consideration. In *conducting media*, the quasistationary field approximation is valid if $1/\omega \gg \epsilon/\sigma$, where ω is the frequency at which the magnetic field varies. For good conductors such as metals, this condition is valid up to frequencies far in excess of those encountered in the operation of FCGs, MMGs and FEGs [2].

The integral form of Maxwell's equations describes the relationship between field vectors, charge densities and current densities over extended regions of space. They are usually used to solve boundary-value problems that possess complete symmetry. However, the fields and their derivatives do not need to be continuous functions. Applying *Stoke's theorem*:

$$\int_s (\nabla \times \mathbf{H}) \cdot d\mathbf{s} = \oint_C \mathbf{H} \cdot d\mathbf{l} \quad (2.8)$$

to an open surface s bounded by a closed curve C , yields *Ampere's Law* (which states that the line integral of the magnetic field over a closed path

is equal to the current enclosed):

$$\oint_C \mathbf{H} \cdot d\mathbf{l} = I_s, \quad (2.9)$$

where $I_s = \int \mathbf{j} \cdot d\mathbf{S}$ is the total current flowing through S. In a similar manner, *Faraday's law* (which states that the electromotive force (EMF) or electric field appearing at the open-circuited terminals of a loop is equal to the time rate-of-change of the magnetic flux linking the loop) can be derived:

$$\oint_C \mathbf{E} \cdot d\mathbf{l} = - \int_S \frac{\partial \mathbf{B}}{\partial t} \cdot d\mathbf{s} = - \frac{d}{dt} \int_S \mathbf{B} \cdot d\mathbf{s}. \quad (2.10)$$

The magnetic induction can also be expressed in terms of the number of magnetic lines of force that pass through a given surface, which is called the *magnetic flux*, Φ ($T \cdot m^2$ or Webers), and is defined by:

$$\Phi = \oint \mathbf{B} \cdot d\mathbf{s}. \quad (2.11)$$

When $\Phi = 0$, this expression is known as *Gauss's Law*, which asserts that the magnetic flux through any closed Gaussian surface must be zero.

The power density of electromagnetic waves is given by:

$$\mathbf{S} = \mathbf{E} \times \mathbf{H}^*, \quad (2.12)$$

where \mathbf{S} (W/m^2) is the Poynting vector and \mathbf{H}^* is the complex magnetic field. The equation governing the time-domain Poynting vector can be derived by subtracting the dot product of Eq. (2.1) with \mathbf{E} from the dot product of Eq. (2.2) with \mathbf{H} . Using the vector identity:

$$\mathbf{H} \cdot \nabla \times \mathbf{E} - \mathbf{E} \cdot \nabla \times \mathbf{H} = \nabla \cdot (\mathbf{E} \times \mathbf{H}), \quad (2.13)$$

it can be shown that:

$$\nabla \cdot (\mathbf{E} \times \mathbf{H}) = -\mathbf{H} \cdot \frac{\partial \mathbf{B}}{\partial t} - \mathbf{E} \cdot \frac{\partial \mathbf{D}}{\partial t} - \mathbf{J} \cdot \mathbf{E}. \quad (2.14)$$

Assuming that $\mathbf{J} = 0$ and using the constitutive relations of Eqs. (2.5) and (2.6), Eq. (2.14) can be rewritten as:

$$\nabla \cdot (\mathbf{E} \times \mathbf{H}) = -\frac{\partial}{\partial t} \left(\frac{B^2}{2\mu} \right) - \frac{\partial}{\partial t} \left(\frac{\epsilon E^2}{2} \right). \quad (2.15)$$

The quantity in the first set of parenthesis is the energy stored in the magnetic field and the quantity in the second set is the energy stored in the electric field.

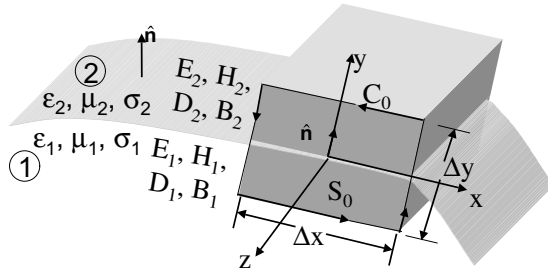


Fig. 2.1 Geometry for boundary conditions of (a) tangential and (b) normal components of electric and magnetic fields.

In general, most problems of interest involve free space with conducting boundaries. The electromagnetic equations apply in both regions — i.e. free space and the conductor, and they are coupled by their *boundary conditions*. Identifying the two media as 1 and 2, and assuming the conductor has finite conductivity (Fig. 2.1), Maxwell's equations can be used to derive the following boundary conditions [1]:

- The tangential component of the electric field is continuous across an interface between two media, provided there are no impressed magnetic current densities on the interface:

$$\hat{n} \times (\mathbf{E}_2 - \mathbf{E}_1) = 0, \quad (2.16)$$

where \hat{n} is a unit vector normal to the interface between the two media.

- The tangential component of the magnetic field across an interface is discontinuous by an amount equal to the electric current density, \mathbf{j} (A/m^2), flowing on the surface:

$$\hat{n} \times (\mathbf{H}_2 - \mathbf{H}_1) = \mathbf{j}. \quad (2.17)$$

Clearly, the tangential component of \mathbf{H} is continuous at the interface if $\mathbf{j} = \mathbf{0}$.

- The normal components of both the electric flux density and the electric field at an interface on which a surface charge density resides are discontinuous by an amount equal to the surface charge density:

$$\hat{n} \cdot (\mathbf{D}_2 - \mathbf{D}_1) = \rho_e, \quad (2.18)$$

$$\hat{n} \cdot (\mathbf{E}_2 - \mathbf{E}_1) = \rho_e. \quad (2.19)$$

When $\rho_e = 0$, these fields are continuous at the interface.

- The normal components of the electric field intensity across an interface are discontinuous:

$$\hat{n} \cdot (\varepsilon_2 \mathbf{E}_2 - \varepsilon_1 \mathbf{E}_1) = 0. \quad (2.20)$$

- The normal components of the magnetic flux density across an interface between two media where there are no sources are continuous:

$$\hat{n} \cdot (\mathbf{B}_2 - \mathbf{B}_1) = 0. \quad (2.21)$$

- The normal components of the magnetic field intensity across an interface are discontinuous:

$$\hat{n} \cdot (\mu_2 \mathbf{H}_2 - \mu_1 \mathbf{H}_1) = 0. \quad (2.22)$$

2.3 Circuit Elements and Equations

The basic components of most explosive pulsed power circuits include resistors, capacitors, inductors, transformers, switches, transmission lines and the load. These devices are categorised as *passive elements*, which are devices that cannot supply an average power that is greater than zero over an infinite time interval [3]. The resistor usually transforms the energy it receives into heat, while the inductor and capacitor are energy storage devices. Circuits also contain *active elements*, which are devices capable of providing an average power that is greater than zero over an infinite time interval to an external device [1]. Examples of active elements include batteries and generators in traditional circuits and FCGs, FEGs, FMGs, MMGs and EMHDGs in explosive pulsed power circuits.

2.3.1 Circuit Elements

2.3.1.1 Resistors

The resistor is the simplest passive device and is governed by Ohm's law, which states that the voltage across many types of conducting materials is directly proportionate to the current flowing through the material, $V = IR$, where the proportionality constant, R , is called the resistance and has units of ohms ($\Omega = \text{volts/amps} = \text{V/A}$). When the voltage is plotted against current, the plot is usually a straight line passing through the origin and the resistor is said to be linear. When the plot is not straight, it is said to be

nonlinear. Examples of devices with a nonlinear resistance are zener diodes, tunnel diodes and fuses. The ratio of current-to-voltage is also typically a constant and is called the *conductance*, $G = I/V$, and its units are mhos (A/V). The power dissipated in resistors is $P = IV = I^2R = V^2/R$ and has units of watts (W). Resistance can be used to define two commonly used terms: *short circuit* and *open circuit*. A short circuit is where the resistance is zero ohms, which means the voltage across a short circuit must be zero, although the current may have any value. An open circuit is where the resistance is infinite, which means that the current across the open circuit is zero, regardless of what the voltage is across it.

2.3.1.2 Inductors

Inductors are passive devices that are capable of storing and delivering finite amounts of energy. They store energy in magnetic fields. It was found empirically that the voltage induced across an inductor is proportional to the rate of change of the current that produces the magnetic field: $V = LdI/dt$, where L is the symbol for inductance and has units of Henrys (H). This definition for inductance is valid only if L is constant, which is not the case for FCGs. When the inductance varies in time, the voltage expression becomes $V = d(LI)/dt = LdI/dt + IdL/dt$. In the case of the FCG, the second term on the right-hand side of this equation denotes its time varying inductance. Since the voltage induced across an inductor depends on the rate of change of the current or of the inductance, the inductor appears to be a short circuit to direct current (DC). The power stored by an inductor is $P = IV = LI dI/dt$. Integrating over time, the energy stored in an inductor is $LI^2/2$ in joules (J). In summary, some characteristics of inductors are [3]:

- There is no voltage across an inductor if the current flowing through it does not change in time.
- A finite amount of energy can be stored in an inductor even if the voltage across it is zero, such as when the current flowing through it is constant.
- It is impossible to change the current through an inductor by a finite amount in zero time — i.e. an inductor resists an abrupt change in the current, which implies the charging process will have a finite rise time and the discharging process will have a finite fall time.
- Ideal conductors never dissipate energy, they only store it. This is, of course, not true of real inductors that have an inherent resistance.

2.3.1.3 Capacitors

Like inductors, capacitors are passive devices capable of storing and delivering finite amounts of energy. Capacitors store energy in electric fields. Capacitance was empirically found to be the ratio of the electric charge, Q , in coulombs, stored in the capacitor to the voltage across it, $C = Q/V$, and has units of farads (F). Alternatively, the voltage-current relationships are $I = CdV/dt$ or $V = (1/C) \int Idt$. The power stored in a capacitor is $P = IV = CVdV/dt$ and, integrating over time, the energy is $CV^2/2$. Some important characteristics of capacitors are [3]:

- The current through a capacitor is zero if the voltage across it does not change in time, which means that a capacitor appears to be an open circuit to DC.
- A finite amount of energy can be stored in a capacitor even if the current flowing through it is zero, such as when the voltage across it is constant.
- It is impossible to change the voltage across a capacitor by a finite amount in zero time, which means it will have a finite rise time when charging and fall time when discharging.
- Ideal capacitors never dissipate energy; they only store it. This is, of course, not true of real capacitors.

2.3.1.4 Transformers

Transformers are networks containing two or more coils that are magnetically coupled. In the transformer shown in Fig. 2.2, the inductor L_1 is called the *primary* and the inductor L_2 is called the *secondary* of the transformer. There are two inductances associated with the transformer: *self inductance* and *mutual inductance*. The self inductance is just the normal inductance of each separate coil and is defined by LdI/dt . The physical basis for the

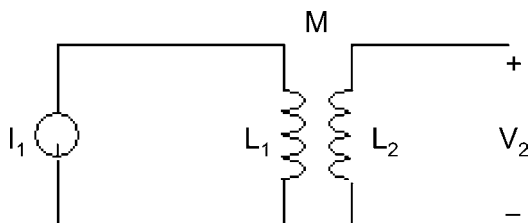


Fig. 2.2 Circuit with a transformer.

voltage-current characteristics of inductors depends on (1) the production of a magnetic flux by a current, where the flux is proportional to the current, and (2) the production of a voltage by a time varying magnetic field, where the voltage is proportional to the time rate of change of the magnetic field. Therefore, it can be concluded that the voltage is proportional to the time rate of change of the current. Mutual inductance results from an extension of this same argument. A current flowing in one coil establishes a magnetic flux about that coil and also about a second coil in the vicinity of the first. The time varying flux surrounding the second coil induces a voltage across the terminals of the second coil, which is proportional to the time rate of change of the current flowing in the first coil. Considering the simple model in Fig. 2.2, the current $I_1(t)$ flowing through L_1 establishes a voltage $V_2(t)$ across the terminals of L_2 . The mutual inductance can now be defined by the relationship $V_2(t) = M_{21}dI_1(t)/dt$, where the order of the subscripts on M_{21} indicates that a voltage response is induced in L_2 by a current in L_1 . If the system in Fig. 2.2 is reversed, the voltage induced in L_1 by a current in L_2 is $V_1(t) = M_{12}dI_2(t)/dt$. It can be shown by using the energy relationships that $M_{12} = M_{21} = M$. The voltage due to the mutual inductance is independent of and in addition to any voltage due to self inductance, which means that the voltage across each coil is the sum of its self and mutual inductances — i.e. $V_1 = L_1dI_1/dt + MdI_2/dt$ and $V_2 = L_2dI_2/dt + MdI_1/dt$. There is an upper limit on the magnitude of the mutual inductance. It can be no greater than the geometric mean of the self inductances of the two coils, between which the mutual inductance exists, and is defined by the *coupling coefficient* k , where $k = M/\sqrt{L_1L_2}$ and has a value of $0 \leq k \leq 1$. The value of the coupling coefficient can be increased by locating the coils physically closer, winding or orienting them to provide a larger common magnetic flux, or providing a common path through a material that serves to concentrate and localise the magnetic flux.

Transformers tend to have a magnetic core to provide flux linkage between the primary and secondary windings, particularly when the windings are separated on the core, and to raise the inductance of the primary winding to reduce the magnetising current. Unlike common iron or ferrite transformers in which the core materials are used to channel the magnetic flux through the winding to assure flux linkage, the *air-core transformer* strongly depends on the physical proximity of all the turns of one winding with respect to all the turns of the other. Consequently, their coupling coefficients are lower than that of magnetic core transformers, particularly with respect to high gain transformers that have thick windings. However,

because air core transformers do not have magnetic cores, their current carrying capacity is not limited by saturation of the magnetic core materials or frequency limited by composition of the core. Therefore, air core pulse transformers [4] are typically used in applications involving very high peak powers (up to 100 GW), high currents (MA) and/or ultra-high radio frequencies (RF) (MHz).

There are two basic types of high voltage — i.e. megavolt, air core pulse transformers: single-layer helical wound transformers and spiral strip transformers. They differ from each other in the configuration of their secondary windings, which accounts for a significant difference in their resistance to insulation failure from fast pulses. Primary windings of either type, which can either be single or multiple turn, may be designed in a variety of ways without affecting the electrical breakdown characteristics of the transformer. To achieve high voltage isolation, the low-voltage primary winding is typically placed outside the secondary in either type of transformer so that the high-voltage output of the secondary can be let out through the centre of the assembly. In order to provide high voltage standoff between the primary and secondary windings, insulation is installed in the space between the windings. This space can be uniform or tapered in the longitudinal direction. When tapered, the insulation thickness increases with the voltage along the length of the coils. In spiral-strip transformers, voltage standoff is largely a function of the radial thickness of the secondary winding because the turns directly overlay each other. The winding stack has a pure radial voltage gradient between the high-voltage inner turns and the low-voltage outer turns. In both cases, the insulation is usually oil. Both transformers have two common problems: electrical breakdown between the windings and partial shorting caused by eddy currents induced in the structural components.

There are several different uses for pulse transformers in electronic circuits, including voltage or current step-up or step-down, impedance matching, DC isolation, pulse polarity inversion and pulse differentiation.

2.3.1.5 *Switches*

Pulsed power systems often require the use of switches and, in many cases, these switches must be capable of handling terawatts of power and of having jitter times of nanoseconds [5]. The switch is the second most important component in a pulsed power system, with the explosive generator being the most important component, since they connect the generator to the load

and play a key role in controlling the rise time, shape and amplitude of the pulse produced by the generator. Over the years, two types of high power switches have been developed: closing and opening switches. The type of switch used will depend on which type of pulsed power system was selected for a particular application. In some applications, both types of switch are needed.

An example of how *closing switches* are used is presented in Fig. 2.3. As the capacitive store, C , is being charged, the closing switch S_C remains open. When this switch is closed, the capacitive store delivers its energy to the load Z . The energy transfer efficiency depends on the characteristics of the load, the circuit parameters and the properties of the switch itself. In practice, the energy transfer efficiency is no higher than 80%. Examples of closing switches include self-breaking and triggered spark gap, thyatron, triggered pseudospark, photoconductive semiconductor and magnetic switches.

An example of how *opening switches* are used is presented in Fig. 2.4. In this case, the energy stored in the capacitive store is temporarily transferred to an inductive store L . During this transfer operation, the opening switch S_O is kept closed and the switch S_C is kept open. When the current through the inductive store reaches a desired value, the initially closed switch S_O opens and the initially opened switch S_C closes, transferring

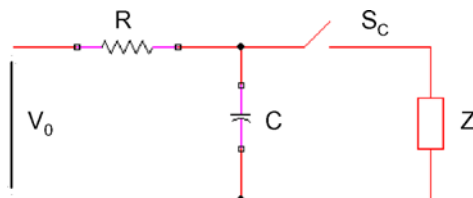


Fig. 2.3 Circuit with closing switch S_C .

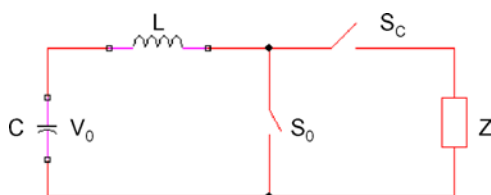


Fig. 2.4 Circuit with opening switch S_O .

some of the inductively stored energy to the load. In this case, the maximum energy transfer efficiency is less than the ideal efficiency of 25%, which is significantly less than that achieved with a capacitive store. The advantage of inductive stores with opening switches is that they can deliver significantly higher energy densities than can capacitive stores. Examples of opening switches include exploding wire and foil, plasma erosion opening and plasmodynamic switches.

The process of closing or opening switches can be achieved by either self-breakdown or external triggering. In either case, the basic principle of switching is the same — i.e. at the proper time, the properties of the closing switch medium (or opening switch medium) are changed from that of an insulator (or conductor) to that of a conductor (or insulator). The mediums used in switches include vacuum, gases, liquids, solids and plasmas. Since there is no universal formula or recipe for switches, each switch must be designed on an individual basis for each application in which it is to be used. However, there are certain parameters that are common to all switches including [5]:

- Hold-off voltage — the maximum static voltage that can be applied to the switch before electrical breakdown occurs between the main electrodes. If the switch is pulse charged, the pulsed hold-off voltage can be greater than the maximum static hold-off voltage. The magnitude of the pulsed hold-off voltage depends on the rise time of the applied voltage pulse.
- Voltage fall time — after breakdown is initiated, the fall time is the time interval during which the voltage drops from its hold-off value to that across the impedance of the switch during current flow through the switch.
- Recovery time — the time interval during which the voltage reverses its polarity.
- Trigger pulse — a fast external pulse used to initiate the switching process. This pulse can be in the form of a voltage, laser or particle beam pulse.
- Delay time — the time interval between the time the trigger pulse is at its peak value and the time at which the switch starts to close or open.
- Current rise time — the time interval required for the current to rise from 10 to 90% of its peak value.
- Current pulse width or length — the time duration of the full-width-half-maximum (FWHM) of the current pulse.

- Peak power — the maximum value of the product of the voltage and current, which occurs at the same time.
- Peak reverse voltage — the maximum value of the reverse voltage.
- Peak reverse current — the maximum value of the reverse current.
- Energy transferred — the time integral of the product of the voltage and current.
- Recharge time — the time interval between the end of the recovery time and the time at which the voltage recovers to its hold-off value.
- Life time — the total number of normal switching operations beyond which the switch no longer functions properly.
- Reliability — the ratio of the number of successful operations of the switch to the total number of operations within the life time of the switch.

The hold-off voltage of switches ranges from several hundred volts to a few tens of kilovolts in the case of semiconductor switches and from several tens of kilovolts to several megavolts in the case of spark gap switches. Peak currents delivered by switches range from a few tens of amps to a few kiloamps for vacuum tube switches and from a few kiloamps to a few megamps for spark gap switches. Of the various switches available, the most commonly used in explosive pulsed power are the spark gap closing switch and the exploding wire or foil opening switch. Both switches are relatively simple to design and build, robust, and well studied. The main difficulty with the opening switch is that as much as 50% of the energy from the power source is dissipated in the switch. However, there are explosively driven opening switches, such as the explosively formed fuse (EFF), that may offer some advantages over currently used fuses. The EFF has interrupted currents ranging from 19 to 25 MA, diverting the current to low inductance loads, and operated at powers up to 6 TW. For a more detailed discussion of switches, see references [5–7].

2.3.1.6 *Transmission Lines*

A *transmission line* consists of any two conductors between which a voltage can be applied and which can transmit an electric current. In most cases, there is no clear-cut distinction between a transmission line and an electric circuit. Whether two conductors should be treated as a transmission line or as an electric circuit depends on two factors: the length of the conductors and the wavelength of the applied voltage. If the wavelength is very long

compared to the length of the conductors, it is considered to be an electric circuit, otherwise, it is regarded as a transmission line.

In pulsed power systems, the transmission line serves several important functions including [5]:

- Pulse sharpening — i.e. producing very fast rise time pulses with a pulse length determined by the length of the line.
- Transmission of a large amount of power — i.e. transmit simultaneously high currents and voltages with high fidelity and fixed propagation time to a load tens of metres away.
- Pulse shaping — i.e. with proper switching, reshape an incoming pulse to form a pulse with a desired shape, such as one with a flat top. When used in this role, the transmission line is referred to as a *pulse forming line* (PFL).
- Intermediate energy storage — i.e. temporarily store the incoming energy from a main energy store, such as a Marx generator, inductive store or explosive pulsed power generator. When used in this role, the intermediate storage line is usually placed between the main energy storage devices and an PFL.

In addition to classifying transmission lines according to their function, they can also be classified according to their basic structure, including:

- Simple transmission lines.
- Double transmission lines (Blumlein lines).
- Multiple (or stacked) transmission lines.
- Magnetically insulated transmission lines (MITL).

Simple transmission lines have the advantage of being simple to construct and operate, but the disadvantage of only supplying half the charging voltage to the load. To deliver higher voltages to the load, the other types of transmission lines are more appropriate. The Blumlein consists of two simple transmission lines that are charged in parallel and discharged in series and with the proper termination can deliver an output voltage nearly as high as the charging voltage. The stacked transmission line, with proper switching and termination, can deliver considerably higher voltages or currents than the other types of transmission lines. If high voltage is desired, the individual lines are stacked together in series discharge configuration and, if high current is desired, they are stacked in parallel discharge configuration. The MITL works on an entirely different principle to the other

transmission lines. It utilises a magnetic field to inhibit the electrons in the transmitted current from reaching the other conductor in the transmission line. This is a good insulation technique that permits the construction of very compact transmission lines that are capable of transmitting very high powers.

Finally, transmission lines can be classified according to their geometric configuration, including:

- Coaxial (cylindrical).
- Parallel cylindrical.
- Strip.
- Helical.
- Tapered.

For more detailed information on transmission lines, see Refs. [5] and [8].

2.3.1.7 *Insulation*

One of the essential components in high voltage systems is electrical insulation. Without proper insulation, high voltages cannot be maintained due to electrical breakdown. According to [5], insulators are dielectric materials that provide high resistance to the passage of electric current. In general, good insulators should have a resistivity no less than $10^{10} \Omega \cdot \text{cm}$. Some examples of common insulating materials are given in Table 2.1. As noted in [3], solids tend to have a higher resistivity than liquids, but liquids and gases are used in most high voltage devices, since these materials can recover after electrical breakdown and solids are irreparably damaged. In addition, the *breakdown field strength* or *dielectric strength*, which is defined to be the

Table 2.1 Room temperature dielectric constants for some common insulators [3].

Material	Dielectric Constant	Material	Dielectric Constant
Air (1 atm)	1.00053	Glass	4.5–10
N ₂ (1 atm)	1.0005	Mica	3–7
SF ₆ (1 atm)	1.002	Mylar	2.8
Water	80.4	Teflon	2.8
Castor Oil	4.5	Polyvinyl Chloride	3.0–3.5
Transformer Oil	2.2–2.5	Polyethylene	2.5–2.6
Glycerin	44.0	Silicon Oil	2.5

maximum electric field that an insulator can withstand without breakdown of gas and liquid insulators is described by certain known relationships such as

$$E_B t^{1/3} A^{1/10} = k, \quad (2.23)$$

where E_B is the breakdown field strength in MV/cm, t is time in μ s, A is the cross-sectional area of the electrodes in cm^2 and k is a constant associated with a given parallel plate electrode configuration. Examination of this equation reveals that although the dielectric strength of a given insulator material is an intrinsic property of the material itself, its magnitude is influenced by external factors such as charging time and electrode geometry. For example, if a system is charged fast enough, significantly higher dielectric strengths can be achieved, and if materials with higher dielectric strengths are used, the stored energy density, of capacitors for example, can be increased, thus permitting the volume of the system to be made smaller.

In addition to resistivity and dielectric strength, another important property of insulating materials is its *dielectric constant*, ϵ . The dielectric constants of some common insulators are presented in Table 2.1. The dielectric strength of a material influences how it may be used. For example, if high energy density is required, then an insulating material with high dielectric constant should be used, since the energy density is directly proportional to the dielectric constant. On the other hand, if high energy transfer rate is required, then an insulator with a lower dielectric constant should be used, since the speed of electromagnetic waves is inversely proportional to the square root of the dielectric constant.

Since high voltage systems tend to operate under severe conditions, other properties such as thermal and mechanical properties must also be taken into account. For example, in FCGs there are high pressures generated by magnetic and mechanical forces, and high temperatures arising from the detonation of high explosives. These can lead to fracturing, softening, deformation, ablation, grazing and/or current tracking [5].

2.3.2 Circuit Equations

There are two methods for solving circuit problems. First is the *lumped element network* method, where it is assumed that the electrical conductors have zero resistance, inductance and capacitance or that they are lumped together as an added circuit element. The other method is the *distributed element network*, where it is assumed that the electrical conductors consist

of an infinite number of vanishingly small resistive, capacitive and inductive elements. Both methods are used in solving explosive pulsed power circuits.

In either case, Kirchhoff's current and voltage laws are used to solve these circuits. *Kirchhoff's current law* states that the algebraic sum of all currents entering any node is zero. *Kirchhoff's voltage law* states that the algebraic sum of the voltages around any closed path in a circuit is zero. As an example of a lumped circuit, consider the LCR circuit with two loops shown in Fig. 2.5. Applying Kirchhoff's current law to node A and applying Kirchhoff's voltage law to the two loops in the circuit, the following set of differential equations is obtained:

$$\begin{aligned} I_1 + I_2 &= I \\ R_1 I_1 + \frac{Q(t)}{C} - V(t) &= 0 \\ L \frac{di_2}{dt} + R_2 I_2 - \frac{Q}{C} &= 0, \end{aligned} \quad (2.24)$$

where $Q(t)$ is electric charge stored in the capacitor and the resistance, inductance, and capacitance are assumed to be constants.

As an example of a distributed element network, consider the simple transmission line in Fig. 2.6. Since passive circuits consist only of resistive, capacitive and inductive elements, the equivalent circuit equation for a transmission line will only contain these elements. Considering the two very long parallel conductors suspended in air in Fig. 2.6(a) and assuming that the wavelength of the applied voltage is shorter than the total length of the line, the equivalent circuit diagram of this transmission line can be drawn as shown in Fig. 2.6(b). In this circuit, R is the series resistance per unit length of conductor in ohms per unit length, L is the series inductance in henries per unit length, R_i is the shunt resistance in ohms per unit

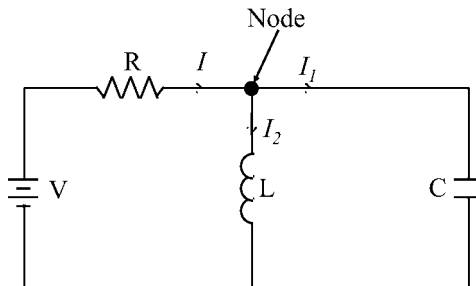


Fig. 2.5 Circuit diagram of an *LCR* circuit with two loops.

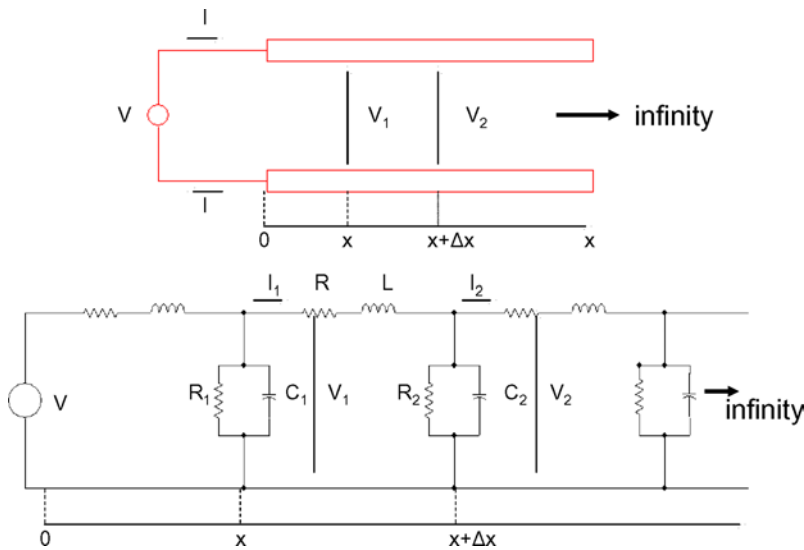


Fig. 2.6 (a) Two long conductors of a transmission line suspended in air and (b) equivalent circuit diagram of this transmission line.

length, C_i is the shunt capacitance in farads per unit length and Δz is an increment of length. Applying Kirchhoff's law around the loop abcd, the circuit equations for this transmission line are:

$$\begin{aligned} V_1 &= R\Delta z I_1 + L\Delta z \frac{\partial I_1}{\partial t} + V_2 \\ I_1 &= I_2 + G\Delta z V_2 + C\Delta z \frac{\partial V_2}{\partial t} \end{aligned} \quad (2.25)$$

where G is the conductance in mhos per unit length and is equal to the reciprocal of a R_i . It should be noted that in transmission line theory, R represents the imperfection of the conductor and G the imperfection of the insulator. When solid insulation is used at very high frequencies, the dielectric loss may be considerable. This has the same effect on the line as true ohmic leakage and is a major contribution to G at these frequencies. Rearranging these equations and letting $\Delta z \rightarrow 0$, the general differential equations for a transmission line are:

$$\begin{aligned} \frac{\partial V}{\partial z} &= -RI - L \frac{\partial I}{\partial t} \\ \frac{\partial I}{\partial z} &= -GV - C \frac{\partial V}{\partial t}. \end{aligned} \quad (2.26)$$

For uniform transmission lines, R , L , C and G are constants, although in practice, the functional forms of these parameters are seldom known. The voltage difference in Eq. (2.26) is caused by the current I flowing through the resistor R and the charging of the inductor L at a rate of dI/dt . The difference in current between the two ends of the transmission line is due to the current caused by the voltage acting on the shunt conductor G and the displacement current through the capacitor C caused by the voltage changing at a rate of dV/dt . These two equations, together with the boundary conditions, will, in principle, yield both steady-state and transient solutions.

2.3.3 Transient Circuits

Transient phenomena are defined to be all phenomena that cannot be classified as steady-state [9]. *Steady-State* phenomena are those phenomena in which there is a constant response to a constant forcing function — e.g. externally applied voltage or mechanical force, or a uniform periodic response to a uniform periodic forcing function. The generators described in this book do not provide a steady-state forcing function to their output circuit, so their circuits are classified as *transient circuits*.

Examples of transient forcing functions are pulses, exponentially increasing or decreasing voltages, damped voltages and spikes. There are three classes of transients. The first is *compound transients*, which occur in circuits containing more than one loop or that have some kind of coupling. The second is *switching transients*, which are associated with the establishment or interruption of the steady state or the switching of elements into or out of a circuit during the transient period. The third is *transient transients*, which occur in circuits in which the applied EMF is changed in any manner during the transient period. In *dissipative systems*, transients are exponentially damped and decrease in magnitude as the steady state is approached.

As an example, when a constant voltage V is applied across an inductor L and a resistor R , the self inductance of the inductor prevents the current from increasing from its initial value of zero to its ohmic or steady state value of V/R . When the voltage source is reduced or removed, the energy stored in the inductor, $LI^2/2$, is returned to the circuit. Again, the current must approach its steady state value of V/R . In both cases, the circuit is undergoing a transient change. The mathematical expression that describes this transient is $I = V(1 - e^{-Rt/L})/R$, where the transient behavior is

represented by the exponential term in the parenthesis. This expression indicates that steady state is only attained in an infinite amount of time. In practical circuits, the current reaches 90% of its steady state value in a few seconds or less. In the case of the circuits powered by explosive driven power supplies, transients usually last only microseconds, since the circuit is destroyed by the explosive charge.

Analysis of transient circuits normally requires solving differential equations. The two methods used to analytically solve these equations make use of either Fourier integrals and transforms or Laplace transforms. The Laplace transform has been found to be a more powerful tool, since it can be applied to a wider range of functions.

2.4 Electromagnetic Phenomena

2.4.1 Magnetic Diffusion

If a magnetic field is localised within a certain spatial domain, then, according to Maxwell's equations, the current that maintains this field must circulate on the boundaries of the domain. If the boundaries are ideal conductors, this current is concentrated in a thin surface layer and does not penetrate into the conductive material. If the conductor possesses a certain resistance, the charge carriers are scattered in the lattice and the thickness of the current layer increases with time. This current layer is called the *skin layer* and its thickness is known as the *skin depth* (Fig. 2.7).

To study the penetration of magnetic fields into *incompressible, electrically isotropic, conducting media*, Maxwell's equations and Ohm's law are used. Assuming the electrical conductivity is a material constant and independent of space and time, then $\sigma = \sigma_0$. Substituting Eqs. (2.9) and (2.10)

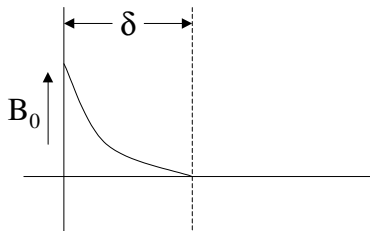


Fig. 2.7 The current layer on the surface of real conductors has a thickness called the skin depth. Skin depth depends on the conductivity of the conductor and the frequency of the pulsed field.

into the curl of Eq. (2.7) yields:

$$\nabla \times (\nabla \times \mathbf{H}) = \sigma_0 \nabla \times \mathbf{E} + \varepsilon \frac{\partial}{\partial t} (\nabla \times \mathbf{E}). \quad (2.27)$$

By using the identity:

$$\nabla \times \nabla \times \mathbf{A} = \nabla(\nabla \cdot \mathbf{A}) - \nabla^2 \mathbf{A} \quad (2.28)$$

and Eqs. (2.7) and (2.8), Eq. (2.27) is transformed into the *wave wave equation*:

$$\nabla^2 \mathbf{H} = \sigma_0 \frac{\partial \mathbf{B}}{\partial t} + \varepsilon \frac{\partial^2 \mathbf{B}}{\partial t^2}. \quad (2.29)$$

In a conducting medium, the displacement currents can be neglected in comparison with the conduction currents and the last term of Eq. (2.29) can be omitted. This reduces the wave equation to the *magnetic diffusion equation*:

$$\nabla^2 \mathbf{H} - \frac{1}{\kappa_0} \frac{\partial \mathbf{H}}{\partial t} = 0, \quad (2.30)$$

where $\kappa_0 = 1/\sigma_0 \mu$ is the *magnetic diffusivity*.

The diffusion of magnetic energy into incompressible conductors is accompanied by an inflow of energy that appears in the form of magnetic energy and Joule heat generated as a result of eddy currents. Complications arise if the conductivity σ is not constant, because the diffusion becomes nonlinear. If the conductor is a metal, there are even further complications such as melting of its surface layer and the formation of instabilities at the metal-field interface. An additional complication arises if the compressibility of the material is taken into account. In fact, compressibility of the conductor sets the most stringent limitations on the generation of ultra-high magnetic fields in FCGs [2]. Compression of the conductor by the magnetic pressure results in its inner layer moving at a lower velocity than would be the case if it were incompressible.

The depth of the skin layer in a conductor with constant electrical conductivity can be estimated by using the equation

$$\delta = \sqrt{\frac{2}{\omega \mu \sigma}} \quad (2.31)$$

where μ is the magnetic permeability and σ is the electrical conductivity of the conducting material and ω is the frequency of the pulsed field. The time

$$\tau_s = \frac{1}{2} \pi \mu \sigma \delta^2 \quad (2.32)$$

is that required for the magnetic field to penetrate to a depth equal to that of the skin layer and is called the *skin time*. Magnetic compression is accompanied by an increase in magnetic field strength and magnetic energy, provided the time interval during which the cavity compresses the magnetic field in an FCG is much less than τ_S .

2.4.2 Magnetic Force

A conductor carrying a current density \mathbf{j} in a magnetic field $\mathbf{B} = \mu\mathbf{H}$ experiences a force per unit volume called the *magnetic stress* :

$$\mathbf{F}_M = \mathbf{j} \times \mathbf{B}. \quad (2.33)$$

Neglecting the displacement term in Eq. (2.5) and substituting $\nabla \times H$ for j in the above equation yields:

$$\mathbf{F}_M = (\nabla \times \mathbf{H}) \times \mathbf{B} = \mu \left[(\mathbf{H} \cdot \nabla) \mathbf{H} - \frac{1}{2} \nabla H^2 \right]. \quad (2.34)$$

It can be shown that the magnetic force acting on a conductor carrying a current can be expressed in terms of the surface field alone [2].

Likewise, a conductor moving through a magnetic field experiences a similar force, which is the basic operating principle of the FCG. To illustrate this, consider Fig. 2.8. As the rectangular loop is pulled out of the magnetic field with velocity v , a force is exerted on the electrons. This is the *Lorentz force*:

$$\mathbf{F}' = q\mathbf{v}_d \times \mathbf{B}, \quad (2.35)$$

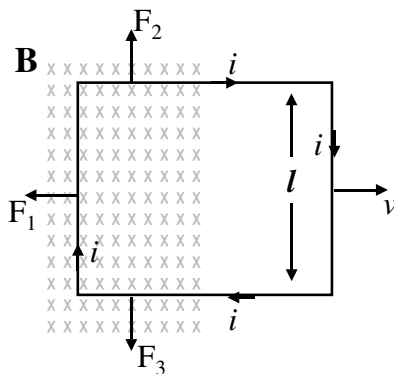


Fig. 2.8 Forces are exerted on a rectangular loop moving through a magnetic field.

where q is electric charge and \mathbf{v}_d is the drift velocity of the charge carriers (electrons) in the wire. The drift velocity is related to the current density by $v_d = j/nq$, where n is the charged particle density. If l is the length of a section of wire and A is its cross-sectional area, then the total force on this section is:

$$F = nlAF' = ilB, \quad (2.36)$$

where $i = jA$. Making the appropriate substitutions, Eq. (2.36) becomes:

$$\mathbf{F} = i\mathbf{l} \times \mathbf{B}. \quad (2.37)$$

According to Faraday's law, a change in magnetic flux induces an electromotive force (EMF) in the conductor:

$$V = -\frac{d\Phi}{dt} = -\frac{d}{dt}(Blx) = -Bl\frac{dx}{dt} = -Blv, \quad (2.38)$$

where x is the distance the rectangular loop is displaced and v is the speed at which it is moved. This EMF sets up a current in the loop:

$$i = \frac{V}{R} = \frac{Blx}{R}. \quad (2.39)$$

Substituting this expression into Eq. (2.38) yields an expression for the force on the wire:

$$F = \frac{B^2l^2v}{R}, \quad (2.40)$$

if it is assumed that the \mathbf{l} and \mathbf{B} are perpendicular. It should be noted that the magnetic force on the conductor is directly proportional to the square of the magnetic field.

2.4.3 Magnetic Pressure

Consider a conductor whose surface is subjected to a magnetic pulse $\mathbf{H}(t)$. For simplicity, it is assumed that the conductor is infinitely thick in the x -direction and planar in the y - and z -directions, and that the magnetic field lines are parallel to its surface. Neglecting the displacement current, Eq. (2.12) becomes:

$$j_y = -\frac{\partial H}{\partial x}. \quad (2.41)$$

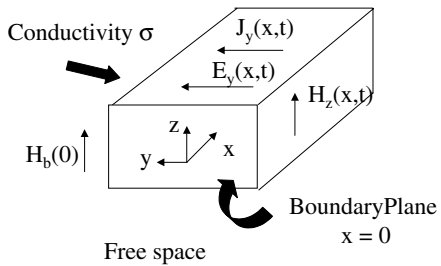


Fig. 2.9 Magnetic pressure is generated at the surface of a conductor when a magnetic pulse is applied.

Substituting this expression into Eq. (2.33) and integrating along the x -axis gives the hydrodynamic pressure at a depth x (Fig. 2.9):

$$p(x, t) = - \int_0^x \frac{\partial H_z}{\partial x} B_z dx = p_H - \frac{1}{2} \mu H^2(x, t), \quad (2.42)$$

where

$$p_H = \frac{1}{2} \mu H^2(0, t) \quad (2.43)$$

is the *magnetic pressure* due to the magnetic field at the surface of the conductor.

2.4.4 Electric Fields

Faraday's law of induction states that a changing magnetic field produces an electric field. For example, when a magnetic field is compressed by a closed conductor, an EMF, $V = d\Phi/dt$, is induced around the conductor. The work done by the EMF on a unit charge is qV and, from another point of view, the work done by the electric force, qE , to move the charge through a distance l is qEl . Equating these two expressions for work yields:

$$V = El. \quad (2.44)$$

Generalising this expression yields:

$$V = \oint \mathbf{E} \cdot d\mathbf{l} = - \frac{d\Phi}{dt}. \quad (2.45)$$

Thus, as magnetic flux is compressed in an FCG, electric fields are induced in the conductor, and these, in turn, circulate a current.

Another way of looking at the relationship between magnetic and electric fields is to consider the force acting on a conductor moving through a

magnetic field by using the Lorentz force:

$$\mathbf{F} = q(\mathbf{E} + \mathbf{v} \times \mathbf{B}). \quad (2.46)$$

Dividing both sides by q yields an expression for the electric field, \mathbf{E}^* , detected by an observer moving with the conductor:

$$\mathbf{E}^* = \mathbf{E} + \mathbf{v} \times \mathbf{B}. \quad (2.47)$$

If the external electric field is $\mathbf{E}^* = 0$, the electric field generated by the motion of the conductor is:

$$\mathbf{E} = -\mathbf{v} \times \mathbf{B}. \quad (2.48)$$

The electric fields generated within FCGs can greatly effect their efficiency through such energy loss mechanisms as electrical breakdown in the insulator or between various components.

2.4.5 Electrical Breakdown

In explosive generators, electrical breakdown can occur in several types of media including gases, liquids, dielectrics and vacuum. For example, in FCGs, breakdown can occur in the gases between the expanding armature and the stator or in the insulating materials between the windings of the stator, while in FEGs it can occur within the volume or on the surface of its ferroelectric material. Electrical breakdown is also the basis upon which many high-voltage closing and opening switches work. The basic principle of switch operation is that at the proper time a change occurs in the properties of the switch medium — i.e. it changes from that of an insulator to that of a conductor or vice versa. This involves either elimination of breakdown (opening switch) or initiation of breakdown (closing switch). A brief introduction to the various types of electrical breakdown that can occur in explosive pulsed power generators will be presented in this section.

Electrical breakdown is a statistical phenomenon. That is, the time at which breakdown will occur cannot be predicted, but the probability of breakdown occurring for certain field conditions and geometries can be calculated. At the microscopic level, breakdown requires the presence of charged particles, typically electrons, since they have a greater mobility than do ions, that have acquired enough energy from an applied electric field to ionise the material and create additional charged particles. In order for the electrons to acquire enough energy between collisions to cause ionisation, their mean free path in the material must be sufficiently large. Since

the mean free path will depend on the density of the material, the electric breakdown strength should also depend on density, which is the case. As the density of a material increases, so too does its breakdown threshold. Thus, the state of a material — i.e. whether it is gaseous, liquid or solid, will affect its breakdown threshold. This plus differences observed in the initiation and evolution of discharges necessitates that the treatment of breakdown in gases, liquids and solids be done separately.

2.4.5.1 Gas Breakdown

The process of gaseous ionisation and breakdown involves many parameters and interactions that have both temporal and spatial dependency [5]. Most of the existing theories are qualitative or semi-quantitative in nature. Early theoretical work on gas breakdown was carried out by Townsend. His model was based on the steady state, one-dimensional continuity equations for electrons and positive ions. The Townsend formula for the current, i , generated during gaseous breakdown is:

$$i = \frac{i_0 e^{\alpha d}}{1 - \gamma(e^{\alpha d} - 1)}, \quad (2.49)$$

where α is the Townsend first ionisation coefficient, d is the distance between two electrodes and γ is the dielectric strength factor. An analytical expression for Paschen's law, which describes how breakdown voltage varies with gas pressure, is:

$$V_b = \frac{Bpd}{\ln \left\{ \frac{APd}{\ln(1+1/\gamma)} \right\}}, \quad (2.50)$$

where A is the cross-sectional area of the electrodes, p is pressure, and B arises from the following empirical formula for α :

$$\alpha = Ap \exp \left(1 - \frac{Bpd}{V} \right). \quad (2.51)$$

This expression for breakdown voltage has been experimentally tested and found to be valid only for values of $pd \leq 200$ mm Hg·cm. For larger values of pd , Townsend's formula is not in agreement with the experimental data.

In order to account for the limitations of the Townsend breakdown model, a new model, called the *steamer breakdown* model, was developed. The basic idea is that at a certain stage in the development of a single avalanche, photoionisation of the gas becomes the predominant process for producing secondary electrons, which leads to the formation of secondary

Table 2.2 Relative dielectric strength of several gases [3].

Gas	Relative Dielectric Strength, γ
N ₂	1.0
CO ₂	0.9
SF ₆	2.3–2.5
Freon	2.4–2.6
CCl ₄	6.3

avalanches and eventually gas breakdown. The critical field, E_r in (V/cm), at which breakdown occurs is

$$E_r = 5.3 \times 10^{-7} \frac{\alpha e^{\alpha x}}{(a/p)^{1/2}}, \quad (2.52)$$

where x is the distance the avalanche has progressed to and p is the gas pressure. The streamer breakdown model has been experimentally tested and found to be in agreement with the data for large values of pd . It is particularly successful in explaining filamentary breakdown.

Static Voltage Gas Breakdown Electrical breakdown of gases, when a static voltage is applied, may be classified as being one of two types: breakdown in uniform fields and breakdown in non-uniform fields. The breakdown voltage of an air gap in a uniform field is

$$V_b = 6.72(pd)^{1/2} + 24.36(pd), \quad (2.53)$$

where V_b is the breakdown voltage in kilovolts, d is the gap width in centimetres and p is the gas pressure in bars. For other gases, the breakdown voltage in a uniform field may be estimated by multiplying the above formula for air by the dielectric strength factor γ for the gas of interest (see Table 2.2):

$$V_{bg} \simeq \gamma V_b, \quad (2.54)$$

where V_{bg} is the breakdown voltage for gases other than air.

Electrical breakdown of gases in non-uniform fields is a more complex problem, since it is dependent on electrode geometry, as well as gas pressure and gap separation. One practical approach for finding an analytical expression for the breakdown voltage in a non-uniform field, $V(p, r, d)$, where r is the radius of curvature of the electrodes, is to find the maximum field strength, E_m ,

$$E_m = f E_0, \quad (2.55)$$

Table 2.3 Field enhancement factors for some common electrode configurations, where r is the radius of the cylinder or sphere and d is the distance between the outside surfaces of the cylinders or spheres with the outside surfaces of adjacent cylinders, planes, or spheres [3].

Electrode Configuration	<i>f</i> -factor
Sphere-Plane	$0.9(r + d)/r$
Sphere-Sphere	$0.9(r + d/2)/r$
Cylinder-Plane	$0.9d/r \ln[(r + d)/r]$
Parallel Cylinders	$0.9d/\{2r \ln[(r + d/2)/r]\}$
Perpendicular Cylinders	$d/\{2r \ln[(r + d/2)/r]\}$
Coaxial Cylinders	$d/\{r \ln[(r + d)/r]\}$
Concentric Spheres	$(r + d)/r$

where $E_0 = V/d$ and f is the field enhancement factor, which is a function of the gap separation and the electrode radius of curvature. By taking E_{mb} as the breakdown field, the breakdown voltage can be estimated by using,

$$V_b = (E_{mb}/f)d. \quad (2.56)$$

Expressions for the field enhancement factor of different electrode configurations can be found in Table 3.5, page 51 of [5] (partially reproduced here in Table 2.3). For example, the field enhancement factor for parallel cylinders is $0.9d/\{2r \ln[(r + d/2)/r]\}$, where r is the radius of the cylinders and d is the distance between the outer surfaces of the cylinders. The breakdown field, E_{mb} , is normally measured, but in some cases can be estimated. For parallel cylinders, the following expression can be used to estimate the breakdown field: $E_{mb} = 24.6p + 6.7(p/0.23r)^{1/2}$, where d and r have units of centimetres, p units of atmospheres, and V_b units of kilovolts.

Pulsed Voltage Gas Breakdown In the case of pulsed voltage breakdown, there are two effects that must be taken into account:

- The statistical time delay required for the initial electrons to be produced.
- The time required for subsequent streamer formation and propagation.

If the field is uniform and the pulse rise time exceeds a few hundred nanoseconds, these two effects are insignificant and can be ignored, and the static breakdown formula presented above can be used to approximate the breakdown voltage for pulsed fields.

If the field is non-uniform or the pulse rise time is less than a few tens of nanoseconds, the rise time and peak voltage of the impulse must be

taken into account. For large gaps with divergent fields, an approximate expression for the breakdown voltage is

$$V_b = K_{\pm} \times p^n d^{5/6} t^{-1/6}, \quad (2.57)$$

where V_b has units of kilovolts, p has units of atmospheres, d has units of centimetres, and t has units of microseconds. The time t is defined to be the time it takes for the voltage to exceed 89% of the breakdown voltage. The constants K and n depend on the type of gas used and the polarities of the electrodes. Their values for some gases are given in Table 2.4. This formula applies for gas pressures ranging from 1 to 5 atmospheres.

2.4.5.2 Liquid Breakdown

Breakdown in liquids is less understood than breakdown in gases. In the case of gases, both diffuse and filamentary breakdown are observed, but in liquids luminous filamentary channels tend to form. The dielectric strength of most liquids tends to lie between 100 and 1000 kV/cm, which is significantly higher than that of gases at high pressure. The pulsed breakdown voltage for deionised water and oil by uniform fields can be approximated by,

$$V_b = K_{\pm} A^{=1/10} dt^{-1/3}, \quad (2.58)$$

where K_{\pm} (see Table 2.5) is a constant and depends on the liquid and the polarity of the pulse, d has units of centimetres and t has units of microseconds.

Table 2.4 K and n values for some gases [3].

Material Constant	Air	Freon	SF ₆
K_+	22	36	44
K_-	22	60	72
n	0.6	0.4	0.4

Table 2.5 Breakdown constants for oil and water used in coaxial pulse lines with centre conductors [3].

Parameter	Oil	Water
K_+	0.5	0.3
K_-	0.5	0.6

microseconds. The time t is defined to be the time it takes for the voltage to reach 63% of its maximum value.

In non-uniform fields, the breakdown field for water may be approximated by

$$E_{\pm} = \alpha K_{\pm} A^{n_{\pm}} t^{-1/3}, \quad (2.59)$$

where E_{\pm} is the breakdown field with units of MV/cm and is polarity dependent, K_{\pm} and n_{\pm} are constants and are polarity dependent, A is the electrode area within 90% of the peak electrical field with units of cm^2 and α is a function of the field enhancement factor, f , and is defined by the following expression:

$$\alpha = 1 + 0.12(f - 1)^{1/2}. \quad (2.60)$$

2.4.5.3 Solid Breakdown

The breakdown strength of solids is at least an order of magnitude greater than that for liquids. There are multiple breakdown mechanisms in solids including [3]:

- Intrinsic Breakdown, which occurs when the applied fields cause electrons in the insulator to transition across their forbidden energy gap from the valence band to the conduction band.
- Streamer Breakdown, which is conceptually similar to streamer breakdown in gases in that when the avalanche exceeds a certain critical size, breakdown occurs.
- Thermal Breakdown, which occurs when an insulator is stressed electrically due to currents and when there are dielectric losses due to polarisation and heat is continuously generated. If this heating exceeds the rate of heat loss, thermal breakdown occurs.
- Erosion Breakdown, which occurs when voids and cavities, which exist within the insulator or are generated under shock conditions, are filled with gaseous or liquid mediums that have lower breakdown strengths than that of the solid. Thus, normal stand-off voltages for the solid may exceed the breakdown strength of the material in these cavities and cause breakdown.
- Tracking Breakdown, which is due to the formation of permanent conducting paths, usually carbon, along the insulator surface because of degradation of the insulator.

The breakdown strength of solids tends to decrease the longer the field is applied and as its volume increases. Since the streamers that form during breakdown have a short transient time, the breakdown field is nearly independent of pulse length down to a few nanoseconds. A practical expression for the breakdown field of solids is

$$E_b = KM^{-1/10}, \quad (2.61)$$

where E_b has units of MV/cm, the volume, M , has units of cm^3 and K is a constant (see Table 2.6). For thin sheets, the standard deviation of the breakdown field decreases and the breakdown strength becomes nearly independent of the volume.

2.4.5.4 *Surface Flashover*

Surface flashover is defined to be the electrical discharge that occurs along or near the surface of an insulator. There are many different forms of surface breakdown depending on the geometrical configuration of the system. The physical mechanisms that are responsible for surface flashover are not clear and are the subject of ongoing research.

2.5 Summary

In this chapter, we have considered the following fundamental electromagnetic principles and devices:

- Maxwell's field equations, which are needed to understand and model the various processes that occur during the operation of explosive pulsed power generators.

Table 2.6 Values of K for several solid insulators [3].

Material	K
Polyethylene	2.5
Teflon	2.5
Polypropylethylene	2.9
Perspex	3.3
Mylar	3.6

- The basic components and materials that make up explosive pulsed power circuits — i.e. resistors, capacitors, inductors, transformers, switches, transmission lines and insulating materials.
- The equations needed to solve explosive pulsed power circuits — i.e. Kirchhoff's Voltage and Current Laws.
- The various electromagnetic fields, forces and phenomena that arise during generator operation and that affect their performance — i.e. magnetic diffusion, magnetic forces, magnetic pressure, electric fields and electrical breakdown.

Bibliography

- [1] C. A. Balanis, *Advanced Engineering Electromagnetics*, John Wiley & Sons, New York (1989).
- [2] S. Fich, *Transient Analysis in Electrical Engineering*, Prentice-Hall, Inc., New York (1951).
- [3] A. Guenther, M. Kristiansen and T. Martin (eds). *Opening Switches*, Plenum Press, New York (1987).
- [4] W. H. Hayt and J.E. Kemmerly, *Engineering Circuit Analysis*, 3rd Edition, McGraw-Hill Book Company, New York (1978).
- [5] G. Knoepfel, *Pulsed High Magnetic Fields*, North-Holland Publishing Company, Amsterdam (1970).
- [6] S. T. Pai and Q. Zhang, *Introduction to High Power Pulse Technology*, World Scientific, Singapore (1995).
- [7] W. J. Sarjeant and R.E. Dollinger, *High-Power Electronics*, TAB Books, Inc., Blue Ridge Summit (1989).
- [8] P. W. Smith, *Transient Electronics: Pulsed Circuit Technology*, John Wiley & Sons, Queensland (2002).
- [9] I. Vitkovitsky, *High Power Switching*, Van Nostrand Reinhold Company, New York (1987).

This page intentionally left blank

Chapter 3

Fundamentals of Shock Waves and High Explosives

3.1 Introduction

Since high explosives are the primary source of energy in explosive driven pulsed power sources, it is necessary that we understand their basic chemical and physical properties, how they interact with materials and the tools that are needed to make them function in a desired way. Since explosives tend to generate shock wave pressures, an understanding of shock waves is also required. Therefore, in this chapter, a brief introduction to explosives, shock waves and their interactions will be presented.

3.2 Shock and Detonation Waves

The surfaces of conductors in FCGs, FEGs and FMGs are subjected to very strong transient forces produced by the detonation of explosives and by their interaction with very strong electric and/or magnetic fields. Since the pressure applied to the surface of a conductor is transmitted to its interior in the form of a shock wave, some knowledge of shock waves, their propagation and their effects on materials is required in order to analyze generator performance.

3.2.1 Stress and Strain

When external forces are applied to the surfaces of real materials, their shape changes. It has been observed that the amount of *strain* (amount of distortion) produced in a material is directly proportional to the *stress* (force per unit area) placed on the material. Stresses can be classified as either *normal* or *tangential (shear)*. In the case of normal stress, the force

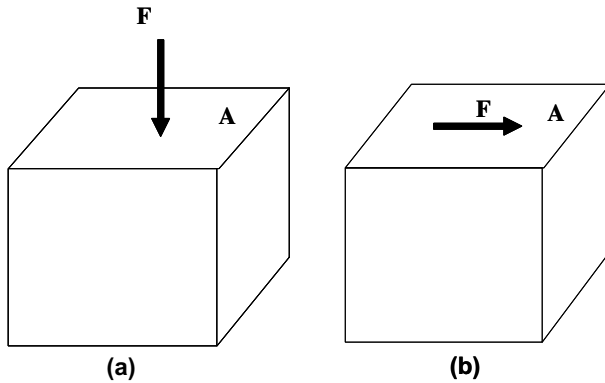


Fig. 3.1 Stress can be classified as either (a) normal or (b) tangential.

is applied perpendicular to the surface (Fig. 3.1(a)), and in the case of tangential stress, it is applied parallel to the surface (Fig. 3.1(b)).

These stresses can generate one of four types of strain: tensile, compressive, shear and volumetric. *Tensile strain* occurs when forces are applied perpendicular to the ends of a rod and stretch it (Fig. 3.2(a)). Tensile strain is defined to be the ratio of the change in length of the rod to its original

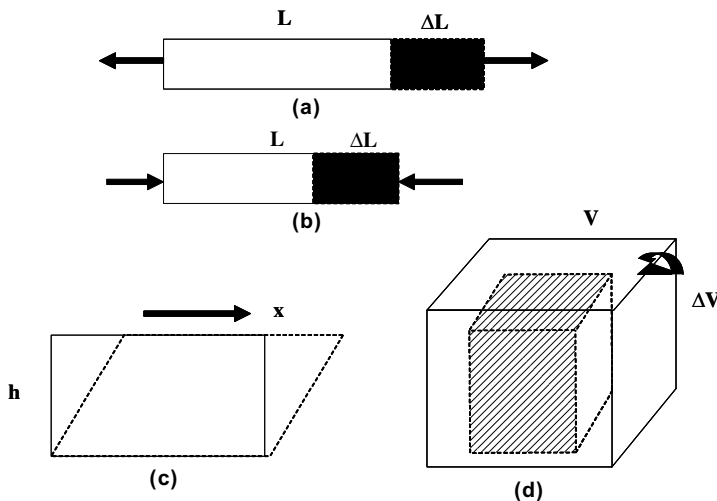


Fig. 3.2 Stresses can generate one of four types of strain: (a) tensile, (b) compressive, (c) shear and (d) volume.

length. *Compressive strain* occurs when forces are applied perpendicular to the ends of a rod and compress it (Fig. 3.2(b)). Compressive strain is defined in the same way as tensile strain. *Shear strain* occurs when forces are applied parallel to the surface of a body and shifts one of its faces relative to its opposite face (Fig. 3.2(c)). Shear strain is defined to be the ratio of the displacement of the face, x , to the transverse dimension of the body, h . *Volume strain* occurs when forces are applied perpendicular to the faces of a body and causes its volume to change. Volume strain is defined to be the ratio of the change in volume to the initial volume of the body (Fig. 3.2(d)). In the case of shock waves, only compressive stresses and strains are observed.

A typical stress-strain curve is presented in Fig. 3.3. The stress-strain relationship is linear up to a point called the *elastic limit* or *yield point*. At or beyond this limit, the material, if the stress is removed, will no longer return to its original shape or dimensions. That is, the deformation is no longer *reversible*. When a material is strained beyond its elastic limit, it undergoes *plastic deformation*, which causes the material to exhibit fluid behavior, and it is in this region that the shock pressures generated by most explosives are found.

3.2.2 Sound Velocity

As a consequence of the compressibility of gases, liquids and solids, a disturbance introduced at some point in the substance will propagate through it at a finite velocity called the *velocity of sound*. The velocity of sound in a

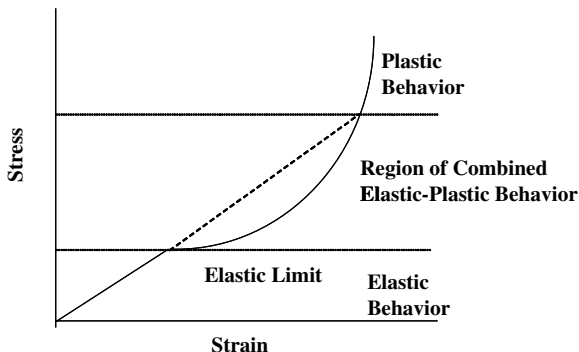


Fig. 3.3 Stress-strain curves.

medium depends on the elasticity of the material and its density. Sound typically travels faster through media with higher elasticity and/or lower density. If the pressures are such that the material is still in the elastic region, the velocity of sound is constant. The square of the velocity of sound, c , is proportional to the ratio of the change in pressure to the change in density:

$$c^2 = \frac{\partial P}{\partial \rho}. \quad (3.1)$$

This means that in the elastic region, the pressure and density are linearly proportional to each other. However, when the stresses exceed elastic limit, the velocity of sound waves increases as the pressure or density increases, which means that the pressure and density are no longer linearly proportional.

3.2.3 Shock Waves

A *shock wave* is a discontinuous high pressure disturbance moving through matter [1–4]. The pressures in strong shock waves stress solid materials far beyond their elastic limits. Since differences among the stress components are limited by the stress yield, the principal stress components are almost equal and the stress can be approximated by its average value — i.e. pressure. The energy, e , particle velocity, u , pressure, P , and density, ρ , on either side of a shock discontinuity propagating at a velocity U are as shown in Fig. 3.4.

To explain how shock waves are formed, consider Fig. 3.5. At point A, the pressure is low and, therefore, the velocity of sound is low. In addition, the velocity of the particles is low. Therefore, the velocity of the pressure wave is low. At point B, the wave velocity is higher than at point A, because the wave velocity increases as the pressure increases when the elastic limit

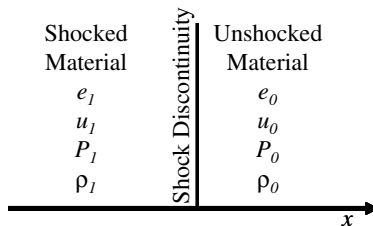


Fig. 3.4 Shock discontinuity propagating at a velocity U and transitioning a material from state $(P_0, \varrho_0, e_0, u_0)$ to state $(P_1, \varrho_1, e_1, u_1)$.

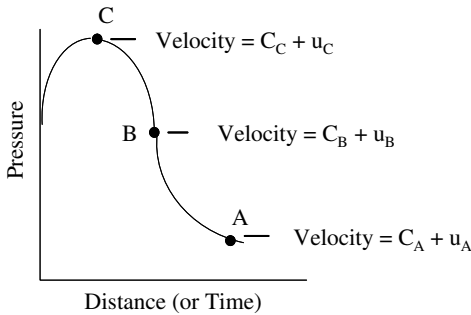


Fig. 3.5 The pressure at point A is low, which means that the velocity of sound is low. The pressure at points B and C is higher, which means that the velocity of sound is higher at these points. These differences in velocity cause the wave to steepen into a shock wave.

of the material is exceeded. The particle velocity is also higher. Therefore, the pressure wave at point B is higher than at point A. The same can be said of point C. Since the velocity of the pressure wave is higher at the higher pressures along the front of the wave, the wave steepens into a shock wave.

To mathematically describe shock waves, there are two coordinate systems available: Eulerian and Lagrangian. To understand the difference, consider the example of a train. If the observer is standing on the side of a railroad track and observing an experiment being performed on a flat car moving at some speed, he makes one set of measurements. In this case, he is in the *Eulerian coordinate system*. On the other hand, if a person on the flat car makes the same set of measurements, he will obtain a different set of values. This second person is in the *Lagrangian coordinate system*. The difference in the measurements is the velocity of the train. In dealing with shock waves, it is mathematically simpler to work in the Lagrangian coordinate system — i.e. to assume that the observer is moving with the shock wave.

There are five variables required to describe shock waves: particle velocity, u , density, ρ , pressure, P , internal energy, e , and shock wave velocity, U . Therefore, five equations are required to solve for these five variables. Three of the equations are based on the mass, momentum and energy conservation laws. In the case of shock waves, these conservation equations do not depend upon the process, but merely on the initial and final states, since these variables change discontinuously across the shock front. These three conservation relationships collectively are called the *Rankine-Hugoniot jump equations*.

Applying the principles of conservation of mass, momentum and energy to a shock wave passing through a material gives rise to the equations:

$$\frac{\rho_1}{\rho_0} = \frac{U - u_0}{U - u_1} \quad (3.2)$$

representing the conservation of mass,

$$P_1 - P_0 = \rho_0(u_1 - u_0)(U - u_0) \quad (3.3)$$

representing the conservation of momentum, and

$$e_1 - e_0 = \frac{P_1 u_1 - P_0 u_0}{\rho_0(U - u_0)} - \frac{1}{2}(u_1^2 - u_0^2), \quad (3.4)$$

representing the conservation of energy. In these equations, P is the shock wave pressure (Pascals, Pa), U is the shock velocity (m/s), u is the particle velocity (m/s), ρ is the density (kg/m^3) and e is the internal energy (J/kg). The subscripts 0 and 1 refer to the state of the unshocked and shocked materials, respectively. Usually, pressure is reported in GPa ($1 \text{ GPa} = 10^9 \text{ Pa} = 10^9 \text{ N}/\text{m}^2 = 10^4 \text{ bars}$) and the velocity in km/s. Conveniently, $1 \text{ km/s} = 1 \text{ mm}/\mu\text{s}$, where the latter units are comparable to the dimensions and time intervals arising in the analysis of explosive pulsed power sources.

If the state of the material into which a shock is propagating is known, Eqs. (3.2)–(3.4) provide three relationships with the five unknown quantities P_1 , u_1 , ρ_1 , e_1 and U . One of these quantities, e.g. the pressure or the particle velocity in the material behind the shock, is a measure of the strength of the shock and must be specified as a boundary condition. The additional relationship needed to completely characterise the shock wave depends on the material behavior. In the context of shock physics, this relationship is called the *Hugoniot curve* (or simply a *Hugoniot*), which is the locus of states achieved by passing a shock into a material in a given initial state. In other words, the Hugoniot is an equation of state that gives all of the equilibrium states in which a material can exist and is written in terms of internal energy, pressure and specific volume. A Hugoniot curve can relate any two of the variables in question and a Hugoniot relationship between any two of the variables can be transformed into a relationship between any other two of these five variables.

Experimental measurements indicate that the response of materials in a given initial state to shock compression can often be represented by the Hugoniot relation [1]:

$$U = c_0 + u_0 + s(u - u_0), \quad (3.5)$$

Table 3.1 Hugoniot values for unreacted explosives [6].

Explosive	Density (g/cm ³)	c_0 (km/s)	s	Range Limitation (Shock Velocity)
Comp B	1.700	2.95	1.58	
	1.710	1.20	2.81	4.40–5.04
Comp B (Cast)	1.700	2.49	1.99	3.57–5.02
	1.903	2.74	2.6	
HMX	1.891	2.901	2.058	
	1.80	3.01	1.72	
Octol	1.803	2.21	2.51	3.24–4.97
PBX-9011-06	1.790	2.225	2.644	4.1–6.1
PBX-9404-03	1.721	1.89	1.57	2.4–3.7
PBX-9404	1.84	2.310	2.767	<3.2
PETN	0.82	0.47	1.73	
RDX	1.0	0.4	2.00	
TNT (Pressed)	0.98	0.366	1.813	1.05–3.26
TNT (Cast)	1.614	2.390	2.050	3.034–5.414

in which c_0 and s are measured parameters that depend on the initial thermodynamic state of the material. The values of these parameters for some explosives are presented in Table 3.1. This equation is broadly applicable to describing the response of materials to compression by strong shocks, but requires refinement when phase transitions are encountered and at low stresses where elastoplastic phenomena often dominate observed responses. An example of another Hugoniot curve that can be derived from the linear $U-u$ Hugoniot in Eq. (3.5) is the $P-\rho$ Hugoniot, which is obtained by combining Eqs. (3.2), (3.3) and (3.5):

$$P_1 - P_0 = \rho_0 \left(1 - \frac{\rho_1}{\rho_0} \right) \left[1 - s \left(1 - \frac{\rho_1}{\rho_0} \right) \right]^{-2}. \quad (3.6)$$

When the boundary forces that produce a shock are removed, a *decompression wave* (also called a *rarefaction* or *release wave*) originates at the boundary and propagates into the interior of the material. When heat conduction is neglected, the decompression wave is a smooth wave, rather than the discontinuous shock wave that is observed on compression. Each decompression wavelet advances at the rate $c(\rho) + u$, where c is the speed of sound at the point in the wave where the density is ρ . The speed of sound at the point immediately behind the shock wave exceeds U , but decreases with the decrease in ρ that occurs as the shock wave passes. Because of this decrease in the rate of advance of the wavelets, the decompression wave spreads as it propagates. The speed of sound in the material immediately behind the

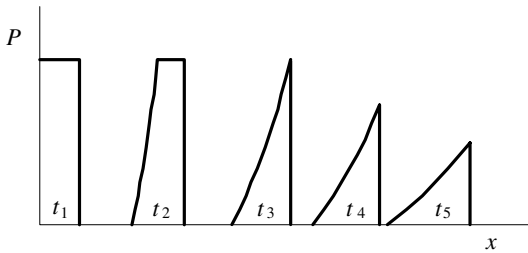


Fig. 3.6 This sketch of an attenuating pressure pulse is based on the premise that the pressure applied to the boundary to produce the shock is sustained until $t = t_0$, at which time it is removed. The decompression wave introduced into the material at this time overtakes the shock at $t = t_3$ and the attenuation process begins.

shock exceeds the shock velocity, so that the decompression overtakes the shock wave. This causes attenuation, which decreases both the energy and pressure changes produced by the shock wave. When the rarefaction wave overtakes the shock wave, the pressure pulse becomes sawtooth-shaped, decreasing in amplitude and increasing in length as the attenuation process proceeds, as shown in Fig. 3.6. Eventually, the shock wave becomes a sound wave.

3.2.4 Detonation Waves

When energetic materials undergo combustion, there are two possible processes by which the reaction zone can propagate into the unreacted material: deflagration and detonation. *Deflagration* is where the reaction zone passes relatively slowly ($\sim 1 \text{ mm}/\mu\text{s}$) across the unreacted energetic material and the gaseous combustion products flow in a direction opposite to that of the reaction zone. *Detonation* is where the reaction zone passes at supersonic speeds ($\sim 2\text{--}10 \text{ mm}/\mu\text{s}$) across the unreacted energetic material and the gaseous combustion products flow in the same direction as that of the reaction zone. The detonation process is strongly directive, which is responsible for an essential property that is not obvious; that is, the detonation products just behind the shock wave flow in the same direction as the motion of the detonation wave. It is this condition that is responsible for sustaining the detonation front.

A *detonation wave* is a shock wave that is supported by an exothermic chemical reaction. This reaction continuously adds energy to the shock wave, maintaining its strength. When the chemical energy liberated at a shock front exceeds that required to sustain the shock wave, it will grow in

strength. When it is too little, the detonation wave will be attenuated by an overtaking decompression wave, as in the case of a nonreactive shock. In the case of a detonation, there exists an equilibrium amplitude at which the chemical energy produced is just sufficient to maintain a steady shock. In this case, the shock propagates at a constant velocity called the *detonation velocity* and has a constant pressure and particle velocity called the *Chapman-Jouguet pressure* and *velocity*, respectively.

High pressures and temperatures are produced by the rapid release of chemical energy by the explosives. Typically, the chemical reaction is 90% complete within 1 ns to 1 μ s. This energy goes into the motion of the explosive products, which creates the high pressures (a few tens of gigapascals) and temperatures (2,000–4,000 K) required to drive the chemical reaction. The shock waves associated with detonation travel at velocities between 1,500 and 9,000 m/s in solids and liquids. The rate at which the material decomposes is governed by the speed at which the material transmits the shock wave, not by the rate of heat transfer.

In a reactive medium, the structure of the detonation wave is more complicated than a pressure pulse, because of the exothermic reaction occurring within it (Fig. 3.7). The wave front moves at the detonation velocity and initiates the explosive reaction as it passes through the material. The reaction takes place in a *reaction zone* immediately behind the shock front. The end of the reaction zone is called the *Chapman-Jouguet (C-J) plane* and its state is characteristic of the explosive used. The hot, high-pressure gas formed by the reaction couples energy into other materials as it expands.

The reaction zone is bounded by two surfaces that isolate it from the regions before and behind it. The first surface is the shock surface that

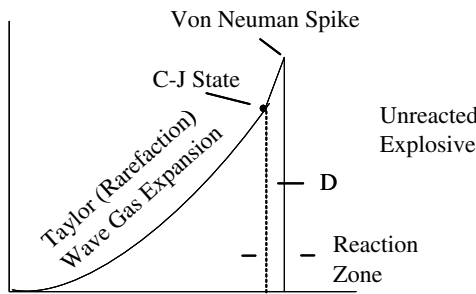


Fig. 3.7 Schematic illustration of a Chapman-Jouguet detonation wave. This waveform consists of a detonation front followed by a simple decompression wave called a Taylor wave.

initiates detonation in the unreacted explosive and that travels at super-sonic speeds relative to the unreacted material, thus preventing leakage of pressure ahead of the shock. The second surface is called the choked flow state and it moves at the local speed of sound in the framework of the moving shock front. To consider the effects of this latter surface, consider an observer riding with the shock front and looking back into the reaction zone. The observer sees an increasing amount of energy being released in the reaction zone as a function of distance. This energy release serves to accelerate the flow away from the shock front and reduce the pressure. As the flow speed at the end of the reaction zone is completed, the flow speed at the choke flow becomes equal to the local speed of sound in the frame of reference moving with the shock wave. As a result, the flow becomes choked and stops any further pressure decrease in the reaction zone. Therefore, what happens in the reaction zone determines if the detonation is self-propagating or not.

The C-J model for high explosives is a one-dimensional model that assumes that the rate of chemical reaction is infinite and therefore that the length of the reaction zone is zero rather than finite. These assumptions lead to the prediction that the detonation velocity is constant and that the values of D_{CJ} and P_{CJ} are independent of the initiating shock strength and depend only on certain properties of the explosive before and after the passage of the detonation front; that is, the initial density of the unreacted explosives, the liberated energy density of the explosive and the pressure-volume response of the unreacted explosive (e.g. the mechanical equation of state). Today, there are 3-D detonation models, called Detonation Shock Dynamics (DSD) models, that take into account the effects of finite rates of reaction and, therefore, finite reaction zone lengths behind the detonation front. The length of the reaction zone effects several things, including the detonation speed, and places limits on the minimum size of explosive and the minimum input pressure that will lead to detonation.

The length of the reaction zone cannot be easily measured, but can be deduced from its effects on other parameters. These lengths vary from as little as a hundredth of a millimetre for some high-density explosives up to several centimetres for blasting agents. The length of the reaction zone is important, because it appears to control the detonation velocity in the non-ideal detonation region. It appears that explosives with thick reaction zones have a greater effect on the ratio of the detonation velocity to the diameter of the explosive charge, than do explosives with thin reaction zones.

As the shock wave travels through the explosive, it accelerates continuously with increasing amplitude until it reaches a steady state. Steady state is reached when the energy generated by the reaction equals the energy lost to the surrounding medium as heat and the energy used to compress and displace the explosive material. At steady state, the velocity of the detonation wave is supersonic [5].

As noted above, the detonation process can be regarded as a wave that is preceded by a shock wave which advances with constant velocity D into the unreacted explosive material and which is followed by a zone of chemical reaction as shown in Fig. 3.8. For the detonation wave to move forward, its velocity in the reaction zone must equal the sum of the velocity of sound, c , and the velocity of the flowing explosive material, U :

$$D = U + c. \quad (3.7)$$

When the velocity of the explosive particles is very low, the shock wave will be weak and its velocity approaches the speed of sound. Under these conditions, detonation will not take place. However, when the velocity of the explosive particles is high, the shock wave will travel faster than the speed of sound and detonation occurs.

3.2.5 Detonation Jump Equations

The explosives and inert materials used in FCGs, FEGs and FMGs are solids, but the detonation pressures are so high that their material strength

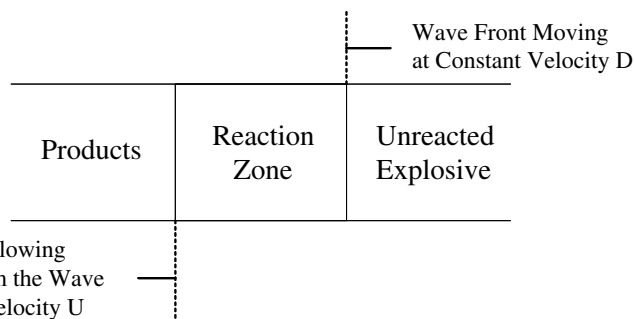


Fig. 3.8 The detonation process is preceded by a shock wave which advances with constant velocity D into the unreacted explosive material and which is followed by a zone of chemical reaction.

may be neglected and the detonation process can be described by the reactive fluid equations. Furthermore, energy transport by heat conduction, viscosity and radiation may be neglected when compared to the energy being transported by the detonation wave and due to the speed of the chemical reaction. Employing these assumptions, a simple fluid dynamic model, referred to as the *CJ theory*, is used to describe the detonation process. This theory is a generalisation of the theory of shock waves and relates the detonation wave velocity to the properties of the gases behind the detonation wave front. The CJ theory assumes that all the chemical energy is released at the detonation front, so that the reaction zone has no thickness. The detonation wave is thus approximated by a self-sustained supersonic wave traveling through the explosive at constant velocity.

The shock equations, Eqs. (3.2)–(3.4), apply to a detonation wave just as they do to a nonreactive shock, with the exception that the chemical energy released in the reaction must be taken into account. In this case, where the pressure and particle velocity are zero in the material ahead of the detonation shock, Eqs. (3.2)–(3.4) can be written as:

$$\frac{\rho_{\text{CJ}}}{\rho_0} = \frac{D}{D - u_{\text{CJ}}} \quad (3.8)$$

and

$$P_{\text{CJ}} = \rho_0 u_{\text{CJ}} D, \quad (3.9)$$

where P_{CJ} is the CJ pressure, ρ_{CJ} is the CJ density and u_{CJ} is the CJ particle velocity at the C-J plane, ρ_0 is the density of the unreacted material and D is the detonation velocity.

If the initial density of all the unreacted explosives is plotted versus their CJ density, curve fitting the data shows that the relationship between these two quantities is

$$\rho_{\text{CJ}} = 1.386 \rho_0^{0.96}. \quad (3.10)$$

It has been shown [6], that

$$P_{\text{CJ}} = \frac{\rho_0 D^2}{4}, \quad (3.11)$$

is a good approximation for the CJ pressure. Using Eq. (3.11) and the mass and momentum conservation laws, the following expression for ρ_{CJ} is derived:

$$\rho_{\text{CJ}} = \frac{4}{3} \rho_0. \quad (3.12)$$

When Eqs. (3.10) and (3.12) are plotted, there is good agreement between the calculated and measured data, except at lower densities, where the calculated values underestimate the value of ρ_{CJ} .

Using Eqs. (3.9)–(3.11), an expression for the relationship between the CJ pressure and the detonation velocity can be derived:

$$P_{\text{CJ}} = \rho_0 D^2 (1 - 0.7125 \rho_0^{0.04}). \quad (3.13)$$

Knowing only the detonation velocity and the initial density of an explosive, its CJ pressure can be estimated to within $\pm 5\%$ of the experimentally measured values. For example, if an explosive has a density of 1.43 g/cm^3 and a detonation velocity of 6.95 km/s , then its CJ pressure is 19.15 GPa .

The detonation velocity depends on the density of the high explosive. For most explosives, the relationship between the detonation velocity and the density of the unreacted explosives is linear:

$$D = a + b\rho_0, \quad (3.14)$$

where a and b are empirical constants that depend on the type of explosives used. Thus, how explosives are packed into explosive power sources and therefore, its density, could affect the overall performance of these generators.

3.3 Explosives and Explosive Components

3.3.1 Explosives

In FCGs and EMHDGs, the source of energy is that which is stored in the explosives. In FMGs and FEGs, the source of energy is that stored in their ferromagnetic and ferroelectric elements respectively, which is released by explosive generated shock waves. Therefore, a brief description of high explosives and their chemistry and thermodynamics are presented. Enough information is presented so that the reader can estimate the detonation velocity of, and the energy generated by pure and mixtures of explosives. For more detailed information, it is recommended that the reader refers to the books by J. Akhavan entitled *The Chemistry of Explosives* [5], P. W. Cooper entitled *Explosives Engineering* [6], and W. Fickett and W. C. Davis entitled *Detonation: Theory and Experiment* [7].

According to Fowler, Garn and Caird [8], explosives offer two unique advantages in compressing magnetic flux. The first is that the compression times, which is on the order of a few microseconds, are short enough that

the cylindrical metal armatures, which trap the flux, behave essentially as perfect conductors. The second is that the magnitude of the magnetic fields generated by flux compression is determined by the pressures the driver-armature systems are capable of sustaining. Since magnetic pressures on the order of millions of atmospheres are generated, it is clear that explosives are necessary to contain these fields, even momentarily.

According to W.C. Davis at LANL [9], ‘The science of high explosives is basically a coupling of chemistry and fluid mechanics. While each of these fields is in itself quite well-developed and sophisticated, high-explosives science is surprisingly primitive. The fluid-mechanical phenomenon of detonation is reasonably well understood, but the detailed chemical reaction and thermomechanics that cause a detonation are still largely a mystery.’ Davis states there are two reasons why the science of explosives is not well understood:

- It is difficult to perform measurements in the interior of a detonating explosive. However, the development of lasers has made it possible to selectively investigate chemical phenomena on time scales of less than 100 ps.
- The study of explosives technology in the past did not place high priority on understanding the details of the detonation process.

However, the technology of explosives and of the components for initiating and controlling detonation of explosives is highly developed [4–7]. There are many explosive materials, although only a few have sufficient power and detonate with the reproducibility required for use in high performance pulsed power sources. Only a few of these materials satisfy the additional requirements of safety and stability that may be associated with specific applications. The explosives used in explosively driven power sources are almost entirely those in the class called *secondary high explosives*, a category comprised of materials with a sensitivity between that of the easily detonable *primary explosives* and that of the very insensitive *tertiary explosives*. Primary explosives will detonate when subjected to heat or shock, while secondary explosives only detonate when subjected to shocks produced by primary explosives. Primary explosives are used in blasting caps and other initiating devices, but are unsuitable for use as main-charges. Tertiary explosives are the safest materials to use, but often prove impractically difficult to initiate, do not function well in small amounts and are less powerful than the best available secondary explosives. Materials such as

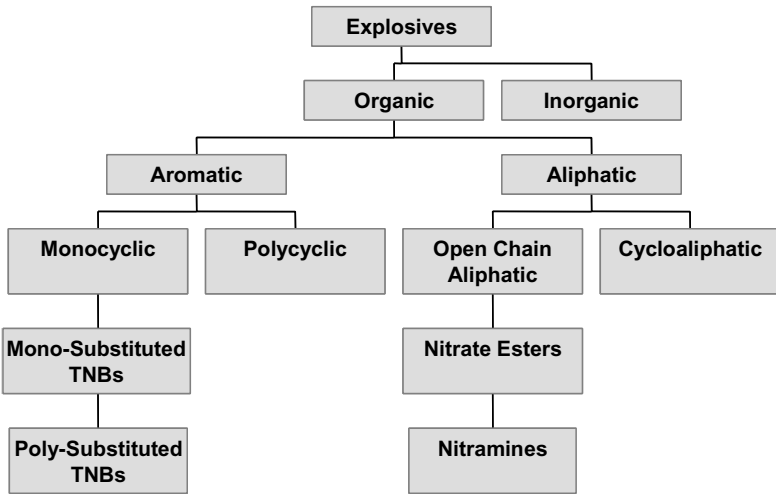


Fig. 3.9 Categories of explosives [6].

pyrotechnics and *propellants* (e.g. gun powder) are used to accelerate projectiles in some types of generators such as FEGs, EMHDGs and MMGs, but are not suitable for driving FCGs and FMGs.

3.3.1.1 Categories of Explosives

Almost all explosives used in explosive pulsed power sources are organic compounds (Fig. 3.9) formed from the elements C, H, N and O, and are called *CHNO explosives*. Their molecular structures are usually quite complicated. Explosive materials are often mixtures of explosive compounds and include polymeric binders that affect their mechanical properties, safety, etc., but are not intended to alter their detonation performance. Explosives of this class liberate their detonation energy by molecular decomposition and reformation into detonation products such as CO₂, N₂ and H₂. The detonation process for many of these explosives does not require atmospheric oxygen, since they contain both the fuel and the oxidiser. A traditional secondary high explosive is trinitrotoluene (TNT), which is easily melted and cast into the shapes required for explosive pulsed power sources and other applications. More powerful explosives in the same class are hexahydrotrinitrotriazine (also called RDX, cylonite or hexogen) and cyclotetramethylenetetranitramine (HMX). These cannot be cast to shape, but granules of the compounds can be mixed into molten TNT and the

mixture cast in much the same way as TNT. More powerful (but also more expensive) explosives can be made by coating granules of RDX and HMX with polymeric binders and pressing the resulting mixture into high-density billets, which are then machined to the required shape. These explosives are called *polymer bonded explosives* (PBX). The first PBX composition was developed at Los Alamos in 1952, when they embedded RDX in plasticised polystyrene. Teflon was used as a binder for HMX during the 1960s and early 1970s. Polymer bonded explosives based on RDX and RDX/PETN have been developed and are referred to by the name *Semtex*. Properties of several secondary high explosives are listed in Table 3.2.¹

3.3.1.2 Chemistry of Explosives

As noted above, most explosives are organic compounds. However, there are inorganic explosives such as ammonium nitrate, mercury fulminate, lead azide and silver azide. These types of explosive will not be considered in this book, since their only use in explosive pulsed power is in detonators. Organic explosives can be further classified as being either aliphatic or aromatic. Aliphatic explosives consist of open chain aliphatic compounds (Fig. 3.10) and cycloaliphatic compounds (Fig. 3.11). Aromatic explosives contain the benzene ring (Fig. 3.12) and can either be monocyclic (containing a single benzene ring) (Fig. 3.13) or polycyclic (containing multiple benzene rings) (Fig. 3.14).

When explosives react, they produce energy by a process called *oxidation*. An oxidation reaction is a chemical reaction in which a fuel reacts with

Table 3.2 Properties of selected secondary high explosive [6].

Explosive	Chemical Formula	Theoretical Density (kg/m ³)	Detonation Velocity (km/s)	Estimated CJ Pressure (GPa)
PETN	C ₃ H ₅ N ₃ O ₈	1780	8.26 (1770)	30 (1670)
RDX	C ₃ H ₆ N ₆ O ₆	1810	8.7 (1770)	34 (1770)
HMX	C ₄ H ₈ N ₈ O ₈	1900	9.11 (1890)	39 (1890)
TNT	C ₇ H ₅ N ₃ O	1650	6.93 (1640)	21 (1630)
TATB	C ₆ H ₆ N ₆ O ₆	1940	7.76 (1880)	29 (1880)
NM	CH ₃ NO ₂	1130	6.35 (1130)	13 (1130)

¹ Numbers in parenthesis are densities in kg/m³. Data from Ref. 1.10. The ‘TATB’ of density 1880 kg/m³ is the plastic bonded explosive PBX 9502, which is 95/5 wt% TATB/Kel-F and is one of the most powerful tertiary explosives.

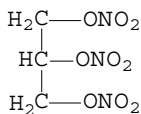


Fig. 3.10 Aliphatic explosive — nitroglycerine.

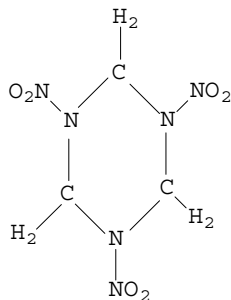


Fig. 3.11 Cycloaliphatic explosive — cyclo-1,3,5-trimethylene-2,4,6,-trinitamine (RDX).

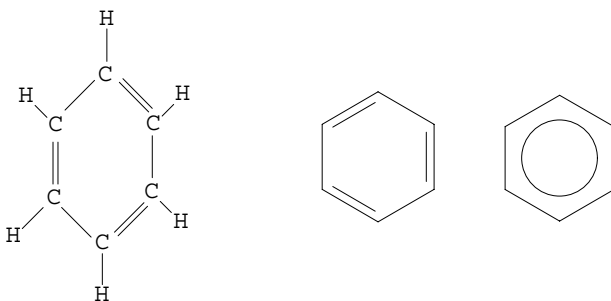


Fig. 3.12 Various methods for representing the benzene ring.

an oxidising agent. For example, the aliphatic compound ethane (a fuel) reacts with oxygen (an oxidising agent) according to the reaction:



However, a separate source of oxidising agent is not necessary for all explosives. It can exist as part of the same molecule that contains the fuel. In fact, most explosives contain the oxidising agent in the form of *substitute groups*, which are atoms or groups of atoms that have replaced hydrogen atoms in

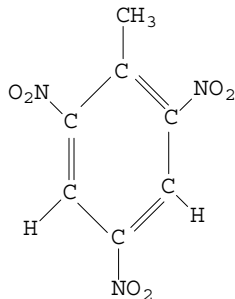


Fig. 3.13 Aromatic explosives — trinitrotoluene (TNT).

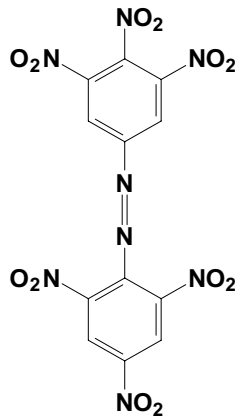
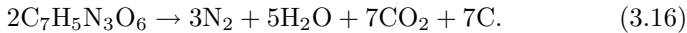


Fig. 3.14 Polycyclic aromatic explosives — Hexanitroazobenzene (HNAB).

hydrocarbons. For example, in the case of nitroglycerine (Fig. 3.10), the oxidiser is the $-\text{ONO}_2$ group and the fuel is the hydrocarbon $-\text{CH}_2-\text{HC}-\text{CH}_2-$. The self-oxidising reaction for the aromatic explosive TNT is:



A list of oxidiser and fuel groups is presented in Table 3.3.

3.3.1.3 Explosive Thermochemistry

A chemical reaction is a process whereby one or more chemical species change their molecular configuration to one that is different. These reactions are accompanied by the release or absorption of energy. If the reaction

Table 3.3 Molecular substitute groups common to many explosives [6].

Name	Formula
Oxidiser Group	
Nitrate	—ONO ₂
Nitro	—NO ₂
Nitroso	—NO
Hydroxyl	—OH
Carboxyl	—COOH
Aldehyde	—CHO
Ketone	—CO
Chloro	—Cl
Fluoro	—F
Difluoramine	—NF ₂
Fuel Groups	
Methyl	—CH ₃
Ethyl	—CH ₂ —CH ₃
Butyl	—CH ₂ —CH ₂ —CH ₂ —CH ₃
Imino	—NH
Amino	—NH ₂
Ammonium	—NH ₄

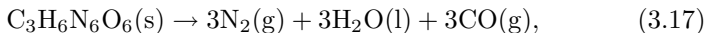
releases energy to the environment, it is referred to as *exothermic*, and if it absorbs energy from the environment, it is referred to as *endothermic*. Reactions involving explosives are exothermic.

This energy is stored in the chemical bonds of the reactants as *internal energy* (*U*). The internal energy of a substance is defined to be the total energy that it possesses by virtue of the presence, relative positions and/or movement of its molecules, atoms and subatomic species. Internal energy consists of the following energies:

- Translational energy of the chemical species, which is significant in the case of gases, where translational motion is nearly unrestricted in contrast to solids and liquids.
- Rotational energies of molecules and groups of atoms that are free to rotate.
- Vibrational energy of atoms in molecules and electrons moving within the atom.
- Potential energy resulting from the attractive and repulsive forces acting between molecules, atoms, electrons and nuclei.

This latter energy depends on the molecular structure of the molecules and on the proximity of atoms and molecules — i.e. if it is a solid, liquid or gas. Since the internal energy of the reactants is different from the internal energy of the products, energy is either released or absorbed by the chemical system.

If the number of reactant molecules is different from the number of product molecules, the volume, especially if gases are involved in the reaction, will change if the pressure is constant. Therefore, work is done that is equal to $P\Delta V$, where P is pressure and ΔV is the change in volume. For example, in the reaction:



the number of molecules has increased from one to nine, six of which are gaseous molecules. Therefore, detonation of this explosive causes the volume to increase, doing work on its environment

The sum of the internal energy and work per unit amount of material (either mass or moles) is called the *enthalpy* (H) — i.e. $H = U + P\Delta V$. The units of energy used are either calories (cal) or joules (J), where 1 cal = 4.1840 J. The difference in the reactant and product enthalpies is called the *heat of reaction*, ΔH_r^0 .

The absolute enthalpy cannot be determined for a substance, which means that only changes in enthalpy can be calculated. In order to simplify calculation of the heats of reaction, an arbitrary *thermodynamic standard state* is defined against which all changes in enthalpy for chemical reactions are referenced. This standard state for most calculations is defined to be 25 C and 1 atm. pressure.

In order to calculate the heat of reaction, the *heat of formation* is used. The heat of formation is the enthalpy change that occurs in making a particular compound from its elements, where both the compound and elements are at standard conditions (25 C and 1 atm. pressure) and they are in their normal state (solid, liquid or gas) at these conditions. The heat of formation at standard conditions is denoted by ΔH_f^0 . The heat of formation is always given on a per mole basis, and its units are calories/mole, kilocalories/mole or joules/mole. By convention, the heat of formation of all free elements, when they are in their normal state at standard conditions, is zero. The heats of formation of compounds have been measured and tabulated, some of which are presented in Table 3.4. Examining this table, it can be seen that some of the heats of formation are positive and some are

Table 3.4 Heats of formation at standard conditions (25 C, 1 atm) for some explosives and their by-products [6].

Explosive	State	Molecular Mass	Heat of Formation, ΔH_f^0
Explosive			
Lead Azide	s	291	+112
Nitroglycerine	l	227.1	-88.6
PETN	s	316.2	-128.7
RDX	s	222.1	+14.71
TNT	s	227.1	-16.0
Explosive By-products			
CO	g		-26.4157
CO ₂	g		-94.0518
H ₂ O	g		-57.7979
H ₂ O	l		-68.3174
NO	g		+21.600
N ₂ O	g		+19.49
NO ₂	g		+8.091

negative. Positive heats of formation indicate the reaction is endothermic and negative negative heats of formation indicate it is exothermic.

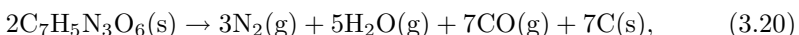
Knowing the standard heats of formation, the heat of reaction can be calculated at standard conditions. The heat of reaction at standard conditions is equal to the difference in the heat of formation of the products and that of the reactants:

$$\Delta H_r^0 = \sum \Delta H_f^0(\text{products}) - \sum \Delta H_f^0(\text{reactants}). \quad (3.18)$$

In the case of explosives, the energy released when it detonates is called the *heat of detonation* (ΔH_d^0) and is defined by the expression:

$$\Delta H_d^0 = \sum \Delta H_f^0(\text{detonation products}) - \sum \Delta H_f^0(\text{explosive}). \quad (3.19)$$

As for the heat of formation, if the heat of reaction is positive then the reaction is endothermic and if it is negative, the reaction is exothermic. In order to illustrate how the heat of reaction or detonation is calculated, consider the detonation of TNT. The chemical formula of TNT is C₇H₅N₃O₆ and it detonates according to the reaction:



where the letters enclosed in the parenthesis denote the state (g — gas, l — liquid, s — solid) of the particular chemical compound. The enthalpy of formation of a compound depends on its state. The formula for calculating

the heat of detonation for this reaction is:

$$\Delta H_d^0 = [3\Delta H_f^0(\text{N}_2) + 5\Delta H_f^0(\text{H}_2\text{O}) + 7\Delta H_f^0(\text{CO}) \\ + 7\Delta H_f^0(\text{C})] - 2\Delta H_f^0(\text{C}_7\text{H}_5\text{N}_3\text{O}_6). \quad (3.21)$$

Note that the coefficients from the balanced chemical equation are used in the formula for calculating the heat of detonation. Looking up the heat of formation of each compound in Table 3.4 and substituting these values into Eq. (3.21), the heat of detonation is calculated to be -494 kcal/mole . That is, the detonation of TNT generates 494 kcal of energy per mole of explosive.

As pointed out by Cooper [6], the composition of the products of real explosives, even when the same explosive is used from shot to shot, is not the same. The composition depends on a number of factors including:

- Initial density and temperature.
- Degree of confinement.
- Particle size and morphology.
- Dimensions and shape of the explosive charge, which affect the pressure and temperature behind the detonation front.
- Various equilibria among the product molecules.

Thus, the energy generated by an explosive will vary from the ideal values calculated in the above example when any of the above factors change.

3.3.1.4 *Chemical Kinetics*

Chemical kinetics is the study of the rate of change of chemical reactions in time. These reactions can be very fast — e.g. instantaneous reactions such as detonations, or very slow — e.g. rusting of iron. In explosive reactions, the rate of reaction is very fast and is dependent on the composition (in terms of the activation energy), temperature, pressure and concentration of the reactants.

Most chemical reactions require that energy be initially applied to start the reaction. This energy is called the *activation energy*. In the case of explosives, the activation energy is supplied by the detonator, which raises the temperature of hot spots. If the energy generated by these hot spots is less than the activation energy, no reaction takes place, but if it is greater than the activation energy then a chain reaction occurs (Fig. 3.15). The magnitude of an explosive's activation energy is a measure of the ease with

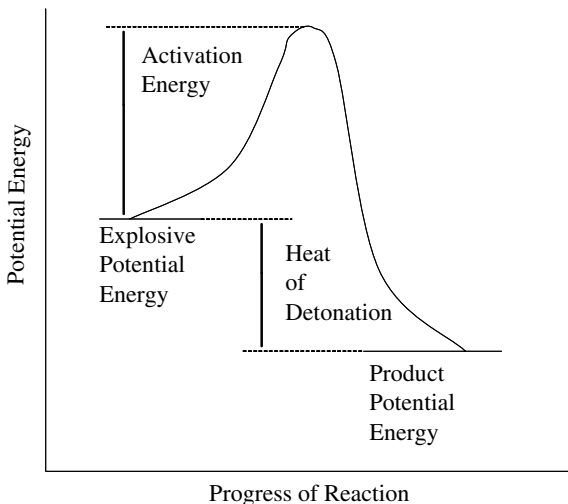


Fig. 3.15 If the energy generated by a chemical reaction is greater than the activation energy, a chain reaction, such as detonation, can occur.

which an explosive will initiate. The higher the activation energy, the more difficult it will be to initiate the explosive.

As noted above, the rate of reaction of an explosive depends on the magnitude of its activation energy and the temperature at which the reaction takes place. As the temperature is raised, an exponentially greater number of the molecules possess the necessary activation energy in the form of molecular kinetic energy. That is, the higher the temperature, the faster the molecules move, which means that more of them possess sufficient kinetic energy to break the chemical bonds of the reactants when they collide so that new bonds can form. The rate of reaction, therefore, increases exponentially as the temperature increases and is described by *Arrhenius's equation*:

$$k = Ae^{-E/RT}, \quad (3.22)$$

where k is the *rate constant*; A is a constant, called the *Arrhenius parameter* or *collision factor*, and is relatively independent of temperature, but is dependent on the chemical composition of the explosive; E is the activation energy in kJ/mole; T is the absolute temperature in degrees Kelvin and $R = 8.314 \text{ J mol}^{-1} \text{ K}^{-1}$ is the *universal gas constant*. The exponential, $e^{-E/RT}$, is a measure of the fraction of colliding molecules that chemically

Table 3.5 Activation Energy, E , and collision factor, A , for some primary and secondary explosives [6].

Explosive	Activation Energy (kJ/mole)	Collision Factor
Primary Explosives		
Mercury Fulminate	105	10^{11}
Silver Azid	167	
Lead Azide	160	
Secondary Explosives		
Nitroglycerine	167	10^{19}
PETN	196	$10^{19.8}$
RDX	199	$10^{18.5}$
Picric Acid	242	$10^{22.5}$
TNT	222	10^{19}
HMX	220	$10^{19.7}$

react. That is, if the activation energy is low; i.e. $E \rightarrow 0$, the exponential approaches unity, $e^{-E/RT} \rightarrow 1$, which implies that all the colliding molecules react. Conversely, if the activation energy is high, the exponential approaches zero, which implies that the colliding molecules do not react.

Primary explosives have low activation energies compared to secondary explosives. Therefore, it takes less energy to initiate a primary explosive, which makes it more sensitive to external stimuli and thus, more difficult to handle. The activation energy and collision factor for some explosives are presented in Table 3.5.

3.3.1.5 Factors That Affect Explosives

In addition to chemical composition, there are a number of other factors that affect the detonation properties of explosives. These include density, mixture composition, geometry, physical dimensions and temperature. These other factors are considered in this section.

Density It was shown earlier that the detonation pressure and detonation velocity are dependent upon the initial density of the unreacted explosives. When estimating the properties of explosives, calculations are usually based on the use of the Theoretical Maximum Density (TMD). The theoretical mass density is the maximum density that an explosive can have, which implies there are no voids or air pockets in the explosive and the explosive is uniformly distributed throughout its volume. Eremenko [10, 11] found that the TMD of an explosive can be estimated by using the following

simple linear relationship between the density and the hydrogen content of the substitute organic molecules:

$$\rho_{TMD} = a_i - k_i H, \quad (3.23)$$

where a_i and k_i are constants and H is the percent by mass of hydrogen in a molecule of the explosive. The values of a_i and k_i depend upon the structural group to which the explosive molecule belongs. Cooper [6] gives a detailed account of how to calculate the TMD.

Since the density of explosives affects its detonation velocity, an empirical relationship between the detonation velocity and the density of unreacted explosive that works for most explosives has been developed:

$$D = a + b\rho, \quad (3.24)$$

where a and b are empirical constants specific to each explosive and ρ is density. If the detonation velocity is known at one density, e.g., TMD, it can be found at a different density by using:

$$D_2 = D_1 - b(\rho_1 - \rho_2). \quad (3.25)$$

For most applications, the density only varies over a small range and the value of b can be assumed to be equal to 3. This value of b is the average value of b taken from data for a number of explosives. This approximation is normally good when the density of the explosive does not change by more than 10 to 15%. For example, if PETN has a detonation velocity of 8.29 km/s and a TMD of 1.77 g/cm³, its detonation velocity is 7.99 km/s when the density is 1.67 g/cm³. The measured detonation velocity at this density is 7.89 km/s, which means the error is 0.13%. The density and characteristic detonation velocity at TMD for several explosives is given in Table 3.6.

Composition The detonation velocity of a mixture, D_{mix} , of explosives can be calculated by using [6]:

$$D_{\text{mix}} = \sum D_i V_i, \quad (3.26)$$

where D_i is the detonation velocity at TMD of the individual explosives or the characteristic velocity of the nonexplosive components and V_i is the *volume fraction* of the component. This formula also works for mixtures with additional oxidisers, inert filters and voids. This is achieved by assigning an *equivalent characteristic velocity* to the nonexplosive components. The equivalent characteristic velocities of various fillers and oxidisers are given in Table 3.6.

Table 3.6 Density and characteristic detonation velocity at TMD for several explosives and additives [6].

Material	Density, ρ (g/cm ³)	Characteristic Velocity, D_{TMD} (km/s)
Pure Explosives		
HMX	1.90	9.15
RDX	1.81	8.80
TNT	1.654	6.97
PETN	1.78	8.59
Polymers and Plasticisers		
Beeswax	0.92	6.50
Kel-F Elastomer	1.85	5.38
Polyethylene	0.93	5.55
Polystyrene	1.05	5.28
Teflon	2.15	5.33
Inorganic Additives		
Air or Void	—	1.5
Al	2.70	6.85
KClO ₄	2.52	5.47
SiO ₂	2.21	4.0

Once the detonation velocity and density of an explosive or mixture of explosives are known, the Chapman–Jouguet (CJ) pressure, P_{CJ} , can be found by using:

$$P_{CJ} = \frac{\rho D^2}{\gamma + 1}, \quad (3.27)$$

where γ is the ratio of specific heats of the detonation product gases and the detonation pressure is in GPa, density is in g/cm³ and detonation velocity is in km/s. Since the composition of the detonation product gases of most explosives is fairly similar, the value of γ , when the explosive density is in the range from 1 to 1.8 g/cm³, is approximately 3.

Dimensions If a cylindrical column of explosive is detonated and its detonation velocity measured, it is found that this velocity changes as the diameter of the column changes. That is, the velocity decreases as the diameter of the column decreases. This is due to energy losses in the radial direction. When the diameter of the column is small, the energy losses in the radial direction are larger relative to the energy generated at the detonation front. A plot of the detonation velocity versus the reciprocal of the diameter, d , of a column of composition B is presented in Fig. 3.16. As $1/d$ approaches zero, the detonation velocity approaches that of a column

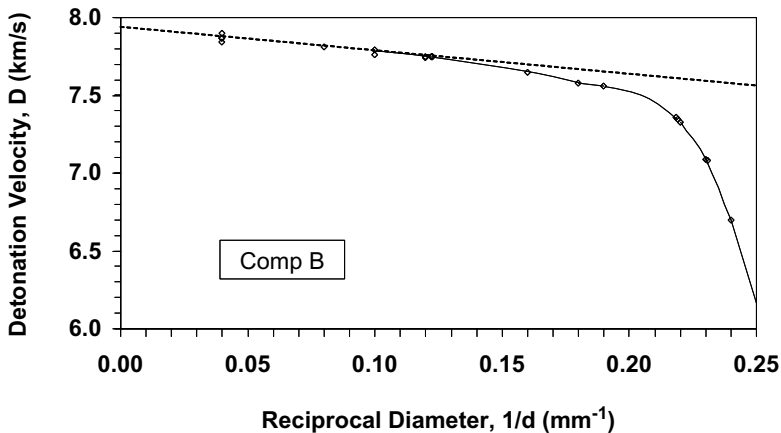


Fig. 3.16 Plot of the detonation velocity as a function of the reciprocal of the diameter of a column of composition B.

having infinite diameter (uniaxial). The detonation velocity at this point is called the *ideal detonation velocity* and is denoted by D_I . Knowing D_I , the velocity for composition B can be calculated for the linear portion of the curve by using:

$$\frac{D}{D_I} = 1 - a \frac{1}{d}, \quad (3.28)$$

where a is a constant and is the slope of the linear portion of the curve. The value of a varies from explosive to explosive and is different for the same explosive at different initial conditions, including temperature, density and particle size.

As noted by Cooper [6], when a cylindrical column of explosives is detonated at one end, the detonation grows spherically from a point. However, after the detonation front moves some distance along the column, the detonation wave ceases to grow spherically and maintains a constant radius of curvature. If the explosive charge is made larger, this transition point moves out further, but the ratio of the radius of curvature to charge diameter remains constant. This ratio has different values for different explosives. One of the implications of this is that the work done by the pressure at the end of the column of charge is not only a function of the pressure, but also of the ratio of the length, L , to the diameter, d , of the column. It has been found that as L/d increases, so does the effectiveness of the explosive.

However, at some maximum value of L/d , the effectiveness of the explosive stops increasing and levels off.

Temperature It has been found that raising the temperature of explosives actually lowers its CJ pressure and detonation velocity. This is due to the fact that raising its temperature causes it to expand, thus lowering its density. Since the detonation velocity is roughly linearly proportional to the density, decreasing the density decreases the detonation velocity. However, the required density will depend on the particular application for the explosive. For example, lower-density explosives are used to expand metal tubes, since more energy is transferred to the tube, due to its confinement of the explosive. But if the explosive is to be used to collapse metal tubes, a higher-density explosive is required, since it is applied as a layer to the outside surface of the tube, which means the confinement effect of the tube is gone and the inertia of the product gases confines the energy transfer to the tube. There is an optimal density for the explosive when used to implode metal tubes. If the density of the explosive is too low, its products, containing almost all the kinetic energy, will be transported into the environment at very high speeds. If it is too high, both the metal and the product gases will move slowly and less than an optimal fraction of the energy is transferred to the tube. Therefore, the optimal density for any particular application must be calculated.

3.3.1.6 Explosive Power

In an explosive reaction, heat and gases are generated that do work on their environment. Explosives are rated according to their explosive power; that is, they are rated as to whether they are low or high power. This is quantified by introducing the terms *explosive power* and *power index*. Explosive power is defined to be the product of the volume of gas, V , generated and the heat of detonation, which is designated by the symbol Q :

$$\text{Explosive Power} = Q \times V. \quad (3.29)$$

The value of the explosive power for a particular explosive is then compared to that of a standard, which is picric acid, to determine its power index:

$$\text{Power Index} = \frac{Q \times V}{Q_{\text{picric acid}} \times V_{\text{picric acid}}}. \quad (3.30)$$

Table 3.7 The power index of some primary and secondary explosives taking picric acid as the reference standard [6].

Explosive	Q kJ/g	V (dm ³ /g)	$Q \times V (\times 10^4)$	Power Index (%)
Primary Explosives				
Mercury Fulminate	1755	0.215	37.7	14
Lead Azide	1610	0.218	35.1	13
Secondary Explosives				
Nitroglycerine	6194	0.740	458.4	171
PETN	5794	0.780	451.9	167
RDX	5036	0.908	457.3	169
HMX	5010	0.908	454.9	168
TNT	4476	0.740	331.2	115
Picric Acid	3250	0.831	270.1	100

The power indexes of some primary and secondary explosives are presented in Table 3.7. Note that the explosive powers and power indexes of secondary explosives are much higher than those for primary explosives.

3.3.2 Explosive Train

Explosive systems use a number of explosive components in addition to the main charge. The *explosive train* consists of a fire set that provides the electrical current required to initiate the detonator, the cabling required to connect the fire set to the detonator, the detonator and the main explosive charge. *Detonators* are used to initiate detonation of the main charge. There may be *explosive lenses* or other configurations that are used to control the shape of a detonation wave. Explosive lenses produce plane waves at distances of from tens to hundreds of millimetres from a single initiation point. Converging cylindrical detonation waves and other configurations can also be produced. Explosive trains may also include *mild-detonating fuses*, a slender column of high explosive in a metal sheath and *explosive delay lines* [6]. Mild-detonating fuses can be used to propagate a detonation to an explosive driven switch or other device that may be located away from the main charge. Mild-detonating fuses are usually made with a small amount of explosive material and are confined in such a way that other materials and components are protected from any damage that the fuse might produce. Explosive delay lines are used to initiate a series of detonators at different times. By changing the length of the delay line to a given detonator, the

time it initiates can be controlled. Explosive delay lines are usually made from strips of Detasheet, which is a plastic explosive.

3.3.2.1 Detonators

Detonators can be classified as either non-electric or electric. Non-electric detonators are divided into four major categories: flame or spark, friction, stab and percussion. Electric detonators fall into three categories: hot-wire, exploding bridge wire (EBW) and exploding foil initiator (EFI). Electric detonators are universally used in explosive pulsed power systems. Of these, the EBW and the EFI are the safest, since unlike electric blasting detonators, which contain a primary explosive (lead azide), these detonators contain only secondary explosives (PETN). Therefore, they require higher currents and voltages to cause detonation, since the bridgewire or foil must be electrically exploded to generate the shock waves needed to initiate the secondary explosives.

Exploding bridgewire detonators (Fig. 3.17) are typically used to initiate the main charge by electrically vaporising (exploding) a thin gold or gold/platinum alloy wire (0.001 to 0.003 inches in diameter and 0.010 to 0.100 inches in length) in contact with a pellet of a granular secondary explosive such as PETN, which is usually pressed to a 50% granular density. Additional explosives may be included in the detonator to ensure that it provides a sufficiently strong stimulus to initiate the main explosive charge. For a bridgewire to explode, currents of several hundred amps to thousands of amps with a fast rise time (on the order of $200\text{ A}/\mu\text{s}$) are required. The energy needed to cause the bridgewire to explode must be delivered within a fraction of a microsecond. Normally, low-inductance, high-voltage capacitors are used in the fire sets for EBWs. The advantage of EBW detonators,

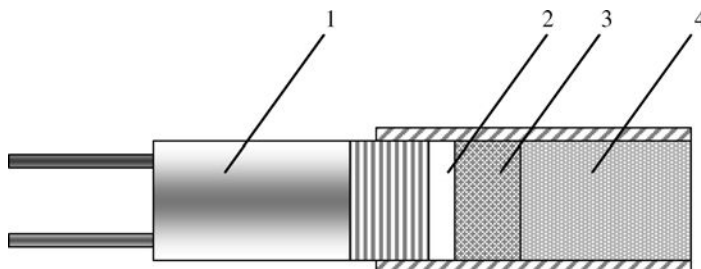


Fig. 3.17 Diagram of an exploding bridgewire (EBW) detonator: 1 — molded head, 2 — bridgewire, 3 — initiating explosive and 4 — high-density explosive.

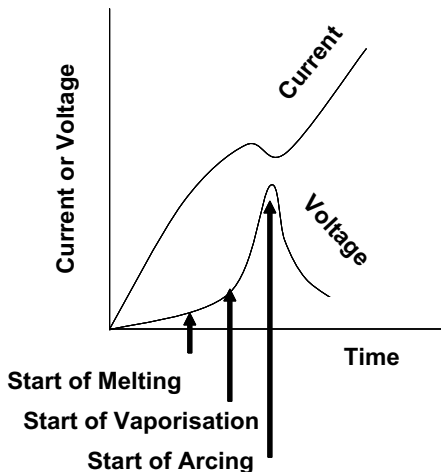


Fig. 3.18 Operation of the EBW occurs in three steps: melting, vaporisation and arcing.

in addition to greater safety, is their short initiation delay and their uniformity of performance. These latter characteristics facilitate their use in systems where precisely timed initiating stimuli must be provided at several different places in the system.

According to Cooper [6], when sufficient current flows through the EBW to cause the bridgewire to explode, the explosion process occurs in three steps (see Fig. 3.18). The first step is bridgewire heating to near its melting temperature. During this process, the resistance of the bridgewire also increases. The second step is bridgewire melting, which happens in such a short time that inertia prevents it from moving away from its initial location. As the temperature of the melted bridgewire continues to increase towards its vaporisation point, its resistance continues to increase. Upon vaporising, the resistance increases rapidly, which causes the current to suddenly decrease at this point. So much current is passing through the dense vapor, it continues to be heated. The third step is explosive expansion of the vaporised bridgewire material. As a stable electric arc forms in the expanding metal vapor, the resistance drops and the current increases, thus driving the metal vapor shock even harder. This entire process takes only tens of nanoseconds.

As suggested by the description in the previous paragraph, the resistance of the EBW is extremely nonlinear during its detonation process. Its resistance starts out very low, milliohms to tens of milliohms, increases

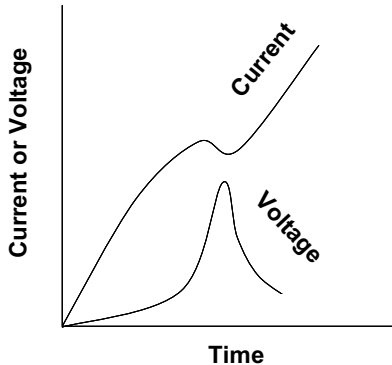


Fig. 3.19 The dynamic resistance of an EBW.

until it peaks at a maximum value of a few ohms, and then decays to a value higher than its original value [6, 12]. This resistance change is illustrated in Fig. 3.19. The dynamic resistance must be accounted for in any mathematical analysis of the EBW.

Since the bridgewire explosion occurs so fast, there is no appreciable heat transfer. Thus, the energy required to bring the bridgewire to a critical explosion state is a constant [6, 12]. The energy balance for the EBW can thus be written as

$$I^2 R(E) dt = m dE \quad (3.31)$$

where $R(E)$ is the dynamic resistance of the bridgewire, m is its mass and E is energy. The dynamic resistance of the bridgewire includes both the resistance change due to its change in temperature and that due to its change in state. The resistance of the wire is equal to the resistivity, $\gamma(E)$, of the wire times its length, L , and divided by its cross-sectional area, A :

$$R(E) = \frac{m A dE}{A}. \quad (3.32)$$

The mass of the bridgewire is equal to its density, ρ , times its volume, which is the product of the length of the wire and its cross-sectional area:

$$m = \rho A L. \quad (3.33)$$

Substituting these definitions into Eq. (3.31) yields

$$I^2 dt = \rho A^2 \frac{dE}{\gamma(E)}. \quad (3.34)$$

Integrating from the start of current flow to the time at which the bridge bursts yields the following equation

$$\int_0^{t_b} I^2 dt = \rho A^2 \int_0^{E_b} \frac{dE}{\gamma(E)}, \quad (3.35)$$

where t_b is the bridgewire burst time and E_b is the bridgewire burst energy. The integral on the right-hand side of the equation can, for all practical purposes, be considered to be a constant that depends only upon the material from which the bridgewire is made [6]. Since the density of the bridgewire depends only upon the type of material used and since the cross-sectional area of the bridgewire is directly proportional to the square of its diameter, several factors in Eq. (3.46) can be lumped together to yield the expression

$$\int_0^{t_b} I^2 dt = K_b D^4, \quad (3.36)$$

where D is the diameter of the bridgewire and K_b is a constant, called the *burst action coefficient*, which depends only on the type of material used to make the bridgewire. The integral on the left-hand side of this equation is called the *burst action* and it is designated by the symbol G_b and is a function of the properties of the bridgewire material and its diameter:

$$G_b = K_b D^4. \quad (3.37)$$

The burst action is equal to the area under the current squared versus time curve in Fig. 3.20, which is bounded by the time period ranging from start of current flow to burst time. Attainment of burst does not depend on the

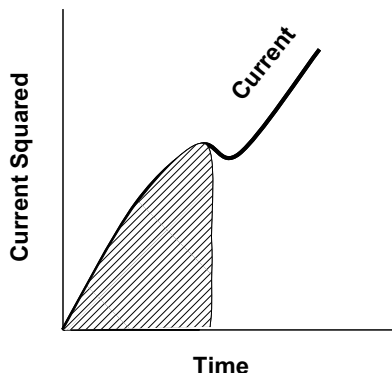


Fig. 3.20 The burst action is equal to the area under the current squared vs. time curve.

shape of the current pulse, but rather on time and current. As Cooper [6] points out, attainment of bridgewire burst is a necessary, but not sufficient condition to form a shock that will cause the EBW explosive charge to detonate.

An analytical expression for G_b was derived by Tucker [12]. Assuming that the firing circuit is an LRC circuit, the following differential equation can be written

$$L \frac{dI}{dt} + I(R(E) + R) + \frac{1}{C} \int I dt = 0, \quad (3.38)$$

where L , R and C are the circuit inductance, resistance and capacitance, respectively. The dynamic resistance of the bridgewire, although relatively high at its peak value ($\sim 10 \Omega$), is usually negligible compared to the overall circuit resistance and thus, can be neglected. If $R(E)$ is not negligible, then Eq. (3.38) must be solved numerically. Neglecting $R(E)$, the analytical solution of Eq. (3.38) is

$$I = \frac{V_0}{L\omega} e^{-(Rt/2L)} \sin(\omega t), \quad (3.39)$$

where V_0 is the initial voltage on the capacitive discharge unit and

$$\omega = \sqrt{\left(\frac{R}{2L}\right)^2 - \frac{1}{LC}}. \quad (3.40)$$

Squaring the current in Eq. (3.39), substituting it into Eq. (3.36) and integrating with respect time yields the following expression for G_b :

$$G_b = A \left(\frac{2L\omega^2}{R} \left[1 - \exp\left(-\frac{Rt_b}{L}\right) \right] - B \right), \quad (3.41)$$

where

$$A = \frac{V_0^2}{L\omega[(R/L)^2 + \omega^2]}$$

and

$$B = \left[\left(\frac{R}{L} \right) \sin \omega t_b + 2\omega \cos \omega t_b \right] \exp\left(-\frac{Rt_b}{L}\right) \sin \omega t_b.$$

Assuming $L = 1.0 \mu\text{H}$, $R = 1.0 \Omega$, $C = 1.0 \mu\text{F}$ and $V_0 = 2.0 \text{kV}$, then $G_b = 0.11 \text{ A}^2\text{s}$ for a gold bridgewire with a diameter of 1.5 mil.

If it is further assumed that the input current to the bridgewire is a 'ramp' with a rise time equal to that of the current pulse in the LRC

circuit, then

$$I = \frac{V_0}{L} t \quad (3.42)$$

and

$$G_b = \left(\frac{V_0}{L} \right)^2 \frac{t_b^3}{3}. \quad (3.43)$$

Substituting Eq. (3.43) into Eq. (3.42), the burst current of the bridgewire is found to be

$$I_b = \sqrt[3]{\frac{3V_0 G_b}{L}}. \quad (3.44)$$

Note that the burst current is directly proportional to the cube root of the product of the initial capacitor voltage and the burst action, and is inversely proportional to the cube root of the circuit inductance.

In order for the EBW explosive charge to detonate, a critical energy fluence must be exceeded. The pressure and duration of the shock wave generated by the bursting bridge is a function of the burst current (or peak burst power). Thus, there is a minimum current below which the initial pressing of explosive in the EBW will not detonate. This *minimum burst current* (or *threshold burst current*) is not only dependent upon the properties of the bridgewire, but also upon the properties (density, particle size and specific surface area of the particles) of the explosives used in the EBW [6]. For a EBW loaded with PETN, Cooper gives the following expression for the minimum burst current:

$$i_{bth} = 850D/L^{1/2}. \quad (3.45)$$

If the bridgewire has a length, L , of 40 mil (0.040 inches) and diameter, D , of 1.5 mil (0.0015 inches), the minimum burst current is ~ 200 A. The properties of some commercial EBWs are provided in Table 3.8.

In summary, two criteria must be met in order to ensure detonation of the explosive charge in an EBW. First is attainment of the bridgewire's burst action, which depends on the type of bridgewire material used and its diameter. Second is attainment of the minimum burst current, which depends on the bridge's dimensions, the properties of the explosive charge and the fire set's electrical parameters.

Table 3.8 Properties of some commercial detonators produced by RISI.

Name of Explosives	Bridgewire Diameter (mils)	Bridgewire Length (mils)	PETN Mass (mg)	RDX Mass (mg)	Threshold Burst Current (A)
RP-1	1.5	40	251	375	190
RP-2	1.5	30	32	18	220
RP-80	1.5	40	80	123	180
RP-81	—	—	80	450	180
RP-87	1.5	20	26	43	210

3.3.2.2 Fire Set and Cabling

The *fire set* is an electronic device which discharges a pulse of electric current into a firing circuit containing the detonators. The critical factor in the design of fire sets and their transmission cables is that they deliver sufficient energy levels at sufficient rates to the bridgewire to ensure that it will reliably detonate the *initial pressing* of PETN in the detonator. The fire set most commonly used with EBWs is a *capacitive discharge unit* (CDU). It consists of a prime power source (batteries or the power grid), voltage converter that converts AC current to DC and that up-converts the voltage, a high voltage storage capacitor and a triggered switch that switches the stored energy into the firing circuit at the proper time. For engineering applications, the CDU should

- Fire reliably.
- Generate reproducible output current waveforms.
- Minimise prefireing.
- Trigger precisely and reproducibly with a short delay time.
- Initiate a variety of detonator combinations, including firing through relatively long firing lines.

The maximum current and the rise time of the current discharge is limited by the impedance of the fire set itself. Thus, for a given charge voltage on the CDU, the lower its internal impedance, the higher its maximum discharge current will be. In addition, the rate at which the electrical energy is deposited in the bridgewire — i.e. the di/dt , is proportional to the voltage and inversely proportional to inductance:

$$\frac{di}{dt} \propto \frac{\text{voltage}}{\text{inductance}}. \quad (3.46)$$

This means that the higher the voltage and/or the lower the inductance of the firing circuit, the shorter the rise time of the current. Since most fire sets operate at fixed voltages, this means that only the inductance can be varied. This is why the type, length and electrical properties of the cabling used to connect the fire set to the detonator must be taken into account.

According to Cooper [6], the impedance characteristics of some typical CDUs are (see Table 3.9):

- Capacitance: $1\text{--}10 \mu\text{F}$.
- Resistance: $50\text{--}150 \text{ m}\Omega$.
- Inductance: $50\text{--}150 \text{ nH}$.

The impedance characteristics of some common EBW cables are listed in Table 3.10. The impedance of these cables is a function of both their construction and their length. Comparing the impedance values of these cables with those of the fire sets, it can easily be seen that if the cable is too long, its impedance will exceed that of the fire set. Therefore, the cabling is ultimately the limiting factor in determining the current level and rise time at the detonator input.

3.4 Interaction of Detonation Waves with Materials

3.4.1 Impedance

When an explosive is in contact with another material, the detonation wave, which is itself a shock wave, interacts with the surface of the material and generates a shock wave within it. The degree of this interaction depends

Table 3.9 RISI capacitive discharge units. Type 'C' cable is a high voltage coaxial cable and twin lead blasting wire is a high voltage cable with a Polyethelene insulator.

Fire Set	Output V, I	Output Energy	Maximum Distance from Fire Set to Explosive Charge (ft)	
			Twin Lead Blast Wire	Type 'C' Cable
FS-9	3000 V, 1000 A	4.5 J	100	300
FS-61B	4000 V	—	100	300
FS-17	4000 V, 1500 A	8.0 J	100	300
FS-43	4000 V, 1500 A	8.0 J	100	300
FS-62B	4000 V	—	100	300

Table 3.10 Impedances of Common EBW Detonator Cables [6].

Cable Type	Resistance (mΩ/ft)	Capacitance (pF/ft)	Inductance (Hn/ft)	Approximate Transmission Time (ns/ft)
C	10	50	66	1.5
L	50	30	90	1.5
RG-213	3	30	80	1.5
No. 20	20	20	200	1.7

on the *shock impedance*, Z , of the explosive and of the material. The shock impedance of a material is defined to be the product of its initial density and the shock velocity, U , within it:

$$Z = \rho_0 U. \quad (3.47)$$

The shock impedance of the explosive products is defined to be the initial density of the unreacted explosive and the detonation velocity:

$$Z_{\text{det}} = \rho_0 D. \quad (3.48)$$

From the momentum equation

$$P = \rho_0 u U = Z u, \quad (3.49)$$

where u is the particle velocity, it can be seen that the shock velocity increases as the pressure increases. However, although the impedance also increases, it does so rather slowly, which implies that it can be treated as a constant within reasonable ranges. The impedance is sufficiently constant to allow a differentiation between low impedance and high impedance materials. When a shock wave passes from a low impedance material into a high impedance material, the shock pressure increases and vice versa.

Therefore, when the explosive products of detonation interact with the surface of a material, two possible cases must be considered: when the impedance of the material is greater than that of the explosive and when the impedance of the explosive is greater than that of the material. When $Z_{\text{material}} > Z_{\text{det}}$, the detonation produces a shock pressure at the interface that is higher than the CJ pressure that propagates into the material and a shock wave that propagates into the explosive products (Fig. 3.21). When $Z_{\text{material}} < Z_{\text{det}}$, the detonation produces a shock pressure at the interface lower than the CJ pressure and a partial rarefaction wave is reflected back into the compressed reaction product gases.

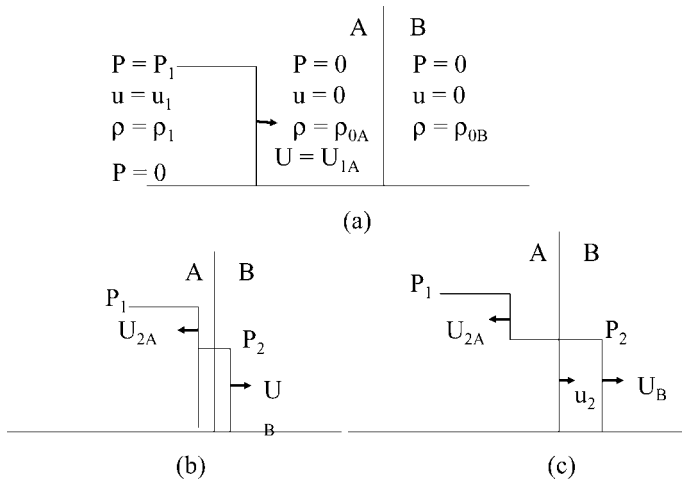


Fig. 3.21 In (a) the shock wave is moving through material A (the explosive) toward the interface with material B. (b) When the impedance of the material is greater than that of the explosive, the detonation shock produces shock waves at the interface that propagate both into the material and the explosive products. (c) When the impedance of the explosive is greater than that of the material, a partial rarefaction wave is reflected back into the compressed reaction product gases.

3.4.2 Gurney Equations

Measures of the output of explosives are usually based upon the strength of the shock wave or the chemical energy content of the explosive, which depend on such quantities as detonation velocity, CJ pressure or heat of detonation [13]. These quantities provide an understanding of the relative output of one explosive in comparison to another, but do not provide a measure of how fast an explosive can, for example, drive a metallic armature in an FCG. In the 1940s, R.W. Gurney at the US Army Ballistic Research Laboratories in Aberdeen, MD proposed two assumptions that would facilitate estimating the terminal velocity of explosively driven fragments. These assumptions are now referred to as the *Gurney Model*.

This model was based upon the energy and momentum balances and was devised to calculate the velocities of fragments from explosive-metal systems of widely varying sizes and proportions. As noted by Zukas and Walters [14], shock waves play a very important part in the transfer of energy from the detonation of confined explosives to its surrounding metallic case, and Gurney's assumptions provided a way of mathematically tracing the various components of the device. Gurney assumed that:

- The detonation of a given explosive releases a fixed amount of energy per unit mass and that this energy is converted into the kinetic energy of the driven material (the armature in the FCG) and the detonation product gases.
- The product gases have a uniform density and a linear one-dimensional velocity profile in a spatial coordinate system.

The Gurney model may be applied to any explosive-metal system with a cross-section that undergoes one-dimensional translational motion in a direction perpendicular to its surface, regardless of the direction of motion of the detonation wave. The *Gurney energy*, E , in kcal/g, is assumed to be that energy converted from chemical energy in the initial state to kinetic energy in the final state. This kinetic energy is partitioned between the metal and the detonation product gases. It is also assumed that the velocity of the metal is constant throughout its thickness and that the velocity of each metal and gaseous element is normal to the axis. Using these assumptions, an energy balance can be written for any simple symmetric geometry, which can be integrated to provide an analytical expression for the final velocity of the metal in terms of the Gurney energy and the ratio of the total mass of the metal, M , to the total mass of the explosives, C .

The terminal velocity of the metal depends on the geometry of the device and whether the device is explosive or implosive. In order to understand this relationship, consider the cylindrical shell filled with high explosives in Fig. 3.22. It is assumed that the velocity of the gases that result from

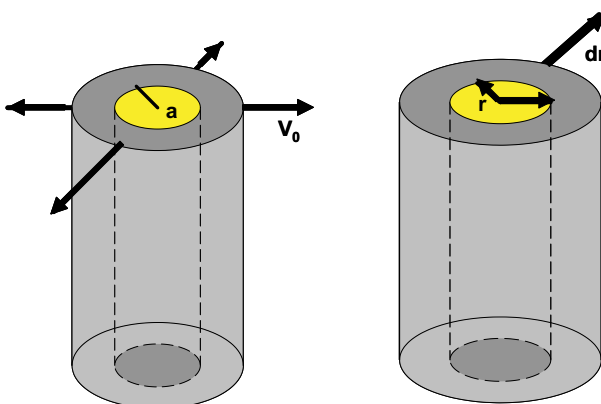


Fig. 3.22 Diagrams (a) of a cylindrical shell filled with high explosives and (b) of an element of gaseous by-product of the explosive.

the detonation vary linearly from the core to the outside of the explosive cylinder. In order to simplify the analysis, wave propagation effects, energy consumption by deformation and fracture, and the fact that the detonation starts at one end of the cylinder and moves along the axis of the cylinder are ignored. Assuming that the inner radius of the cylinder is a , that its radius is r at some given point in time during expansion and that the velocity varies linearly, the velocity of the cylinder is given by:

$$V = V_0 \frac{r}{a}, \quad (3.50)$$

where V_0 is the initial velocity of the cylinder and V is the velocity of the cylinder after expanding to a radius of r .

Assuming that the shell does not fragment, the total kinetic energy (KE) is equal to the kinetic energy of the cylindrical shell and the kinetic energy of the gases generated by the explosives:

$$KE = \frac{1}{2}MV_0^2 + \frac{1}{2} \int V^2 dm_g, \quad (3.51)$$

where M is the mass of the cylindrical shell and m_g is the mass of the gaseous products. Assuming the gases take on a tube-shape and selecting an increment of this tube, the mass of this element of gas is

$$dm_g = \rho dV = 2\pi r \rho dr, \quad (3.52)$$

where ρ is the density of the explosives. Substituting Eqs. (3.50) and (3.52) into Eq. (3.51) yields:

$$\begin{aligned} KE &= \frac{1}{2}MV_0^2 + \frac{1}{2} \int_0^a V_0^2 \frac{r^2}{a^2} 2\pi r \rho dr \\ &= \frac{1}{2}MV_0^2 + \frac{1}{4}\pi V_0^2 a^2 \rho. \end{aligned} \quad (3.53)$$

Since $\rho = C/\pi a^2$, where C is the mass of the explosive charge, this equation becomes:

$$KE = \frac{1}{2}MV_0^2 + \frac{1}{4}CV_0^2. \quad (3.54)$$

Equating this kinetic energy to the chemical energy of the explosive (E) and rearranging, an expression for the initial velocity of the cylinder can be found:

$$V_0 = \sqrt{2E} \left(\frac{M}{C} + \frac{1}{2} \right)^{-\frac{1}{2}}. \quad (3.55)$$

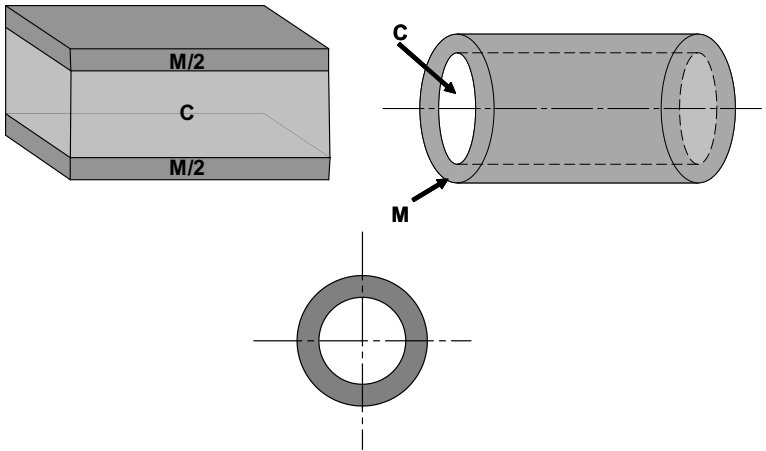


Fig. 3.23 Simple symmetric geometries used to derive the Gurney equations: (a) planar, (b) cylindrical and (c) spherical.

This equation is called the *Gurney equation*, which relates the velocity of the cylinder to the ratio of the masses of the cylinder and of the explosive charge. The factor $\sqrt{2E}$ always appears in the Gurney equations. Since this factor has the dimensions of velocity, it is known as the *Gurney characteristic velocity*, or simply *Gurney velocity*, for a given explosive. The velocity for other geometries can be similarly derived. The initial velocity for a flat sandwich geometry (Fig. 3.23a) is

$$V_0 = \sqrt{2E} \left(\frac{M}{C} + \frac{1}{3} \right)^{-\frac{1}{2}} \quad (3.56)$$

and that for a spherical geometry (Fig. 3.23b) is

$$V_0 \sqrt{2E} \left(\frac{M}{C} + \frac{3}{5} \right)^{-\frac{1}{2}}, \quad (3.57)$$

where the above equations were derived for exploding systems. Similar equations can be derived for imploding systems, but they tend to be more complicated. The equations for imploding cylindrical and spherical geometries, as well as for asymmetric explosive-metal configurations, are presented in [13]. As a rule of thumb, LANL has found that the assumption that the gurney velocity is one-third that of the detonation velocity of the explosives to be a good approximation.

3.4.3 Taylor Angle Approximation

In deriving the Gurney equations, it was assumed that the detonation wave and thus, the metal, moves in a direction normal to its surface. This is not the case for end initiated helical FCGs, where the detonation wave encounters the metal cylinder at a grazing incidence angle. In order to model the expansion of the armature in the helical FCG, another model, called the *Taylor Angle Approximation*, must be used.

In Fig. 3.24, a detonation wave is moving parallel to the surface of a metal plate. As a result, the plate is deflected an angle θ , the Taylor angle,² from its original position. It is assumed that the metal plate achieves its final velocity instantaneously and that it undergoes pure rotation — i.e. there is no shear flow or changes in the length or thickness of the plate.

Referring to Fig. 3.24, the end of the deflected plate element that was initially at P will be at P' after it is launched. Since it is assumed that the length of the plates do not change, the lengths \overline{OP} and $\overline{OP'}$ will be the same — i.e. $\overline{OP} = \overline{OP'}$. A line drawn from O perpendicular to $\overline{PP'}$, bisects angle θ and line $\overline{PP'}$, since OPP' is an isosceles triangle. If the time t is measured from the time the detonation wave passes point P , the lengths of the lines can be related to the detonation velocity, D , of the explosive and

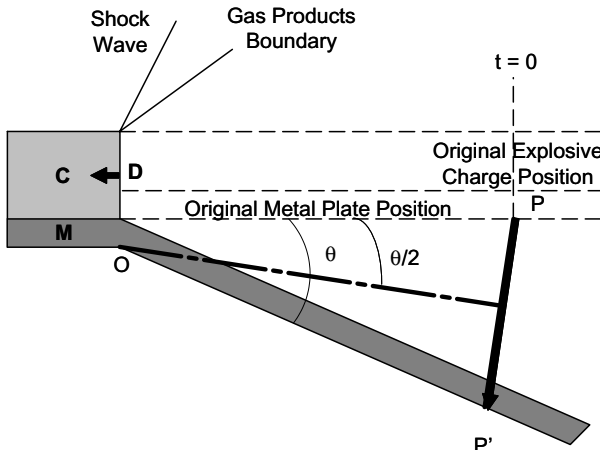


Fig. 3.24 Taylor angle approximation.

²Neuber [15] calls this angle the Gurney angle, but the traditional name in the explosives community is Taylor angle.

the velocity, V , of the deflected metal plate:

$$\overline{OP} = Dt \quad (3.58)$$

$$\overline{PP'} = Vt. \quad (3.59)$$

Since the line from O that bisects the line $\overline{PP'}$, the resulting right triangle can be used to relate the deflection angle to V and D :

$$\sin \frac{\theta}{2} = \frac{\overline{PP'}/2}{\overline{OP}} = \frac{Vt}{2Dt} = \frac{V}{2D}. \quad (3.60)$$

The velocity V can be estimated by using the Gurney equations.

3.5 Summary

In this chapter, attention was focused on

- Shock and detonation waves and their characteristics.
- Explosives, their chemical and thermodynamic properties, those factors that affect their effectiveness and those components needed to properly utilise them.
- How explosives and shock waves interact with materials.

Armed with this knowledge, we can now better understand what is required to design explosive pulsed power generators. When designing explosive pulsed power generators, several things must be taken into account:

- Shape of the shock wave in order to yield optimal performance — e.g. in FEGs.
- Shock pressures needed to generate a desired effect.
- Detonation velocity, which depends on the type of explosive used and its properties such as density, diameter, since a minimum diameter is needed to maintain detonation and composition, if there is a need higher for CJ pressures.
- Effective initiation system.
- Shock impedance matching — e.g. in FEGs and FMGs to ensure effective depolarisation.
- Interaction of the explosive and shock waves with materials, since these interactions determine the expansion angle in FCGs and effective coupling in FEG and FMG.
- Calculations of parameters such as the Taylor angle in FCGs.

Bibliography

- [1] M. B. Boslough and J. R. Assay, *High-Pressure Shock Compression of Solids*, eds. J. R. Assay and M. Shahinpoor (Springer-Verlag, New York, 1993), pp. 7–42.
- [2] D. S. Drumheller, *Introduction to Wave Propagation in Nonlinear Fluids and Solids*, Cambridge University Press, Cambridge (1998).
- [3] R. Cheret, *Detonation of Condensed Explosives*, Springer-Verlag, New York (1993).
- [4] R. Engleke and S. A. Sheffield, *High-Pressure Shock Compression of Solids III*, eds. L. Davison and M. Shahinpoor (1998), pp. 173–239.
- [5] J. Akhavan, *The Chemistry of Explosives*, Thomas Graham House, Cambridge (1998).
- [6] P. W. Cooper, *Explosives Engineering*, Wiley-VCH, New York (1996).
- [7] W. Fickett and W. C. Davis, *Detonation: Theory and Experiment*, Dover Publications, Inc., Unabridged Edition, New York (2001).
- [8] C. M. Fowler W. B. Garn and R. S. Caird, Production of Very High Magnetic Fields by Implosion, *Journal of Applied Physics* **31**(3) (1960) 588–594.
- [9] W. C. Davis, High Explosives: The Interaction of Chemistry and Mechanics, *Los Alamos Science* **2**(1) (1981).
- [10] L. E. Eremenko, Interrelationship Between Density and Structure in Explosives, *Proceedings of the 11th Symposium on Explosives and Pyrotechnics*, Philadelphia (1981).
- [11] L. E. Eremenko, Density Calculation of Aromatic Crystals Using Their Structure, *Proceedings of the 8th International Pyrotechnics Symposium*, Colorado (1982).
- [12] T. J. Tucker, Explosive Initiators, *Proceedings of the 12th Annual Symposium of the New Mexico Section of the ASME* (Albuquerque, NM, 2–3 March 1972).
- [13] M. A. Meyers, *Dynamic Behavior of Materials*, Wiley-Interscience, New York (1994).
- [14] *Explosive Effects and Applications*, eds. J. A. Zukas and W. P. Walters, Springer-Verlag, New York (1998).
- [15] A. Neuber, *Explosively Driven Pulsed Power: Helical Magnetic Flux Compression Generators*, Springer, Berlin (2005).

This page intentionally left blank

Chapter 4

Measurement Techniques

The physics of explosive pulsed power is a blend of detonics and electromagnetism. *Detonics* is the science of detonation that provides information about the performance of explosives and the energy transformation processes that occur in generators. *Electromagnetism* complements detonics by providing information about the ultrahigh electric and magnetic fields and the electric currents and voltages generated during these energy transformation processes. Thus, a mix of diagnostic tools is needed when testing explosive pulsed power systems.

In explosive pulsed power, a wide spectrum of measurements must be made, usually under very harsh conditions generated by the explosives. In addition, the generation of very high voltages, currents and fields tends to complicate these measurements. Therefore, this chapter focuses on various techniques currently used to diagnose the behavior of explosive pulsed power systems and to measure their output. Thus, attention is focused on two broad categories of measurements: those associated with the measurement of very high voltages, currents and fields and those associated with diagnosing the detonation process.

4.1 High Power Electrical Measurements

In explosive pulsed power experiments, the most common electrical parameters measured are voltage and current from which power and energy can be calculated. Since these generators tend to produce very high peak values (kiloamps to megamps, kilovolts to megavolts) and their pulse lengths and rise times tend to be very short (subnanoseconds to many microseconds), the methods ordinarily used to measure these electrical parameters are no longer adequate to make accurate measurements. In this section,

several techniques for measuring all four of these parameters will be briefly discussed.

In general, the following instruments are needed to make electrical measurements: oscilloscopes, current monitors, high voltage monitors and probes, attenuators, resistors, capacitors and coaxial cables. How these devices are used will become apparent as the various measurement techniques introduced in this section are described.

4.1.1 *Voltage Measurements*

Several techniques for measuring high voltage have been developed and they include the resistive voltage divider, the capacitive voltage divider and the optical voltage monitor. Each technique has its advantages and disadvantages, which will be discussed along with its principles of operation.

4.1.1.1 *Resistive Voltage Divider*

Due to its simplicity and its wide range of applicability, the *resistive voltage divider* is probably the most widely used device for making voltage measurements. These dividers have several advantages including easy construction, less noise and simple electrical properties. The basic circuit diagram for an ‘ideal’ voltage divider is shown in Fig. 4.1. The voltage divider consists of two branches — i.e. a high-voltage branch with resistor R_1 and a low-voltage branch with resistor R_2 . The voltage across the low-voltage branch, R_2 , is measured directly and the unknown voltage across the high-voltage

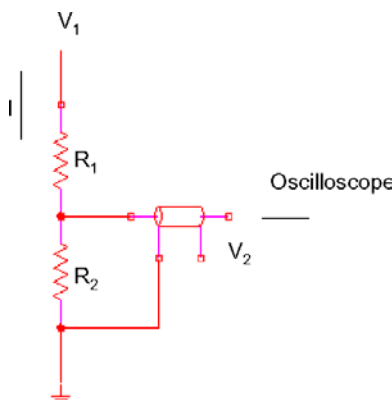


Fig. 4.1 Resistive voltage divider.

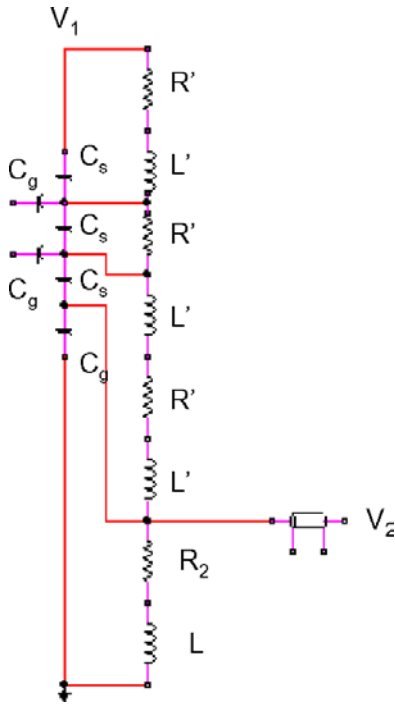


Fig. 4.2 Resistive voltage divider with stray inductances and capacitances.

branch, R_1 , is calculated by using the formula

$$V_2 = \frac{R_2}{R_1 + R_2} V_1. \quad (4.1)$$

The circuit diagram for a more realistic voltage divider is presented in Fig. 4.2. It includes inductances and stray capacitances, which cannot be ignored. Since solving this circuit can be rather tedious, it is initially assumed that the stray capacitances are negligible and that the equivalent circuit diagram becomes that shown in Fig. 4.3. Solving this circuit, the relationship between the measured voltage V_2 and the unknown voltage V_1 is

$$V_2 = \frac{V_1 R_2}{R_1 + R_2} \left[1 - \exp\left(-\frac{R_1 + R_2}{L_g} t\right) \right], \quad (4.2)$$

where L_g is the total inductance of the circuit. From this equation, it can be seen that the greater the value of $L_g/(R_1 + R_2)$ in the exponential term, the greater the original waveform of the unknown voltage is distorted.

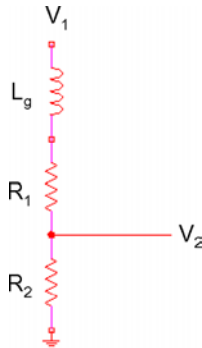


Fig. 4.3 Resistive voltage divider taking into account stray inductances, but not stray capacitances.

Therefore, it is essential that the circuit inductance be kept as small as possible. According to Pai and Zhang [1], this can be accomplished by using liquid or film resistors in the high-voltage branch. They point out that the general rule for designing resistive voltage dividers with inductance is that the following condition should be met

$$\frac{L_g}{R_1 + R_2} < \frac{t_r}{20}, \quad (4.3)$$

where t_r is the rise time of the unknown voltage pulse that is to be measured.

Now let's consider the case where the circuit inductance is negligible, but the stray capacitances are not. For this case, the circuit diagram now becomes that shown in Fig. 4.4. Solving this circuit, the relationship

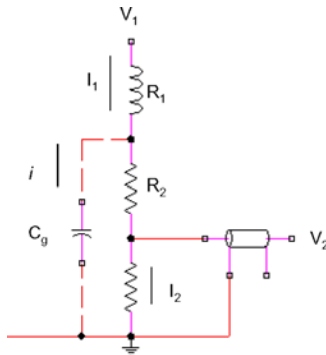


Fig. 4.4 Resistive voltage divider taking into account stray capacitance, but neglecting stray inductance.

between the measured voltage V_2 and the unknown voltage V_1 is

$$V_2 = \frac{V_1 R_2}{R_1 + R_2} \left[1 - 2 \sum_{n=1}^{\infty} (-1)^n \exp\left(-\frac{n^2 \pi^2}{C(R_1 + R_2)} t\right) \right], \quad (4.4)$$

where C is the total stray capacitance between the voltage divider and the ground plane. Since stray capacitances are always present in real circuits, the rise time of the measured voltage pulse is always greater than that of the actual pulse. According to Pai and Zhang [1], the general rule for designing resistive voltage dividers with stray capacitance is that the following condition be met

$$C(R_1 + R_2) < \frac{t_r}{0.23}. \quad (4.5)$$

Minimising the inductance and stray capacitances to meet the two conditions in Eqs. (4.3) and (4.5) will yield a practical voltage divider with minimal measurement error.

Self capacitance of the divider elements tends to give rise to unwanted distortions at the beginning of the output signal (overshoot or undershoot), and stray capacitance tends to reduce the frequency bandwidth of the divider. The stray capacitance, or leakage current, is due to the electric lines of force between the probe and the earth. In order to reduce the distortions caused by self capacitance and stray capacitance, two modifications to the resistive voltage divider have been proposed. The first was to add a self-compensating circuit to nullify the self capacitance and the second was to employ electric field contouring and matching methods to minimise the stray inductance.

Another source of error in making voltage measurements with a resistive voltage divider is the impedance mismatch at the input and output ends of the cable connecting the divider to, for example, an oscilloscope. If the impedance at the two ends of the cable are not properly matched, the voltage pulse will be reflected. Superimposing the original pulse on to the reflected pulse may seriously distort the waveform of the original pulse. These mismatches can be reduced by either connecting a parallel resistor at the input end of the measuring device (Fig. 4.5) or a series resistor at the output end of the divider (Fig. 4.6). In Fig. 4.5, the resistor R_0 should have a value identical to the characteristic impedance of the cable, Z_0 . In Fig. 4.6, the resistor R_m should have a value that meets the condition $R_2 + R_m = Z_0$. When $R_m \geq Z_0$, the series connection is not needed.

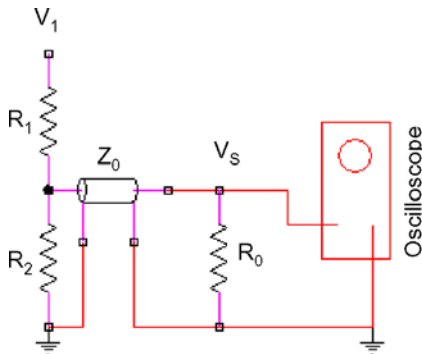


Fig. 4.5 Resistive voltage divider with resistance connected in parallel to the measuring device to reduce mismatches.

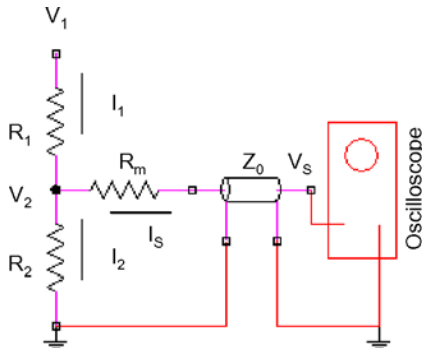


Fig. 4.6 Resistive voltage divider with a series resistor at the output end of the voltage divider to reduce mismatches.

The relationship between the measured voltage V_S and the unknown voltage V_1 for the parallel connection case in Fig. 4.5 is

$$V_S = V_1 \frac{R_2 R_0}{R_1 R_2 + R_1 R_0 + R_0 R_2}. \quad (4.6)$$

The relationship between the measured voltage V_S and the unknown voltage V_1 for the series connection case in Fig. 4.6 is

$$V_S = V_1 \frac{R_2}{R_1 + R_2}. \quad (4.7)$$

Generally, the parallel connection in Fig. 4.5 is preferable because it is simpler to implement.

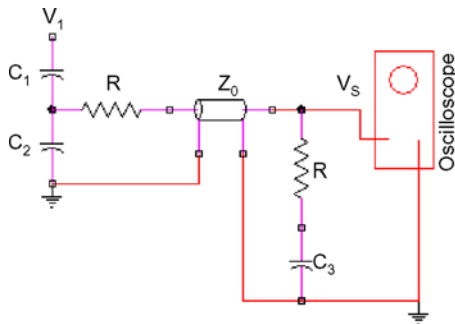


Fig. 4.7 Capacitive voltage divider.

4.1.1.2 Capacitive Voltage Divider

The basic structure of the *capacitive voltage divider* (Fig. 4.7) is quite similar to that of the resistive voltage divider with the exception that the resistors are replaced with capacitors. As in the case of the resistive voltage divider, the capacitive voltage divider has a high-voltage branch with capacitor C_1 and a low-voltage branch with capacitor C_2 . Since C_1 is usually much smaller than C_2 , the total capacitance of the capacitive voltage divider is $C \approx C_1$, where C_1 is usually a few picofarads. One of the advantages of the capacitive voltage divider is that its small capacitance draws very little current from the main circuit, thus having practically no effect on it. Other advantages are its responsiveness and its wide bandwidth. Its main disadvantage is its susceptibility to undesirable oscillations at its output, which are caused by the presence of inductances in the circuit. Thus, low-inductance capacitors should be used. Another disadvantage is RC coupling, which causes the output voltage to decay exponentially. This problem can be prevented by designing the circuit so that $R = Z_0$ and $C_1 + C_2 = C_3 + C_k$, where Z_0 is the impedance of the coaxial cable and C_k is the stray capacitance in the circuit. The relationship between the measured voltage V_S and the unknown voltage V_1 is

$$V_S = V_1 \frac{C_1}{2(C_1 + C_2)}. \quad (4.8)$$

Capacitive voltage dividers are frequently used to measure pulses generated by systems capable of producing peak powers on the order of a terawatt and pulse lengths of 10 to 100 ns, since they are immune to interference caused by the strong electromagnetic fields produced by these systems.

4.1.1.3 Optical Voltage Monitors

The previous two methods for measuring voltage do so by consuming a small amount of the power generated by the explosive generator. For instance, the resistive voltage divider draws a small amount of current from the generator in order to measure its output. Instead of measuring the voltage directly, it is possible to measure it indirectly by measuring changes in the properties of some materials induced by electric and magnetic fields. One family of techniques relies on electric and magnetic field induced changes in the optical properties of certain materials. This family includes those techniques based on the Kerr, Pockels and Faraday effects. All of these techniques are based on the use of materials that rotate polarised light when the material is subjected to electric or magnetic fields. The amount of rotation depends on the strength of the electric and magnetic fields generated. The *Kerr effect* is the anisotropic change in the index of refraction of light in response to an electric field. The degree of rotation of polarised light passing through a Kerr type material is proportional to the square of the electric field strength. The *Pockels effect* is the linear change in the index of refraction that is proportional to the electric field strength. The *Faraday effect* is a magnetic effect, where the degree of rotation of polarised light is proportional to the magnetic field strength. The advantages of these measurement techniques are immunity to electromagnetic interference, high sensitivity and small size.

Attention is focused on the Pockels cell, since it is capable of measuring voltages up to 1 MV, when it is capacitively coupled. The optical and electrical arrangement described by Pai and Zhang [1] is shown in Fig. 4.8. The high voltage, V_0 , to be measured is capacitively coupled from the transmission line to the Pockels cell via an antenna, A. The crystals used in Pockels cells are typically potassium dihydrogen phosphate (KDP), deuterated KDP (KD*P) and lithium niobate (LiNbO_3), since they exhibit large Pockels effects. The sensor unit is passive and is connected to the laser detector unit by optical fibers, so that the detector is totally isolated from the high-voltage source.

According to Pai and Zhang [1], if the Pockels cell is placed between crossed polarisers and a quarter wavelength plate, the input intensity, J_0 , of the laser light is related the cell's output intensity, J , by the formula

$$J = J_0 \sin^2 \frac{\pi}{2} \left(\frac{V}{\beta} + \frac{1}{2} \right), \quad (4.9)$$

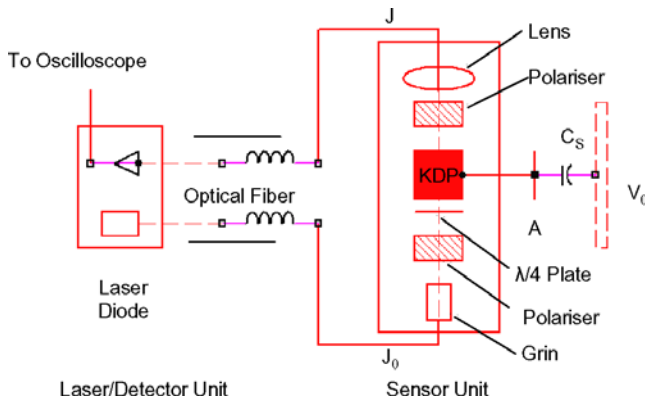


Fig. 4.8 Optical voltage monitor based on the Pockels cell.

where $\beta = \lambda/(2n_0^3\gamma_{63})$ is a constant that depends on the wavelength λ and where n_0 and γ_{63} are optical constants associated with the particular crystal used. The relationship between the measured voltage V and the unknown voltage V_0 is

$$V = V_0 \frac{C_s}{C_s + C_p}, \quad (4.10)$$

where C_p is the capacitance of the Pockels Cell and C_s is the capacitance between the high-voltage conductor and the antenna. By measuring the intensity of the light passing into and out of the crystal and by using Eq. (4.9), the voltage V can be calculated, which is then used to calculate V_0 by using Eq. (4.10).

4.1.2 Current Measurements

Several techniques for making high current measurements have been developed and include the pure resistance shunt method, Rogowski coil, Pearson current monitor, current viewing monitor, cavity current monitor and magneto-optical current monitor. Each technique has its advantages and disadvantages, which will be discussed along with their principles of operation.

4.1.2.1 Pure Resistive Shunt Method

The pure resistive shunt method is used to measure high peak pulse currents when highly accurate measurements and the simplest calibration procedures

are desired. This method is capable of subnanosecond rise time responses. It has added advantages in that it is only responsive to the current that flows through it and that its calibration is independent of its location in the circuit carrying the current to be measured. Some disadvantages are that it does absorb some of the energy from the circuit carrying the current to be measured and that a means must be designed to either nullify or avoid sensing any significant self-inductive voltage drops across the shunt's resistive element and any voltage induced due to mutual field coupling between the current bearing circuit and the shunt's sensing circuit. The latter is necessary in order to maintain a simple relationship between the current bearing circuit and the shunt sensing circuit — i.e. the resistance of the shunt.

The pure resistive shunt method consists of a specially designed resistive shunt inserted into the circuit carrying the current to be measured. The current is measured by measuring the voltage drop across it. Shunts are designed to sense only the noninductive resistive voltage drop across the resistive element. The measured voltage drop is in phase with, and is directly related to the current pulse passing through the shunt resistance. The pulse width response is limited by the energy deposition in the shunt. If the amount of energy deposition must be increased, then the length, diameter and resistive film thickness of the shunt element must be increased, which also lengthens the rise time response of the resistive shunt circuit. Small shunts are used to measure fast rising pulses and large shunts are used to measure large currents — i.e. hundreds of kAs to MAs.

4.1.2.2 *Rogowski Coil*

The *Rogowski coil* is a field coupled sensor capable of measuring current pulses with amplitudes of several hundred kiloamperes and rise times of a few nanoseconds. As can be seen in Fig. 4.9, it consists of a helical coil of wire formed into a loop to form a torus with the lead from one end passing back through the center of the coil to the other end, so that both terminals are at the same end of the helical coil. A conductor carrying the unknown current that is to be measured passes through the loop. The magnetic field generated by the unknown current induces a weak current in the Rogowski coil, which is measured directly. The voltage induced in the Rogowski coil is directly proportional to the rate of change of the unknown current. In other words, the Rogowski coil is similar to a transformer in



Fig. 4.9 Rogowski coils.

that the cable carrying the unknown current acts like a single turn primary and the Rogowski loop acts like the secondary.

A device similar to the Rogowski coil was first described by Chattock [2] in 1887, but it was Rogowski and Steinhaus [3], who first used it to measure electric current. It is widely used today, because it [4, 5]:

- Has a very wide bandwidth.
- Has the capability of measuring high currents with exceedingly fast rise times. The same size coil can measure currents ranging from 100 A to 100 kA.
- Has no saturation limits, since the coil is not damaged by over current.
- Provides its own isolation.
- Is easy to use, since the coil can be relatively thin and flexible.
- Does not intrude on the circuit it is measuring, since there is no discernible loading of the circuit carrying the unknown current and since the impedance it introduces into the circuit is typically a few picohenrys.
- Has very good linearity, since no magnetic materials are used.
- Does not require that the coil be circular or that the cable carrying the unknown current be centrally located within the loop.
- Can be easily built in the laboratory.
- Is expendable, since it is not expensive to build.

Depending on its design and how it is used, the Rogowski coil can be used to measure either the magnitude and the shape of a pulse, if an integrator is used, or the time rate of change of the unknown current [1]. Figure 4.10 shows the equivalent circuit diagram for a Rogowski circuit. The governing

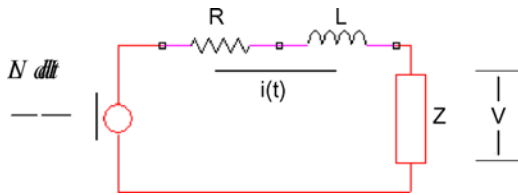


Fig. 4.10 Equivalent circuit diagram of a Rogowski circuit.

equation for the voltage drop around the circuit is

$$\frac{L}{N} \frac{dI}{dt} - L \frac{di}{dt} - (R + Z)i = 0, \quad (4.11)$$

where I is the unknown current, i is the current induced in the Rogowski coil, N is the number of turns in the Rogowski coil, R is the resistance of the Rogowski coil and Z is the signal impedance.

Passive Rogowski Coil Techniques: According to Pai and Zhang [1] and Ray and Hewson [5], there are three passive methods by which the Rogowski coil can be used to measure current.

Self-Integrating Rogowski Coils: If the rise time, t_c , of the unknown current, I , is such that

$$t_c \ll \frac{L}{R + Z}, \quad (4.12)$$

or $L/(R + Z)$ is greater than the current pulse length, then the third term of Eq. (4.11) can be neglected and it reduces to

$$V = iZ = \frac{I}{N}Z. \quad (4.13)$$

The voltage is directly proportional to the current, thus the name *self-integrating Rogowski coil*. If N is large and Z is small, this particular design can be used to measure fast rising, high amplitude current pulses by measuring the voltage V across the impedance Z .

These coils have a number of advantages including the output voltage being essentially frequency independent, the rise time of a symmetrically excited coil being limited by the external circuit parameters or the transit time through a single minor winding turn in the coil, insensitivity to electron impact or photo induced currents, and less cable attenuation of the signal from the coil, since the output of the coil is proportional to the current rather than the time derivative of the current.

Passive Differentiating or L/R Rogowski Coils: If the rise time is such that

$$t_c \gg \frac{L}{R + Z}, \quad (4.14)$$

or $L/(R+Z)$ is much shorter than the current pulse length, then the second term in Eq. (4.11) can be neglected and it reduces to

$$V = iZ = \frac{LZ}{N(R + Z)} \frac{dI}{dt}. \quad (4.15)$$

The voltage is linearly proportional to dI/dt , thus the name *differentiating Rogowski coil* or *I-dot probe*. This arrangement allows one to measure the rate of change of current in time.

The advantages of this type of Rogowski coil are its simple construction and its capability to generate a high output voltage for a given coil area. Its disadvantages are that it can generate high output voltages that are frequency dependent and that its output signal may be attenuated by the coaxial cables connecting it to the oscilloscope, it can generate an integrated signal with a rise time no faster than $L/(R+Z)$ and sometimes much slower, it can generate high voltages that can over-volt the coil or other components and its output is sensitive to electron impact that can cause changes that are integrated.

Passive Integrating RC Rogowski Coil: If a capacitor is added in series to the impedance Z in the circuit in Fig. 4.10, then Eq. (4.11) becomes

$$\frac{L}{N} \frac{dI}{dt} - L \frac{di}{dt} - (R + Z)i - \frac{1}{C} \int i dt = 0. \quad (4.16)$$

Assuming that the condition given in Eq. (4.14) holds and that C is sufficiently large, the second and fourth terms in Eq. (4.16) can be neglected and the voltage V_c across the capacitor can be found by using the expression

$$V_c = \frac{1}{C} \int i dt = \frac{LI}{NC(R + Z)}. \quad (4.17)$$

By measuring the voltage across the capacitor and using Eq. (4.17), the amplitude and shape of the unknown current can be determined. The addition of the capacitor makes the output voltage directly proportional to the current and not the derivative of current. This circuit is referred to as a

passive RC integrator. It has a disadvantage in that its response time is usually slow due to its large RC constant.

Active Integrating Rogowski Coils: At low frequencies (50–60 Hz), the coil voltage is typically very small — i.e. on the order of a few $\mu\text{V/A}$, unless the coil is exceptionally sensitive. Therefore, electronic integration must be used.

The *active integrating Rogowski current sensor* consists of three components [6]. The first is the Rogowski coil, where the output voltage at its open terminals is proportional to the time derivative of the current flowing in a conductor passing through the coil. The second element is the integrator that integrates the output voltage of the Rogowski coil. The integrator usually consists of three elements, an input resistor, feed back resistor that reduces DC drift and integration capacitor. Integration of the Rogowski coil's output does not usually pose a problem when there is no DC component, the current is sufficiently large and the Fourier frequency components of the current lie above a certain minimum value [6]. A third element is a circuit with an operational amplifier that resets the integrator to zero when the current being measured goes to zero. Resetting the integrator prevents the integration of the integrator's offset voltages and biases from growing too large.

There are two types of operational amplifiers used in active integrating Rogowski coils: inverting and non-inverting. Figure 4.11 shows a Rogowski circuit with a conventional inverting integrator. The resistor R_0 , which is part of the integrating circuit, is connected to the end of the cable that is connected to the Rogowski coil to reduce the cable capacitance, which could reduce the bandwidth of the coil. The Rogowski coil is terminated with the

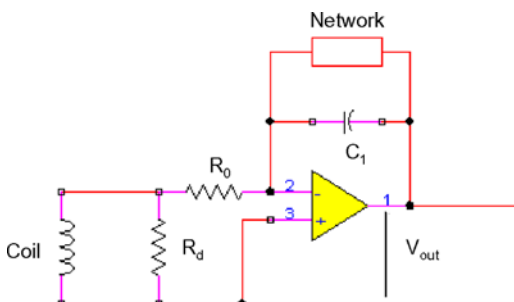


Fig. 4.11 Rogowski circuit with inverting integrator.

damping resistor R_d . The damping resistance is greater than the characteristic impedance of the coil, since it has been found that the Rogowski circuit will yield a better transient response for step changes in the measured current. The value of the resistance R_0 is generally much greater than that of R_d . The main disadvantages of using inverting operational amplifiers are the generation of high frequency ringing and opposite polarity pre-shoot that are superimposed on the output waveform following a transient change in the measured current. The high frequency oscillations are due to the interaction of the cable dynamics with that of the operational amplifier. In order to reduce the magnitude of the ringing and the pre-shoot, a filter may be added to the transducer output, but this will significantly reduce the bandwidth, which could otherwise be achieved.

Figure 4.12 shows a Rogowski circuit with a non-inverting operational amplifier. At high frequencies, the integration is done by the passive R_0C_0 network and the operational amplifier acts as a unity gain amplifier. At low frequencies, the passive R_0C_0 network has unity gain and the integration is done by the operational amplifier, which has an integration time constant of R_1C_1 . The advantages of the non-inverting integrator are that there is no capacitive coupling from the non-inverting amplifier to the output, thus eliminating the pre-shoot effect and the need for an output filter, and that the dynamics of the cable and the R_0C_0 network are de-coupled from the

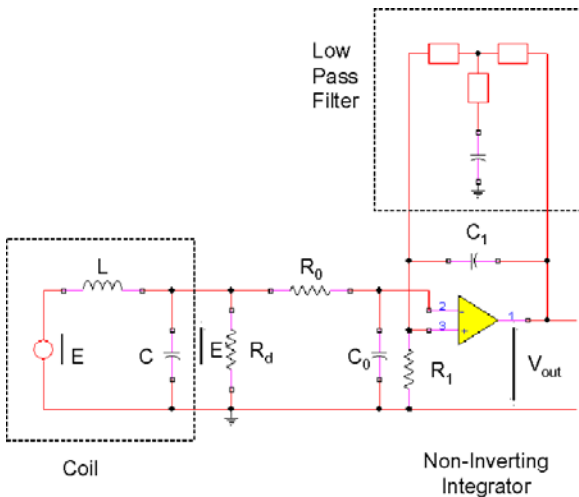


Fig. 4.12 Rogowski circuit with non-inverting operational amplifier.



Fig. 4.13 Pearson coil.

dynamics of the operational amplifier by its high input impedance, thus eliminating the source of oscillations, provided the coil and cable are properly terminated. The disadvantages of the non-inverting integrator are the need for three stages of integration (two passive and one active), which requires accurate matching of two sets of circuits with different time constants, thus making set-up and calibration difficult; L/r integration of the higher frequencies, which could lead to high frequency oscillations and improper termination of the Rogowski coil; the impossibility of correctly terminating both the Rogowski coil and the connecting cable, since they have widely differing characteristic impedances and limited bandwidth.

4.1.2.3 Pearson Current Monitor

Pearson Current Monitors [13] are current monitoring transformers with ferromagnetic cores that were originally developed by Pearson Electronics, Inc. in the 1950s to measure pulse currents, but are now widely used today to measure more complicated transients and periodic signals with frequencies ranging from a few hertz to several megahertz. When using a Pearson current monitor, typically an oscilloscope and a coaxial cable with an impedance of 50 ms are all that are required to make current measurements. Like the Rogowski coil, the conductor carrying the unknown current is passed through a hole in the Pearson current monitor, which is connected to the oscilloscope via a coaxial cable. The voltage waveform displayed on the oscilloscope will be a faithful reproduction of the unknown current waveform within the limitations of the rise time and droop specified

for the particular model of Pearson current monitor used. The amplitude of the voltage displayed on the oscilloscope will be linearly proportional to the amplitude of the unknown current. The current can be found by knowing the sensitivity in volts per ampere of the oscilloscope. The rise time (10–90%) of these monitors typically ranges from 2 to 100 ns and the droop values typically ranges from 0.1% per microsecond to 0.5% per millisecond. The advantages of the Pearson current monitor are its physical isolation from the circuit under test, which eliminates ground currents, and that it can be used at low sensitivity without ringing, both of which are encountered when using current viewing resistors.

4.1.2.4 Current Viewing Resistor

When the current from an explosive generator flows through certain resistive materials, the voltage drop across these materials can be measured. This voltage can then be used to calculate the current by using Ohm's law. If this resistive material is used in a device as shown in Fig. 4.14, then it is called a *Current Viewing Resistor* (CVR). Current viewing resistors are rugged high frequency resistors designed to sustain very high peak powers and currents. Inherent to CVR design is the coupling between their major electrical parameters — i.e. resistance, band pass, energy capacity and wattage rating, which makes it possible to design them to cover a broad range of specifications.

An example of a current viewing resistor is the tubular or coaxial CVR shown in Fig. 4.14. A cavity filled with resistive material and covered with a thin foil is located on the outer conductor. When a current I flows through

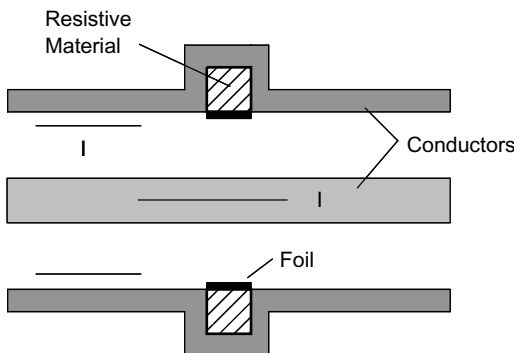


Fig. 4.14 Current viewing resistor.

the conductor, a voltage drop forms across the resistive material, which is measured. If the inner radius of the resistive material is r , its outer radius is a , and its length is l , then, according to Pai and Zhang [1], the current can be calculated by knowing the measured voltage and using the formula

$$V = \frac{I\eta l}{\pi^{3/2} a \delta \tau^{1/2}} e^{-1/4\tau}, \quad (4.18)$$

where $\delta = a - r$, $\tau = \eta t / (\mu \delta^2)$, t is time and η and μ are the resistivity and permeability of the resistive material respectively. The CVR is typically a four-terminal device so that the contacts for the measuring equipment are independent of the current carrying elements. One disadvantage is that when they are connected directly to high voltage, high current sources, they are susceptible to electromagnetic interference.

4.1.2.5 Cavity Current Monitor

The basic structure of the *Cavity Current Monitor* (CCM) is similar to that of the CVR in that cavities are machined into the current carrying conductors. The difference is that the cavities in the CVR are filled with a resistive material, whereas in the CCM the cavities are empty. Because of the presence of the resistive material, the operation of the CVR is based on Ohm's law; whereas the operation of the CCM is based on Faraday's law.

In the CCM, a resistor is connected across the cavity. The resistor leads connected to the cavity walls form a closed loop that serves as a magnetic pickup coil. When current flows through the conductor, a voltage drop develops across the cavity that corresponds to the rate of change of magnetic flux in the cavity. An array of magnetic pickup loops is usually used to sample the changes in flux at different locations along the current path in the cavity. The signals picked up by each coil are combined by delivering them through cables, having the same length, to a summing circuit. The output of the summing circuit is then integrated using a passive RC integrator to yield a signal proportional to the unknown current being measured. According to Pai and Zhang [1], the voltage output from the passive integrator is given by

$$V = \frac{1}{RC} \frac{\mu_0 A I}{(N + 1) \Delta l}, \quad (4.19)$$

where A is the cross-sectional area of the pickup loop, Δl is the distance between the coils, RC is the time constant of the integrator and N is the number of loops used. The CCM is easy to construct, simple to operate and

can measure current pulses with amplitudes ranging up to megamps and rise times of subnanoseconds.

4.1.2.6 Magneto-Optical Current Sensor

Operation of the *magneto-optical current sensor* is based on Faraday rotation. It consists of a glass bar inserted into a single-loop coil on the conductor carrying the current to be measured and placed between a polariser and an analyser oriented at an angle of $\pi/4$ relative to each other. When linearly polarised light of intensity J_0 passes through the glass, its intensity changes due to the rotation of its polarisation vector. According to Pai and Zhang [1], the angle the polarisation vector rotates is related to the current by the expression

$$\theta = KV_c I \quad (4.20)$$

where K is a calibration factor that must be determined experimentally and V_c is the Verdit constant of the glass used. The intensity of the light at the analyser is

$$J = J_0 \alpha (1 + \sin 2\theta) \quad (4.21)$$

where α is the attenuation coefficient and must be determined experimentally. Using Eqs. (4.20) and (4.21) and the measured intensity J , the unknown current I can be determined. Due to their electrical isolation and electromagnetic noise immunity, the magneto-optical current sensor generally yields much cleaner results.

4.1.3 Power and Energy Measurements

In addition to knowing the currents and voltages generated by pulsed power systems, it is often desirable to know how much power and energy they generate, as well as their impedance. Direct measurement of power, energy and impedance is generally not necessary, since they can be calculated from the measured values of the time dependent current and voltage by using the following relationships:

$$\text{Power } P(t) = V(t)I(t) \quad (4.22)$$

$$\text{Energy } E(t) = \int_0^t V(t)I(t)dt \quad (4.23)$$

$$\text{Impedance } Z(t) = V(t)/I(t). \quad (4.24)$$

4.2 Pulsed Electric and Magnetic Field Measurements

The sensors used to measure electric and magnetic fields can be separated into four classes: antennas, current monitor transformers, B-dot (or surface current) probes and D-dot (or surface charge) probes. In addition to these traditional sensors, other types of sensor based on new principles are being developed. One such sensor is a fast pulsed magnetic field sensor based on thin polycrystalline films. A brief description of each class of sensor will now be provided.

4.2.1 B-Dot Probes

The B-dot probe (Fig. 4.15) measures the time derivative of the tangential component of a magnetic field at the surface of a conductor. This is equivalent to measuring the time rate of change of the surface current per unit length, where the unit length is perpendicular to the direction of current flow. B-dot sensors consist of a cylindrical loop. The basic principle behind B-dot probes is that a time varying magnetic field induces a current in the conducting coil. The output voltage from the coil is proportional to the cross-sectional area of the coil, the number of turns in the coil and the temporal characteristics of the magnetic field:

$$V = A \cdot \frac{dB}{dt},$$

where A is the equivalent area of the sensor in m^2 , B is the magnetic flux density in Teslas and V is the output voltage from the sensor. Integration of the output voltage from the B-dot probe yields the time-averaged magnetic field value.



Fig. 4.15 EG&G multi-turn loop or B-dot free field sensor.

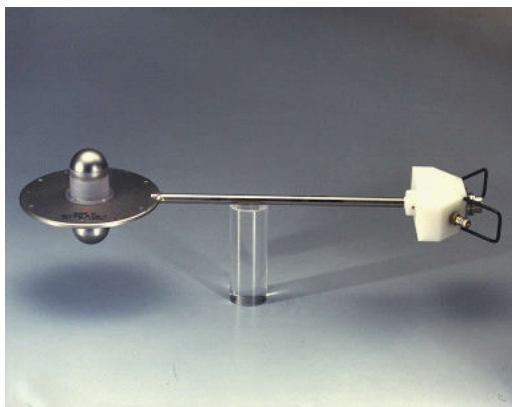


Fig. 4.16 EG&G asymptotic conical dipole or D-dot free field sensor.

4.2.2 *D-Dot Probes*

The D-dot probe (Fig. 4.16) measures the time derivative of the normal component of an electric field at the surface of a conductor. This is equivalent to measuring the time rate of change of the surface charge density.

The D-dot sensor consists of two conductive hemispherical shells mounted on opposite sides of a conductive base plate by means of dielectric spacers. In a time varying electric field, current is generated on each shell. This current is then picked off each shell with 200Ω strip lines, which are connected to a 100Ω output cable at the center of the sensor. The output voltage, V , of the sensor is

$$V = RA \frac{dD}{dt},$$

where R is the characteristic impedance of the sensor (100Ω), A is the equivalent area of the sensor in m^2 and D is the magnitude of the electric displacement in coulombs/ m^2 .

4.2.3 *Current Monitor Transformer*

The current monitor transformer is used to measure the total current flowing through a conductor. Changing electric and magnetic fields can induce currents in conductors. Like the B-dot sensor, the current monitor transformer senses the magnetic field, not current, generated by these induced currents. One type of current monitor transformer is the Pearson current

monitor, which has been previously discussed. It should be noted that the output of the current monitor transformer is proportional to the total current, not its time derivative as in the case of the B-Dot probe.

4.2.4 Antennae

There is a wide choice in antenna types and sizes, so there is considerable flexibility in choosing the type best for measuring a particular parameter. Most antennae tend to be monochromatic — i.e. they tend to operate best at one frequency determined by the dimensions of the antenna. However, the transient signals produced by explosive pulsed power systems tend to be broadband — i.e. radiating multiple frequencies at the same time. So, if possible, one would like to use a broadband antenna. Some antennae that have been used in explosive pulsed power tests will be discussed below.

4.2.4.1 Dipole Antenna

The dipole antenna is a monochromatic antenna — i.e. its length determines which wavelength it will receive. It consists of a conductor split at its center (see Fig. 4.17). Output transmission lines are attached to the two conductors at the center of the antenna. This is called a center-fed dipole antenna. The antenna in Fig. 4.17 is horizontally polarised, so their orientation is important when making measurements. The half-wavelength version of the dipole antenna tends to have a figure-eight radiation pattern with the maximum fields being perpendicular to the antenna and the nulls being at the ends of the antenna. These antennae are sensitive to ground reflections, because the interaction between the ground and the antenna depend on antenna height, frequency, ground conductivity and dielectric constant. For example, as the antenna's height decreases, its radiation pattern tends to shift from a figure-eight pattern to a more omnidirectional pattern with significant radiation at the ends of the antenna.

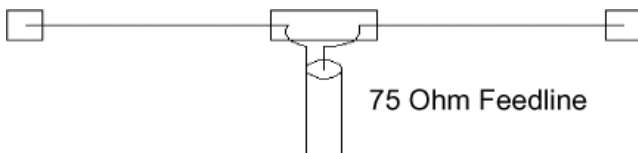


Fig. 4.17 A schematic diagram of a simple half-wave dipole antenna.

4.2.4.2 Monopole Antenna

The monopole antenna is also a monochromatic antenna. It consists of a quarter wavelength vertical conductor connected to its recording equipment by a coaxial cable (see Fig. 4.18). Typically, the center conductor of the coaxial cable is attached to the base of the antenna and its outer conductor is grounded. Thus, the earth serves as an image conductor, in which case, the monopole acts as a vertically polarised dipole with an omnidirectional radiation pattern in the horizontal plane.

4.2.4.3 Log Periodic Antenna

The log periodic antenna is a pseudo frequency independent antenna. It consists of a parallel array of center-fed half-wavelength dipoles, which are fed 180 degrees out of phase (see Fig. 4.19). The dipole lengths increase along the length of the antenna, which means each dipole is designed to receive a different wavelength. For an incoming broadband signal, the most efficient reception occurs at that dipole in the array that corresponds to a half wavelength of that which it is designed to receive. The longer element behind a particular dipole acts as a reflector, whereas the shorter dipole just in front of the particular element acts like a director. Other dipoles in the antenna are not of the proper length to be in resonance. The bandwidth of the antenna is roughly bounded by the wavelengths equal to twice the dipole lengths at the two extreme ends of the log periodic antenna.

4.2.4.4 Vivaldi Antenna

The Vivaldi antenna is a coplanar broadband antenna. It consists of a metallised dielectric sheet (usually PCB) with copper sheets cut to the desired

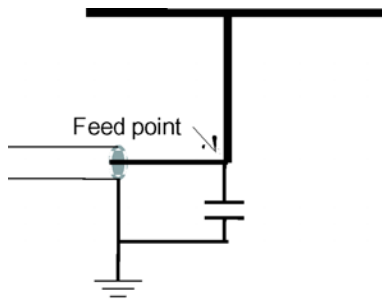


Fig. 4.18 A schematic diagram of a T-monopole antenna.



Fig. 4.19 Log periodic Antenna (from Wikipedia, the free encyclopedia).

shape and plated on both of its sides. The shape of the flare of the antenna determines most of its antenna characteristics. Vivaldi antennas are linearly polarised. Since the Vivaldi antenna is exponentially tapered, an infinitely long antenna with this shape would be essentially frequency independent. At a given wavelength, only a specific section of the exponential will actually radiate or receive efficiently. As the wavelength is changed, the radiation will occur from a different section, which is scaled in proportion to that wavelength. The bandwidth of the Vivaldi antenna is limited by the physical size of the antenna. The feed of the Vivaldi antenna determines its high-frequency limit and the aperture determines its low-frequency limit. The Vivaldi antenna is capable of producing a symmetrical radiation pattern even though it is a planar structure. The proper taper can provide an almost constant beam width over a very wide frequency band. The gain of the antenna is proportional to its length.

Vivaldi antennae have several advantages including being broadband, which means they are suitable for receiving ultra wideband signals, easy and inexpensive to construct, and easy to impedance match to their output circuit. Because of these advantages, these antennae are ideal as expendable broadband antennae for explosive pulsed power experiments. One such antenna that has been used in explosive pulsed power tests is shown in Fig. 4.20.

4.2.5 Thin Film Sensors

There has been recent work [7, 8] to develop pulsed magnetic field sensors that operate at room temperature and can measure relatively high



Fig. 4.20 Vivaldi antenna (courtesy of A.H. Stults, Army Aviation and Missile Research, Development and Engineering Center).

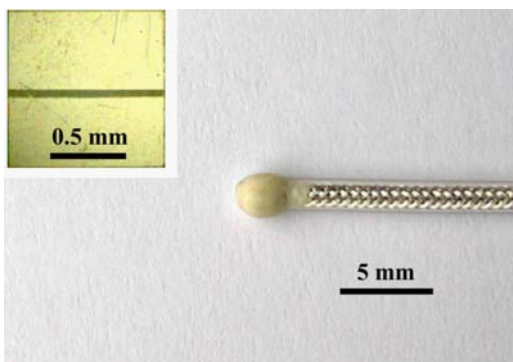


Fig. 4.21 Picture of colossal magnetoresistance (CMR) sensor with cable. A view of the die of the sensor is shown in the inset (courtesy of Saulius Balevicius and Nerija Zurauskienė, Semiconductor Physics Institute, Vilnius, Lithuania).

magnetic fields (10–20 T) with long pulse lengths (milliseconds). One such sensor (Fig. 4.21) is based on polycrystalline $\text{La}_{0.33}\text{Ca}_{0.67}\text{MnO}_3$ thin films. The discovery of colossal magnetoresistance (CMR) in manganites led to the development of these sensors. It has been found that these polycrystalline films exhibit small anisotropy, which means they do not saturate at high magnetic fields, and “memory” effects, which makes it possible to measure pulses with short decay times. It has also been found that these polycrystalline films have a magnetoconductance that varies linearly with magnetic field strengths up to 47 T.

Typical pulsed magnetic field waveforms measured using the CMR sensor and a B-dot sensor are shown in Fig. 4.22. The blue line in the figure is for magnetic field measurements made using the B-dot sensor and the

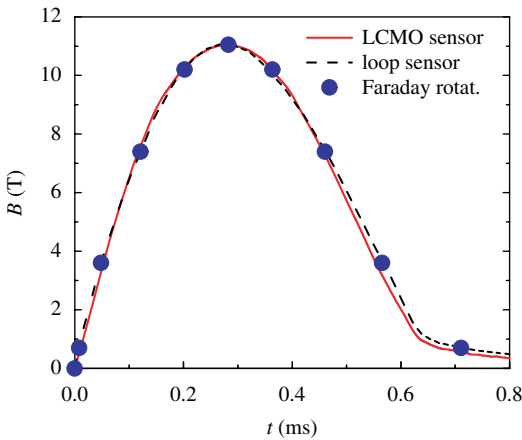


Fig. 4.22 Transient magnetic field measurements made using a CMR sensor placed close to a railgun (courtesy of Saulius Balevicius and Nerija Zurauskienė, Semiconductor Physics Institute, Vilnius, Lithuania).

black line is for the magnetic field measurements made with the thin film sensor. The magnetic film was placed parallel to the surface of the substrate and the direction of the bias current. As can be seen, both methods gave similar results. Then the magnetic film was placed perpendicular to the magnetic field. The data shows that the memory effect was not present in these films. Thus, it can be concluded the thin film sensor can record the absolute values of magnetic fields independent of the orientation of the field relative to the sensor and the direction of the bias current. This can be seen in Fig. 4.23. The sensor is sensitive to the absolute value of the magnetic field, which gives it an advantage over B-dot probes that senses the derivative of the magnetic field.

In order to validate the sensor, it was used to measure magnetic field changes in a railgun. Dynamic experiments were performed using well-known experimental techniques, which allowed reliable solid contact up to 1100 m/s. Figure 4.21 shows the results of a typical shot: the signals of a CMR and a loop sensor, as well as the total current, are shown. Note that at the time (about 2.1 ms) the projectile passed the sensor, its velocity was about 740 m/s. The figure also includes two curves obtained from simulations using the MEGA code. These calculations were performed for the “static” case — i.e. before the projectile has started moving. It was successfully demonstrated that the sensor could record high transient magnetic

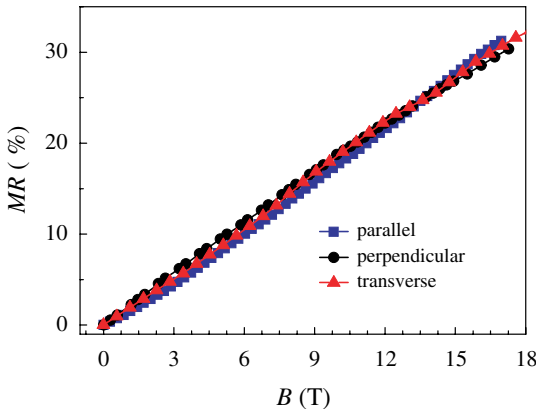


Fig. 4.23 Comparison of a measurement made with a thin film magnetic sensor with that made by a B-dot probe (courtesy of Saulius Balevicius and Nerija Zurauskienė, Semiconductor Physics Institute, Vilnius, Lithuania).

fields during railgun operation. The measured magnetic field amplitudes ranged up to 4 T with rise times of 50 μ s.

4.3 Detonic Measurement Techniques

In addition to electromagnetic measurements, the dynamic behavior of the explosive pulsed power generator's components must also be measured in order to monitor their behavior during operation and to optimise their performance. These dynamic measurements can be divided into two types: those associated with the explosive, e.g. detonation velocity, and those associated with the acceleration of the conductors and insulators that make up the generator. In addition to knowing the bulk velocities of these components, we also need to know how their geometry changes in time, the surface conditions of the various components, and the temperature and pressure at various times during generator operation. To make these measurements, techniques such as high-speed photography, interferometry and x-ray photography are used. In this section, a brief introduction to the techniques used to measure high strain rate and shock propagation events associated with explosive pulsed power generators will be presented. Techniques for measuring the properties of explosives can be found in Ref. 9.

According to Graham and Asay [10] and Meyers [11], the detectors used to diagnose high strain rate and shock propagation events can be classified

as follows:

- Wave or particle time of arrival detectors, which are used to determine velocity.
- Discrete particle displacement versus time detectors.
- Continuous particle displacement versus time detectors.
- Stress versus time detectors, which include piezoresistive and piezoelectric detectors that record voltage and current that can be converted to stress.
- Cinematography, which includes high-speed cameras, flash X-rays, holography and Doppler radars.

Graham and Asay [10] point out that mechanical measurement tools cannot be used to diagnose shock wave propagation events because they are too slow. Thus, electromagnetic and optical diagnostics must be used. Detailed descriptions of all the techniques discussed in this Section, as well as others, can be found in References [11] and [12].

4.3.1 Time of Arrival Detectors

Time of arrival detectors are used to measure velocity by sequentially spacing multiple detectors along the path of interest (Fig. 4.24), such as the stator in an FCG. The earliest time-of-arrival detectors were electrically charged pins and flash gaps. A more recent detector is the optical pin. All three detectors rely on the generation of an electrical pulse that can be recorded.

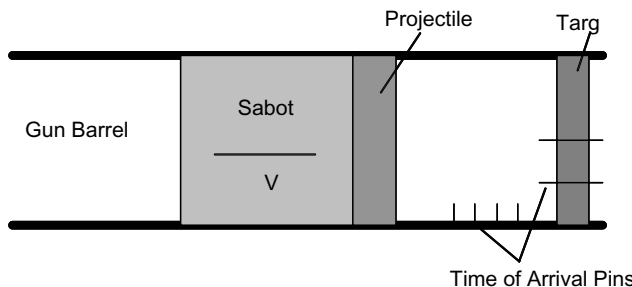


Fig. 4.24 Gun-launched projectile with multiple time-of-arrival detectors (electrically charged pins) for detecting the location of the projectile and for estimating its velocity.

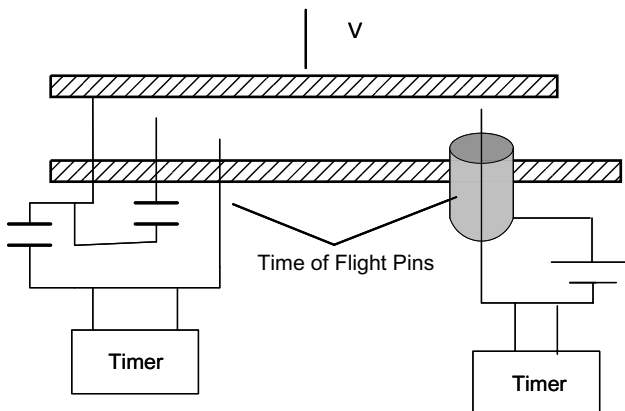


Fig. 4.25 Schematic drawing of a simple electrically charged pin set up. On the left-hand side, the pins are set up for detecting moving metallic projectiles, while on the right-hand side they are set up for detecting moving nonmetallic projectiles.

A schematic drawing of how simple electrically charged pins are used is shown in Fig. 4.25. On the left-hand side of Fig. 4.25, the pins are electrically charged so that when they make contact with a moving metallic surface, a small current is generated and recorded by a high-speed oscilloscope. If the moving surface is not metallic, then the arrangement on the right-hand side of Fig. 4.25 should be used. These are coaxial pins, which protrude from a small metallic tube. Electrical contact between the pin and tube is made when the center pin collapses upon impact by the moving surface. A potential difference between the pin and tube is established by charging a capacitor, which discharges when the pin and tube make contact. Since the moving surface compresses the air ahead of it, the resulting pressure in this compressed region may ionise the air, making it electrically conducting. This ionised air can short out the pins. Since this is undesirable, the region being compressed should be filled with a nonionising gas or evacuated.

The flash gap detector consists of a small container filled with a gas that readily ionises when the container is compressed by a moving surface. The ionised gas generates a flash of light that can be recorded by a high-speed framing or streak camera.

A more modern version of the flash gap is the optical pin. The optical pin consists of a glass microballoon (hollow glass spheres with a diameter less than 1 mm) filled with an easily ionisable gas (xenon or argon) placed in contact with one end of an optical fiber. When the microballoons are impacted by the moving surface, the gas is ionised and produces a flash of

light that is carried by the optical fiber to a photomultiplier or a streak camera. The advantage of optical pins over flash gaps is that they are very small.

4.3.2 Surface Displacement Detectors

The most successful surface displacement detector is that based on laser interferometry, which was first invented in the 1960s [11]. A more sophisticated laser interferometer for measuring velocity is the *Velocity Interferometer System for Any Reflector* (VISAR), which was developed in the early 1970s.

If two laser beams having the same wavelength are offset in distance or if they have slightly different wavelengths, then their interaction will form an interference pattern. Laser interferometry is based on detecting and measuring the changes in these interference fringes caused by displacement or movement of the reflecting surface being monitored. This is done by comparing a laser beam reflected from a surface that has moved to a reference laser beam, in the case of *displacement interferometry*, or by Doppler shifting of frequency caused by a moving reflecting surface, in the case of *velocity interferometry*.

The basic features of a displacement interferometer are shown in Fig. 4.26. The beam from the laser is divided into two beams by the beam splitter S. One half of the beam is reflected back off the surface to be displaced and the other half goes through the splitter and is reflected off a stationary mirror. The latter beam is the reference beam that remains

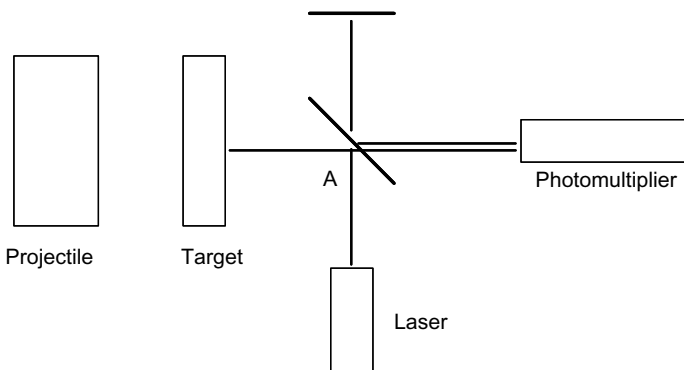


Fig. 4.26 Displacement interferometer.

unchanged during the measurement. The two beams are reunited and enter a photomultiplier.

The displacement of the sample will produce an interference pattern. If the rate at which the interference pattern changes is measured, then the velocity of the displaced surface can be calculated by using

$$U(t) = \frac{\lambda}{2} \frac{dF}{dt}, \quad (4.25)$$

where $U(t)$ is the velocity of the displaced surface, λ is the wavelength of the laser and dF/dt is the fringe frequency — i.e. the rate of change in the fringe spacing. A window is often placed between the back of the surface to be displaced and the laser to prevent jetting and irregular deformation of the surface. Common window materials are polymethylmethacrylate (PMMA), fused silica, Z-cut sapphire and lithium fluoride. When a window is used, a correction term must be added to Eq. (4.25) to account for changes in the index of refraction caused by the window. Equation (4.25) now becomes

$$U(t) = \frac{\lambda}{2(1 + \Delta V/V)} \frac{dF}{dt}, \quad (4.26)$$

where $\Delta V/V$ is the correction term.

Displacement interferometers provide velocity information by measuring the change in fringe spacing with respect to time. Velocity interferometers provide velocity information by using only the fringe spacing. In a velocity interferometer, one of the beam legs is delayed with respect to the other by a few nanoseconds. The delay is produced by passing the beam to be delayed through a glass etalon or lens system (see Fig. 4.27). The direct and delayed

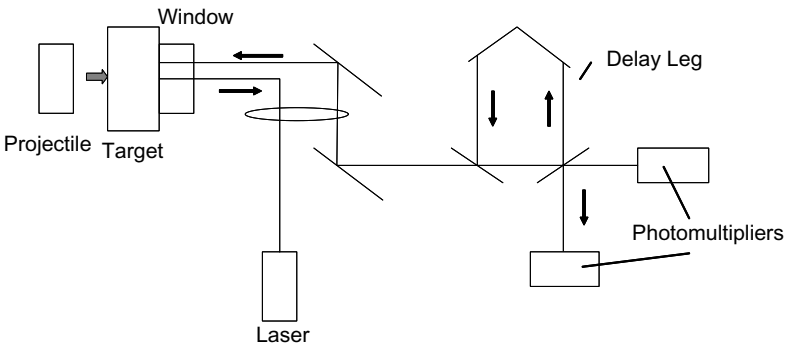


Fig. 4.27 Velocity interferometer.

laser beams will have close, but not equal, frequencies, which produce an interference pattern. The velocity of the moving surface is given by

$$U\left(t - \frac{\tau}{2}\right) = \frac{\lambda}{2\tau} F(t), \quad (4.27)$$

where τ is the optical delay time, $U(t - \tau/2)$ is the velocity at time $t - \tau/2$ and $F(t)$ is the fringe count. If a window is used, a correction term must be included:

$$U\left(t - \frac{\tau}{2}\right) = \frac{\lambda}{2\tau} \frac{1}{1 + \Delta V/V} F(t). \quad (4.28)$$

There are two types of velocity interferometers: the VISAR system and the Fabry-Perot system. The VISAR system has the advantage that it can be used with irregular surfaces. The Fabry-Perot interferometer uses two parallel plates separated by a distance L that are normal to the beam and produce the interference pattern. This adds the complication that a streak camera must be used to record the fringe pattern, since photomultipliers can't be used.

4.3.3 Stress Versus Time Detectors

4.3.3.1 Piezoresistive Gages

Piezoresistive materials are those materials whose electrical resistivity changes with pressure. They have been used in gages that record pressures under quasi-static conditions. As early as 1911, Bridgman [11] used Manganin coils immersed in pressurised fluids to accurately measure pressure. Manganin is an alloy of copper, manganese and nickel (24 wt% Cu, 12 wt% Mn and 4 wt% Ni) that is electrically sensitive to changes in pressure, but insensitive to changes in temperature at atmospheric pressure. Thus, the effects of shock heating are minimal. Manganin gages are best suited for measuring pressures greater than 5 GPa and have been used to measure pressures up to 100 GPa.

A schematic drawing of a piezoresistive pressure gage is shown in Fig. 4.28. The gages are embedded in insulating materials such as Kapton, mica or Teflon. The piezoresistive material can be either in the form of wires or foils. The resistance of the gage is approximately 50Ω , but it can be made lower. A power supply delivers current to the gage a few milliseconds prior to the arrival of the shock wave to prevent burnout of the gage. The voltage change across the gage, which is caused by the change in resistance induced by the shock wave, is recorded with an oscilloscope.

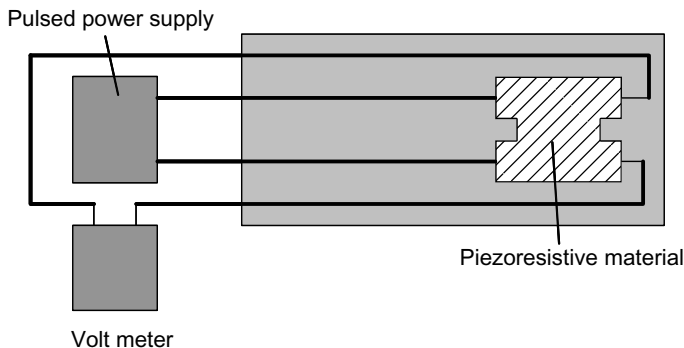


Fig. 4.28 Photoresistive gage.

4.3.3.2 Piezoelectric Gages

Piezoelectric materials are those materials that generate an electric current when stressed. Quartz, lithium niobate and some polymers such as PVDF are examples of piezoelectric materials used in piezoelectric gages. The advantage of these pressure gages over piezoresistive gages is that they do not need an external power supply, since they generate their own electrical power. There are two piezoelectric gage geometric configurations: thin-element and thick-element. In the case of the thin-element configuration, the thickness of the piezoelectric element is much smaller than the length of the pulse being measured, while in the case of the thick-element configuration, the entire pulse length occupies only a fraction of the thickness of the piezoelectric element. In the 1980s, F. Bauer [13] in France introduced an even thinner configuration when he developed the PVDF piezoelectric gage.

4.3.4 Cinematographic and Flash X-Ray Techniques

Since the operation of explosive generators are dynamic events, methods were developed to visually record them. These methods include high-speed photography and flash radiographs. While the human eye can only resolve times of 0.05 s, modern high-speed photography can resolve times approaching 10^{-13} s. High-speed photography has proven to be a very valuable tool in recording and diagnosing the operation of explosive pulsed power generators.

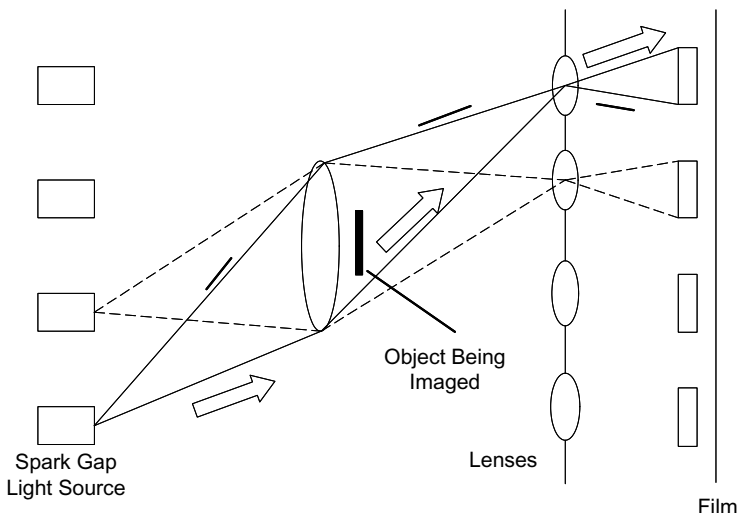


Fig. 4.29 Cranz-Schardin camera for producing shadowgraphs.

4.3.4.1 *Shadowgraphs*

In this method, rapid flashes of light are used to create an image (shadow of the object being recorded) on film. The flashes of light are produced by spark gap generators, simple spark circuits and lasers. Spark gap generators can produce exposure times as short as 5 ns, while lasers can produce femtosecond exposure times. An example of a shadowgraph camera is the Cranz-Schardin camera (Fig. 4.29), which is a multi-spark gap camera developed by Cranz and Schardin [14] in 1929. These cameras were found to be ideally suited for studying stress wave propagation and fracturing.

The Cranz-Schardin camera has an array of spark gap light sources and an array of lenses. When the light sources are activated sequentially, a cinematographic effect is generated. The Cranz-Schardin camera is easy to use, its framing rate can easily be adjusted from 20,000 to 800,000 frames per second and its interframe time may be varied from spark to spark for observing a single dynamic event.

4.3.4.2 *Rotating-Mirror and Rotating-Drum Cameras*

The rotating-mirror camera has an objective lens that forms an image on a rotating mirror and a gas-driven turbine that rotates the mirror at high speeds. The mirror reflects the image of the device under test on to film

in a large drum. The mirror is typically a beryllium substratum with an aluminum coating. Beryllium is used because it is one of the few known substances that can withstand the centrifugal forces generated at rotations speeds of 20,000 revolutions per second. The aluminum coating is protected by a vapor deposited quartz coating that makes the surface reflective and durable. The image can be recorded in either a framing or streak mode. When this camera is used in the framing mode, the rotating mirror forms successive images of the object on a long strip of film at framing speeds up to 25 million frames per second. When the camera is used in the streak mode, a slit is placed between the objective and the relay lens, which permits continuous monitoring of the object at speeds up to $30\text{ mm}/\mu\text{s}$, but does not record an image of it.

The rotating-drum camera has a film track which lies on the inside of a cylindrical drum. The rotating drum is driven by an electric motor, controlled by an electronic control unit or variable power supply. The streak version of the rotating-drum camera records a line image reflected on the film by a stationary mirror and can record up to $0.3\text{ mm}/\mu\text{s}$. The framing version of the rotating-drum camera has a mirror mechanically coupled to the drum. Successive faces of the mirror reflect light through relay lenses at regular intervals. The relay lens focuses the light onto film, creating regularly space discrete frames. These cameras can record up to 200,000 frames per second. Faster recording rates are possible if the drum rotates in a housing that is evacuated to reduce air friction. This allows the drum to reach higher speeds with less power consumption, reduced temperature increase and slight loss of image resolution due to turbulence.

4.3.4.3 *Image Converter and Electronic Cameras*

A wide range of cameras based on electronics, fiber optics and microchannel plate technologies now exist. Conventional optical instruments are limited in speed by the exposure time needed to create an image on film. However, electronic cameras can use devices that magnify light gathering capability. Image converter tubes convert photons to an array of electrons that are analogous to the image. The electron image is electrostatically focused, deflected and shuttered to produce a record of the device being imaged. The non-mechanical manipulation of the image permits extremely fast recording speeds and provides the greatest flexibility in timing and duration of the exposures. A phosphor screen in the image converter tube reproduces the optical image by converting the electrons back to photons that are

transferred to film or video. Image converter cameras produce a streak record by rapid deflection of the electron image from a slit across a photoanode and a frame record by electrostatically deflecting and shuttering of the image on successive regions of the photoanode. Image converter cameras can also produce synchroscan images using periodic light sources repetitively pulsed at high frequency. The electron image is repeatedly swept across the photoanode at a frequency tuned to that of the incident light. The overlapping low-level streak images of the periodic image accumulate on a recording medium, producing a high resolution record under low light conditions.

Another class of electronic cameras is the charge-coupled device (CCD) camera. Charge-coupled imaging devices have a silicon chip on which a large array of photoelectric detectors are etched. Each photoelectric detector corresponds to a pixel. As light falls on these pixels, a negative charge is generated by the base material as a result of the photoelectric effect. This array of charges is read and digitised to form the image. This is an inherently slow process, but advances in CCD imaging technology have made them useful for high speed imaging.

Another electronic camera is the CMOS based Image Intensified Phantom High Speed Digital Camera. These cameras are capable of covering the visible light and ultraviolet portions of the spectrum, resolutions of 800×600 pixels at frame rates of 4,800 frames per second and maximum recording speeds of greater than 100,000 frames per second at reduced resolution.

4.3.4.4 Flash X-Ray Radiography

Flash X-ray Radiography is probably the major diagnostic tool used to study dynamic deformations. It is especially useful when working with explosive detonations, since the gaseous products produced by the explosives mask the view of optical cameras. In most applications, X-rays are used in a penetration mode although there are some cases where they are used in a diffraction mode. The shadowgraph or radiograph generated by the penetration mode will provide information about the device of interest, while the diffraction mode gives information about the structure of the materials inside the generators and the nature of the shock waves being generated [11].

Typical X-ray generators [12] used to produce shadowgraphs generate energies in the range from 100 keV to 2 MeV, pulse lengths of approximately 50 ns, and doses at 1 m of 10 to 100 mrad. Analysis of these images is generally limited to defining the position or edge of an object. Higher energy



Fig. 4.30 X-ray photograph of a helical FCG. Image taken with a 450-kV CW X-ray system (courtesy of A.H. Stults, Army Aviation and Missile Research, Development and Engineering Center).

and higher dose X-ray generators make it possible to generate radiographs, instead of shadowgraphs, of all the areas penetrated by the X-rays. The X-ray machines required to produce radiographs require energies between 3 and 300 MeV, dose rates between 20 and 500 rad at 1 m and pulse durations between 30 and 200 ns. Flash radiographs obtained with penetrating X-rays can be quantitatively analysed. For example, tomography can be used to reconstruct the material density cross-section of the device under test, even when the device is in a fireball caused by high explosives and moving at several kilometers per second.

The radiograph of a helical FCG is shown in Fig. 4.30.

4.4 Summary

In this chapter, several devices for measuring the electromagnetic and detonic parameters of explosive pulsed power generators have been introduced. Of these devices, the Rogowski and Pearson coils, high voltage probes and antennae of various types are commonly used to make electromagnetic measurements. High-speed cameras, interferometers and X-rays are commonly used to make detonic measurements. As new materials are developed, other types of sensors, such as the thin film magnetic sensor, will become available.

Bibliography

- [1] S. T. Pai and Q. Zhang, *Introduction to High Power Pulse Technology*, World Scientific, Singapore (1995).
- [2] A. P. Chattock, On a Magnetic Potentiometer, *Philosophical Magazine and Journal of Science* **24**(5) (1882) 94–96.
- [3] W. Rogowski and W. Steinhaus, Die Messung der Magnetischen Spannung, *Archiv fur elektrotechnik* **1**(4) (1912) 141–150.
- [4] W. F. Ray and C. R. Hewson, High Performance Rogowski Current Transducers, *Record of the IEEE Industry Applications Conference* **5** (2000) 3083–3090.
- [5] W. R. Ray and C. R. Hewson, Rogowski Transducers for Measuring Large Magnitude Short Duration Pulses, IEE Symposium on Pulsed Power, Digest Number 2000/053 (2000) 23/1–23/4.
- [6] A. Radun, An Alternative Low-Cost Current-sensing Scheme for High-Current Power Electronics Circuits, *IEEE Transactions on Industrial Electronics* **42**(1) (1995) 78–84.
- [7] J. Novickij, R. Kacianauskas, A. Kaceniauskas, Balevicius, N. Zurauskiene, and V. Stankevic, Axial Magnetic Field Measurements of Pulsed Solenoids, *Elektronika ir Elektrotehnika* **2**(51) (2004) 15–19.
- [8] S. Balevicius, N. Zurauskiene, V. Stankevic, S. Kersulis, J. Novickij, L. L. Altgilbers and F. Clarke, High Pulsed Magnetic Field Sensor Based on La-Ca-Mn-O Thin Polycrystalline Film, *ACTA Physica Polonica A* **107**(1) (2004) 207–210.
- [9] M. Suceska, *Test Methods for Explosives*, Springer-Verlag, New York (1995).
- [10] R. A. Graham and J. R. Asay, High Temperatures–High Pressures **10** (1978) p. 355.
- [11] M. A. Meyers, *Dynamic Behavior of Materials*, John Wiley & Sons, New York (1994).
- [12] *Tactical Missile Warheads*, AIAA Progress in Astronautics and Aeronautics, **155** (1993).
- [13] F. Bauer, in *Shock Waves in Condensed Matter*, eds. W. J. Nellis, L. Seaman and R. A. Graham (American Physical Society, 1981), p. 251.
- [14] C. Cranz and H. Schardin, Kinematographie auf Ruhendem Film und mit Extrem Hofer Bildfrequenz, Zeits. F. Physik **56** (1929) p. 147.

Chapter 5

Flux Compression Generators

I. R. Smith and B. M. Novac of Loughborough University in the United Kingdom define *Flux Compression Generators* (FCGs) to be ‘any closed conducting cage surrounding a magnetic field produced either by a current flowing through it or by external means, which can be made to reduce its volume. The movement of the cage should be sufficiently rapid (μs) to prevent massive magnetic diffusion through the cage. The forces to produce the movement could be explosive (solid, liquid, and gaseous or even nuclear) or electromagnetic (produced by external coils). The total energy of the system is increased by the work done as the metallic cage moves against the internal magnetic pressure, and very high voltages and currents with very rapid rates-of-change are correspondingly induced.’

In this book, FCGs are defined to be devices that convert the chemical energy of high explosives into electromagnetic energy by using the explosives to mechanically compress a magnetic field completely enclosed within a metallic boundary. That is, they utilise a three-step energy conversion process: chemical \rightarrow kinetic \rightarrow electrical [1]. The initial detonation energy is first transformed into the kinetic energy of a rapidly expanding or collapsing armature. This kinetic energy is then transformed into electrical energy through electromagnetic interaction of the armature with a seed magnetic field. The efficiency of this conversion process is governed by the detailed physics of the detonation process and is limited by a number of loss mechanisms including Joule heating, magnetic diffusion, electrical breakdown and mechanical limitations of the armature and insulator material. The magnetic field configuration and the FCG design play a significant role in terms of magnetic diffusion losses and magnetic flux compression efficiency.

There are two main applications for FCGs. The first is as a source of intense magnetic fields. These FCGs are called *field generators* and are

sometimes referred to as Type I, Mark I, MC-I, or MK-I generators in various publications. The second is as a source of electrical power. These generators are called *current generators* and are sometimes referred to as Type II, Mark II, MC-II or MK-II generators [2–4]. In this book, attention is focused on the Type II generator, since the subject of this book is power sources.

5.1 Classifications of FCGs

As in most fields of study, a special nomenclature has evolved over the years for these types of generators. In common with conventional practice, the moving conductors are frequently called *armatures* (or *liners*) and the fixed conductors are often called *stators*. When there is little chance of confusion, the devices described in this chapter are often simply called ‘generators’.

Other generic names found in the literature, together with appropriate abbreviations, include: *Magnetic Flux Compression Generators* (MFCGs), *Magnetic Flux Compressors* (MFCs) and, particularly in the Soviet, and now Russian, literature, *Magnetocumulative Generators* (MCGs) or *Explosive Magnetic Generators* (EMGs). None of these abbreviated descriptions are perfect, but for the time being, they are the names that appear in common use. As will be discussed in the following paragraphs, there are several classes of these generators in common use, each class having some characteristics that may make it more suitable for a specific application. The most commonly used generators usually carry a name descriptive of their class, often indicative of the shape of their conducting components. Examples are ‘coaxial generators’, ‘plate generators’ and ‘spiral or helical generators’. While these generator classes may, externally, bear little resemblance to each other, they all operate on the same principles outlined below. The shapes that the conductors of an FCG can take are limited by the available explosive initiation systems. In other words, for some geometries there are no initiation systems that can support it.

All FCGs are essentially amplifiers and operate basically the same way:

- Seed magnetic flux injection.
- Initiation of the explosive charge.
- Detonation driven expansion or contraction of the armature.
- Magnetic flux trapping between the armature and the stator with magnetic flux diffusion into both the stator and the armature.

- Rapid magnetic flux compression as the kinetic energy of the armature is transformed into magnetic pressure.
- Forced reduction in generator inductance, yielding a fast rise time current pulse.

As noted earlier, the shape of these conductors can take on different forms including planar, cylindrical, toroidal and spherical. Therefore, FCGs are classified according to the shape of their conductors and include:

- Plate generators.
- Strip generators.
- Bellows generators.
- Cylindrical implosion/explosion generators.
- Coaxial generators.
- Helical (or spiral) generators.
- Disk generators.
- Loop generators.
- Spherical generators.
- Semiconductor generators.
- Superconducting generators.

Each class of generator has its advantages and disadvantages. For example, plate generators tend to be faster than the other types of generators, while helical generators have a geometry more suitable for many applications and tend to produce higher current and energy gains. A brief description of some of these generators, preceded by a historical review and a more detailed description of their principles of operation, is given below. The next chapter will be dedicated to the helical generator, since it is the most studied and the most widely used in practical applications.

By way of introduction to how these generators work, let's consider the helical FCG in Fig. 5.1. It consists of a seed source, coil or solenoid called the *stator*, explosive filled metallic tube called the *armature* or *liner*, output circuit, power conditioning equipment (opening and closing switches, transformers, peaking inductors and/or transmission line) and load. When peak current from the seed source (typically a capacitor bank or batteries with a voltage up-converter) flows through the stator, the high explosive (HE) is initiated at one end of the armature, causing it to flare out to form a cone that makes contact with a *crowbar*, thus trapping the magnetic flux inside the generator. As the cone moves along the length of the generator, shorting each turn of the stator in turn and compressing the magnetic field, the

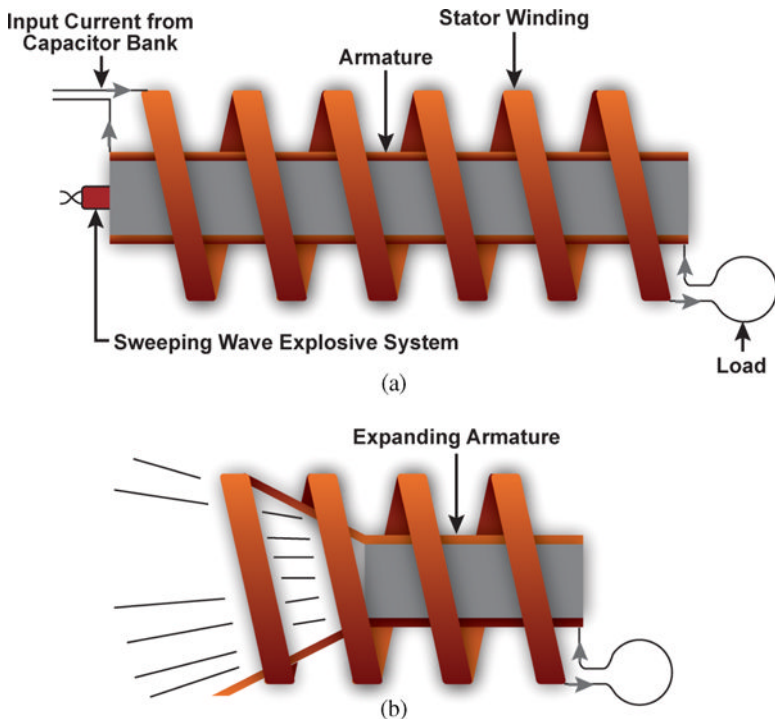


Fig. 5.1 Sketch of a helical generator with its load coil, (a) before and (b) after explosive initiation.

current flowing through the stator increases. The resulting current pulse is then conditioned to meet the input requirements of the load.

5.2 Historical Perspectives

The FCG was independently conceived in the early 1950s by scientists at the Los Alamos National Laboratory (LANL) in the United States and the All-Soviet Scientific Institute of Experimental Physics (VNIIEF), also known as Arzamas-16, in the Soviet Union. Over the intervening years to the present, work to develop and apply these generators has continued in several countries.

According to an unpublished report [2] in 1944 by J.L. Fowler, magnetic compression was first used during World War II at LANL to measure the implosion of explosive-driven liner systems. In 1954, W.B. Garn, at the

suggestion of Edward Teller and F.J. Willig, conducted flux compression experiments to generate high magnetic fields. In 1957, C.M. Fowler resumed this work [6]. A series of patents for various designs of FCGs were applied for in the United States. In 1962, J.S. Foster, J.R. Wilson and A. MacDonald [7] applied for a patent for a helical generator in which they described the basic theory of these generators. Others were filed by J.L. Hilton and M.J. Morley [8], K.K. Allport [9], A.M. Stott [10] and H. Knoepfel [11]. The first book discussing FCGs was published by Knoepfel [3] in 1970.

In 1951, A.D. Sahkarov at the Kurchatov Institute in the Soviet Union independently proposed using imploding devices to compress magnetic fields [12]. In 1952, R.Z. Lyudaev and others [12] conducted the first implosion experiments to generate ultra-high magnetic fields. The first journal article proposing magnetic field compression was published in 1957 by Ia.P. Terletskii [13]. Terletskii suggested using this method for particle acceleration. The first experimental paper was published by C.M. Fowler, W.B. Garn and R.S. Caird in 1960 [14]. Other prominent scientists in Russia who played a key role from the beginning in developing magnetic field compression technology were A.I. Pavlovskii and V.K. Chernychev.

An extensive number of publications on FCGs have been published over the years, including a substantial number in Russian journals. For a broader view, the reader may consult the 11 published volumes [15–26] that comprise the proceedings of the ‘Megagauss Conferences’, as well as three books [2–4] and two monographs [27, 28] devoted to this subject. From the previously cited publications and the proceedings of the various IEEE Pulsed Power and Power Modulator Conferences, that usually contain a number of related papers, a fairly complete view may be obtained of where work on FCGs has been done, as well as the key people involved. It should be noted that VNIEF in Russia, in particular, continues its excellent work in developing and applying FCGs and that there are relatively new, and in some cases, aggressive programs in Australia, Canada, China [29, 30], France [31], Germany [32, 33], Iran, Japan [34], The Netherlands [35], South Africa [36], South Korea [37, 38], Sweden [39] and Ukraine [40]. Also, a consortium of universities including Texas Tech, Texas A&M, University of Missouri in Rolla and the University of Texas in Austin in the United States and Loughborough University in the United Kingdom have spent 5 years working on a Multidisciplinary University Research Initiative (MURI) program to investigate the basic physics of FCGs, as well as other explosive driven power sources [41]. Additionally, Texas A&M University had a program to develop micro FCGs [42]. Other universities that have recently investigated FCGs

and their applications are the University of Missouri in Columbia for mine detection [43], the University of Alabama in Huntsville for micro fusion propulsion [44] and the University of Missouri in Rolla for pulsed power.

5.3 Principles of Operation

5.3.1 General Principles

The fundamental operating principle of FCGs is based on the conservation of flux in a perfectly conducting circuit. While the idea of perfect conductors cannot be realised, minimising flux losses in the real conductors of FCGs and in the circuit elements that they drive is a fundamental goal in generator design.

The basic principles of FCG operation [2, 3, 28] may be illustrated with the use of Fig. 5.2. The sketch is an idealised version of a plate generator, which will be discussed in more detail later. Basically, it consists of a conducting rectangular box, an input slot at the upper left and a slab of high explosive on the upper plate. Current, usually supplied from a capacitor bank, is passed through the input slot to induce an initial magnetic flux within the box. The current, I , is assumed to flow uniformly over the width of the box. The length l and width w of the box are assumed to be sufficiently large, compared to the height x , so that edge effects can be neglected. The high explosive is detonated at such a time that it closes the input slot at peak current, or peak magnetic flux within the box, and then continues to drive the top metal plate downward. A fundamental result from

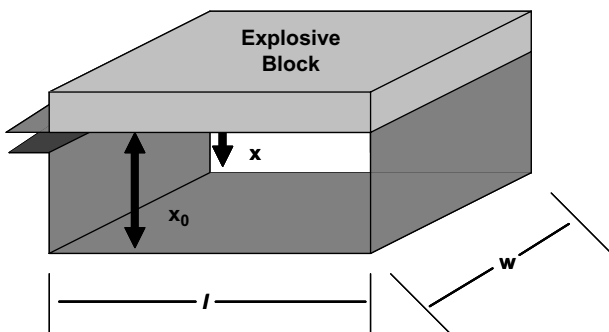


Fig. 5.2 Planar implosion system, illustrating the principles of FCG operation.

Maxwell's equations is that magnetic flux is conserved when bounded by a perfect conductor regardless of the subsequent distortion or displacement of the conducting boundaries [45]. As a first approximation, it is assumed that once the input slot is closed, the box is now a bounding perfect conductor.

Note that as the top plate of the generator is driven downward, the volume enclosing the flux is reduced, and thus, the average magnetic field must increase. A complete mathematical solution of most FCG problems is formidable, usually requiring the full set of three-dimensional (3D) magnetohydrodynamic (MHD) equations and knowledge of the constitutive relations for the materials used to construct the generator under extreme conditions. Progress in code development continues to be good, but it will be some time before complete treatments of all but the simplest FCGs will be available. Consequently, varying degrees of simplification are employed in analysing FCG performance. In [45], for example, it is shown that the magnetic fields, and their accompanying electric fields, actually build up by electromagnetic waves reflecting back and forth from the top and bottom plates. However, for time scales that are long compared to the transit times (on the order 10^{-9} to 10^{-10} seconds) of these waves, the fields may be calculated from the current in an adiabatic fashion without introducing significant error.

Assuming no flux losses and negligible edge effects, the new magnetic field B can be calculated when the top plate moves from its initial height x_0 to a new lower height x and when the initial field is B_0 . Applying the principle of magnetic flux conservation yields

$$\phi = B_0 l x_0 = \phi(x) = B l x. \quad (5.1)$$

For this example, the edge effects are ignored and the magnetic field B is assumed to be parallel to the flux compressing conductors. In this case, the magnetic stress on the conductors is compressive and is normally treated as a magnetic pressure exerted on the conductors [46]. In this case, the magnetic pressure and the energy density of the magnetic field are equal to $B^2/2\mu$ (Pascals or joules/m³). Using Eq. (5.1), the magnetic energies, $(B^2/2\mu)V$, for the example plate generator, are

$$E_0 = \frac{B_0^2}{2\mu} l w x_0; \quad E(x) = \frac{B^2}{2\mu} l w x = E_0 \frac{x_0}{x}, \quad (5.2)$$

where E_0 and E are the initial and final energies respectively. The energy increase is easily shown to be equal to the work done by the top plate

moving against the magnetic pressure:

$$W = \int F ds = \int_{x_0}^x \frac{B^2}{2\mu} lw(-dx) = E(x) - E_0. \quad (5.3)$$

While it is somewhat more satisfying to work with magnetic fields, by far most of the analyses of generator circuits are carried out by using an engineering or lumped parameter approach. Thus, currents are usually used instead of magnetic fields and the geometry of the generators is accounted for by inductances, although physical effects encountered later, such as flux losses and magnetic forces, do employ the use of fields. The inductance, L , is so defined that when it is multiplied by the generator current, the magnetic flux is linked to the current. For the parallel plate configuration in Fig. 5.2, the field and current are related by

$$B = \frac{\mu I}{w}. \quad (5.4)$$

Substituting this expression into Eq. (5.1), the generator inductance is found to be

$$L(x) = \frac{\mu lx}{w}. \quad (5.5)$$

With these substitutions, Eqs. (5.1) and (5.2) become

$$\phi = L_0 I_0; \quad \phi(x) = L(x)I; \quad (5.6)$$

$$E_0 = \frac{1}{2} L_0 I_0^2; \quad E(x) = \frac{1}{2} L(x)I^2 = E_0 \frac{L_0}{L(x)}. \quad (5.7)$$

In general, Eqs. (5.1) and (5.6), which describe the conservation of flux in perfectly conducting systems, can be rewritten as

$$\frac{d\phi}{dt} = \frac{d(BA)}{dt} = \frac{d(LI)}{dt} = 0. \quad (5.8)$$

Equation (5.8) is also a statement that the voltage around the circuit, $d\phi/dt$, is zero. If the last term in Eq. (5.8) is expanded and Eqs. (5.4) and (5.5) are used, the following expression is obtained:

$$I \frac{dL}{dt} + L \frac{dI}{dt} = Blv + L \frac{dI}{dt} = 0. \quad (5.9)$$

These terms are readily identifiable as the *motional voltage* across the moving conductor, or generator armature, and the *inductive voltage* across the remaining inductance in the generator.

5.3.2 Some Important Generator Parameters

Since FCGs are not ideal devices and have a variety of intrinsic and ohmic losses, a number of parameters have been introduced to account for their nonideal behavior and to measure their relative effectiveness. In order to simplify this discussion, let's consider a cylindrical implosion generator in which an annular explosive charge [47] is used to cylindrically compress the volume within a liner. Since the implosion time is considerably shorter than the time it takes for the magnetic flux to diffuse out of the liner, the flux $\phi = \pi r^2 B$ is compressed and the magnetic field is amplified by a factor $\gamma_M = B/B_0 = \lambda r_{\min}^2/r_0^2 = \lambda \gamma_G$, where r_0 is the initial radius of the liner, r_{\min} is the smallest radius attainable due to magnetic pressure, $\lambda = \phi/\phi_0$, which is the *flux loss coefficient* and $\gamma_G = r_0^2/r_{\min}^2$, which is the *geometrical compression ratio*. If the compression is ideal and flux is conserved, λ is equal to 1.

Using these parameters, the *energy amplification* or *energy gain* is defined by $W_M/W_{M0} = \lambda^2 \gamma_G$, where W_{M0} is the initial and W_M is the final electromagnetic energy enclosed within the system. Since most FCGs do not rely on a cylindrical imploding geometry, it is more appropriate to express the compression factor in terms of electric current and inductance, $L = \phi/I$, so that, $I/I_0 = \lambda L_0/L = \lambda \gamma_L$.

In Chapter 6, another parameter called the *figure of merit*, α , will be introduced. The figure of merit was first introduced by Fowler, Garn and Caird [14] and is used to compare measured results with those predicted for lossless conditions. It is defined by the expression $(I_f/I_0)_{\text{measured}} = (I_f/I_0)_{\text{theoretical}}^\alpha$. When $\alpha = 1$, the energy gain is ideal or lossless and, when $\alpha = 0.5$, there is no energy gain.

5.3.3 Generator Impedance

The circuit diagram for a circuit containing a generator, with time varying inductance L and a fixed inductive load L_1 that is to be energised, is shown in Fig. 5.3. An inductance symbol with an arrow is commonly used to indicate a generator. Allowance is made for source or waste inductance

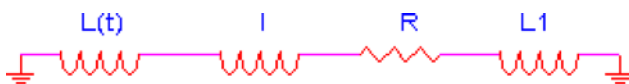


Fig. 5.3 Circuit diagram for an FCG (variable inductor) powering a series connected load, L_1 , source inductance, l_0 , and resistance R .

(from various external leads to the load, residual generator inductance, etc.) and circuit resistance, which are indicated by l and R , respectively, in the circuit diagram. The equation governing the performance of this circuit is then:

$$\frac{d}{dt} [(L + l + L_1) I] + IR = 0. \quad (5.10)$$

Two consequences that follow from Eq. (5.10) are:

- If $R = 0$, the circuit is perfectly conducting and the circuit flux $(L + L_1 + l)I$ is conserved. Clearly, as L decreases, the current I increases.
- When $R \neq 0$, the equation expands as follows:

$$\left[\frac{dL}{dt} + R \right] I + (L + L_1 + l) \frac{dI}{dt} = 0. \quad (5.11)$$

Since generator inductances are forcibly reduced, dL/dt is negative. The absolute value of dL/dt is usually called the internal impedance of the generator. It may vary widely during the time the generator is operational. However, it is clear from Eq. (5.11) that the generator impedance must exceed the resistance R at least part of the time during generator operation or the current will not amplify.

As noted earlier, IdL/dt is the voltage across the moving armature that serves to drive the entire circuit. Multiplication of Eq. (5.10) by I leads to

$$\frac{1}{2} \frac{dL}{dt} I^2 + \frac{d}{dt} \left(\frac{1}{2} LI^2 \right) + \frac{1}{2} l \frac{dI^2}{dt} + \frac{1}{2} L_1 \frac{dI^2}{dt} + I^2 R = 0. \quad (5.12)$$

Equation (5.12) is a power equation in which the last four terms are the rates at which energy is delivered to the remaining generator inductance, the source inductance, and the load inductance and is used to heat the resistance R . The negative first term, $(I^2/2)(dL/dt)$, is the power delivered by the generator to the other circuit elements. As shown by Eq. (5.11), the generator impedance, on average, must exceed the circuit resistance for current amplification. As shown by Eq. (5.12), the generator impedance, on average, must exceed twice the circuit resistance for the inductive load energy to amplify.

In some cases, skin losses in the generator can be represented by a generator resistance. In such cases, the resistance depends upon the generator action in a complex way. Among the significant factors affecting the resistance are changes in conductor skin depth, temperature and path length as generator action proceeds. For illustrative purposes, however, consider the case where R in Eq. (5.10) can be considered to be an explicit function of

time. If, further, the inductances in the generator circuit are also functions of time only, then the solution of this equation is

$$I(t) = I_0 \frac{L_T(0)}{L_T(t)} \exp \left[- \int_0^t \frac{R}{L_T(y)} dy \right], \quad (5.13)$$

where the total circuit inductance $L + l + L_1$ is represented by L_T . The inductive energy E of the circuit is

$$E(t) = E_0 \frac{L_T(0)}{L_T(t)} \exp \left[-2 \int_0^t \frac{R}{L_T(y)} dy \right]. \quad (5.14)$$

5.3.4 Example: An Idealised Generator

For purposes of illustration, consider the generator pictured in Fig. 5.2, whose inductance is assumed to be given by Eq. (5.5). Assuming that the top plate moves with a constant velocity v , starting from an initial plate separation x_0 , Eq. (5.5) becomes

$$L = L_0(1 - t/\tau), \quad (5.15)$$

where

$$L_0 = \mu l x_0 / w \quad (5.16)$$

and

$$\tau = x_0/v. \quad (5.17)$$

At time τ , the top plate has contacted the fixed bottom plate and generator action has been completed. The time τ is called the *generator burnout time*. Assuming that l , L_1 and R are constant, Eqs. (5.13) and (5.14) reduce to

$$I(t) = I_0 \left[\frac{L_T(0)}{L_T(t)} \right]^{1-R\tau/L_0}, \quad (5.18)$$

$$E(t) = E_0 \left[\frac{L_T(0)}{L_T(t)} \right]^{1-2R\tau/L_0}. \quad (5.19)$$

Here, as before, the total circuit inductance $L + l + L_1$ is represented by L_T .

At burnout, $t = \tau$, the current and energy are at a maximum. The energy is distributed between the two inductances l_0 and L_1 in proportion to their inductive values. Therefore, the maximum current and energy, E ,

into the load L_l , are

$$I(\tau) = I_0 \left[\frac{L_T(0)}{L_T(\tau)} \right]^{1-R\tau/L_0}, \quad (5.20)$$

$$E(\tau) = E_0 \frac{L_1}{L_1 + L_0} \left[\frac{L_T(0)}{L_T(\tau)} \right]^{1-2R\tau/L_0}. \quad (5.21)$$

The generator impedance $|dL/dt|$, from Eq. (5.15), is

$$|dL/dt| = L_0/\tau. \quad (5.22)$$

As expected, Eqs. (5.20) and (5.21) show that the generator impedance must exceed R for current gain and must exceed $2R$ for energy gain.

To gain a feeling for the magnitudes involved, lets return to the simplified parallel plate generator. If the following parameter values are assumed:

- Initial Inductance: $L_0 = 0.3 \mu\text{H}$
- Load Inductance: $L_1 = 10 \text{ nH}$
- Source Inductance: $l = 2 \text{ nH}$
- Resistance: $R = 3 \text{ m}\Omega$
- Burn Time: $\tau = 10 \mu\text{s}$
- Initial Current: $I_0 = 1 \text{ MA}$,

then,

- Total Initial Inductance: $L_T(0) = 0.312 \mu\text{H}$
- Total Final Inductance: $L_T(\tau) = 0.012 \mu\text{H}$
- Generator Impedance: $|dL/dt| = 0.03 \Omega$
- Exponent: $R\tau/L_0 = 0.100$.

From these values, the initial magnetic energy is found to be $E_0 = \frac{1}{2}L_T(0)I_0^2 = 0.156 \text{ MJ}$. With $R\tau/L_0 = 0.100$, the current and energy at generator burnout can be found from Eqs. (5.20) and (5.21): $I(\tau) = 18.77 \text{ MA}$ and $E_1(\tau) = 1.762 \text{ MJ}$. Finally, note that at burnout, the internal armature voltage is $(|dL/dt| I)_\tau = 563 \text{ kV}$ and the power supplied by the generator is $(0.5|dL/dt| I^2)_\tau = 5.28 \text{ TW}$.

It is clear that good generator practice calls for minimum stray circuit resistance and source inductance. If the resistance were negligible, the burnout current would increase to 26 MA and the load energy to 3.38 MJ. If the source inductance were also negligible, the peak current and energy would be 31 MA and 4.81 MJ, respectively.

It is clear that a parallel plate generator of this type is not well suited for powering loads that are resistive. Some generators, described later, can

achieve burnout impedances in the low-ohm range and may be used to directly power some resistive loads. However, impedance matching techniques are usually more effective, particularly when the load impedance exceeds a few ohms. These techniques will be described later.

Much effort has been expended in developing approximate expressions for generator inductances. The difficulty in doing this arises because the concept of inductance is itself somewhat artificial. When an inductance can be defined, it is a geometric quantity that relates the circuit flux to the total circuit current and is determined from the specific boundary conditions. Part of the complexity in calculating the inductance of generators arises because their geometric configurations vary with time, which results in a subsequent redistribution of currents and a variation in current skin depths in the conductors. In some cases, particularly when very large currents are generated, some of the generator elements can be moved by magnetic forces and this also modifies the inductance.

It should not be concluded that the inductance approach is fraught with insurmountable difficulties. Indeed, by introducing suitable approximations for factors such as skin depth and current concentration, generator models have been developed that lead to almost quantitatively correct predictions. Even the simplest models usually lead to qualitatively correct results. In any event, until mathematical solutions can be obtained from first principles, we will have to be satisfied with these approximate treatments.

5.3.5 *Advantages and Disadvantages*

The advantages of FCGs will mainly be considered, since most of their disadvantages are rather obvious. The disadvantages include:

- The hazards of working with high explosives to both personnel and nearby equipment.
- Environmental effects such as loud noise must be considered. In some cases, firing shots in explosive containment vessels can mitigate these effects, but such vessels usually limit explosive charges to relatively small sizes.
- The normal electrical hazards associated with initial energy sources, such as capacitor banks, tend to compound the problems of working with high explosives.
- Experimental facilities devoted to explosive flux compression are specialised, usually requiring considerable isolation from nearby structures,

and must be carefully controlled to avoid inadvertent access by outside people.

- Limiting access to highly sophisticated explosive facilities is a requirement for working with any explosive generators. Even though such facilities may be available to outside users, the product costs could be high, in part because of the mandatory requirements put on shipping, accountability and, in some cases, physical security.
- These devices are single shot by their nature.
- Even though the loads themselves are not necessarily destroyed (such as a rail gun or electron beam diode), the generators, or at least most of their components, are destroyed.

In view of these disadvantages, it is clear that it would be foolish to use such power sources if other, more conventional sources could be used at comparable costs. There are, however, a number of advantages that make them attractive for applications. Among them are those described below.

5.3.5.1 High Energy and Power Density

Most explosives have an energy content of 2–5 MJ/lb. At explosive-to-electric conversion efficiencies of only 2–3%, electrical energies of many tens of kilojoules can be delivered per pound of explosive at very high power levels. Thus, these generators are good for applications where weight and volume are limited. The ‘Birdseed’ experiments [48], accomplished with 50-year-old technology, illustrate this point. High-energy, generator-powered plasma guns were installed in rockets and fired into the ionosphere (~ 200 km altitude). Energy (~ 400 kJ) was supplied by a flux compression generator system. At that time, other power supplies could not have met the volume and mass constraints imposed by the rocket used in the experiments.

5.3.5.2 Adaptability

Most generators can be altered to meet varying load requirements without extraordinary difficulty, particularly when contrasted with most other installed energy sources such as capacitor banks. Examples of this adaptability will be discussed later.

5.3.5.3 Pulse Shape Effects

From Eq. (5.11), it can be seen that there is a basic difference between the shape of a generator current pulse and that, for example, from a capacitor

discharge. As noted from this equation, since the dL/dt of the generator is negative, the current can only increase if dI/dt is positive. Thus, increasing voltage across the load, $L_1 dI/dt$, is accompanied over much of the generator run by increasing current, and therefore, increasing magnetic field. In other words, when the electric fields are large, the magnetic fields are also large. There have been a number of cases where the potential for electric breakdown in generator-powered loads is thought to have been averted, thanks to this built-in magnetic insulation effect. This may be contrasted with the typical capacitor discharge, where maximum voltage occurs at zero current.

This pulse shape, in some cases, has a negative feature in that it is sometimes difficult to get a large initial dI/dt when it is required, as is the case for some Z -pinch configurations. For example, sheath formation in plasma focuses appears to be poor if the initial dI/dt is low [49].

The shape of the generator pulse also has advantages, for some applications, in reducing unwanted metal displacement or heating. Generators, being low-impedance devices, usually operate more effectively when powering loads with high currents. The resulting magnetic fields exert pressures on the conducting elements and can lead to unwanted displacements. To get a feeling for these displacements, consider the downward motion of the bottom plate of the generator shown in Fig. 5.2. Let M be the mass-per-unit area of the plate and let's assume that the magnetic field increases from a low value to a value B_M in time T . For simplicity, the time variation of B is assumed to be represented by the n th power of time:

$$B(t) = B_M(t/T)^n. \quad (5.23)$$

The equation of motion for the plate, with y in the downward direction, is

$$M \left(\frac{d^2y}{dt^2} \right) = B_M^2 \left(\frac{t}{T} \right)^{2n} / 2\mu. \quad (5.24)$$

The displacement to time T is then

$$\Delta y = B_M^2 T^2 / [(2\mu M)(2n+1)(2n+2)]. \quad (5.25)$$

Frequently, initial loading (seeding) is supplied by capacitor discharge in a quarter period. The value $n = 1/2$ is a good approximation for this current wave form. On the other hand, $n = 2$ is fairly representative of the wave form supplied by FCGs, at least over a substantial part of its operating time. Using Eq. (5.25), it is found that the capacitor discharge would displace the plate about five times more than the current supplied by a generator. To put this into perspective, if the generator in Fig. 5.2 was

loaded to 50 T (about 400 kA/cm) in a time of 15 μ s and if the density of the plates were 25 kg/m² (approximately 1/8 in. thick copper), then the plate would be displaced by approximately 0.3 mm with the generator supplying the initial current or by approximately 1.5 mm with the capacitor bank supplying the initial current. While this analysis is qualitative, the effects are real and good generator design requires careful attention be paid to undesired component motion.

Other effects mitigated by the generator pulse shape include I^2R heating, the action integral and flux diffusion. More details about these effects are available in [50] and specifically for capacitor bank loadings in [51]. Knoepfel [52] showed that flux penetration (diffusion) into a conductor is also reduced when using faster rising pulses.

5.3.5.4 Powering Parallel Loads

In many cases, a second inductive load may be switched into a generator circuit, such as shown in Fig. 5.4. In this figure, the generator L is series connected to the load L_1 and I_0 is the initial current. At a later time τ , a second inductive load L_2 is switched into the circuit. At this time, the generator inductance has been reduced to L_τ . For purposes of illustration, consider an idealised circuit (no resistance), so that flux is conserved. Up to time τ , the current I flows only in the upper branch of the circuit and has a value of:

$$I = \frac{I_0(L_0 + L_1)}{L + L_1}; \quad t \leq \tau. \quad (5.26)$$

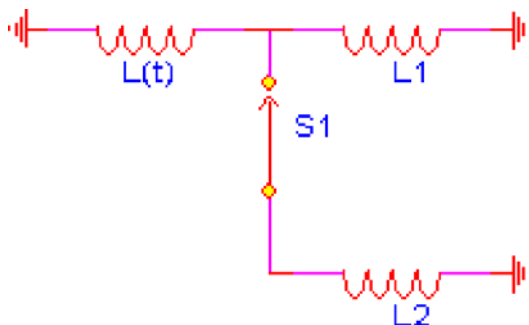


Fig. 5.4 Circuit diagram of an FCG driving parallel loads, where the second load, L_2 , is switched in at time τ .

At time, τ , the second circuit is switched in. At this time, the flux in the upper circuit remains at $I_0(L_0 + L_1) = I(\tau)(L_\tau + L_1)$. In the second circuit, consisting of the generator and load L_2 , the flux is that in the generator, $I_\tau L_\tau$, since current has not started to flow in L_2 . At a later time, the currents are I_1 and I_2 and the flux relations are:

$$\begin{aligned} L(I_1 + I_2) + L_1 I_1 &= I_0(L_0 + L_1); \\ L(I_1 + I_2) + L_2 I_2 &= I_0(L_0 + L_1)L_\tau/(L_\tau + L_1); \end{aligned} \quad (5.27)$$

when $t \geq \tau$. At burnout ($L = 0$), the final peak currents are:

$$\begin{aligned} I_1 &= \frac{I_0(L_0 + L_1)}{L_1}, \\ I_2 &= \frac{I_0(L_0 + L_1)L\tau}{L_2(L_\tau + L_1)}. \end{aligned} \quad (5.28)$$

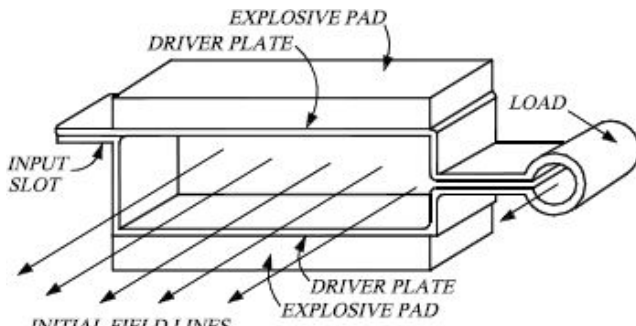
Interestingly, the peak current and the energy in L_1 are just the same as though L_2 had not been switched in. This points out another fundamental difference between flux compression generators and other sources of fixed energy. In its effort to conserve flux, the generator will attempt to deliver the additional energy required to power other loads switched into the circuit. The assumption is that the available energy in the explosive far exceeds the magnetic energies involved. In practice, the situation is somewhat different. The presence of resistances in the circuit affects the peak currents obtained. Further, the generator conductors are forced to carry higher total current and this can adversely affect the generator performance. Still, on several occasions this effect has proven beneficial when inadvertent short circuits have arisen in generator systems. While generator performance is usually significantly degraded in such cases, short circuits do not always cause the catastrophic effect that would have resulted had the power source been a capacitor bank.

5.4 Specific Types of Generator

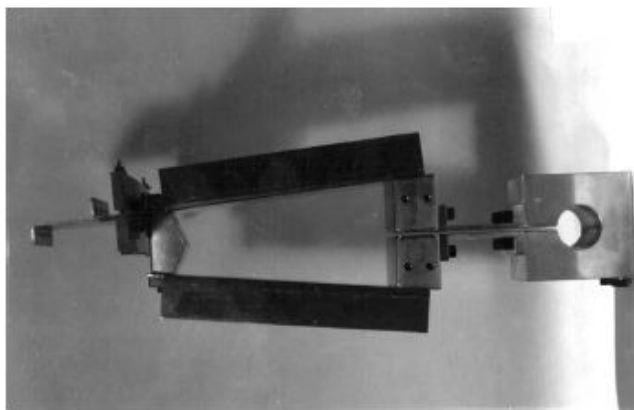
Many types of generator have been conceived, but relatively few are practical. Design limitations are set by the ability to machine or otherwise fabricate components, including the explosives, availability of explosive initiation systems and avoiding excessive losses. The types of generator in most common usage will now be considered, which, for the most part, is an update to the discussion in [53].

5.4.1 Plate Generators

Plate Flux Compression Generators (PFCGs), or simply *Plate Generators*, so-named because their conductors are plates driven by explosives simultaneously detonated over their surface areas, are presently the fastest operating FCGs available for powering external loads. Figure 5.5(a) shows such a generator, where both the top and bottom plates are overlaid with explosives. Initial flux is supplied to the generator and load by passing current through the input slot. The explosives are simultaneously initiated over the surfaces to close the input slot at, or near peak flux in the system. Plate generator burnout occurs when the two plates collide at the generator center.



(a)



(b)

Fig. 5.5 (a) Sketch of a plate generator with a cylindrical load coil and (b) photograph of a tapezoidal version of the plate generator.

By way of example, typical dimensions which can vary widely depending upon the application might be: top and bottom plates made from 0.3175-cm-thick 6061 aluminum that are 12.7 cm wide and 50.8 cm long and initially separated by 12.7 cm. The explosive charge is a 5.08-cm thick layer of PBX 9501. Closure time for these conditions is somewhat over 14 μs and the plates collide with a relative speed of about 10 mm/ μs .

Neglecting corrections for the edge effect, the initial inductance of these generators is given by Eq. (5.16). For the dimensions cited above, the edge effect correction factor is approximately 0.5, but approaches unity near plate collision or generator burnout time. In these generators, it is customary to rate them by squares; that is, the length of the generator divided by its width. There are about four squares in the PFCG depicted in Fig. 5.5. From Eq. (5.16), the inductance per square is then $L_{\text{per square}} = 1.257 \times 10^{-6} x_0$ Henrys/square, where x_0 has units of meters. Near burnout, the PFCG internal impedance is relatively large. With collision velocities approaching 10⁴ m/s, $|dL/dt| > 0.01 \Omega$ per square. Generators of this class have been used in many applications, particularly those requiring short pulses at high current, voltage and power levels. Near burnout, they can deliver multimegapampere currents at terawatt power levels to low-inductance loads with pulse half-widths of less than a microsecond. They are easily adaptable to variations that may be required. Plate widths can be controlled to allow for greater current-carrying capacity, while lengths and separations can also be controlled to vary initial generator inductance and burn time, respectively. Caird *et al.* [54, 55] have discussed this generator class in detail and give more realistic models for its performance. They also consider the case where the two driven plates are not parallel, giving rise to the ‘trapezoidal’ plate generator shown in Fig. 5.5b. This construction results in a different output pulse shape, which may be more suitable for some applications.

One application for the plate generator will be briefly mentioned. Freeman *et al.* [49] have successfully powered a Dense Plasma Focus (DPF) with plate generators, obtaining yields of 3×10^{11} DD neutrons. The only power conditioning required was a closing switch that switched the DPF into the circuit 3 to 4 μs before generator burnout.

5.4.2 Strip Generators

A Strip Flux Compression Generator (SFCG), or simply *Strip Generator*, so-named because its active elements are arbitrarily long strips of copper

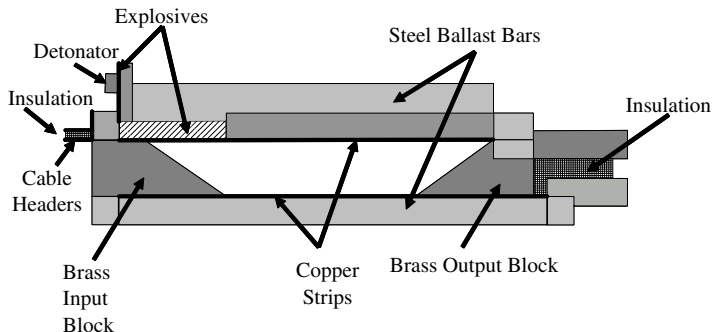


Fig. 5.6 Sketch of a strip generator. The ballast bars help resist generator expansion due to magnetic forces.

and explosive, is shown schematically in Fig. 5.6. Its most useful characteristic is the capacity to carry relatively high currents (up to megampere peak values) for long times (on the order of milliseconds). Initial inductances vary considerably with the particular dimensions selected, but are typically in the low microhenry range. Although one of the earliest generator types developed, some of its detailed construction features were not published until after it proved to be a useful power source for railguns [56, 57]. The generator consists of long parallel strips of copper, one of which is overlaid with explosive sheets, together with input and output blocks for capacitor bank cable input leads and for connection to the load, respectively. The long edges of the upper copper strip are bent up to add structural rigidity. The strip then assumes the form of a shallow U-shaped channel. For one of the commonly used SFCGs, the copper strips are about 57-mm wide, 1.6 mm thick and 2.45 m long and are separated by 51 mm. Two layers of DuPont C-8 Detasheet explosive, 45-mm wide, are placed over the upper copper strip. To minimise expansion of its components from magnetic forces, steel ballast bars, 51-mm wide and 12.7 to 25.4 mm thick, are laid on top of the Detasheet explosive and directly under the bottom copper strip. The input and output wedges are cut from 51 mm square brass bar stock and then drilled and tapped individually to accommodate cable input header attachments and to make output connections to the various loads tested. In some applications, where larger currents were required, its cross-sectional dimensions were doubled, while the copper strip, explosive and ballast bar thicknesses remained the same.

Initial flux is supplied to the generator by a capacitor bank located at the firing site. The detonator is fired shortly before maximum current

is delivered to the generator and load. The resultant detonation of the explosive strip closes the current input slot, thus trapping the magnetic flux. As detonation proceeds, the top plate is driven into the bottom plate, thereby pushing the flux into the load.

This class of generators is by far the cheapest to fabricate. Its parameters may be easily changed: the strip length can be varied to change the output pulse length; the plate width and thickness varied to suit current demands; the plate separation varied to alter the generator inductance and the plate width varied along its length to give added flexibility in controlling the output pulse shape. By using relatively simple load input header adjustments, two or more of these generators have been fired simultaneously into a load, connected in parallel for greater current-carrying capacity or in series for greater gain.

A related class of generators, often called *Bellows Generators*, was described by Herlach *et al.* [58] and by Bichenkov [59]. In the bellows generator, the explosive strip is sandwiched between two conducting strips, both of which are driven outward towards stationary return conductors. Thus, the strip generator described here has the appearance of half of a bellows generator. The bellows generator clearly makes more efficient use of the explosive and it should be easier to ballast the outer conductors. They have been found to perform very well, especially for shorter lengths. In general, however, they are more expensive to fabricate and it is not so easy to vary their dimensions.

5.4.3 Cylindrical Implosion System

Several views of a *Cylindrical Implosion System* are shown schematically in Fig. 5.7. Two of the sketches show the system before detonation. The initial assembly consists of a thin-walled cylinder centered within a ring of explosive charge to which is attached a ring of high-quality detonators. The thin-walled metal cylinder is the generator armature (or liner). An initial flux is induced within the liner, in most cases by passing current through coils external to the system. Detonation of the charge is timed to correspond to peak flux in the liner. The third sketch shows the position of the liner at a later stage in the implosion.

This class of generator is of historical interest because it was the first FCG for which experimental results were published in the open literature [14]. These generators were developed for use in imploding liner plasma compression experiments [60].

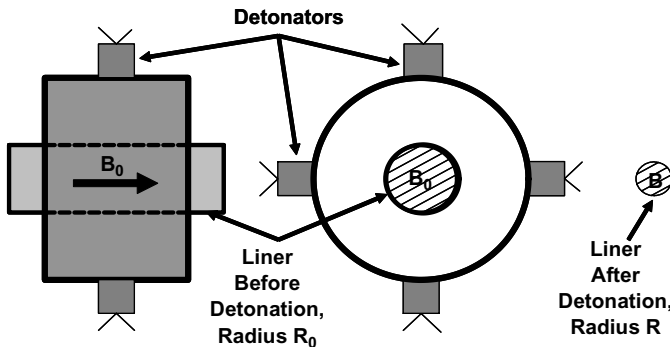


Fig. 5.7 Side (left) and end (center) views of a cylindrical implosion system before detonation and an end view during implosion (right).

If the liner in Fig. 5.7 was perfectly conducting, then, from flux conservation, the magnetic field would increase inversely as the square of the radius: $\phi = B_0 R_0^2 = BR^2$. The magnetic pressure exerted on the liner would therefore increase inversely as the fourth power of the radius. Hoyt and Kazek [14] made a number of hydrodynamic calculations for perfect flux compression. They showed that the magnetic pressures got large enough to stop the inward motion of the liner and drive it outward. This minimum radius is now called the *turn-around radius*. The magnetic field attains its maximum value at this radius. Magnetic fields in excess of 10 MG were reported in Ref. 14. The time resolved data suggested the existence of a turn-around radius, but not conclusively. Somewhat later, Besancon *et al.* [61] carried out an extensive study of these high-field systems. Pavlovskii and his co-workers [62, 63] have developed very reproducible systems, called MC-1 generators, and have used them in a number of high-field investigations. In the early 1990s, relations between Los Alamos scientists and their counterparts at Arzamas-16 had progressed to the stage that plans were made for joint experiments. Several MC-1 generators were purchased for use in a set of high-field solid-state studies, together with some Los Alamos high field systems. An overview of that shot series is given by Fowler and Freeman [64]. The success of that series led to another ultra-high magnetic field shot series in which scientists from several different countries and universities were invited to participate. A summary of the results of this second shot series, called Dirac II, is given by Clark [65]. Boyko *et al.* [66] have recently produced record fields, up to 2,800 T, by extending the techniques developed by the Pavlovskii team.

There have been many studies devoted to the diffusion of magnetic fields into the liner. A number of these calculations are given in Ref. 3. In particular, the calculations reported by Kidder [see 3] were advanced for the time and contain points that are still pertinent today. In modeling the experiments reported on in Ref. 14, it was concluded that the effects of field diffusion into the liner did not affect the peak field maxima appreciably, but they occurred at a somewhat smaller radius than that predicted, assuming perfect liner conductivity.

5.4.4 Coaxial Generators

The upper sketch in Fig. 5.8 shows a *Coaxial Flux Compression Generator* (CFCGs) and its load coil. Generators of this type are, upon occasion, also called *Cylindrical Flux Compression Generators* or, more simply, *Coaxial Generators*. The basic generator components include the stator, the outer cylinder and the armature, the explosive-loaded inner cylinder. The load coil pictured is annular or doughnut-shaped. Initial current is supplied by a capacitor bank, or commonly, by another FCG, through the annular input slot at the left. Arrows show that the current flows along the outside cylinder, through the load coil and back through the armature. Magnetic field lines B , indicated by circles and crosses, are circular or tangential. They

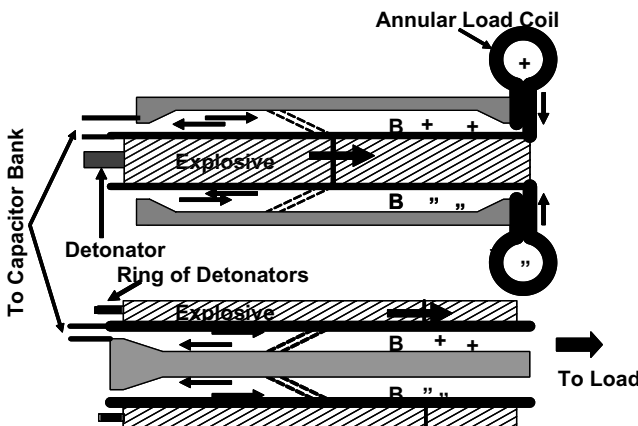


Fig. 5.8 Sketches of coaxial or cylindrical generators powering an annular load (shown only in the upper view). Most often, the explosive and armature are inside the stator, as shown in the upper sketch. Upon occasion, the armature and explosive are outside the stator, as shown in the lower sketch.

encircle the armature and are restricted essentially to the annular space between the stator and the armature and to the load coil.

Detonation of the armature explosive is again timed to close the input current slot at such time that maximum current or flux is in the system. As the detonation proceeds, the armature expands into a conical front, which moves at the detonation velocity.

The lower sketch in Fig. 5.8 shows a variant of this class of generator. Here, the central cylinder plays the role of stator while the outer cylinder becomes the armature.

These generators have low impedance, but are extremely rugged, can carry very large currents and are quite efficient in conserving flux. They are frequently built as an extension of a helical generator, whose armature has been extended in length to power the coaxial section. It is common to find that this stage of such a multi-stage generator accounts for much of their overall gain. In some cases, the stators have been especially contoured to approximately match the armature expansion angle so that closure in this last section is almost simultaneous near burnout to increase its effective impedance [67]. In another variant, the armature explosive is detonated simultaneously, on axis, to increase the impedance. Performance details of two generators of this type are given in Ref. 68. A photograph of one such coaxial generator [69] is shown in Fig. 5.9 (foreground). An initial current of 6 MA was supplied by a ‘booster’ generator (the LANL Mark IX), which can be seen attached to the coaxial generator by a number of parallel coaxial cables. The inside diameter of the stator at the generator output end was about 55.9 cm. This gave a circumference of about 175 cm to carry the output current, which was sufficient for the maximum calculated current of 160 MA. The maximum current delivered to a low-inductance load (a few nH) was \sim 161 MA. The Los Alamos ‘Ranchero’ generator [69] has both an aluminum stator and an aluminum armature. The stator has a diameter of 30.5 cm. It has been tested to currents exceeding 50 MA and should be capable of generating some 90 MA into low inductance loads. It was designed to be cost-effective and to allow for series or parallel staging of more than one generator.

As noted earlier, generators with such coaxial outputs can carry large currents that are on the order of a MA per cm width for typical operational times. The disk generators, described in the next section, also deliver final currents in a coaxial way and, thus, can also carry currents of this magnitude. One version of these generators has an output diameter of a meter and can deliver nearly 300 MA to low-inductance loads.

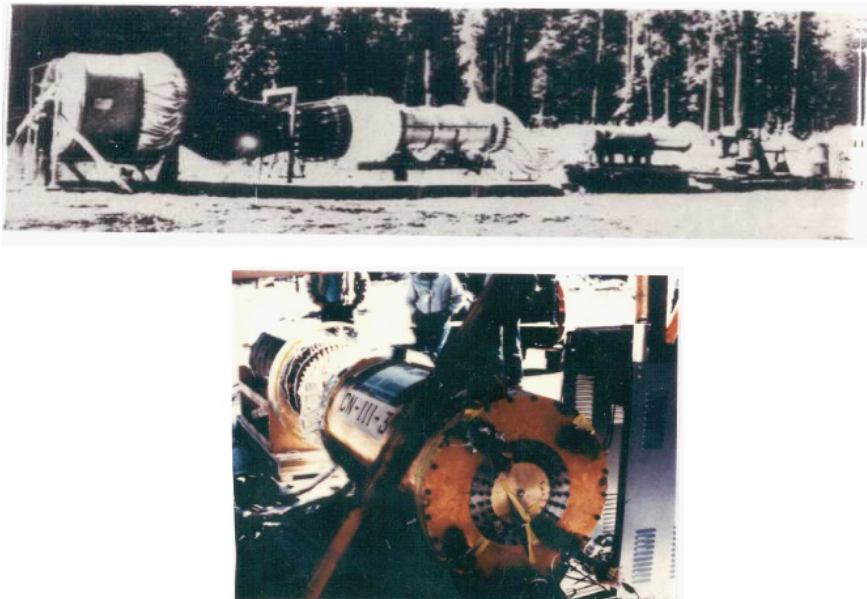


Fig. 5.9 The top photograph shows a series of increasingly large helical generators boosting a final output coaxial generator. The lower photograph shows a coaxial generator with a helical booster generator.

5.4.5 Disk Generators

Figure 5.10(a) shows the radial cross-section of a *Disk Flux Compression Generator* (DFCG), also known as a *Disk Generator*, developed by Chernyshev and his co-workers [70]. The entire device is a figure of revolution about a center line. As can be seen, the device is of modular construction, two of which are shown in the sketch. Solid lines show the current carrying disks and the cross-hatched regions are the explosive components. Magnetic field lines are azimuthal, as in the coaxial generator discussed in the previous section, and the flux is mainly confined within the generator cavity regions that are ultimately compressed by the explosive. When peak magnetic flux is attained, from a capacitor bank discharge for example, the current input opening is closed by firing, for example, a ring of detonators. At about the same time, the main charges are detonated, driving the cavity plates together as the detonation front progresses radially outward. Flux is ultimately transferred to the toroidal load coil through the outer coaxial transmission line. This geometric arrangement is quite favorable for generating large currents, since, as generator action proceeds

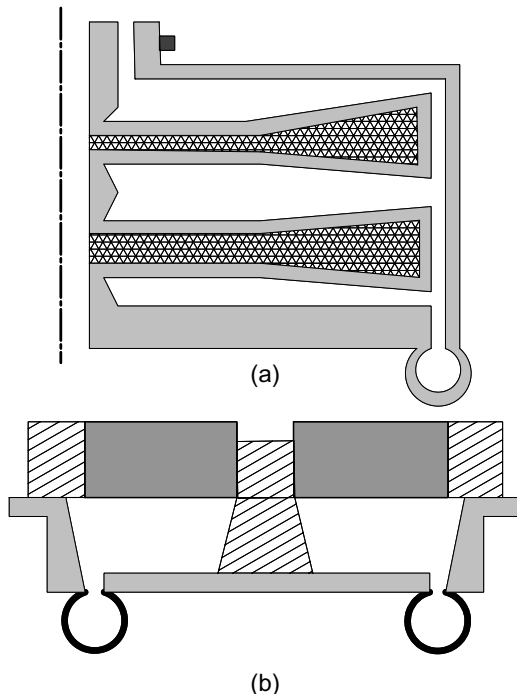


Fig. 5.10 (a) Disk generator and (b) post generator. In (a), the complete generator is a figure of revolution about the center line. The explosive, shown cross-hatched, is initiated near the cylindrical axis. Two explosive stages are shown, but many stages can be assembled in series. In (b), the explosive is initiated over the top annular surface. These systems can be made very fast, but lack the current carrying capacity that type (a) has.

and currents increase, so does the cross-section of the conductors. Similarly, there is an increase in the amount of explosive with radius. This makes for more efficient use of the explosive, since current, power and energy delivered by the generator increase toward burnout. Demidov *et al.* [71] described a three-module generator, with outer conductor diameter of 1 meter, which delivered a current of over 250 MA into a 3-nH load or about 97 MJ of energy. The initial current was 13.7 MA and, thus, the current multiplication factor was 18.7. The explosive-to-electric energy conversion efficiency was stated to be 14%, giving an estimated explosive weight on the order of 100 kg. The generator burn time was about 60 μ s and a peak dI/dt value of 2.2×10^{13} amp/s was obtained. Lindemuth *et al.* [72] describe an experiment done jointly by LANL and VNIIEF at Sarov, Russia, in which a large disk

generator was used to implode a cylindrical aluminum alloy liner weighing about 1 kg. The liner was magnetically accelerated radially inward to a velocity of about 6.5 km/s with an estimated kinetic energy of more than 20 MJ. The disk generator had 5 modules with outer diameter of 1 meter. A helical generator supplied the initial current.

Figure 5.10(b) shows a ‘simultaneous’ disk or post generator described by Fowler, Hoeberling and Marsh [73]. Current is injected radially, generating azimuthal magnetic field lines that encircle the central post. The explosive ring is detonated simultaneously over its top surface. The angles between the glide cylinders and the central post, together with the support post and ring, were selected such that the top or driver plate remained approximately parallel to the bottom plate. With about 4.5 kg of explosives and an initial current of 1.08 MA, a final current of 30.8 MA was achieved, yielding a current gain ratio of 28.5. This generator was designed for short burn times, with a consequently large dI/dt value of 3×10^{13} amp/s. As noted in reference [73], tests with this generator showed a definite improvement in performance when the driver plate was accelerated in a nearly shockless manner. This generator was first tested with the explosive charge in direct contact with the driver plate and then with the explosive standing off the plate. This latter method resulted in a nearly shockless acceleration of the plate and better performance.

It was mentioned earlier that generators were often given names by their developers to emphasise some aspect of their construction. The name of the Los Alamos generator just described was given as ‘disk’ before the authors were aware of the generators, previously described, developed by Chernyshev, which were also called disk generators. Needless to say, the developers of the LANL generator have deferred to the high-performing Chernyshev generators and now refer to their own generators as ‘post’ generators.

5.4.6 Loop Generators

A generator intermediate to that of the high-speed helical generator that can generate currents in the range of 5–20 MA and the coaxial and disk generators that have generated currents in the range of 60–300 MA is the *Loop Flux Compression Generator* (LFCG), or more simply the *Loop Generator* (Fig. 5.11). The stator of this generator is a single wide loop with two cuts. One cut serves as the input for the seed current and the second as the output. These generators are simple in design and relatively low-cost to

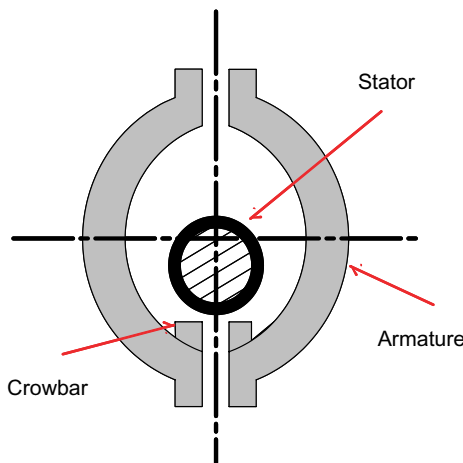


Fig. 5.11 End view of an LFCG. Note that the armature is not centered with the stator.

produce. Their characteristics include relatively high volume energy densities ($200\text{--}250\text{ MJ/m}^3$) and surface current densities (0.70–0.80 MA/cm). They can operate with a wide range of loads with inductances ranging from a few nH to some tens of nH. They are very convenient devices for doing experiments, since they can easily be filled with high explosives at any time because the HE charging process is an independent process. It is also convenient to connect these generators in series or in parallel.

As described above, the loop generator consists of an outer wide loop with two cuts and an inner cylinder filled with high explosives. A capacitor bank or another booster generator provides the initial current to the outer loop or stator. The center of these two loops are offset, with the center of the inner loop nearer to the input of the outer loop. The explosive charge is simultaneously initiated along its axis using a detonator chain. When the explosive is detonated, the inner cylinder expands and the portion near the input closes the input terminals at the moment the seed current reaches peak value. The portion of the cylinder furthest from the input continues to expand, compressing the magnetic field and forcing it into the load. Compression of the magnetic field by every portion of the cylinder ensures optimal generation of current density. These generators have a relatively low current gain of 7 to 10 and an e-fold time of about 9 to 12 μs . Loop generators were first described by Lukasik [74]. His generators were small and designed to make large magnetic fields in very small volumes. Their

best-performing generators achieved a field multiplication of 26, resulting in a magnetic field of 133 T.

Later experiments with much larger generators and loads were conducted by Vasyukov [75]. He tested a single loop generator with a loop diameter of 30 cm and a width of 60 cm that had an inductance of 87 nH. This generator delivered 50 MA, 10 MJ and 30 to 35 kV to an 8 nH load. He then connected three of these generators in series to a 30 nH load. The total inductance of the three generators was 260 nH. This system generated 46 MA of current, 30 MJ of energy and 4 TW of power. Higher currents could have been generated by connecting the generators in parallel or by increasing the width of the generators. The characteristics of these generators are discussed in some detail by Altgilbers *et al.* [2].

The most recent work on LFCGs is that of Shkuratov *et al.* [76–79]. They developed miniature explosive driven LFCGs with volumes as small as 54 cm³. The initial current and magnetic flux in the LFCG was generated by an explosive driven transverse ferromagnetic generator. A schematic diagram of a FMG-LFCG-load system is presented in Fig. 5.12 and cut-away views of the LFCG are presented in Fig. 5.14. The equivalent circuit diagram for their FMG-LFCG system is shown in Fig. 5.13, where the FMG portion of the circuit includes the FMG as a source of EMF and a pulse generating coil with resistance R_{FMG} and inductance L_{FMG} . The LFCG portion of the circuit includes the resistance, R_{LFCG} , and inductance, L_{LFCG} , of the LFCG, a closing switch and a load Z_{Load} . The LFCG (see Fig. 5.14) consists of a single-turn aluminum armature and a single-turn copper stator, the centers of which are offset to facilitate crowbarring by the two

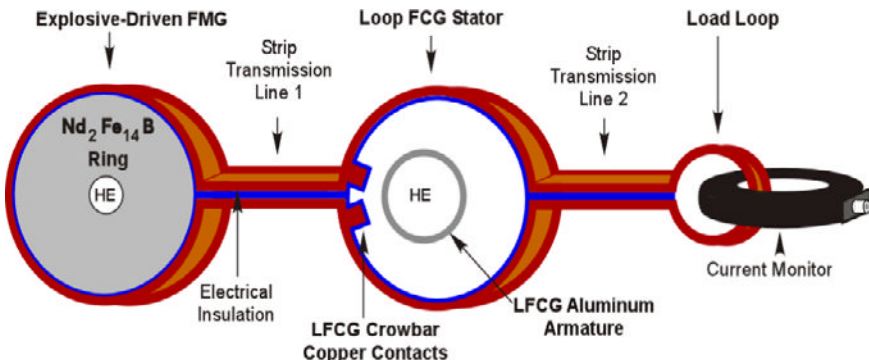


Fig. 5.12 Schematic diagram of an FMG-LFCG-load system [79].

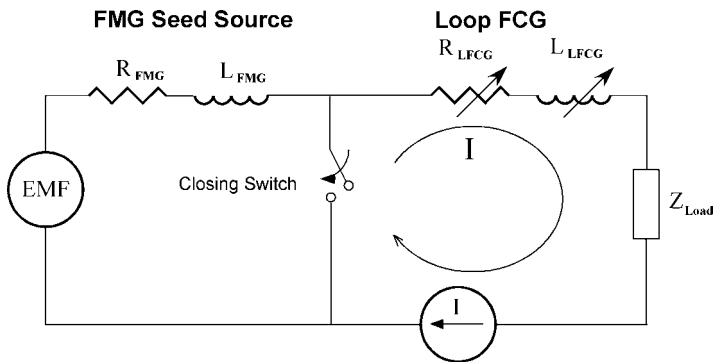


Fig. 5.13 Equivalent circuit diagram for an FMG-LFCG-load system [79].

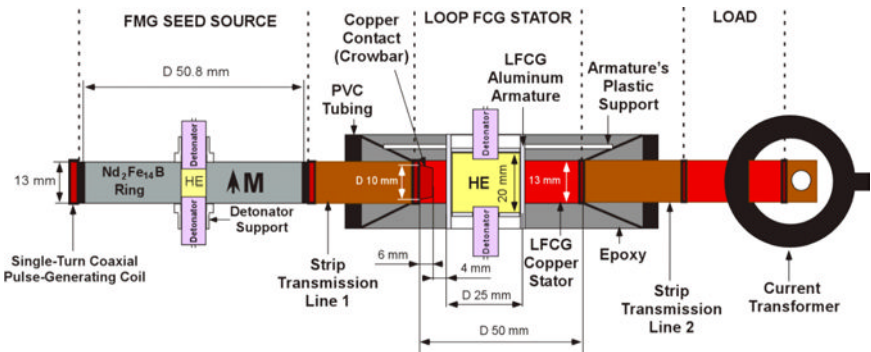


Fig. 5.14 Cutaway view of an FMG-LFCG-load system [79].

copper contacts in the stator. The stator was limited to a width of 13 mm, since this is the maximum width that would allow nearly simultaneous detonation of the explosive charge in the armature with a single detonator. The armature had a diameter of 38 mm and a length of 25 mm and was filled with 20 g of HE. When the armature expands and contacts the two copper contacts, the FMG seed source is disconnected from the LFCG and the current in the stator increases due to the compression of the magnetic flux trapped inside the LFCG. Typical waveforms produced by the FMG and by the FMG-LFCG are presented in Fig. 5.15. The inductances of the LFCG and the load that generated the waveforms in Fig. 5.15 were $L_{LFCG} (100 \text{ kHz}) = 72 \text{ nH}$ and $L_{Load} (100 \text{ kHz}) = 57 \text{ nH}$, respectively. The maximum output current produced by the LFCG was 4.73 kA. The current

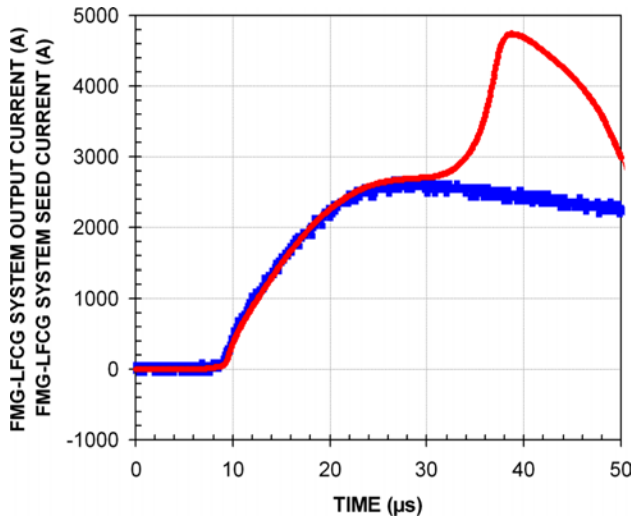


Fig. 5.15 Current from FMG seed source (blue) and current from FMG-LFCG combination (red) [79].

amplification factor was 1.89. The total flux loss was $65.8 \mu\text{Wb}$, which is 19.6% of the initial flux.

An alternative design (see Fig. 5.16) was proposed by one of the authors of this book. The new design proposes to use ‘keepers’, which are magnets placed over the open ends to the LFCG to trap the flux between the armature and stator. The keepers also serve to further increase the magnetic field within the LFCG and to prevent expulsion of the magnetic field from the annular region during compression.

Altgilbers *et al.* [80] developed a semi-empirical analytical model for the FMG-LFCG system. They treated the LFCG as an equivalent inductive-resistive (LR) circuit connected to an inductive load. The inductance and resistance of the LFCG were assumed to be time dependent, as was the input current from the FMG. Several characteristic times, which had to be determined empirically, were introduced. A comparison of the calculated and experimental results are presented in Fig. 5.17 and, as can be seen, there is good agreement between them.

5.4.7 Helical or Spiral Generators

More has been written about *Helical Flux Compression Generators* (HFCGs), or simply *Helical Generators* (Fig. 5.18), because of their

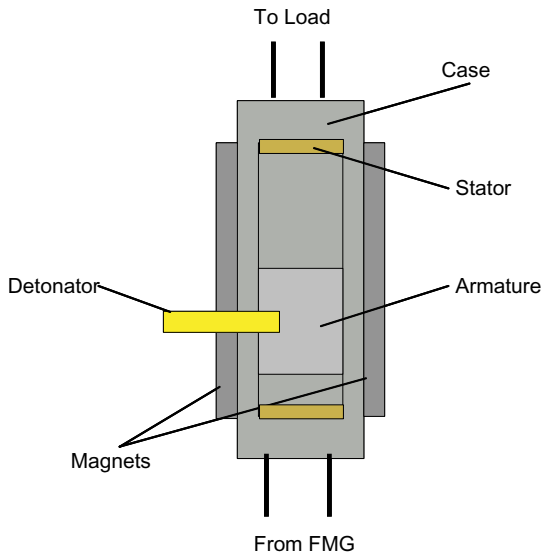


Fig. 5.16 Loop MCG with end disk magnets. One disk magnet has a hole for the detonator. Seed current is supplied by an FMG (not shown). These end magnets will increase and confine the magnetic field during compression.

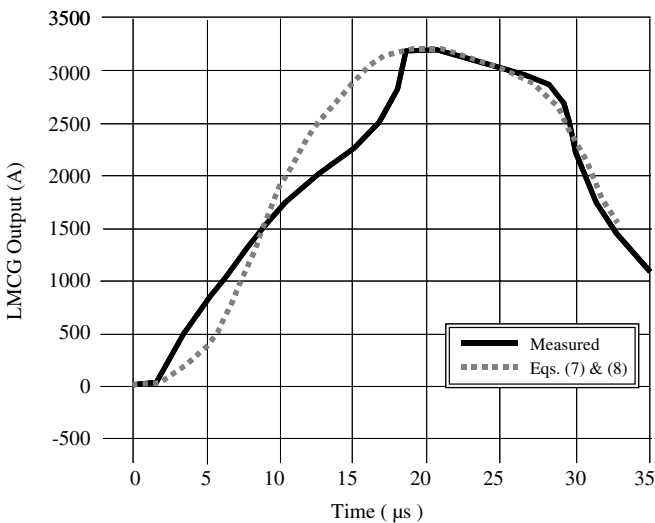


Fig. 5.17 Waveforms of the seed current (blue) delivered by the FMG to an LFCG with no explosives (calibration shot) and of the seed current delivered to an LFCG with explosives (red).

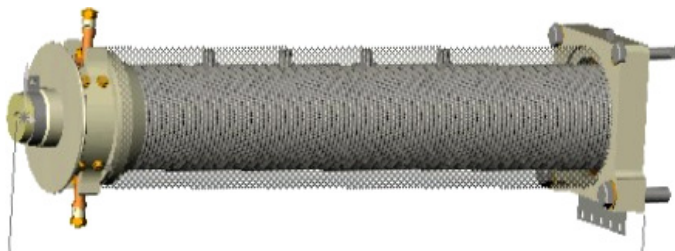


Fig. 5.18 Side views of a helical FCG.

potentially high current and energy gains, and because the explosive system required is relatively simple and requires only single point initiation for a conventional generator. In fact, the entire next chapter of this book is dedicated to covering many aspects of these extremely useful explosive generators. With this in mind, the discussion of the HFCG in this section is abbreviated to simply point out that the stator in this case is a helical or solenoidal winding. The explosive in the central stator is detonated with a propagating explosive initiation, thus expanding the stator and compressing the magnetic flux.

5.4.8 *Simultaneous Helical Generators*

The Simultaneous Helical Generator developed at Los Alamos [81–83] will be briefly described. In this generator, the armature explosive is detonated simultaneously on axis. In this case, the generator burn time is governed only by the time it takes for the armature to move radially outward and make contact with the windings. Thus, the generator inductance is reduced to zero in a short period of time, leading to high internal impedance. As noted in the Refs. 81–83, flux diffusion losses can be large. The generator gains are therefore relatively small, but the device has since been shown to power loads at much higher voltages near burnout than does the conventional helical generator. Using this approach, it is possible to design explosive generators that have source impedances on the order of 1 Ohm.

5.4.9 *Shock Wave Generators*

In the early 1960s [84], it was discovered that certain dielectrics, such as silicon, and oxidised metal powders, like aluminum powder, become electrically

conducting under static and shock compression. It was also found that under static compression, the conductivity of silicon increases monotonically with increasing pressure and reaches the conductivity of classic metals. In addition, it was also found that shock compression of silicon causes metallisation to occur when the Hugoniot Elastic Limit is exceeded. The difference between static compression conductivity and shock conductivity was found to be six orders of magnitude at a pressure of 15 GPa. This physical phenomenon led researchers to believe that it may be possible to use shock induced metallisation of solids to efficiently compress magnetic flux [85–88].

As seen in the preceding sections of this chapter, traditional FCGs convert the energy from high explosives into electromagnetic energy by using metallic liners to compress magnetic fields. There are several loss mechanisms associated with this traditional approach for converting energy that lead to considerable loss of magnetic flux [2]. As a result, new techniques were sought to reduce these magnetic flux losses. As noted above, it was well known that certain materials, including semiconductors and insulators, will transition from an electrically nonconducting state into an electrically conducting state when subjected to high pressures, increasing their conductivity by 6 to 8 orders of magnitude. Some substances that exhibit this property in addition to silicon and aluminum powder are germanium, selenium, gray tin, silicon oxide, cesium iodide, germanium iodide and lithium niobate (LiNbO_3). Using this property of these materials, FCGs referred to as *Shock Wave* or *Semiconductor Flux Compression Generators* (SWFCG), or simply *Shock Wave Generators* (SWS) or *Semiconductor Generators*, were developed and tested. The advantages of SWSs over conventional FCGs are:

- More efficient transfer of chemical energy from the explosive to the shock wave,
- Practically complete compression of the magnetic field within the working volume,
- Increased initial magnetic field in the generator because the energy is concentrated,
- Independence of the time it takes to create the seed field,
- Freedom from instabilities, such as Rayleigh-Taylor instabilities, associated with the imploding liner in conventional FCGs,
- Faster operation, which is determined by the shock velocity.

The SWS was first proposed in 1978 by E.I. Bichenkov [87–97] at the Larent'ev Institute of Hydrodynamics in Russia. The same idea was independently proposed by K. Nagayama [98–102] in 1981 at the University of Kumamoto in Japan. In the intervening years, development of these generators has been carried on by S.D. Gileev and A.M. Trubachev in Novosibirsk [103–115], A.B. Prishchepenko and A.A. Barmin [116–121] in Moscow, I.R. Smith and B.M. Novac in the United Kingdom [122–123], G. Bjarnholt and others in Sweden [124–127], Pai *et al.* [128], Gatilov *et al.* [129], Velikovich [130], Tracy *et al.* [131], Kolosenok *et al.* [132] and D. Hemmert and S. Holt [133–135]. A diagram and a photograph of a spherical SWFCG built by Prishchepenko are shown in Fig. 5.19. The narrow tracks visible on the surface are explosive delay lines and used to detonate the high explosive in some prescribed manner so as to achieve a uniform implosion. Permanent magnets are used to create the seed magnetic field and the working material is cesium iodide. A more detailed description of these generators is given in [2]. Until very recently, all generators of this type have used implosive geometries and have taken advantage of the convergent

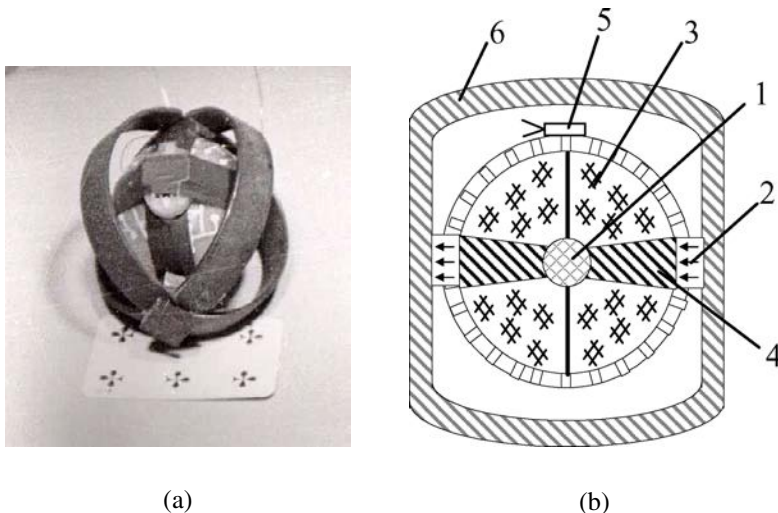


Fig. 5.19 Shock wave source developed by A.B. Prishchepenko. It consists of 1 — working body (CsI), 2 — permanent magnets, 3 — high explosives, 4, 5 — magnetic field concentrators, and 6 — detonator. The white lines on the body of the device are explosive delay lines configured to ensure uniform implosion.

nature of the shock wave. Recent work has been done by the authors on divergent shock wave generators.

Within recent times, there have been a number of advances in our understanding of SWSs. Some recent theoretical advances are:

- Kolosenok *et al.* [132] reported that shock wave compression of magnetic fields in solid materials is not as strongly limited by magnetic pressure as it is in conventional FCGs. For example, Hemmert *et al.* [133, 134] reported that one can compress magnetic fields in aluminum powder when the magnetic pressures generated by the compression process are an order of magnitude greater than the amplitude of the shock waves driving the flux compression.
- Velikovich [130] has reported that electrical breakdown in the uncom-pressed material ahead of the shock wave may be the most restricting condition in the operation of SWSs.
- Investigations by Barmin and Prischepenko [116], Kolosenok [132] and Tracy *et al.* [131] of CsI monocrystals and by Bichenkov [96] of powders suggested that when the shock wave converges towards the center of a SWS, the ionised shock front decelerates and there is an oscillatory com-pression mode, where the pressure, material density and local magnetic flux density oscillate behind the shock front.

Some recent experimental advances are:

- While investigating shock induced changes in the electrical conductivity of aluminum powder for use in closing switches for ultracompact explosive generators such as FEGs, Hemmert *et al.* [133, 134] found that the change in conductivity is independent of grain size, but may be influenced by the method used to pack the powder. In other words, the gain of the SWS is related to the porosity of the Al powder.
- Hemmert, Holt and Krile [133, 134] also found that high voltage hold-off tests showed a large difference in hold-off capabilities for different grain sizes, with the larger grains performing the worst. They concluded the use of aluminum powder in compact explosive closing switches appeared possible for low-voltage applications and that the use of nanopowders may achieve higher hold-off voltages.

Of all the recent papers related to the SWS, two papers by Gilev [113, 135] are probably the most relevant. Gilev points out that current

models for the SWS are based on a number of assumptions: 1) the material is incompressible, 2) the electrical conductivity increases just behind the shock front, but does not change later, 3) the electrical conductivity does not depend on pressure and 4) the electrical conductivity is very high so that magnetic diffusion losses from the uncompressed region is negligible. As is self-evident, this model does not take in the compressibility of the material, shock-induced metallisation, effects due to magnetic compression, shock dynamics, and so on. In order to account for these shortcomings, Gilev developed a magnetoelectrical experimental technique for studying the insulator-metal transition under shock compression. Some of the results from his studies are:

- The thickness of the skin layer of course powders is smaller than the thickness of the shock transition zone, which implies that magnetic compression is only effective in fine powders, not course powders.
- Metallisation of aluminum powder only occurs within the shock front and not in a elastic precursor proposed by Novac [123]. In fact, Gilev saw no evidence of the precursor wave being formed.
- The electrical conductivity of silicon and selenium increases by 5 and 12 orders of magnitude respectively without a noticeable delay (within a few nanoseconds) under shock compression.
- The pressure dependency of the electrical conductivity consists of two parts: a steep rise in conductivity followed by a plateau. The plateau conductivity corresponds to that of the metallic state. This plateau regime does not depend on the type of doping or impurities that may be present. The metallic state tends to be metastable in that when the stress is released there is a temporary delay in the reverse transition.
- The threshold pressure for metallic transition in silicon is about 10 GPa and metallisation occurs at approximately 12 GPa.
- Metallisation in selenium occurs at about 21 GPa. Powered selenium undergoes metallic transition at a lower pressure than solid selenium.
- As the shock pressure increases in powdered aluminum, its conductivity increases sharply, reaches a maximum and then decreases. This behavior reflects the combined effects of compression and heating by the shock wave.

In summary, Gilev has established that shock wave compression of magnetic fields in solids is feasible and that it is more effective when the materials are fine powders.

5.4.10 *Summary of Generator Classes*

In summary, the various classes of FCGs all operate on the same principle, yet each has its own unique set of capabilities:

Plate Generators

- Have low gain, but are very fast.
- Often require very little power conditioning.

Strip generators

- Can generate long pulses.
- Can only generate limited currents.
- Are cheap to build.

Loop Generators

- Are simple and inexpensive to build.
- May be made small.
- May be combined in series and in parallel.

Cylindrical Generators

- Have low gain.
- Can generate very large currents and energies in low inductance loads.

Disk Generators

- Have characteristics similar to cylindrical generators.
- Are versatile due to their modular construction.

Helical or Spiral Generators

- Have high current and energy gains.
- Often require power conditioning.
- Are widely used as a ‘booster’ for other generators.

Semiconductor Generators

- Require complicated detonator arrays.
- Are less prone to instabilities encountered in conventional helical FCGs.
- Are rugged, compact and efficient.

5.5 Losses and Efficiencies

Generator efficiency is usually defined as the ratio of the magnetic energy produced by the explosive generator to the energy content of the explosive. In most cases, efficiency is not considered to be an important factor. In fact, as noted earlier, in most cases the energy content of the explosive is considered so large that it is not considered a limitation on generator performance and is therefore treated as a virtually inexhaustible source of energy available to meet the energy needs required for flux conservation. Nevertheless, there are situations where higher efficiency is desired. These arise when overall system size or weight is at a premium, when danger of fragment or blast damage to nearby components must be minimised or to reduce the size and weight of containment vessels in which shots are fired. Efficiencies are more dependent on the various losses that can occur during generator operation and on the load's characteristics. Generator losses are generally categorised as those related to magnetic diffusion and those arising from mechanical effects.

5.5.1 *Diffusion Related Losses*

The magnetic fields within the generator diffuse into its conductors and it is generally non-recoverable. The basic principles of diffusion are well-known [3]. For simple geometries, the major uncertainty lies in the value of the electrical conductivity. Some of the complexities may be seen by considering Fig. 5.2. The explosive drives the top plate, but not the bottom plate. If the explosive is in direct contact with the upper plate, then a shock wave is generated in the plate with a corresponding temperature rise. Thus, there is a decrease in electrical conductivity from this effect over and above that caused by current heating. This also occurs in the bottom plate. The situation is even more complicated since the top plate is subjected to various waves, both shock and release waves, during its motion. This leads to corresponding spatial and temporal variations in both temperature and pressure throughout the plate thickness. However, much of the average temperature increase arises from the first shock that passes through the plate, which is subsequently mitigated by a release at the free surface. The severity of the first shock may be greatly reduced by standing off the explosive from the plate or by interposing a low-density foam between the explosive and the plate. This is frequently done, but sometimes other circumstances prohibit it.

In spite of these complexities, it is usually possible to qualitatively account for the flux losses by using diffusion theory, provided the geometries are relatively simple and the current densities are not too high. However, it has been found empirically that, in some situations, the losses become anomalously high when the magnetic fields exceed certain values for long enough times. Bichenkov and Lobanov [136] noted the onset of high losses in a copper strip generator when the magnetic fields approached about 400 kg. Fowler *et al.* [28] observed a similar onset in brass coils when the fields exceeded 500 kg. It is possible that these effects arise partly from crack formation in some of the conductors [137], since a magnetic field of 500 kg has a magnetic pressure of about 10 kbars, which is above the elastic limit of brass.

In most situations, the generator's conductors are thick compared to the skin depths they develop during generator operation. Thus, the flux loss by diffusion resides in the conductors and can be approximately calculated from skin depth estimates, provided the magnetic fields do not get too high [138, 139].

There are, however, situations where skin depths are not small compared to the conductor thickness. These cases arise when relatively thin conductors carry currents for long times. In this case, additional flux is lost by radiation from the outer conductor surface. This situation was discussed by Fowler [139, 140].

5.5.2 *Mechanical Related Losses*

Major losses generally occur because of flux trapping and unwanted component motion arising from magnetic pressure. *Flux trapping* or *pocketing* (not to be confused with the flux trapping associated with dynamic transformers in multi-stage HFCGs) occurs when part of the magnetic flux is inadvertently isolated from the generator and load. This can happen in a number of ways.

5.5.2.1 *Mechanical Tolerances*

If the plates in the plate generator shown in Fig. 5.5 are thicker on the input side than on the load or output side, plate closure would occur earlier on the output side, leaving flux trapped between the lagging plates on the input side. The eccentricity of the armature or variations in the armature wall thickness could cause premature contact with a downstream stator turn. This would result in the trapping of flux between this turn and the

unshorted upstream turns. Chernyshev and his co-workers [141] examined the consequences of armature eccentricity in considerable detail.

5.5.2.2 *Moving Contact Effects*

With the exception of cylindrical implosion systems, all of the generators described in this and the next chapter require moving metallic contacts (the point at which the armature and stator make contact during generator operation) to carry the current during generator operation. These contacts are sometimes rough or bumpy and, in any case, frequently have some conducting metal spray running ahead of the major hard contact. It is difficult to quantify the resulting flux loss for lengthy contact regions, as in the strip generator in Fig. 5.6, where the strip lengths may be as long as 3 m. It is thought that this may be a significant loss mechanism. Bichenkov and Lobanov [136] and Knoepfel [3] address this point.

5.5.2.3 *Explosive Produced Jets*

Jets arise in a number of ways. If the jets arise from explosive-metal interactions, they are usually conductive enough to form an alternate flux-trapping current path. Imperfections in either the explosive or the metal in the armature of a helical generator, for example, can lead to jets that will short to a stator turn before the armature makes major contact and, thus, lead to flux loss. Metallic jets can also be produced at sliding contacts, such as between the moving plates and the side glide blocks of the generator shown in Fig. 5.5. Since these jets move ahead of the plates, they produce a short circuit in front of the output slot before generator action has ceased. These jets caused considerable trouble in the earlier stages of plate generator development. Guided in part by the classic study on jets by Walsh *et al.* [142] and later work by Caird [143], this problem was eventually solved by careful selection of the angle between the glide planes and the moving plates, and by proper location of the explosive.

5.5.2.4 *Undesired Component Motion*

Unwanted motion of metallic components can lead to reduced performance (Fig. 5.20), since the motion increases the inductance of the system. Two examples of this effect are shown in Fig. 5.20. Flash x-ray photography reveals massive motion of the metal conductors connecting a strip generator to a railgun. These motions, of course, can arise when other power sources are used, but they are especially serious for flux compression generators,

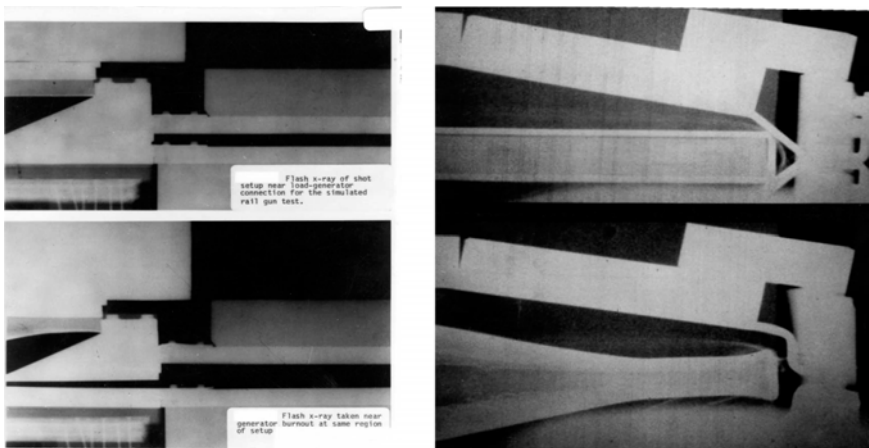


Fig. 5.20 Undesirable motion caused by magnetic forces. Upper Views show two different assemblies before firing. Lower views show displacement and distortion of metal components near generator burnout caused by magnetic forces.

since the maximum theoretical energy gains are rigorously controlled by circuit inductances.

5.5.3 *Efficiencies*

The efficiency at which explosive energy is converted into electromagnetic energy is limited by a number of factors including the particular pulse characteristics required by the load and any special requirements imposed by the explosive charge.

As an example of the influence of the load on efficiency consider Eq. (5.14). Even if the generator system is lossless, i.e. both l and R are negligible, the maximum energy that can be delivered to a load L_1 is $E_1 = E_0(L_0 + L_1)/L$. It is clear that if L_1 is comparable to the initial generator inductance L_0 , the final load energy would at most be double the initial energy.

The disposition of the explosive is also significant. Often, more explosives than ideally required are needed for practical reasons. For example, in the cylindrical implosion system of Fig. 5.7, there are practical limits on how closely spaced the detonators may be mounted. The wall thickness of the explosive ring must be large compared to the detonator spacing otherwise perturbations from the detonation points will affect the subsequent liner motion.

Generators in which the explosives are confined by the armature are normally more efficient. In the cases of the helical generator, the loop generator and the coaxial generator, the explosives are confined by the armatures and do maximum work against them. If the explosives are unconfined on one surface, only a portion of the explosive energy is used to drive the armatures. Under some conditions, part of the lost energy can be recovered by *tamping* the explosive; that is, by putting some heavy ballasting material such as steel plates or concrete over the explosive. The resulting gains are, however, not very large.

Efficiencies are not often reported. However, under some circumstances, relatively high values have been obtained. In all cases, the ratio of the generator inductance to the load inductance has been chosen to have relatively high values and the explosives have been armature confined. Bichenkov and Lobanov [136] reported efficiencies of 12–14% using a bellows-type strip generator. Morin and Videl [144] reported a 13% efficiency using a helical generator followed by an in-line coaxial generator. Pavlovskii *et al.* [145] reported efficiencies of ~20% with helical-coaxial generators, when used under specialised conditions. A word of caution is in order in rating generator efficiencies. Usually, the useful energy delivered to a load L_1 is defined to be $0.5L_1I^2$. However, the total generator electrical energy output is the integral of the power delivered. This energy is frequently as much as 50% higher than the load energy, since the generator must supply sufficient energy to account for resistive losses, flux trapped in conductor skins and expansion of metal components. Degnan *et al.* [146], for example, described a helical generator that delivered 10 MJ of energy to an inductive load, but the integrated power (i.e. energy) delivered by the generator was 15 MJ. Pavlovskii and his co-workers [147] have cited similar results.

Frequently, efficiencies can be increased, but at an increase in cost. For the case of the cylindrical implosion system in Fig. 5.8, the thickness of the explosive charge can be reduced in some cases if more detonators are used. However, high-quality detonators, which are required for such systems, are expensive. In another study, Fowler [148] doubled the efficiency of a helical generator by boring out half of the armature explosive and reducing the armature wall thickness somewhat. However, additional explosive machining nearly doubled the cost of the explosive.

In summary, efficiencies can be relatively good in certain applications. Usually, existing efficiencies can be increased, but often at increased cost. In most cases, improved efficiency is not particularly important although several exceptions were listed earlier. Generally speaking, the major criteria

are whether or not significant weight and volume reductions can be made by using explosive generator power sources and, in some cases, whether or not other reasonable power sources can meet the load's power requirements.

5.6 Power Conditioning

Many of the power handling and conditioning techniques used in nonexplosive pulsed power systems have been adapted to perform explosive pulsed power conditioning. Among these are opening and closing switches, transformers and transmission lines.

5.6.1 *Switches*

Switches, either closing or opening, and often both, are normally required in power conditioning. General treatments of this subject are available in several references, such as the books *Opening Switches* [149] and *High Power Switching* [150], which contain comprehensive reviews of these switching technologies.

5.6.1.1 *Closing Switches*

Most *closing switches* used at Los Alamos are activated by detonators, including those that switch in the capacitor banks normally supplying the initial flux to the FCG. The configuration usually employed consists of an insulator, such as polyethylene, Mylar, polypropylene, captan, etc., sandwiched tightly between two metal plates. One of the plates is connected to an active circuit and the other is connected to the circuit to be switched in. Detonators are mounted on one of the plates over small holes drilled through the plate. Upon initiation, the detonators produce small jets that puncture the insulation, thus allowing current flow from the plate connected to the active circuit to the plate connected to the circuit to be switched in. This type of switch has proved to be quite reliable. Premature switch breakdown during capacitor bank charge-up is usually as disastrous as failure of the switch to close. If the switch fails to close, the timing sequence of the usual shot is such that the generator's explosives are detonated anyway. If the switch breaks down prematurely, often the explosive is not detonated, but the magnetic forces produced by the early current flow will frequently tear up the generator and may break up the explosive, scattering undetonated pieces over the firing table.

Another type of closing switch occasionally used depends upon the two plates discussed above shorting to each other when the voltage difference across the plates reaches a certain preset value. As normally used here, the insulation used between the plates has been selected to break down at a certain voltage. Once that voltage level has been reached, the insulation breaks down, thus letting current flow through the plates and that part of the circuit that was to be switched in.

5.6.1.2 *Opening Switches*

Two kinds of *opening switches*, when required, have been used in most Los Alamos FCG experiments. They are electrically exploding wires or foils, simply called fuses, and explosively formed fuses (EFFs).

Fuses: The study and use of *fuses* has been around for a long time. Generally speaking, they are used to open a circuit branch or to become so resistive that current flow in the circuit branch is greatly reduced and shunted to another branch of the circuit. Generally, as the fuse resistance increases, so does the voltage, IR , across the fuse. In the case of FCGs, fuses are generally designed to not only open one circuit branch, but also to put a high voltage across the new circuit being shunted or switched into the system. Information on the history, behavior and applications of fuses can be found in the four collections of papers published between 1959 and 1968 in the books entitled *Exploding Wires* edited by Chace and Moore [151].

When used with FCGs, fuses are usually made from metal foils or a number of parallel wires. These fuses are usually *tamped* to inhibit expansion of the fuse material. Foils, for example, are often placed between heavily clamped plates and wires are frequently embedded in materials like quartz sand. If expansion is unlimited, the expansion kinetic energy can dwarf the internal energy at certain stages of fuse heating. In order to calculate the performance of a well-tamped fuse being used as a circuit element, the fuse length, l , in the direction of current flow and the cross-sectional area, A , of the foil or wires must be given, as well as their specific resistivity, $\rho(E)$, and material density, D , which are often assumed to be a function of the specific electrical energy, E , deposited in the fuse. Figure 5.21, modeled roughly after the data of DiMarco and Burkhardt [152], shows a plot of resistivity vs. specific energy for well-tamped copper foils of various dimensions. The lower curve was for very thin, short foils. Up to the onset of vaporisation, which occurs when the specific energy is about 1.3 MJ/kg, the fuse's specific resistivity is largely independent of dimensions. Except for very thin foils,

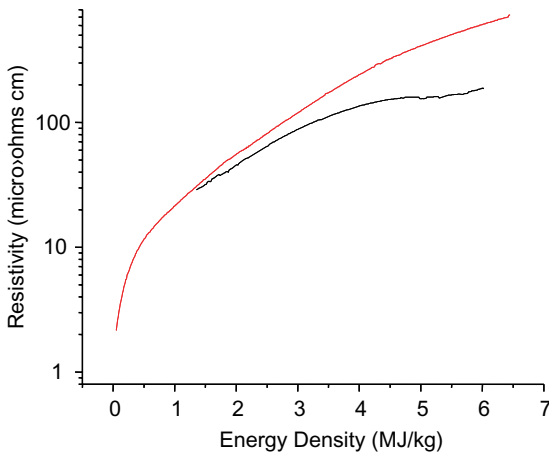


Fig. 5.21 Resistivity vs. specific energy for copper. The lower curve is DiMarco and Burkhardt [151] data for very thin, short foils and the upper curve is calculated data from Lindermuth [152].

specific resistivities up to 3–4 MJ/kg are still reasonably good, with a data spread of 15–30%. These values are consistent with the data collected for wires. At higher energy densities, above 5 MJ/kg, there is more scatter in the data. Proper accounting for all the factors affecting fuse behavior would be a formidable task indeed. Lindemuth *et al.* [153] have, however, developed a code that accounts for many factors not normally treated in fuse calculations and shows favorable agreement with experimental results for various FCG-fuse experiments. It has been found, however, that, in many cases, using the simple equation for resistivity given below yields results not too different from those obtained with more sophisticated codes. The following equation, which is used to calculate resistivity, is a rough fit to the DiMarco-Burkhardt data (upper curve of Fig. 5.21):

$$\rho(E) = 1.7 + 20 \times E + 2.0 \times E^3 \mu\text{ohm-cm}, \quad (5.29)$$

where

$$E = \int I^2 R dt / M \text{ joules/kg}, \quad (5.30)$$

$$R = l\rho(E)/A, \quad (5.31)$$

$$M = lAD(E). \quad (5.32)$$

The above equations are solved iteratively with the generator circuit equations. For heavily tamped fuses, D and A are assumed to be constant.

For untamped fuses, there is generally a huge uncertainty in estimating the density from which the area, A , is obtained, which suggests that there are wide variations in the physical properties of the fuse throughout its volume. The general complexity of this subject is illustrated by Webb *et al.* [154].

In fuse technology, the term *Action* is frequently encountered and it is mathematically defined by the following expression:

$$\text{Action} = \int I^2 dt. \quad (5.33)$$

Tucker and Neilson [155], for example, found a better correlation of some properties of fuses with Action, rather than with specific energy. In particular, fuse designs have sometimes been based upon Action integrals, rather than on specific energies. This integral also appears in the analysis of magnetically accelerated plates and of bridge wire detonators.

Figure 5.22 is a sketch of an early application of fuses employed in an FCG powered experiment reported on by Damerow *et al.* [156]. The demands on the fuse were to deliver a predetermined voltage across a Θ -pinch coil a few microseconds before generator burnout. The thickness of the dielectric material between the two switch plates was chosen to break down at a desired voltage. Laboratory tests confirmed that breakdown voltages could be controlled to within 5–10% of the pre-selected voltage, as indeed they did on a subsequent successful series of shots. A Russian team has employed the same technique in FCG-powered Vircator experiments. As a final comment, before using a fuse in an expensive shot, it goes without saying that considerable pre-testing should have been done.

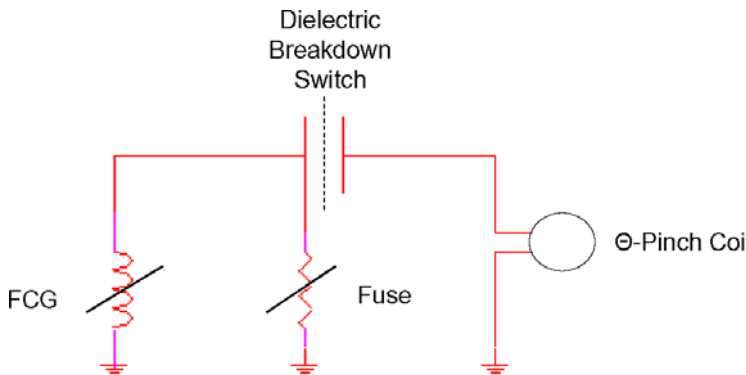


Fig. 5.22 FCG powered Θ -pinch with fuse and dielectric breakdown switch.

Explosive Formed Fuses: Figure 5.23 shows the basic elements of an *Explosively Formed Fuse* (EFF). The inner metallic cylinder, one of the current carrying conductors, is driven radially outward at the appropriate time by a central explosive charge. The circular grooves in the Teflon insulator are used to nearly cut through the conductor, leaving a thin foil at the cut. These switches are sometimes referred to as *cutter switches*, but as Goforth and Marsh [157] noted from various 2-D hydrodynamic calculations, the actual action is one of greatly thinning the portions of the conductors in the grooves, in essence forming much of the conductor into a thin foil, as in a foil fuse. In a later paper, Goforth *et al.* [158] reported on being able to switch a current of about 20 MA into a load in a time of 2 μ s. Earlier, Chernyshev *et al.* [159] used a planar version of this switch.

5.6.2 Transformer Coupling

Large impedance loads, not capable of being powered effectively by direct connection to an FCG, can be effectively energised by transformer coupling to the generator.

5.6.2.1 Powering a Large Inductance

Equation (5.14) shows that the maximum energy (at generator burnout) that can be delivered by a generator with initial inductance L_0 to a series connected load L_1 in the absence of circuit resistance and source or loss inductance is

$$E = \frac{E_0(L_0 + L_1)}{L_1}. \quad (5.34)$$

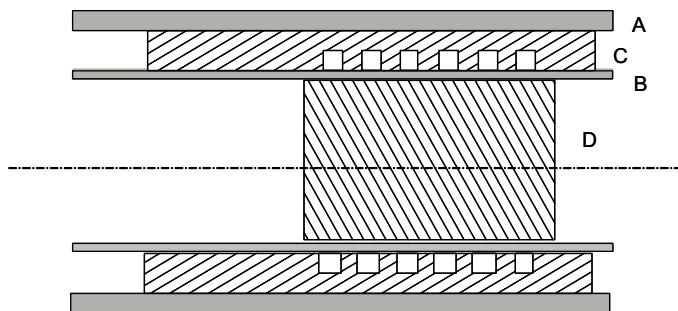


Fig. 5.23 Explosively Formed Fuse: A — outer conductor, B — inner conductor, C — grooved Teflon insulator, and D — explosive initiated simultaneously on axis.

Thus, an FCG could, even under ideal conditions, at most deliver twice the initial circuit energy to a load whose inductance equaled or exceeded that of the initial inductance of the generator.

The situation is different, however, if the load is connected to the secondary coil of a transformer coupled to its primary coil that is powered by an FCG, as shown in Fig. 5.24. In this figure, the primary circuit contains the generator's inductance $L(t)$, the resistance R_1 , the source or loss inductance l_0 and the transformer's primary inductance L_1 . The secondary circuit contains the transformer's secondary inductance L_2 , the resistance R_2 and the inductance L_3 , which is the load that is to be energised. Provisions are made to close the secondary circuit at a later time through the switch shown in the figure. The currents I_1 and I_2 flow through the two circuits. The primary and secondary circuits are mutually coupled with an inductance, M , which can also be expressed in terms of a *coupling coefficient* k ,

$$M = k\sqrt{L_1 L_2}. \quad (5.35)$$

For purposes of illustration, both resistances are set equal to zero, which allows the currents to be found by algebraically solving the simple flux conservation laws. Up to switch time τ , the current I_1 flows only in the primary circuit, which is determined by using

$$(L(t) + l_0 + L_1)I_1 = (L_0 + l_0 + L_1)I_0 = \Phi_0, \quad t \leq \tau. \quad (5.36)$$

At switch time, the current $I_1(\tau)$ is given by

$$I_1(\tau) = \frac{\Phi_0}{L(\tau) + l_0 + L_1} \quad (5.37)$$

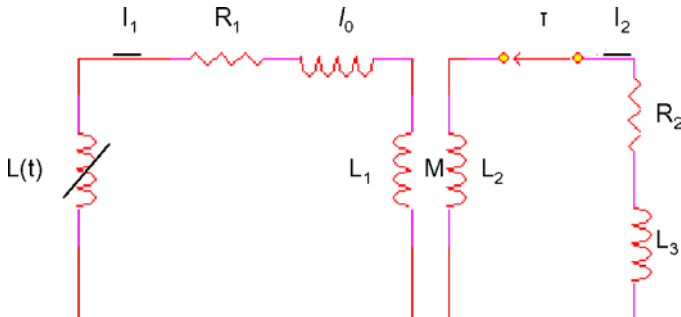


Fig. 5.24 Circuit diagram showing how FCGs power larger impedance loads, L_3 and R_2 , through an impedance matching transformer.

and the flux in the secondary circuit, Φ_2 , is

$$\Phi_2 = MI_1(\tau). \quad (5.38)$$

After switch time, using Eqs. (5.36) and (5.38), the conservation of flux yields the following circuit equations

$$(L(\tau) + l_0 + L_1)I_1 + MI_2 = \Phi_0, \quad (5.39)$$

$$MI_1 + (L_2 + L_3)I_2 = \Phi_2 = M \frac{\Phi_0}{L(\tau) + l_0 + L_1}. \quad (5.40)$$

At generator burnout, $L(t) = 0$, the above equations become

$$I_2(\text{burnout}) = \frac{-ML(\tau)\Phi_0}{(L(\tau) + l_0 + L_1)[(L_2 + L_3)(l_0 + L_1) - M^2]}. \quad (5.41)$$

Choosing optimum values for the transformer inductances can increase I_2 at burnout. This will, of course, increase the energy delivered to the load, L_3 . As an example, assuming the other parameters are fixed and using of Eq. (5.41), the current I_2 at burnout is optimised by proper choice of the transformer secondary inductance

$$L_2(\text{optimum}) = \frac{L_3}{1 - k^2 \frac{L_1}{L_1 + l_0}} \cong \frac{L_3}{1 - K^2}, \quad (5.42)$$

where the *effective coupling coefficient* K is defined by the formula

$$K^2 = \frac{k^2 L_1}{L_1 + l_0}. \quad (5.43)$$

From Eqs. (5.41) and (5.42), the equation for the burnout current gain when the secondary inductance is optimum becomes

$$\frac{I_2(\text{burnout})}{I_0} = \frac{-K}{2\sqrt{1 - K^2}} \cdot \frac{L_0 + l_0 + L_1}{L(\tau) + l_0 + L_1} \cdot \frac{L(\tau)}{\sqrt{L_3(l_0 + L_1)}} \quad (5.44)$$

and the corresponding equation for the load energy at burnout becomes

$$\frac{1}{2} L_3 I_2^2(\text{optimum}) = \frac{E_0}{4} \cdot \frac{L_0 + l_0 + L_1}{l_0 + L_1} \cdot \left(\frac{L(\tau)}{L(\tau) + l_0 + L_1} \right)^2 \cdot \frac{K^2}{1 - K^2}, \quad (5.45)$$

where, E_0 is the initial circuit energy — i.e. $E_0 = 0.5(L_0 + l_0 + L_1)I_0^2$.

As an example, the energy gain ratio, $0.5L_3I_2^2/E_0$, can be calculated for an inductive load of $L_3 = 10 \mu\text{H}$. Using parameter values of: $L(0) = 10 \mu\text{H}$, $L_1 = 0.1 \mu\text{H}$, $l_0 = 0.05 \mu\text{H}$ and $k = 0.85$, assuming that the secondary switching is delayed until $L(\tau) = 2 \mu\text{H}$, and using the parameter $K^2 = k^2 L_1 / (L_1 + l_0)$ and Eq. (5.44), the secondary inductance should be $L_2(\text{optimum}) = 19.29 \mu\text{H}$, and from Eqs. (5.44) and (5.45), the energy and current gains are $0.5L_3I_2^2/E_0 = 13.60$ and $I_2/I_0 = 3.719$, respectively.

This example illustrates several points:

- An energy gain of 13.60 is respectable from a generator whose initial inductance is no larger than that of the load. It should be recalled that a maximum gain of 2 could be realised by directly powering the load with the FCG.
- When the secondary is not optimised, the energy gain is reduced, but only slightly, even when the L_2 values are substantially greater than that required for the optimum energy. On the other hand, the gain drops off rather quickly for L_2 values much less than the optimum value.
- When the secondary is not optimised, the current and energy gains are reduced, but only slightly for values of L_2 greater than that for the optimum current.
- The factor $K^2/(1 - K^2)$ in the energy gain equation varies from 4.26 for $K = 0.9$ to 0.56 for $K = 0.6$. This shows the importance of a high coupling coefficient, k , and of minimising the source inductance, l_0 . If l_0 had been zero in the numerical example given above, the energy gain ratio would be 38.1. It is clear that for given values of k and l_0 , K_2 improves with an increase in the primary inductance L_1 . However, this decreases the value of the other energy gain factors.
- The factor $[L(\tau)/(L(\tau) + l_0 + L_1)]^2$ changes relatively slowly until $L(\tau)$ drops to a few times the residual inductance, $l_0 + L_1$. The difference in gain from switching the secondary in quite late, $L(\tau) = 1 \mu\text{H}$, to quite early, $L(\tau) = 9 \mu\text{H}$, results in a gain decrease of only 22%. This result is important in power conditioning, when the pulse length required by the load must be much shorter than the basic generator burn time.
- Multiplication of Eq. (5.41) by L_3 gives the flux in load L_3 at burnout. Using the optimum value of $L_2 = 19.29 \mu\text{H}$ and the corresponding value of $M = 0.85 \cdot \sqrt{(0.1)(19.29)} \mu\text{H}$, the ratio of flux in L_3 to ϕ_0 , the initial circuit flux, is 7.15. This flux increase in L_3 over the initial circuit flux is usually called *flux multiplication*. At first thought, this seems to be almost a contradiction in terms, since the flux in a perfectly conducting circuit

cannot increase. The answer lies, of course, in that the large negative fluxes in the secondary inductors, $L_2 I_2$ and $L_3 I_2$, are almost balanced by the large positive mutual inductive flux, $M I_1$, in the secondary circuit.

5.6.2.2 Powering Large Resistances

In some cases, the loads to be energised are mainly resistive and include such devices as flash lamps, some diodes, and laser cavities. From Eq. (5.11), it is known that the load resistance must be substantially less than the average generator impedance to be powered directly in an effective way. With rare exceptions, this limits load resistances to less than an ohm. However, with proper selection of the transformer inductances in Fig. 5.24, resistive loads having greater resistance placed in the secondary circuit can be efficiently energised. The coupled circuit equations for the circuit in Fig. 5.24 cannot, in general, be solved analytically in tractable form. Consequently, the equations have been numerically solved in a fairly general way. The primary circuit consists of the generator inductance, $L(t)$, the source or loss inductance, l_0 , the primary transformer inductance, L_1 , and the resistance, R_1 . The secondary circuit contains the transformer's secondary inductance L_2 , the load resistance R_2 , provisions for a load inductance L_3 and a closing switch that functions at time τ . The transformer's mutual inductance is M , which is expressed in terms of the coupling coefficient $k = M/(L_1 L_2)^{1/2}$.

The generator inductance is written explicitly as

$$L(t) = L_0[1 + A(t/T_1) + B(t/T_1)^2 + C(t/T_1)^3], \quad (5.46)$$

where L_0 is the initial generator inductance and T_1 is the generator burnout time. The values of A , B and C may be selected somewhat arbitrarily, provided that $L(t)$ decreases monotonically to zero as $t \rightarrow T_1$. Equation (5.46) is general enough to represent fairly well the inductive behavior of a plate generator. Letting $A = 1$, $B = C = 0$, Eq. (5.46) reduces to Eq. (5.15), which can be used to approximately represent the plate generator. However, for most of the examples given below, the following values have been used: $L_0 = 10\mu\text{H}$, $T_1 = 100\ \mu\text{s}$, $A = -0.75$, $B = -1.5$ and $C = 1.25$. These values result in $L(T_1) = 0$ and $dL(T_1)/dt = 0$ and give a flex point in the inductance at $t = 0.2T_1$. This behavior is qualitatively characteristic of many helical generators. The primary resistance R_1 may be a fixed resistance or it may also include a fuse. When fuses are used here, they are considered to be made of copper and their performance is assumed to be governed by Eqs. (5.29)–(5.32). Thus, the fuse input parameters consist only of the

fuse length and cross-sectional area. Most of the examples to follow do not incorporate a fuse. It is effectively removed from the circuit by giving it a ridiculously large cross-sectional area, such as 0.5 m^2 . For later examples, where it is used, it is somewhat surprising how well these equations yield results in reasonably good agreement with calculations employing more sophisticated models, such as those developed by Lindemuth *et al.* [153].

Energising with no Transformer: As a first example, let's consider directly energising a $20\ \Omega$ load with an FCG. The primary resistance R_1 becomes that of the load. The source inductance is $l_0 = 0.1\mu\text{H}$ and the initial current is $I_0 = 200\text{ kA}$. The inductance L_1 is taken as zero and the secondary circuit suppressed by setting $k = 0$. The initial inductive energy in the system is $E_0 = 0.1LI_0^2 = 202\text{ kJ}$. Upon solving the circuit equations, it is found that only 202.8 kJ are delivered to the $20\ \Omega$ load and almost all of it is delivered in a time of only $2\text{--}3\ \mu\text{s}$. If the circuit inductance L_c does not change, the initial inductive energy would be transferred to the resistive load according to

$$E_R(t) = 0.5L_cI_0^2(1 - e^{-2Rt/L_c}). \quad (5.47)$$

With an initial inductance of $10.1\ \mu\text{H}$ and a resistance of $20\ \Omega$, 99.9% of the initial energy would be delivered to R in less than $2\ \mu\text{s}$. In this time, according to Eq. (5.46), the generator inductance has decreased by only about 1%, but there is almost no flux left in the generator to compress. In total, the generator managed to deliver only an additional 800 J to the original inductive energy of 202 kJ.

Energising Through a Transformer: Let's now consider powering the same $20\ \Omega$ resistor through a transformer. In this case, R_2 of Fig. 5.24 is the $20\ \Omega$ load. However, a standard problem (see Table 5.1) will first be solved and the effects of varying some of the parameters investigated. The upper curve of Fig. 5.25 shows the energy deposited in the $20\ \Omega$ load as a function of time. At generator burnout, which occurs at $100\ \mu\text{s}$, 1.26 MJ of energy has been deposited, the primary current exceeds 4 MA and there is a considerable amount of inductive energy stored in the circuits. This results in an additional transfer of energy to the load beyond generator burnout as the currents decay. In this case, the final energy delivered to the load reaches 1.77 MJ . Ninety eight per cent of this final load energy is delivered in less than $300\ \mu\text{s}$ or somewhat less than $200\ \mu\text{s}$ after burnout. In general, however, it would be difficult to keep the explosive from blowing the circuit apart for such a long time. However, as seen in Fig. 5.25, over

Table 5.1 Device parameters for the Standard Problem.

Primary Circuit	
Generator Equations	(5.39) and (5.40)
Primary Inductance	$L_1 = 0.50 \mu\text{H}$
Source or Loss Inductance	$L_0 = 0.1 \mu\text{H}$
Resistance	$R_1 = 0.005 \Omega$
Initial Current	$I_1(0) = 200 \text{ kA}$
Secondary Circuit	
Secondary Inductance	$L_2 = 800 \mu\text{H}$
Secondary Loss Inductance	$L_3 = 0.50 \mu\text{H}$
Load Resistance	$R_2 = 20 \Omega$
Initial Current	$I_2(0) = 0$
Switch Time	$TS = 0$
Fuze	None
Coupling Constant	
$k = M/(L_1 L_2)^{1/2} = 0.90$	

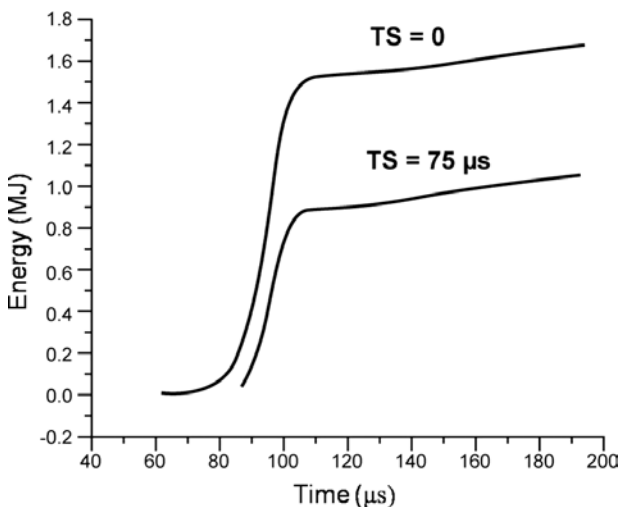


Fig. 5.25 Energy delivered to a 20Ω load vs. time: upper curve is for the standard problem in Table II; lower curve is the same, except the secondary circuit is switched in at $75 \mu\text{s}$.

1.5 MJ is delivered to the load in $110 \mu\text{s}$, or only $10 \mu\text{s}$ beyond burnout, making it relatively easy to protect the rest of the circuit. The lower curve shows the effect of switching in the secondary circuit $75 \mu\text{s}$ after the start of generator operation. The curves in Fig 5.26 show the voltage developed

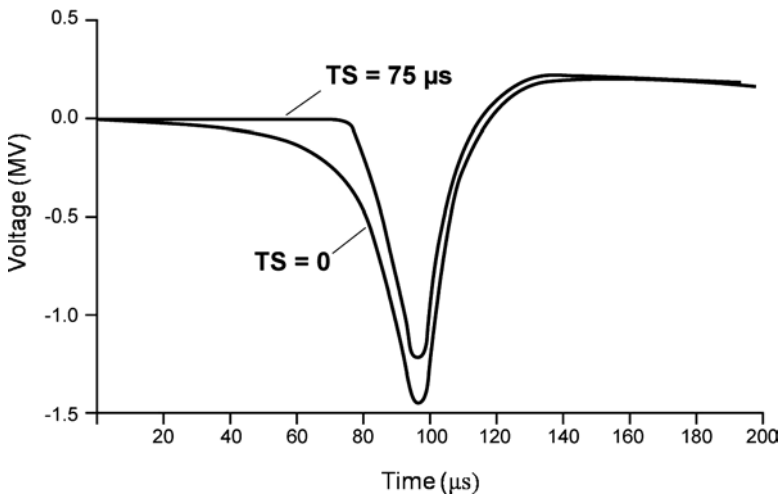


Fig. 5.26 Voltage developed across 20Ω load vs. time for the standard problem ($TS = 0$) and for the standard problem, except the secondary circuit is switched in at $TS = 75 \mu s$.

across the 20Ω load for switch times of 0 and $75 \mu s$ after generator start. In the former case, it reaches a peak of nearly 1.5 MV a little before generator burnout and, although reduced, still exceeds 1 MV for the latter case.

Let's now consider how variations in some of the parameters influence the energy delivered to the load at generator burnout and the final energy actually delivered to the load.

Variation in Primary Source Inductance: With a reduction of the source inductance from $0.1 \mu H$ to $0.05 \mu H$, the energy at burnout increases from 1.26 MJ to 1.69 MJ and the final energy increases from 1.77 MJ to 2.28 MJ . Good generator design calls for minimising the primary source inductance, particularly when transformers are used.

Variation in Primary Resistance: On the one hand, if the primary resistance in the standard problem is reduced from 0.005Ω to 0.002Ω , the energy at burnout increases from 1.26 MJ to 1.76 MJ and the total energy from 1.77 MJ to 2.57 MJ . On the other hand, an increase of the resistance to 0.008Ω decreases these energies to 0.91 MJ and 1.25 MJ , respectively. Coaxial cables are often used to connect generator outputs to the load. Since the cable braids are frequently thin compared to their skin depths, they may be characterised by a resistance and an inductance per unit length. If

the cables are not too long, a sufficient number may be paralleled to keep the resistive losses manageable. Most of the other metallic conductors in a generator circuit are relatively thick compared to their skin depths. Losses in those elements should be treated as source inductance losses that vary with time [139].

Variation in Coupling Coefficient: If the coupling coefficient is reduced from 0.9 to 0.8, the load energy at burnout is reduced from 1.26 MJ to 0.75 MJ and the total energy from 1.77 MJ to 1.16 MJ. A number of transformers, used in applications where FCGs are the power source, have been constructed with $k = 0.9$. However, it is rare to find expendable transformers with k exceeding 0.85 capable of withstanding voltages of a megavolt or more. Some of these transformers will be discussed later.

Variation in Transformer Inductance: As with energising inductances, there are optimum values for the transformer's primary and secondary inductances for maximum energy delivery to resistive loads. Figure 5.27 shows how the energy delivered to a $20\ \Omega$ load varies with the

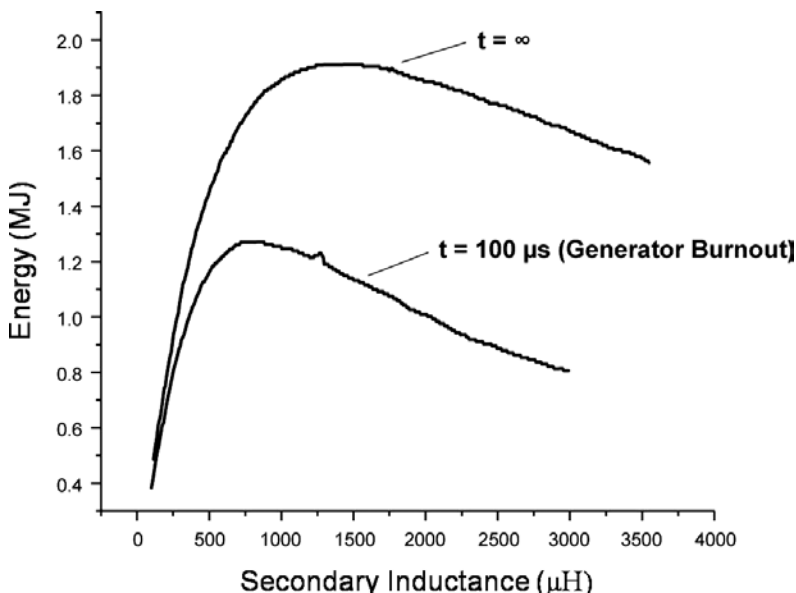


Fig. 5.27 Variation of energy delivered to a $20\ \Omega$ load as a function of transformer secondary inductance. All other circuit parameters are those given for the standard problem in Table II. The lower curve gives the energy delivered up to the time of generator burnout, $t = 100\ \mu\text{s}$; the upper curve gives the total energy delivered, $t = \infty$.

secondary inductance, assuming that the other circuit parameters remain at the values prescribed for the standard problem. The lower curve gives the energy delivered up to the time of generator burnout, while the upper curve gives the final energy. As can be seen in Fig. 5.27, a secondary inductance of about $800 \mu\text{H}$ delivers a maximum energy of 1.26 MJ to the load at generator burnout, while an inductance of about $1500 \mu\text{H}$ delivers the maximum total energy to the load. These curves are typical in that they show a relatively rapid rise in energy delivered to the load with increasing inductance up to the optimum value and a rather gradual fall-off in delivered energy for inductances beyond the optimum. A similar behavior is observed for variations in the primary inductance. For this example, the optimal primary and secondary inductances are $L_1 = 0.35 \mu\text{H}$ and $L_2 = 685 \mu\text{H}$, respectively. For these inductances, 1.29 MJ of energy is delivered to the 20Ω load at generator burnout. In this particular example, which has a rather wide range of values for both L_1 (0.2 to $0.7 \mu\text{H}$) and L_2 (500 to $2000 \mu\text{H}$), the generator still delivers load energies no less than 75% of the optimum value.

Variation in Secondary Switch Closure Time: In some applications, it is undesirable to have the load in the circuit during the entire generator burn time. For the typical generator, with its rising current pulse, the load energy and voltage are not degraded seriously, even when the secondary circuit is not switched in until late in the generator run. The curves in Figs. 5.25 and 5.26 marked $TS = 75 \mu\text{s}$ show the time evolution of energy delivered to the load and of the voltage across the load respectively when the load is switched in at $75 \mu\text{s}$. As seen in these figures, the energy delivered at generator burnout is still over 0.7 MJ , while the peak voltage remains high at 1.2 MV . The rise times are, of course, also shorter. Figure 5.28 shows how some of these quantities vary with switch closure time. Curve *A* shows the energy delivered to the load at generator burnout, curve *B* shows the total energy delivered to the load and curve *C* shows the peak voltage developed across the load. As noted, these values drop off very little for switch times as late as $50 \mu\text{s}$. Even for switch times as late as $80 \mu\text{s}$, over half a megajoule is delivered to the load at generator burnout and the peak voltage developed still exceeds a megavolt. The small ripple in the total final energy near burnout might be an artifact due to the simple energy algorithm used in the code. However, the general circuit behavior is quite complicated, so a physical cause for this behavior cannot be ruled out. In any event, it is not evident that there

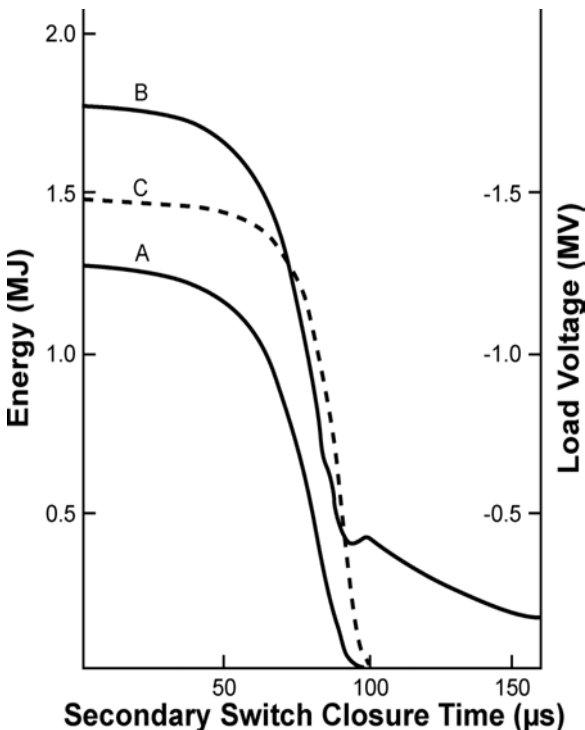


Fig. 5.28 Variation of load parameters vs. secondary circuit switch time. All other circuit parameters are those for the standard problem in Table II. Curve A gives the energy delivered to the $20\ \Omega$ load at generator burnout, $T = 100\ \mu s$. Curve B gives the total energy delivered to the load, $t = \infty$, while curve C gives the peak voltage developed across the $20\ \Omega$ load.

are any advantages to switching in the load after burnout in the present situation.

Variation in Load Size: As can be seen by examining Fig. 5.27, transformer secondary inductances of hundreds of microhenrys are required to power a $20\ \Omega$ load effectively. This is not too surprising, in that it might be expected that RT_1/L has a magnitude on the order of unity, where L is some weighted inductance of the transformer. With $R = 20\ \Omega$ and $T_1 = 100\ \mu s$, L might be expected to be in the millihenry range. As inferred from Fig. 5.27, secondary currents must approach 75 kA in order to develop voltages of nearly 1.5 MV across the $20\ \Omega$ load. It would be very difficult to build secondary inductances in the millihenry range of a reasonable size

that could carry this current and retain a large coupling coefficient. On the other hand, smaller secondary inductances would be expected if the load resistance was smaller. For example, if the load resistance was reduced to $2\ \Omega$ in the standard problem, the inductances are $80\ \mu\text{H}$ for maximum energy delivered at burnout ($1.24\ \text{MJ}$) and about $160\ \mu\text{H}$ for maximum total energy ($1.92\ \text{MJ}$). These energies are about the same as those delivered to the $20\ \Omega$ load, but the secondary inductances are much more reasonable. However, it should be noted that the peak voltage across the $2\ \Omega$ load is less than $0.5\ \text{MV}$, or less than a third of that developed across the $20\ \Omega$ load.

Variation in Generator Burn Time: If the burn time of the generator is reduced, it might be expected that the optimum transformer inductance would be correspondingly reduced. As an example, if the burn time T of the standard problem was reduced to $20\ \mu\text{s}$, the optimal secondary inductance is about $170\ \mu\text{H}$ for delivering a maximum energy at burnout of $1.95\ \text{MJ}$ to the $20\ \Omega$ load and somewhat over $600\ \mu\text{H}$ to deliver a maximum total energy of about $4\ \text{MJ}$. These values are to be compared to $800\ \mu\text{H}$ and $1,600\ \mu\text{H}$ for the standard problem, where $T_1 = 100\ \mu\text{s}$. Peak voltages across the load, which occur a few microseconds before burnout, exceed $4\ \text{MV}$ in these calculations. These large voltages are expected since the generator inductance is wiped out in one-fifth of the time. The larger energies have a more complicated explanation. The shorter operation time has two effects. First, the energy deposited in the load is reduced because the currents flow for shorter times. Second, for the same reason, the resistance in the primary circuit has less time to attenuate the primary current. Coupled with the faster rate of change, the increased secondary currents more than offset the effect of having less time for the load to accumulate energy.

Experimental Example: As an experimental example, the results of a shot described by Erickson *et al.* [160], in which a plate generator was used to power a resistive load through a transformer, are presented. The plate generator had an initial inductance of $174\ \text{nH}$ and a burn time of $7.7\ \mu\text{s}$. The primary inductance was $27.3\ \text{nH}$ and the secondary inductance was $19\ \mu\text{H}$. The load was an encapsulated solution of copper sulfate having a resistance of $25.5\ \Omega$. The measured primary-secondary coupling coefficient was 0.76. Estimates of the loss terms were: primary source inductance, $7\ \text{nH}$; primary resistance, $1.3\ \text{m}\Omega$ and secondary stray inductance, $400\ \text{nH}$. With an initial current of $900\ \text{kA}$ and therefore, an initial inductive energy of about $84\ \text{kJ}$,

the following results were obtained:

- Peak voltage across load: 1.08 MV,
- Load energy at burnout: 23 kJ,
- Total load energy: 40 kJ.

The computer simulation used the approximate expression in Eq. (5.15) for the plate generator. Given that $L_0 = 0.174 \mu\text{H}$ and $T_1 = 7.7 \mu\text{s}$, the coefficients for Eq. (5.46) were $A = -1$, $B = C = 0$, assuming the loss terms and transformer parameters are those cited above. The values predicted by the code were:

- Peak voltage across load: 1.24 MV,
- Load energy at burnout: 32 kJ,
- Total load energy: 48 kJ.

The agreement between calculated and measured values is reasonable in view of the fact that the plate generator model was overly simplistic, as noted earlier [54, 55]. The primary load coil was switched into the circuit at the start of generator burn. Before this time, the current was carried by a ‘ballast’ load, without which the circuit would be incomplete. This load remained in the circuit during the complete shot. However, as seen from Eq. (5.27), where L_τ is essentially L_0 , the peak primary current (I_2 as used in the equation and Fig. 5.4, where L_2 in the figure is assumed to be the primary of the transformer in this example) is not affected much by the presence of the parallel ballast load.

The voltage pulse rose to its peak (at about generator burnout) rapidly and also dropped rapidly after peaking, with a pulse FWHM of $1.2 \mu\text{s}$. Both the voltage pulse shape and the energy delivered to the load were quite satisfactory for the proposed use.

However, the total energy of 40 kJ delivered to the load was less than the initial inductive energy in the system. The causes for this arise from the presence of relatively high loss terms and rather poor coupling of the primary and secondary of the transformer. In comparison, for the same problem with no primary resistance, the primary source inductance decreased to 1 nH and the coupling coefficient increased to 0.9, yielding a peak voltage greater than 3 MV, an energy of about 140 kJ at generator burnout and a total energy of nearly 180 kJ. *These results point out again the importance of minimising the loss terms and increasing the transformer’s coupling*

coefficient, in particular for energy sources that are based on the principle of flux conservation.

Fuse in Primary Circuit of Transformer: With a properly dimensioned fuse in the primary circuit of a transformer, the primary current drops rapidly as the fuse resistance increases. This leads to a large negative value of the primary dI/dt , with a corresponding positive voltage induced in the secondary circuit. This technique, particularly when using FCG drivers, was first proposed by Reinovsky *et al.* [161]. Good fuse design calls for maintaining the fuse resistance low until generator burnout is approached, so that the basic generator current gain is not reduced too much before fuse action. In some respects, this behavior makes the interesting part of the generator action, at least for transformer purposes, occur in much shorter times. Thus, much smaller inductances are required to efficiently power the load than are required without the fuse.

Let's consider the standard problem again, but now incorporate the fuse in the primary circuit. The fuse has heretofore been suppressed by giving it a ridiculously large cross-sectional area that has forced its resistance to remain very low. There are many parameters that can be juggled when optimising the operating characteristics of a fuze. However, Reinovsky, Lindemuth and Vorthman [162] have developed a model based in part on the work of Lindemuth *et al.* [153] that allows assignment of the fuse parameters and of the secondary inductance for optimum performance. In the present example, with a primary inductance of $0.5 \mu\text{H}$ and load resistance of 20Ω , near optimum values for the fuse are a length of 1.75 m , cross-sectioned area of $2.5 \times 10^{-5} \text{ m}^2$ and secondary inductance of $45 \mu\text{H}$.

As noted earlier, as the fuse resistance suddenly increases, the primary dI/dt becomes negative with a resultant positive voltage induced in the secondary circuit. However, before the fuse resistance changes substantially, the primary dI/dt is positive and a normal negative voltage is induced in the secondary. In many cases, this earlier negative part of the secondary voltage pulse is undesirable. However, it may be eliminated without too much loss by delayed switching in the secondary circuit. Figure 5.29 shows the secondary voltage across a 20Ω load for several different secondary closing switch times. As the switch time is further delayed, the negative voltage peak continually diminishes. At a switch time of about $94 \mu\text{s}$, it disappears altogether. Peak positive voltages exceed 1.2 MV for switch times as late as $98 \mu\text{s}$. The curves for load energy vs. time in Fig. 5.30 show a flex point at the moment in time at which peak negative voltage occurs, reflecting

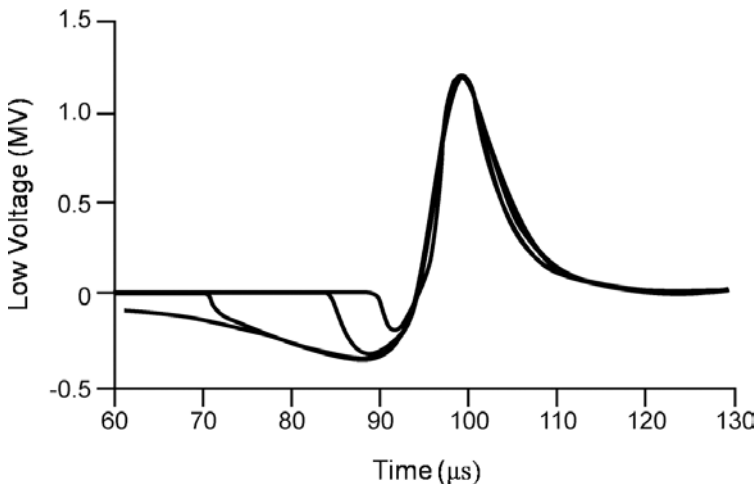


Fig. 5.29 Voltages developed across $20\ \Omega$ load with a fuse in the primary circuit. As noted in the text, a much lower secondary inductance may be used. In this case, the optimum value is $L_2 = 45\ \mu\text{H}$. The four curves correspond to secondary switch times of 0, 70, 85 and 90 μs . The negative voltage pulse disappears entirely for switch times exceeding 94 μs .

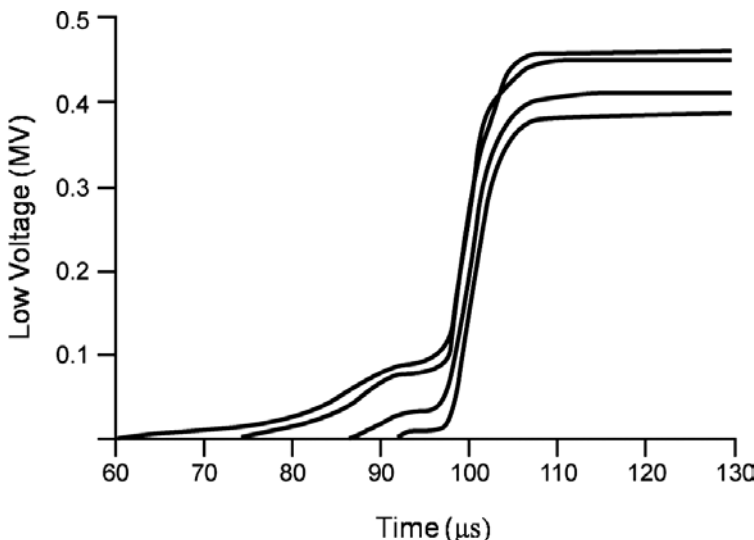


Fig. 5.30 Energies delivered to a $20\ \Omega$ load corresponding to the conditions displayed in Fig. 5.24. It may be noted that the total energy delivered does not diminish much even when the secondary circuit is switched into the circuit as late as 90 μs .

the contribution of this part of the voltage pulse. This behavior, of course, disappears for switch times after $94\ \mu s$. The energy delivered from the rising part of the voltage pulse (obtained by subtracting the energy at the flex point from the total energy delivered) is surprisingly independent of the switch time (up to $98\ \mu s$) and equals about 370 kJ .

Advantages to this approach are large inductance gains and longer burn times, which may be used with reasonably sized secondary inductances. Calculations indicate that these systems can operate effectively with somewhat lower coupling coefficients. Problems can arise, however, from the development of large primary voltages, inability to hold close tolerances on the fuses and difficulties in controlling secondary switch times. Reinovsky, Lindemuth and Vorthman [162] have obtained secondary voltages exceeding a megavolt across high resistance loads using this technique.

5.6.3 *Transformers*

Most of the primary coils in generator powered transformers consist of a single-turn hollow cylinder machined from a solid block or fabricated by bending a plate to the required diameter. In either case, the coils are powered directly through an axial input slot in the cylinder walls. Sometimes the primary coil is switched into the circuit at a later time, while balast loads carry the generator current before switching. Some other types of primary coils will be described below.

For primary coils of this kind, the secondary coil usually consists of a cylindrical dielectric core, overwound with enough conducting turns to produce the required secondary inductance. The secondary coil is then placed within the cylindrical primary coil. The secondary turns are usually wound in the form of a single layer helix or as tape-wound coils. Normally, the lengths of both the primary and the secondary coils are about the same. For either kind of coil, the coupling coefficient is approximately equal to the square of the ratio of the primary coil radius to the mean radius of the secondary coil. These radii must include the current skin depths, which will reduce the coupling coefficient from that calculated by using the mechanical radii. For very high voltages, more insulation between the primary and the secondary will also reduce the coupling.

5.6.3.1 *Helical-Wound Coils*

Helical wound coils are often used when the secondary voltages are not too high. In this case, it is possible to get very high coupling coefficients.

Khristoforov *et al.* [163] reported on a number of experiments where various inductive and resistive loads (up to $1.3\ \Omega$) were successfully powered using transformers of this kind. Coupling coefficients were very high — i.e. 0.94. Energy gains, which is defined to be the ratio of the final load energy to the initial generator energy, approaching 10 were achieved in some experiments. For resistive loads, the energy at generator burnout was frequently about half the final energy. Load voltage maxima were generally low (typically in the vicinity of 10 kV), except for the larger resistive loads where 170 kV was reported for one experiment. The generator employed was a long strip generator with a burn time of about $300\ \mu s$. In an earlier report, Christiansen, Garn and Fowler [164] reported similar results, but employed a helical generator with an effective burn time of approximately $100\ \mu s$. The coupling coefficient was reduced to about 0.8 to reduce the voltage in key parts of the secondary circuit. Fowler *et al.* [165] studied the performance of transformers of this kind in very high magnetic fields. Several different wire materials and dielectric substrates were used. Even for copper wire, transformer integrity was maintained in external magnetic fields as high as 160 T. However, the $\mathbf{j} \times \mathbf{B}$ forces on the wires drove them radially inward into the dielectric substrate, thus further reducing the already rather low initial coupling coefficients. Loads of various kinds were powered, including resistances ranging from 0.4 to $40\ \Omega$, inductances ranging from about 10 to $40\ \mu H$ and, in one case, a $7.15\ \mu F$ capacitor. Generally, the energies delivered were quite small. Only when the external fields were 40 T or less did the delivered energy approach that initially in the generator.

Reinovsky *et al.* [166] have worked with a class of helical generators, where the primary coil of the transformer was simply an extension of its stator windings. Sometimes more than one turn was used for the primary. The secondary coil consisted of a helical coil wound closely over the primary coil. Bichenkov, Prokopiev and Trubachev [167] reported on similar experiments, where the secondary winding covers not only the primary coil but the generator stator winding as well. That part of the secondary winding over the active part of the stator is wiped out by the expanding armature along with the stator. By reversing the winding direction of the primary turns, they obtained coupling coefficients of opposite signs in the two regions of the secondary coil. An analysis of the resulting equations shows that inductive loads may be powered more effectively by this method rather than by the more conventional methods described above. Some experimental data cited supports these calculations.

5.6.3.2 Tape-Wound Coils

Tape-wound secondary coils were used by Erickson *et al.* [160] in the megavolt systems mentioned earlier. These coils were wound from thin copper sheets around a dielectric mandrel, much like a roll of aluminum foil, but with insulation between the turns. Their construction draws heavily on the techniques described by Martin, Champney and Hammer [168]. In the present case, the turns were loosely wound, resulting in a rather low coupling coefficient of 0.76. In the most successful configuration, the outermost turn of the secondary coil was attached to one end of the single-turn primary coil. Thus, the high-voltage side of the secondary appeared on the inner turn, farthest away, and therefore, most insulated from the primary. With plate generators serving as the power supply, megavolt potentials were obtained across resistive loads of $25.5\ \Omega$. These results were considered particularly gratifying in that the entire secondary package was contained within a primary coil with a 4-in diameter. In an effort to improve the coupling coefficients, Freeman *et al.* [169] developed larger diameter coils with more closely packed turns. Coupling coefficients in the range of 0.90 were obtained. Open-circuit voltages in excess of 600 kV were obtained with plate generator power sources. Transformers designed for higher voltages suffered mainly from creep breakdown. Turn-to-turn breakdowns were not observed, which was encouraging. Figure 5.31 shows (a) photograph and (b) drawing of a tape-wound transformer developed by the Institute of Electromagnetic Research in Kharkov, Ukraine.

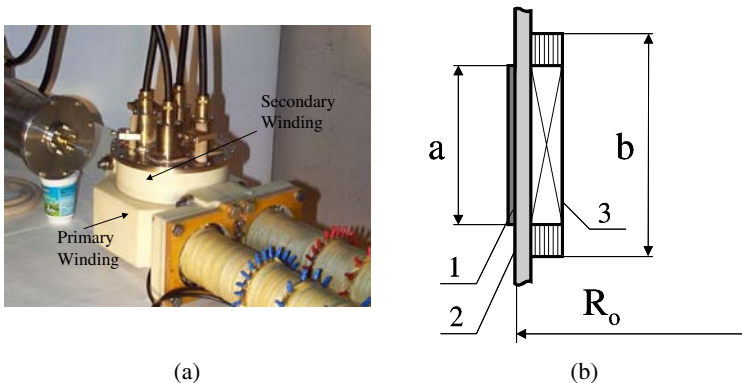


Fig. 5.31 (a) Photograph and (b) sketch of tape wound impulse transformer: 1 — primary winding, 2 — insulating layer and 3 — secondary winding (courtesy of the Institute of Electromagnetic Research, Kharkov, Ukraine).

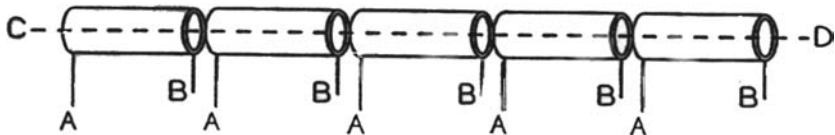


Fig. 5.32 Sketch showing the construction of a coaxial cable transformer.

5.6.3.3 Coaxial cable transformers

Figure 5.32 shows the construction of a coaxial cable transformer. The outer braid is broken into N segments, $A - B$, where N is the number of turns required for the secondary. The ends marked A are attached together and serve as one of the primary coil input leads. The ends marked B are attached together and serve as the other primary input lead. Thus, all $A - B$ segments are in parallel. The center core CD serves as the secondary. The pulse generated across CD tends to be N times the primary pulse. While the origin of this technique is not known, it has been used at LANL for at least 50 years. Coupling coefficients for these transformers can be quite high. Values exceeding 0.97 at 500 kHz were measured at Los Alamos using very low inductance coaxial cables (22 nH/ft) [170]. However, high voltage limits are set by the breakdown strength of the coaxial cable. These transformers have been further developed by Pavlovskii *et al.* [171]. A number of transformer configurations powering various loads are described by these authors.

5.6.4 Generator Flux Sources (Seed Sources)

All flux compression generators require that an initial (or seed) magnetic field exist within the working volume of the generator. It is this initial field that the FCG amplifies. There are two methods for seeding FCGs. The first is *direct seeding* by which the initial field is established by using the flux compression generator geometry — i.e. passing an electric current through the generator circuit and inducing the initial field in FCGs working volume. The second method is *indirect seeding* by which the initial magnetic field is established within the working volume of the FCG by using either permanent magnets or an external coil that is not part of the FCG circuit.

A prime power source, such as a capacitor bank, is typically used to generate the initial flux in the FCG. These sources are also called *seed sources*. While capacitor banks are typically used to seed FCGs, other seed sources, such as external permanent and electromagnets, batteries, FEGs

and FMGs, have also been used. In addition, it is sometimes necessary to use one FCG to seed a second FCG. All three of these cases will be considered in this section.

5.6.4.1 Capacitive Seed Sources

Capacitor banks are normally used to supply the initial flux to an FCG. They are usually series connected to the generator and the initial flux is generated by the current flowing from the capacitor bank through the generator. In this case, care must be taken not to exceed the structural strength limits of the generator, since the accompanying magnetic forces tend to move the generator components according to Eq. (5.25). This equation shows that component motion may be reduced by decreasing the time T required to generate the required initial flux, increasing the effective mass of the conductors, or otherwise inhibiting their motion. A highly effective way to inhibit stator coil motion in helical generators was developed by Pavlovskii *et al.* [145]. They overcast their stators with a layer of concrete. This not only supports the coil turns well, but also seems to reduce the shrapnel range from the ensuing explosion. In the case of plate generators, the aluminum plates are light, their current loading density is high. The initial weight of the explosive serves as additional tamping material. Without this additional weight, the plates would separate substantially during their initial seeding period.

Reduction in loading time can be accomplished by using higher voltage capacitor banks of equivalent energy. Fowler and Caird [172] describe a generator designed to receive an initial loading of 600–700 kJ, normally obtained from two modules of a capacitor bank connected in parallel. By connecting the two modules in series, the time required for transfer of energy was cut in half. Under these conditions the generator encountered no difficulty in accepting energies in excess of a megajoule. Finally, it is known that for a typical sine wave discharge from a capacitor bank into a generator, very little flux is added to the generator in the last 10–20% of the quarter period, yet much of the integral of the square of the current (i.e. the action integral) evolves during this time period. It is, therefore, more or less standard practice to start generator action sometime before peak currents are generated by the seed source. Not only are generator component motions substantially reduced, but so too are heating effects in the conductors. As a general rule, most generators are designed so that their seeding times are short, seldom exceeding a millisecond and usually much

less. This, unfortunately, mainly eliminates the use of the power grid or batteries as a source of seed current. Vorthman *et al.* [173] described a battery powered source, but this ultimately charges a capacitor, which actually seeds the generator.

5.6.4.2 *External Seed Coils*

Flux may also be induced in some generators by external fields. In a few cases, permanent magnets have been used. Generally speaking, however, such systems become very massive and expensive if more than a few joules of magnetic energy are required by the generators. However, pulsed fields generated in external coils can be effective flux sources. This is particularly true when initial axial magnetic fields are required by the generator, such as in helical generators or in cylindrical implosion systems [174]. In most cases [175], the time constants of the external coils are too short for the magnetic field to penetrate the generator conductors. Thus, the generators must remain open-circuited during the loading. Another advantage of this technique is that there are no net translational forces on the generator components during loading. There is, of course, some field diffusion into the conductors, with consequential heating, and there are net compressive forces on the conductors. Under normal circumstances, these effects are not a serious problem. A disadvantage of these systems is that some generators do not allow good coupling to external coils. For example, it is difficult to get a coupling coefficient as high as 0.5 between a suitable external coil and a plate generator.

5.6.4.3 *Booster Generators*

The type of generator used to power a load is selected on the basis of being best able to deliver the pulse required by the load for it to operate optimally. For various reasons, the initial energy requirements for such generators may not be readily accessible from prime energy sources such as capacitor banks. In this case, the required energy may be supplied by another generator, called a *booster generator*. The use of one generator to energise another is known as *staging* or *boosting*. Even a cursory inspection of the literature will reveal many examples of staging or boosting. One of the most common examples is to use a helical generator to power a coaxial generator connected in series with it. Frequently, the armature for the helical generator is simply extended into the coaxial generator. In general,

booster generators are connected in series with low-inductance generators, such as plate and coaxial generators, to seed them.

The situation is different for boosting large generators such as most helical generators. These generators are usually boosted in one of the following two ways. In the first method, the booster generator first delivers energy to a low-inductance load. This load serves as the primary of a transformer. The secondary of the transformer is then selected to most effectively deliver energy to the generator to be boosted. This generator is essentially a fixed inductive load before detonation of the armature explosive. Equations (5.34) to (5.45) contain the idealised results governing this process. Pavlovskii and his co-workers [171] discussed several staged systems, some of them employing two or more boosting stages, where energy gain ratios (final output electrical energy divided by initial electrical energy) are many thousands. The transformers normally employed are made from coaxial cable, as described earlier. In the second method, the booster generator again delivers energy to a low-inductance load but in this case, the second generator fits inside the booster load and thus obtains its flux inductively from the booster generator. This method has been referred to by such names as *flux capture*, *flux trapping* or *dynamic transformer*. There has been some discussion as to which of the methods is more effective. Cnare, Kaye and Cowan [176] lean toward the transformer coupling method, but point out advantages and disadvantages of both methods, while Chernyshev *et al.* [177] argue in favor of the flux trapping method. The arguments supporting these positions are mainly analytical. There are, however, practical considerations that may be the determining factors. The very large coupling coefficients obtainable with coaxial cable transformers are certainly beneficial, but secondary voltages must be maintained below the cable breakdown limits. The flux trap systems are usually simple to construct, but often require awkward topologies.

5.6.4.4 Permanent Magnets, FEGs and FMGs

Over the years, permanent magnets, ferroelectric (or piezoelectric) generators and ferromagnetic generators have been considered potential candidates as seed sources for FCGs and some limited experiments have been performed. Recent advances have made these seed sources more viable, especially with current interest in mini and micro FCGs. Boydston *et al.* [178], Prishchepenko *et al.* [179], Littrell *et al.* [180] and Andreas *et al.* [181] have used permanent magnets to seed FCGs with some success. Freeman

and his colleagues at Texas A&M [182] have built and tested a series of micro generators, which were 2.54 cm long and had stator inner diameters of 2.54 cm. The armatures had an outer diameter of 1.27 cm and a wall thickness of 0.889 mm. All of these units had stators containing 16 turns of a single length of 12-gage magnet wire with a center tapped load connection. The armatures with glide planes were machined from single pieces of 1100 aluminum. The explosive loads extended 1.27 cm beyond the inside attachment of the glide planes on both ends. Two Reynolds RP-501 detonators were used to simultaneously initiate approximately 9.8 g of C-4 explosive. They used Nd-Fe-B ring magnets with inner bores of 1.27 cm and outer diameters of 3.175 cm. The residual flux of these magnets was about 12 kg at the pole face. Using less than 10 g of C-4, they have generated in excess of 1 kA of current. They have subsequently built and tested other variants of these permanent magnet FCGs.

Shkuratov *et al.* at Texas Tech [183–196] and later at Loki, Inc. [76–79, 191–195] developed a series of explosive driven transverse FMG seed sources [183] for driving miniature and medium size FCGs. These FMGs contained cylindrical Nd₂Fe₁₄B ferromagnets with a hole drilled along their axis and pulsed generating coils wound on the ferromagnet. The explosive charge was loaded in the central hole of the ferromagnet. Two different approaches were used to seed the FCG with the FMG. The first approach was to connect the output of the FMG to the stator of the FCG [76–79, 191–195]. This approach was successfully used to seed both helical FCGs and loop FCGs [79, 189, 194, 195]. Schematic diagrams and the equivalent circuit diagram of the devices used in this first approach are shown in Figs. 5.12–5.14. The FMG has a total volume of 25 cm³, used 0.6 g of RDX based high explosive and produced a seed current pulse with an amplitude of 2.5 kA and a rise time of 28 µs (Fig. 5.15). When medium size FCGs were seeded by using this first approach, their output current exceeded 33 kA [195]. The second approach was based on transformer coupling of the pulsed generating coil of the FMG to the stator of the FCG. In other words, there was no direct coupling of the FMG with the FCG. Several FMG-FCG systems based on this second approach were successfully built and tested [194].

Arzamas-16 in Russia and Diehl in Germany have considered both PEGs and FEGs as potential seed sources for small- and medium-size FCGs. The Agency for Defense Development in South Korea [196] has successfully used FMGs to seed medium-size FCGs. Texas Tech University in the United States successfully developed and tested a series of compact battery based high-current seed sources for driving medium-size FCGs [197, 198].

5.7 Summary

After almost 60 years, researchers are still designing, building and testing FCGs and they continue to learn from their experiences. Today, several countries have efforts ranging from fledging to systematic and well-funded programs (see Table 5.2). Enough information has been accumulated so that it is now possible to classify the various types of FCGs according to several different schemes. However, it is convenient to first separate them into two groups: Class I or Mk I generators that are implosive systems and designed to generate high magnetic fields and Class II or Mk II generators designed to deliver high energies and high currents to external loads.

Some of the schemes used for classifying FCGs include [5]:

- Geometric Shape: Mk I generators are cylindrical, while Mk II generators can be cylindrical-coaxial, helical, disk, plate, strip, bellows and spherical.
- Explosive Initiation Scheme: planar surface, line, axial, cylindrical using a cylindrical wave generator or spherical.
- Time Rate-of-Change of Inductance: the dL/dt can be either constant as in the case of plate, bellows, cylindrical coaxial and single-pitch helical generators or variable as in the case of variable pitch helical generators.

Table 5.2 Members of the ‘Megagauss Club’ [5].

Country	Magnetic Flux Density (MG)	Energy (MJ)	Current (MA)	Program Start Year
USA	14	50	320	1950
Russia	28	100	> 320	1952
UK	5	10	20	1956
France	11	8.5	24	1961
Italy	7	2	16	1961
P.R. China	—	—	2	1967
Japan	6.2	—	8	1970
Poland	3.5	—	0.8	1973
Germany	3.1	—	1.2	1975
Romania	7.5	0.5	12	1979
Ukraine	—	—	> 1	1993
Sweden	—	—	0.4	1994
South Africa	—	—	0.88	1995
South Korea	—	0.2	2	1999
Czech Republic	—	—	0.025	2001
Iran	—	—	—	2004

- Compression Time: FCGs can be classified as fast with operation times of less than 10 microseconds, or slow with operation times of tens to hundreds of microseconds.

Since helical FCGs are the most commonly used in practice, there are variations of them that could be used to classify them [5]:

- Fast Pulse: the length of the explosive charge determines their operating time, but this time can be reduced by either employing two-ended initiation or inductive coupling and late crowbarrring.
- High Efficiency: this can be obtained either by dL/dt optimisation or using a nested design.
- High Voltage: this can be achieved by using either an inductive feed with axial initiation or Marxing.
- High Current: this can be accomplished by either shaping the helical coil and/or armature, or using tilted turns and by parallel ‘battery’ coupling or using low-value inductive/resistive loads.
- High Energy: high-energy generators use an optimal dL/dt grading to maintain a constant high electric field and a high value inductive/resistive load.
- High Energy/Current Multiplication: very high energy (or current) multiplication can only be achieved by using a chain of inductively coupled generators.
- Generator Size: generator size does have an impact on the operation and imposes design difficulties, so a scheme for classifying generators by size was developed and is presented in Table 5.3.

Each generator design poses its own unique set of design problems.

- Large Generators: Design problems include large magnetic forces, high voltage insulation and electrical breakdown. Numerical modeling challenges include modeling the coil and armature, accounting for 2D movement and modeling contact delays.
- Medium Generators: Design problems include high-voltage insulation, large magnetic forces, electrical breakdown and energy efficiency. Numerical modeling challenges include 1D radial coil motion, accounting for the total resistance, and electric field distributions.
- Mini Generators: Design problems include energy efficiency, nonlinear diffusion, armature cracks and 2π -clocking. Numerical modeling challenges include accounting for electric field distributions and the total resistance.

Table 5.3 Principle parameters of the four categories of helical MCGs (from Ref. 5).

Parameter	Large	Medium	Mini	Micro
Length (mm)	1000–2500	500–1500	100–500	< 100
Diameter	250–500	100–250	40–100	< 40
Total Mass (kg)	200–2000	10–200	0.2–10	< 0.2
Explosive Mass (kg)	20–200	1–20	0.05–1	< 0.05
Current (MA)	10–50	1–10	0.5–5	< 0.1
Energy (MJ)	10–100	0.2–10	0.1–0.5	< 0.1
Compression Time (μ s)	100–300	50–200	10–50	< 10

- Micro Generators: Design problems include manufacturing, tight tolerances, armature cracks, voltage breakdown, maximum current and 2π -clocking. Numerical modeling challenges include accounting for total resistance, exotic loss mechanisms, contract point delays and micro-jets.

In the next chapter, attention will be focused on the helical FCG, since it is the most studied of all the generators due to its applicability to a number of practical problems and since it has been the subject of recent intensive research and development in several countries.

Bibliography

- [1] C. W. Hawk, *Plasma Pulsed Power Generation*, NIAC Report No. 98–01 (May, 1999).
- [2] L. L. Altgilbers, M. D. J. Brown, I. Grishnaev, B. M. Nova, I. R. Smith, I. Tkach and Y. Tkach, *Magnetocumulative Generators* (Springer-Verlag, New York, 2000).
- [3] G. Knoepfel, *Pulsed High Magnetic Fields*, North-Holland Publishing Company, New York (1970).
- [4] A. Neuber (ed.), *Explosively Driven Pulsed Power: Helical Magnetic Flux Compression Generators* (Springer-Verlag, Berlin, 2005).
- [5] B. M. Novac and I. R. Smith, Brief History and Classification of Magnetic Flux Compression Generators, *Journal of Electromagnetic Phenomena* **3**(11) (2003) 358–365.
- [6] C. M. Fowler, R. S. Caird and D. J. Erickson (eds.), *Megagauss Technology and Pulsed Power Applications* (Plenum Press, New York, 1987).
- [7] J. S. Foster, J. R. Wilson and C. A. McDonald, *Electric Generator*, Patent No. 4,370,576, Submitted (21 Feb. 1962).
- [8] J. L. Hilton and M. J. Morley, *Single Pulse Power Generator*, Patent No. 3,356,869, Submitted (13 Nov. 1963).

- [9] J. J. Allport, *Electrical Power Generator*, Patent No. 3,337,76, Submitted (9 Oct. 1964).
- [10] A. M. Stott, *Electrical Pulse Generator*, Patent No. 3,259,769, Submitted (30 Jan. 1964).
- [11] H. Knoepfel, *Generator for Currents in the Order of Mega-Amperes. Through the Use of Explosives*, Patent No. 3,478,231, Submitted (20 May 1966).
- [12] M. Cowan and R. B. Spielman (eds.), *Megagauss Magnetic Field Generation and Pulsed Power Applications* (Nova Science Pub., New York, 1994).
- [13] I. A. Terletskii, Properties of Very Strong Magnetic Fields by Rapid Compression of a Conducting Shell, *Sov. Phys. JETP* **32** (1957) 301.
- [14] C. M. Fowler, W. B. Garn and R. S. Caird, Production of Very High Magnetic Fields by Implosion, *Journal of Applied Physics* **31**(4) (1960) 588–594.
- [15] H. Knoepfel and P. Herlach (eds.), *Proceedings of the Conference on Megagauss Magnetic Field Generation by Explosives and Related Topics* (Euratom, Brussels, 1966).
- [16] P. Turchi (ed.), *Megagauss Physics and Technology* (Plenum Press, New York and London, 1980).
- [17] V. M. Titov and G. A. Shvetsov (eds.), *Ultrahigh Magnetic Fields, Physics, Techniques, and Applications* (Nauka, Moscow, 1984).
- [18] C. M. Fowler, R. S. Caird and D. J. Erickson (eds.), *Megagauss Technology and pulsed Power Applications* (Plenum Press, New York and London, 1987).
- [19] V. M. Titov and G. A. Shvetsov (eds.), *Megagauss Fields and Pulsed Power Systems* (Nova Science Publishers, Inc., New York, 1990).
- [20] M. Cowan and R. B. Spielman (eds.), *Megagauss Magnetic Field Generation and Pulsed Power Applications* (Nova Science Pub., New York, 1994).
- [21] V. K. Chernyshev, V. D. Selemir and L. N. Plyashkevich (eds.), *Megagauss and Megampere Pulse Technology and Applications* (Sarov, VNIIIEF, 1997).
- [22] H. J. Schneider-Muntau (ed.), *Megagauss Magnetic Field Generation, Its Application to Science and Ultra-High Pulsed-Power Technology* (World Scientific Publishing Company, Singapore, 2004).
- [23] V. D. Selemir and L. N. Plyashkevich (eds.), *Megagauss-9* (VNIIIEF, Sarov, 2004).
- [24] M. von Ortenberg (ed.), *Megagauss X* (VNIIIEF, Sarov, 2005).
- [25] *Megagauss XI*, in publication (London, 2006).
- [26] G. F. Kiuttu, R. E. Reinovsky and P. J. Turchi (eds.), *Proceedings of the 2006 International Conference on Megagauss Magnetic Field Generators and Related Topics and the International Workshop on High Energy Liners and High Energy Density Applications* (Institute of Electrical and Electronics Engineers, Inc., Santa Fe, NM, 2007).
- [27] F. Herlach, Megagauss Magnetic Fields, *Prog. in Phys. X, part 1* (1968) 341–417.

- [28] C. M. Fowler, R. S. Caird and W. B. Garn, An Introduction to Explosive Magnetic Flux Compression Generators, Los Alamos National Laboratory Report, LA-5890-MS (I975).
- [29] X. Gong, M. Cai, Y. Chen, S. Zhong and C. Sun, A Compact Magnetic Flux Compression Generator Driven by Explosives, Ref. 4, pp. 417–424.
- [30] Q. Sun, C. Sun, X. Gong, W. Xie, Z. Liu, W. Dai, Y. Chi, and S. Fu, An Effective Explosive Magnetic Flux Compression Generator with 102 nH Inductance Load, Preprint, *Megagauss-9*, VNIIIEF, Sarov (2004), pp. 185–188.
- [31] M. Bavay, P. L'Eplattenier, C. Mangeant, F. Hamann, Ph. Monjaux, F. Lassalle, F. Bayol, D. Huet, G. Avrillaud and B. Lalle, The Magnetic Flux Compression Scheme as a Power Amplification & Pulse Shaping Stage, *ICOPS 2002*, Canada (2002).
- [32] G. Staines, Compact Sources for Tactical RF Weapon Applications, *AMEREM 2002*, Annapolis, Maryland (2002).
- [33] G. Staines, Rheinmetall Sets out Its Energy Weapon Stall, International Defense Review, Jane's International Group (Feb. 2003).
- [34] Y. Kakudate, S. Usuda, H. Yukoi, M. Yoshida, S. Fujiwars, R. Kameyama and M. Miyanoto, Study on the Explosive-Driven Magnetic Generator for Large Current Production, *Journal of Japan Explosives Society* **57** (1996) 123–128.
- [35] R. Bouma, TNO, private communications.
- [36] G. Turner, Nuclear Energy Corporation of South Africa, Private Communication (2003).
- [37] J. W. Ahn, J. H. Kuk, J. Lee, J. S. Choi, C. H. Kim, and J. H. Ryu, Output Characteristics of Serially Connected Magneto-Cumulative Generators, *Megagauss-9* (VNIIIEF, Sarov, 2004), pp. 223–227.
- [38] H. Kuk, J. W. Ahn and H. H. Lee, Output Characteristics of the Cascade MCG System Consisting of Several MCGs Connected in Parallel, *Megagauss-9* (VNIIIEF, Sarov, 2004), pp. 217–222.
- [39] Gert Bjarnholt, FOI, Sweden, private communications.
- [40] Institute of Electromagnetic Research, www.iemr.vl.net.ua.
- [41] M. Kristiansen, P. Worsey, B. L. Freeman and F. Stefani, *Explosive-Driven Pulsed Power Generation (MURI 98)*, Report No. AFOSR MURI 00-2 (1 Sept. 2000).
- [42] J. C. Boydston, B. M. Freeman and A. R. Luginbill, Fast Helical Flux Compression Generator using a 50-mm Form Factor, *ICOPS 2002*, Alberta, Canada (May 2002).
- [43] T. G. Engel and N. B. VanKirk, Design and Development of a Novel Flux Compression Generator for Mine Detection, *IEEE Transactions on Plasma Science* **35**(1) (1999) 245–249.
- [44] M. Turner, Experiments in Magnetic Flux Compression Using a Plasma Armature, NASA/CR-2003-212169 (Feb. 2003).
- [45] C. M. Fowler, W. B. Garn and R. S. Caird, Production of Very High Magnetic Fields by Implosion, *J. Appl. Phys.* **31** (1960) 588–594.

- [46] J. A. Stratton, *Electromagnetic Theory*, McGraw-Hill Book Company, Inc., New York and London (1941). This book, written more than a half-century ago, remains one of the classic treatments of the subject. The electromagnetic stress and strain energy tensors occur frequently in the text, but are carefully indexed. Rationalised MKS units are used throughout.
- [47] B. M. Dobraty and P. C. Crawford, *LLNL Explosive Handbook, Properties of Chemical Explosives and Explosive Simulates*, January 31 (1985), report UCRL-52997, Change 2 (from National Technical Information Service, U.S. Department of Commerce, 5285 Post Royal Road, Springfield, VA 22161).
- [48] C. M. Fowler, D. B. Thompson, W. B. Garn and R. S. Caird, LASL Group M-6 Summary Report: The Birdseed Program, Los Alamos National Laboratory Report, LA-5141-MS (January 1973).
- [49] B. L. Freeman, R. S. Caird, D. J. Erickson, C. M. Fowler, W. B. Garn, H. W. Kruse, J. C. King, D. E. Bartram and P. J. Kruse, Plasma Focus Experiments Powered by Explosive Generators, *Megagauss Fields and Pulsed Power Systems*, eds. V.M. Titov and G.A. Shvetsov (Nova Science Publishers, Inc., New York, 1990), pp. 136–144.
- [50] C. M. Fowler, R. S. Caird and W. B. Garn, *An Introduction to Explosive Magnetic Flux Compression Generators*, Los Alamos National Laboratory Report LA-5890-MS (1975), pp. 25–27.
- [51] C. M. Fowler, R. S. Caird, W. B. Garn and D. B. Thowson, The Los Alamos Flux Compression Program from its Origin, *Proceedings of the Conference on Megagauss Magnetic Field Generation by Explosives and Related Topics*, eds. H. Knoepfel and F. Herlach (Euratom, Brussels, 1966), pp. 7–8.
- [52] H. Knoepfel, *Pulsed High Magnetic Fields*, Figs. 3.2 and 3.3 and Eq. (3.32), North-Holland Publishing Company (Amsterdam and London, 1970), pp. 49–54.
- [53] C. M. Fowler, R. S. Caird, W. B. and Garn, An Introduction to Explosive Magnetic Flux Compression Generators, Los Alamos National Laboratory Report LA-5890-MS, (1975), pp. 4–11.
- [54] R. S. Caird, C. M. Fowler, D. J. Erickson, B. L. Freeman and W. B. Garn, A Survey of Recent Work on Explosive-Driven Magnetic Flux Compression Generators, *Energy Storage, Compression and Switching*, Vol. 2, eds. V. Nardi, H. Sahlin and W. H. Bostick (Plenum Press, New York, 1983), pp. 1–18.
- [55] R. S. Caird, D. J. Erickson, C. M. Fowler, B. L. Freeman and J. H. Goforth, A Circuit Model for the Explosive Driven Plate Generator, *Megagauss Fields and Pulsed Power Systems*, eds. V. M. Titov and G. A. Shvetsov (Nova Science Publishers, Inc., New York, 1990), pp. 246–253.
- [56] C. M. Fowler, R. S. Caird, D. J. Erickson, B. L. Freeman, and J. C. King, Explosive Flux Compression Generators for Rail Gun Power Sources, *IEEE Trans. Mag.* **18**(1), (1982) 64–67.
- [57] C. M. Fowler, D. R. Peterson, J. F. Kerrisk, R. S. Caird, B. L. Freeman and J. H. Goforth, Flux-Compression Strip Generators, *Megagauss Fields and Pulsed Power Systems*, eds. V. M. Titov and G. A. Shvetsov (Nova Science Publishers, Inc., New York, 1990), pp. 282–291.

- [58] F. Herlach, H. Knoepfel and R. Luppi, Magnetic Field and Current Amplification with Non-Cylindrical Explosive Systems, *Proceedings of the Conference on Megagauss Magnetic Field Generation by Explosives and Related Topics*, eds. H. Knoepfel and F. Herlach (Euratom, Brussels, 1966), pp. 287–304 (See Figs. 3 and 4 and related text.)
- [59] E. I. Bichenkov, Explosive Generators, *Sov. Phys. Doklady* **12** (1967) 567–569.
- [60] Atomic Energy Research in the Life and Physical Science (report of the U.S. Atomic Energy commission, available from the Superintendent of Documents, U.S. Government printing Office, Washington DC, 1960), p. 104.
- [61] J. E. Beasancon, J. Morin, and J. M. Vedel, Production de champ magnétique intense par implosion de tubes en cuivre non fendus, *C. R. Acad. Sc Paris*, t. 271, Ser. B, August (1970), pp. 397–399.
- [62] A. I. Pavlovskii, N. P. Kolokolchikov, O. M. Tatsenko, A. I. Bykov, M. I. Dolotenko and A. A. Karpikov, Reproducible Generation of Multimegagauss Magnetic Fields, *Megagauss Physics and Technology*, ed. P. Turchi (Plenum Press, New York and London, 1980), pp. 627–439.
- [63] A. I. Pavlovskii, A. I. Bykov, M. I. Dolotenko, A. A. Karpikov, N. P. Kolokolchikov, V. I. Mamyshev and O. M. Tatsenko, Limiting Value of Reproducible Magnetic Field in Cascade Generator MC-I., *Megagauss Technology and Pulsed Power Applications*, eds. C. M. Fowler, R. S. Caird and D. J. Erickson (Plenum Press, New York, 1987), pp. 37–54.
- [64] C. M. Fowler and B. L. Freeman, The Los Alamos-Arzamas-16 High Magnetic Field Shot Series, Ancho Canyon Site, 1993, Los Alamos National Laboratory report: LA-UR-94-2802.
- [65] R. G. Clark, Dirac Series: Results and Challenges, *Megagauss Magnetic Field Generation, Its Application to Science and Ultra-High Pulsed-Power Technology*, ed. H. J. Schneider-Muntau (World Scientific Publishing Company, Singapore, 2004), pp. 12–21.
- [66] B. A. Boyko, A. I. Bykov, M. I. Dolotenko, N. P. Kolokol'chikov, I. M. Markevtsiev, O. M. Tatsenko and A. M. Shuvalov More than 20 MG Field Generators in the Cascade magnetocumulative MC-1 Generator, *Megagauss Magnetic Field Generation, Its Application to Science and Ultra-High Pulsed-Power Technology*, ed. H.J. Schneider-Muntau (World Scientific Publishing Company, Singapore, 2004), pp. 61–66.
- [67] S. Felber, R. S. Caird, C. M. Fowler, D. J. Erickson, B. L. Freeman and J. H. Goforth, Design of a 20 -MJ Coaxial Generator, Ref. 3, pp. 321–329.
- [68] M. G. Sheppard, B. L. Freeman, R. L. Bowers, J. H. Brownell, C. M. Fowler, J. N. Fritz, A. E. Greene, S. P. Marsh, T. A. Oliphant, D. L. Tubbs and D. L. Weiss, Design, Testing, and Modeling of a High-Gain Magnetic Flux-Compression Generator, *Megagauss Technology and Pulsed Power Applications*, eds. C. M. Fowler, R. S. Caird and D. J. Erickson (Plenum Press, New York, 1987), pp. 479–488.
- [69] J. H. Goforth, W. T. Atchison, C. M. Fowler, R. E. Keinigs, H. Oona, D. G. Tasker, D. B. Reisman, P. T. Springer and R. C. Cauble, Design of High

Explosive Pulsed Power Systems for 20 Mb Isentropic Compression Experiments, *Megagauss Magnetic Field Generation, Its Application to Science and Ultra-High Pulsed-Power Technology*, ed. H. J. Schneider-Muntau (World Scientific Publishing Company, Singapore, 2004), pp. 137–147.

- [70] V. K. Chernyshev, B. E. Grinevich, V. V. Vahrushev and V. I. Mamyshev, Scaling Image of 90 MJ Explosive Magnetic Generators, *Megagauss Fields and Pulsed Power Systems*, eds. V. M. Titov and G. A. Shvetsov (Nova Science Publishers, Inc., New York, 1990), pp. 347–350.
- [71] V. A. Demidov, A. I. Kraev, V. I. Mamyshev, A. A. Petrukhin, V. P. Pogorelov, V. K. Chernyshev, V. A. Shvetsov and V. I. Shpargin, Three-Module Disk Explosive Magnetic Generator, Ref. 5, pp. 351–354.
- [72] I. R. Lindemuth, C. A. Ekdahl, C. M. Fowler, R. E. Reinovsky, S. M. Younger, V. K. Chernyshev, V. N. Mokhov and A. I. Pavlovskii, US/Russian Collaboration in High Energy Density Physics Using High Explosive Pulsed Power: Ultrahigh Current Experiments, Ultrahigh Magnetic Fields Applications and Progress Toward Controlled Thermonuclear Fusion, *IEEE Transactions on Plasma Science*, **21**(6) (1997) 1357–1372.
- [73] C. M. Fowler, R. F. Hoeberling and S. P. Marsh, Disk Generator with Nearly Shockless Accelerated Driver Plate, *Megagauss Fields and Pulsed Power Systems*, eds. V. M. Titov and G. A. Shvetsov (Nova Science Publishers, Inc., New York, 1990), pp. 337–345.
- [74] S. J. Lukasik, G. W. Zepko and R. I. Jameson, Magnetic Flux Compression in an Expanding Geometry, *Proceedings of the Conference on Megagauss Magnetic Field Generation by Explosives and Related Topics*, eds. H. Knoepfel and F. Herlach (Euratom, Brussels, 1966), pp. 397–419.
- [75] V. A. Vasyukov, Explosive Magnetic Generators of a Loop Type Operating within a Middle Range of Fast Current Pulses (15–45 MA), *Megagauss and Megampere Pulse Technology and Applications*, eds. V. K. Chernyshev, V. D. Selemir and L. N. Plyashhevich (Sarov, VNIIEF, 1997), pp. 292–293.
- [76] S. I. Shkuratov, E. F. Talantsev, J. Baird, L. L. Altgilbers, P. T. Tracy and A. H. Stults, Autonomous Completely Explosive Pulsed Power System Based on Loop FCG and Shock Wave FMG Seed Source, *Megagauss XI*, London (September, 2006), to be published.
- [77] S. I. Shkuratov, E. F. Talantsev, J. Baird, L. L. Altgilbers, and A. H. Stults, A New Concept for Constructing Autonomous Completely Explosive Pulsed Power System: Transverse Shock Wave Ferromagnetic Primary Power source and Loop Flux Compression Amplifier, *Proceedings of the 2006 International Conference on Megagauss Magnetic Field Generators and Related Topics*, eds. G. F. Kiutti, R. E. Reinovsky and P. J. Turchi, IEEE Catalog Number: CFP06MEG-PRT (2007), pp. 331–336.
- [78] S. I. Shkuratov, E. F. Talantsev, J. Baird, L. L. Altgilbers, and A. H. Stults, Explosive Driven Mini-System based on Shock Wave Ferromagnetic Seed Source and Loop Magnetic Flux Compression Generator, Digest of Technical papers, *16th International Pulsed Power Conference* (2007), pp. 1141–1145.

- [79] S. I. Shkuratov, J. Baird, E. F. Talantsev and L. L. Altgilbers, Electric Discharge Caused by Expanding Armatures in Flux Compression Generators, *Appl. Phys. Letters* **94** (2009) 171502.
- [80] L. L. Altgilbers, P. T. Tracy, J. Burch, T. X. Zhang and S.T. Wu, Analytic Model for the Loop Magnetocumulative Generator, Megagauss XI, London (September 2006), to be published.
- [81] R. S. Caird and C. M. Fowler, Conceptual Design for a Short-Pulse Explosive-Driven Generator, *Megagauss Technology and Pulsed Power Applications*, eds. C. M. Fowler, R. S. Caird and D. J. Erickson (Plenum Press, New York and London, 1987), pp. 425–431.
- [82] C. M. Fowler, R. S. Caird, B. L. Freeman and S. P. Marsh, Design of the Mark 101 Magnetic Flux Compression Generator, *Megagauss Technology and Pulsed Power Applications*, eds. C. M. Fowler, R. S. Caird and D. J. Erickson (Plenum Press, New York and London, 1987), pp. 433–439.
- [83] B. L. Freeman, C. M. Fowler, J. C. King, A. R. Martinez, J. B. VanMarter, L.R. Veeser, and J.E. Worthman, Testing of the Mark 101 Magnetic Flux Compression Generator, *Megagauss Technology and Pulsed Power Applications*, eds. C.M. Fowler, R.S. Caird, and D.J. Erickson (Plenum Press, New York and London, 1987), pp. 441–445.
- [84] S. Minomura and H. G. Drickamer, *J. Phys. Chem. Solids* **23** (1962) 451.
- [85] S. D. Gilev and A. M. Trubachev, Metallization of Monocrystalline Silicon Under Shock Compression, *Phys. Stat. Solids B* **211** (1999) 379–383.
- [86] S. D. Gilev and A. M. Trubachev, MC Generator based on Powered Aluminum, Izd. Institute of Hydrodynamics, Sib. Otd. Akad., NAUK SSSR, No. 48, Novosibirsk (1980).
- [87] E. I. Bichenkov, S. D. Gilev and A. M. Trubachev, MC Generators using Transition of a Semiconducting Material into a Conducting State, *Prikl. Mekh. Tekh. Fiz.* **5** (1980) 125–129.
- [88] E. I. Bichenkov, S. D. Gilev and A. M. Trubachev, Magnetic Course Generators using the Transition of a Semiconductor material into a Conducting State, *J. Appl. Mech. Tech. Phys.* **21** (1980) 678–682.
- [89] E. I. Bichenkov, S. D. Gilev and A. M. Trubachev, Shock Wave MC Generators, *Ultrahigh Magnetic Fields*, eds. V. M. Titov and G. A. Shvetson (Nauka, Moscow, 1984), pp. 88–93.
- [90] E. I. Bichenkov, S. D. Gilev and A. M. Trubachev, Shock Wave Method of Generating Megagauss Magnetic Fields, *J. Appl. Mech. Tech. Phys.* **28** (1987) 331–339.
- [91] E. I. Bichenkov, S. D. Gilev and A. M. Trubachev, Shock Wave Method for Generation of Megagauss Magnetic Fields, *Megagauss Technology and Pulsed Power Applications*, eds. C. M. Fowler, R. S. Caird and D. J. Erickson (Plenum, New York, 1987), pp. 89–105.
- [92] E. I. Bichenkov, S. D. Gilev, A. M. Ryachun and A. M. Trubachev, Magnetic Field Compression by Shock Induced Conduction Waves in High Porosity Materials, *J. Appl. Mech. Tech. Phys.* **37** (1996) 785–793.

- [93] E. I. Bichenkov, Structure of a Stationary Current Wave Produced by a Shock Wave in a Conducting Material with a Transverse Magnetic Field, *Fiz. Gorenija Vzryva* **33**(4) (1997) 113–127.
- [94] E. I. Bichenkov, Electromagnetic Field and Current Waves Generated by a Shock Wave Entering a Conductor with a Transverse Magnetic Field, *Prikl. Mekh. Tekh. Fiz.* **38**(2) (1997) 19–25.
- [95] E. I. Bichenkov, Shock Wave Driven Flux Compression Technique, *Mega-gauss Magnetic Field Generation, Its Application to Science and Ultra-High Pulsed Power Technology*, ed. H. J. Schneider-Muntau (World Scientific, Singapore, 2004), pp. 593–598.
- [96] E. I. Bichenkov, Two Alternatives of Magnetic Cumulation, *J. Appl. Mech. Tech. Phys.* **41**(5) (2000) 792–805.
- [97] E. I. Bichenkov, Electrodynamic Effects Accompanying the Propagation of Current Carrying Shock Waves in a Transverse Magnetic Field, *Combustion, Explosion, and Shock Waves* **36**(6) (2000) 809–815.
- [98] K. Nakayama, New Method of Magnetic Flux Compression by means of the Propagation of Shock Induced Metallic Transition in Semiconductors, *Appl. Phys. Lett.* **38** (1981) 109–110.
- [99] K. Nagayama, T. Oka and T. Mashimo, Experimental Study of a New Mechanism of Magnetic Flux Cumulation by the Propagation of Shock Compressed Conductive Region in Silicon, *J. Appl. Phys.* **53** (1982) 3029–3037.
- [100] K. Nagayama and T. Mashimo, Magnetohydrodynamic Study of Flux Cumulation by the Propagation of Shock Compressed Conductive Region in Semiconductors, *Ultrahigh Magnetic Fields*, eds. V. M. Titov and G. A. Shvetsov (Nauka, Moscow, 1984), pp. 270–277.
- [101] K. Nagayama and T. Mashimo, Explosive Driven Magnetic Flux Compression by the Propagation of Shock Compressed Conductive Region in Highly Porous metal Powders, *J. Appl. Phys.* **61** (1987) 4730–4735.
- [102] K. Nagayama and T. Mashimo, Magnetohydrodynamic Study of the Interaction of Magnetic Flux with High Pressure Shock Waves in Metal Powder, *Shock Tubes and Waves*, ed. H. Grenig (Aachen: VCH, 1987), pp. 881–887.
- [103] S. D. Gilev and A. M. Trubachev, Production of Strong Magnetic Fields by Shock Waves in a Medium, *Sov. Tech. Phys. Lett.* **8** (1982) 396–397.
- [104] S. D. Gilev and A. M. Trubachev, Obtaining Strong Magnetic Fields with Magnetocumulative Generators Based on Porous Material, *J. Appl. Mech. Phys.* **24** (1983) 639–643.
- [105] S. D. Gilev and T. Yu. Mikailova, Current Wave in Shock Compression in Matter in a Magnetic Field, *Tech. Phys.* **41** (1996) 407–411.
- [106] S. D. Gilev, Effect of the Conductivity of a Shock Compressed Substance on the Electromagnetic Response of a Shock Formed Set of Conductors, *Combustion, Explosion, and Shock Waves*, **33**(4) (1997) 504–511.
- [107] S. D. Gilev and T. Yu. Mikailova, The Development of a Method for Measuring a Condensed Matter Electroconductivity for Investigation of Dielectric-Metal Transitions in a Shock Wave, *J. Phys. IV, France*, **5** Colloq. C3 (EURODYMAT 97) (1997) 211–216.

- [108] S. D. Gilev and T. Yu. Mikhailova, Electromagnetic Field and Current Waves in a Conductor Compressed by a Shock Wave in a Magnetic Field, *Combustion, Explosion, and Shock Waves* **36**(6) (2000) 816–825.
- [109] S. D. Gilev and T. Yu. Mikhailova, Electromagnetic Field Formed by Shock Compression of a Conducting Magnetic, *Combustion, Explosion, and Shock Waves* **39**(6) (2003) 704–714.
- [110] S. D. Gilev and A. M. Trubachev, Metallization of Silicon in a Shock Wave: Metallization Threshold and Ultrahigh Defect Densities, *J. Phys.: Condens. Matter* **16** (2004) 8139–8153.
- [111] S. D. Gilev, Electrical Conductivity of Metal Powders under Shock Compression, *Combustion, Explosion, and Shock Waves* **41** (2005) 599–609.
- [112] S. D. Gilev, Semiconductor-Metal Transition in Selenium Shock Compression, *Combustion, Explosion, and Shock Waves* **51** (2006) 860–866.
- [113] S. D. Gilev, Shock Wave Cumulation of Magnetic Field: Building Physical Model of the Phenomenon, Proceedings of Megagauss XI (in publication), London, September (2006).
- [114] S. D. Gilev, Electrode Gauge as Instrument for Studying Shock Compression and Metallization of the Substance, *Combustion, Explosion, and Shock Waves* **43**(5) (2007) 598–606.
- [115] S. D. Gilev, Semiconductor-Metal Transition in Selenium under Shock Compression, *Technical Physics* **51** (2006) 860–866.
- [116] A. A. Barmin, O. S. Mel'nik, A. B. Prishchepenko, O. L. Filippova, A. Sh. Shakhabzob and M. V. Shchelkachev, Losses of Electromagnetic Energy in Compression of a Magnetic Field by a Jump of the Second Kind, *Izv. Akad. Nauk SSSR, Mekh. Zhidk. Gaza* **6** (1988) 166–170.
- [117] A. A. Barmin, O. L. Filippova and O. E. Mel'nik, Disintegration of a Single Crystal by means of an Imploding Shock Wave in the Presence of a Magnetic Field, Report No. 4032, Institute of Mechanics, Moscow (1991).
- [118] A. B. Prishchepenko, Electromagnetic Weapons in Air Defense, *Air Defense Herald* **7** (1993) 51–55.
- [119] A. A. Barmin and A. B. Prishchepenko, Compression of a Magnetic Field in a Single Crystal by a Strong Converging Ionizing Shock Wave, *Megagauss Magnetic Field Generation and Pulsed Power Applications*, Apart 1, eds. M. Cowan and R.B. Spielman (Nova Science Publishers, Inc., Commack, NY, 1994), pp. 35–40.
- [120] A. B. Prishchepenko, A. A. Barmin, V. V. Markov and O. E. Mel'nik, Magnetic Field Compression by Converging Ionizing Shock Wave in Alkali Halogenide Single Crystal, *Megagauss and Megampere Pulse Technology and Applications*, Part 1, eds. V. K. Chernyshov, V. D. Selemir and L. N. Plyashkevich (RFND-VNIIEF, 1997), pp. 152–156.
- [121] A. A. Barmin and M. S. Rumnenko, Investigation of the Process of Compression of a Magnetic Field by a Strong Ionizing Shock Wave in a CsI Crystal, *Fluid Dynamics* **37**(3) (2002) 484–495.
- [122] B. M. Novac, I. R. Smith, D. F. Rankin and M. Hubbard, An Insulator-Metallic Phase Transition Cascade for Improved Electromagnetic Flux

- Compression in Θ -pinch Geometry, *IEEE Trans. Plasma Sci.* **32** (2004) 1960–1965.
- [123] B. M. Novac, I. R. Smith and S. E. Goh, Monitoring the Velocity of the Insulator-Metallic Phase Transition in Aluminum Powder Under Shock Loading, *J. Phys. D: Appl. Phys.* **34** (2001) 174–176.
 - [124] G. Bjarnholt, S. M. Golberg and S. E. Nyholm, Compression of the Magnetic Flux by Imploding Ionizing Shock Waves, *11th IEEE International Pulsed Power Conference*, Vol. 2 (1997), pp. 1497–1502.
 - [125] H. Almstrom, G. Bjarnholt, S. M. Goldberg and M. A. Libermann, On the Methods of Generation of Ultrahigh Pulsed Magnetic Field, *Megagauss and Megampere Pulse Technology and Applications*, Part 1, eds. V. K. Chernyshev, V. D. Selemir and L. N. Plyashkevich (RFND-VNIIEF, 1997), pp. 144–151.
 - [126] H. Almstrom, G. Bjarnholt, S. M. Golberg and M. A. Libermann, Numerical Modeling of Magnetic Flux Compression by Cylindrical Imploding Ionizing Shock Wave, *Megagauss and Megampere Pulse Technology and Applications*, Part 1, eds. V. K. Chernyshev, V. D. Selemir and L. N. Plyashkevich (RFND-VNIIEF, 1997), pp. 453–462.
 - [127] S. E. Nyholm, Numerical Simulation of Shock Wave Driven Flux Compression with MFCICS, Sci. Report No. FOA-R-98-00776-612-SE (1998).
 - [128] V. V. Pai, Ya. L. Luk'yanov, I. V. Yakovlev and G. E. Kuz'min, Variation of the Magnetic Field in a Powder Metallic Medium upon Explosive Compaction, *Combustion, Explosion, and Shock Waves* **36**(6) (2000) 826–831.
 - [129] L. A. Gatilov and I. V. Kuleshov, Electrical Conductivity of Cesium Iodide Behind a Shock Front at Pressures up to 100 GPa, *Fiz. Tverd. Tela* **23** (1981) 2848.
 - [130] A. L. Velikovich, Limit possibilities of magnetic field compression method by converging shock waves (in Russian), *J. Techn. Phys.* **62** (1992) 47–59.
 - [131] P. Tracy, L. Altgilbers, I. Merritt and M. Brown, Shock Compression of Magnetic Fields in CsI, *Megagauss Magnetic Field Generation, Its Application of Science and Ultra-high Power Pulsed-Power Technology*, ed. H. J. Schneider-Muntau (World Scientific, Singapore, 2004), pp. 450–457.
 - [132] S. V. Kolosenok, V. S. Soukhomlinov, Yu. A. Tolmachev, L. L. Altgilbers, Evaluating the Limits of Shock Wave Magnetic Flux Compression in Solids, *Electromagnetic Phenomena* **7**(2(19)) (2007) 170–174.
 - [133] D. Hemmert, S. Holt and J. Krile, Electrical Breakdown of Aluminum Powder in Shock-Wave Driven Pulsed Power Systems, *10th Directed Energy Professional Society*, Huntsville, Nov. (2007).
 - [134] D. Hemmert, J. Dickens, J. Mankowski, J. Walter, S. Holt and M. Kristiansen, Shock Induced Conductivity of Aluminum Powder for Closing Switches for Ultracompact Explosive Generators, unpublished paper (2007).
 - [135] S. D. Gilev, Magnetoelectrical Technique for Studying the Insulator-Metal transition under Shock Compression, *Journal of Physics D: Applied Physics* **40** (2007) 4631–4635.

- [136] E. I. Bichenkov and V. A. Lobanov, Limiting Currents and Losses in Unshaped Flat and Coaxial Magnetic Compression Generators, *Fizika Gorenija Vzryva* **16**(5) (1980) 46–47.
- [137] H. Knoepfel, Very High Electromagnetic Density Research at Frascati up to the Seventies and Beyond, *Megagauss Technology and Pulsed Power Applications*, eds. C. M. Fowler, R. S. Caird and D. J. Erickson (Plenum Press, New York, 1987), pp. 7–18. (See Figs. 5 and 6).
- [138] B. L. Freeman and D. G. Rickel, Los Alamos National Laboratory, private Communication. They have satisfactorily explained flux losses in simultaneous helical generators using reasonable skin-depth calculations.
- [139] C. M. Fowler, Losses in Magnetic Flux compression Generators, Part 1, Linear Diffusion, Los Alamos National Laboratory, Report LA-9956, Part 1 (1984) p. 12.
- [140] C. M. Fowler, Losses in Magnetic Flux Compression Generators, Part 2, Radiation Losses, Los Alamos National Laboratory Report, LA-9956-MS, Part 2 (1988), pp. 11–12 and 39–40.
- [141] V. K. Chernyshev, E. I. Zharinov, S. A. Kazakoo, V. K. Busin, V. E. Vaneev and M. I. Korotkov, Magnetic Flux Cutoffs in Helical Explosive Magnetic Generators, *Megagauss Technology and Pulsed Power Applications*, eds. C. M. Fowler, R. S. Caird and D. J. Erickson (Plenum Press, New York, 1987), pp. 455–469.
- [142] J. M. Walsh, R. G. Shreffler and F. J. Willig, Limiting Conditions for Jet Formation in High Velocity Collisions, *J. Appl. Phys.* **24**(3) (1953) 349–359.
- [143] R. S. Caird, Los Alamos National Laboratory, private communication.
- [144] M. Jacques Morin and J. Vedel, Generateurs de Courants Intenses par Conversion d'Energie Explosive en Energie Electrique, *C. R. Acad. Sc. Paris*, t. 272, Ser. B (1971) 1–4.
- [145] A. I. Pavlovskii, R. Z. Lyudaev, V. A. Zolotov, A. S. Seryoghin, A. S. Yuryzhev, M. M. Kharlamov, V. Ye Gurin, G. M. Spirov and B. S. Makaev, Magnetic Cumulation Generator Parameters and Means to Improve Them, Ref. 2, pp. 557–583.
- [146] J. H. Degnan, W. L. Baker, C. M. Fowler , R. S. Caird, D. J. Erickson and B. L. Freeman, Test of 10 Megajoule Electrical Output Magneto-Cumulative Generator, *Ultrahigh Magnetic Fields, Physics, Techniques, and Applications*, eds. V. M. Titov and G. A. Shvetsov (Nauka, Moscow, 1984), pp. 352–358.
- [147] A. I. Pavlovskii, R. Z. Lyudaev, L. L. Sel'Chenkov, A. S. Seryoghin, V. A. Zolotov, A. S. Duryzhev, D. I. Zenkov, V. Ye. Gurin, A. S. Boriskin and V. F. Basmanov, A Multiwire Helical Magnetic Cumulation Generator, Ref. 2, pp. 585–593.
- [148] C. M. Fowler, Los Alamos National Laboratory, private communications.
- [149] A. Guenther, M. Kristiansen and T. Martin (eds.), *Opening Switches* Plenum-Press, New York and London (1987).
- [150] I. Vitkovitsky, *High Power Switching*, Van Nostrand Reinhold Company, New York (1987).

- [151] W. G. Chace and H. K. Moore (eds.), *Exploding Wires*, Vol. 1 (1959), Vol. 2 (1962), Vol. 3 (1964) and Vol. 4 (1968), Plenum Press, New York.
- [152] J. N. DiMarco and L. C. Burkhardt, Characteristics of a Magnetic Energy Storage System Using Exploding Foils, *J. Appl. Phys.* **41**(9) (1970) 3894–3899.
- [153] I. R. Lindemuth, J. H. Brownell, A. E. Greene, G. H. Nickel, T. A. Oliphant and D. L. Weiss, A Computational Model of Exploding Metallic Fuses for Multimegajoule Switching, *J. Appl. Phys.* **57**(9) (1985) 4447–4460.
- [154] F. H. Webb, H. H. Hilton, P. H. Levine and A. V. Tollestrup, The Electrical and Optical Properties of Rapidly Exploding Wires, Ref. *Megagauss and Megampere Pulse Technology and Applications*, eds. V. K. Chernyshev, V. D. Selemir and L. N. Plyashhevich, Vol. 2, Sarov, VNIIIEF (1997), pp. 37–74.
- [155] T. J. Tucker and F. W. Neilson, The Electrical Behavior of Fine Wires Exploded by a Coaxial Cable Discharge System, Ref. *Megagauss and Megampere Pulse Technology and Applications*, eds. V. K. Chernyshev, V. D. Selemir and L. N. Plyashhevich, Vol. 1, Sarov, VNIIIEF (1997), pp. 73–82.
- [156] R. A. Damerow, J. C. Crawford, C. M. Fowler, R. S. Caird, K. J. Ewing, W. B. Garn and D. B. Thompson, An Explosive Generator Powered Theta-Pinch, Sandia Laboratories Report SCRR-6951 (1969).
- [157] J. H. Goforth and S. P. Marsh, Explosively Formed Fuse Opening Switches for Use in Flux Compression Generator Circuits, Ref. *Megagauss Fields and Pulsed Power Systems*, eds. V. M. Titov and G. A. Shvetsov (Nova Science Publishers, Inc., New York, 1990), pp. 515–526.
- [158] J. H. Goforth and 37 other authors, Procyon: 18 MJ, 2 μ s Pulsed Power System', Digest of Technical Papers, 10th IEEE International Pulsed Power Conference, eds. W.L. Baker and G Cooperstein, (1995), pp. 478–483.
- [159] V. K. Chernyshev, G. S. Volkov, V. A. Ivanov and V. V. Vakhrushev, Study of Basic Regularities of Formation of Multi-MA Current Pulses with Short Risetimes by EMG Circuit Interruption, *Megagauss Physics and Technology*, ed. P. Turchi (Plenum Press, New York and London, 1980), pp. 663–675.
- [160] D. J. Erickson, R. S. Caird, C. M. Fowler, B. L. Freeman, W. B. Garn and J. H. Goforth, A Megavolt Pulse Transformer Powered by a Fast Plate Generator, *Ultrahigh Magnetic Fields, Physics, Techniques, and Applications*, eds. V. M. Titov and G. A. Shvetsov (Nauka, Moscow, 1984), pp. 333–341.
- [161] R. E. Reinovsky, R. G. Colclaser, J. M. Welby and E. A. Lopez, Energy Storage Transformer Power Conditioning Systems for Megajoule Class Flux Compression Generators, *Megagauss Technology and Pulsed Power Applications*, eds. C. M. Fowler, R. S. Caird and D. J. Erickson (Plenum Press, New York, 1987), pp. 575–582.
- [162] R. E. Reinovsky, E. Lindemuth and J. E. Vorthman, High Voltage Power Condition Systems Powered by Flux Compression Generators, 7th IEEE Pulsed Power Conference, eds. B. Bernstein and J. Shannon, Monterrey, (1989), pp. 971–974.

- [163] B. D. Khristoforov, I. I. Divnov, N. I. Zotov and O. P. Karpov, Experimental Research on Explosive-Driven Magnetic Generator Performance with Resistive-Inductive Load, *Megagauss Physics and Technology*, ed. P. Turchi (Plenum Press, New York and London, 1980), pp. 527–532.
- [164] D. E. Christiansen, W. B. Garn and C. M. Fowler, Explosives Flux Compression Devices Project, DARPA Order Number 21619, Los Alamos Scientific Laboratory Report M-32, pp. 17–46, August (1973).
- [165] C. M. Fowler, R. S. Caird, D. J. Erickson, B. L. Freeman and W. B. Garn, Pulse Transformer Operation in Megagauss Fields, *Megagauss Physics and Technology*, ed. P. Turchi, Plenum Press, New York and London, 1980), pp. 275–285.
- [166] R. E. Reinovsky, private communication.
- [167] I. Bichenkov, V. S. Prokopiev and A. N. Trubachev, Magnetic Flux Transformation in Inductively Coupled Systems Using Magnetic Cumulation, *Megagauss Fields and Pulsed Power Systems*, eds. V. M. Titov and G. A. Shvetsov (Nova Science Publishers, Inc., New York, 1990), pp. 601–606.
- [168] J. C. Martin, P. D. Champney and D. A. Hammer, Notes on the Construction Methods of a Martin High Voltage Pulse Transformer, Rept. Cornel Univ. School of Electr. Eng., CU-NRL/2 (1967).
- [169] B. L. Freeman, D. G. Rickel, A. Ramrus and B. E. Strickland, High-Voltage Pulsed Transformer Development, *Megagauss Fields and Pulsed Power Systems*, eds. V. M. Titov and G. A. Shvetsov (Nova Science Publishers, Inc., New York, 1990), pp. 587–594.
- [170] Coupling coefficients were measured as a function of frequency for a number of coaxial transformer configurations using different kinds of coaxial cables. Interested readers may contact the author for details.
- [171] A. I. Pavlovskii, R. Z. Lyudaev, L. N. Pljashkevich, A. M. Shuvalov, A. S. Kravchenko, Yu. I. Plyashkevich and V. A. Vasyukov, Transformer Energy Output Magnetic Cumulative Generator, *Megagauss Physics and Technology*, ed. P. Turchi (Plenum Press, New York and London, 1980), pp. 611–626.
- [172] C. M. Fowler and R. S. Caird, The Mark IX Generator, 7th IEEE Pulsed Power Conference, eds. B. Bernstein and J. Shannon, Monterrey (1989), pp. 475–479.
- [173] J. E. Vorthman, C. M. Fowler and R. F. Hoeberling, A Battery Powered Flux Compression Generator, *Megagauss Fields and Pulsed Power Systems*, eds. V. M. Titov and G. A. Shvetsov (Nova Science Publishers, Inc., New York, 1990), pp. 437–440.
- [174] See for example, C. M. Fowler, W. B. Garn and R. S. Caird, Production of Very High Magnetic Fields by Implosion, *Journal of Applied Physics* **31** (1960) 588–594; A. I. Pavlovskii, N. P. Kolokolchikov, O. M. Tatsenko, A. I. Bykov, M. I. Dolotenko and A. A. Karpikov, Reproducible Generation of Multimegagauss Magnetic Fields, *Megagauss Physics and Technology*, ed. P. Turchi (Plenum Press, New York and London, 1980), pp. 627–439; and B. L. Freeman, D. G. Rickel, A. Ramrus and B. E. Strickland, High-Voltage Pulsed Transformer Development *Megagauss Fields and Pulsed*

- Power Systems*, eds. V. M. Titov and G. A. Shvetsov (Nova Science Publishers, Inc., New York, 1980), pp. 587–594.
- [175] F. Herlach, Megagauss Magnetic Fields Progress in Physics, Part 1, pp. 341–417 (1968) (pp. 365–367 gives a discussion of field diffusion through unslotted liners, such as used in cylindrical implosion systems, for more reproducible results).
 - [176] E. C. Cnare, R. J. Kaye and M. Cowan, An Explosive Generator of Cascade Helical Stages, *Ultrahigh Magnetic Fields, Physics, Techniques, and Applications*, eds. V. M. Titov and G. A. Shvetsov (Nauka, Moscow, 1984), pp. 50–56.
 - [177] V. K. Chernyshev, E. I. Zharinov, V. E. Vaneev, A. I. Ionov, V. N. Buzin and Y. G. Bazanov, Effective Comparison of Explosive Magnetic Cascade Systems, *Megagauss Fields and Pulsed Power Systems*, eds. V. M. Titov and G. A. Shvetsov (Nova Science Publishers, Inc., New York, 1990), pp. 355–365.
 - [178] J. C. Boydston, B. M. Freeman and A. R. Luginbill, Fast Helical Flux Compression Generator using a 50-mm Form Factor, ICOPS 2002, Alberta, Canada, May (2002).
 - [179] A. B. Prishchepenko, Devices Build Around Permanent Magnets For Generating an Initial Current in Helical Explosive Magnetic Generators, *Instruments and Experimental Techniques Part 2* **38**(9) (1995) 515–520.
 - [180] D. M. Littrell, M. W. Heyse, K. A. Jamison, E. R. Parkinson, H. Zmuda, M. J. Matyac and M. A. Cash, Miniature Flux Compression Generators for Pulsed Telemetry, *Megagauss-9*, VNIEF, Sarov (2004), pp. 174–184.
 - [181] A. A. Neuber, S. I. Shkuratov, T. A. Holt, E. F. Talantsev, J. C. Dickens, J. W. Walter and M. Kristiansen, All-Explosive Pulsed Power Generator Systems, *Megagauss-9*, VNIEF, Sarov (2004), pp. 232–238.
 - [182] B. L. Freeman, L. L. Altgilbers, C. M. Fowler, J. C. Boydston, J. M. Ferguson, B. A. Lindeburg, A. D. Luginbill and T. E. Tutt, Similarities and Differences Between Small FCG's and Larger FCG's, *Journal of Electromagnetic Phenomena* **3**(12) (2003) 467–476.
 - [183] S. I. Shkuratov, E. F. Talantsev, J. C. Dickens and M. Kristiansen, Transverse Shock Wave Demagnetization of Nd₂Fe₁₄B High-Energy Hard Ferromagnetics, *J. Appl. Phys.* **92** (2002) 159–162.
 - [184] S. I. Shkuratov, E. F. Talantsev, J. C. Dickens and M. Kristiansen, Ultra-compact Explosive-Driven High-Current Source of Primary Power Based on Shock Wave Demagnetization of Nd₂Fe₁₄B hard Ferromagnetics, *Rev. Sci. Instrum.* **73** (2002) 2738–2742.
 - [185] S. I. Shkuratov, E. F. Talantsev, J. C. Dickens and M. Kristiansen, Seed Currents Produced by Ultracompact Explosive-Driven Transverse Shock Wave Ferromagnetic Generator of Primary Power in a Coaxial Single-Turn Seeding Coil of a Magnetocumulative Generator, *Proceedings of IXth International Conference on Megagauss Magnetic Field Generation and Related Topics (Megagauss-IX)*, eds. V. D. Selemir and L. N. Plyashkevich (2002), pp. 247–254 .

- [186] S. I. Shkuratov, E.F. Talantsev, J.C. Dickens, and M. Kristiansen, Dimensional Effects for Explosive-Driven Ferromagnetic Primary Power Source Seeding a Magnetocumulative Generator, *Proceedings of IXth International Conference on Megagauss Magnetic Field Generation and Related Topics (Megagauss-IX)*, eds. V. D. Selemir and L. N. Plyashkevich (2002), pp. 255–267.
- [187] S. I. Shkuratov, E. F. Talantsev, J. C. Dickens and M. Kristiansen, Currents Produced by Explosive Driven Transverse Shock Wave Ferromagnetic Source of Primary Power in a Coaxial Single-Turn Seeding Coil of a Magnetocumulative Generator, *J. Appl. Phys.* **93** (2003) 4529–4535.
- [188] E. F. Talantsev, S. I. Shkuratov, J. C. Dickens and M. Kristiansen, An Autonomous Completely Explosive Pulsed Power Mini-System, *Proceedings of IXth International Conference on Megagauss Magnetic Field Generation and Related Topics (Megagauss-IX)*, eds. V. D. Selemir and L. N. Plyashkevich (2002), pp. 239–246.
- [189] F. Talantsev, S. I. Shkuratov, J. C. Dickens and M. Kristiansen, Completely Explosive Pulsed Power Minisystem, *Rev. Sci. Instrum.* **74** (2003) 225–230.
- [190] S. I. Shkuratov and E. F. Talantsev, Powering the Coaxial Single-Turn Seed Coil of a Magnetocumulative Generator by an Explosive-Driven Shock Wave Ferromagnetic Primary Source, *Journal of Electromagnetic Phenomena* **3**(4(12)) (2003) 452–467.
- [191] S. I. Shkuratov, E. F. Talantsev, J. Baird, L. L. Altgilbers, and A. H. Stults, New Design for Seeding a Helical FCG with a Shock Wave Ferromagnetic Generator, *Proceedings of Megagauss XI International Conference (Ultrahigh magnetic Fields: Their Science, Technology and Application)*, eds. I. Smith and B. Novac (London, U.K., 2006), In press.
- [192] S. I. Shkuratov, E. F. Talantsev, J. Baird, L. L. Altgilbers and A. H. Stults, Completely Explosive Pulsed Power FMG-FCG System, *Proceedings of Megagauss XI International Conference (Ultrahigh magnetic Fields: Their Science, Technology and Application)*, eds. I. Smith and B. Novac (London, U.K. 2006), In press.
- [193] S. I. Shkuratov, E. F. Talantsev, J. Baird, L. L. Altgilbers, and A. H. Stults, Compact Autonomous Completely Explosive Pulsed Power System Based on Transverse Shock Wave Demagnetization of Nd2Fe14B and Magnetic Flux Compression, *IEEE Proceedings of 2006 International Conference on Megagauss Magnetic Field Generation and Related Topics*, eds. J. F. Kiutti, R. E. Reinovsky and P. J. Turchi (2007), pp. 337–342.
- [194] S. I. Shkuratov, E. F. Talantsev, J. Baird, L. L. Altgilbers, A. H. Stults, Transformer-Type Seeding System of a Helical FCG Based on a Transverse Shock Wave Ferromagnetic Generator, *IEEE Proceedings of 2006 International Conference on Megagauss Magnetic Field Generation and Related Topics*, eds. J. F. Kiutti, R. E. Reinovsky and P. J. Turchi (2007), pp. 313–318.
- [195] S. I. Shkuratov, E. F. Talantsev, J. Baird, L. L. Altgilbers, A. H. Stults, Compact Autonomous Completely Explosive Pulsed Power System, Digest

- of Technical papers, *16th IEEE International Pulsed Power Conference*, (2007), pp. 1347–1351.
- [196] J. S. Choi, J. Lee, J. H. Kuk, M. S. Seo and D. W. Yim, *A Study of the Optimization of Design and Modeling in Explosively-Driven Ferromagnetic Generators*, AMEREM, Annapolis, MD (2002).
 - [197] M. Elsayed, T. Holt, T. Young, A. Neuber, J. Dickens, M. Kristiansen, L. L. Altgilbers and A. H. Stults, High-Current Compact FCG Seed Source Implementing Solid State Switching, *Proceeding of the 2008 IEEE International Power Modulator and High Voltage Conference* (2008), pp. 25–28.
 - [198] M. Elsayed, A. Neuber and M. Kristiansen, Fast-Charging Compact Seed Source for Magnetic Flux Compression Generators, *Review of Scientific Instruments* **79** (2008) 124702.

Chapter 6

Helical Flux Compression Generators

Having surveyed the various types of FCGs, their associated ancillary equipment (seed sources and power conditioning), and their advantages and disadvantages, attention is now focused on one particular type of generator; namely, the *Helical Flux Compression Generator* (HFCG), or simply *helical* or *spiral generator*. The reason for this emphasis is that the HFCG is the most studied and utilised of all the explosive pulsed power devices (see Table 6.1). More has been written about helical flux compression generators because of their potentially high current and energy gains when compared to other generators. Also, their explosive initiation systems are relatively simple, since conventional HFCGs require only single point initiation. However, from a physics viewpoint, they are also the most complex generator of all of the designs considered in Chapter 5.

Figure 6.1(a) shows the basic components of an HFCG. At the lower right is a fixed external load coil with inductance L_1 , which is to be energised by the generator. The HFCG itself consists of an outer helical winding, called the stator, together with an explosive loaded metal cylinder, known as the armature. Initial flux may be supplied to the generator and its series load coil by a capacitor bank. It can be seen that the armature itself serves as part of the conducting circuit. When the explosive is detonated, the armature expands, creating a conical metal front that moves at the explosive detonation velocity. The detonation is timed such that this conical front shorts out the generator input at, or near peak current or, equivalently, peak flux in the generator. This also effectively isolates the capacitor bank from the generator system. After closure of the current input, the conical front proceeds along the armature and makes point contact with the helical turns of the stator. The armature contact point propagates azimuthally along the length of the generator with the pitch of the stator. Figures 6.1(b)

Table 6.1 Examples of helical generators that have been built and tested since the 1950s.

Name	Year	Country	Peak Current (MA)	Peak Voltage (kV)	dI/dt (TA/s)	Armature Diameter (cm)	Length (m)
Potok	1953	Russian	40	540	0.18		
Mark IX	1989	US	30		0.63	17.3	1.12
Mark 101	1986	US	2.11	470	0.00255	10	60
Flexy-1	1989	UK	7.3	118	0.08		0.42
Flexy-3	1995	UK	4.2	88	0.08		0.25
Flexy-4	1995	UK	2.5	58	0.06		0.42
EF-3		Romania	2.8				
Ranchito	1995	US	4.2	170	0.055	10.06	1.52
MCG-50	1997	Russia	0.338	46.5	0.034	5.0	0.40
MCG-60	1998	Russia	0.047	177		6.0	0.40
MCG-100	1998	Russia	6.8	50		10.0	0.70
MCG-200	1998	Russia	20				1.50
7-4 Helical	1979	China	0.915			4.12	0.264
Helical MCGJ	2005	US	1.9	50	0.092	15	0.40
Two-stage Helical	2001	US/Russia	0.0156	90	0.028	5.0	0.8

through 6.1(h) give different views of the generator during its operation. The inductance of the HFCG is roughly proportional to the square of the number of turns in the helix and inversely proportional to the remaining length over which the turns are spaced. The HFCG inductance thus varies continuously, assuming no turn skipping or other stray motions, with time from its initial value of L_0 until burnout, at which time armature motion has ceased.

Helical FCGs have large initial inductances because of the coupling between the many turns of their helix. Many mathematical models have been proposed to describe the operation of these generators. These models are usually for rather specific constructions that have a specific set of operating parameters. The magnetohydrodynamics involved is clearly three-dimensional (3D) and there are uncertainties in the physical properties, such as the electrical conductivity at very high energy densities, of the materials used to construct the generators. However, code development is making steady progress and a number of codes have been developed that, with suitable benchmarking with experimental results, have proven to be very useful.

Generally, the initial inductance of helical FCGs ranges from a few microhenrys to a few tens of microhenrys, although some have had

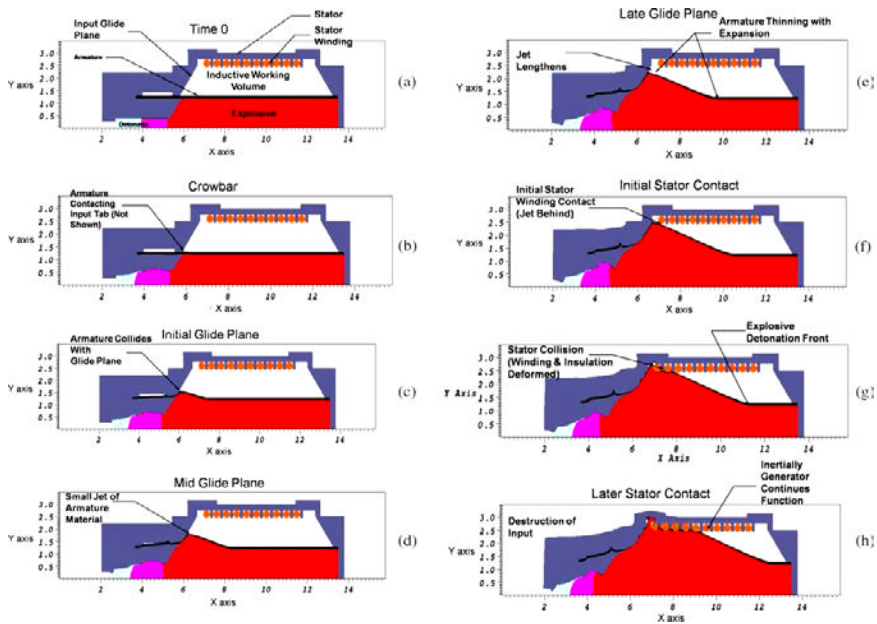


Fig. 6.1 Snapshots are shown from an ALE3D hydrodynamic simulation of an HFCG. At time = 0, the various components of the simulated generator are annotated. Significant features are noted in later frames.

inductances as high as several hundred microhenrys. The energy gain factors of HFCGs that have appropriate inductive loads and that have very low initial loading — (seeding) may be several hundred or more, which drops to a few tens when the output energy is very large i.e. greater than 10 MJ. Helical generator operation or ‘burn’ time, largely controlled by the length of the explosive charge in the armature, generally ranges from about ten microseconds to a few hundred microseconds.

Controlling the current density is a primary objective in the design of these generators. Generally, linear current densities should be kept less than 400 kA/cm of conductor width for the operating times given in the previous paragraph in order to have good generator operation. Thus, a helical generator designed to generate a current of 25 MA should have an output turn width of at least 62 cm. At the input end of the HFCG, the turns can be narrow and closely packed since the currents are small. At this stage of generator burn, the time rate of change of inductance is relatively large and the associated internal generator impedances can exceed an ohm. However, as the end of generator burn is approached, the

internal impedance drops rapidly due to the rapidly decreasing inductance per stator length in a properly designed generator. Although generator output currents continue to increase, the peak internal voltage, $|dL/dt| I$, will peak well before burnout.

Of the many papers written on this class of generators, the following have been singled out as particularly instructive. The first description of this class of generators was given by Cummings and Morley [1], although these generators had been developed and used earlier at both American and Russian laboratories and perhaps in other countries as well. Shearer *et al.* [2] discussed a number of design details, including the generation and handling of the internal voltages in these generators. Crawford and Damerow [3] discussed a class of HFCGs, where the armature explosive was detonated at both ends, which essentially cuts the generator burn time in half. The stator is thus symmetric about the mid point of the axis of this generator, where the output to the load is located. This technique significantly reduces the adverse effects of skin-loss and conductor displacement, both of which increase approximately as \sqrt{t} . Nevertheless, special design features are required in such a HFCG to avoid forming a mid-plane, cylindrical jet that cuts or shorts the stator before generator burnout. Morin and Vedel [4] discussed a helical generator where the turn pitch and width were varied continuously to accommodate for the increased current during generator operation. Also noteworthy is the completeness of their analysis describing HFCG performance. Pavlovskii and his co-workers [5–7] discussed many HFCG design improvements. First was the use of a concrete overcast to support the stator. Second was to account for increased current carrying capacity as current generation continued during generator operation. This was accomplished by paralleling (called *bifurcating* within the FCG community) the conductors in a stage, often followed by one or more additional bifurcations in following stages. This process results in many parallel conductors at the output end of the FCG, enabling it to carry the final current. Each such bifurcation increases the pitch of the windings. Third was the development of a family of HFCGs that produced output currents ranging from low to very high and that had provisions for coupling them together in such a fashion that the output of a smaller generator supplies the input energy to a larger generator. This process, in which one generator, usually smaller, supplies the initial energy to a larger generator, is called *boosting*. Due to the large possible gains of HFCGs, boosting is one of their major uses. These generators are sometimes operated in series and/or parallel. The Pavlovskii team tested four large helical generators in parallel, which

delivered a very large energy of 60 MJ to a load. For an excellent, more recent discussion of helical generators, the paper by Novac *et al.* [8] should be consulted. This paper provides detailed construction techniques, which are not commonly given or discussed elsewhere.

Often special care must be taken in the design of the stator to minimise voltages — i.e. the internal generator drive voltage, $I(dL/dt)$. As noted by Fowler *et al.* [9], by equating this expression to a constant voltage, V , and by using a model to express the current as a function of the inductance, the inductance, which limits the internal voltage so that it does not exceed V , can then be determined as a function of time (or distance along the stator, as determined from the explosive detonation velocity). This model contains information about the load inductance and about the stator winding design best suited for this load. Chernyshev *et al.* [10] have rather faithfully reproduced such a calculated inductance in a generator requiring 15 sections, where each had a specified number of turns, wire diameter and pitch.

It was mentioned earlier that component displacement is proportional to the square root of the time. It is critical that unwanted component displacement should not occur during initial loading or seeding of the generator. The Los Alamos Mark IX helical generator, developed by Fowler *et al.* [11], was designed to deliver up to 35 MA. It was wound with #00 copper wire, with a diameter of 0.927 mm or 0.365", by starting with 5 parallel wires at the generator input end, followed by 3 successive bifurcations, and ending with 40 parallel turns at the generator output. The generator delivered 7–10 MJ into various loads when powered initially with 400–450 kJ from a 600 kJ, 20 kV capacitor bank module. To increase the output, the generator required additional initial loading — i.e. about 900 kJ, which was accomplished by using two modules. When these modules were connected in parallel, the combination of additional loading time and increased current resulted in sufficient internal motion within the generator that some turns were apparently shorted together. This resulted in considerably reduced generator performance. Caird [12] then connected the two modules in series. This provided the same initial loading current, but in about two-thirds of the time. The generator easily accepted this loading and performed well, delivering 18 MJ and 25 MA to the load.

When used to power various loads, some type of power conditioning is usually required. Often, an opening switch, fuse or transformer is used. These are discussed in Sec. 5.6.2. Some of the applications in which these power conditioning techniques were used were discussed in Sec. 5.6. In some

cases, the power conditioning may only require a closing switch, which is perhaps the simplest form of power conditioning.

6.1 Basic Theoretical Treatment

A simple circuit diagram of an FCG circuit is shown in Fig. 6.2. Applying Kirchhoff's voltage law, the equation that describes this circuit is

$$\frac{d}{dt} [(L_G(t) + L_T + L_L) I(t)] + R(t)I(t) = 0, \quad (6.1)$$

where $L_G(t)$ is the time dependent inductance of the FCG, L_T is the inductance of the transmission line, L_L is the inductance of the load and $R(t)$ is the dynamic resistance of the circuit. Solving this equation yields an expression for the current

$$I(t) = I_0 \frac{L_0}{L(t)} \exp \left[-\int_0^t \frac{R(\tau)}{L(\tau)} d\tau \right], \quad (6.2)$$

and for the energy in the system

$$E(t) = E_0 \frac{L_0}{L(t)} \exp \left[-2 \int_0^t \frac{R(\tau)}{L(\tau)} d\tau \right], \quad (6.3)$$

where $L_0 \equiv L_G(t=0) + L_T + L_L$ is the initial inductance, I_0 is the initial current and $E_0 = (L_G(t=0) + L_T + L_L)I_0^2/2$ is the initial energy in the circuit. Examining these equations, it is clear that increasing the ratio of the initial inductance to the final inductance ($L_F = L(t = \text{burnout}) = L_T + L_L$) increases the generator's current and energy outputs. However, making the final inductance as small as possible is not always feasible due to the requirements of the load. Making the initial inductance larger is also problematic since this increases the overall size of the FCG and may

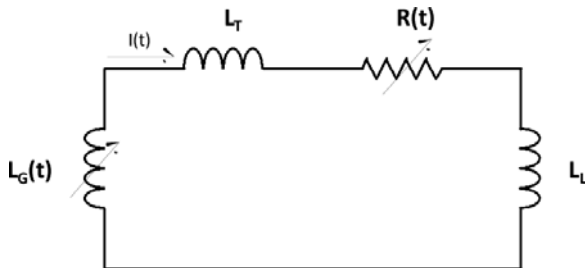


Fig. 6.2 Equivalent circuit diagram of an HFCG with a load.

increase the overall resistance $R(t)$, which will reduce the output of the generator [13, 14].

An effective way to increase the output of an HFCG is to increase its dL/dt . This is usually done by reducing the time it takes to eliminate the inductance of the generator. There are several ways of accomplishing this:

- Selecting the proper type and mass of explosives and the proper type of armature material. Armatures are normally made of either copper or aluminum. Higher armature velocities are achieved with aluminum, rather than with copper.
- Double end initiation, which complicates the design of the HFCG.
- Tapering the armature at an angle slightly larger than the opening angle produced by detonation of the explosive in the armature.
- Simultaneously initiating the explosive charge along the length of its axis — i.e. simultaneous axial initiation.

These modifications will, within limit, lead to shorter pulse lengths, higher output impedance and higher output voltage.

Letting $L(t) = L_G(t) + L_T + L_L$ and differentiating with respect to time, Eq. (6.1) becomes

$$I \frac{dL}{dt} + L \frac{dI}{dt} + IR(t) = 0, \quad (6.4)$$

where dL/dt is the driving term, has a negative value since the inductance decreases in time and is mathematically responsible for the current increasing in time. However, it is almost impossible to model all the losses in an HFCG. Since experience shows that this equation always overestimates the results observed experimentally, a correction factor must be introduced into the driving term to account for intrinsic losses. Introducing this correction factor, Eq. (6.4) now becomes

$$I \cdot \alpha \cdot \frac{dL}{dt} + L \frac{dI}{dt} + IR(t) = 0, \quad (6.5)$$

where α is called the *intrinsic flux loss parameter* or *figure of merit* and has a value between 0 and 1. When $\alpha = 0$, the equation reverts back to that for a passive RL circuit — i.e. Eq. (6.1), and when $\alpha = 1$, the generator behaves ideally with no intrinsic losses. Typically, the value of α lies between 0.7 and 0.95 depending on the size of the generator, its geometry, the detonation velocity of the explosives and other factors. If it is assumed that α is time

independent, the solution of Eq. (6.5) is

$$I(t) = I_0 \left(\frac{L_0}{L(t)} \right)^\alpha \exp \left[- \int_0^t \frac{R(t)}{L(t)} dt \right]. \quad (6.6)$$

At present, it is not possible to predict the value of α . It can only be determined by comparing the calculated results with the experimental data.

Rewriting Eq. (6.5)

$$\frac{dI}{dt} = -\frac{I}{L} \left(\alpha \frac{dL}{dt} + R \right), \quad (6.7)$$

some simple design rules can be developed [14]:

- Since L is decreasing in time, dL/dt is negative, which implies that the condition $-\alpha dL/dt > R$ must be met to have a positive current gain.
- For similar reasons, the condition $(1 - 2\alpha)dL/dt > 2R$ must be met to have a positive energy gain.
- For the previous two conditions to be met by HFCGs, the pitch on the detonator end must be small to overcome the large initial resistance, whereas the pitch toward the output end of the generator must be larger to keep the maximum induced voltage, $d(LI)/dt$, in the generator below the electrical breakdown threshold of the insulation in the system.

6.2 Figures of Merit

Since figures of merit are commonly used, further discussion of this subject is warranted. Of the various geometries for FCGs, the helical FCG is the most complicated generator to model and build [14]. As was seen in the previous chapter, there are a number of interrelated issues associated with manufacturing, materials, tolerances and operation. In addition, there are a number of basic physics issues, such as how current is transferred between the armature and the stator at the contact point and the armature-stator contact mechanics, which, so far, have precluded accurate modeling of these generators. Most models only approximate the performance of FCGs and these models typically have an adjustable parameter in the code to enable tweaking the calculated results with those obtained experimentally. Therefore, an approach that accounts for these differences is the introduction of a figure of merit into the model to assess the experimental performance of helical FCGs.

Letting I_0 be the initial current, I_f the final current, L_0 the initial inductance and L_f the final inductance, a practical measure of performance is α , which is called the *figure of merit* (or in Russian literature, the *perfectness factor*) and is quantitatively defined by the following relationship for the *current gain* [13, 14]:

$$\text{Current Gain} = G_I = \left(\frac{I_f}{I_0} \right)_{\text{experimental}} = \left(\frac{I_f}{I_0} \right)_{\text{ideal}}^{\alpha} = \left(\frac{L_0}{L_f} \right)^{\alpha}, \quad (6.8)$$

where the subscripts on the parenthesis refer to the theoretical or ideal gain and to the experimentally measured gain. The general derivation for this figure of merit was given in the previous section. A second method for determining the figure of merit is to use the *energy gain*, which is more demanding of generator performance than current gain:

$$\text{Energy Gain} = G_E = \frac{E_f}{E_0} = \frac{\frac{1}{2} L_f I_f^2}{\frac{1}{2} L_0 I_0^2} = \left(\frac{L_0}{L_f} \right)^{2\alpha-1}. \quad (6.9)$$

In deriving these expressions, the transmission line inductance was included in the generator inductance and the resistance was neglected. When $\alpha = 1$, there are no losses, and when $\alpha \leq 0.5$, there is no energy gain. In general, larger values of α are achieved by using HFCGs with diameters > 50 mm, widely spaced turns, lower current densities and smaller theoretical current gains [14].

As the expanding armature moves along the length of the generator, the contact point between the armature and the stator makes a spiral motion. Neuber [14] has found it instructive to look at the figure of merit as a function of the angular frequency of the motion of the contact point. To derive a relationship between α and the angular frequency, it was assumed that the armature has constant diameter and that the stator is a long solenoid with closely space turns. The inductance of the long solenoid can be approximated by the formula

$$L_0 = \mu_0 N^2 \frac{A}{l}, \quad (6.10)$$

where N is the number of turns, A is the cross-sectional area of the solenoid and l is its length. The annular cross-sectional area between the armature and stator is $\pi(r/2)^2 - \pi(d/2)^2$, where r is the diameter of the stator and d is the diameter of the armature. Factoring out $1/d^2$, the annular cross-sectional area is $A = \pi[(r/d)^2 - 1]d^2/4 = \pi[x^2 - 1]d^2/4$, where x is the ratio of the diameter of the stator to that of the armature and is called the *expansion ratio*. In practical generators, this ratio is typically about 2.

Substituting this expression into Eq. (6.10) gives the following expression for the inductance

$$L_0 = \mu_0 \frac{\mu(x^2 - 1)}{4} N^2 \frac{d^2}{l}. \quad (6.11)$$

The angular frequency, ω , is defined to be $2\pi\nu$, where ν is the number of turns completed per unit time, which is related to the detonation velocity by the formula $v_d \cdot N/l$. In other words, the frequency at which the contact point moves around the helix is the axial velocity of the contact point times the number of complete cycles it makes per unit length of solenoid. Therefore, the angular frequency of the contact point is

$$\omega = 2\pi v_d \frac{N}{l}. \quad (6.12)$$

The volume of the space between the armature and the stator is its cross-sectional area times the length of the solenoid:

$$V = \frac{\pi(x^2 - 1)}{4} d^2 l. \quad (6.13)$$

Substituting Eqs. (6.11) and (6.12) into Eq. (6.13) yields the following relationship between ω , L and V :

$$\omega = \frac{2\pi v_d}{\sqrt{\mu_0}} \sqrt{\frac{L_0}{V}}. \quad (6.14)$$

This formula does not take into account variations in pitch. It can be used to calculate the average value of ω for HFCGs by using the initial inductance of the generator and the volume between the armature and stator, or for calculating the value of ω for individual sections within the HFCG. From this equation, it can be seen that as the volume of the generator decreases, the angular frequency of the contact point increases. Neuber [14] plotted the angular frequency versus the figure of merit (Fig. 6.3) for several HFCGs having various sizes. From this analysis, he found that as the angular frequency increases, with a corresponding decrease in the volume of the generator, its figure of merit decreases. Helical FCGs with a diameter of a few millimeters have an angular frequency of more than 30 rad-MHz. Such generators are not suitable for pulsed power applications because an energy gain of 10 or more is normally required to make the HFCG useful in most practical applications although there may be exceptions.

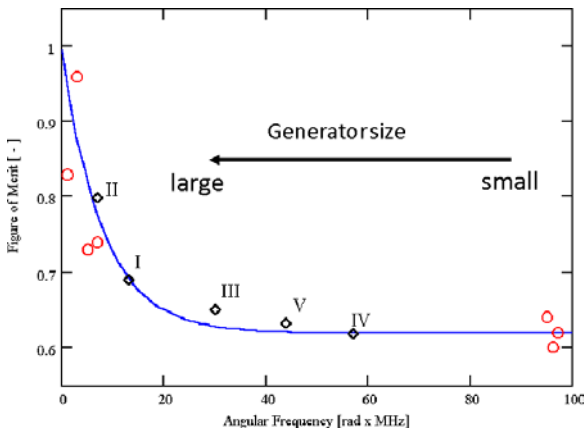


Fig. 6.3 Dependence of the figure of merit α on the contact point's angular frequency, which depends on the diameter of the generator, for FCGs with constant diameter armatures.

6.3 Loss Mechanisms

There are three major sources of loss in HFCGs:

- Electrical: magnetic diffusion, electrical breakdown and intrinsic losses.
- Mechanical: armature fracturing, material defects and voids in the explosive charge.
- Geometrical: turn skipping due to improper alignment or stator irregularities, surface imperfections and stator geometry.

In this section, each loss mechanism will be discussed separately.

6.3.1 Electrical Loss Mechanisms

6.3.1.1 Magnetic Diffusion

The most basic loss mechanism in HFCGs is magnetic flux diffusion into its metal conductors. If the resistivity of the conductors remains constant during the times of interest, then the magnetic diffusion is considered to be *linear*. If the resistivity of the conductors is significantly affected by magnetic diffusion during the times of interest, then it is considered to be *nonlinear*. In the case of nonlinear diffusion, ohmic heating increases the temperature, which increases resistivity, which in turn, increases diffusion. The onset of nonlinear diffusion depends on the change in resistivity of the material

and the shape and amplitude of the magnetic pulse. Detailed theoretical treatments of diffusion are given by Knoepfel [15, 16] and Neuber [14].

Some practical implications of magnetic diffusion are:

- When the magnetic field exceeds a certain critical value, the magnetic diffusion becomes nonlinear. As a rule, this occurs when the *linear current density*, the current flowing through a conductor per unit width orthogonal to the direction of the current flow, exceeds -400 kA/cm , depending on the operating time of the HFCG and the materials used to construct it. For example, if stainless steel is used, nonlinear diffusion will occur earlier or at lower linear current densities.
- As a rule of thumb, when the pulse rise time is 10 to 10's of microseconds in copper or aluminum, the limiting linear current density is $\leq 1 \text{ MA/cm}$. For longer rise times, the limiting linear current density is in the range from 500 to 750 kA/cm . If the pulse rise time is one microsecond or less, the limiting linear current density can be higher than 1 MA/cm .
- Since the passage of the explosive shock wave may have a significant impact on the temperature of the conductor and its resistivity, methods to lower shock intensity will improve HFCG performance. On the microsecond time scales, heating due to the passage of the shock wave through the material, deformation and heat from explosive products causes the temperature and the associated resistivity of the armature to increase. This jump in resistivity typically happens early in the HFCG run: i.e. relative to the final current doubling from the generator. The net effect is that the effective onset of nonlinear magnetic diffusion may occur at significantly lower currents than would initially be expected.
- The thickness of the conductors used in HFCGs should be greater than their magnetic skin depth to avoid excessive magnetic flux loss during generator operation. When designing a helical generator, thinning of the armature wall thickness during its expansion should be taken into account.

6.3.1.2 Electrical Breakdown

Electrical breakdown can occur between the metallic components in the HFCG, as well as within their insulators and insulating gases. The explosive generated shock waves and those reflected between the armature and stator can substantially heat the insulating gases and possibly weakly ionise them. At the same time, the gas is being compressed as the armature expands

toward the stator. The effect of the increased pressure is to shorten the recombination time for any ionisation that may be occurring. Thus, the attributes of the gas used in an HFCG are time dependent and generally not well characterised.

Using a shock tube with a flyer plate, Neuber [14] and Freeman *et al.* [17] investigated the attributes of using SF₆ instead of air as the insulating gas in HFCGs. In summary, they found that under shock conditions SF₆ maintains better insulating properties than air. However, flyer plates move at slightly higher velocities through air. The net conclusion is that these differences suggest SF₆ may not always be the best bulk insulator for HFCGs. The best fill gas will depend on the design constraints imposed on the generator and the conditions under which it is used.

6.3.1.3 Contact Point Resistance Model

Flux loss due to joule heating is inevitable since the geometry of HFCGs and the real materials used to construct them introduce resistance. These losses can be reduced by making changes to the geometry of the generator, selecting low-resistance conducting materials and bifurcating the stator windings. However, joule heating is not the only mechanism that increases the resistance to current flow and flux loss. These other losses are referred to as *intrinsic losses* and are accounted for by the intrinsic loss factor in Eq. (6.5).

To give physical meaning to the *intrinsic loss factor*, Kiuttu and Chase [18] developed a resistance model for the armature-stator contact point. They also developed an analytical expression that estimates the rate of magnetic field diffusion in the vicinity of the contact point. When converted to a flux loss rate, they found that it scales nonlinearly with the instantaneous current. The resulting effective resistance is proportional to the square root of the current. They further found that the contact resistance generally increases throughout generator operation despite the fact that the overall HFCG resistance decreases as the generator length decreases. And finally, they found that the contact resistance usually dominates toward the end of generator operation and ultimately limits the gain of most helical generators.

Kiuttu and Chase postulated that there is a point, which they call the *critical point*, (Fig. 6.4) in the region near the contact point where most of the flux behind it diffuses into the conductors and most of the flux ahead is advected ahead toward the load. They further postulated that if the flux



Fig. 6.4 Kiuttu and Chase divide the helical FCG into sections separated by two points: Critical Point, where the local Magnetic Reynolds Number is unity, and the Transition Point, where the wire-to-wire proximity effect is equal to the wire-to-armature proximity effect [18].

per unit length in the armature-stator gap at the critical point could be determined and that if it is multiplied by the critical point velocity, v_{cp} , then the effective voltage and the resistance across the generator at that point can be found. Thus, the three parameters that must be found are the location of the critical point, its velocity and the flux per unit length at that point.

To find the location of the critical point, they introduced the *Magnetic Reynolds Number*, R_m . It is a dimensionless quantity that relates the relative importance of flux advection to that of diffusion and is defined to be the ratio of the time it takes to move flux a distance, l , in vacuum to the time it takes for it to diffuse the same distance into a resistive medium:

$$R_m = \frac{l^2/D_m}{l/v} = \frac{lv}{D_m}, \quad (6.15)$$

where $D_m = \eta/\mu_0$ is the magnetic diffusivity, η is the material resistivity and μ_0 is the permeability of free space. When R_m is a large, diffusion is not important, but when $R_m = 1$, the flux diffuses about as rapidly as it is pushed forward by the moving conductor. The Magnetic Reynolds Number can be used to determine the critical gap distance, g :

$$g \approx \frac{\eta R_m}{\mu_0 v}. \quad (6.16)$$

Since these critical gap distances are very small, there are strong armature-stator proximity effects that make the surface fields very strong, causing nonlinear diffusion. The nonlinear resistivity can be approximated by

$$\eta = \eta_0(1 + \beta Q), \quad (6.17)$$

where η_0 is a reference resistivity, Q is the specific energy density and β is the temperature coefficient.

The simplified analytic form for the nonlinear contact resistance model developed by Kiuttu and Chase is

$$R_{cp} = \mu_0 n r_s \left(\frac{I}{\pi} \right)^{1/2} \left(\frac{D}{r_w} \right)^{3/4} \left(\frac{2\eta_0 \beta}{3 \sin \theta} \right)^{1/4}, \quad (6.18)$$

where n is the number of turns per unit length, r_s is the inside radius of the stator, D is the detonation velocity of the explosive, r_w is the radius of the wire in the stator and θ is the armature cone half-angle. This equation shows that the contact point resistance is nonlinear and scales as the square root of the current. It depends weakly on the properties of the materials used to construct the generator and the armature expansion angle. This model appears to give good results when applied to small, simple HFCGs and to medium generators.

6.3.2 Mechanical Loss Mechanisms

In general, major losses due to mechanical effects are caused by flux trapping and unwanted component motion arising from magnetic pressure. *Flux trapping* or *pocketing* occurs when part of the magnetic flux is inadvertently isolated from the generator and load. This can happen in a number of ways.

6.3.2.1 Mechanical Tolerances

If the plates in a plate generator are thicker on the input side than on the load or output side, plate closure would occur earlier on the output side, leaving flux trapped between the lagging plates on the input side. Similarly, eccentricity of the armature or variations in the armature wall thickness of a HFCG could cause premature contact with a downstream stator turn. This would result in flux loss between this turn and the unshorted upstream turns. Chernyshev and his co-workers [19] examined the consequences of armature eccentricity in considerable detail.

6.3.2.2 Expansion and Fracturing

Examination of the high-speed photography of expanding HFCG armatures used in ‘case motion tests’ reveal that axial cracking can form on the outer surface of the armatures. These linear cracks appear in both aluminum and copper armatures when the strain rates to which they are subjected exceed a certain value. The time at which cracking occurs is primarily determined by the initial anneal state of the armature material. These longitudinal cracks

begin on the surface of the armature at the detonator end of the armature and, in some cases, stop their extension at identical distances along the cylinders, depending on the exact failure mode. Since electric currents flow in a circumferential direction along the outer surface of the armature, the formation of cracks could interrupt the flow of this current and, thus, flux compression. A more likely outcome is that crack formation leads to arcing across opening gaps in the armature. Unfortunately, arcing creates a very hot plasma, which causes the stator insulation to break down before the sliding contact reaches that location. Thus, this armature arcing may cause the current flowing from the armature to the stator to jump ahead of the sliding contact, which results in significant magnetic flux trapping. The magnetic flux, now trapped in the region between the sliding contact and the arc, is lost to the compression process [14], which has the direct result of causing poor FCG performance.

Metals tend to break when stressed beyond their strength limitations or when subjected to high strain rates. In the case of metal cylinders, this limit is reached when the cylinder is expanded to more than twice its original diameter. As noted above, explosive expansion produces circumferential strains that can cause cracks that extend along the length of the armature. However, fracturing may occur much sooner than expected if the metal of the armature is not fully annealed. In some cases, it has been found that the fractures do not extend the entire length of the armature, as would be expected if they are purely the result of explosive expansion. There are instances when this fracturing occurs at much lower armature diameter expansion ratios than might normally be expected.

A different source of fracturing is the result of a radial shock passing through the armature and causing spallation — i.e. the formation of flakes of material from the surface of the armature opposite to the surface that the shock wave entered. It has long been known by researchers that the length of the detonator end of the armature had to be extended about two armature diameters beyond the stator crowbar for the generator to operate properly. One manifestation of armature fracturing only occurs over a distance equal to two diameters of the armature at the detonator end of the armature. A distinction that sets this fracturing, which is called *longitudinal fracturing* (Fig. 6.5), apart from normal overexpansion of the armature tube is that this fracturing begins on the outer surface of the cylinder, while normal explosive expansion fracturing begins on the inner surface. Longitudinal fracturing stops at two armature diameters from the detonator end of the armature, which is when the inner surface fracturing catches up with the

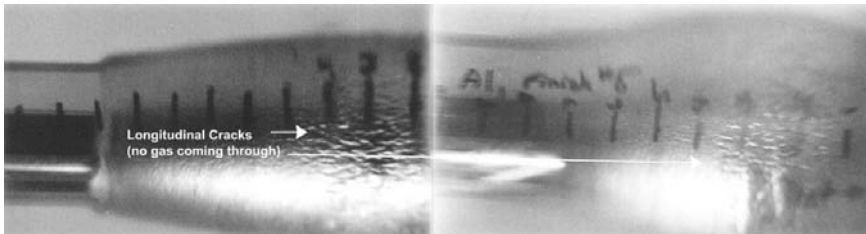


Fig. 6.5 Longitudinal cracking in an expanding armature. Longitudinal cracking is caused by virtual spallation.

spalled surface fracturing. Therefore, it was concluded that longitudinal fracturing is due to shock dynamics in this segment of the armature during detonation. The best explanation was provided by Dr. Jason Baird in his dissertation at the University of Missouri in Rolla, in which he proposed that the mechanism that causes longitudinal fracturing is a variation of the spallation process called *virtual spallation*. Spallation occurs when a shock wave passes through a metal and reflects from an outer surface, thus putting the material under tension. If the tension exceeds the strength of the metal, a layer of metal will detach and move away from the bulk of the metal. Virtual spallation is the same process with the exception that the underlying metal is still accelerating, and in some cases, catches up with the spalled surface. The effect is that the metal has failed, but the bulk of the metal and the spalled pieces continue to move as a unit. The failure of the surface is what gives the armature an ‘orange peel’ texture, as opposed to the smooth metal surface observed in a propagating detonation drive armature. Simultaneously initiated FCGs without a staging layer will produce an orange peel on the outer surface of its armature. Longitudinal fracturing, however, is likely to be caused by a similar process, but because of a different vector direction of shock travel in the starting end of the armature, the fractures form parallel to the major axis of the armature instead of parallel to the surface of the armature. These ‘incipient’ fractures open much sooner in the armature expansion process than fractures caused by the mechanical effects of expansion.

In summary, Baird found that:

- Shock wave and timing studies predict that cracks form at the locations and times observed in case motion tests.
- When the detonator is fired, a spherical detonation wave is formed. This causes the end of the armature to form a bulb-shaped structure (Fig. 6.6),

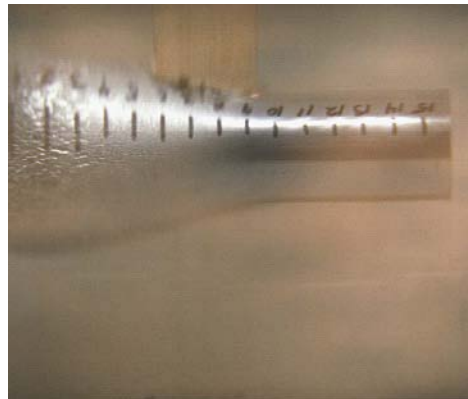


Fig. 6.6 Armature ‘bulbing’ is due to the formation of a spherical detonation wave by the detonator. Armature ‘bulbing’ may lead to improper crowbarring and 2 $\frac{1}{2}$ -clocking unless the system is carefully designed with this effect in mind.

rather than a conical plane. Geometric optics, applied to the detonation wave, indicates that the point where the detonation wave changes from spherical to semi-planar is where the virtual spall and longitudinal fracturing stops.

- Mach stems (Fig. 6.7) were predicted to form in the region where longitudinal fracturing stops. They alter the pressure distribution next to the explosive-armature interface, which causes the detonation wave to lose

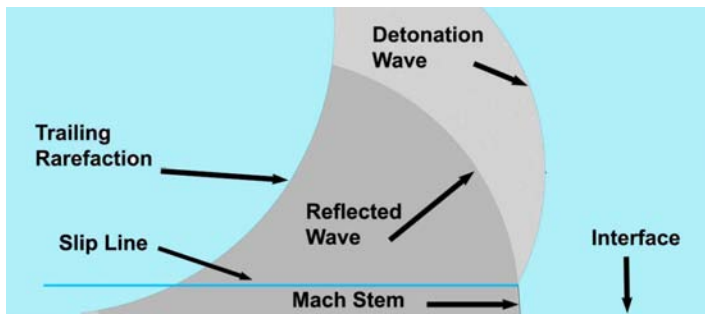


Fig. 6.7 Mach stems or Mach wave interactions form near the interface between two media having different densities. Mach stems are formed when shock waves impinging on a surface combine with those reflected from the same surface. The resulting wave has a ‘Y’ shape, where the bottom leg of the ‘Y’ is the mach stem. The Mach stem travels through the medium at Mach (sonic) speed.

contact with the interface at about the same point where the longitudinal fracturing stops.

- Hydrodynamic simulations indicate the presence of alternating compressions and tensions within the armature in the region where the virtual spallation and longitudinal fracturing begins, and that the tensile stresses exceed the ultimate tensile strength of the armature material in this region, thus forming crack initiation points.
- These initiation points coalesce under low cyclic fatigue, which is caused by the alternating stresses, and form incipient fractures.
- The incipient fractures open during explosive expansion and form premature cracking.

Except in the case of armature expansion beyond strain rate limits, detonation wave phenomenon, such as transmission, reflection and refraction of shock waves and trailing rarefactions, are capable of producing incipient fractures at the locations and times where the cracking may begin on the outer surface of the armatures — i.e. virtual spallation and longitudinal fracturing. The fractures are caused by shock wave reflections, not expansion due to detonation. Later in time, the expansion only opens the fractures once they are initiated. In any event, proper design and/or positioning of the glide plane can and will eliminate the flux loss that may be associated with this phenomenon.

6.3.3 Geometrical Loss Mechanisms

6.3.3.1 Moving Contact Effects

Helical generators require moving metallic contacts to carry the current during generator operation. These contact points sometimes encounter rough or bumpy surfaces and frequently have some conducting metal spray running ahead of them, both of which can lead to significant losses. It is difficult to quantify the resulting flux loss when there are lengthy contact regions, such as in helical generators with a large winding length or in strip generators. Bichenkov and Lobanov [20] and Knoepfel [21] have examined these loss mechanisms.

6.3.3.2 Explosive Produced Jets

Explosive produced jets arise in a number of ways. If these jets arise from explosive-metal interactions, they are usually conductive enough to form

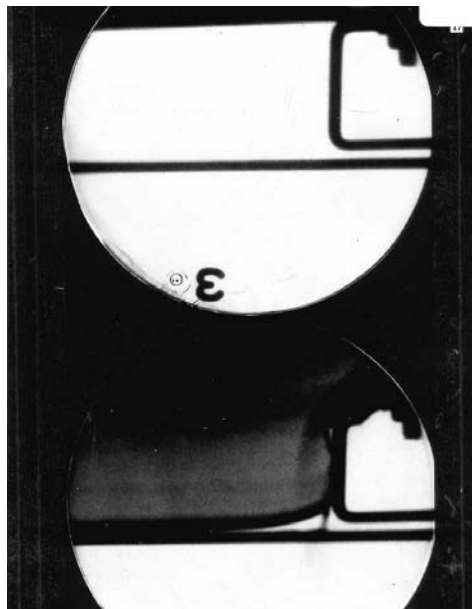


Fig. 6.8 Destructive jet formed due to poor HE-metal configuration. This is a classic example of a jet dividing the compression volume of a plate FCG at exactly the wrong time. Essentially, the run has completed and the remaining flux density is high, but half the compression volume has been eliminated. (Courtesy of C.M. Fowler, Los Alamos National Laboratory.)

alternative flux trapping current paths. Imperfections in either the explosive or the metallic parts of the armature in a helical generator can lead to jets that will short to a stator turn before the armature makes major contact with the stator, which leads to flux loss. Metallic jets can also be produced at sliding contacts, such as the moving plates of the generator with the side glide blocks as shown in Fig. 6.8. Since these jets move ahead of the plates, it is clear that they would produce a short circuit in front of the output slot of the generator before generator action has ceased. Guided in part by the classic study on jets by Walsh *et al.* [22] and later work by Caird [23], this problem was solved by careful selection of the angle between the glide planes and the moving plates, and by proper location of the explosive.

6.3.3.3 Explosive Packing and Voids

When generators are hand packed with explosives, there have always been concerns about the uniformity of the explosive charge and the possible

existence of voids. The explosive can be hand loaded by using two methods. The first is to roll the high explosive into balls and then tamp it into the armature. It was believed this technique would introduce small random voids and low-density regions within the explosive charge. The second method is to form 2 cm disks and to push them into the armature. It was believed that this method could potentially introduce mold line type voids in the explosive charge. In this case, the armature would almost certainly experience a radial jet from the explosive underneath its location. To understand the impact of voids on generator operation, 4 mm diameter spherical glass beads were introduced into an explosive charge at various points to simulate voids. In one set of experiments the beads were placed along the charge-armature interface and in another set they were inserted into the body of the charge. The tests established that concerns about hand-packing were unfounded, so long as care is exercised to ensure that each portion of explosive charge is knitted closely with previously loaded portions to prevent armature surface irregularities during expansion. From these studies, the only voids that appear to affect armature expansion are those located at or near the explosive-armature interface, which one might intuitively expect.

6.3.3.4 Undesired Component Motion

Unwanted motion of metallic components can lead to reduced generator performance, since the motion increases the inductance of the system. Two examples of this effect are shown in Fig. 6.9. Flash x-ray photography revealed massive motion of the metal conductors connecting a strip generator to a railgun. These motions, of course, can arise when other power sources are used, but they are especially serious for flux compression generators, since the maximum theoretical energy gains are rigorously controlled by circuit inductances.

6.4 Seed Sources for HFCGs

All magnetic flux compression generators, including HFCGs, are energy amplifiers. This means they require a prime or initial energy source to provide the magnetic flux that will be subsequently compressed. Even though HFCG performance is relatively independent of how the initial flux is generated, the prime power (seed) source must meet certain

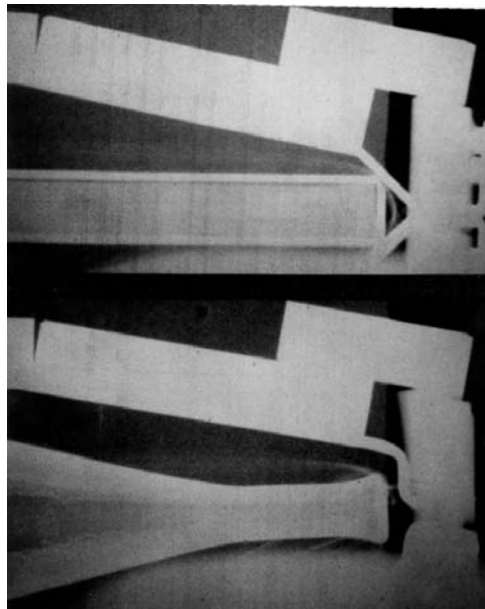


Fig. 6.9 Magnetic forces have compressed or moved the explosive charge in this strip generator. (Courtesy of C.M. Fowler, Los Alamos National Laboratory.)

requirements:

- It must deliver the initial flux to the proper location at the proper time to ensure optimal performance of the generator.
- Its output pulse characteristics must be known to ensure proper timing of main explosive charge detonation.
- Its output pulse should have a relatively short rise time to reduce flux diffusion into the armature, to prevent premature and excessive heating of the stator windings and to avoid unwanted movement of conductors within the generator.

In the case of HFCGs, seven seed sources have been used and they include:

- Capacitive energy stores.
- Batteries.
- Permanent magnets.
- Explosive-driven flux compression generators, also called booster generators.

- Explosive-driven ferroelectric generators.
- Explosive-driven ferromagnetic generators.
- Explosive magnetohydrodynamic generators.

In this chapter, only the first three types of seed energy source will be discussed. The ferroelectric and ferromagnetic generators will be discussed in the respective chapters devoted to these generators.

6.4.1 Capacitive Energy Stores

The capacitive energy store is the most commonly used seed source, since it is simple to use, reliable and easily accessible to researchers. Most HFCG circuits with capacitive seed sources driving the stator coil can be modeled as a simple LRC circuit, where

$$R < 2\sqrt{\frac{L}{C}}. \quad (6.19)$$

and R is the total system resistance, L is the total system inductance and C is the seed source capacitance. Since the initial magnetic field within the HFCG is proportional to the seed current, it is also directly proportional to the initial voltage on the capacitive store — i.e. $B_0 \propto V_{0\text{cap}}$. The initial magnetic field will peak at $T = \pi\sqrt{LC}/2$. The maximum seed current is proportional to $I_{\max} \propto V_0 \sqrt{C/L}$.

If there are limitations on the capacitive seed source size or voltage, an auxiliary winding outside the stator can be used to initialise the HFCG. For example, if a lower voltage seed source is preferable, then a single turn winding can be, and has been used by several groups, especially Pavlovskii's group. This single-turn seed winding would have a relatively small system R and L , which means there would be a higher current produced to give the same magnetic field that might be generated by directly seeding the HFCG with a higher voltage capacitive store. Further advantages of this initialisation approach are that conductor heating and possible conductor displacements within the generator are avoided, since the generator is an open circuit and not carrying current.

6.4.2 Batteries

This approach is really a variation of the capacitive seeding approach, with the exception that the initial energy comes from a set of small batteries.

In general, one cannot directly seed an explosive generator using solely batteries because the internal resistance of the batteries is too high to produce a reasonable current or a suitably short rise time for the seed current pulse.

Battery powered capacitive discharge seed sources have been used to seed small and medium HFCGs. One such seed source is shown in Fig. 6.10 [24]. It has an overall volume less than 200 cm^3 and a diameter less than 55 mm; it uses 10 miniature 12 V batteries and stores 10 J in a $20 \mu\text{F}$ capacitor. The battery voltage is stepped up to 1 kV with a 10 W DC-DC converter. This particular seed source was designed for a $10 \mu\text{H}$ inductive load. It is capable of delivering about 1 kA at 1 kV for $10 \mu\text{s}$. It was found that the most critical aspect in designing this seed source was the proper selection of batteries.

6.4.3 Permanent Magnets

Max Fowler and his team at Los Alamos initially used the magnet from a magnetron to provide the initial magnetic fields for their tests in 1951.



Fig. 6.10 Compact battery/capacitor powered seed source developed by HEM Technologies for small and medium FCGs. The energy density is roughly 30 mJ/cm^3 . (Courtesy of D. Hemmert.)

According to Pavlovskii [25], A.D. Sahkarov first proposed converting the chemical energy of explosives into electromagnetic energy in 1951 and suggested the first FCG design (a helical-coaxial generator) in 1952. By 1956, his team had optimised the helical-coaxial generator, minimised flux losses, investigated using permanent magnets as seed sources and used transformers to build cascaded multi-element systems. The first paper discussing the use of permanent magnets as seed sources for MK-2 type generators was by Gurin *et al.* [26] in 1966. They reported achieving an output current of 100 kA. In 1994, Boyko *et al.* [27] reported the idea of using permanent magnets as seed sources for HFCGs was first proposed by A.D. Sakharov. Sakharov proposed placing a coil inside the annulus of a permanent magnet, but it was concluded the energy inside the solenoid was too small. This led Pavlovskii to establish a program to investigate several techniques for using permanent magnets to seed FCGs. Some of most techniques investigated by Pavlovskii included using:

- Shock waves to cause permanent magnets to transition through their Curie points.
- Explosives to break magnetic circuits.
- Explosives to propel a magnet through a closed contour.
- Explosives to compress a magnetic field in the air gap of a permanent magnet.

The first is the basis of the ferromagnetic generator, the third the moving magnet generator and the fourth the permanent magnet FCG. R.Z. Lyudaev proposed using various FMG designs as a seed source for FCGs. In 1995, A.B. Prishchepenko [28] developed a HFCG, in which permanent magnets were used to provide the seed field. The magnets were oriented in such a way to concentrate the fields within the helix. However, a significant portion of the field was not enclosed in the helix and thus, not compressed. Prishchepenko developed an alternative design in which he placed two semi-cylindrical magnets at each end of the coil and used two semi-cylindrical magnetic yokes, made of magnetically soft steel, to help concentrate the field inside the helix. The slits between the two semi-cylindrical magnets at each end and between the two halves of the yokes were filled with a dielectric material having a dielectric strength of several hundred volts in order to prevent shunting the generator when it began to function. Prishchepenko points out that this design only makes sense if the length of the helix is short — i.e. on the order of the radius of the helical coil. In 1997, V.V. Golovnina *et al.* [29] proposed some alternative designs for a permanent

magnet seeded HFCG. The most recent work on permanent magnet seeded HFCGs was done by Freeman [30] and Neuber [14].

6.5 HFCGs with Simultaneous Axial Initiation

The highest impedance explosive generators are a class of helical systems in which their explosive charge is simultaneously axially initiated along the length of their armatures. In this case, the dL/dt impedance of the generator may be as high as $1\ \Omega$. Thus, if the final HFCG current was to be 500 kA, the associated voltage would be 500 kV [31]. For some loads, such performance would obviate the need for any pulse forming network. The advantages offered by this class of generator were such that Los Alamos expended significant efforts in the late 1980s to develop them, which was reported on at the Megagauss V conference [32]. Later, at the Megagauss VI Conference in Albuquerque, Fortov's group [33] reported a similar developmental effort. These generators are difficult to build because the initiation system for the explosive is very demanding and usually quite expensive.

In the simultaneous helical generator, the usual end initiation system is replaced by an initiation system that simultaneously initiates the explosive along the entire length of its axis. Thus, the detonation wave propagates radially outward from the center of the armature. This causes the armature to expand as a cylinder, rather than as a propagating cone. As noted earlier, the effective impedance of any explosive flux compression generator is dL/dt and is measured in ohms. The impedance of end initiated HFCGs is proportional to the detonation velocity of the explosive. However, the impedance of simultaneous HFCGs is approximated by the total inductance divided by the expansion time of the armature. Their effective impedance can be very high compared to that of end-fired HFCGs and can approach $1\ \Omega$. Their associated output voltages can also be rather large. This, of course, raises the issue of voltage control within and around the generator.

The best understood example of this class of generator is the Mark 101 flux compression generator (see Fig. 6.11), which was developed and tested at Los Alamos. The tapered-thickness aluminum armature had an inner diameter of 11.43 cm and an average outer diameter of 23.66 cm. The PBX-9501 explosive charge had an outer diameter of 20.32 cm. A 1.27-cm thick layer of polyurethane foam with a density of $0.1\ \text{g}/\text{cm}^3$ was inserted between the explosive and the armature to soften the initial shock on the

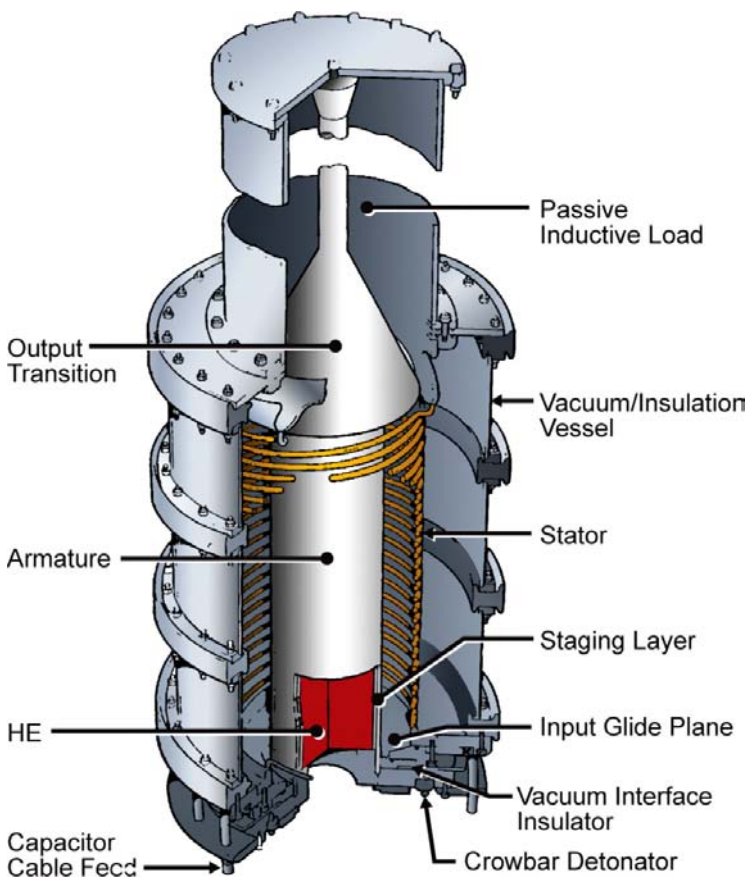


Fig. 6.11 This drawing of the Mark 101 generator shows its key components including the location of the foam staging layer. (Courtesy of C.M. Fowler, Los Alamos National Laboratory.)

armature. Given that the detonation velocity of PBX-9501 of is $8.8 \text{ mm}/\mu\text{s}$, the final armature velocity was estimated to be approximately $4.5 \text{ mm}/\mu\text{s}$. With an expansion radius of 6 cm, the expected run time at the input end of the generator was about $13.4 \mu\text{s}$, while at the output end it was a bit slower at $16 \mu\text{s}$.

The stator had a 4-parallel wire, 7.5 turn winding with an inner radius of 17.85 cm. The initial generator inductance was $5.36 \mu\text{H}$, and the passive load inductance was $0.6 \mu\text{H}$. Thus, the ideal (lossless) gain was estimated to be 9.9:1. However, it must be remembered that unlike a conventional helical

generator, the entire stator is in the active circuit throughout essentially the entire generator run. With this in mind, the estimated practical gain was estimated to be 5.5:1, where this number will vary in the downward direction with increasing initial current. While one of the low current tests used a hard vacuum, 5×10^{-5} torr, for insulation, most of the tests used ambient pressure SF₆.

In one low-current test, the seed current was 129 kA, which was provided by a 3,000 μ F capacitor bank charged to 6.3 kV. The rise time of the current was approximately 229 μ s. A clear time of 5 μ s was added to ensure proper crowbar. The recorded peak current was 600 kA, which represents a current gain of 5.0:1 (see Fig. 6.12). The maximum dI/dt was 8.7×10^{10} A/s and the recorded voltage was 39 kV. Two high-current tests were conducted and were essentially identical to within the experimental error. The second of these shots had an initial current of 380 kA and a final current of 1.58 MA, for a current gain of 4.16:1 (see Fig. 6.13). As noted earlier, this test was expected to have a reduced gain from the low-current test because of flux losses in the conductor skin layers. The measured dI/dt was 1.8×10^{11} A/s and the measured voltage was 62 kV. However, if one computes the load voltage as $L \cdot dI/dt$, the voltage across the generator load should have been 108 kV, a very respectable voltage for a generator without a PFN. Indeed, it was subsequently found that one of the input cables from the capacitor bank had shorted to ground, which would certainly compromise direct voltage measurements.

In summary, it has been demonstrated that the simultaneous helical generator performs at levels near those initially predicted. This FCG has the advantage over normal HFCGs in that it can develop relatively high output impedances and voltages. The disadvantages of this explosive initiation system are that they tend to be somewhat expensive, generate internal voltages that are quite large and to be prone to several failure modes. However, it should be noted that further development was terminated with the high-current test described above and was never resumed. Thus, it can be concluded that this is a promising generator geometry, but it is certainly not a mature technology at this time.

6.6 Cascaded HFCGs

Cascaded FCGs consist of multiple generators connected in some combination of series, parallel and/or series-parallel configurations. Figure 6.14

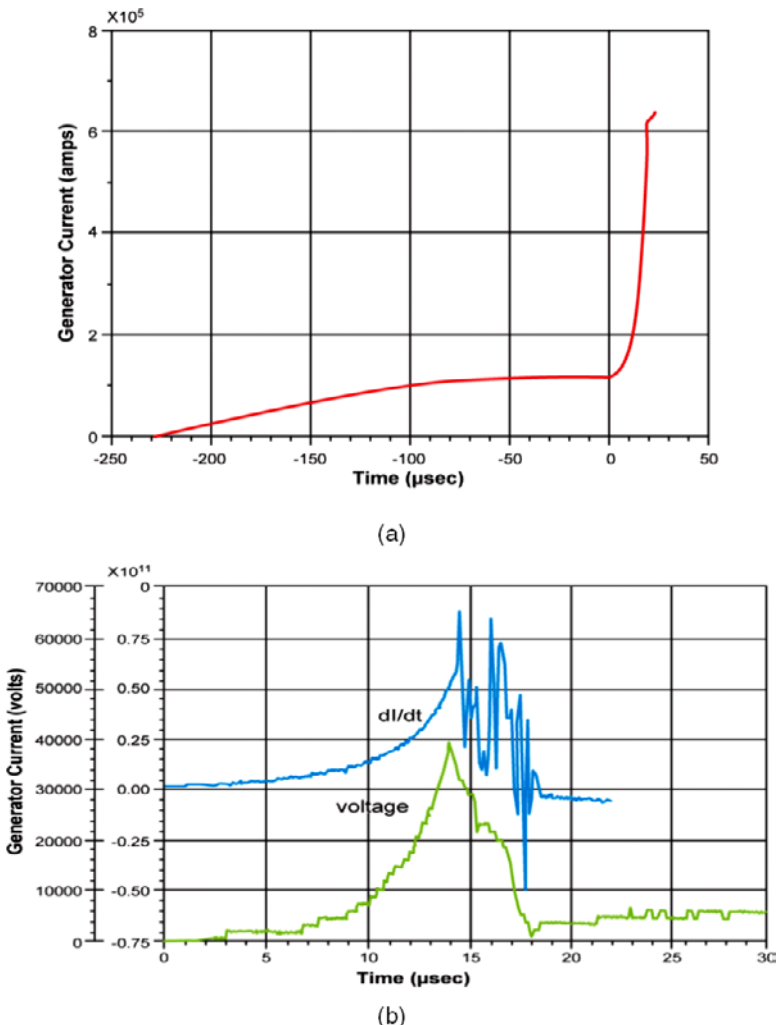


Fig. 6.12 (a) The current trace for a low current, SF₆ insulated experiment shows a multiplication of 5.0:1. (b) The voltage and dI/dt traces for the low current SF₆ insulated experiment show maximum values of ~39 kV and $\sim 8.7 \times 10^{10}$ A/s, respectively.

shows three FCGs at VNIEF connected via transformers in series. When generators are connected in parallel configurations, the Russians often referred to the arrangement as a *battery*. In fact, the Russians — mostly at Arzamas 16 (Sarov) — have used these configurations extensively. The circuit arrangement was initially used in the 1950s and reported on in the

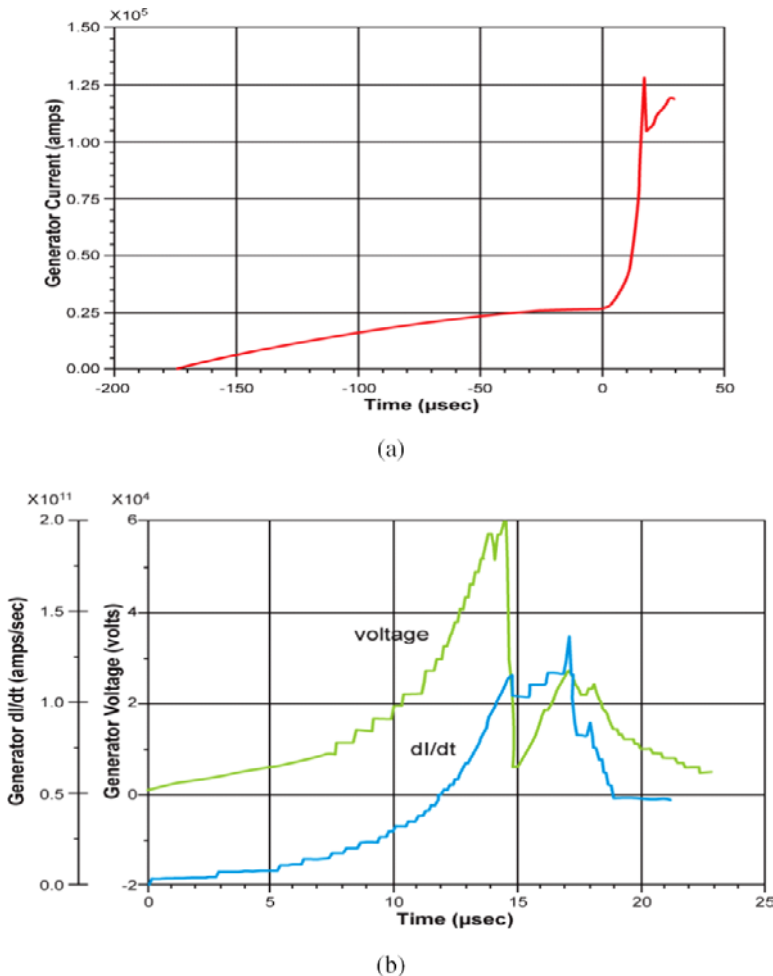


Fig. 6.13 (a) The current trace for a high-current SF₆ insulated experiment, which utilised a hard-drawn copper wire stator, shows a maximum current of approximately 1.24 MA. (b) The associated voltage and dI/dt traces for the high-current experiment, which shows maximum values of 60 kV and 1.15×10^{11} A/s, respectively.

open literature at the first Megagauss Conference. Invariably, the goal of these systems is to start with a relatively small initial energy and then multiply this seed energy to much larger values. The United States' efforts generally did not use extensive collections of generators, either in their early research or later, because high-quality capacitors were available to provide the initial energy for the experiments being performed. For example, Bykov



Fig. 6.14 Series connected FCG cascade at the All Russian Institute of Experimental Physics. The FCGs are connected via open-air transformers.

et al. [27] have reported starting with 0.2 J of energy from permanent magnets and, after six stages of compression, delivering approximately 100 MJ to a very high-current disk generator (see Fig. 6.15). The net energy gain for this system was $\sim 5 \times 10^8 : 1$. In such systems, helical flux compression generators are always used in the booster generator stages because of their relatively high initial inductance. Typically, the voltage from one generator may need to be increased by using a transformer to couple to the next stage of amplification. Again, the Russians have been the masters of this technique, as shown in their paper on transformer coupling of generators presented at Megagauss II [34]. In subsequent Megagauss Conferences, the Russians continue to report on their use of expendable helical flux compression generators as energy amplifiers.

6.7 Practical Design and Optimisation of HFCGs

6.7.1 *Philosophy*

Before one begins to design an explosive pulsed power (EPP) system, regardless of the type of generator, there are philosophical considerations

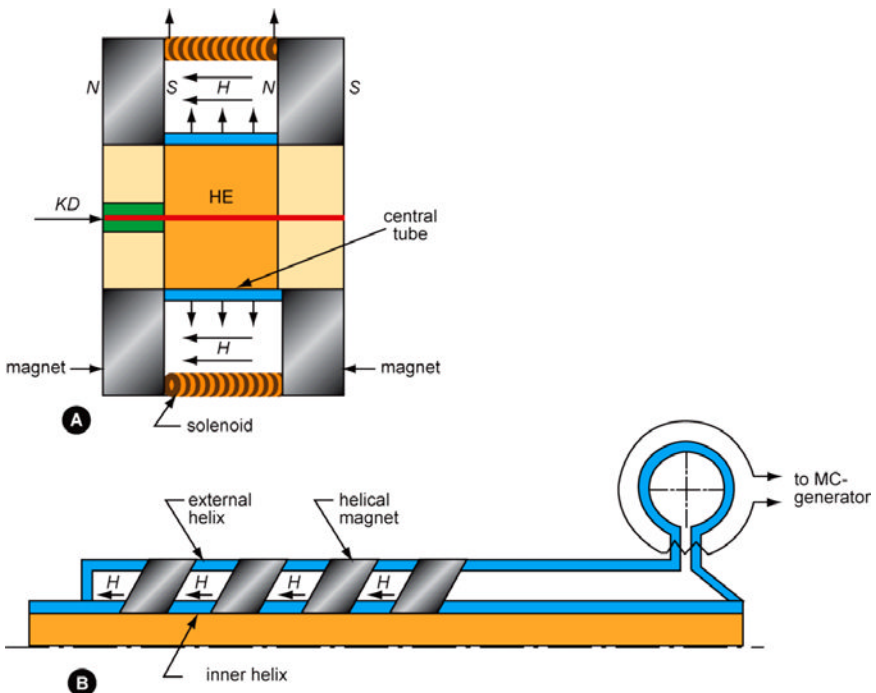


Fig. 6.15 Permanent magnet FCGs proposed by Lyudaev: (a) FCG with annular magnets and (b) FCG with helical magnets.

that need to be taken into account. Failure to do so may well lead to very serious issues for the program involved, or worse a dead-end design that will not meet the power supply requirements. The first question that should be asked is whether or not the application can practically use conventional pulsed power, rather than EPP. The reason for this is that one can move from a destructive, single-shot power supply to a multi-shot, usually non-destructive, power supply. This was typically the first question that Max Fowler would ask whenever a new application was presented to his group at Los Alamos. Quite often the answer was and still is ‘no’, due to space and weight limitations, energy requirements or a combination thereof. However, with time and the development of advanced materials, an increasing number of projects can now use conventional pulsed power whereas earlier the answer was clearly a requirement for an EPP system. Nevertheless, there continue to be many instances in which an EPP power supply is the only answer.

The second consideration is that an ‘off-the-shelf’ explosive generator design is almost never appropriate. FCGs, in general, and HFCGs, in particular, are relatively low-impedance power supplies, especially near the end of their run. This being the case, the behavior of the load as a function of time significantly impacts the FCG’s performance. Therefore, the generator design should always be tailored for the specific application. One can indeed simply treat the generator as a low impedance source of current, but this leads us to a third and closely related issue that must be considered. One should always design an EPP system in such a way as to minimise the requirements on the pulse forming network (PFN) to the greatest extent possible and practical. Experience shows that when an EPP system fails or performs poorly, the problem nearly always occurs in the PFN and not in the FCG. Thus, the reliability needs of an explosive system lead one to attempt to minimise or eliminate the PFN whenever possible. Of course, there are very practical limits as to how far one can proceed in this direction, so the whole issue ends up being one of balance and compromise.

A final consideration that needs to be taken into account before launching into generator design and optimisation is that an FCG is basically an amplifier of the current and energy provided by its initial energy or seed source. While tests have demonstrated the ability to start an FCG with 1 J of energy and end with several megajoules, the typical application does not usually accommodate either the volume nor mass required for such a feat. To be more specific, limitations of the seed source results in limitations of the energy and current available or, in other words, the overall efficiency of the FCG. The efficiency issue comes up when it is noticed that the energy density of explosives is 3–5 MJ/kg, which equates to 3–5 kJ/g. Most explosives have densities of 1.5 g/cm³, so the volumetric energy density is 4.5–7.5 kJ/cm³. If the FCG can convert as much as 50% of this energy density into electrical power, then it would indeed be an impressive power supply. However, it must be considered that the conditions for achieving ideal energy conversion from explosives to electricity include perfect tamping of the explosive charge, stopping the armature against the magnetic field as it touches the stator and revocation of the second law of thermodynamics. Clearly, this last requirement is out of the question. In addition, neither of the first two conditions are practical, in part because the seed source has limitations. As a result, a more achievable and practical FCG conversion efficiency is $\leq 1\%$.

To summarise, there are several concepts and issues that a designer should address before plunging into a new generator design. These are:

- Consider whether or not the task at hand can be accomplished by using a conventional pulsed power system.
- Always design the generator for the application.
- Always minimise the task of the pulse forming network, or eliminate it entirely, if and/or when possible.
- Realistically consider the efficiency in the context that the FCG is an amplifier limited by its seed source and that achieving maximum efficiency may be counterproductive to the task at hand.

If a designer will stop to consider these four issues before beginning to design an FCG powered system, the eventual design will typically be more robust and better able to adjust to circumstances that will always come up as the project continues.

6.7.2 Preliminary Design

Once the issues in the previous section have been addressed, the designer must next assess the range of gains that may be required from the HFCG, when working with a seed source that will fit into the confines of the application being considered and when driving a load either directly or through a PFN. At this point in the process, the design problem is generally a multi-variate challenge with insufficient information to enable definitive decisions or, in other words, a poorly posed mathematical problem. The reason for this situation is because for any circumstance there are probably multiple solutions that will achieve the desired goals with varying degrees of elegance and reliability. At this point, the designer should perform ‘back of the envelope’ calculations and not resort to computer simulations. Once computer simulations are involved, several decisions have already been made that may or may not be appropriate at this time in the design process.

For systems with armature diameters ≥ 5 cm, gains on the order of a few hundred ($\geq 100 : 1$) in current are not unreasonable for single stage helical generators. Thus, if a gain exceeding this range is needed, the problem will be complicated by the need to use either a more capable seed source or multiple generators to achieve the desired outputs. On the other hand, if the armature diameter is ≤ 2.54 cm, gains of only a few tens (10–30:1) should be expected with minimal energy gain in the first stage or two. The reason for this reduction in gain is related to the point contact model developed by

Kiuttu and Chase. Obviously, in a very confined space, the design challenges are more severe or even impractical. In these cases, losses pose especially difficult challenges to avoid energy losses per stage. Assuming the space limitations can be addressed, a system that uses one or more boosting stages will be necessary. By using closely coupled transformer interconnections, staging may be achieved with relatively low losses, provided the internal voltages can be properly controlled.

6.7.3 Advanced Design

By this point in the design process, computer design tools, such as CAGEN or SCAT95, can now be used to simulate the electrical performance of FCGs. Codes such as CTH, ALE3D, ALEGRA or other similar codes can be used to simulate the hydrodynamic performance of FCGs. One aspect that a designer must keep in mind is that these are explosive systems and suffer from all of the mechanical limitations that any mechanical system will experience. The difficulties of coupling mechanical time scales with electrical time scales must be remembered and used to enable some of the design trades that will simply have to be made. Finally, as indicated earlier, under sufficient initial loading by the seed source, which may begin to significantly affect the kinetic energy of the armature motion, initial conductor motion is possible and should be taken into account. Finally, these are explosive systems and do not exist after the event, so only as much effort should be put into the system design as is required to make it work properly. Any effort beyond this is a waste of time and money.

6.8 Small versus Large HFCGs

To date, most applications have required the use of medium to large HFCGs. However, as new applications are developed, the requirement for small (micro and mini) generators has increased. The problem is that HFCG performance does not scale linearly with its size. Therefore, in order to develop small generators with gain, the similarities and differences between small and large HFCGs must be understood.

Of the various FCG geometries described in Chapter 5, the HFCG is the most complicated, thus making it the most difficult to develop and build. For example, in large generators, it is difficult to align the armature relative to the center line of the stator to prevent turn skipping. This problem

becomes even more difficult as the diameter of the generator decreases. Neuber [14] and Freeman *et al.* [35] have studied the similarities and differences of small and large HFCGs. In Neuber's book, a *small HFCG* is considered to be one that has an overall diameter of less than 50 mm.

There have been relatively few studies dedicated to small HFCGs. The first experimental study appears to have been conducted at Sandia National Laboratory by Grover *et al.* [36] and the first theoretical study by Stuetzer [37]. They investigated a HFCG that had a closely wound stator with as many as 100 turns of thin (1 mm or less diameter) wire and with a volume of approximately 100 cm³. These generators were different from the other, larger contemporary generators in that they generated far less energy and had a much closer spacing between the turns in the stator. More than 150 were tested and it was found that there are considerable variations in their electrical data, which they attributed to not being able to control the generator's mechanical tolerances. It was concluded that in order to improve the performance of these generators, they had to reduce mechanical tolerances, improve armature design and utilise new insulating materials that have high-voltage hold-off capability under normal conditions, but at the same time undergo rapid breakdown under mechanical shock.

Abe and Chase [38] from Lawrence Livermore National Laboratory tested a 600 cm³ HFCG with a 4-stage close wound copper stator with bifurcations from stage to stage, relative high armature-stator contact velocity and high-current multiplication factor. Three loads were tested: short circuit, constant resistance and constant inductance. They found that the performance of these generators is inversely proportional to the impedance of the load, thus stressing the importance of matching the impedance of the load to that of the small HFCG in order for it to operate optimally.

Prishchepenko [39] and Demidov [40] in Russia also conducted studies of small HFCGs. Prishchepenko tested a series of HFCGs ranging in diameter from 36 to 50 mm with both tapered and cylindrical armatures. They found that their small generators could power high-impedance loads through electroexplosive opening switches.

Brooker *et al.* [41] in the United Kingdom developed and tested two types of small HFCGs. Both types of generator had 30 mm diameter aluminum armatures filled with 0.25 kg of high explosives. The first had a hand-wound stator with round, insulated copper wire, while the other stator was wound in groves precision machine on copper cylinders and potted with epoxy resin. The performance of the hand-wound generators was erratic due to turn skipping and the current and energy gains decreased

from 20 and 13.8 to 2.2 and 1.1 respectively, as the seed current increased from 1 kA to 9 kA. The current and energy gains of the machined HFCGs increased from 9.4 and 0.115 to 14.2 and 2.7 respectively as the seed current increased from 5.2 kA to 10 kA, but the flux efficiency of the machined stator was less than that of the wire-wound stator. This reduced efficiency was thought to be the result of electrical breakdown due to the lack of insulation between the armature and the stator.

The most recent study of small HFCGs was that done by Texas Tech University and Texas A&M University. These two universities independently built and tested HFCGs with armature diameters ranging from 0.95 cm to 3.8 cm. In addition, they tested generators with constant diameter and tapered armatures and/or constant diameter and tapered stators.

Based on their studies, Texas Tech University and Texas A&M found the following similarities between small and large HFCGs [14]:

- Increasing the wire diameter increases the generator's figure of merit. This is thought to be due to two causes. First, larger wire diameter means there is more surface available to carry the current, which reduces the current density on the conductors and lowers the magnetic field for a given electric current. Second, increasing the wire diameter also increases the spacing between the turns in the stator, which reduces diffusion losses.
- Using round magnet wire instead of square magnet wire yields better performance. The reason for this difference can be simply explained by assuming the magnetic field will diffuse into the corners of the square wire more quickly and be lost to the system for compression.
- Decreasing the ideal gain of small HFCGs tends to increase their figure of merit and their energy gain. That is, using a passive load with a larger inductance relative to the smaller inductance of the FCG increases the figure of merit.

Some of the differences between large and small HFCGs are:

- Increasing the seed current to a small HFCG tends, within limits, to increase their figure of merit, which is not the case for large HFCGs. One reason might be that the higher seed currents required by larger generators lead to nonlinear magnetic diffusion, which increases magnetic flux loss. Another explanation is that higher seed currents may cause unwanted mechanical displacement of the generator's components. Both these effects would decrease the figure of merit of the generator.

- Tapering the armature or stator of a small HFCG tends to increase their figure of merit and, thus, their current and energy gains. This is not true of larger generators, since the higher voltages generated by shortening the output pulse of the generator by tapering its armature or stator — i.e. reducing the closing angle between the armature and stator, leads to electrical breakdown.
- Achieving current gains greater than 10:1 in small HFCGs is difficult to do, which is not true of large generators. This is probably the most significant finding of the Texas Tech study since it implies that alternative HFCG designs must be developed for those applications requiring small generators. Later work by Loki Incorporated showed that higher gains in small HFCGs are possible and have demonstrated gains approaching 100:1 by utilising optimised designs not available to Texas Tech.

In summary, small HFCGs tend to have current gains of 10:1 or less, while large generators tend to have current gains greater than 100:1 or more. In other words, the figure of merit of small generators is ≤ 0.6 , while large generators have figure of merits ranging from 0.7 to more than 0.8. There is some evidence that the performance of small HFCGs can be improved by using faster explosives and by using simultaneous axial initiation.

6.9 Computer Models

Several computer codes have been developed to model the operation of HFCGs including:

- CIRC, which was developed at Lawrence Livermore National Laboratory, is a lumped circuit code for HFCGs [42].
- SCAT95, which was developed at Los Alamos by M. Yapuncich, W. Deninger and R. Gribble, is a general circuit analysis code with provisions for several types of FCGs [43]. This code is a derivative of the earlier SCEPTRE circuit code developed at Berkeley.
- CAGEN, which was developed by CARE'N Company, is a commercially available code for HFCGs [44]. This code now includes the Kiuttu and Chase contact point resistance model.
- TTU, which was developed at Texas Tech University, is a PSPICE based circuit analysis code with an empirically adjustable factor to account for losses for HFCGs [45].

- FCGSCA, which was developed by SAIC, is a circuit analysis code specifically developed for HFCGs [46].
- Tracy Code, which was developed by P. Tracy for the U.S. Army Space and Missile Defense Command, is a circuit analysis code with empirically adjustable factors for HFCGs [47].
- Loughborough Codes, which were developed by I.R. Smith and B.M. Novac at Loughborough University, are 2D circuit and 3D MHD codes for HFCGs [48]. Loughborough University has also developed a fast code to model HFCGs with multi-sectioned stator windings, where each section can have a different (but constant) pitch and where the number of turns in each section may be chosen arbitrarily [49].
- NECSA, which was developed by G. Turner at the Nuclear Energy Corporation of South Africa, is a circuit analysis code for HFCGs [50].
- ALEGRA, which was developed by Sandia National Laboratories, is a 3D MHD simulation code, which was primarily designed to model Z-pinch machines.
- ALE3D, which was developed by Lawrence Livermore National Laboratory, was initially a 3D hydrodynamic code that has recently been modified to include magnetic fields.
- CALE, which was developed by Lawrence Livermore National Laboratory, is a 2D Lagrangian/Eulerian code with a circuit model added to enable the inclusion of magnetic fields.

As noted earlier, these codes work reasonably well, but they all need adjustable parameters to match the calculations with experimental results. These adjustable parameters are an indication of our imperfect understanding of the loss mechanisms within FCGs. However, the contact resistance model developed by Kiuttu and Chase may be a way forward in eliminating the need for these adjustable parameters.

6.10 Summary

In this chapter, we have reviewed many of the theoretical and practical aspects of the helical flux compression generator that should be considered when designing these generators as power supplies. While the HFCG has been, and continues to be the most universally used FCG, it is also the most complex. In the same spirit, we have presented a design philosophy and approach for developing a useful HFCG. Then, some

application configurations and advanced designs were discussed. Finally, a list of computer codes that are or have been used to design these generators was presented. One should remember that these generators range in sophistication from a simple ‘pipe bomb’ inserted into a helical coil that provides joules of energy to very extensive designs capable of producing megajoules of energy and megaamperes of current. Due to their wide range of output parameters, HFCGs remain the single most useful generator design.

Bibliography

- [1] D. B. Cummings and M. J. Morley, Electrical Pulses from Helical and Coaxial Generators, in *Proceedings of the Conference on Megagauss Magnetic Field Generation by Explosives and Related Topics*, eds. H. Knoepfel and P. Herlach (Euratom, Brussels, 1966), pp. 451–470.
- [2] J. W. Shearer, F. P. Abraham, C. M. Aplin, B. P. Benham, J. E. Faulkner, F. C. Ford, M. M. Hill, C. A. McDonald, W. H. Stephens, D. J. Steinberg and J. R. Wilson, Explosive-Driven Magnetic-Field Compression Generators, *Journal of Applied Physics* **39**(4) (1968) 2102–2116.
- [3] J. C. Crawford and R.A Damerow, Explosively Driven High-Energy Generators, *J. Appl. Phys.* **39**(11) (1968) 5224–5231.
- [4] M. Jacques Morin and J. Vedel, Generateurs de Courants Intenses par Conversion d’Energie Explosive en Energie Electrique, *C. R. Acad. Sc. Paris t. 272*(Ser. B) (1971) 1–4.
- [5] A. I. Pavlovskii, R. Z. Lyudaev, V. A. Zolotov, A. S. Seryoghin, A. S. Yuryzhev, M. M. Kharlamov, V. Ye Gurin, G. M. Spirov and B. S. Makaev, Magnetic Cumulation Generator Parameters and Means to Improve Them, in *Megagauss Physics and Technology*, ed. P. Turchi (Plenum Press, New York and London, 1980), pp. 557–583.
- [6] A. I. Pavlovskii, R. Z. Lyudaev, L. L. Sel’Chenkov, A. S. Seryoghin, V. A. Zolotov, A. S. Duryzhev, D. I. Zenkov, V. Ye. Gurin, A. S. Boriskin and V. F. Basmanov, A Multiwire Helical Magnetic Cumulation Generator, in *Megagauss Physics and Technology*, ed. P. Turchi (Plenum Press, New York and London, 1980), pp. 585–593.
- [7] I. Pavlovskii, R. Z. Lyudaev, A. S. Kravchenko, V. A. Vasyukov, L. N. Pljashkevich, A. M. Shuvalov, A. S. Russkov, V. Ye. Gurin and B. A. Boyko. Formation and Transmission of Magnetic Cumulation Generators Electromagnetic Energy Pulses, in *Megagauss Physics and Technology*, ed. P. Turchi (Plenum Press, New York and London, 1980), pp. 595–609.
- [8] B. M. Novac, I. R. Smith, H. R. Stewardson, P. Senior, V. V. Vadher and M. C. Enache, Design, Construction and Testing of Explosive-Driven Helical Generators, *J. Phys. D—Appl. Phys.* **28** (1995) 807–823.
- [9] R. S. Caird Characterization of the Mark IX Generator M-6 Technical Note, No. 17, Los Alamos National Laboratory Report: LA-UR (1987), pp. 87–4211.

- [10] R. S. Caird and C. M. Fowler, Conceptual Design for a Short-Pulse Explosive-Driven Generator, in *Megagauss Technology and Pulsed Power Applications*, eds. C. M. Fowler, R. S. Caird and D. J. Erickson (Plenum Press, New York and London, 1987), pp. 425–431.
- [11] C. M. Fowler, R. S. Caird, B. L. Freeman and J. B. VanMarter, Performance of the Mark IX Helical Flux Compression Generator, M-6 Technical Note No. 5, Los Alamos National Laboratory Report (December, 1983).
- [12] R. S. Caird, Characterization of the Mark IX Generator, M-6 Technical Note, No. 17, Los Alamos National Laboratory Report: LA-UR (1987), pp. 87–4211.
- [13] C. M. Fowler and L. L. Altgilbers, Magnetic Flux Compression Generators: a Tutorial and Survey, *Journal of Electromagnetic Phenomenon* **3**(11) (2003) 305–357.
- [14] *Explosively Driven Pulsed Power: Helical Magnetic Flux Compression Generators*, ed. A. Neuber (Springer-Verlag, Berlin, 2005).
- [15] H. Knoepfel, *Pulsed High Magnetic Fields*, North-Holland Publishing Company, Amsterdam and London (1970).
- [16] H. Knoepfel, *Magnetic Fields: A Comprehensive Theoretical Treatise for Practical Use*, John Wiley & Sons, New York (2000).
- [17] D. J. Dorsey and B. L. Freeman, Electrical Properties of Sulfur Hexafluoride in Explosive Generator Environments, *IEEE 12th International Conference on Pulsed Power* (1999), pp. 762–764.
- [18] G. F. Kiuttu and J. B. Chase, An Armature-Stator Contact Resistance Model for Explosively Driven Helical Magnetic Flux Compression Generators, 2005 IEEE Pulsed Power Conference (2005), pp. 435–440. *Recent Advances in Modeling Helical FCGs, Proceedings of Megagauss XI* eds. G. F. Kiuttu, J. B. Chase, D. M. Chato and F. D. Peterson (Santa Fe, Omnipress, 2006), pp. 255–264.
- [19] V. K. Chernyshev, E. I. Zharinov, S. A. Kazakoo, V. K. Busin, V. E. Vaneev and M. I. Korotkov, Magnetic Flux Cutoffs in Helical Explosive Magnetic Generators, in *Megagauss Technology and Pulsed Power Applications*, eds. C. M. Fowler, R. S. Caird, and D. J. Erickson (Plenum Press, New York and London, 1987) pp. 455–469.
- [20] E. I. Bichenkov and V. A. Lobanov, Limiting Currents and Losses in Unshaped Flat and Coaxial Magnetic Compression Generators, *Fizika Gorenija Vzryva* **16**(5) (1980) 46–47.
- [21] Knoepfel, Very High Electromagnetic Density Research at Frascati up to the Seventies and Beyond, in *Megagauss Technology and Pulsed Power Applications*, eds. C. M. Fowler, R. S. Caird and D. J. Erickson (Plenum Press, New York and London, 1987), pp. 7–18.
- [22] J. M. Walsh, R. G. Shreffler and F. J. Willig, Limiting Conditions for Jet Formation in High Velocity Collisions, *J. Appl. Phys.* **24**(3) (1953) 349–359.
- [23] C. M. Fowler, Los Alamos National Laboratory, private communication.
- [24] D. Hemmert, HEM Technologies, private communication (2005).
- [25] A. I. Pavlovskii, Magnetic Cumulation — A Memoir for Andrei Sakharov, in *Megagauss Magnetic field Generation and Pulsed Power Applications*,

- eds. M. Cowan and R. B. Spielman (Nova Science Publishers, Inc., 1994), pp. 9–22.
- [26] Ya. Gurin, R. Z. Lyudaev, A. I. Pavlovskii, L. N. Plyashkevich and E. N. Smirnov, MC-2 Generator with Permanent Magnets, *Proceedings of the Conference on Megagauss Magnetic Field Generation by Explosives and Related Experiments*, Brussels, Euratom (1966), p. 517.
 - [27] B. A. Boyko, V. E. Gurin, R. Z. Lyudaev and A. I. Pavlovskii, Autonomous Cascade MC-System with Constant Magnets, in *Megagauss Magnetic field Generation and Pulsed Power Applications*, eds. M. Cowan and R. B. Spielman (Nova Science Publishers, New York, 1994), pp. 467–473.
 - [28] A. B. Prishchepenko. Devices Build Around Permanent Magnets For Generating an Initial Current in Helical Explosive Magnetic Generators, *Instruments and Experimental Techniques*, Part 2 **38**(4) (1995) 515–520.
 - [29] V. V. Golovnina, V. P. Isakov, M. V. Lapatin, V. B. Mintsev, and A. Ye. Ushnurtsev, Magnet-Powered Initial Stage of Magnetic Flux Compressor, in *Megagauss and Megaampere Pulse Technology and Applications*, eds. V. K. Chernyshev, V. D. Selemir and L. N. Plyashkevich (VNIEF, 1997), pp. 333–335.
 - [30] B. Freeman, J. Rock and L. Altgilbers, 25 mm Diameter Helical FCG, *4th Annual Directed Energy Symposium*, Huntsville, AL (1990).
 - [31] B. L. Freeman, C. M. Fowler, D. G. Rickel and M. L. Hodgdon, Mark 101 Flux Compression Generator: Development Progress, in *Megagauss Fields and Pulsed Power Systems*, eds. V. M. Titov and G. A. Shvetsov (Nova Science Publishers, New York, 1990), pp. 377–384.
 - [32] D. G. Rickel, B. L. Freeman, C. M. Fowler, J. E. Vorthman and S. P. Marsh, Simultaneous Helical Generator, in *Megagauss Fields and Pulsed Power Systems*, eds. V. M. Titov and G. A. Shvetsov (Nova Science Publishers, New York, 1990), pp. 399–402.
 - [33] V. E. Fortov, Y. V. Karpushin, A. A. Leontyev, V. B. Mintsev and A. E. Ushnurtsev, Testing of Compact Magnetocumulative Generators with Flux Trapping. in *Megagauss Magnetic field Generation and Pulsed Power Applications*, eds. M. Cowan and R. B. Spielman (Nova Science Publishers, New York, 1994), pp. 947–954.
 - [34] P. J. Turchi, (ed). *Megagauss Physics and Technology*, Plenum Press, New York (1980).
 - [35] B. L. Freeman, L. L. Altgilbers, C. M. Fowler and A. D. Luginbill, Similarities and Differences Between Small FCG's and Larger FCG's, *Journal of Electromagnetic Phenomena* **3**(4)(12) (2003) 467–475.
 - [36] J. E. Grover, O. M. Stuetzer and J. L. Johnson, Small Helical Flux Compression Amplifiers, in *Megagauss Physics and Technology*, ed. P. J. Turchi (Plenum Press, New York, 1980), pp. 163–180.
 - [37] O. M. Stuetzer, Theory of Small Compressed Magnetic Flux Current Amplifiers, Sandia Laboratories Technical Report (1979), SAND79-1075.
 - [38] D. K. Abe and J. B. Chase, Experiments with Small Helical Flux Compression Generators, in *Megagauss Magnetic Field Generation and Pulsed*

- Power Applications*, eds. M. Cowan and R. B. Spielman (Nova Science Pub., 1994), pp. 405–409.
- [39] A. B. Prishchepenko, private communication (1997).
 - [40] V. A. Demidov, V. D. Sadunov, S. A. Kazakov, L. N. Plyashkovich, T. V. Trischenko, S. N. Golosov, A. V. Blinov, I. L. Fetisov, M. V. Korotchenko and Ye. V. Sahpovalov, Helical Cascade FCG Powered by Piezogenerator, *Proceedings of the IEEE 12th International Conference on High Power Particle Beams* (1998) 269–272.
 - [41] C. J. Brooker, N. H. Manton and N. McKay, Helical Flux Compressor Development for Compact Pulsed Power Sources, in *Megagauss Magnetic field Generation and Pulsed Power Applications*, eds. M. Cowan and R. B. Spielman (Nova Science Publishers, Inc., 1994), pp. 511–517.
 - [42] J. B. Chase, CIRC: A Specialized Circuit Analysis Computer Simulation Program for a High Explosive Generator Model, in *Megagauss Magnetic Field Generation and Pulsed Power Applications*, eds. M. Cowan and R. B. Spielman (Nova Science Pub., 1994), pp. 397–403.
 - [43] Code distribution is limited. Consult D. G. Tasker, Los Alamos National Laboratory, for details. E-mail: tasker@lanl.gov.
 - [44] J. B. Chase, D. Chato, G. Peterson and P. Pincosy, CAGEN: A Modern, PC Based Computer Modeling Tool for Explosive MCG Generators and Attached Loads, in *Megagauss Magnetic Field Generation, Its Applications to Science and Ultra-High Pulsed Power Technology*, ed. H. J. Schneider-Muntau (World Scientific, Singapore, 2004), pp. 515–520.
 - [45] M. G. Giesselmann, T. Heeren, A. Neuber and M. Kristiansen, Advanced Modeling of a Exploding Flux Compression Generator Using Lumped Element Models of Magnetic Diffusion, in *Proceedings of the IEEE Pulsed Power and Plasma Science Conference*, eds. R. Reinovsky and M. Newton (Las Vegas, NV, IEEE Catalog No. 0101CH37251, 2001), pp. 162–165.
 - [46] R. Parkinson, K. A. Jamison, J. B. Cornette, M. A. Cash, C. M. Fowler and J. D. Goettee, Continued Benchmarking of an FCG Code, in *Proceedings of the 12th IEEE Pulsed Power Conference*, eds. C. Stallings and H. Kirbie (Monterey, CA, IEEE Catalog No.99CH36358, 1999), pp. 724–727.
 - [47] L. L. Altgilbers, I. Merritt, M. D. Brown and P. Tracy, Semi-Empirical Model for the Resistance of Spiral Magnetocumulative Generators, in *Megagauss Magnetic Field Generation, Its Applications to Science and Ultra-High Pulsed Power Technology*, ed. H. J. Schneider-Muntau (World Scientific, Singapore, 2004), pp. 540–545.
 - [48] B. M. Novac, I. R. Smith, I. R., H. R. Stewardson, K. Gregory and M. C. Enache, *Two-Dimensional Modeling of Flux-Compression Generators, IEE Symposium on Pulsed Power*, IEE, London (April, 1998), pp. 361–363.
 - [49] B. M. Novac and I R Smith, *Fast Numerical Modeling of Helical Flux Compression Generators*, Megagauss IX, Russia, to be published (July, 2002).
 - [50] Geoff Turner, *Nuclear Energy Corporation of South Africa*, Private Communication (2003).

This page intentionally left blank

Chapter 7

Magnetic Materials and Circuits

Since several of the explosive pulsed power devices utilise ferromagnetic materials, this chapter is devoted to a review of the properties of these materials and how they are accounted for in electric circuits. In general, a *magnetic circuit* is a circuit that has one or more components made from high permeability materials with a substantially uniform cross section in which magnetic flux is largely confined.

The concept of a magnetic circuit is based on the idea that a constant or slowly varying flux tends to confine itself to the high permeability paths of a ferromagnetic structure in a manner that resembles the tendency of a constant current or slowly varying electric current to confine itself to the high conductivity paths of an electric circuit. This concept suggests there is a similarity between the behavior of a nonlinear resistive circuit with constant or slowly varying currents and the behavior of a ferromagnetic circuit, which is inherently nonlinear, with constant or slowly varying flux [1, 2].

It should be noted that magnetic circuits differ markedly from a simple electric circuit analogue. In electric circuits, the conductors are normally separated from other conductors by an insulating material and the conduction current in the insulating materials is negligibly small in comparison to the current in the conductors. There is no magnetic insulating material with similar properties.

When working with magnetic materials, Maxwell's equations are typically used to calculate their field distributions. However, when working with complex structures in practical devices, these calculations are quite complicated. It is possible to simplify these calculations by using magnetic circuit analysis based on an analogy with DC electrical circuits.

7.1 Properties of Magnetic Materials

The power of lodestone or magnetite to attract iron was first mentioned by Thales in Greece in 600 B.C. The ability of magnetite to magnetise iron was first observed by Socrates. It was not until 1269 A.D. that Peregrines discovered that magnets had ‘poles’. Coulomb (1736–1806) was the first to discover that magnets had two poles (north or positive and south or negative) and to accurately measure the forces between the magnetic poles of long, thin steel rods. He found that the force of attraction or repulsion between two poles is proportional to the product of the strength of the poles and inversely proportional to the square of the distance between them, which is now known as Coulomb’s Law.

7.1.1 *Types of Magnetic Materials*

The origin of magnetism lies in the orbital and spin motions of electrons that make the atom’s magnetic dipoles and how these dipoles interact with each other. There are five different types of magnetic materials, which are best introduced by describing how variously they respond to magnetic fields. This difference in magnetism is due to the fact that in some materials there is no collective interaction of atomic magnetic moments, whereas in other materials there is a very strong interaction. Thus, the magnetic behavior of materials can be classified according to which one of the following five major groups it falls into:

- Diamagnetism.
- Paramagnetism.
- Ferromagnetism.
- Ferrimagnetism.
- Antiferromagnetism.

Materials in the first two groups exhibit no collective magnetic interactions, whereas the materials in the last three groups show long-range magnetic interactions below a critical temperature. Ferromagnetic and ferrimagnetic materials are strongly magnetic, while the materials in the other three groups are weakly magnetic.

Diamagnetic materials are composed of atoms that have no magnetic moment due to all their orbital shells being filled and there being no unpaired electrons. When subjected to a nonuniform magnetic field, diamagnetic materials align perpendicular to the magnetic field and are slightly

repelled by it. *Paramagnetic materials* are composed of atoms, some of which have a net magnetic moment due to unpaired electrons in partially filled orbitals. The individual magnetic moments do not interact magnetically, but in the presence of an external magnetic field, their magnetic moments partially align in the direction of the field, resulting in a net positive magnetisation. Paramagnetic materials are weakly attracted by magnets. *Antiferromagnetic materials* have a large concentration of strongly interacting magnetic atoms and their magnetic moments align in an antiparallel pattern below a certain critical temperature, called the *Curie Temperature*, but behave like a paramagnetic material above this temperature. *Ferromagnetic materials* have a spontaneous magnetism, which exists in the absence of an external magnetic field. The retention of this magnetism distinguishes ferromagnetism from the induced magnetism of diamagnetism and paramagnetism. Ferromagnetic materials exhibit parallel alignment of magnetic moments, resulting in large net magnetisation. However, ferromagnets lose this permanent magnetism when their temperature exceeds their Curie temperature. *Ferrimagnetic materials* possess their own magnetic field due to there being a permanent arrangement in which there are an unequal number of parallel and anti-parallel magnetic domains. In ionic compounds, such as oxides, more complex forms of magnetic ordering can occur as a result of the crystal structure. In ferrimagnets, the magnetic moments of the various sublattices are not equal and result in a net magnetic moment.

Ferromagnetic materials can be further classified as being hard or soft. *Hard magnetic materials* require relatively strong magnetic fields to permanently magnetise them and to reverse or erase this magnetisation; whereas, *soft magnetic materials* require relatively weak magnetic fields to magnetise or demagnetise them.

Ferromagnetic materials are comprised of *magnetic* or *Weiss domains* containing 10^{10} to 10^{15} atoms, whose magnetic moments are spontaneously and fully aligned. These domains are separated by Bloch walls. When a magnetic field is applied, the domains change and the Bloch walls are displaced throughout the crystalline structure, unless they are blocked by imperfections in the structure or by grain boundaries in polycrystalline substances. The imperfections introduce a resistance that prevents the ferromagnetic material from returning to its original state when the field is removed, which is the source of hysteresis. Ferromagnetism also depends on the size of the specimen, the magnitude and frequency of the applied field, temperature and other factors. When the temperature exceeds its Curie temperature,

kinetic movement prevents spontaneous alignment of its magnetic domains and, thus, blocks the material's ferromagnetic properties. The material is then paramagnetic [3]

7.1.2 Properties of Magnetic Materials

The magnetic properties of a material are ultimately determined by the magnetic dipole moment of the atoms that make it up. The magnetic dipole can be represented mathematically in terms of its *magnetic dipole moment*:

$$\mathbf{m} = p\mathbf{d} \quad (7.1)$$

where \mathbf{m} is the magnetic moment, \mathbf{d} is the vector pointing from the negative pole to the positive pole and has a magnitude equal to the distance between the poles and p is the pole strength. When the magnetic dipole moments of the atoms of a material are summed up over a volume element, Δv , the resulting sum is a macroscopic vector quantity, called *magnetisation* \mathbf{M} , which defines the overall magnetic properties of that material.

When solving problems involving magnetic materials, it is important to know the relationship between \mathbf{M} , \mathbf{H} and \mathbf{B} . These relationships depend on the nature of the magnetic material and are usually derived from experiment. In the case of paramagnetic and diamagnetic materials, there exists an approximately linear relationship between \mathbf{M} and \mathbf{H} . If the material is linear and isotropic, the following relationship can be written:

$$\mathbf{M} = \chi_m \mathbf{H}, \quad (7.2)$$

where is χ_m , a dimensionless scalar quantity called the *magnetic susceptibility*. If χ_m is positive, the material is paramagnetic and its magnetic induction strengthened by the presence of a magnetic material, and if χ_m is negative, the material is diamagnetic and its magnetic induction is weakened by the presence of a magnetic material. In general, the χ_m of paramagnetic and diamagnetic materials is quite small — i.e. $|\chi_m| \ll 1$. The relationship between \mathbf{B} and \mathbf{H} is also linear; that is,

$$\mathbf{B} = \mu \mathbf{H}, \quad (7.3)$$

where μ is the permeability and is related to the magnetic susceptibility by

$$\mu = \mu_0(1 + \chi_m). \quad (7.4)$$

The dimensionless ratio

$$\mu_r = \frac{\mu}{\mu_0} = 1 + \chi_m \quad (7.5)$$

is called the *relative permeability* and is sometimes used in place of χ_m . It has a value close to unity for paramagnetic and diamagnetic materials.

Unlike paramagnetic and diamagnetic materials, ferromagnetic materials are nonlinear, which means that Eqs. (7.3)–(7.5), with constant χ_m and μ , do not apply. Assuming the form of Eq. (7.3) still to be valid, then the nonlinearity of ferromagnetic materials can be accounted for by assuming that μ is a function of \mathbf{H} ; i.e. $\mu = \mu(\mathbf{H})$. Referring to Fig. 7.1, if the magnetic intensity, initially zero, is increased monotonically, then the \mathbf{B} – \mathbf{H} relationship will trace out the curve seen in the figure. This curve is called the *magnetisation curve* from which the value of μ can be found; i.e., $\mu = \mathbf{B}/\mathbf{H}$. The maximum permeability occurs at the ‘knee’ in the curve. As \mathbf{H} continues to increase, so does \mathbf{B} ($= \mu_0(\mathbf{H} + \mathbf{M})$), but \mathbf{M} approaches a maximum called *magnetic saturation*. If the magnetic intensity is decreased, the \mathbf{B} – \mathbf{H} relationship does not follow back down the magnetisation curve, but rather follows a new path to a point r . That is, once the magnetisation is established, it does not disappear with the removal of \mathbf{H} . It takes a reversed magnetic intensity to reduce the magnetisation to zero. If \mathbf{H} continues to increase in the reversed direction, then \mathbf{M} will establish itself in the reversed direction, once again reaching a saturation point. If \mathbf{H} now reverses itself, the bottom part of the curve in Fig. 7.1 is generated. The loop formed by this process is called the *hysteresis loop* and arises because the magnetisation, \mathbf{M} , of the material lags the exciting field, \mathbf{H} . The magnitude of \mathbf{B} at point r is called the *retentivity* or *remanence* of the material, which is the induction \mathbf{B} that remains when \mathbf{H} has returned to zero, and

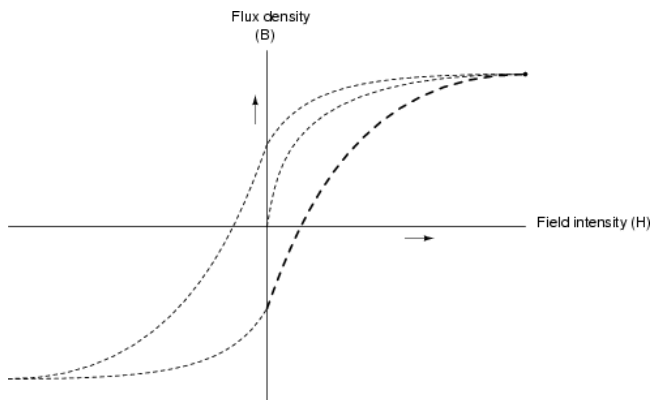


Fig. 7.1 Hysteresis curve for ferromagnetic materials.

the magnitude of \mathbf{H} at point c is called the *coercive force* or *coercivity* of the material, which is the \mathbf{H} required to cancel the remaining inductance. The shape of the hysteresis curve depends on the properties of the ferromagnetic material and the maximum value of \mathbf{H} to which the material is subjected. Once the value of \mathbf{H} is sufficient to produce saturation in the material, the shape of the hysteresis loop does not change as \mathbf{H} continues to increase.

Ferromagnetic materials are used either to increase the magnetic flux in a circuit or as sources of permanent magnets. A portion of the energy expended to magnetise a permanent magnet is magnetically stored by the magnet. In the case of FMGs, the objective is to demagnetise the ferromagnetic material and release this energy in the form of electrical energy. The energy stored in the magnet is

$$W = -\mu_0 VMH, \quad (7.6)$$

where V is the volume of the magnetic field in which the energy is stored.

By way of example, the hard ferromagnets used in the FMGs described in this book are 2-inch diameter and 1-inch thick cylinders made of N35 Nd₂Fe₁₄B, which has the following magnetic properties: residual magnetisation $B_r = 1.23$ T and coercive force $H_c = 899000$ A/m.

7.2 Shock Compression of Ferromagnetic Materials

The magnetic properties of solids can be significantly altered by high pressure shock compression. The Curie temperature of some ferromagnetic materials are strongly dependent on hydrostatic pressure or volume compression. These materials, which are typically iron alloys, can also undergo second-order phase transitions that transform them into denser phases with reduced magnetisation. Shear stresses can alter the direction of remanent magnetisation of both ferromagnetic and ferrimagnetic materials [4].

It has been found that the Curie temperature and saturation levels of iron alloys with 30–40% nickel content are highly sensitive to pressure, suggesting their magnetism is strongly dependent on their volume. Their transition from a ferromagnetic to a paramagnetic state is normally considered to be a second-order phase transition. That is, there are no discontinuous changes in enthalpy, volume and entropy, but there are discontinuous changes in volumetric thermal expansion, compressibility and specific heat. First-order transitions are those with a discontinuous change in enthalpy, entropy and volume. Since the mechanical, physical, chemical and magnetic

properties of solids are strongly dependent on their crystalline structures and since many solids are polymorphic, i.e., they have multiple crystalline structures depending on their ambient conditions, their transition from a ferromagnetic state to a paramagnetic state can be achieved by shock compression, which is the basic process that occurs during FMG operation.

Three mechanisms have been identified as contributing to shock-induced demagnetisation of ferromagnetic materials [4]:

- First-order crystallographic phase transitions in which total demagnetisation occurs.
- Second-order phase transitions between ordered and disordered magnetic states.
- Shock-induced anisotropy, caused by nonhydrostatic strains along with changes in the magnetoelastic properties of the material that produce deviations from magnetic saturation.

In the case of FMGs, the objective is to use an explosive charge to completely demagnetise its ferromagnets and, thus, release as much of the energy stored in its magnets as is possible into its output circuit. In Chapter 8, it will be shown that almost complete demagnetisation of the magnets used in specific FMG designs has been achieved.

7.3 Magnetic Circuits

In order to develop a practical method for analysing circuits with magnetic components, consider the simple structure in Fig. 7.2. It consists of a current carrying coil with N turns and a magnetic core with a mean length l and cross-sectional area A . Assuming the size of this device and its operating frequency are such that the displacement current in Maxwell's equations can be neglected and that the permeability of the core material is very high, so that all the magnetic flux will be confined to the volume of the core, Ampere's law

$$\oint_C \mathbf{H} \cdot d\mathbf{l} = \oint_S \mathbf{J} \cdot d\mathbf{a} \quad (7.7)$$

can be rewritten as:

$$H_c l_c = NI, \quad (7.8)$$

where H_c is the magnetic field strength in the core and NI is the *magnetomotive force* (MMF). The magnetomotive force is the magnetic analogue of

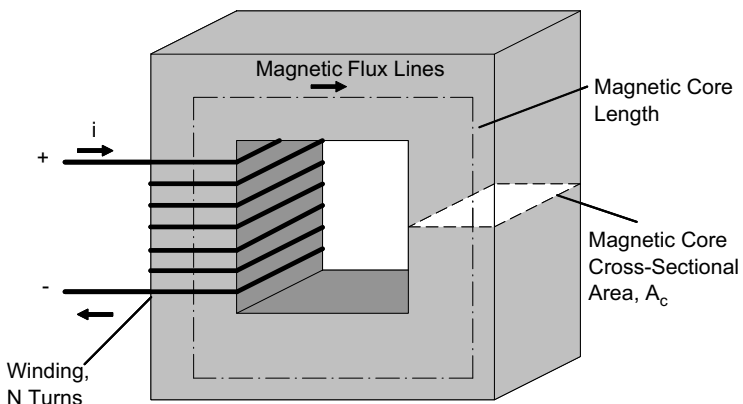


Fig. 7.2 A simple magnetic circuit.

the electromotive force. The magnetic flux that passes through the cross-sectional area of the core is

$$\phi_c = BA, \quad (7.9)$$

where $B_c = \mu H_c$. Combining Eqs. (7.7)–(7.9), the magnetic flux expression becomes

$$\phi_c = \frac{NI}{l_c/(\mu A_c)} = \frac{F}{R_H}, \quad (7.10)$$

where $R_H = l_c/(\mu A_c)$ is called *magnetic reluctance* and $F = NI$ is the magnetomotive force. The permeability of the materials used in magnetic circuits correspond to the conductivity of the materials used in electric circuits. In the magnetic circuit shown in Fig. 7.3 (right figure), the magnetic flux takes the place of the current in the electric circuit in Fig. 7.3 (left), the magnetomotive force takes the place of the emf of the voltage source and the reluctance takes the place of the resistance. Equation (7.10) is the magnetic analogue of Ohm's law. The magnetomotive force has units of ampere turns and the reluctance has MKS units, where l_c has units of meters and A_c has units of meters squared. There is no accepted name for the MKS unit of reluctance.

When a magnetic material is introduced into a magnetic circuit, it opposes any change in magnetic flux. This opposition is called *reluctance* and is the analog of the resistance encountered in electric circuits. Like resistance, the reluctance of a circuit depends upon length of a given magnetic element, its cross-sectional area and the material from which it is made.

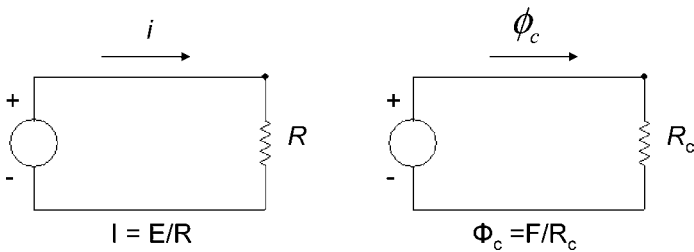


Fig. 7.3 Electric circuit diagram and its analog magnetic circuit diagram for the magnetic circuit shown in Fig. 7.2.

As with resistance in electrical circuits, the equivalent reluctance of a series magnetic circuit is the sum of the reluctances of the elements that comprise the circuit [1, 2, 5]. The magnetic potential difference required to force flux through the reluctance of a portion of magnetic circuit is called *reluctance drop* and it is the magnetic analog of voltage drop.

The *magnetic conductance* of a magnetic circuit is called the *permeance* and is equal to the reciprocal of its reluctance. The equivalent permeance of a number of magnetic paths in parallel is equal to the sum of the permeances of the individual paths [2].

The *magnetic potential gradient* is defined to be the reluctance drop per unit length of circuit and is designated by the symbol H :

$$H = \frac{\text{Reluctance Drop}}{l}. \quad (7.11)$$

It is also called *magnetising force* or *field intensity*. It is analogous to the voltage gradient in electric circuits. When the MMF applied to a magnetic circuit varies in time, so does its magnetic potential gradient. The magnetic potential gradient can be related to the magnetic flux density, $B = \phi/A$, by using the magnetic analog of Ohm's law:

$$\text{Reluctance Drop} = \phi R_H = \phi \frac{l}{\mu A}. \quad (7.12)$$

Rearranging and substituting in the definition of magnetic flux density, it is found that

$$H = \frac{\text{Reluctance Drop}}{l} = \frac{1}{\mu} \cdot \frac{\phi}{A} = \frac{B}{\mu}. \quad (7.13)$$

Thus, the relationship between magnetic potential gradient and magnetic flux density is

$$B = \mu H, \quad (7.14)$$

Table 7.1 Equivalent parameters of electric and magnetic circuits.

Electric Circuit		Magnetic Circuit	
Electrical Parameter	Symbol or Relationship	Magnetic Parameter	Symbol or Relationship
Current Density (Ohm's Law)	$j = \sigma E$	Magnetic Flux Density (Magnetic Ohm's Law)	$B = \mu H$
Electrical Conductivity	σ	Magnetic Permeability	μ
Electric Field	E	Magnetic Field	H
Voltage	$V = \oint E \cdot dl$	Magnetomotive Force	$V_H = \oint H \cdot dl = ni$
Total Current	$I = jA = \frac{V}{R}$	Total Magnetic Flux	$\phi = BA = \frac{V_H}{R_H}$
Resistance	$R = \frac{l}{\sigma A}$	Magnetic Reluctance	$R_H = \frac{l}{\mu A}$
Conductance	$\frac{1}{R}$	Permeance	$\frac{1}{R_H}$

where μ is the permeability of the material used as the magnetic conductor, H is the magnetic potential gradient in ampere turns per meter and B is the magnetic flux density in webers per square meter.

In summary, the equivalent parameters of magnetic and electric circuits are presented in Table 7.1.

7.3.1 Magnetic Circuit Laws

In this section, the magnetic analogue of Kirchhoff's voltage and current laws will be derived [1, 2]. In order to derive the magnetic equivalent of Kirchhoff's voltage law, let's consider the magnetic circuit in Fig. 7.4 and its analogue magnetic circuit in Fig. 7.5. An air gap of length l_g has been introduced into the middle of one of the legs. The magnetic flux in the gap fringes outward, thus increasing its effective cross-sectional area to A_g and reducing the reluctance of the air gap. The presence of the air gap in this magnetic circuit is analogous to a series resistor in an electric circuit. Summing the magnetic potentials, the following circuit equation can be written

$$F = NI = H_c l_c + H_g l_g = \phi_c R_{Hc} + \phi_g R_{Hg}. \quad (7.15)$$

According to Gauss's law,

$$\oint_C \mathbf{B} \cdot d\mathbf{A} = 0, \quad (7.16)$$

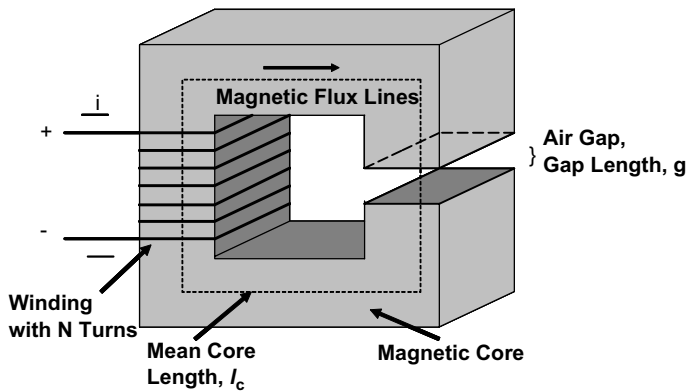


Fig. 7.4 A simple magnetic circuit with an air gap.

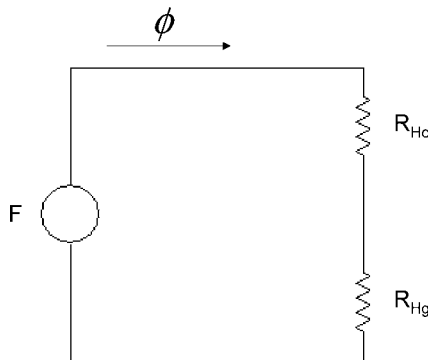


Fig. 7.5 Equivalent magnetic circuit diagram for the magnetic circuit with an air gap shown in Fig. 7.4.

which implies that

$$\phi = \phi_c = \phi_g. \quad (7.17)$$

Therefore,

$$F = (R_{Hc} + R_{Hg})\phi. \quad (7.18)$$

Generalising this expression, the following formula

$$\sum F_i = \sum R_{Hi}\phi_i \quad (7.19)$$

can be interpreted to be the magnetic analogue of Kirchhoff's voltage law.

In order to derive Kirchhoff's current law, let's consider the circuit in Fig. 7.6 with the analogue magnetic circuit diagram shown in Fig. 7.7. Applying Gauss's law, Eq. (7.16), to the T joint in this circuit, it is found that

$$\sum_{i=1}^3 \phi_i = 0. \quad (7.20)$$

Generalising this expression, the following formula

$$\sum_{i=1}^n \phi_i = 0, \quad (7.21)$$

can be interpreted as the magnetic analogue of Kirchhoff's current law.

These two laws can now be used to solve very complex magnetic circuits using all the same techniques used to solve electrical circuits. For magnetic circuits, where its nonlinearity needs to be taken into account, the magnetic

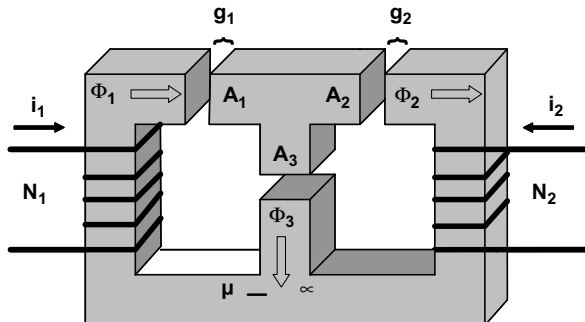


Fig. 7.6 Magnetic circuit with a two-coil system.

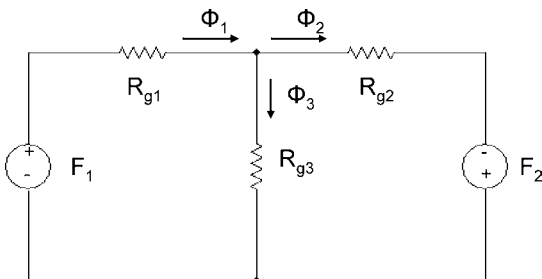


Fig. 7.7 Analog magnetic circuit diagram for the magnetic circuit shown in Fig. 7.6.

reluctance is assumed to be a function of magnetic flux, since the permeability is a function of magnetic field strength or flux density. In this case, numerical methods are needed to solve the circuit.

In summary, the magnetic analogue of Kirchhoff's laws depends on the following three relationships:

- The sum of the fluxes entering a junction in a magnetic circuit is equal to the sum of the fluxes leaving the junction.
- The algebraic sum of the magnetomotive forces equals the algebraic sum of the reluctance drops.
- The difference in magnetic potential between any two points in a magnetic circuit is the same along any path.

7.3.2 Magnetic Circuit Model for Permanent Magnets

Permanent magnets are used to seed FCGs and are the main component in FMGs and MMGs. Since they are a major part of the magnetic circuit, it would be beneficial if they could be treated as a lumped circuit element when analysing these circuits.

For the purposes of this analysis, let's consider a permanent magnet with cross-sectional area A_m and length l_m and let's assume that it has a linear demagnetisation curve with a coercive force of H_c and remanent flux density of B_r . Then an expression for the magnetic equivalent of the voltage drop across the magnet can be written as

$$H_m I_m = \left(\frac{B_m}{\mu_m} - H_c \right) l_m = \frac{l_m}{\mu_m A_m} \phi_m - H_c l_m = R_m \phi_m - F_m, \quad (7.22)$$

where R_m is the reluctance of the magnet and F_m is its magnetomotive force. If the demagnetisation curve is nonlinear, the above circuit model is still valid with the exception that the magnetic permeability must be redefined as follows:

$$\mu_m = \frac{B_m}{H_m + H_c}, \quad (7.23)$$

which is a function of the magnetic field in the magnet. It should be noted that H_m and B_m have opposite polarity. The magnetic circuit models for magnets with (a) linear and (b) nonlinear demagnetisation curves are shown in Fig. 7.8.

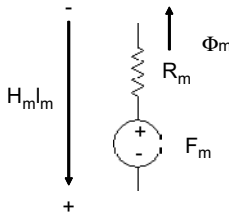


Fig. 7.8 Magnetic circuit model for a permanent magnet.

7.4 Magnetic Loss Mechanisms

There are two loss mechanisms in magnetic materials. First is the tendency of the material to retain its magnetism or to oppose a change in its magnetism, which is called *hysteresis loss*. The second is I^2R heating, which occurs as the result of voltages and subsequent circulatory currents being induced by temporal changes in the magnetic flux and which is known as *eddy current loss*.

7.4.1 Hysteresis Loss

Hysteresis is the result of a magnetic material's desire to retain its magnetism or to oppose a change in its magnetic state. Hysteresis loss is the energy converted into heat because of the hysteresis phenomenon. The occurrence of hysteresis loss is intimately associated with a phenomenon whereby energy is absorbed by a region permeated with a magnetic field. If the region is not a vacuum, then only a portion of the energy taken from a magnetising electric circuit is stored and recovered from the region when the magnetising force is removed. The energy not recovered is converted into heat.

7.4.2 Eddy Current Loss

Whenever the magnetic flux in a conducting material changes in time, an electric field is induced in the material. This field induces an electric current, called *eddy currents*, in the magnetic material. The presence of this current results in an energy loss, i.e., Joule heating, within the material that is proportional to I^2R . Since the flux densities within the material may be relatively large and since the resistivity of the material is not very high, the induced electromotive forces, eddy currents and eddy current losses may

become appreciable. Thus, steps should be taken to minimise these losses. For the case of the FMG, the steps taken to reduce eddy current losses will be discussed in Chapter 8.

To illustrate the conditions that are typically encountered in iron cores, consider the thin metal slab shown in Fig. 7.8. Assuming the slab is permeated by magnetic flux, ϕ , that is changing in time, the electromotive force, emf, induced around the boundary $abcga$, through which the flux is changing, is given by

$$\text{emf} = -\frac{d\phi}{dt}. \quad (7.24)$$

This voltage acting around the circuit $abcta$ induces a current i that circulates around the boundary and sets up a magnetomotive force in a direction that opposes any change in ϕ . This current tends to shield the center of the slab from the magnetic flux, thus reducing the flux density near the center with respect to that at the surfaces. In other words, the total flux tends to concentrate near the surface of the slab. This phenomenon is called the *magnetic skin effect* and is the magnetic analogue of the skin effect observed in electrical conductors.

7.5 Summary

In this chapter, a brief introduction to magnetic materials and their properties has been presented. This discussion included the following topics:

- Classification of the various types of magnetic materials.
- Parameters used to characterise the magnetic properties of materials.
- Effects of shock loading on ferromagnetic materials.
- Principles of magnetic circuits.
- Magnetic loss mechanisms.

Bibliography

- [1] *Magnetic Circuits and Transformers*, Members of the Staff of the Department of Engineering, Massachusetts Institute of Technology, John Wiley & Sons, Inc., New York (1943).
- [2] G. V. Mueller, *Introduction of Electrical Engineering*, 2nd Ed., McGraw-Hill Book Company, Inc., New York (1948).
- [3] H. E. Knoepfel, *Magnetic Fields: A Comprehensive Theoretical Treatise for Practical Use*, John Wiley & Sons, Inc., New York (2000).

- [4] R. A. Graham, *Solids Under High-Pressure Shock Compression: Mechanics, Physics, and Chemistry*, Springer-Verlag, New York (2003).
- [5] J. R. Reitz, F. J. Milford and R. W. Christy, *Foundations of Electromagnetic Theory*, Addison-Wesley Publishing Company, Reading (1980).

Chapter 8

Ferromagnetic Generators

8.1 Explosive Driven Soft Ferromagnetic Generators

The first attempt to develop explosive driven Ferromagnetic Generators (FMGs) as power supplies was performed at Sandia National Laboratories in the late 1950s. The first papers describing pulsed power generation by this type of electrical transducer were published by Anderson *et al.* [1] in 1957 and by Kulterman *et al.* [2] in 1958. This ferromagnetic transducer was based on the demagnetisation of a closed soft ferromagnetic core by shock waves generated by an accelerated projectile. A schematic diagram of this transducer is shown in Fig. 8.1. Its basic operating principle [1, 2] is the rapid change of the magnetic flux, due to shock demagnetisation of the ferromagnet, in the coil wound on one arm of the closed soft ferromagnetic (silectron steel) core. This change in flux induces an Electromotive Force (EMF) pulse at the output terminals of the coil.

In 1966, Besancon *et al.* [3] conducted detailed investigations of explosive driven ferromagnetic transducers similar to those described in Refs. 1 and 2. They used three types of soft ferromagnetic materials (Fe-Ni, Fe-Co-V, Fe-Co) as the closed ferromagnetic cores in their generators. It was demonstrated that these generators, loaded with high-resistance loads, are capable of producing high-voltage pulses with amplitudes exceeding 100 kV. Detailed investigations of the phase transformations induced in soft ferromagnetic materials by shock waves are described in Refs. 4–11.

8.2 Explosive Driven Soft Ferromagnetic Generator Limitations

There are two important principles that prevent the generators described in Refs. 1–3 from being prime energy sources. They are the key physical

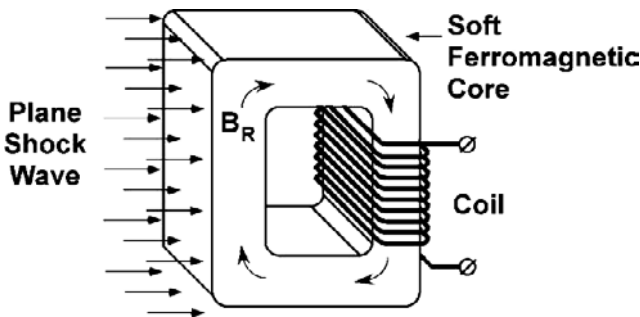


Fig. 8.1 Schematic diagram of an explosively driven electrical transducer based on the shock wave demagnetisation of a closed soft ferromagnetic core [1–2].

principles that determine whether or not FMGs can be used as ‘prime’ energy sources.

- The generators described in Refs. 1–3 are not autonomous sources of prime power. Their closed soft ferromagnetic cores had to be magnetised to saturation by external electrochemical batteries immediately before explosive operation. In other words, these generators require a seed source.
- The electromagnetic energy density that can be stored by soft ferromagnets is extremely low.

The magnetostatic energy, E , stored in a magnetised body can be expressed in terms of the volume integral of the scalar product $(B \cdot H)$, where B is the magnetic flux density and H is the magnetic field intensity of the ferromagnetic material, taken at each point in the magnetic medium:

$$E = -0.5 \iiint_V (B \cdot H) dv \quad (8.1)$$

Most soft ferromagnetic materials typically possess very high residual magnetisation, B_r , which for some materials can exceed 2 T. At the same time, these materials have extremely low (less than 1 Oe) coercive forces, H_c . Correspondingly, the maximum energy product, $(B \cdot H)_{\max}$, and the magnetostatic energy stored in soft ferromagnets are very low.

An expression for the total energy delivered by an FMG to a load circuit, $W(\infty)$, can be written as follows:

$$W(\infty) = \int_0^{+\infty} I(t) \cdot U(t) \cdot dt \quad (8.2)$$

where $I(t)$ is the electric current in the load circuit and $U(t)$ is the electric potential across the load. It follows from the general thermodynamic laws that the total energy, $W(\infty)$, delivered by a generator to a load circuit cannot exceed the energy, E , initially stored in the ferromagnet (see Eq. (8.1)). There are no grounds to believe that explosively demagnetised soft ferromagnetic cores can efficiently deliver energy to loads.

A breakthrough in the development of explosive driven ferromagnetic transducers was made in the late 1990s by Shkuratov *et al.* [12–28] at Texas Tech University. The basic idea behind this new approach was to exclusively use hard ferromagnetic materials in FMGs.

Hard ferrimagnets and ferromagnets possess significantly lower (about two times for ferromagnets and four times for ferrimagnets) residual magnetisation, B_r , than that of the best soft ferromagnetic materials. At the same time, the coercive force, H_c , of hard ferrimagnets and ferromagnets is from 4 to 8 orders of magnitude higher than that of soft ferromagnets. Correspondingly, the maximum energy product, $(B \cdot H)_{\max}$, and the magnetostatic energy (Eq. (8.1)) stored in hard ferromagnets is at least 4 orders of magnitude greater than that of soft ferromagnets. The magnetostatic energy density for commercially available hard ferromagnetic materials reaches 0.2 J/cm^3 .

Hard ferromagnets have one more important advantage in comparison with soft ferromagnetic materials. A hard ferromagnet does not require a seed source to magnetise it prior to explosive and electrical operation of the FMG. It stores its magnetostatic energy for long periods of time, making the FMG a completely self-contained system. Ferromagnetic generators using hard ferromagnets can be smaller, lighter and simpler than those using soft ferromagnets.

Even though hard ferromagnets store a large amount of magnetostatic energy, this does not mean that the energy can be released by shock wave action. It was earlier reported by Johnson [29] that it is not possible to demagnetise hard ferromagnets with a high amplitude shock wave. However, it was later shown by Shkuratov *et al.* [13] that this is not the case.

Experimental investigations of shock induced phase state transitions in hard ferrimagnets and ferromagnets were performed by Shkuratov *et al.* [13] at Texas Tech University in the late 1990s, 40 years after the initial investigations of magnetic phase transitions in soft ferromagnetic materials. As a result of these studies, it was for the first time demonstrated that high-energy hard ferrimagnets ($\text{BaFe}_{12}\text{O}_{19}$) and ferromagnets ($\text{Nd}_2\text{Fe}_{14}\text{B}$)

undergo ferrimagnetic/ferromagnetic-to-paramagnetic phase state transitions under longitudinal (the shock wave propagates along the magnetisation vector M) shock compression [12–14]. This physical effect was the basis for the development of more energetic types of explosive driven prime power sources, i.e. the FMGs [12–15].

In 2002, South Korean researchers published a paper [30] devoted to the development of generators utilising longitudinal shock wave demagnetisation of $\text{Nd}_2\text{Fe}_{14}\text{B}$ ferromagnets. Prishchepenko *et al.* [31] proposed using ferromagnetic generators as a prime power source for compact microwave systems.

Two years after demonstrating that longitudinal shock waves can demagnetise hard ferrimagnetic and ferromagnetic materials, Shkuratov *et al.* [16–18] at Texas Tech University observed that transverse (when the shock wave propagates across the magnetisation vector M) shock waves can also demagnetise $\text{Nd}_2\text{Fe}_{14}\text{B}$ ferromagnets. The discovery of transverse shock demagnetisation of hard ferromagnets offered a straightforward way to design and construct miniature high-current and high-voltage generators of prime power [16–28].

Research and development of shock wave FMGs were conducted at Texas Tech University from 1998 through 2003. Since 2004, S.I. Shkuratov and J. Baird have continued systematic studies of FMGs at Loki Incorporated. During ten years of intensive research and development work, a variety of FMGs were designed, constructed and tested. As a result of these efforts, it is now possible to produce highly reliable compact high-voltage and high-current FMGs [19–28, 32].

This chapter gives detailed descriptions of shock induced ferromagnetic effects, designs of miniature FMGs, results of the operation of these generators with different types of loads and design and performance characteristics of completely explosive driven FMG-FCG pulsed power systems.

Some of the results described in this chapter were presented at various international and national conferences and workshops; however, some of the results herein are presented for the first time.

8.3 Pressure Induced Magnetic Phase Transitions in Hard Ferromagnets

The first problem that needs to be solved relative to utilising the energy stored in hard ferromagnets for the generation of pulsed power is to find those hard ferromagnetic materials that can be transformed to the

paramagnetic state by shock wave compression. The second problem is how to efficiently deliver the magnetostatic energy, E , stored in hard ferromagnets to the pulse generating circuit of the FMG in a short (microsecond or submicrosecond) period of time, Δt , to provide high output power levels:

$$P(t) = \frac{\Delta E}{\Delta t}. \quad (8.3)$$

Consider a hard ferromagnet that stores 5 J of magnetostatic energy. If this stored energy is released by a shock wave over a period of 5.0 μs , the output power of the FMG can reach a value of:

$$P(t) = \frac{\Delta E}{\Delta t} = \frac{50 \text{ J}}{5 \times 10^{-6} \text{ s}} = 10^6 \text{ W}. \quad (8.4)$$

If this same magnetic phase transition takes tens or hundreds of milliseconds, the output power of the FMG would be too low for many applications.

The permanent ferromagnetic materials that store the greatest amount of magnetostatic energy are rare earth hard Nd₂Fe₁₄B ferromagnets [33]. In this section, the results of studies by Shkuratov *et al.* [13–15] of the longitudinal shock wave compression of Nd₂Fe₁₄B ferromagnets will be presented.

8.3.1 Longitudinal Shock Wave Demagnetisation of Nd₂Fe₁₄B

A schematic diagram of the experimental device, described in Ref. 14, that was used to investigate longitudinal demagnetisation of Nd₂Fe₁₄B ferromagnets is shown in Fig. 8.2. The device consisted of a plastic body, high explosive charge, single RISI RP-501 Exploding Bridgewire (EBW) detonator, Nd₂Fe₁₄B ferromagnetic cylinder magnetised along its axis and single-turn diagnostic coils wound on the ferromagnet. A planar shock wave was initiated at one end of the Nd₂Fe₁₄B cylinder, which propagated through the ferromagnet along the magnetisation vector M (Fig. 8.2). The shock wave was generated by 16.5 to 18.5 grams of C-4 high explosives.

The test objects [13–14] were solid Nd₂Fe₁₄B cylinders, with a diameter of 2.22 cm and a length of 2.54 cm, magnetised along their axis. The parameters of the Nd₂Fe₁₄B ferromagnet (commercial grade 35) in a closed magnetic circuit were: residual flux density $B_r = 1.23 \text{ T}$, coercive force $H_c = 8.99 \times 10^5 \text{ A/m}$, maximum-energy product $BH_{\max} = 0.279 \text{ J/cm}^3$; industry tolerance: $B_r \pm 5\%$, $H_c \pm 8\%$ and $BH_{\max} \pm 10\%$ and Curie temperature $T_c = 312^\circ\text{C}$.

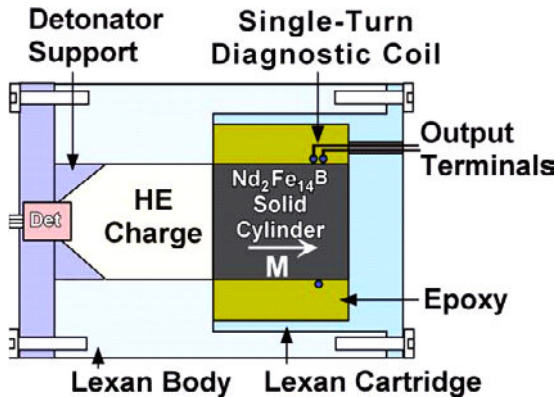


Fig. 8.2 Schematic diagram of the explosive device used to generate $E_g(t)$, waveforms by longitudinally shock depolarising a $\text{Nd}_2\text{Fe}_{14}\text{B}$ ferromagnetic cylinder [14].

The magnetic circuit used to test the $\text{Nd}_2\text{Fe}_{14}\text{B}$ samples was an open circuit (Fig. 8.2). In order to determine the magnitude and distribution of the initial magnetic flux density, B_0 and the initial magnetic flux, Φ_0 , three-dimensional computations were conducted (the accuracy of these computations were no less than 0.03%). The technique described in Refs. 22 and 23 was used for these computations. The initial magnetic flux density, B_0 and magnetic flux, Φ_0 , were calculated at planes offset by 0.05, 0.50 and 1.00 cm from the butt end of the $\text{Nd}_2\text{Fe}_{14}\text{B}$ cylinder and are presented in Fig. 8.3 and in Table 8.1.

After detonation of the HE charge (Fig. 8.2), the $\text{Nd}_2\text{Fe}_{14}\text{B}$ cylinder was subjected to longitudinal shock wave compression. Propagation of the longitudinal shock wave through the $\text{Nd}_2\text{Fe}_{14}\text{B}$ ferromagnet and generation of EMF are shown schematically in Fig. 8.4.

If the shock wave demagnetises the $\text{Nd}_2\text{Fe}_{14}\text{B}$ — i.e. the ferromagnetic cylinder partially or completely loses its initial magnetic flux Φ_0 , the change in magnetic flux, $d\Phi(t)$, generates an EMF pulse, $E_g(t)$, in the diagnostic coils wound on the cylinder in accordance with Faraday's law

$$E_g(t) = -\frac{d\Phi(t)}{dt}, \quad (8.5)$$

where dt is the time it takes for the magnetic flux $d\Phi(t)$ to change.

Integration of the $E_g(t)$ waveform from 0 to t

$$\Delta\Phi(t) = - \int_0^t E_g(t) \cdot dt \quad (8.6)$$

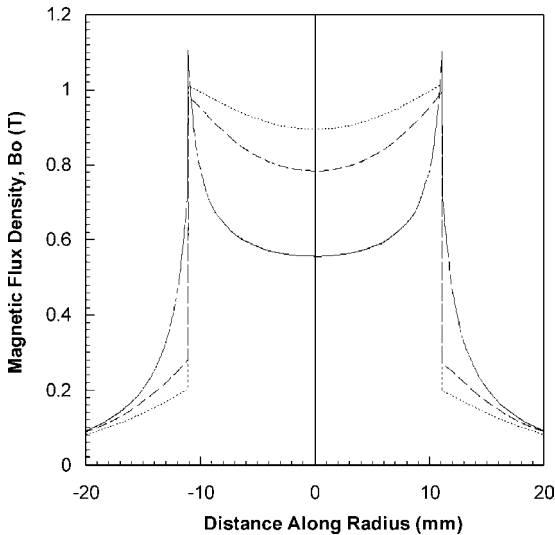


Fig. 8.3 Calculated magnetic flux density B_0 inside and outside a $\text{Nd}_2\text{Fe}_{14}\text{B}$ cylinder (diameter $D = 2.22$ cm, length $h = 2.54$ cm) at 1.0 cm (dotted line), 0.5 cm (dashed line) and 0.05 cm from the butt end of the cylinder [14].

Table 8.1 Initial magnetic flux calculated at different positions of the diagnostic induction coils and experimentally measured magnetic flux losses.

Single-turn coil positions (mm)	10.0	5.0	0.5
Calculated initial flux, Φ_0 (μWb)	368	334	212
Experimental flux loss, $\Delta\Phi_f$ (μWb)	$-(341 \pm 38)$	$-(316 \pm 25)$	$-(202 \pm 18)$

yields the magnetic flux $\Delta\Phi(t)$ lost in time t . The numerical value of the integral

$$\Delta\Phi_f = - \int_0^{+\infty} E_g(t) \cdot dt \quad (8.7)$$

gives the value of the total magnetic flux loss.

The test setup used to measure the $E_g(t)$ waveforms is shown in Fig. 8.5. The diameter of the wire used to make the single-turn diagnostic inductive coils was 0.81 mm. The wire was coated with plastic insulation that had a thickness of 0.37 mm. The single-turn coils had a diameter of 23.9 mm and a cross-sectional area of 4.486 cm^2 . Miniature Hewlett-Packard 1160 A passive probes with an input impedance of $10 \text{ M}\Omega$ and capacitance of 9 pF were also used in the experiments.

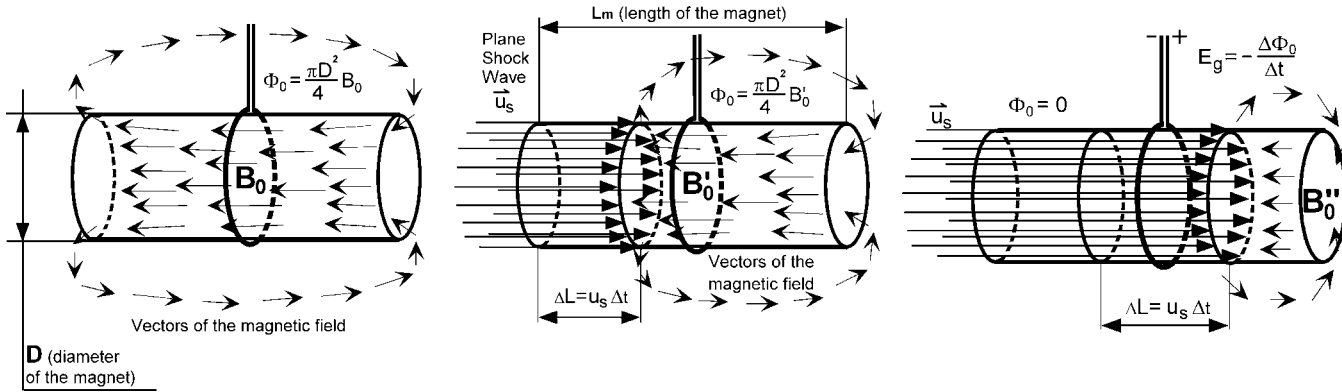


Fig. 8.4 Schematic diagram illustrating the propagation of a longitudinal shock wave through a $\text{Nd}_2\text{Fe}_{14}\text{B}$ ferromagnetic cylinder and the generation of electromotive force, $E_g(t)$, due to shock wave demagnetisation. The shock wave (a) is initiated at the front face of the ferromagnet, (b) travels through the magnetic cylinder and (c) passes through the winding.

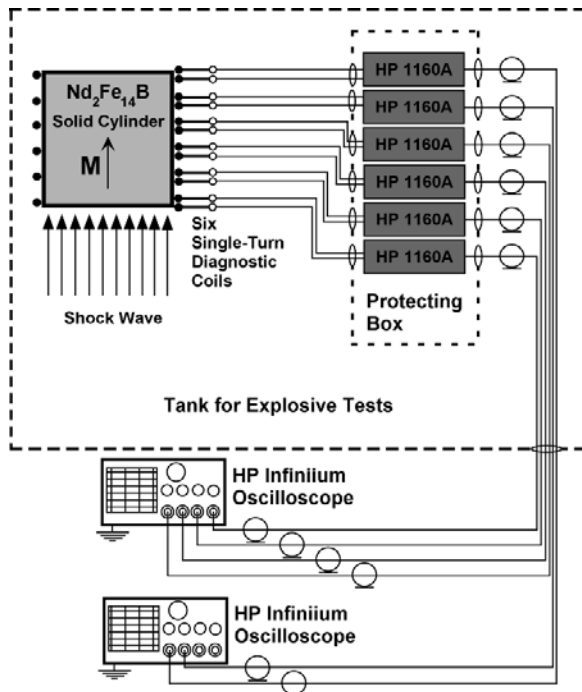


Fig. 8.5 Test setup for measuring the electromotive force, $E_g(t)$, waveform generated by a single-turn diagnostic coil wound on a Nd₂Fe₁₄B ferromagnet subjected to longitudinal shock wave compression [14].

Typical experimental $E_g(t)$ waveforms recorded by the single-turn diagnostic coils located at distances of (a) 0.5, (b) 5.0 and (c) 10.0 mm from the butt end of the Nd₂Fe₁₄B cylinder and the corresponding magnetic flux losses are presented in Fig. 8.6. Special measures were taken to prevent relative motion of the magnet with respect to the single-turn diagnostic coils.

The shape and amplitude of the $E_g(t)$ waveforms (for the corresponding positions of the single-turn diagnostic coils) were very reproducible in all experiments. Relevant values of $\Delta\Phi_f$, obtained by integration of the experimental $E_g(t)$ waveforms, are listed in Table 8.1.

As can be seen in Table 8.1, the magnetic flux losses, $\Delta\Phi_f$, are almost equal to the initial values of the magnetic flux Φ_0 for all three single-turn diagnostic coils. The spread in the experimental values of the magnetic flux losses, $\Delta\Phi_f$, does not exceed the industry tolerance for the

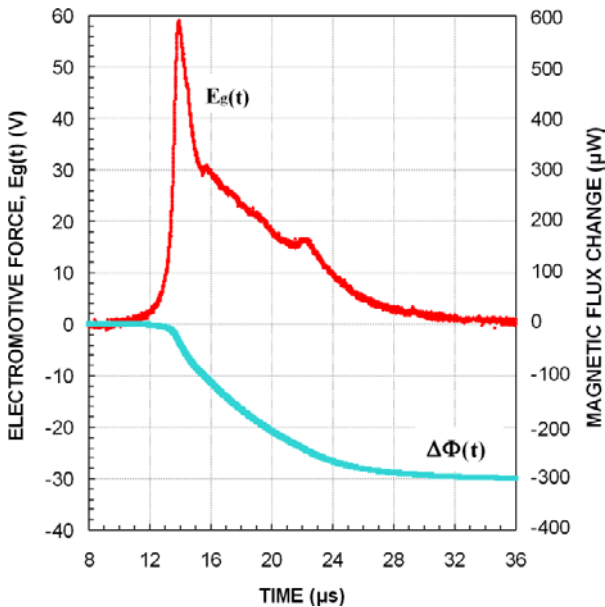


Fig. 8.6 Typical waveform of the electromotive force, $E_g(t)$, generated by a single-turn diagnostic coil wound on a $\text{Nd}_2\text{Fe}_{14}\text{B}$ cylinder ($D = 2.22 \text{ cm}$, $h = 2.54 \text{ cm}$) and located 5.0 mm from the butt end of the magnet (Fig. 8.5) [14]. The corresponding change in the magnetic flux is also shown.

principal magnetic parameters of the $\text{Nd}_2\text{Fe}_{14}\text{B}$ samples tested. These results are direct evidence of the almost complete shock demagnetisation of the $\text{Nd}_2\text{Fe}_{14}\text{B}$ ferromagnets.

8.3.2 Pressure in Shock Compressed $\text{Nd}_2\text{Fe}_{14}\text{B}$ Ferromagnets

The high shock pressures used to demagnetise $\text{Nd}_2\text{Fe}_{14}\text{B}$ ferromagnets cause both mechanical compression of its crystal lattice and shocked induced increases in its temperature. It is more probable that demagnetisation is due to a magnetic phase transition or a structural phase transition, or a series of such transitions, within the bulk of the $\text{Nd}_2\text{Fe}_{14}\text{B}$ crystal.

In order to estimate the shock wave pressure that induces magnetic phase transformations in $\text{Nd}_2\text{Fe}_{14}\text{B}$, the Hugoniot equations for C-4 and for $\text{Nd}_2\text{Fe}_{14}\text{B}$ were solved simultaneously [14]. In accordance with [34], the

detonation product Hugoniot equation is

$$P = 2.412P_{CJ} - \left(1.7315 \frac{P_{CJ}}{U_{CJ}}\right) U_P + \left(0.3195 \frac{P_{CJ}}{U_{CJ}^2}\right) U_P^2, \quad (8.8)$$

where P is pressure, CJ denotes the Chapman-Jouguet state and U_P is particle velocity.

The Hugoniot for $\text{Nd}_2\text{Fe}_{14}\text{B}$ is still unknown. Therefore, a technique found in Ref. 35 was used to estimate the Hugoniot of $\text{Nd}_2\text{Fe}_{14}\text{B}$. This technique was developed to calculate the Hugoniots for alloys and is based on using the Hugoniots of the various components of the alloy. Taking into account that the Hugoniot of boron is not available and that boron makes up such a small portion of the alloy (1% by mass, 3.2% by relative atomic volume), the presence of boron in the alloy was neglected. Using this approximation, the relative atomic volumes of Fe and Nd are 70.5% and 29.5%, respectively. Utilising the data presented in Refs. 35 and 36, the Hugoniots for Fe and Nd are:

$$U_S(\text{Fe}) = 4.63 + 1.33U_P \quad (8.9)$$

and

$$U_S(\text{Nd}) = 2.2 + 1.83U_P, \quad (8.10)$$

respectively, where U_S is the shock wave velocity.

In accordance with [35], the Hugoniot for the $\text{Nd}_2\text{Fe}_{14}\text{B}$ alloy was found to be:

$$U_S(\text{Nd}_2\text{Fe}_{14}\text{B}) = 3.913 + 1.475U_P. \quad (8.11)$$

The shock wave velocity, U_S , in $\text{Nd}_2\text{Fe}_{14}\text{B}$ was determined from analysis of the $E_g(t)$ waveforms. The peaks in the $E_g(t)$ waveforms could confidently be associated with the time at which the shock wave front crossed the plane of the respective single-turn coils. Based on this observation, the velocity of the shock wave front through $\text{Nd}_2\text{Fe}_{14}\text{B}$ was estimated to be $U_S = 5.03 \pm 0.08 \text{ km/s}$. Using Eq. (8.11) and the calculated shock velocity, the particle velocity was calculated to be $U_P = 0.75 \pm 0.02 \text{ km/s}$. Using the basic equation for shock waves in condensed matter [37, 38]

$$P = \rho U_S U_P, \quad (8.12)$$

where ρ is the density of $\text{Nd}_2\text{Fe}_{14}\text{B}$ in its compressed state (in its normal, uncompressed state, $\rho_0 = 7.4 \text{ g/cm}^3$), the pressure produced by the longitudinal shock wave was found to be $P > 28.2 \pm 2.2 \text{ GPa}$.

The pressure exerted by the C-4 at the explosive–Nd₂Fe₁₄B interface can be found by using the Hugoniot of the detonation products (Eq. (8.8)). Substitution of $P_{CJ} = 22.36 \text{ GPa}$, $U_{CJ} = 1.75 \text{ km/s}$ and $U_P = 0.75 \text{ km/s}$ into Eq. (8.8) yields a pressure of $P = 38.7 \text{ GPa}$. The pressure estimates in the bulk Nd₂Fe₁₄B ($P > 28.2 \text{ GPa}$) and at the C-4–Nd₂Fe₁₄B interface ($P < 38.7 \text{ GPa}$) are the lower and upper bounds, respectively, of the pressure generated by the C-4 charge in the Nd₂Fe₁₄B ferromagnet.

The second pronounced peak in Fig. 8.6(c), which is always present in the $E_g(t)$ waveforms recorded by the single-turn diagnostic coils located at positions ranging from 0.04 to 0.1 cm from the top face of the cylinder (see Fig. 8.5), is most likely due to shock waves reflected from the face of the Nd₂Fe₁₄B cylinder furthest from the explosive charge.

As was shown above, longitudinal shock induced ferromagnetic-to-paramagnetic phase transitions have been detected in Nd₂Fe₁₄B ferromagnets. As the phase transition take place, the energy stored in the ferromagnets is released within a short period of time to the pulse generating circuit [13–15]. However, this energy release can be substantially extended in time due to the appearance of pulsed vortex currents in the bulk of the demagnetised ferromagnet. The key parameter that determines the density, magnitude and damping time of these vortex currents in the non-magnetic material is its electrical conductivity [39]. Therefore, it is important to measure the electrical conductivity of the shock compressed Nd₂Fe₁₄B ferromagnets. Measurement of the electrical conductivity of longitudinally shock compressed Nd₂Fe₁₄B was performed by Talantsev *et al.* [40]. It was shown that the conductivity of longitudinally shock compressed Nd₂Fe₁₄B is $\sigma_{sw} = (2.83 \pm 0.24) \times 10^2 (\Omega \text{ cm})^{-1}$, which is 22 times lower than the conductivity of Nd₂Fe₁₄B under normal conditions [40].

8.3.3 High Voltage and High Current Generation by Longitudinally Shock Demagnetising Nd₂Fe₁₄B

To further illustrate the capabilities of miniature FMGs, several high voltage and high current generator designs were built and tested [13–15]. The pulse generating coils (for both high voltage and high current generation) were placed on the second half of the magnets — i.e. on the end furthest from the explosive charge. A description of the test setup used to generate and monitor the high voltages and high currents produced by these FMGs is presented in Refs. 13–15.

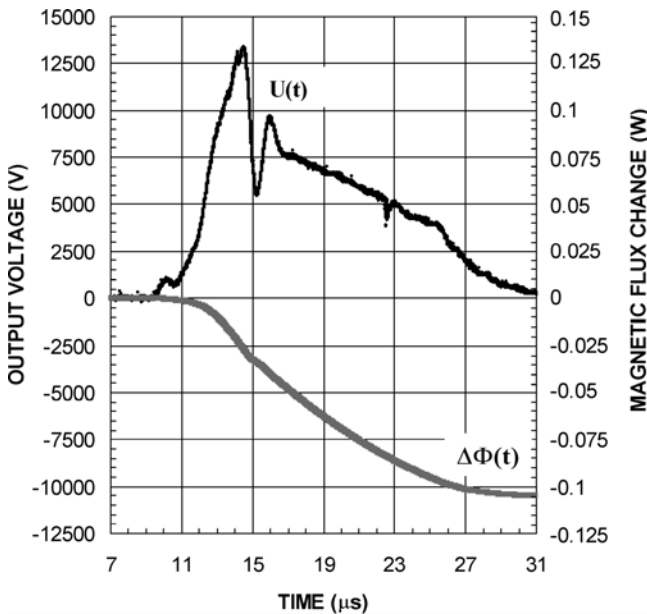


Fig. 8.7 Waveform of the output voltage produced by a high voltage FMG containing 389 turns of copper wire (0.16 mm in diameter) wound on a Nd₂Fe₁₄B cylinder ($D = 2.22$ cm, $h = 2.54$ cm) and its corresponding magnetic flux change [15].

A high voltage FMG, containing 389 turns of copper wire (0.16 mm in diameter) in its pulse generating coil, generated a high voltage pulse with a peak amplitude of $U(t)_{\max} = 13.4$ kV and a FWHM of $8.2 \mu\text{s}$ (Fig. 8.7). The inside diameter of the multi-turn winding was 2.34 cm and its cross-sectional area was 4.3 cm^2 . The outside diameter of the multi-turn winding was 3.12 cm and its cross-sectional area was 7.65 cm^2 . The total magnetic flux $\Delta\Phi_f$ captured by the pulse generating coil was $\Delta\Phi_f = 0.114 \text{ Wb}$ (Fig. 8.7). This corresponds to a specific magnetic flux of $\Delta\Phi_f = 293 \mu\text{Wb}/\text{turn}$, which is close to the initial magnetic flux of $\Phi_0 = 323 \mu\text{Wb}$ averaged over half the length of the Nd₂Fe₁₄B cylinder.

A high current single coaxial turn generator, having diameter of 2.5 cm and a strip width of 1.3 cm, delivered a current pulse with peak amplitude of $I(t)_{\max} = 1,002$ A and FWHM of $165 \mu\text{s}$ (Fig. 8.8) to a load having an absolute impedance of $Z(100 \text{ kHz}) = 87 \text{ m}\Omega$. Note that even $600 \mu\text{s}$ after initiation of the shock wave, the output current $I(t)$ had not dropped to zero and had a value of $I(600 \mu\text{s}) = 25$ A.

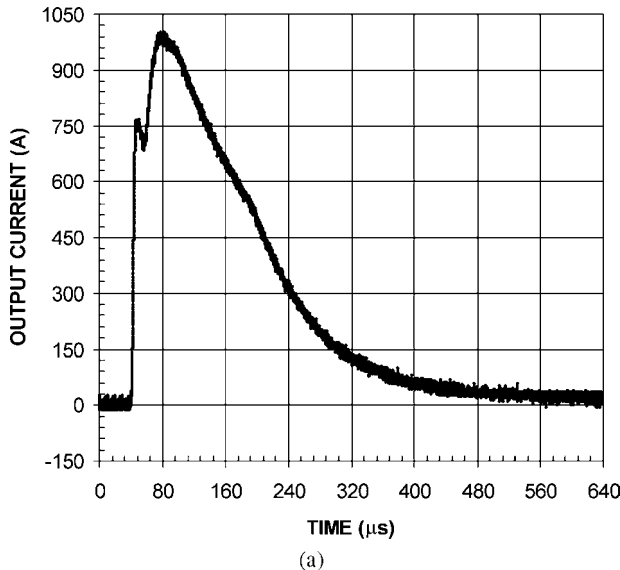


Fig. 8.8 Waveform of the output current pulse delivered by a high current single coaxial turn FMG (2.5 cm outer diameter, 1.3 cm strip width) to a circuit with a load having an absolute impedance of $Z(100 \text{ kHz}) = 87 \text{ m}\Omega$ [15].

In summary, it was experimentally demonstrated that miniature (total volume of 35 cm^3) autonomous FMGs are capable of producing current pulses with a peak amplitude of 1.0 kA and FWHM of $165 \mu\text{s}$, and voltage pulses with a peak amplitude of 13.4 kV and FWHM of $8.2 \mu\text{s}$.

8.4 Transverse Shock Wave Demagnetisation of $\text{Nd}_2\text{Fe}_{14}\text{B}$ Ferromagnets

It was demonstrated in Refs. 13–15 that longitudinal FMGs are completely autonomous compact explosive driven electrical power supplies capable of producing high voltages and high currents. But there are a few design problems with these generators. In order to completely demagnetise $\text{Nd}_2\text{Fe}_{14}\text{B}$ ferromagnets of diameter 22.2 mm, 18 g of C-4 was needed. To demagnetise a $\text{Nd}_2\text{Fe}_{14}\text{B}$ ferromagnet with a diameter of 50 mm, the mass of the HE has to be increased to 75 g and, correspondingly, the dimensions of the plastic body of the generator have to be increased (Fig. 8.2).

It was a matter of great scientific and engineering interest to investigate the demagnetisation of $\text{Nd}_2\text{Fe}_{14}\text{B}$ ferromagnets by explosive driven shock

waves traveling across the magnetisation vector M (transverse shock compression). Another extremely important engineering problem was to find a way to reduce the amount of high explosives needed to demagnetise the Nd₂Fe₁₄B ferromagnets. The problem with transverse FMGs is that the shock wave propagating across the magnetisation vector of the Nd₂Fe₁₄B ferromagnetic cylinders or bars can destroy the diagnostic coils and/or the pulse generating coil before they produce a signal.

One approach to solve this problem was to build in a delay between the time the shock wave demagnetises the ferromagnet and the time it reaches the diagnostic and current generating coils. This was made possible by drilling a hole along the center line of the Nd₂Fe₁₄B cylinder and loading the HE charge into this hole. The problem was that the diameter of the hole should not be too big, because it would significantly reduce the volume of the magnetic material and, correspondingly, the magnetic energy stored in the ferromagnet. A hole of relatively small diameter can hold no more than 1.5 g of high explosives. This is more than 10 times less than the amount of high explosives used in longitudinal FMGs [12–15]. A key question was: will the chemical energy from 1 g of HE be enough to demagnetise Nd₂Fe₁₄B ferromagnets of diameter 25 mm and length 19 mm? Transverse shock wave compression of Nd₂Fe₁₄B ferromagnets were studied by S. I. Shkuratov and E. F. Talantsev [16–18] at Texas Tech University in 2001. The results of these studies are described in this section.

A schematic diagram of the FMG used to investigate transverse demagnetisation of Nd₂Fe₁₄B ferromagnets is shown in Fig. 8.9 [16–18]. The ferromagnet investigated was a Nd₂Fe₁₄B hollow cylinder magnetised along its axis. The hole in the center of the cylinder was made by using a water jet to avoid exposing the ferromagnetic material to high temperatures, which would destroy the magnetic state of the sample.

The ferromagnet test samples had an outer diameter of O.D. = 25.4 mm, inner diameter of I.D. = 8.0 mm and length of h = 19.1 mm. The HE charge [0.8 g of desensitised RDX (C-4)] was loaded in the central hole with two RISI RP-501 EBW detonators attached to both ends of the charge (Fig. 8.9). Both detonators were initiated simultaneously — i.e. to within ± 125 ns.

Four single-turn diagnostic coils were wound on the ferromagnet. The coils were made by using Teflon insulated AWG22 wire with a diameter of 1.1 mm. The coils were located ± 3.2 mm and ± 9.5 mm from the center of the magnet. A detailed description of the test setup can be found in Refs. 16–18.

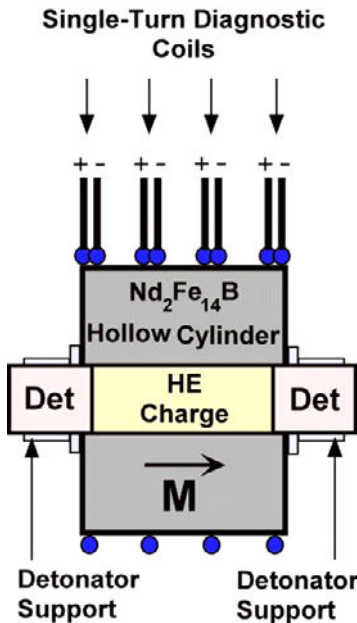


Fig. 8.9 Schematic diagram of the FMG used to investigate the effects of transverse shock wave compression on the magnetic phase state of $\text{Nd}_2\text{Fe}_{14}\text{B}$ ferromagnets [16–18].

8.4.1 *Static Magnetic Flux Initially Stored in $\text{Nd}_2\text{Fe}_{14}\text{B}$ Ferromagnets*

In order to calculate the initial static magnetic flux of the $\text{Nd}_2\text{Fe}_{14}\text{B}$ ferromagnet, the open circuit shown in Fig. 8.9 was used. The initial magnetic field density, B_0 and the initial magnetic flux, Φ_0 , linking the single-turn diagnostic coils were numerically calculated using the technique described in Refs. 22 and 23. The results of the calculation of B_0 at two positions are shown in Fig. 8.10. The magnetic flux linking the diagnostic coils were $\Phi_0(z = \pm 3.2 \text{ mm}) = 237 \mu\text{Wb}$ and $\Phi_0(z = \pm 9.5 \text{ mm}) = 371 \mu\text{Wb}$.

It follows from the calculations performed by Shkuratov *et al.* [16, 22, 23] that the B -field distribution in a hollow ferromagnetic cylinder (Fig. 8.10) is significantly different from that in a solid ferromagnetic cylinder (Fig. 8.3). However, it was demonstrated [16, 22, 23] that in spite of this difference, the hollow ferromagnetic cylinder is capable of creating really high initial magnetic flux, Φ_0 . This initial flux is sufficient to generate prime pulsed power, provided transverse shock wave demagnetisation of the hollow ferromagnet can be achieved experimentally.

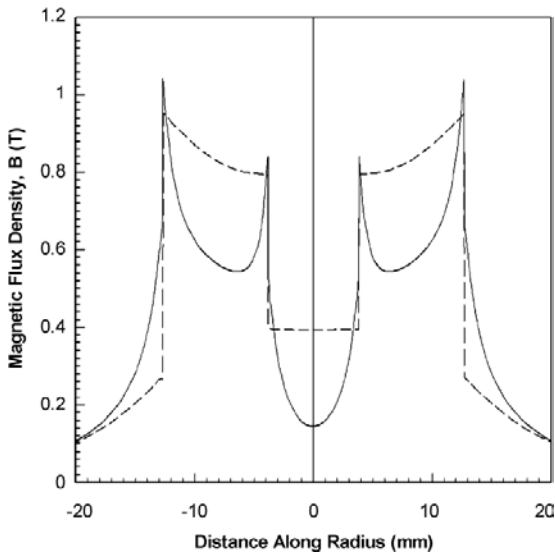


Fig. 8.10 The calculated magnetic flux density B_0 inside and outside a $\text{Nd}_2\text{Fe}_{14}\text{B}$ cylinder (diameter $D = 22.2$ mm, length $h = 25.4$ mm) 10.0 mm (dotted line), 5.0 mm (dashed line) and 0.5 mm from the butt end of the cylinder [16].

8.4.2 Transverse Shock Wave Demagnetisation of $\text{Nd}_2\text{Fe}_{14}\text{B}$ Ferromagnets

After initiation of the HE charge (Fig. 8.9), the shock wave propagates into the body of the ferromagnet across the magnetisation vector M . If the ferromagnetic cylinder loses its initial magnetic flux, Φ_0 , due to transverse shock compression, the change in magnetic flux, $\Delta\Phi(t)$, should generate an EMF pulse, $E_g(t)$, (Eq. (8.5)) in the diagnostic coils wound on the cylinder. Integration of the experimentally measured $E_g(t)$ waveforms (Eq. (8.6)) yields the ferromagnetic material's magnetic flux change, $\Delta\Phi(t)$.

The first transverse shock wave experiments were performed by Shkuratov *et al.* [16] in November 2001. They had little hope that they would get positive results in these experiments because of the very small amount of explosive charge used in the $\text{Nd}_2\text{Fe}_{14}\text{B}$ ferromagnets (0.8 g of C-4) in comparison with the amount used in the longitudinal design (18.5 g of C-4), but the results were much better than expected.

Typical experimental $E_g(t)$ waveforms recorded in these experiments by diagnostic coils located 3.2 and 9.5 mm from the middle of the $\text{Nd}_2\text{Fe}_{14}\text{B}$ cylinder and the corresponding magnetic flux losses are shown in Fig. 8.11.

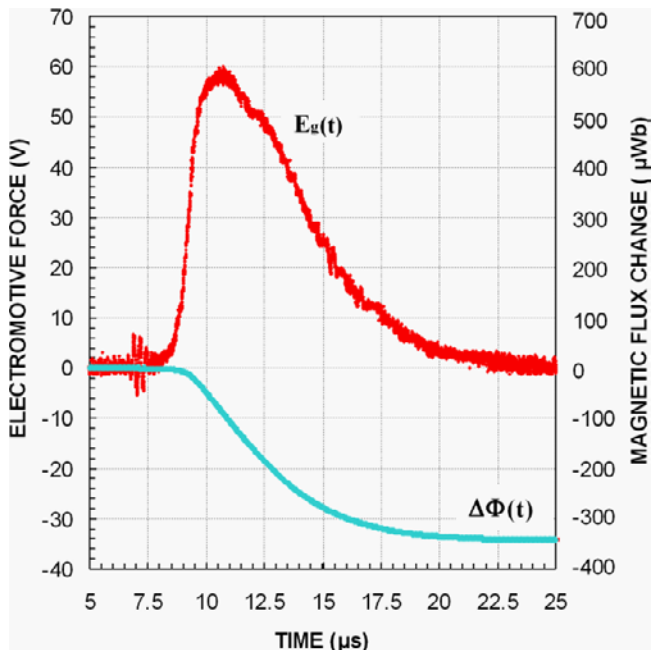


Fig. 8.11 Measured EMF, $E_g(t)$ and the corresponding change in the magnetic flux, $\Delta\Phi$, generated by a single-turn diagnostic coil wound on a hollow Nd₂Fe₁₄B ferromagnetic cylinder at $z = 3.2$ mm [16].

A comparison of the initial magnetic flux, Φ_0 , with the change in magnetic flux recorded in the explosive experiments (Table 8.2) demonstrated that the transverse shock wave accounts for more than 90–92% demagnetisation. An HE charge of less than 1 gram of C-4 demagnetised a ferromagnet having a total volume of 25.4 cm³ and a mass of 81.6 grams.

Table 8.2 Calculated values of the initial magnetic flux at different positions along a completely magnetised hollow ferromagnetic cylinder and the experimentally measured magnetic flux losses of a transverse FMG.

Position of diagnostic coils relative to the center of the Nd ₂ Fe ₁₄ B ferromagnet (mm)	9.5	3.2
Calculated value of the initial flux, Φ_0 (μ Wb)	237	371
Experimental value of the magnetic flux change, $\Delta\Phi_f$ (μ Wb)	-(223 ± 17)	-(345 ± 21)

It follows from Table 8.2 that the magnetic flux losses, $\Delta\Phi_f$, are almost equal to the initial value of the magnetic flux, Φ_0 . The spread in the experimental values of the magnetic flux losses does not exceed the industry tolerance for the principal magnetic parameters of the Nd₂Fe₁₄B samples tested. These results are direct evidence of the almost complete demagnetisation of the Nd₂Fe₁₄B ferromagnets by a transverse shock wave.

The lengthened trailing edge of all the $E_g(t)$ waveforms is interpreted to be the result of a slow damping of the vortex currents caused by the ferromagnetic-to-paramagnetic phase transition in the shock compressed Nd₂Fe₁₄B [37, 38].

8.5 Generation of High Currents by Miniature Transverse FMGs

The overall dimensions of transverse FMGs [16–18] are approximately equal to that of its Nd₂Fe₁₄B ferromagnetic elements. This essentially distinguishes this type of generator from all the other known explosive driven generators [41] in which a considerable part of the generator volume is reserved for a high-explosive charge holder, the generator body and paths for free movement of conductors inside the generators. One possible application of high current FMGs is as seed sources for magnetic flux compression generators (FCGs). Comprehensive studies of the generation of high currents by miniature transverse FMGs were performed by Shkuratov *et al.* [17, 19, 21–23]. The results of these studies are described in this section.

8.5.1 The Physical Principle of Seed Current Generation

The basic cause of current generation by the FMG [17, 22] is the EMF, $E_g(t)$, induced in the pulse generating coil by the decreasing initial magnetic flux of the Nd₂Fe₁₄B ferromagnet in accordance with Faraday's law (Eq. (8.5)). This EMF pulse induces a current in the FMG's output circuit, which in Fig. 8.12 is the FMG-FCG circuit. The electrical circuit of an FMG-FCG circuit consists of an FMG pulse current generating system with an absolute impedance of Z_G and the load with an absolute impedance of Z_L . In this FMG-FCG system, both the generating unit and the load are inductive coils. Thus, the equivalent circuit diagram of the entire system includes the inductance, L_G , and resistance, R_G , of the pulse generating unit and the inductance, L_L , and resistance, R_L , of the load connected in series.

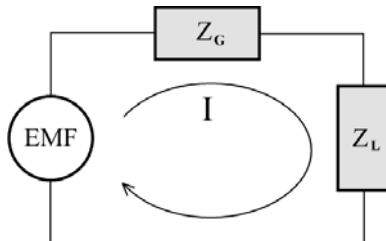


Fig. 8.12 Electrical circuit diagram of a transverse FMG (absolute impedance Z_G) with an FCG seed coil (absolute impedance Z_L) serving as the load.

One possible design of the seed stage for a FMG-FCG pulsed power system consists of two coaxial single-turn low resistance and low inductance coils connected by a strip transmission line. One of the coaxial turns serves as the pulse generating coil of the FMG, while the other is the seed coil of the FCG.

A cut-away view of the high current FMG described in Refs. 17, 19–23 is shown in Fig. 8.13. It contains a hollow Nd₂Fe₁₄B ferromagnetic cylinder, high explosive charge and single-turn coaxial pulse generating coil wound on the ferromagnetic cylinder. The central hole in the Nd₂Fe₁₄B is where the HE charge is loaded. The diameter of the hole for all the Nd₂Fe₁₄B elements studied was 7.6 mm. It was determined by the diameter of the RISI EBW RP-501 detonators that were used. The initiation scheme used

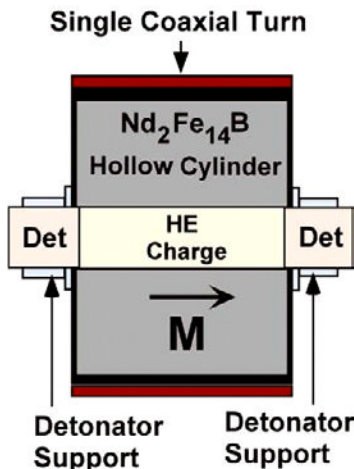


Fig. 8.13 Diagram of a miniature high current transverse FMG [17, 22].

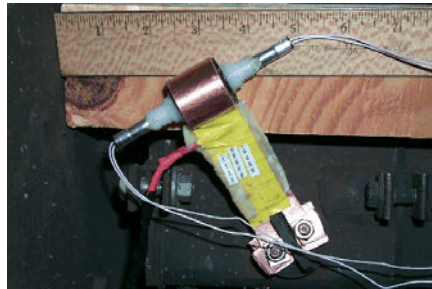


Fig. 8.14 High current transverse FMG just prior to explosive and electrical operation [17].

to fire the two detonators butt-joined to the end faces of the hollow magnet is discussed in Ref. 17.

A photograph of a high current transverse FMG just prior to explosive and electrical operation is shown in Fig. 8.14. Details of the experimental setup and measuring system used to investigate these FMG-FCG systems can be found in Refs. 17, 22 and 23.

8.5.2 Magnetic Flux Changes in Transverse FMGs

The change in the magnetic flux of the ferromagnetic elements is due to ferromagnetic-to-paramagnetic phase transitions that occur in the Nd₂Fe₁₄B because of transverse shock wave compression [16–18]. In accordance with Faraday's law, the change in the magnetic flux, $d\Phi(t)$, during time dt induces an electromotive force $E_g(t)$ in the coil wound on the ferromagnet.

As it was done in Ref. 16, single-turn diagnostic coils were wound on a Nd₂Fe₁₄B hollow cylinder and were placed at different positions along the cylinder's axis. It was found that the EMF, $E_g(z, t)$, generated at different positions had different amplitudes and pulse shapes. Since the miniature FMGs had a single coaxial turn with width h that was equal to the height of the Nd₂Fe₁₄B hollow cylinder h_0 , the average $E_g(t)$ measured in the experiments was the integral of the EMF, $E_g(z, t)$, normalised to the width of the coil

$$E_g(t) = \frac{\int_0^{h_0} E_g(z, t) dz}{h_0}, \quad (8.13)$$

where z is a position along the axis of the hollow ferromagnetic cylinder and $E_g(z, t)$ is the EMF generated in a single-turn coil with width dz and placed at position z . The inner diameter of the coil was 3.2 mm larger than the diameter of the Nd₂Fe₁₄B cylinder on which it was wound. The integral of the magnetic flux normalised to the width h_0 of the coaxial single-turn coil is:

$$\Phi_{0in} = \frac{\int_0^{h_0} \Phi_0(z) dz}{h_0}, \quad (8.14)$$

where $\Phi_0(z)$ is the magnetic flux in the cross-sectional area of the coil.

Faraday's law can now be rewritten as follows

$$E_g(t) = \frac{\int_0^{h_0} E_g(z, t) dz}{h_0} = -\frac{d(\int_0^{h_0} \Phi_0(z) dz / h_0)}{dt}. \quad (8.15)$$

Integration of the EMF waveform from 0 to $+\infty$

$$\Delta\Phi(t) = - \int_0^{+\infty} E_g(t) dt \quad (8.16)$$

yields the experimental value of the change in the normalised magnetic flux in a coaxial single-turn coil.

A series of experiments were performed to obtain the $E_g(t)$ waveforms that were needed to measure the final decrease in the normalised magnetic flux, $\Delta\Phi_f$ (Eq. (8.16)). The FMG was loaded with a miniature Agilent 1160A passive probe of input impedance 10 MΩ. The results of these experiments are presented in Table 8.3. The experimentally recorded $E_g(t)$ waveforms were used to numerically simulate the operation of FMGs. The technique used in these simulations is described in Refs. 22 and 23. This technique makes it possible to simulate the waveforms of the output currents, $I(t)$ and output voltages, $U(t)$, produced by transverse FMGs.

A typical $E_g(t)$ waveform produced by an FMG containing Nd₂Fe₁₄B elements with O.D. = 22.2 mm and h_0 = 25.4 mm (volume V_0 = 8.66 cm³ and mass m = 64.1 ± 1.0 g) and the corresponding magnetic flux losses are shown in Fig. 8.15. The peak value of the induced $E_g(t)$ was 48.8 V and its FWHM was 1.32 μs. The waveform has an extended tail of more than 15 μs.

The computed value of the initial normalised magnetic flux (Eq. (8.14)) for this FMG is

$$\Phi_{0in} = \frac{\int_0^{h_0} \Phi_0(z) dz}{h_0} = 259 \mu \text{ Wb.}$$

Table 8.3 Dimensions, mass, initial magnetic flux and basic output parameters of transverse two FMGs.

Parameter	FMG 1	FMG 2
Element dimensions and mass	O.D. = 2.2 cm, $h_0 = 2.54$ cm, $V_0 = 8.66 \text{ cm}^3$, $m = 64.1$ g	O.D. = 2.54 cm, $h_0 = 1.9$ cm, $V_0 = 8.75 \text{ cm}^3$, $m = 64.8$ g
Mass of C-4	1.2	1.0
Computed initial magnetic flux, Φ_{0in} (μ Wb)	259	331
Measured decrease in $\Delta\Phi_f$ (μ Wb)	234	312
Measured $E_g(t)$ (V)	48.8	71.7
FWHM of $E_g(t)$ (μ s)	1.32	1.80
Calculated seed current $I(t)_{\max}$ (A) and rise time $\tau(\mu\text{s})$ in load with $Z(100 \text{ kHz}) = 41 \text{ m}\Omega$	1700, 13.5	1940, 9.0
Measured seed $I(t)_{\max}$ (A) rise time $\tau(\mu\text{s})$ and FWHM (μ s)	1690, 14.3, 51	1930, 10.5, 100
$I(t)$ in load, $Z = 41 \text{ m}\Omega$		
Calculated $U(t)_{\max}$ (V) and FWHM (μ s) in load with $Z(100 \text{ kHz}) = 41 \text{ m}\Omega$	35.0, 1.8	43.5, 1.8
Measured $U(t)_{\max}$ (V) and FWHM (μ s) in load with $Z = 41 \text{ m}\Omega$	35.8, 2.3	42.5, 2.2
Total charge $Q(\infty)$ (C)	0.08	0.16
Calculated seed current $I(t)_{\max}$ (A), rise time $\tau(\mu\text{s})$, in $Z = 18 \text{ m}\Omega$	2800, 11.6	3000, 9.1
Measured seed current $I(t)_{\max}$ (A), rise time $\tau(\mu\text{s})$, and FWHM (μ s) in $Z = 18 \text{ m}\Omega$	2780, 12.1, 51	3000, 11.7, 59
Calculated $U(t)_{\max}$ (V), FWHM (μ s) in load $Z = 20 \text{ m}\Omega$	30.0, 1.8	27.0, 1.8
Measured voltage $U(t)_{\max}$ (V) and FWHM (μ s) in load $Z = 20 \text{ m}\Omega$	30.1, 1.7	27.1, 1.9
Total charge $Q(\infty)$ (C)	0.12	0.15

Its experimentally measured magnetic flux loss is

$$\Delta\Phi_f = - \int_0^{+\infty} E_g(t) dt = 234 \pm 17 \mu \text{ Wb.}$$

Table 8.3 summarises results obtained for all the types of Nd₂Fe₁₄B investigated. It follows from Table 8.3 and the data presented in Fig. 8.15 that the initial value of the magnetic flux Φ_{0in} that existed in the pulse

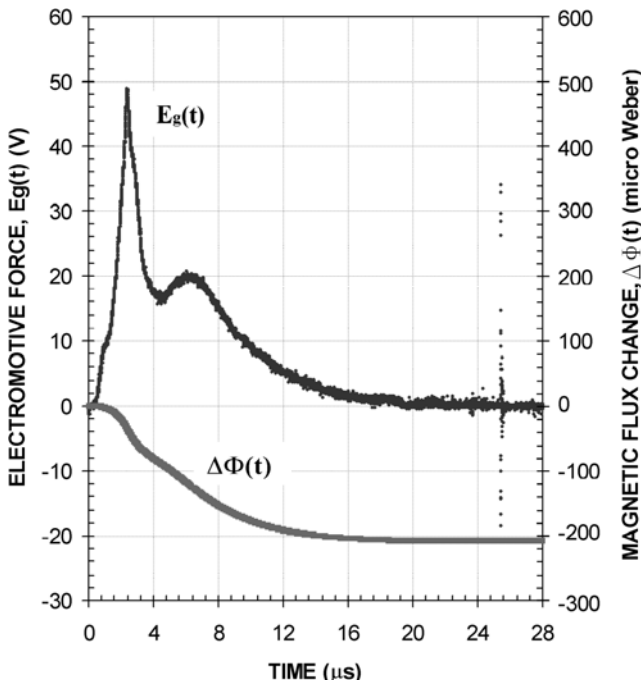


Fig. 8.15 Typical waveform of the electromotive force, $E_g(t)$, generated by a coaxial single-turn coil wound on a Nd₂Fe₁₄B hollow cylinder with O.D. = 22.2 mm and h_0 = 25.4 mm and its corresponding magnetic flux loss, $\Delta\Phi(t)$ [22].

generating coil before shock wave action is practically equal to the experimentally measured magnetic flux lost, $\Delta\Phi_f$, due to the shock wave action. Based on these results, it can be concluded that the integral of the magnetic flux normalised to the width of the pulse generating coil, Φ_{0in} and that the integral of the electromotive force waveform normalised to the width of the coil, $E_g(t)$, are in good agreement.

8.5.3 Currents Produced by Transverse FMGs

Seed current experiments were conducted with two types of coaxial single-turn seed coils having different electrical parameters. These coils were made so that their electrical parameters represented those of a typical coaxial single-turn seed coil of a miniature FCG [41]. The first coil had an impedance with an absolute value of $Z_L(100 \text{ kHz}) = 41 \text{ m}\Omega$. The second coil had an impedance of $Z_L(100 \text{ kHz}) = 18 \text{ m}\Omega$.

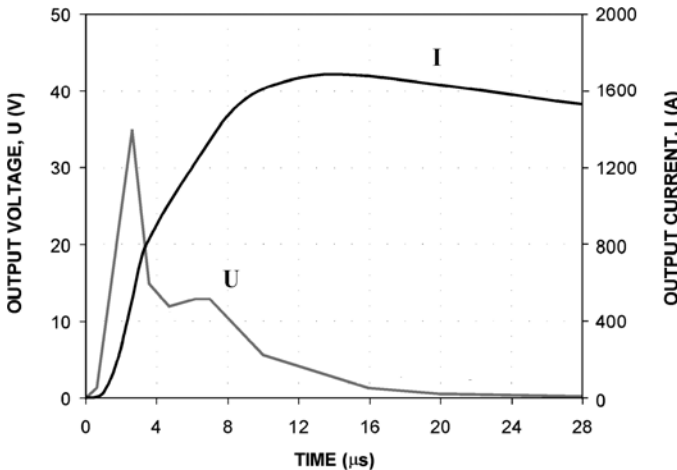


Fig. 8.16 Results of the numerical simulation of the seed current $I(t)$ and the output voltage $U(t)$ produced by a high current FMG containing a Nd₂Fe₁₄B cylinder with O.D. = 22.2 mm and height h_0 = 25.4 mm. The load was a FCG seed coil with an impedance of Z_L (100 kHz) = 41 mΩ [22].

Figure 8.16 presents the results of the numerical simulation of the waveforms of the seed current $I(t)$ and the output voltage $U(t)$ for the first 28 μ s after initiation of the shock wave. The FCG seed coil had an impedance of $Z_L(100 \text{ kHz}) = 41 \text{ m}\Omega$. The calculated peak amplitude of the seed current was $I(t)_{\max} = 1700 \text{ A}$. The risetime, τ , which is defined to be the time it takes the current to rise from 0 to $I(t)_{\max}$, was 13.5 μ s. The calculated peak amplitude of the output voltage pulse was $U(t)_{\max} = 35 \text{ V}$ and its calculated was FWHM 1.8 μ s.

The experimental waveforms of the seed current $I(t)$ and the output voltage $U(t)$ are presented in Fig. 8.17. Comparing Figs. 8.16 and 8.17, it can be concluded that there is good agreement between the experimental and numerically simulated waveforms. The measured peak output voltage was $U(t)_{\max} = 35.8 \text{ V}$. The measured peak value and rise time of the seed current were $I(t)_{\max} = 1700 \text{ A}$ and 14.3 μ s, respectively. The FWHM of the recorded waveform of the output voltage $U(t)$ was 2.32 μ s.

The recorded $I(t)$ waveform is a quasi-rectangular pulse with FWHM 51 μ s (Fig. 8.8). Figure 8.18 also shows the evolution of the charge that passed through the circuit:

$$Q(t) = \int_0^t I(t) dt. \quad (8.17)$$

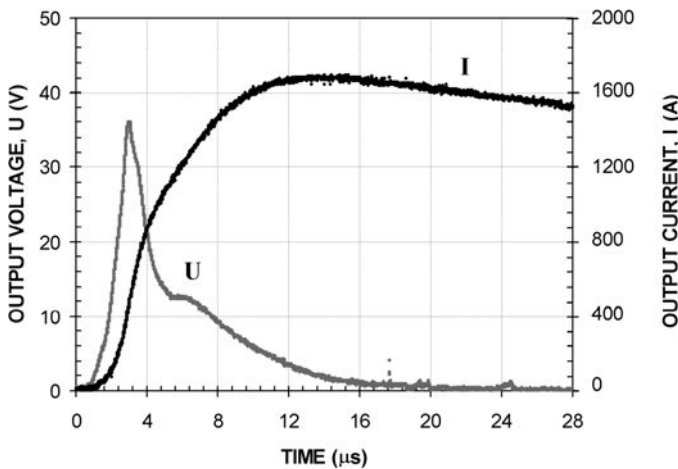


Fig. 8.17 Experimental waveforms of the output current, $I(t)$, (blue) and output voltage, $U(t)$, (red) produced by a high current FMG and recorded over the same period of time as in Fig. 8.16. The load was an FCG seed coil with an impedance of Z_L (100 kHz) = 41 mΩ [22].

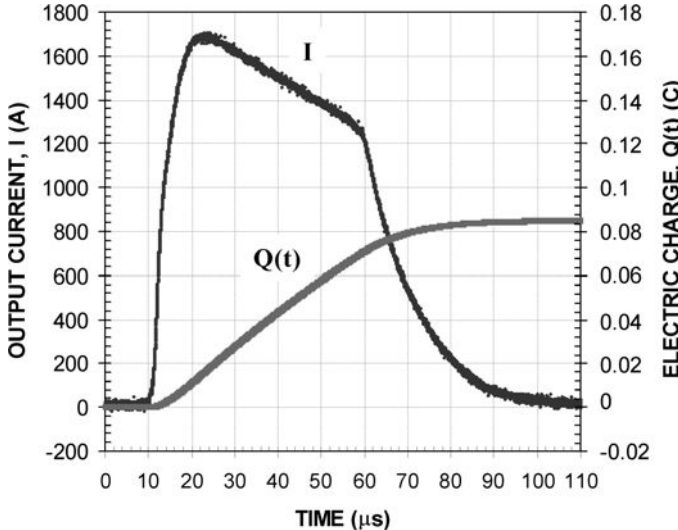


Fig. 8.18 Experimental waveforms of the output current, $I(t)$, and electric charge evolution, $Q(t)$, produced by a high current FMG containing a Nd₂Fe₁₄B cylinder with an O.D. = 22.2 mm and height of h_0 = 25.4 mm. The load was an FCG seed coil with an impedance of Z_L (100 kHz) = 41 mΩ [22].

The total charge that passed through the circuit during the experiment was three orders of magnitude greater than the integrated charge transferred by a piezoelectric, as opposed to a ferroelectric, current source.

Reducing the impedance of the FCG seed coil to $Z_L(100\text{ kHz}) = 18\text{ m}\Omega$ led to an increase in the amplitude of the seed current by a factor of 1.64 (Table 8.3). The experimental value of $I(t)$ reached a maximum value of 2780 A. The amplitude of the calculated seed current pulse was 2800 A. The rise time of the seed current was $12.1\text{ }\mu\text{s}$ and the calculated value was $11.6\text{ }\mu\text{s}$. The recorded amplitude of the output voltage pulse was $U(t)_{\max} = 30.1\text{ V}$ with a FWHM of $1.68\text{ }\mu\text{s}$ and the calculated value was 30.0 V with a FWHM of $1.8\text{ }\mu\text{s}$.

Comparing the experimentally recorded and numerically calculated $I(t)$ and $U(t)$ waveforms (Table 8.3) shows good agreement between the actual and numerically calculated signals. It can be concluded that the methodology, described in Refs. 22 and 23, used to simulate the seed processes in a combined FMG-FCG system provides correct predictions of the FMG seed current amplitude, $I(t)_{\max}$, output voltage, $U(t)_{\max}$ and rise time.

Based on these results, it can be concluded that a twofold decrease in the seed coil dynamic impedance leads to a more than 50% increase in the seed current amplitude and charge transferred, but does not change the current rise time.

Based on these results, it can also be concluded that the volume and weight of the ferromagnetic element are its most important parameters. Ferromagnetic elements with O.D. = 22.2 mm and height $h_0 = 25.4\text{ mm}$ and with O.D. = 25.4 mm and height $h_0 = 19.0\text{ mm}$ have approximately equal volumes and masses — i.e. to an accuracy of 1.5%. However, the amplitude of the seed current generated by an FMG with an Nd₂Fe₁₄B element having an O.D. = 25.4 mm and height of $h_0 = 19.0\text{ mm}$ is about 10% higher than the current produced by an FMG having an Nd₂Fe₁₄B element with an O.D. = 22.2 mm and height of $h_0 = 25.4\text{ mm}$ with the same FCG seed coils. Apparently, Nd₂Fe₁₄B ferromagnets, having a given volume and mass, must have optimal geometrical proportions that deliver the highest seed current amplitudes to certain loads.

In summary, it was experimentally demonstrated that FMGs with a total volume less than 9 cm^3 are capable of delivering current amplitudes of 3 kA with FWHM of $60\text{ }\mu\text{s}$ to single-turn coaxial FCG seed coils. The numerical simulation techniques described in Refs. 22 and 23 used to simulate the seeding process in FMG-FCG systems correctly predicted the waveforms of the output current and voltage produced by the FMG seed source. It follows

from both experimental and simulation results that the amplitude of the FMG output current is directly proportional to the amplitude of the EMF produced by the FMG and to the impedance of the load.

8.6 FMG Analytical Techniques

A numerical simulation technique was developed by Shkuratov *et al.* [22, 23] to model the operation of FMGs. This technique correctly predicts the output current and voltage waveforms produced by FMGs (see Secs. 8.5 and 8.7). Talantsev *et al.* [42, 43] also developed a theoretical model for FMGs and analytical techniques for calculating the amplitudes of the current pulses produced by FMGs. This theoretical model and analytical technique are described in this section.

8.6.1 Analytical Equations

The initial electromagnetic energy stored in an FMG, W_{FMG} , is equal to the initial magnetostatic energy stored in its ferromagnetic element, W_{NdFeB} :

$$W_{\text{FMG}} = W_{\text{NdFeB}}. \quad (8.18)$$

Assuming that the ohmic losses in the FMG-load circuit are negligible, the energy, W_{current} , in the circuit during FMG operation is:

$$W_{\text{current}} = \frac{L_{\text{total}} \cdot I_{\text{max}}^2}{2}, \quad (8.19)$$

where I_{max} is the peak amplitude of the current pulse. The total inductance of the system, L_{total} , is the sum of the inductances of the FMG and the load:

$$L_{\text{total}} = L_{\text{FMG}} + L_{\text{Load}}. \quad (8.20)$$

Taking into account that the FMG has an efficiency coefficient of η_{FMG} , the equation for the initial energy in the FMG-load system is:

$$W_{\text{current}} = \eta_{\text{FMG}} W_{\text{NdFeB}} = \frac{(L_{\text{FMG}} + L_{\text{Load}}) \cdot I_{\text{max}}^2}{2}. \quad (8.21)$$

Equation (8.22) gives the amplitude of the current:

$$I_{\text{max}}(t) = \eta_{\text{current FMG}} \cdot \left[\frac{2W_{\text{NdFeB}}}{(L_{\text{FMG}} + L_{\text{Load}})} \right]^{1/2}, \quad (8.22)$$

where $\eta_{\text{current FMG}} = (\eta_{\text{FMG}})^{1/2}$ is the coefficient of FMG efficiency for the conversion of W_{NdFeB} into a current pulse. The energy W_{NdFeB} can be estimated by using:

$$W_{\text{NdFeB}} = \frac{V \cdot (B \cdot H)_{\max}}{2}, \quad (8.23)$$

where V is the volume of the $\text{Nd}_2\text{Fe}_{14}\text{B}$ element and $(B \cdot H)_{\max}$ is the maximum energy product of the ferromagnetic material. Hence, from Eqs. (8.22) and (8.23), an expression for $\eta_{\text{current FMG}}$ can be found:

$$\eta_{\text{current FMG}} = \frac{I_{\max}(t)}{[(V \cdot (B \cdot H)_{\max}) / (L_{\text{FMG}} + L_{\text{Load}})]^{1/2}}. \quad (8.24)$$

Equations (8.22) and (8.24) were obtained as a direct result of the application of the law of conservation of energy to the FMG-load system. Moreover, no assumptions were made about the physical mechanism by which the ferromagnet undergoes shock wave demagnetisation. Thus, Eqs. (8.22) and (8.24) can be used to analyse both longitudinal [13–15] and transverse [16–23] FMGs.

Another approach used to analyse FMGs [42, 43] is based on the law of conservation of magnetic flux. The initial magnetic flux in the FMG-load system, $\Phi_{\text{FMG-Load}}$, is the magnetic flux that is coupled to the FMG pulse generating coil wound on the $\text{Nd}_2\text{Fe}_{14}\text{B}$ ferromagnet [13–23]:

$$\Phi_{\text{FMG-Load}} = \sum_{n=1}^N \Phi_n, \quad (8.25)$$

where Φ_n is the magnetic flux coupled to the n th turn and N is the number of turns in the FMG coil. The value of Φ_n depends on the parameters and the shape of the ferromagnet and on the disposition of the n th turn on the ferromagnet [13, 16, 18]. The methodology used to calculate the magnetic flux coupled to the FMG pulse generating coils is described in Refs. 22 and 23.

The magnetic flux stored in the ferromagnet is transformed into the magnetic flux of the current, $\Phi_{\text{current}}(t)$, flowing through the FMG-load circuit:

$$\Phi_{\text{FMG-Load}} = \sum_{n=1}^N \Phi_n = \Phi_{\text{current}}(t)_{\max} = (L_{\text{FMG}} + L_{\text{Load}})I_{\max}(t). \quad (8.26)$$

It follows from the law of conservation of magnetic flux that $\Phi_{\text{FMG-Load}}$ must be conserved in the FMG-load system, since it was assumed that losses are negligible.

Thus, a system of two independent equations was obtained [42, 43] for $I_{\max}(t)$. The first equation is Eq. (8.22). The second equation can be obtained from Eq. (8.26):

$$I_{\max}(t) = \frac{\sum_{n=1}^N \Phi_n}{L_{\text{FMG}} + L_{\text{Load}}}. \quad (8.27)$$

This system of equations (Eqs. (8.22) and (8.27)) can be solved by performing successive iterative calculations. Assuming that $L_{\text{FMG}} = 0$, Eq. (8.22) can be used to calculate the first approximation for the current, $I_{\max}^{\text{1st approx}}$. Substituting $I_{\max}^{\text{1st approx}}$ into Eq. (8.27) yields the first approximation for the initial value of the magnetic flux in the system, $\Phi_{\text{FMG-load}} = \sum \Phi_n^{\text{1st approx}}$. A detailed description of the technique used to calculate the magnetic flux coupled by an FMG coil can be found in Ref. 22. The design of the FMG — i.e. the number of turns, N and the disposition of the turns, can also be calculated to the first approximation. This FMG design has an exact inductance value, $L_{\max}^{\text{1st approx}}$. If one makes the assumption that $L_{\text{FMG}} = L_{\max}^{\text{1st approx}}$, Eq. (8.22) will yield the second approximate value for the current, $I_{\max}^{\text{2nd approx}}$. It is obvious that $I_{\max}^{\text{2nd approx}} < I_{\max}^{\text{1st approx}}$. Substituting $I_{\max}^{\text{2nd approx}}$ into Eq. (8.27) yields the second approximation for the initial magnetic flux in the FMG-load system. And so on. In practice, four iterations are enough to get $I_{\max}^{\text{5th approx}} \approx I_{\max}^{\text{4th approx}}$. The matrix $\Phi_n \{\Phi_1, \Phi_2, \dots, \Phi_n\}$ is used to find the number of turns, N , that should be wound in the FMG coil, as well as their disposition on the ferromagnet, for a given value of $\Phi_{\text{FMG-load}}$.

8.6.2 Current Generated by Longitudinal FMGs

An analysis [42, 43] of the operation of longitudinal FMGs described in Refs. 13–15 was performed. The longitudinal FMGs used in this analysis contained Nd₂Fe₁₄B elements (O.D. 2.22 cm and length 2.54 cm) with a volume of 9.8 cm³. The energy product ($B \cdot H$)_{max} of the Nd₂Fe₁₄B ferromagnets (Grade 35) used was 0.279 J/cm³.

The electrical parameters of the longitudinal FMG-load system described in Refs. 13–15 and its output currents are presented in Table 8.4. Substituting the parameters of these systems into Eq. (8.24), the average efficiency coefficient for current transformation, $\eta_{\text{current LFMG}}$, was calculated to be:

$$\eta_{\text{current LFMG}} = 0.314 \pm 0.025, \quad (8.28)$$

Table 8.4 Experimental results and the calculated efficiency using Eq. (8.24) for longitudinal FMGs [13–15].

LFMG pulse-generating coil	Volume of NdFeB V (cm ³)	Total System inductance L _{total} (μH)	Current I _{max} (A)	η _{current LFMG}
4 Turns	9.80	0.490	735	0.311
8 Turns	9.80	0.790	602	0.317

where the actual current produced by the FMG was 0.31 A and the maximum current was calculated to be 1.0 A. The average efficiency coefficient for energy conversion, η_{current LFMG}, found from the analysis of the experimental data reported on in Refs. 13–15 is:

$$\eta_{\text{current LFMG}} = 0.099 \pm 0.06, \quad (8.29)$$

where the actual energy delivered by the FMG was 0.1 J/cm³ and the energy stored in the magnet was calculated to be 1.0 J/cm³. Thus, practically 10% of the energy stored in the longitudinal FMG was transferred to the load.

8.6.3 Current Generated by Transverse FMGs

An analysis [42, 43] of the operation of transverse FMGs described in Refs. 16–18, 22, 23, 44 and 45 was performed. The electrical parameters of the transverse FMG-load system and its output currents are presented in Table 8.5. Substituting the parameters of these systems into Eq. (8.24), the average efficiency coefficient for current transformation, η_{current TFMG}, was calculated to be:

$$\eta_{\text{current TFMG}} = 0.392 \pm 0.015, \quad (8.30)$$

Table 8.5 Experimental results and calculated current efficiency of transverse FMGs Refs. 16–18, 22, 23, 44 and 45.

TFMG pulsed generating coil	Volume of NdFeB V (cm ³)	Total system Inductance L _{total} (μH)	Current I _{max} (A)	η _{current TFMG}
8.5 Turns	8.76	1.14	574	0.392
Single Coaxial Turn	8.76	0.097	1920	0.383
Single Coaxial Turn	25.1	0.108	3030	0.393
Single Coaxial Turn	25.1	0.064	4190	0.400

where the actual current produced by the FMG was 0.39 A and the maximum current was calculated to be 1.0 A. The average efficiency coefficient for energy conversion, $\eta_{\text{current TFMG}}$, for transverse FMGs found from analysis of the experimental data in Refs. 16–18, 22, 23, 44 and 45 is:

$$\eta_{\text{current TFMG}} = 0.154 \pm 0.043, \quad (8.31)$$

where the actual energy delivered by the FMG was 0.15 J/cm³ and the energy stored in the magnet was calculated to be 1.0 J/cm³. Thus, practically 15% of the energy stored in the transverse FMG was transferred to the load.

It follows from Table 8.5 that the $\eta_{\text{current TFMG}}$ coefficient ranges from 0.383 to 0.400, so it is essentially constant for the transverse FMGs described in Refs. 16–18, 22, 23, 44 and 45.

The technique described in Refs. 42 and 43 for calculating the amplitude of the current pulses produced by FMGs was verified through the analysis of experimental data presented in Refs. 13–18, 22, 23, 44 and 45. The amplitude of output current pulses that were calculated by this technique are in good agreement with those obtained experimentally. Based on these results, it can be concluded that the technique described in Refs. 42 and 43 provides highly accurate values for the amplitude of the output current produced by high current FMGs.

8.6.4 Summary

An analytical model for the FMG was described in Refs. 42 and 43. This model is an attempt to describe the fundamental idea of Shkuratov *et al.* [12–18] that the main parameter that determines the output power produced by FMGs is the magnetostatic energy stored in its ferromagnetic elements; in other words, its remnant magnetisation and coercive force, $(B \bullet H)_{\max}$. A previous model of the FMG [1] was based on the idea that the main factor that determines the output current of the FMG was the high initial magnetic flux stored in its ferromagnetic element. In accordance with [12–18, 42, 43], soft ferromagnets, possessing high initial flux, Φ , due to a high value for B_r , cannot be considered to be an effective ferromagnetic element for use in FMGs due to their low initial magnetostatic energy — i.e. low $(B \bullet H)_{\max}$.

The technique presented in Refs. 42 and 43 for calculating the amplitude of the current pulse produced by FMGs is in good agreement with experimentally obtained data. It was found that the energy efficiency of

FMGs is 10% for devices based on longitudinal shock wave demagnetisation and 15% for devices based on transverse shock wave demagnetisation of Nd₂Fe₁₄B ferromagnets.

The difference in the energy efficiency for the two types of FMGs is probably related to differences in their shock demagnetisation kinetics, because the characteristic time for longitudinal shock demagnetisation is longer than it is for transverse shock demagnetisation [40].

8.7 Charging Capacitors with High Voltage Transverse FMGs

Capacitive energy stores, such as the Arkadiev-Marx generator, are widely used in modern pulsed power systems [46]. However, certain special applications require that the pulsed power system be autonomous and that it be compact. In an attempt to make Arkadiev-Marx generators autonomous and compact, electrochemical cells have been used to charge them [47]. However, these cells are not small and require a high voltage converter to produce the high voltage required to charge capacitor banks.

In order to meet these requirements for a compact autonomous pulsed power, Shkuratov *et al.* [24, 25] proposed and experimentally verified that a transverse FMG can charge a capacitor bank. The results of these investigations are described in this section.

8.7.1 High Voltage Transverse FMG Design

One of the problems associated with the operation of explosive driven electrical generators is the destructive action of the explosive charge on the pulse generating system of the device and its related electronic circuit [13, 16–18]. Another problem is the operating time of the first transverse FMGs investigated in Refs. 16–18 did not exceed 12 μ s. The main objectives of the work reported on in Refs. 24 and 25 were to design miniature high voltage transverse FMGs to charge capacitor banks to produce pulsed power systems that operate reliably, decrease the effect of the explosive charge on the system, improve its high voltage insulation and extend its operating time to 50 μ s.

A schematic diagram and photograph of the miniature high voltage transverse FMGs described in Refs. 24 and 25 is shown in Fig. 8.19. A pulse generating coil holder was introduced into the system to protect the pulse

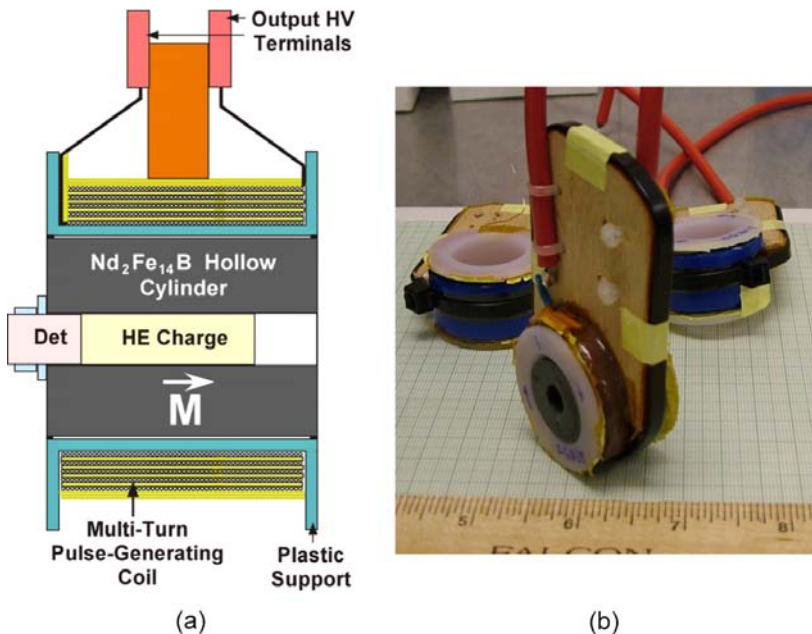


Fig. 8.19 (a) Schematic diagram and (b) photograph of a high voltage transverse FMG [24, 25].

generating coil of the FMG from the mechanical action of the explosive charge for a few tens of microseconds. In addition, the holder provides electrical insulation between the pulse generating coil and the magnet, which are connected to ground via the detonator wires. A 0.75 mm air gap was also introduced between the ferromagnetic element and the insulator (Fig. 8.19) to reduce shock wave propagation into the plastic insulator. All the generators investigated in Refs. 24 and 25 contained Nd₂Fe₁₄B (grade 35) elements with O.D. = 22.2 mm, I.D. = 9.0 mm and length h = 25.4 mm.

8.7.2 Results and Discussion

The basis for the production of high voltage at the output terminals of the transverse FMG is Faraday's law. For a multi-turn coil, the EMF pulse generated is the sum of the voltages produced by each of the turns

$$E_{m\text{-turn}}(t) = \sum_N -\frac{d\Phi_n(t)}{dt}, \quad (8.32)$$

where dt is the time it takes the magnetic flux to change in a given turn, $d\Phi_n(t)$ is the magnetic flux captured by the n th turn of the multi-turn coil and N is the number of turns in the coil.

A typical output voltage waveform produced by a high voltage transverse FMG is shown in Fig. 8.20. The generator contained a 231-turn coil (AWG 28 magnet wire with a diameter of 0.35 mm) with an inner diameter of 27 mm and an outer diameter of 33 mm. The serial resistance and serial inductance of the FMG at 100 kHz were R_S (100 kHz) = 19.4 Ω and L_S (100 kHz) = 1.82 mH, respectively. The generator used 0.6 g of C-4 high explosives, which was initiated by a single RISI RP-501 detonator.

The peak amplitude of the output voltage pulse was $E_{m\text{-turn}}$ ($7.8 \mu\text{s}$)_{max} = 7.45 kV, its FWHM was 5.8 μs and its rise time was τ = 2.6 μs. There were no breaks or distortions in the voltage pulse waveform (Fig. 8.20). After the main pulse, there is a long tail with an amplitude of about 300 V. This means that the pulse generating coil of the transverse FMG is not destroyed for more than 40 μs after the explosives is initiated.

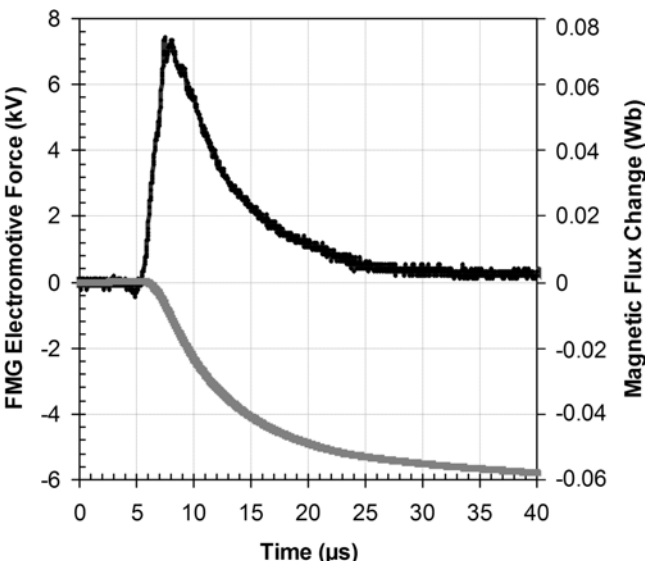


Fig. 8.20 A typical waveform of the output pulse produced by a high voltage transverse FMG with a 231-turn pulse generating coil and the corresponding time history of the magnetic flux change in the generator. The FMG contained a Nd₂Fe₁₄B cylinder with O.D. = 22.2 mm and h = 2.54 mm [25].

The specific peak voltage of the transverse FMG (Fig. 8.20) was $E_{m\text{-turn}}(7.8\ \mu\text{s})_{\max\ spec} = 32.2\ \text{V/turn}$. The specific peak voltage averaged over seven experiments was $E_{m\text{-turn}}(t)_{\max\ spec} = 31.1 \pm 1.4\ \text{V/turn}$.

Figure 8.20 also shows the time history of the magnetic flux change, $\Delta\Phi(t)$, which was obtained by integrating the experimental waveform of the output voltage pulse. The final magnetic flux change in this experiment was $\Delta\Phi(\infty) = \Delta\Phi_{\text{fin}} = 58\ \text{mWb}$ and the specific magnetic flux change was $\Delta\Phi_{\text{fin}\ spec} = 251\ \mu\text{Wb/turn}$. The value of the specific magnetic flux change averaged over seven experiments was $\Delta\Phi_{\text{fin}\ spec} = 231 \pm 20\ \mu\text{Wb/turn}$.

The value of the initial magnetic flux, Φ_0 , in the cross-sectional area of the pulse generating coil, calculated by using the methodology described in Refs. 22 and 23, is $\Phi_0 = 269\ \mu\text{Wb}$. Comparing the experimentally obtained specific magnetic flux change, $\Delta\Phi_{\text{fin}\ spec}$, to the initial value of the magnetic flux, Φ_0 , it can be concluded that more than 85% of the initial magnetic flux stored in the Nd₂Fe₁₄B ferromagnet was transformed into a high voltage pulse.

To further explore the design of high voltage transverse FMGs, several series of experiments [24, 25] with transverse FMGs containing different numbers of turns in the pulse generating coil were performed. Figure 8.21 shows the peak amplitude of the output voltage and the peak specific voltage versus the number of turns in the pulse generating coil. It follows from the experimental results [24, 25] that the peak amplitude of the output voltage is directly proportional to the number of turns. The transverse FMG containing a 727-turn pulse generating coil is capable of producing a pulse with an amplitude of 21.9 kV.

Very reproducible high amplitude voltage pulses generated by FMGs, along with their relatively long pulse durations, make it possible to consider the transverse FMG as a charging source for capacitor banks. To predict the amplitude and waveforms of the voltage pulse produced by a high voltage transverse FMG across a capacitor bank and the charging current waveform, a model to numerically simulate the operation of the transverse FMG-capacitor bank system was developed [24, 25].

Figure 8.22 shows an example of these simulation results. The plot is the calculated waveform of the voltage pulse produced across a capacitor bank with capacitance $C_L = 18\ \text{nF}$ by a transverse FMG containing a pulse generating coil with $N = 252$ turns. The amplitude of the calculated voltage pulse was 6.6 kV and its rise time was 16 μs . The calculated current amplitude ranges from 10 to 14 A.

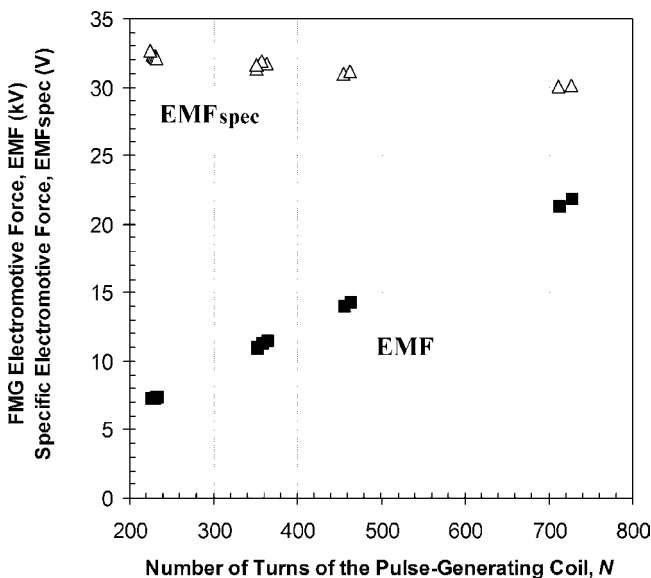


Fig. 8.21 Peak amplitude of the output voltage pulse and the specific voltage produced by transverse FMGs versus the number of turns in the pulse generating coil. The FMGs contained Nd₂Fe₁₄B ferromagnet cylinders with O.D. = 22.2 mm and h = 25.4 mm [24, 25].

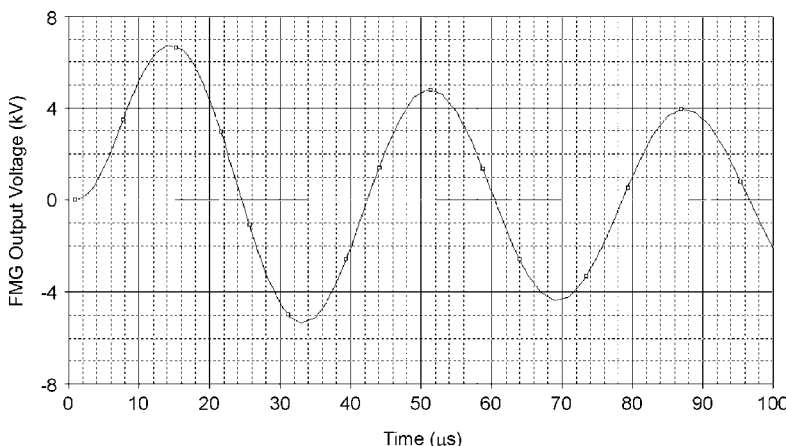


Fig. 8.22 Calculated waveform of the output voltage pulse produced by a transverse FMG across an 18 nF capacitor bank. The pulse generating coil of the transverse FMG contained 252 turns. The FMG contained a Nd₂Fe₁₄B cylinder with O.D. = 22.2 mm and h = 25.4 mm [25].

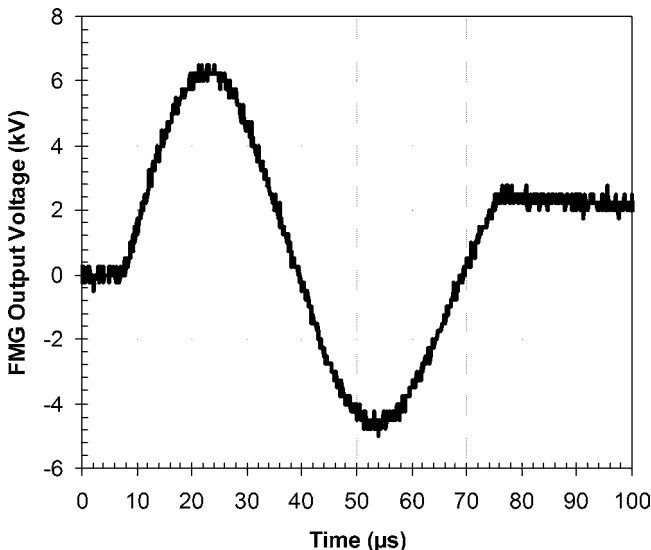


Fig. 8.23 Experimental waveform of the output voltage pulse produced by a transverse FMG across an 18 nF capacitor bank. The pulse generating coil of the transverse FMG contained 252 turns. The FMG contained a Nd₂Fe₁₄B cylinder with O.D. = 22.2 mm and h = 25.4 mm [25].

The experimentally measured high voltage pulse waveform produced by an FMG containing a 252-turn pulse generating coil across a 18 nF capacitor bank is shown in Fig. 8.23. The amplitude of the voltage pulse was $U(t)_{\max} = 6.5 \text{ kV}$ and its risetime was $\tau = 15.2 \mu\text{s}$. There is very good agreement between the results obtained by digital simulations (Fig. 8.22) and the experimental data (Fig. 8.23). The energy delivered to the capacitor bank was $W(t)_{\max} = 0.38 \text{ J}$ [$W(t)_{\max} = C_0 \bullet U(t)_{\max}^2 / 2$]. The corresponding current, $I(t)$, voltage, $U(t)$, and power, $P(t)$, waveforms obtained in this experiment are shown in Fig. 8.24. The output power, $P(t)$, was calculated by taking the product of the instantaneous value of the output voltage, $U(t)$ and the instantaneous value of the output current $I(t)$ — i.e. $P(t) = I(t) \bullet U(t)$. The peak power reached a value of $P(t)_{\max} = 43 \text{ kW}$.

From the voltage and current waveforms, the time at which the pulse generating system of the transverse FMG is destroyed can be determined, which in this case is about $75 \mu\text{s}$. Therefore, the operating time of the transverse FMG is five times longer than the time needed to charge the capacitor bank; which is $\tau = 15.2 \mu\text{s}$, as shown in Figs. 8.23 and 8.24.

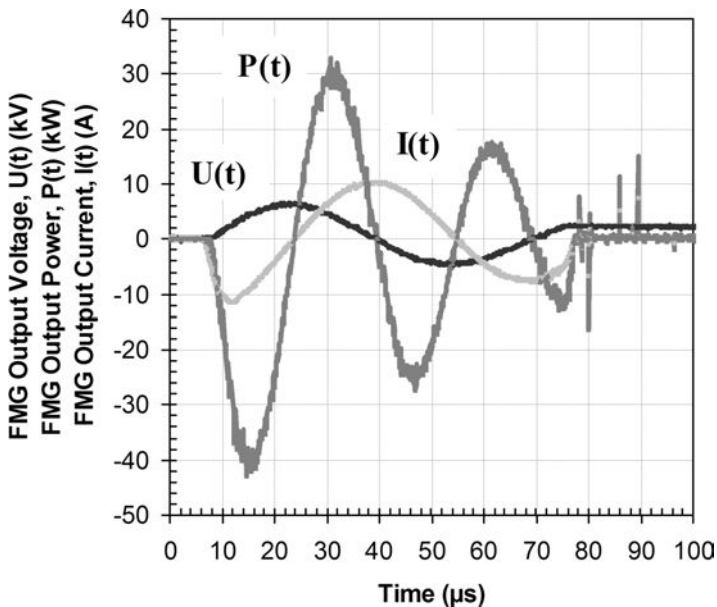


Fig. 8.24 Experimental waveforms of the output current, $I(t)$, voltage, $U(t)$ and power, $P(t)$, produced by a transverse FMG across an 18 nF capacitor bank. The pulse generating coil of the transverse FMG contained 252 turns. The FMG contained a Nd₂Fe₁₄B cylinder with O.D. = 22.2 mm and h = 25.4 mm [25].

8.7.3 Summary

In summary, it has been experimentally demonstrated [24, 25] that it is fundamentally possible to charge a capacitor bank to high voltage with an explosive driven transverse FMG. The significance of any prime power source can be evaluated through its ability to deliver power to a practical load or power conditioning system. Capacitive energy storage devices are the most widely used pulsed power systems and can therefore be considered to be the most important type of load devices for FMGs. It follows from the experimental results reported on in Refs. 24 and 25 that more than 30% of the magnetostatic energy stored in Nd₂Fe₁₄B ferromagnets can be transferred to capacitor banks by transverse FMGs. This demonstrates the real practicality of these explosive driven prime power sources. These results open a straightforward way to design and construct miniature autonomous single-stage and multi-stage systems based on transverse FMGs and capacitive energy stores.

8.8 Miniature High Voltage, Nanosecond FMG System

Another approach for constructing autonomous two-stage, high-voltage FMG-based systems was proposed and developed by Shkuratov *et al.* [26, 52]. The general idea of this system was to utilise an output transforming stage to amplify the output voltage of the FMG. This approach was implemented [26, 52] by combining a high voltage FMG with a spiral Vector Inversion Generator (VIG), which served as the power conditioning stage for the FMG. It was demonstrated, in principle, that it may be possible to amplify the amplitude of the output voltage pulse produced by an FMG by several times and that it may also be possible to compress the voltage pulse length from microseconds to nanoseconds. Details of this system are described in this section.

8.8.1 *Operating Principles*

A schematic diagram of the experimental setup used to investigate the operation of FMG-VIG systems is shown in Fig. 8.25. The FMG was placed inside a detonation tank. The output terminals of the FMG were passed through a port in the detonation tank wall and connected to the input of the VIG and the voltage monitoring system. The general design of the high voltage FMGs used in these experiments is shown in Fig. 8.19. The generator contains a Nd₂Fe₁₄B ferromagnetic element, with O.D. of 22.2 mm, I.D. of 8.0 mm and height of 25.4 mm, high explosive charge, plastic pulse generating coil holder with a multi-turn coil wound on it and high voltage output terminals. The volume of the Nd₂Fe₁₄B ferromagnetic element was 22.5 cm³.

The VIG is a pulse generator, which can store an electric charge at one voltage and discharge it as a pulse having a peak voltage higher than the stored voltage [48, 49]. A schematic diagram of the VIG is shown in Fig. 8.25. The VIG contains alternating layers of two sheets of conductive material and two sheets of electrically insulting material wound together on to a roll, thus forming an open-ended transmission line. If this rolled foil capacitor is charged to voltage U_0 and the spark gap switch is closed, an electromagnetic wave originates from the switch and travels along the VIG's rolled transmission line. As the wave travels, it converts the electrostatic field in the VIG into an electromagnetic field and when it retraces its path after reflection at the end of the transmission line, it converts the electromagnetic field back into an electrostatic field. An output pulse of

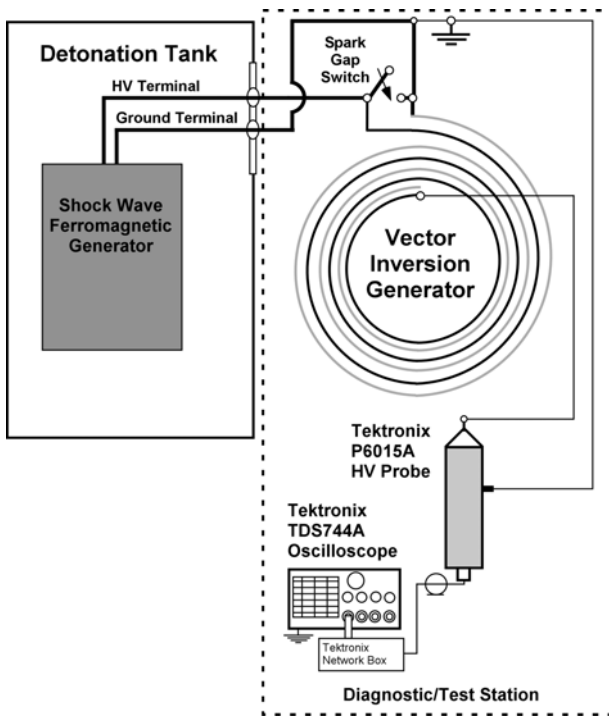


Fig. 8.25 Test setup for an explosive driven FMG-VIG system [26, 52].

amplitude $U_{\text{out}} = 2nU_0$ (n is a number of turns in the roll) with a rise time equal to double the electrical length of the VIG transmission line appears at the contacts of the VIG. The advantages of this system are its simplicity, low cost, configurability and nanosecond rise time. The VIGs used in the experiments described in this section were five-turn units. Their calculated capacitance was 5.6 nF .

8.8.2 Performance of the FMG-VIG System

Operation of the FMG-VIG system is as follows. The FMG produces a high voltage pulse with a pulse length of $5\text{--}8 \mu\text{s}$ that impulse charges the VIG. When the charge voltage exceeds the VIG spark gap hold-off voltage threshold, the VIG erects in a time equal to two wave transit times through the VIG ($\sim 6 \text{ ns}$), producing a transient voltage several times greater than the breakdown voltage of the VIG spark gap switch.

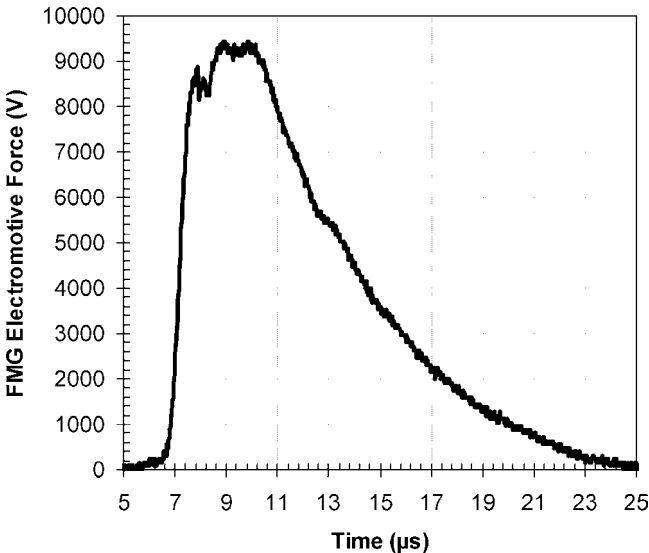


Fig. 8.26 Waveform of the output voltage pulse produced by an FMG with a 257-turn pulse generating coil. The FMG contained a $\text{Nd}_2\text{Fe}_{14}\text{B}$ cylinder with O.D. = 22.2 mm and $h = 19.2$ mm [26].

The first series of experiments [26, 52] was performed with FMGs operating in the open-circuit mode — i.e. where the high voltage probe served as the load. A typical waveform of the output voltage pulse produced by an FMG with a 257-turn pulse generating coil is shown in Fig. 8.26. The amplitude of the high voltage pulse was $U_g(8.3 \mu\text{s})_{\max} = 9.44 \text{ kV}$, its FWHM was $6.67 \mu\text{s}$ and its rise time was $\tau = 1.2 \mu\text{s}$. The slope of the voltage curve, $\Delta U_g(t)_{\max}/\Delta t$, at the moment that demagnetisation begins was $7.87 \text{ kV}/\mu\text{s}$. The amplitude of the voltage pulse averaged over six experiments was $U_g(t)_{\max} = 9.20 \pm 0.26 \text{ kV}$.

The VIG spark gap was characterised in real time just before each FMG-VIG experiment. The spark gap was tuned and set to break at $U = 5.9 \pm 0.3 \text{ kV}$. A typical waveform of a high voltage pulse produced by an FMG-VIG system is shown in Fig. 8.27. The peak voltage amplitude was $U(3.5 \text{ ns})_{\max} = 40.2 \text{ kV}$, its FWHM was 14 ns and its rise time was $\tau = 6.5 \text{ ns}$. The slope of the output voltage curve, $\Delta U(t)_{\max}/\Delta t$, at the moment power generation began was $6.18 \text{ kV}/\text{ns}$. The slope of output voltage, $\Delta U(t)_{\max}/\Delta t$, of the FMG-VIG system increased by approximately three orders of magnitude in comparison with the slope of the output voltage from an FMG. The average value of the amplitude of the peak voltage

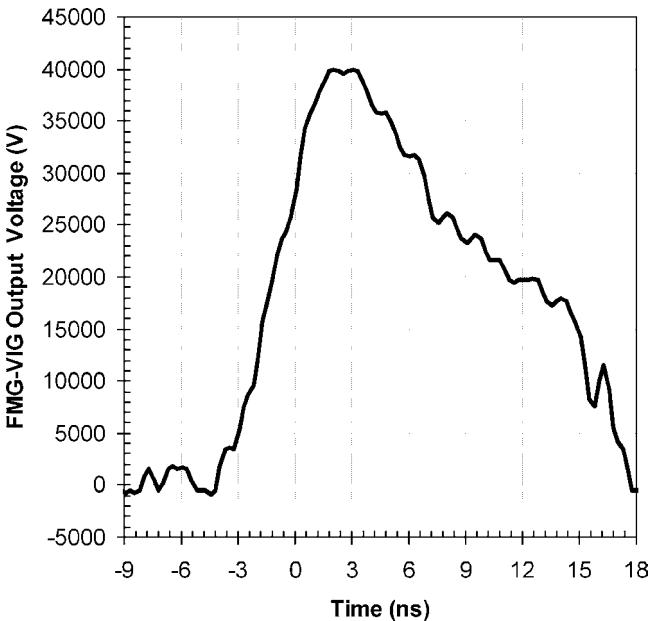


Fig. 8.27 Waveform of the output voltage pulse produced by a FMG-VIG system. The FMG had a 257-turn pulse generating coil [26].

for the FMG-VIG system tested was $U(t)_{\max} = 39.4 \pm 1.9$ kV. The amplitude and shape of the output voltage pulses produced by the FMG-VIG systems tested were very reproducible.

8.8.3 Summary

In summary, operation of the FMG-VIG system was successfully demonstrated by Shkuratov *et al.* [26, 52] for the first time. Adding a VIG stage increases the voltage output of the FMG by a factor of 4, while simultaneously compressing the pulse length to a few nanoseconds. This factor can be increased to 20 by changing the parameters of the VIG. The FMG-VIG combination is a compact high-power, single-shot pulser.

8.9 Explosive Driven FMG-FCG System

Magnetic flux compression generators (FCGs) [50, 51] are the most powerful explosive driven pulsed power amplifiers. A principal feature of the FCG

is the need for a seed source to produce the initial magnetic flux in its working volume. In practice, the initial magnetic flux, Φ , is created in all types of FCGs by an electric current (seed current, I_{seed}) flowing through it prior to explosive operation. The seed current is usually generated by a capacitor bank that is charged by conventional voltage sources, such as the commercial power grid.

The autonomous FMG-FCG systems described in Refs. 44 and 45 offer several advantages, including that they do not require switches, energy stores or converters and nonlinear radio engineering elements.

An autonomous explosive driven FMG-FCG pulsed power system was proposed and experimentally verified by Talantsev *et al.* [44, 45]. It has been experimentally demonstrated [44, 45] that it is feasible to produce pulsed power by harnessing two physical phenomenon: transverse shock wave demagnetisation of a Nd₂Fe₁₄B magnet [16–18] and magnetic flux compression [50–51]. In addition, Shkuratov *et al.* [53–60] proposed and tested alternative autonomous FMG-FCG system designs. The results obtained by Talantsev *et al.* [44, 45] are presented in this section.

8.9.1 FMG-FCG System

A schematic diagram of the experimental setup used to investigate FMG-FCG systems is shown in Fig. 8.28. The FMG-FCG system contained two multi-turn coils connected in series. One of the coils was the pulse generating coil wound on a hollow Nd₂Fe₁₄B magnet with a O.D. of 25.4 mm, I.D. of 7.6 mm and height of 19.2 mm. The other coil was the stator of the FCG. The pulse generating coil on the FMG had an inner diameter of 29.0 mm, consisted of 11.5 turns of copper wire wound in a single layer and had an impedance of $Z(100 \text{ kHz}) = 1.28 \Omega$. The FCG coil consisted of 12 turns of copper wire and had an impedance of $Z(100 \text{ kHz}) = 3.17 \Omega$. The FMG-FCG load consisted of copper wire with an impedance of $Z(100 \text{ kHz}) = 0.2 \Omega$. Details of the FMG-FCG system and its experimental setup can be found in Refs. 44 and 45.

8.9.2 FMG-FCG Performance

The FMG-FCG operates in the following way. When the detonator initiates the high explosives in the FMG, a transverse shock wave is generated that demagnetises the magnet and induces an EMF pulse in the pulse generating coil that, in turn, generates a current pulse, $I_{\text{seed}}(t)$, that flows through the

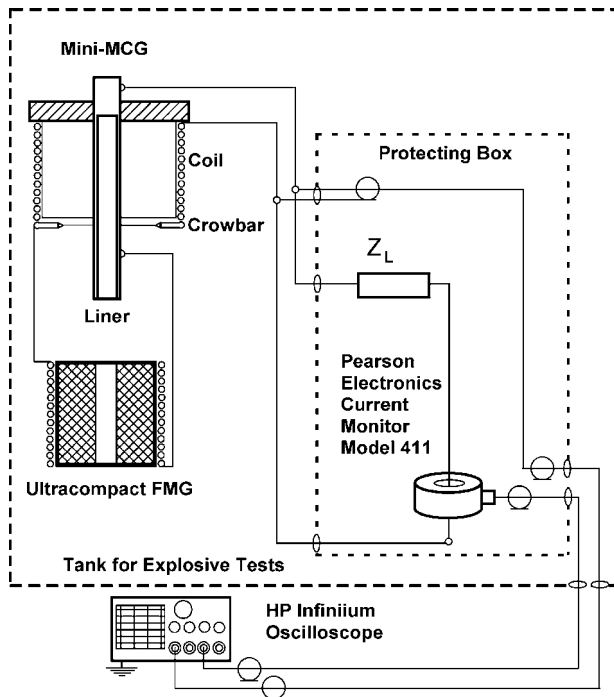


Fig. 8.28 Test setup used to investigate the operation of a FMG-FCG pulsed power system [44, 45].

FMG-FCG-Load circuit (Fig. 8.28). The seed current flowing through the stator of a helical FCG creates a seed magnetic field $B_{\text{seed}}(t)$ within the working volume of the FCG.

In order to measure the magnitude and time characteristics of the seed current in the FMG-FCG-Load circuit, a series of experiments were performed, where the armature of the FCG was not loaded with high explosives and the helical FCG was a passive inductive-resistive element in the circuit. Only the FMG was loaded with explosives.

A typical waveform of the seed current $I_{\text{seed}}(t)$ flowing in the FMG-FCG-Load circuit is shown in Fig. 8.29. The $I_{\text{seed}}(t)$ pulse has a quasi-rectangular shape with a flat top and a FWHM of $83 \pm 5 \mu\text{s}$. The maximum seed current $I_{\text{seed}}(t)_{\max} = 226 \pm 4 \text{ A}$ was achieved between the 20th and the 25th microsecond after ignition of the FMG detonators.

The magnitude of the seed magnetic field, B_{seed} , in the working volume of the FCG, which occurs when the seed current reaches a maximum, can

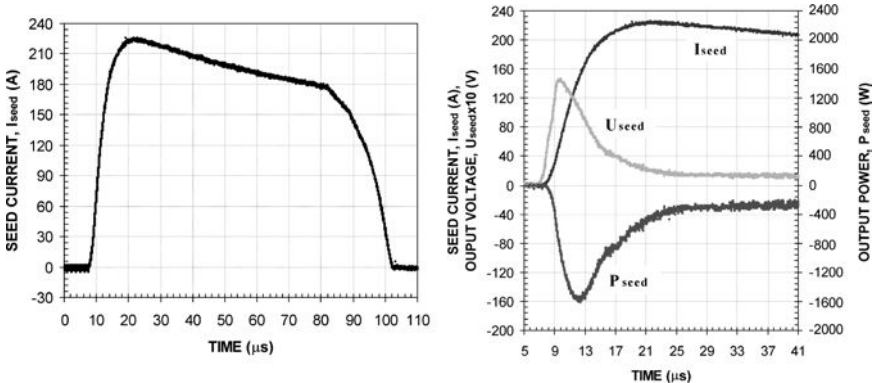


Fig. 8.29 A typical waveform of the seed current pulse flowing through a FMG–FCG–Load circuit. The FMG contained a $\text{Nd}_2\text{Fe}_{14}\text{B}$ cylinder with O.D. = 25.4 mm and h = 38.4 mm [45].

be estimated by using a simple expression for the magnetic field of a long solenoid: $B_{\text{seed}}(21.6 \mu\text{s})_{\text{max}} = \mu_0 n I_{\text{seed}}(21.6 \mu\text{s}) = 0.19 \text{ T}$. Since the maximum seed current, $I_{\text{seed}}(t)_{\text{max}}$ and, hence, the maximum seed magnetic field $B_{\text{seed}}(t)_{\text{max}}$ was achieved between the 20th μs and the 25th μs after ignition of the FMG detonators, it was necessary to delay the ignition of the detonator of the FCG armature so that FCG crowbar occurs within this time interval.

To avoid considerable complications, an initiation scheme was used in which all three detonators — i.e. the two detonators in the FMG and the single detonator in the FCG — were ignited simultaneously [44, 45]. In this case, the delay in FCG crowbar was achieved by increasing the length of the armature of the FCG. In view of the fact that the detonation velocity of C-4 is 0.8 cm/ μs , a delay of 20 μs can be obtained by increasing the length of the FCG armature by 16 cm. A photograph of an FMG-FCG system is shown in Fig. 8.30.

A typical waveform of the current generated in an FMG-FCG-Load circuit, $I_{\text{FMG/FCG/load}}(t)$, is shown in Fig. 8.31. The liner and the crowbar of the FCG were closed at about 25 μs . When the FMG completed its operation, the current rise in the FCG-Load circuit occurred solely due to magnetic flux compression. For comparison purposes, Fig. 8.31 also presents the waveform of the current in the load circuit with the FCG turned off, $I_{\text{seed}}(t)$ — i.e. when the FCG contains no HE.

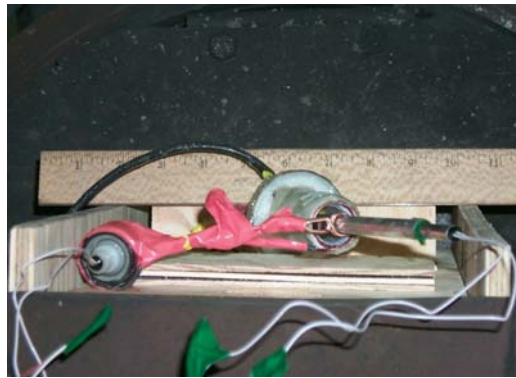


Fig. 8.30 Photograph of a FMG–FCG system [45].

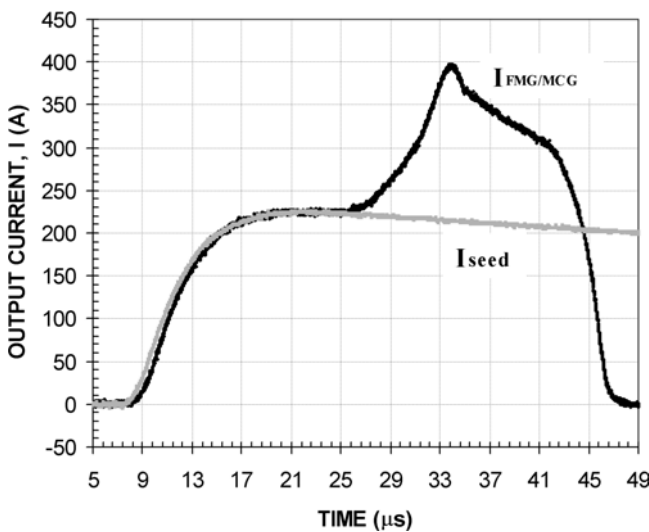


Fig. 8.31 A typical waveform of the output current pulse, $I_{\text{FMG/MCG}/\text{load}}(t)$, produced by a FMG-FCG-Load system and its corresponding seed current pulse, $I_{\text{seed}}(t)$ [45].

The power delivered to the load, $P_{\text{FMG/MCG}/\text{load}}(t)$, increased during the period from $t = 25 \mu s$ to $t = 32.9 \mu s$ by a factor of 17.5; peaking at $P_{\text{FMG/MCG}/\text{load}}(32.9 \mu s) = 5.26 \text{ kW}$ (Fig. 8.32).

The energy delivered to the load, $W_{\text{FMG/MCG}/\text{load}}(t)$, which was determined by taking the integral of the absolute value of the instantaneous

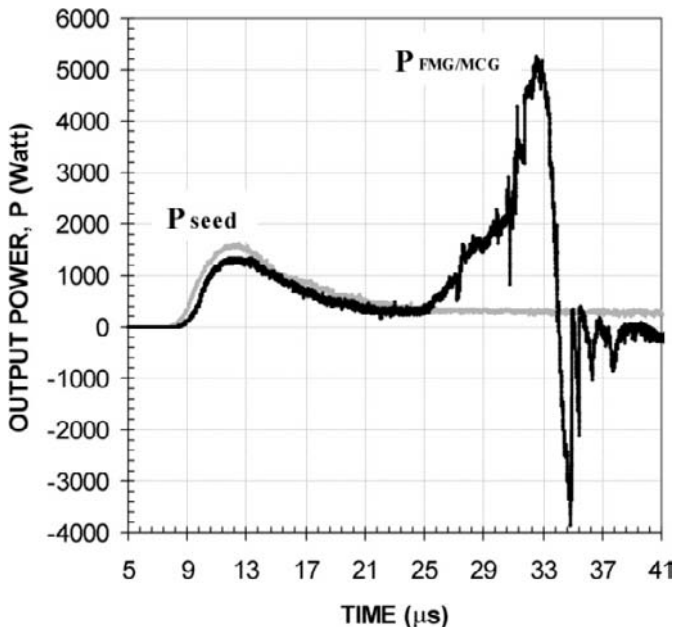


Fig. 8.32 Output power waveforms delivered to a load during the operation of a FMG-FCG-Load system [45].

value of the output power, $|P_{\text{FMG/MCG/load}}(t)|$, with respect to time:

$$W_{\text{FMG/MCG/load}}(t) = \int_0^t |P_{\text{FMG/MCG/load}}(t)| dt$$

increased during the period from $t = 25 \mu\text{s}$ to $t = 34 \mu\text{s}$ — i.e. during the period in which pulsed power is generated by magnetic flux compression, by a factor of 3.0 (Fig. 8.31).

8.10 Summary

From the end of the 1990s to the present time, Shkuratov *et al.* [12–28, 32, 40, 42–45, 52–59] conducted an enormous amount of fundamental and applied research on ferromagnetic generators. The results of this endeavor are summarised below.

- Shock wave demagnetisation of hard Nd₂Fe₁₄B ferromagnets is both feasible and practical [12–18]. Transverse FMGs [16–25] do not require

the use of containers and HE charge holders. The dimensions of transverse FMGs are very close to the dimensions of their Nd₂Fe₁₄B ferromagnets.

- Both high current and high voltage FMGs have been successfully designed, built and tested [13, 15–17, 22–25, 44, 45]. It has been experimentally demonstrated that high current FMGs with a total volume of 9 cm³ are capable of producing currents with amplitudes exceeding 3 kA and with FWHM of 60 µs and that high voltage FMGs with a total volume of 30 cm³ are capable of producing voltage pulses with amplitudes up to 25 kV. It follows from the experimental results in Refs. 24 and 25 that the output voltage amplitude is directly proportional to the number of turns in the pulse generating coil of the FMG.
- Analytical [42, 43] and numerical [22, 23] models have been used to successfully simulate the operation of FMGs. It was shown that the main parameter that determines the output of the FMG is the magnitude of the magnetostatic energy stored in the Nd₂Fe₁₄B element — i.e. $(B \cdot H)_{\max}$. Increasing the volume of the Nd₂Fe₁₄B element (and correspondingly its magnetostatic energy) leads to an increase in the output energy produced by the FMG.
- It was experimentally demonstrated that it is fundamentally possible to charge a capacitor bank to a high voltage with an explosive driven FMG [24, 25]. More than 30% of the magnetostatic energy stored in the Nd₂Fe₁₄B ferromagnetic element in the FMG can be transferred to the capacitor bank. These results offer a straightforward way to design and construct miniature autonomous single-stage and multi-stage pulsed power systems based on FMGs and capacitive energy stores.
- Operation of miniature autonomous high voltage nanosecond FMG-VIG systems [26] were demonstrated. Adding a vector inversion generator increases the voltage output of the FMG by a factor depending on the parameters of the VIG, while simultaneously compressing the pulse to a few nanoseconds. The FMG-VIG combination is an extremely compact high-power, single-shot pulser.
- An autonomous completely explosive driven system based on two successive physical phenomenon — i.e. transverse shock wave demagnetisation of Nd₂Fe₁₄B ferromagnets and magnetic flux compression [44, 45], was successfully demonstrated. This FMG-FCG system needs no capacitive energy stores or electrochemical cells as seed sources, switches, voltage converters and other electronic elements.

Bibliography

- [1] G. W. Anderson and F. W. Neilson, Effects of Strong Shocks in Ferromagnetic Materials, *Bulletin of American Physical Society* **2** (1957) 302.
- [2] R. W. Kulterman, G. W. Anderson and F.W. Neilson, Pulse Generator Based on High Shock Demagnetisation of Ferromagnetic Materials, *J. Appl. Phys.* **29**(3) (1958) 500–501.
- [3] J. E. Besancon, J. L. Champetier, Y. Leclanche, J. Vedel and J. P. Plantevin, Ferromagnetic Transducers, in *Proceedings of International Conference on Megagauss Magnetic Field Generation by Explosives and Related Topics*, eds. H. Knoepfel and F. Herlach (European Atomic Energy Community, Brussels, 1966), pp. 331–348.
- [4] R. A. Graham, Pressure Dependence of the Magnetisation of Invar and Silelectron from 30–450 kbar, *J. Appl. Phys.* **39**(2) (1966) 437–439.
- [5] E. B. Royce, Anomalous Shock-Induced Demagnetisation of Nickel Ferrite, *J. Appl. Phys.* **37**(11) (1966) 4066–4070.
- [6] A. Graham, D. H. Anderson and J. R. Holland, Shock-Wave Compression of 30%Ni-70%Fe Alloys: The Pressure-Induced Magnetic Transition, *J. Appl. Phys.* **38**(1) (1967) 223–229.
- [7] I. G. Clator and M. F. Rose, Shock-Induced Second-Order Phase Change in Invar, *British Journal of Applied Physics* (1967) 853–855.
- [8] R. C. Wayne, Effect of Hydrostatic and Shock-Wave Compressions of a 31.4 at.%Ni-Fe Alloy, *J. Appl. Phys.* **40**(1) (1969) 15–22.
- [9] Lee Davison and R. A. Graham, Shock Compression of Solids, *Physics Reports (Review Section of Physics Letters)* **55**(4) (1979) 255–379.
- [10] V. V. Novikov and V. N. Minyeyev, Magnetic Effects During Shock Loading of Magnetised Ferro- and Ferrimagnetic, *Physics of Combustion and Explosion*, No. 3 (1983), pp. 336–342. Translated from Russian Journal *Fizika Gorenija i Vzryva* **19**(3) (1983) 97–104.
- [11] R. A. Graham, *Solids Under High-Pressure Shock Compression: Mechanics, Physics and Chemistry*, Springer Verlag, NY (1993).
- [12] S. I. Shkuratov, E. F. Talantsev, J. C. Dickens and M. Kristiansen, Longitudinal Shock Wave Demagnetisation of BaFe₁₂O₁₉ Hard Ferrimagnetics, *J. Appl. Phys.* **91** (2002) 3007–3009.
- [13] S. I. Shkuratov, E. F. Talantsev, J. C. Dickens and M. Kristiansen, Compact Explosive-Driven Generator of Primary Power Based on a Longitudinal Shock Wave Demagnetisation of Hard Ferri- and Ferromagnets, *IEEE Transaction on Plasma Science* **30** (2002) 1681–1691.
- [14] S. I. Shkuratov, E. F. Talantsev, J. C. Dickens, M. Kristiansen and J. Baird, Longitudinal-Shock-Wave Compression of Nd₂Fe₁₄B Hard Ferromagnet: The Pressure Induced Magnetic Phase Transition, *Appl. Phys. Letters* **82** (2003) 1248–1251.
- [15] S. I. Shkuratov, E. F. Talantsev, J. C. Dickens and M. Kristiansen, Novel Type of Explosive Driven High-Current and High-Voltage Source of Primary Power Based on Longitudinal Shock Wave Demagnetisation of

- Nd₂Fe₁₄B High-Energy Hard Ferromagnets, in *Proceedings of IXth International Conference on Megagauss Magnetic Field Generation and Related Topics (Megagauss-IX)*, eds. V. D. Selemir and L. N. Plyashkevich (2002), pp. 279–285.
- [16] S. I. Shkuratov, E. F. Talantsev, J. C. Dickens and M. Kristiansen, Transverse Shock Wave Demagnetisation of Nd₂Fe₁₄B High-Energy Hard Ferromagnetics, *J. Appl. Phys.* **92** (2002) 159–162.
 - [17] S. I. Shkuratov, E. F. Talantsev, J. C. Dickens and M. Kristiansen, Ultra-compact Explosive-Driven High-Current Source of Primary Power Based on Shock Wave Demagnetisation of Nd₂Fe₁₄B hard Ferromagnetics, *Rev. Sci. Instrum.* **73** (2002) 2738–2742.
 - [18] S. I. Shkuratov, E. F. Talantsev, J. Baird, L. L. Altgilbers, and A. H. Stults, Transverse Explosive Shock-Wave Compression of Nd₂Fe₁₄B High-Energy Hard Ferromagnets: Induced Magnetic Phase Transition, in *Shock Compression of Condensed Matter, AIP Proceedings*, eds. M. D. Furnish, M. Elert, T. P. Russel and C. T. White **845** (2006) 282–285.
 - [19] S. I. Shkuratov, E. F. Talantsev, J. C. Dickens and M. Kristiansen, Seed Currents Produced by Ultracompact Explosive-Driven Transverse Shock Wave Ferromagnetic Generator of Primary Power in a Coaxial Single-Turn Seeding Coil of a Magnetocumulative Generator, in *Proceedings of IXth International Conference on Megagauss Magnetic Field Generation and Related Topics (Megagauss-IX)*, (eds) V. D. Selemir and L. N. Plyashkevich (2002), pp. 247–254.
 - [20] S. I. Shkuratov, E. F. Talantsev, J. C. Dickens and M. Kristiansen, Autonomous Ultracompact Explosive-Driven High-Voltage Generator Based on Transverse Shock Wave Demagnetisation of Nd₂Fe₁₄B Hard Ferromagnets, in *Proceedings of IXth International Conference on Megagauss Magnetic Field Generation and Related Topics (Megagauss-IX)*, eds. V. D. Selemir and L. N. Plyashkevich (2002), pp. 268–273.
 - [21] S. I. Shkuratov, E. F. Talantsev, J. C. Dickens and M. Kristiansen, Dimensional Effects for Explosive-Driven Ferromagnetic Primary Power Source Seeding a Magnetocumulative Generator, in *Proceedings of IXth International Conference on Megagauss Magnetic Field Generation and Related Topics (Megagauss-IX)*, eds. V. D. Selemir and L. N. Plyashkevich (2002), pp. 255–267.
 - [22] S. I. Shkuratov, E. F. Talantsev, J. C. Dickens and M. Kristiansen, Currents Produced by Explosive Driven Transverse Shock Wave Ferromagnetic Source of Primary Power in a Coaxial Single-Turn Seeding Coil of a Magnetocumulative Generator, *J. Appl. Phys.* **93** (2003) 4529–4535.
 - [23] S. I. Shkuratov and E. F. Talantsev, Powering the Coaxial Single-Turn Seed Coil of a Magnetocumulative Generator by an Explosive-Driven Shock Wave Ferromagnetic Primary Source, *Journal of Electromagnetic Phenomena* **3** (4(12)) (2003) 452–467.
 - [24] S. I. Shkuratov, E. F. Talantsev, J. Baird, L. L. Altgilbers, A. H. Stults and S. V. Kollossenok, Operation of High-Voltage Transverse Shock Wave Ferromagnetic Generator in the Open Circuit and Charging Mode, Digest

- of Technical papers, *15th International Pulsed Power Conference* (2005), pp. 533–536.
- [25] S. I. Shkuratov, E. F. Talantsev, J. Baird, L. L. Altgilbers, and A. H. Stults, Compact Autonomous Explosive-Driven Pulsed Power System Based on a Capacitive Energy Storage Charged by a High-Voltage Shock-Wave Ferromagnetic Generator, *Rev. Sci. Instrum.* **77** (2006) 066107.
 - [26] S. I. Shkuratov, E. F. Talantsev, J. Baird, L. L. Altgilbers, and A.H. Stults, Completely Explosive Autonomous High-Voltage Pulsed Power System Based on Shock Wave Ferromagnetic Primary Power Source and Spiral Vector Inversion Generator, *IEEE Transaction on Plasma Science* **34**(5) (2006) 1866–1872.
 - [27] S. I. Shkuratov, E. F. Talantsev, J. Baird, L. L. Altgilbers, and A. H. Stults, New Concept for Constructing an Autonomous Completely Explosive Pulsed Power System: Transverse Shock Wave Ferromagnetic Primary Power Source and Loop Flux Compression Amplifier, in *IEEE Proceedings of 2006 International Conference on Megagauss Magnetic Field Generation and Related Topics*, eds. J. F. Kiutu, R. E. Reinovsky and P. J. Turchi (2007), pp. 331–336.
 - [28] S. I. Shkuratov, E. F. Talantsev, J. Baird, L. L. Altgilbers and A. H. Stults, A New Concept of Explosive Pulsed Power: Design of Macro Primary Power Sources Based on Elementary Miniature Shock-Wave Ferromagnetic Cells, in *IEEE Proceedings of 2006 International Conference on Megagauss Magnetic Field Generation and Related Topics*, eds. J. F. Kiutu, R. E. Reinovsky and P. J. Turchi (2007), pp. 319–324.
 - [29] J. H. Johnson, Theoretical and Experimental Analysis of the Ferromagnetic Explosively Shocked Current Pulse Generator, *J. Appl. Phys.*, Supplement to **30**(4) (1959) 241–243.
 - [30] J. Lee, J. S. Choi, J. H. Ryu and C. H. Kim, Maximizing Energy Output of Explosively-Driven Ferromagnetic Generators, *Journal of Electromagnetic Phenomena* **3**(3(11)) (2003) 384–391.
 - [31] A. B. Prishchepenko and D. V. Tretyakov, Energy Balance in the System a Ferromagnetic Generator — a Capacitive Load, *Electricity (Elektrichestvo)* **5** (1998) 52–56 (in Russian).
 - [32] A. Prishchepenko and D. Tretyakov, Dissipative Energy Losses in Ferromagnetic Generator of Frequency, in *Proceedings of the 12th IEEE International Pulsed Power Conference, Monterey*, eds. C. Stallings and H. Kirbie (1999), pp. 856–859.
 - [33] R. B. O. Handley, *Modern Magnetic Materials*, John Wiley & Sons, New York (2000).
 - [34] P. W. Cooper, *Explosives Engineering*, VCH Publishers, Inc. NY, USA (1996).
 - [35] R. F. Trunin, *Shock Compression of Condensed Materials*, Part 4, Cambridge University Press, Cambridge, UK (1998), pp. 95–105.
 - [36] L. M. Barker, *Journal of Applied Physics* **45** (1975) 2544.
 - [37] Lee Davison and R. A. Graham, Shock Compression of Solids, *Physics Reports (Review Section of Physics Letters)* **55**(4) (1979) 255.

- [38] R. N. Keeler and E. B. Royce, Shock waves in condensed media, in *Proceedings of the International School of Physics Enrico Fermi*, eds. P. Caldirola and H. Knoepfel (Villa Monastero, Italy, 4–26 July, 1969), Course XLVIII, Academic Press, NY (1971), pp. 51–150.
- [39] H. Knoepfel, *Pulsed Magnetic Field*, Elsevier, NY (1970).
- [40] E. F. Talantsev, S. I. Shkuratov, J. C. Dickens and M. Kristiansen, The Conductivity of a Longitudinal-Shock-Wave-Compressed Nd₂Fe₁₄B Hard Ferromagnetics, *Mod. Phys., Lett. B* **16** (2002) 545–554.
- [41] L. L. Altgilbers, M. D. J. Brown, I. Grishnaev, B. M. Novac, I. R. Smith, I. Tkach and Yu. Tkach, *Magnetocumulative Generators*, Springer-Verlag, New York (2000).
- [42] E. F. Talantsev, S. I. Shkuratov, J. Baird, L. L. Altgilbers, and A. H. Stults, Analytical Method for Calculation of Currents Produced by Shock Wave Ferromagnetic Generators, Digest of Technical papers, 16th International Pulsed Power Conference (2007), pp. 1141–1144.
- [43] E. F. Talantsev, S. I. Shkuratov, J. Baird, L. L. Altgilbers, and A. H. Stults, *Analytical Method for Calculation of Currents Produced by Shock Wave Ferromagnetic Generators*, Acta Polonica A. Submitted for publication (2008).
- [44] Talantsev, S. I. Shkuratov, J. C. Dickens and M. Kristiansen, An Autonomous Completely Explosive Pulsed Power Mini-System, in *Proceedings of IXth International Conference on Megagauss Magnetic Field Generation and Related Topics*, eds. V. D. Selemir and L. N. Plyashkevich (*Megagauss-IX*) (2002), pp. 239–246.
- [45] E. F. Talantsev, S. I. Shkuratov, J. C. Dickens and M. Kristiansen, Completely Explosive Pulsed Power Minisystem, *Rev. Sci. Instrum.* **74** (2003) 225–230.
- [46] G. A. Mesyats, *Pulsed Power*, Kluwer Academic/Plenum Publishers, New York (2005).
- [47] B. A. Jacoby and T. M. York, *Rev. Sci. Instrum.* **51** (1980) 885–888.
- [48] R. A. Fitch and V. T. Seymour, Pulse Generator, Patent of England, United States Patent Office No. 3,289,015, Nov. 29 (1966).
- [49] S. A. Merryman, F. Rose, Z. Shotts, Characterization and Applications of Vector Inversion Generators, Digest of Technical Papers, *13th International Pulsed Power Conference* (2003), pp. 249–252.
- [50] Y. P. Terletskii, Production of Very Strong Magnetic Fields by Rapid Compression of Conducting Shells, *Sov. Phys. JETP* **5** (1957) 301–302.
- [51] C. M. Fowler, W. B. Garn and R. S. Caird, *Journal of Applied Physics* **31** (1960) 588.
- [52] S. I. Shkuratov, E. F. Talantsev, J. Baird, M. F. Rose, Z. Shotts, L. L. Altgilbers, A. H. Stults and S. V. Kollossenok, Completely Explosive Ultra-compact High-Voltage Pulse Generating System, Digest of Technical papers, *15th International Pulsed Power Conference* (2005), pp. 445–448.
- [53] S. I. Shkuratov, E. F. Talantsev, J. Baird, L. L. Altgilbers, and A. H. Stults, New Design for Seeding a Helical FCCG with a Shock Wave Ferromagnetic Generator, in *Proceedings of Megagauss XI International Conference*, eds.

- I. Smith and B. Novac (*Ultrahigh Magnetic Fields: Their Science, Technology, and Application*), London, UK (2006), in press.
- [54] I. Shkuratov, E. F. Talantsev, J. Baird, L. L. Altgilbers, and A. H. Stults, Completely Explosive Pulsed Power FMG-FCG System, in *Proceedings of Megagauss XI International Conference (Ultrahigh magnetic Fields: Their Science, Technology and Application)*, eds. I. Smith and B. Novac, London, UK (2006), in press.
- [55] S. I. Shkuratov, E. F. Talantsev, J. Baird, L. L. Altgilbers and A. H. Stults, Autonomous Completely Explosive Pulsed Power Mini-System Based on Transverse Shock Wave Ferromagnetic Primary Power Source and Ultra-compact Loop FCG, in *Proceedings of Megagauss XI International Conference (Ultrahigh magnetic Fields: Their Science, Technology and Application)*, eds. I. Smith and B. Novac, London, UK (2006), in press.
- [56] S. I. Shkuratov, E. F. Talantsev, J. Baird, L. L. Altgilbers, and A. H. Stults, Compact Autonomous Completely Explosive Pulsed Power System Based on Transverse Shock Wave Demagnetisation of Nd₂Fe₁₄B and Magnetic Flux Compression, in *IEEE Proceedings of 2006 International Conference on Megagauss Magnetic Field Generation and Related Topics*, eds. J. F. Kiutti, R. E. Reinovsky and P. J. Turchi (2007), pp. 337–342.
- [57] S. I. Shkuratov, E. F. Talantsev, J. Baird, L. L. Altgilbers, and A. H. Stults, Transformer-Type Seeding System of a Helical FCG Based on a Transverse Shock Wave Ferromagnetic Generator, in *IEEE Proceedings of 2006 International Conference on Megagauss Magnetic Field Generation and Related Topics*, eds. J. F. Kiutti, R. E. Reinovsky and P. J. Turchi (2007), pp. 313–318.
- [58] S. I. Shkuratov, E. F. Talantsev, J. Baird, L. L. Altgilbers and A. H. Stults, Compact Autonomous Completely Explosive Pulsed Power System, Digest of Technical papers, 16th International Pulsed Power Conference (2007), pp. 1347–1351.
- [59] S. I. Shkuratov, E. F. Talantsev, J. Baird, L. L. Altgilbers, and A. H. Stults, Explosive-Driven Mini-System Based on Shock Wave Ferromagnetic Seed Source and Loop Magnetic Flux Compression Generator, Digest of Technical papers, 16th International Pulsed Power Conference (2007), pp. 1141–1145.
- [60] S. I. Shkuratov, E. F. Talantsev, J. Baird and L. L. Altgilbers, Electrical Discharge in Flux Compression Generators: The Dominant Role of Explosively Expanding Armature, *Applied Physics Letters* (submitted).

Chapter 9

Ferroelectric Materials and Their Properties

9.1 Introduction

All dielectrics can be polarised by applying an external electric field. However, some dielectrics, under certain conditions, also possess a naturally occurring *spontaneous polarisation* due to their crystalline structure and are called *ferroelectrics*. According to M. Budimir [1], a crystal is defined to be ferroelectric when it has at least two orientation states of spontaneous polarization in the absence of an external electric field and can be shifted from one to another of these states by an electric field. This definition is an oversimplification, since whether or not a material is ferroelectric also depends on other factors such as crystalline perfection, electrical conductivity, pressure and temperature, all of which affect the orientation of the polarisation of the material.

In this chapter, the fundamental properties of ferroelectric materials will be examined, with particular attention focused on Lead Zirconate Titanate (PZT), which is the material that has been extensively used by the authors in their explosive-driven ferroelectric generators that are the subject of Chap. 12. Since the operation of FEGs rely on the depolarisation of PZT via phase transitions or domain shifting, a detailed discussion of phase transitions is presented in Chap. 11. The operation of FEGs also relies on shock compression of ferroelectric materials, which has been under study since the 1950s. Therefore, a brief review of the extensive literature on shock compression of ferroelectric materials is presented in Chap. 11.

9.2 Historical Perspectives

In 1880, Pierre and Jacques Curie observed that when certain solids, like tourmaline crystals, are subjected to mechanical stress that an electrical

charge accumulates on their surface, thus forming electric fields across the bulk of the material. In 1881, Hankel called this phenomenon *piezoelectricity* ('piezo' being the Latin word for 'pressure') and Lipmann deduced the inverse effect by employing thermodynamics [2]. In 1910, Voigt published *Lehrbuch der Kristallphysik*, which described in detail the complex electromechanical relationships in piezoelectric crystals. The first to use piezoelectric materials in a practical application was Langevin in France during World War I, when he developed a piezoelectric ultrasonic transducer for submarine detection.

Unlike piezoelectricity, which is a linear reversible process, *ferroelectricity*¹ is the complex interaction of the dielectric and elastic properties of highly nonlinear, anisotropic, polarisable, deformable crystals [3]. The roots of ferroelectricity can be traced back to the work of J. Valasek in the 1920s [4–9], who at the time was investigating the piezoelectric properties of Rochelle salt (potassium sodium tartrate), which was first produced by P. Seignette in La Rochelle, France in 1655. Valasek was the first to use the term 'Curie Point' to describe the onset of polar ordering in Rochelle salts below certain temperatures. The anomalous properties of Rochelle salt i.e. extremely high dielectric and piezoelectric response, was for a considerable time called Seignette electricity. The term ferroelectricity was not commonly used until the early 1940s.

Valasek found that Rochelle salts exhibited several interesting properties, such as pyroelectricity and optical activity. He also recognised that some of the effects observed in Rochelle salt resembled some of the magnetic properties of iron. Based on his studies, he reported to a meeting of the American Physical Society in Washington in 1920 that '... the dielectric displacement, D , electric intensity, E , and polarization, P ', of Rochelle salt 'are analogous to B (magnetic flux), H (magnetic field), and I (electric current) in the case of magnetism'. He added that there is '... a hysteresis in P analogous to magnetic hysteresis. This would suggest a parallelism between the behavior of Rochelle salt as a dielectric and steel, for example, as a ferromagnetic substance' [4]. Rochelle salt was the only known ferroelectric material until 1935, when it was found that potassium dihydrogen phosphate (KDP) also exhibited ferroelectric properties. A major turning point in ferroelectricity came in 1941, when it was discovered that a number

¹The term 'ferroelectric' arises from the observation that ferroelectric materials are the electrical analogues of ferromagnetic materials, not because they are associated with iron.

of mixed oxides, such as TiO_2 and BaO , which forms barium titanate, crystallised with a perovskite structure and exhibited unusual dielectric properties — i.e. permittivities 1000 times higher than those of any other known ceramics at the time. During World War II, the study of piezoelectric and ferroelectric materials expanded in the U.S., Japan and Russia [10, 11]. The first patent on ferroelectrics was filed in 1941 [12] and the first working piezoelectric ceramic transducer built in 1945 [13]. In the early 1950s, Japanese researchers [11] began to investigate the ferroelectric properties of lead titanate and lead zirconate and their mixtures. In the mid-1950s, Jaffe and co-workers [11] formulated the first piezoceramics based on these compounds to create lead zirconate titanate (PZT). From the late 1950s until the present, a variety of ferroelectric materials have been identified, which are used in a number of commercial and military applications.

9.3 Electromechanical Effects in Ferroelectric Materials

A general property of all dielectric materials, no matter if they are crystalline, amorphous, polar or centrosymmetric, is electrostriction. When an electric field is applied to an insulating material, it can cause the material to undergo a slight change in shape — i.e. become mechanically deformed, where this deformation is called *electric field induced strain* or *electrostriction*. Reversing the electric field does not reverse the direction of the deformation. The change in the dimensions of the dielectric is the result of a reorientation of its molecules by the applied external electric field. In addition, if the electric field is not uniform, the dielectric material will tend to move. For example, if the relative permittivity of the dielectric is higher than that of its surroundings, it will tend to move into a region of higher electric field strength. The amount of strain (S) induced in the material is proportional to the square of the polarisation (P):

$$S = QP^2, \quad (9.1)$$

where Q is the *electrostrictive coefficient*.

Another property of some crystalline materials is piezoelectricity. The *piezoelectric effect* is observed when a mechanical stress induces electric polarisation in a material due to the distortion of the unit cells of the crystal. The *direct piezoelectric effect* is a linear reversible process, where the magnitude of the polarisation is dependent on the magnitude of the stress and the direction of the polarity is dependent on the type of stress — i.e.

tensile or compressive. The direct piezoelectric effect is always accompanied by an *inverse* or *converse piezoelectric effect*, where a solid is strained when placed in an external electric field. Electrostriction is not the same as the converse piezoelectric effect, since the latter is defined to be primarily an electromechanical effect — i.e. the strain is proportional to the electric field, whereas electrostriction permanently deforms the crystal and is proportional to the square of the electric field. Electrostrictive materials do not spontaneously polarise, i.e. they do not generate charge under stress, but do experience a change in permittivity, which is called the *converse electrostrictive effect*. To further clarify the difference between electrostriction and the piezoelectric effect, Jaffe *et al.* [14] stated that in electrostriction the ‘sign (direction) of the deformation is independent of the polarity of the field, and proportional to even powers of the field.’ In contrast, deformation due to the piezoelectric effect is linear with respect to the electric field — i.e. within the elastic limit of the material, and changes direction when the electric field is reversed.

The direct and inverse piezoelectric effects are mathematically described by their respective equations of state, which are the basic relationships between the electrical and mechanical properties of ferroelectric materials:

$$D = \varepsilon^T E + dT \quad (9.2)$$

$$S = dE + s^E T, \quad (9.3)$$

where D is the dielectric displacement, E is the electric field, T is the mechanical stress, S is the mechanical strain, d is the piezoelectric coefficient, ε is the permittivity and s is the mechanical compliance. The superscript T means the piezoelectric material is under constant stress — i.e. a mechanically free condition, and the superscript E means that it is under constant electric field — i.e. a short-circuit condition.

A necessary condition for the piezoelectric effect to occur is that there has to be a lack of a center of symmetry in the material’s crystalline structure. There are 32 classes or point groups of crystals, of which 11 have a center of symmetry (centrosymmetric) and 21 do not have a center of symmetry (see Fig. 9.1). When there is a lack of symmetry, the net movement of positive and negative ions with respect to each other as a result of stress will produce an electric dipole. When there is a centrosymmetry, the centers of the positive and negative charges will still coincide, even after deformation of the crystal due to stress. Of the 21 non-centrosymmetric crystal classes, 20 are piezoelectric.

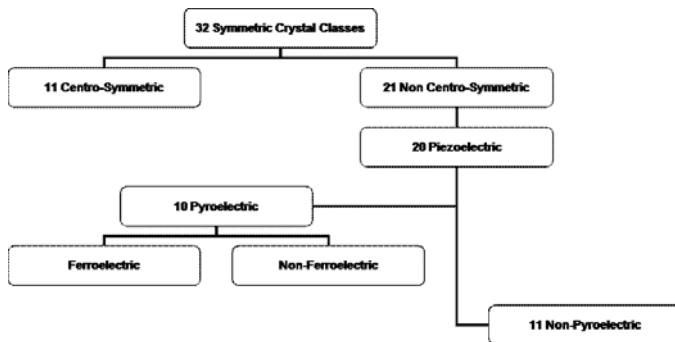


Fig. 9.1 Crystal classifications.

Of the 20 classes of crystals that are piezoelectric, 10 have a unique polar axis and are called polar crystals. Even when no external stress is being applied, those 10 classes of crystals with unique polar axes have a permanent electric dipole moment within their unit cells and are, thus, said to be spontaneously polarised. *Spontaneous polarisation* (P_S) is defined to be the magnitude of the dipole moment per unit volume or the magnitude of the electrical charge per unit area on the surface perpendicular to the axis of spontaneous polarisation. The magnitude of the spontaneous polarisation depends on temperature (Θ). The temperature dependence of spontaneous polarisation is called the *pyroelectric effect* and crystals that exhibit this property are called *pyroelectrics*. The pyroelectric effect is mathematically described by the formula

$$\Delta P_S = p\Delta\Theta, \quad (9.4)$$

where p is the *pyroelectric coefficient*. Changing the temperature of a pyroelectric changes the value of its electric dipole moment.

A subgroup of the pyroelectric classes of crystals is the *ferroelectrics*. As noted earlier, ferroelectrics are polar materials that have at least two equilibrium orientations for the spontaneous polarisation vector in the absence of an external electric field and that can have their spontaneous polarisation switched between these two equilibrium orientations by an applied external electric field. Crystalline ferroelectric materials can be either single crystals or polycrystalline ceramics, the latter of which are currently in wide use.

A *ferroelectric crystal* is a dielectric material that has a net dipole moment even in the absence of an external electric field [15, 16]. This net dipole moment is due to the center of positive charge in the crystal not

coinciding with the center of the negative charge due to its crystalline structure, which, as noted earlier, is referred to as spontaneous polarisation. If an electric field is applied to a ferroelectric material and then slowly reversed and plotted against the resulting change in polarisation of the material, a hysteresis loop (Fig. 9.2) is generated, much like for ferromagnetic materials. Once a ferroelectric material has been poled to saturation and the poling electric field is removed, the remaining polarisation is called the *remnant polarisation*, which is an important property relative to FEG operation. Most non-ferroelectric dielectrics will not form much of a hysteresis loop and the electric moment of these materials is not affected by the application of an external electric field, even when the applied field reaches values that cause electrical breakdown within the crystal.

Ferroelectricity usually disappears above a certain temperature called the *transition* or *Curie temperature*. When the temperature of a ferroelectric material exceeds the Curie temperature, the material is no longer ferroelectric and is said to be *paraelectric*. The Curie temperature is also the temperature at which the dielectric constant of a ferroelectric material peaks. When the temperature of a ferroelectric material exceeds its Curie point, it still behaves electrostrictively.

Like ferromagnetic materials, ferroelectric materials tend to form *domains* in which the unit cell dipoles that make up the domain are aligned in parallel to make the domain polar. Crystals where polar domains are

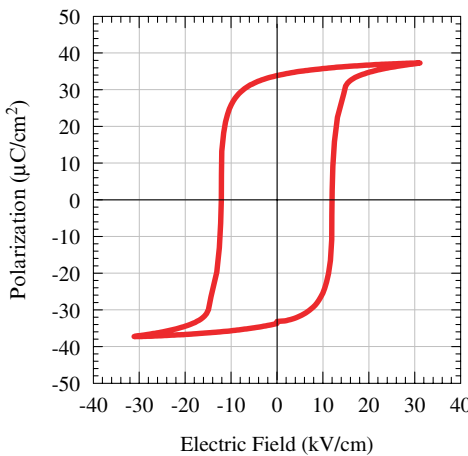


Fig. 9.2 Hysteresis curve for a ferroelectric material.

aligned anti-parallel — i.e. where half the domains are aligned with their dipoles oriented in one direction and the other half are aligned with their dipoles oriented in the opposite direction and where adjacent domains are oppositely polarised, so that there is a net center of symmetry and there is no net polarisation, are called *antiferroelectrics*. This anti-polar orientation arises because the dipole-dipole interaction energy is lowered. In anti-polar crystals, where the free energy of the anti-polar state does not differ appreciatively from that of the polar state, externally applied mechanical stresses or electric fields can transition the material to a parallel state (ferroelectric state). Of course, the opposite is true as well — i.e. a stress can also cause a ferroelectric material to transition into an antiferroelectric state, which is what occurs in FEGs that use PZT 95/5 as their ferroelectric element.

To further understand the differences between the paraelectric, ferroelectric and antiferroelectric states, consider the relationship between the applied electric field E and the induced polarisation P . In the case of paraelectric materials, a plot of P versus E is linear. In the case of ferroelectric materials, a hysteresis curve (Fig. 9.3) results, due to the transition of the spontaneous polarisation between positive and negative directions. In the case of antiferroelectric materials in low electric fields, the induced polarisation is proportional to E , but when the electric field exceeds a critical value, the crystal becomes ferroelectric and a hysteresis curve results. After removal of the external field, the crystal returns to its original anti-polar state and no spontaneous polarisation is observed. A plot of P versus E for an antiferroelectric material results in a double hysteresis curve (Fig. 9.3).

In even simpler terms, the difference between ferroelectrics and piezoelectrics can be summarised as follows: ferroelectric materials have ferroelectric domains and piezoelectric materials do not. The constitutive response of these two materials can be divided into types. The response of a piezoelectric material to external mechanical or electrical stresses is linear, reversible and includes time independent displacements of ions within a unit cell. The constitutive response of ferroelectric materials to external mechanical and electrical stresses is nonlinear, irreversible and time dependent, since the irreversible switching of the spontaneous polarisation and/or movement of domain walls occurs in an incremental fashion.

All ferroelectric crystals are also piezoelectric, since a stress applied to the crystal will change their electric polarisation or, similarly, an externally applied electric field will cause the crystal to become strained. However, it should be noted that a crystal may be piezoelectric without being ferroelectric. By way of example, quartz is piezoelectric, but not

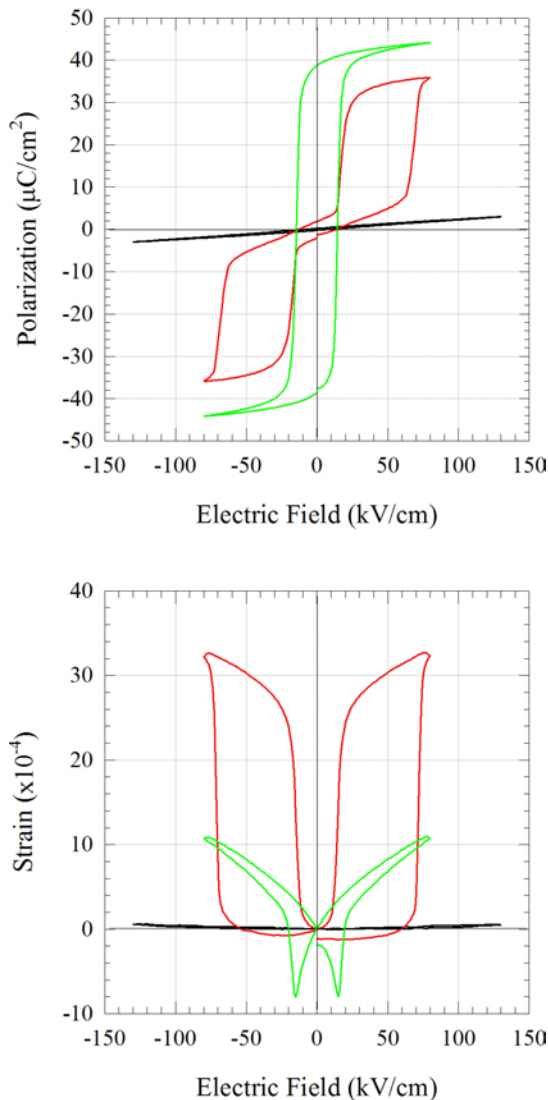


Fig. 9.3 Double hysteresis curve of an antiferroelectric material. The black curve represents the case where the electric fields are not high enough to switch the material from the antiferroelectric state to the ferroelectric state; the red curve represents the case where the composition of the material is closer to the phase boundary so that the antiferroelectric-to-ferroelectric switching field is lower and has a butterfly loop; and the green curve is for the case where the composition of the ferroelectric material is on the ferroelectric side of the phase transition and has a typical ferroelectric loop. (Courtesy of W. Hackenberger and E. Alberta, TRS Technologies.)

ferroelectric, whereas barium titanate is both. All ferroelectric crystals are also pyroelectric.

The parameters of FEGs are closely related to the elastic, dielectric, piezoelectric and ferroelectric properties of the materials from which they are made. Since the discovery of the ferroelectric effect, it has been found that many materials exhibit ferroelectric properties. However, only a few of these materials are suitable for practical applications. Their suitability is determined by the relationship of their mechanical stresses/deformations with their fundamental electrical parameters.

9.4 Piezoelectric Figures of Merit

There are several parameters [15] that are used to specify the electromechanical properties of ferroelectric materials. These parameters will be discussed in this section. The common units of measurement for these parameters are listed in Table 9.1.

9.4.1 Dielectric Constant/Permittivity

The *Dielectric constant (relative permittivity)*, K , is defined as the dielectric displacement per unit electric field. It is also defined as the ratio of the charge stored on a slab of material with electrodes with a certain voltage across them to that stored on identical electrodes with vacuum between them and with the same voltage across them — i.e. the ratio of the permittivity of the material to that of vacuum ($K = \epsilon/\epsilon_0$). Permittivity is a

Table 9.1 Piezoelectric figures of merit and their metric units of measure.

Symbol	Name	Unit
T	Stress	N/m ²
ϵ	Permittivity	F/m
E_{br}	Dielectric Strength	MV/m
P	Polarisation	C/m ²
s	Elastic Compliance	m ² /N
c	Elastic Stiffness	m ² /N
d	Piezoelectric Charge Constant	C/N
g	Piezoelectric Voltage Constant	Vm/N
k	Electromechanical Coupling Factor	—
Z	Acoustic Impedance	Ns/m ⁵

physical quantity that describes how an electric field affects and is affected by a dielectric medium. It is a measure of the polarisability of a material. It is determined by measuring the ability of a material to polarise in response to an electric field, and, thereby, reduce the field inside the material. Thus, permittivity relates to a material's ability to transmit (or 'permit') an electric field. For example, the permittivity determines the capacitance of the ferroelectric element, which impacts the relationship between the FEG and its load. The higher the capacitance of the FEG, the higher the capacitive load it can effectively drive. The value of the permittivity will depend on whether the material is under constant stress or under constant strain ('clamped state'). Ferroelectric materials often have very high dielectric constants.

9.4.2 Dielectric Strength

The dielectric strength, E_{br} , of a dielectric is the maximum electric field strength that it can withstand intrinsically without breaking down, i.e., without experiencing failure of its insulating properties. The field strength at which breakdown occurs for a given case is dependent on the respective geometries of the dielectric and of the electrodes with which the electric field is applied, as well as the rate of increase of the applied electric field. Because dielectric materials usually contain minute defects, the practical dielectric strength will be a fraction of the intrinsic dielectric strength seen for ideal — i.e. defect-free, materials.

9.4.3 Remnant Polarisation

When an external electric field is applied across a ferroelectric material, the dipoles within the material become increasingly aligned until no further polarisation is observed. The material is then fully polarised or saturated. If the external field is reduced to zero, the dipoles become less strongly aligned; however, they do not return to their original alignment, since there are several preferred alignment directions within the crystal. Therefore, there is still a very high degree of alignment and the material remains polarised at some value lower than the saturation polarisation. The polarisation at this point is called the *remnant polarization*, P_r , and determines the maximum amount of charge that can be coupled from the FEG into a load.

9.4.4 Coercive Field

The *coercive field*, E_c , for a ferroelectric material is the electric field required to switch its polarisation from its remnant [P_r] polarisation to zero polarisation [$P = 0$]. The value of E_c for a ferroelectric crystal is dependent on many parameters including its thermal and electrical history, environmental factors and the area of its switching electrodes.

9.4.5 Compliance

The *elastic compliance*, s , of a material is defined to be the strain produced per unit stress. It is the reciprocal of the *modulus of elasticity* or *elastic stiffness*, c , of the material. The elastic compliance has very different values, depending upon whether the electric field within the material is maintained at zero (short-circuited) or whether the electric displacement remains constant (open-circuited).

9.4.6 Piezoelectric Charge Constant or Piezoelectric Coefficient

The *piezoelectric charge constant*, commonly called the *piezoelectric coefficient*, d , is defined to be the electric polarisation, P , generated in a material per unit of mechanical stress, T :

$$P = dT. \quad (9.5)$$

Other definitions include the short circuit charge density developed per unit of applied stress and the strain developed per unit of electric field. It is a measure of the electric charge induced on the electrodes in response to a mechanical stress or the mechanical strain achieved when an electric field is applied across a ferroelectric material under constant stress.

9.4.7 Piezoelectric Voltage Constant

When an external stress, T , is applied to a piezoelectric material, the magnitude of the induced electric field, E , is related to the applied stress by the *piezoelectric voltage constant*, g :

$$E = gT. \quad (9.6)$$

Other definitions include the open-circuit field developed by a given stress and the strain developed per unit of applied electric field. The piezoelectric

charge and voltage constants are related to each other by the following expression:

$$g = \frac{d}{k\epsilon_0}. \quad (9.7)$$

The factor ϵ is the relative permittivity of the material and ϵ_0 ($= 8.854 \times 10^{-12} \text{ F m}^{-1}$) is the permittivity of free space. Materials with a high g constant are desirable when generating voltages by mechanical stress.

9.4.8 Electromechanical Coupling Factor

The *electromechanical coupling factor*, k , is a measure of the ability of a ferroelectric material to convert mechanical energy into electrical energy and vice versa and is defined by:

$$k^2 = \frac{\text{Stored Electrical Energy}}{\text{Input Mechanical Energy}}. \quad (9.8)$$

Other related figures of merit are the *energy transmission coefficient*, λ_{\max} , defined by the expression

$$\lambda_{\max} = \left. \frac{\text{Output Electrical Energy}}{\text{Input Mechanical Energy}} \right|_{\max} \quad (9.9)$$

and the *efficiency*, η , defined by the expression

$$\eta = \frac{\text{Output Electrical Energy}}{\text{Consumed Mechanical Energy}}. \quad (9.10)$$

The coupling factor is related to the piezoelectric charge constant by the expression

$$k^2 = \frac{d}{(s^E \epsilon^T)^{1/2}}, \quad (9.11)$$

where s^E is the short-circuited compliance and ϵ^T is the permittivity at constant stress — i.e. when the element is free to deform.

9.4.9 Acoustic Impedance

The *acoustic impedance*, Z , is a parameter used to evaluate the acoustic energy transfer between two materials and is defined by the expression:

$$Z = \frac{\text{Pressure}}{\text{Area Velocity}}. \quad (9.12)$$

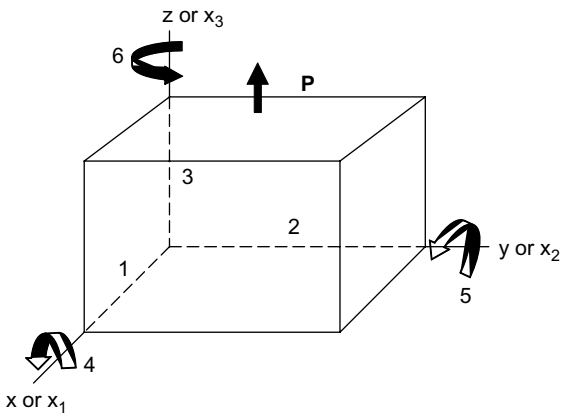


Fig. 9.4 The orthogonal system used to describe piezoelectric and ferroelectric materials.

In a solid, this expression becomes:

$$Z = \rho c, \quad (9.13)$$

where ρ is density of the material and c is the longitudinal velocity of the wave propagating in the material.

9.5 Notation

Ferroelectric generators operate either in the longitudinal (axial) mode (shock wave moving parallel to the polarisation) or the transverse (normal) mode (shock wave moving perpendicular to the polarisation). The various parameters associated with ferroelectric materials are tensors: electric field and polarisation are first order tensors (3 components), stress and dielectric permittivity are second order tensors (9 components), piezoelectricity is a third order tensor (27 components), elasticity is a fourth order tensor (81 components), and so on. Certain components of these tensors are more important than others with respect to each mode. The contributions of each tensor component will depend on a number of factors, including which composition of the PZT is used, the stress levels applied, the direction in which these stresses are applied, types of dopants added, electrical breakdown strength and so on. All these parameters are interrelated in a complex manner.

Since many of the parameters associated with ferroelectricity are either vectors or tensors, a directionality indexing is required. This indexing is analogous to that used in crystallography. In order to standardise this indexing, the polarisation vector is usually set parallel to the z or 3rd axis of a right-handed Cartesian coordinate system. Those physical quantities associated with ferroelectric materials are given the subscripts 1, 2 and 3, which correspond to the x -axis, y -axis and z -axis, respectively, of the Cartesian coordinate system (see Fig. 9.4). The shear stresses and shear strains can be represented either in tensor or vector notation. In matrix notation, there are mechanical shear stresses about the x -axis, y -axis and z -axis, the corresponding strains are designated 4, 5 and 6, respectively. The relationship between the tensor components and the vector components of stress and strain are given by

$$\begin{bmatrix} S_1 \\ S_2 \\ S_3 \\ S_4 \\ S_5 \\ S_6 \end{bmatrix} = \begin{bmatrix} \varepsilon_{11} \\ \varepsilon_{22} \\ \varepsilon_{33} \\ 2\varepsilon_{23} \\ 2\varepsilon_{31} \\ 2\varepsilon_{12} \end{bmatrix} = \begin{bmatrix} \varepsilon_1 \\ \varepsilon_2 \\ \varepsilon_3 \\ \varepsilon_4 \\ \varepsilon_5 \\ \varepsilon_6 \end{bmatrix} \quad \text{and} \quad \begin{bmatrix} \sigma_{11} \\ \sigma_{22} \\ \sigma_{33} \\ \sigma_{23} \\ \sigma_{31} \\ \sigma_{12} \end{bmatrix} = \begin{bmatrix} \sigma_1 \\ \sigma_2 \\ \sigma_3 \\ \sigma_4 \\ \sigma_5 \\ \sigma_6 \end{bmatrix} = \begin{bmatrix} T_1 \\ T_2 \\ T_3 \\ T_4 \\ T_5 \\ T_6 \end{bmatrix}$$

For the piezoelectric coefficients, the first subscript corresponds to the electrical term and the second to the mechanical term. For example, d_{31} is the coefficient relating the electric field along the polar axis to the elongational strain perpendicular to the axis. The coefficient d_{15} relates the electric field applied at right angles to the polar axis to the induced shear strain. The coefficient g_{31} describes the electric field induced in direction 3 (z -axis in Fig. 9.4) by a mechanical stress acting in direction 1 (x -axis in Fig. 9.4), and s_{33} is the ratio of the electric field induced in direction 3 to the mechanical stress in direction 3.

Using matrix notation, the piezoelectric constitutive equations of state (Eqs. (9.1) and (9.2)) can now be rewritten in the following form:

$$D_i = \varepsilon_{ij}^T E_j + d_{ij} T_j \quad (9.14)$$

$$S_i = d_{ij} E_j + s_{ij}^E T_j. \quad (9.15)$$

It should be noted that these are the constitutive equations for linear piezoelectric materials. When applying these equations to ferroelectric

materials, the coefficients s , d and ε are no longer constants, but rather functions of stress and electric field and of their rate of rise or fall.

By way of example [17], consider the case of where a small stress or a weak electric field is applied to a ferroelectric ceramic along its poling direction. Equations (9.14) and (9.15) can now be rewritten as follows:

$$D_3 = \varepsilon_{33}^T E_3 + d_{33} T_3 \quad (9.16)$$

$$S_3 = d_{33} E_3 + s_{33}^E T_3. \quad (9.17)$$

where the subscript 3 indicates the poling direction. If the stress is set equal to zero, which means that the sample is free to expand unhindered (unclamped), Eqs. (9.16) and (9.17) are no longer coupled and the strain and the electric displacement are now functions of the electric field. Similarly, if the electric field is set equal to zero, which corresponds to a short-circuit condition, the strain and electric displacement are now functions of the stress. The piezoelectric constant, d_{33} , is the same in both cases. This example illustrates the equivalence of the direct and converse piezoelectric response of the ferroelectric ceramic.

Now if a large stress or electric field is applied, the ferroelectric ceramic will have a significant hysteresis due to irreversible domain switching in the material. These irreversible changes take a finite amount of time, which implies that the hysteresis curve depends on the rate at which the signal is ramped up or down. Thus, the coefficients ε_{33}^T , s_{33}^E and d_{33} are no longer constants, as in the piezoelectric case, but are now functions of the amplitude of the mechanical or electrical stress and the rate at which the stress rises and falls.

9.6 Ferroelectric Materials

There are several classes of ferroelectric material: single-crystal, ferroceramics, ferropolymers, ferrocomposites and ferrofilms. For the most part, only ferroceramics and ferropolymers have been used in explosively driven FEGs, but for completeness a brief description of each class is given below.

9.6.1 Single-Crystals

Some of the most commonly used single-crystal piezoelectric and ferroelectric materials are quartz, lithium niobate (LiNbO_3) and lithium tantalate

(LiTaO₃). Single-crystal ferroelectric materials are anisotropic and exhibit different material properties depending on the cut of the material and the direction of the bulk or surface wave propagation.

9.6.2 *Ferroceramics*

Ferroceramics are polycrystalline ferroelectric materials with a perovskite crystal structure that contain a large divalent metal ion, such as barium or lead, and a tetravalent metal ion, such as titanium or zirconium. Two common ferroceramics are barium titanate (BaTiO₃) and lead zirconate titanate (PZT). The ferrocерamic PZT is widely used because of its superior ferroelectric properties. There are different formulations of PZT, depending on the ratios of Zr to Ti used and the amount and types of dopants added. For example, PZT 95/5 implies that the Zr:Ti ratio is 95:5. It has been found that when PZT 95/5 is modified with 2% niobium, the nominal state of this material is ferroelectric, but it is near an antiferroelectric state. Bound electric charge is readily released by shock compression, when the material transitions from its ferroelectric state to its antiferroelectric state.

9.6.3 *Ferropolymers*

When certain polymers, such as polyvinylidene difluoride (PVDF), are drawn and stretched in certain directions when being fabricated, they are transformed into a microscopically polar phase. Piezopolymers tend to have small *d* and high *g* piezoelectric constants, to be lightweight and have soft elasticity.

9.6.4 *Ferrocomposites*

Ferrocomposites are composed of ferroceramics and a polymer phase. The advantages of these composites are their high coupling factors, low acoustic impedance, mechanical flexibility and tailorability.

9.6.5 *Thin Films*

Thin film ferroelectric materials are produced by sputter-depositing binary compounds, such as zinc oxide (ZnO) or aluminum nitride (AlN), on various substrates. Thin films based on ZnO have poor piezoelectric coupling properties, so alternatives such as PZT thin films are being developed.

9.7 Lead Zirconate Titanate (PZT)

Since PZT has been the ferroceramic of choice for use in FEGs, their physical and electrical properties will be examined in this section. The output of the FEG depends on many factors including the direction of propagation of the shock wave relative to the direction of polarisation, shock pressures, electrical characteristics of the load circuit (short-circuit, open-circuit, capacitive, resistive, or inductive), composition of the PZT, material properties (grain size, crystalline structure), presence of dopants, degree of poling, type of transition the PZT undergoes (polarised → nonpolarised, ferroelectric → antiferroelectric), failure modes (fracturing, electrical breakdown), properties of the fill or potting material used, physical constraints (clamped or unclamped), and so on. In other words, the materials used in FEGs require the proper mix of good electrical, shock and mechanical properties.

9.7.1 PZT Properties

Lead zirconate titanate (PZT) is synthesised from lead, titanium and zirconium, and is a member of the family of ferroelectric ceramics, having a perovskite crystalline structure. The general chemical formula for perovskite molecules is ABO_3 . Perovskite crystals have a cubic unit cell with a large cation (A) on the corners, a smaller cation (B) in the body center and oxygen anions (O) in the centers of the faces. The structure is a network of corner linked oxygen octahedra, with the smaller cation filling the octahedral holes and the larger cations filling the dodecahedral holes [14]. The piezoelectric, dielectric and mechanical properties of PZT can be adjusted by replacing the A or B cations with other cations, such as Na^+ , K^+ , Bi^{+3} and La^{+3} for the A cations and Nb^{+5} , Fe^{+3} , Sb^{+5} , Fe^{+5} , Al^{+3} and Cr^{+3} for the B cations. These cations are classified as either being acceptor or donor dopants. If the substitute ion has a higher positive charge than the ion it is replacing, it is called a *donor*. If the substitute ion has a lower positive charge than the ion it is replacing, it is called an *acceptor*.

The perovskites PbZrO_3 and PbTiO_3 form a continuous series of solid solutions of the form $\text{PbZr}_{1-x}\text{Ti}_x\text{O}$, where x can vary from 0 to 1. These solid solutions can undergo a rich variety of ferroelectric (FE), paraelectric and antiferroelectric transitions brought on by changes in composition, temperature, electric field and/or stress. They also exhibit large spontaneous polarisation and piezoelectric coefficients.

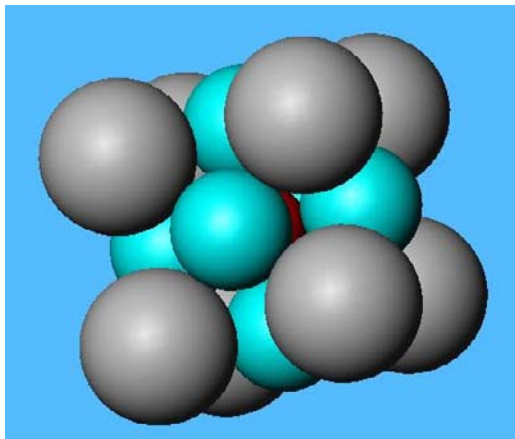


Fig. 9.5 Crystalline structure of PZT. The atoms are scaled for lead zirconate, with Zr at the center.

Above its Curie temperature, PZT has a cubic perovskite crystal structure (see Fig. 9.5) and is paraelectric — i.e. no dipoles are present. Its relative dielectric constant and coupling coefficient have a distinct maximum in the vicinity of the Curie temperature. Below its Curie temperature, its cubic lattice is distorted to either a high temperature rhombohedral, low temperature rhombohedral or tetragonal crystalline structure, depending on the relative compositions of PbZrO_3 and PbTiO_3 , and dipoles are formed. The phase diagram for PZT is shown in Fig. 9.6. The rhombohedral and tetragonal phases are separated by an almost temperature independent *Morphotropic* (composition dependent) *Structural Boundary* (MPB) at which there is an abrupt structural change in the PZT's crystalline structure. The MPB depends on the relative composition of lead zirconate and lead titanate. It is not a sharp boundary, but rather a temperature dependent range of compositions over which there is a mixture of tetragonal and monoclinic phases. At room temperature, the two phases coexist when the concentration of lead titanate lies between 45 and 48%.

The piezoelectric activity of PZT peaks in the region of the MPB. It has been suggested by Moulson [18] that this increase in activity is due to relatively large ionic displacements associated with either mechanical or electrical stress — i.e. induced rotation of the monoclinic axis.

When the mixture is rich in Zr, the high temperature paraelectric phase will transition from the cubic phase structure into either a rhombohedral ferroelectric phase or orthorhombic antiferroelectric (AFE) phase

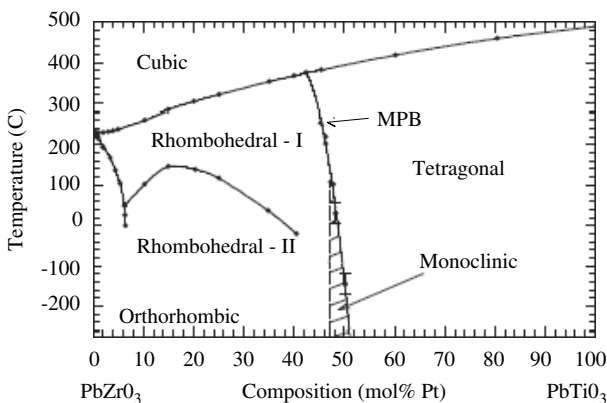


Fig. 9.6 Phase diagram for PZT (courtesy of W. Hackenberger and E. Alberta, TRS Technologies).

upon cooling. The rhombohedral ferroelectric region actually consists of two phases: a high temperature phase of symmetry denoted by R3m and a low temperature phase of symmetry denoted by R3c, the latter of which has a unit cell double that of the former.

In the FEG experiments conducted by the authors, the particular composition used in most of their experiments was Zr rich EC-64 produced by the EDO Corporation. This composition has a high coercive field, high coupling coefficient and low dielectric loss under high driving fields. Its composition is $\text{Pb}(\text{Zr}_{52}\text{Ti}_{48})\text{O}_3$. This particular composition undergoes a polarised-to-unpolarised transition when shocked as the result of domain switching, which is a lossy process with a large portion of the stored energy being converted into heat. The ferroelectric properties of EC-64 are provided in Table 9.2.

A particularly interesting member of the Zr rich PZT family that the authors used in many of their FEGs is one having a composition of $\text{PbZr}_{0.95}\text{Ti}_{0.05}\text{O}_3$ (PZT 95/5) doped with a small amount of Nb to stabilise the R3c phase and to reduce dielectric losses. When cooled at a pressure of 1 bar, it transforms from the paraferroelectric (PF) phase to the R3m phase and then, near room temperature, to the R3c phase. Application of a modest pressure causes the R3c phase to transition into the AFE phase. In other words, under certain conditions PZT 95/5 2Nb lies near a boundary separating the FE and AFE phases. At ambient conditions, it is ferroelectric and can be poled, but if the pressure is increased to ~ 0.3 GPa, it is

Table 9.2 Mechanical, electrical and piezoelectric properties of EC-64 produced by EDO Corporation.

Properties	Metric Units
Mechanical Properties	
Density	7.5 g/cm ³
Elastic Modulus	78 GPa
Electrical Properties	
Curie Temperature	320 °C
Dielectric Constant	1300
Dissipation Factor	0.40
Piezoelectric Properties	
Longitudinal Coupling Factor, k_{33}	0.71
Transverse Coupling Factor, k_{31}	0.35
Planar Coupling Factor, k_p	0.60
Transverse Charge Coefficient, d_{31}	-127×10^{-12} m/V
Longitudinal Voltage Coefficient, g_{33}	25×10^{-3} Vm/N
Longitudinal Charge Coefficient, d_{33}	295×10^{-12} m/V
Transverse Voltage Coefficient, g_{31}	-10.7×10^{-3} Vm/N
Mechanical, Q	4000

near its AFE phase boundary and the bound charge in a poled sample can be rapidly released. Using dielectric measurements and neutron diffraction studies, Avdeev, Jorgensen and Short [19] showed that the thickness and the size of the sample have a significant influence on the boundary between the FE and AFE phases when subjected to stresses due to anisotropic cell contractions. Based on work done by Sandia National Laboratory and others, this particular composition considerably outperforms the EC-64 by delivering much higher open-circuit and load voltages. The properties of PZT 95/5 produced by TRS Technologies are presented in Table 9.3.

The TRS PZT 95/5 [18] is formulated to provide maximum discharge efficiency during shock compression. There are two variants of TRS PZT: monolithic and multilayer to achieve maximum high voltage and high current, respectively. Conventionally fired TRS high voltage PZT 95/5 can achieve open-circuit voltages of up to 115 MV/m (theoretical limit) and charge densities of approximately 0.32 C/m². The high-voltage variant of their PZT can be produced as blocks, cylinders, rings and plates (Fig. 9.7). Both thick film silver and thin nickel/gold electrodes can be applied. The size ranges up to 2–3 inches wide for the plates and thicknesses up to 2 inches for the cylinders. The high current variant of their PZT can be produced as rectangular or circular plates up to 1 inch wide with an active layer of thicknesses as thin as 30 µm.

Table 9.3 Specifications of TRS PZT 95/5 (courtesy of TRS Technologies). Quantities denoted by * measured at 25 C, 1 V and 1 kHz.

Properties	Metric Units
Dielectric Constant and Loss* — Unpoled (-/%)	350/2.00
Dielectric Constant and Loss* — Poled (-/%)	295/1.97
Dielectric Constant* — Depoled (-)	225 est.
Dielectric Constant (MV/m)	8.0
Remanent Polarisation, P_r (C/m ²)	0.32–0.38
Coercive Field, E_c (MV/m)	1.2
Piezoelectric Coefficients, d_{33}/d_{31} ($\times 10^{-12}$ C/N)	68/-16
Piezoelectric Coefficients, g_{33}/g_{31} ($\times 10^{-3}$ Vm/N)	26.3/-6.0
Piezoelectric Coupling, $k_p/k_{31}/k_t$ (-)	0.18/0.11/0.46
Elastic Compliance, $s_{11}^E/s_{12}^E/s_{33}^E$ ($\times 10^{-12}$ m ² /N)	7.68/-1.97/8.37
Elastic Stiffness, $c_{11}^E/c_{12}^E/c_{33}^E$ ($\times 10^9$ m ² /N)	130/-508/120
Acoustic Velocity/Poisson Ratio (m/s)	4200/0.26
Thickness Mode, N_t/Q_m (Hz·m)	2100/15

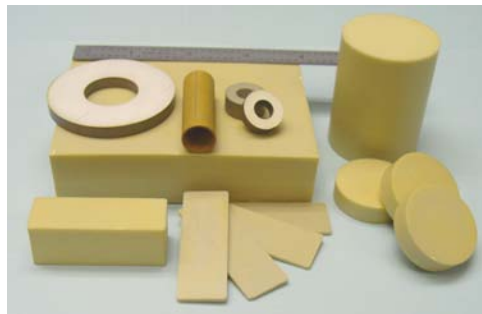


Fig. 9.7 Samples of PZT 95/5 produced by TRS Technologies (courtesy of Wes Hackenberry and Ed Alberta).

The performance characteristics of TRS PZT 95/5 are presented in Fig. 9.8. The temperature dependencies of TRS's high voltage and high current PZT 95/5 are presented in Figs. 9.9 and 9.10, respectively. The Nb doped version of PZT 95/5 undergoes a ferroelectric-to-antiferroelectric transition when shocked, which is an instantaneous low-loss process.

9.7.2 Important PZT Parameters

In working with explosively driven PZT, certain mechanical, electrical and piezoelectric properties are more important than others. For example, in the

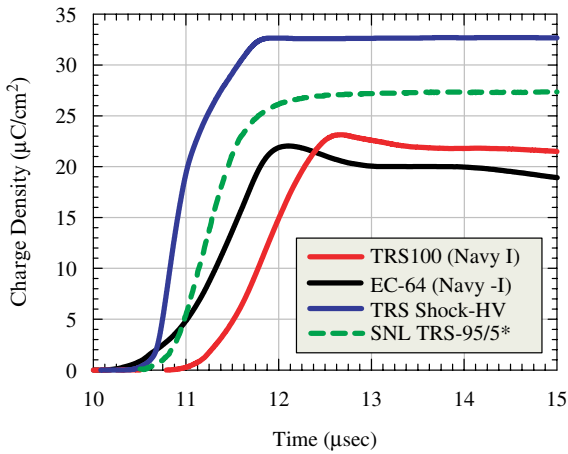


Fig. 9.8 Charge per unit electrode area released during explosive depolarisation of several ferroelectric compositions including TRS 95/5 (Shock-HV), two Department of Defense Type I piezoelectrics (TRS100 and EDO EC-64) and data from the literature for Sandia PZT 95/5 with controlled porosity (Furnish *et al.* [31]).

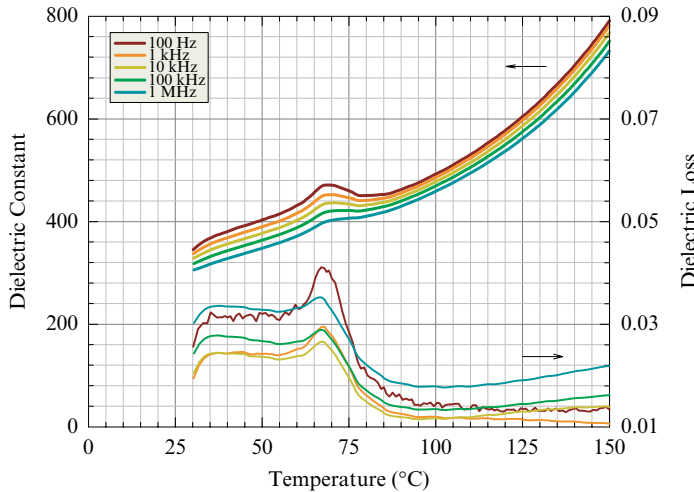


Fig. 9.9 Dielectric constant and dielectric loss vs. temperature and frequency for PZT 95/5. The anomaly near 70°C is a phase transition between two different rhombohedra ferroelectric phases. The Curie temperature is above 150°C .

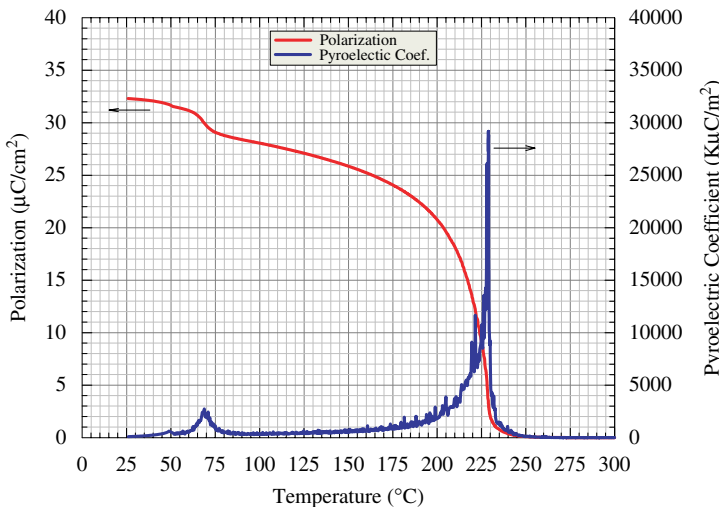


Fig. 9.10 PZT 95/5 remnant polarisation vs. temperature and the resulting pyroelectric coefficient (linear relationship between polarisation and temperature). The polarisation goes to zero at the Curie temperature (230°C) when the pyroelectric coefficient is at a maximum. The rapid decrease in polarisation above 175°C indicates thermally induced depoling.

FEG, stress drives the material into a smaller volume, thus the hydrostatic component of the stress is important. Uniaxial compressive stress parallel to the polarisation will first drive domain switching followed by phase transformation, possibly causing the electrical output to spread out in time. Uniaxial stress perpendicular to the polarisation does not drive domain switching, but the hydrostatic component of the stress drives a phase transformation.

Two parameters that contribute to the final electric field (open circuit) in the case of PZT 95/5 are the dielectric permittivity in the depoled state and the threshold electric field or dielectric strength for an electric field driven phase transformation from the AFE to the FE states. The latter threshold is stress dependent — i.e. the higher the stress, the higher the electric field. Relative to the FEG with PZT 95/5 elements, the two parameters that will increase the explosively generated energy density are the remnant polarisation, which needs to be as large as possible, and the dielectric permittivity in the AFE state, which must be as small as possible.

If it is assumed that the stress drives the material into the AFE state under short-circuit conditions and then an electric field is applied, the

electric field should produce a double hysteresis loop associated with driving the material from the AFE state to the FE state. A further increase in stress makes the AFE state more stable, so the field necessary to drive the material to the FE state is higher. If the circuit had been initially open, an applied stress would have driven the electric field up. The maximum field is found by extrapolating the linear part of the $D - E$ curve all the way up to the initial polarisation level.

To further understand the importance of the ferroelectric properties upon FEG operation, both their intrinsic and extrinsic effects need to be understood. Intrinsic effects have to do with the shifting of ions within a unit cell, while extrinsic effects are concerned with the moving of domain walls around.

9.7.2.1 Intrinsic Effects

Considering the schematic of the lead titanate unit cell shown in Fig. 9.11, this perovskite unit cell can be thought of as a positively charged ion (the central titanium ion) in a negatively charged cage (the oxygen octahedron

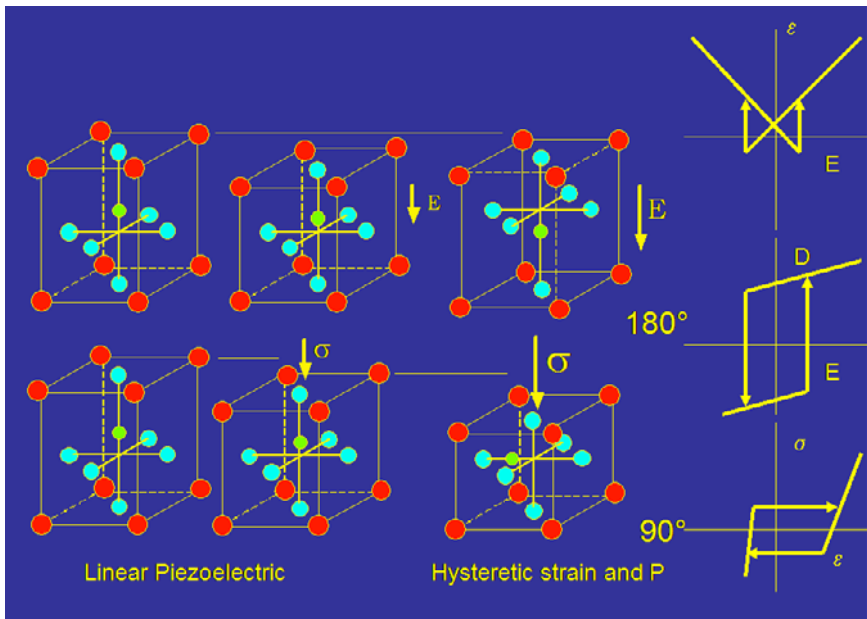


Fig. 9.11 Diagram illustrating the intrinsic properties of PZT.

cage). If an electric field is applied, the ions move relative to one another and the crystal structure distorts. The relative motion of the ions changes the dipole moment of each unit cell. The dipole moment per unit volume is the definition of polarisation. The easier it is to move the ions around, the larger the dielectric constant of the material. If the unit cell is ‘clamped’ so the shape of the unit cell cannot change, i.e., the ions are prevented from moving much, the constant strain dielectric constant would have a much lower value than when unclamped. A larger dielectric constant typically means flatter energy wells, which means it is easier for the ions to move. This implies a lower stiffness and larger piezoelectric constant. The compliance is the inverse of the stiffness and is typically measured at constant electric field, which means electrodes must be applied to the material and short-circuited to prevent voltage build up at the surface when the crystalline structure is deformed. If the measurements are done open circuit, an electric field is generated that tends to hold the ions in their original positions, thus stiffening the material.

9.7.2.2 Extrinsic Effects

Figure 9.12 shows two types of domain walls in PZT: 90 degrees and 180 degrees. When an electric field is applied, the 90-degree wall moves, causing a large strain change due to strain differences across the walls. The domain motion tends to be an irreversible process that generates heat and results in hysteresis. When a domain wall moves, there is a large change in polarisation that significantly increases the dielectric constant. Donor doping (soft PZT) tends to make it easier for domain walls to move (higher dielectric constant) and acceptor doping (hard PZT) tends to make it harder for walls to move (lower dielectric constant). Higher dielectric

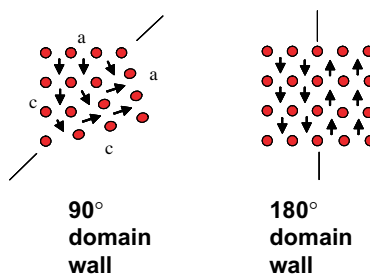


Fig. 9.12 Diagram illustrating the extrinsic properties of PZT.

constant means higher losses associated with domain motion, but it also means higher piezoelectric coefficients. Easier domain wall motion also lowers the stiffness (higher compliance).

9.7.2.3 PZT 95/5

For a poled piezoelectric like PZT 95/5 [20], the dielectric constant, K , is related to the piezoelectric properties and the elastic constant by the following formula:

$$K = \frac{d_{33}^2}{\varepsilon_0 S_{33} E R_{33}^2}, \quad (9.18)$$

where k_{33} is the coupling coefficient, d_{33} is the piezoelectric coefficient and s_{33} is the elastic compliance. Note that the subscript on d_{33} denotes the charge density developed per unit of mechanical stress or, alternatively, the strain developed per unit of electric field strength, in the polarisation direction. The subscript 33 in s_{33} is the ratio of the mechanical strain in direction 3 to the mechanical stress in direction 3, where direction 3 is the direction long which the polarisation vector lies. Relative to the FEG, this would be the longitudinal mode. The formula indicates that materials with high d_{33} will have a high K or, conversely, materials with a low K will have a low d_{33} . It is not possible to decouple these effects — i.e. these two parameters cannot be changed independently of each other.

A more fundamental relationship is the formula $K \sim dP/dE$, which is the rate of change in polarisation with respect to electric field. For a poled ceramic, the dielectric constant will gradually decrease as the electric field increases, since the material is approaching saturation. When a poled ferroceramic is depolarised, it yields an energy density of $e = P_r \cdot E$ in joules/cm³, where P_r is the remnant polarisation — i.e. the charge per unit area stored in the ceramic — and E is the electric field that develops between the sample electrodes when the ceramic is shock depolarised. The dielectric constant determines how high E will be according to the equation $E = P_r/K\varepsilon_0$. Therefore, a lower dielectric constant will result in a higher electric field and a higher energy density. However, in practice, the electric field is limited by the material's breakdown strength rather than the dielectric constant. Note that for PZT 95/5, the dielectric constant of interest is in the shocked induced antiferroelectric phase.

PZT 95/5 has a lower dielectric constant ($K = 200\text{--}300$) than other conventional forms of PZT ($K = 1500$); therefore, it potentially has a

much higher energy density, assuming a high breakdown strength can be achieved. Therefore, PZT 95/5 is preferable for FEGs over other forms of PZT because it has a higher P_r and a lower dielectric constant to produce higher energy densities. This is just the opposite of the situation for capacitors, where energy is being stored in an applied electric field rather than generating an electric field due to a phase change in FEGs. Increasing the energy density in a capacitor requires an increase in the dielectric constant. In summary, shock discharging a high dielectric constant material requires more mechanical work to yield a large electric field, while for capacitors a high dielectric constant material can do more work at a given electric field than a low dielectric material.

If a ferroceramic is being completely depoled (ferroelectric effect), the piezoelectric constant is not relevant, but if the material is not being depoled (piezoelectric effect), the piezoelectric constant is important to the generation of electric charge and, therefore, electric field across the element, from an applied stress. The direct piezoelectric effect relates the electric displacement to the applied stress by the formula: $P_i \sim D_i = d_{ij}T_j$, where d_{ij} is the piezoelectric coefficient in pC/N, D_i is the electric displacement and T_j is the applied stress. If the material is not being depoled, then the piezoelectric coefficient should be as high as possible; however, the dielectric constant will also be high, which limits the energy density, so there will be a trade-off that results in compositions like EC-64 being the optimum for stress, not shock, generated charge applications. In summary, PZT 95/5 has a low piezoelectric coefficient and would not be the best material for generating electric charge using the piezoelectric coefficient. Thus, P_r is more important than d_{ij} when depolarising PZT 95/5. The relationship between P_r and d_{ij} is very complex and highly material specific.

The compliance is related to other properties. As d_{33} increases, the compliance tends to increase. PZT 95/5 is much stiffer than other commercial ferroelectrics, thus it has a low d_{33} , which means it requires more electrical energy to mechanically deform it through the piezoelectric effect. Compliance does not matter very much when shock depolarising a material. For the case of PZT 95/5, the amount of stress-induced volume change during a phase transition would be more important than the compliance. If an FEG that uses a very small amount of HE is desired, then the compliance may become more important.

PZT 95/5 has a number of advantages over other PZT compositions including

- Energy is converted from mechanical energy to electrical energy in a field induced phase transition, which means it can be rapidly discharged.
- Capacitance increases with voltage.
- Very fast discharge times ($<1\ \mu\text{s}$).
- High charge-discharge efficiency (80–90%).
- High-energy densities ($>10\ \text{J/cm}^3$).

9.7.3 Fabrication of PZT

According to Moulson [18], common powder technologies are used to fabricate PZT ceramics. The highest coefficient values are achieved when

- The composition is nearly stoichiometric.
- The fluxing agents and impurities are kept to a minimum.
- The density is as high as possible.

All the constituents of PZT can be precipitated from nitrate solutions or by calcining citrates that contain A-site and B-site ions in a 1:1 ratio. Most compositions at present contain PbO as a major constituent which, despite its volatility at 800°C , must be retained at sintering temperatures that could be as high as 1300°C . Therefore, the atmosphere around the PZT, when fired, must be controlled. *Calcination* (a process that causes the constituents of a mixture to interact by interdiffusion of their ions to reduce the extent of diffusion that must occur during sintering to make a homogeneous body) is carried out in alumina pots with lids. When the PZT undergoes final *sintering* (a process by which a coherent mass is formed by heating without melting), the mixture is surrounded by lead-rich powders, such as PbZrO_3 . Final firing is usually carried out in batch electric kilns.

Simple shapes are formed by die-pressing, bodies of uniform shape are formed by extrusion, thin plates are formed by extrusion and rings are formed by slip casting. Electrodes are applied after machining to the desired shape or finish by applying a suitably formulated silver-bearing paint or by sputtering Ni-Cr or gold on the surface of the PZT. The specimens are poled in transformer oil at temperatures ranging from 100 to 150°C with applied fields ranging from 1–4 MV/m. The temperature and voltage are optimised to yield the maximum piezoelectric coefficients without allowing leakage current to reach levels that could cause thermal runaway and electrical breakdown [18].

9.7.4 Factors that Affect PZT

There are several factors that affect the behavior of PZT, including chemical composition, dopants, density, porosity, particle size, temperature, manufacturing techniques, potting material (requires good mechanical, shock, and electrical properties), shock strength and electric field strength.

9.7.4.1 Dopants

In order to meet the specific requirements for certain applications, piezoelectric ceramics can be modified by doping them with ions which have a valence different to the ions in the lattice. Piezoelectric PZT ceramics having a composition that is near the MPB can be doped with ions to form *hard* and *soft* PZTs. Hard PZTs are doped with acceptor ions such as K^+ , Na^+ (for A site) and Fe^{+3} , Al^{+3} , Mn^{+3} (for B site), creating oxygen vacancies in the lattice. Hard PZTs usually have lower permittivities, smaller electrical losses and lower piezoelectric coefficients. These are more difficult to pole and depole, thus making them ideal for rugged applications. Soft PZTs are doped with donor ions such as La^{+3} (for A site) and Nb^{+5} , Sb^{+5} (for B site) leading to the creation of A and B site vacancies in the lattice. The soft PZTs have higher permittivities, larger losses, higher piezoelectric coefficients and are easier to pole and depole. They can be used for applications requiring very high piezoelectric properties.

According to Jaffe *et al.* [14], the entire family of compositions of PZT with A site additives has a characteristic set of properties:

- Increased dielectric constant.
- Increased remnant polarisation.
- High dielectric loss.
- Increased elastic compliance.
- High piezoelectric coupling factor.
- Low coercive field.
- Relatively square hysteresis loops.
- Greatly increased electrical volume resistivity.
- Anomalously low aging rates.
- Easier nonelastic mechanical deformation.

Haccart, Remiens and Cattan [21] showed that when PZT with a Zr/Ti ratio of 54/46, which is at the MPB for PZT, was doped with Nb, the grain sizes increased and that the dielectric constant and the piezoelectric

coefficient reached their maximum values when the Nb concentration was 2%. When PZT 95/5 is doped with 2% Nb, its nominal state is ferroelectric that lies near an antiferroelectric phase boundary.

9.7.4.2 *Density and Porosity*

Setchell [22] looked at the effects of microstructures on PZT 95/5. *Dynamic yield* is the term given to the observation that an elastic precursor is followed by a plastic wave in plate impact experiments. In the case of porosity, dynamic yield is likely associated with pore collapse and may actually initiate fracture, rather than help to avoid fracture. By adding different types and amounts of organic pore formers to PZT 95/5 prior to bisque firing and sintering, Setchell found that differences in porous microstructured materials having the same initial density have little effect on the mechanical and electrical shock properties of PZT 95/5, but that the initial density of the material has a significant impact. In a follow-on study, Setchell found that when large pore formers are used in materials with the same initial density, the shock properties are insensitive to microstructural differences, but that the smallest pore formers did have an impact in that there was a significantly higher threshold for dynamic yielding due to increased initial density.

Increasing the yield threshold has both advantages and disadvantages. On the one hand, the shock stress required for rapid and complete depoling is only a few tenths of a GPa below the threshold stress for yielding, so increasing the yield strength could reduce the formation of fractures and thus, reduce the probability of electrical breakdown. On the other hand, increasing the initial density and thus, the yield threshold, increases the bound charge and shock velocity, which may not be desirable. Setchell pointed out that materials with limited microstructures would have a broader range of shock pressures for effective depoling without altering other characteristics.

9.7.4.3 *Encapsulating Materials*

Ferroelectric generators are typically filled with an encapsulating or potting material to hold the ferroelectric elements in place, to achieve impedance matching of the shock wave with the elements, and to control the properties of the shock wave. The properties of these potting materials can be affected by temperature changes and/or by adding various materials.

Setchell and others [23, 24] have investigated the effects of temperature on the shock compression of these encapsulating materials, namely epoxy, with and without additives. They also investigated the effects of different compositions of alumina (polycrystalline Al_2O_3) additive on the shock properties of epoxy.

Setchell and his co-workers examined the effects of temperature over an initial temperature range of -50°C to $+70^\circ\text{C}$. They found that there was a clear trend of increasing inelastic features in compressive waveforms with decreasing temperature and that these temperature effects are more pronounced in epoxies with the alumina additive. In both cases, the release wave speeds decreased as the temperature decreased. The epoxies without the alumina tended to be viscoelastic, while the epoxies with alumina were highly dispersive and had no elastic regime.

Setchell also found that increasing the volume fraction of alumina resulted in steadily increasing Hugoniot states, wave rise times and release wave velocities. He also observed that the difference between the release wave and shock wave velocities increased significantly as the concentration of alumina increased, resulting in stronger wave attenuation. Changes in the size and shape of the alumina particles had little affect with the exception that they tended to cause viscous spreading of the shock wave profiles during shock compression.

9.7.4.4 Shock and Electric Field Amplitudes

Investigating the shock response of normally poled PZT 95/5 to uniaxial strain, Setchell *et al.* [25, 26] found that the amplitude of the shock wave and of the electric field within the PZT element has an impact on the amount of electric current delivered to an external load. The peak electric fields generated within the element were varied by varying the output circuit resistance, since a portion of the depoling current is retained on the element electrodes to account for the capacitance of the PZT sample, and the shock pressures were varied by varying the velocity of an impacting flyer plate. The shock pressures were varied from 0.6 to 4.6 GPa, and the peak electrical fields within the sample were varied from 0.2 to 37 kV/cm. Setchell found that a nearly constant current, which was governed simply by the remnant polarisation and the shock velocity, was achieved when the pressure was 2.4 GPa and the electric field was at its lowest value. Also, decreasing the shock pressure and increasing the electrical field within the sample resulted in reducing the amount of current

delivered to the load, which is an indication that the field retards the depoling kinetics.

9.7.5 Optimisation of PZT for FEGs

There is an ongoing effort by TRS Technologies and HEM Technologies [27–29] to optimise the properties of PZT for use in FEGs. For comparative purposes, they investigated 4 different cylindrical PZT materials of different thicknesses: High Voltage (HV) Shock Discharge Elements, High Current (HC) Shock Discharge Elements and two Type I Navy PZT elements — i.e. EDO EC-64 and TRS-100. High voltage and high current shock discharge elements are made from PZT 95/5. All these elements are specially designed to operate in the ferroelectric depolarisation regime, unlike other commercial ferroelectrics, which are designed to resist depolarisation. Table 9.4 lists the dimensions and piezoelectric properties of these elements.

Two sets of measurements were made using these materials: a shock depolarisation test into a low-impedance load and a dielectric breakdown test. The results of the dielectric strength measurements are presented in Fig. 9.13 and of the shock depolarisation measurements in Table 9.5. Based on the limited testing done, it is clear that the Shock HV and HC samples outperform the other types of PZT used in FEGs. The thick Shock HV samples produce almost an order of magnitude more power without power conditioning systems, making them the better material for direct drive applications.

In summary, the goal is to increase the energy density delivered to the output circuit by PZT 95/5. This is achieved by maximising the remnant polarisation in the ferroelectric phase, achieving complete depolarisation by

Table 9.4 List of materials used in HEM/TRS assessment of various PZT materials for use in FEGs.

Materials	Height (mm)	Diameter (mm)	d_{33} (pC/N)	ε_r
TRS Shock HV Thick	5.08	25.4	75	300
TRS Shock HV Thin	0.91	25.4	75	300
TRS Shock HC Thick	2.79	25.4	75	300
TRS Shock HC Thin	1.60	25.4	75	300
EC-64	5.08	25.4	290	1300
TRS-100	5.08	25.4	350	1450

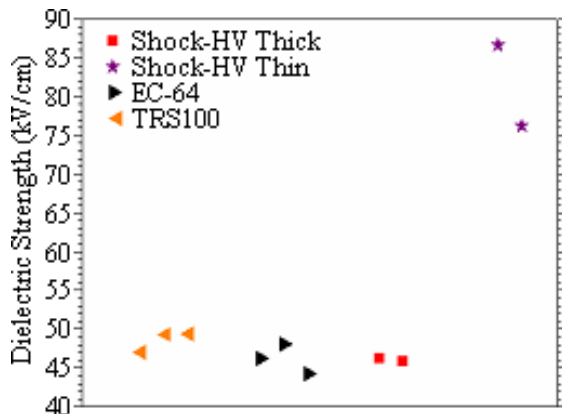


Fig. 9.13 Measured dielectric strengths of several different types of PZT used in FEGs [26–28].

Table 9.5 Shock depolarisation measurements of various PZT materials used in FEGs [26–28].

Measured Parameter	Shock HC Thick	Shock HC Thin	Shock HV Thick	Shock HV Thin	EC-64	TRS-100
Capacitance (nF)	487	250	0.27	1.47	1.15	1.28
Current (A)	151	55.1	327	47	113	117
Voltage (V)	170	60.9	361	52.6	124	131
Power (kW)	25.5	3.36	118	2.47	13.8	15.2
Energy (mJ)	68.9	22.6	35.1	0.32	9.89	16.7
Energy Density (mJ/cm ³)	48.9	27.9	13.7	0.69	3.85	6.50
Charge (μC)	700	458	165	6.1	112	123
Pulse Width (μs)	3.85	8.88	0.34	0.13	0.95	1.02
Rise Time (μs)	1.48	2.10	0.20	0.07	1.13	0.73

the shock wave, maximising DC resistivity and maximising the dielectric breakdown strength of the element.

9.7.6 PZT Failure Modes

Understanding the failure mechanisms of ferroelectrics is critical to setting design margins, material acceptance and FEG reliability. Acceptance testing of PZT 95/5 used in high voltage devices is limited by high voltage breakdown that occurs late in time as the shock wave propagates through a test sample. In recent years, Setchell *et al.* [30] found a previously unknown

failure mechanism. They now believe that in a PZT 95/5 element being compressed well beyond its dynamic yield threshold, failure occurs near the front of the PZT bar, resulting in significant material damage, followed by a loss in dielectric strength during the subsequent unloading due to the unsupported shock structure. At cold temperatures, this failure mechanism is exacerbated.

In summary, the main failure mechanisms in PZT appear to be fracturing of the material and electrical breakdown across fractures or on the surface of the material.

9.8 Chapter Summary

In summary:

- The primary parameter that affects FEG performance is the remnant polarisation, of the ferroelectric material. The remnant polarisation is directly proportional to the energy density of the shock loaded material.
- When the FEG is operated in an open-circuit mode, the electric field is limited by the breakdown strength of the ferroelectric material.
- The piezoelectric properties of ferroelectric materials have no influence on FEG performance.
- The volume of the ferroelectric sample does not effect its properties. However, porosity (low density) tends to reduce the ferroelectric properties in proportion to the volume fraction of pores. The exact dependence of these properties on porosity does depend on which property is being considered. That is, the elastic constants have a different dependence on porosity than do the dielectric properties. Most of the functions that relate the properties of a ferroelectric material to porosity are empirical in nature.
- PZT 95/5 can be produced by conventional ceramic manufacturing techniques and may be made in a wide range of shapes and sizes.
- The ferroelectric material PZT 95/5 differs from other commercial PZT materials in the following ways:
 - The electrical breakdown strength of shock depoled PZT 95/5 is higher than that of commercial PZTs.
 - The open circuit stored energy density of PZT 95/5 is three to four times higher than that of commercial PZTs.

- The voltage generated by FEGs with PZT 95/5 is two to three times higher than that produced by FEGs with commercial PZT.
- The pressure induced phase transition of PZT 95.5 to its anti-ferroelectric phase results in complete depolarisation at around 0.3 GPa.

9.9 Suggested Reading on Ferromagnetic Materials

- W. G. Cady, *Piezoelectricity: An Introduction to the Theory and Applications of Electromechanical Phenomena in Crystals*, Dover Publications (1964).
- T. Mitsui, I. Tatsuzaki and E. Nakamura, *An Introduction to the Physics of Ferroelectrics*, Gordon and Breach, New York (1976).
- J. M. Herbert, *Ferroelectric Transducers and Sensors (Molecular Crystals and Liquid Crystals)*, Gordon and Breach (1982).
- G. Smolenskii, *Ferroelectrics and Related Materials (Ferroelectricity and Related Phenomena)*, TH-ROUTL (1984).
- G. W. Taylor, *Piezoelectricity*, Routledge Press, New York (1985).
- Y. Zhiwen, *Ferroelectrics Research in the People's Republic of China: A Special Issue of the Journal Ferroelectrics*, Routledge (1990).
- C. Z. Rosen, B. V. Hiremath and R. E. Newnham, *Piezoelectricity*, AIP Press (1992).
- F. Jona and G. Shirane, *Ferroelectric Crystals*, Dover Publications (1993).
- K. Uchino, *Ferroelectric Devices*, CRC Press (2000).
- M. E. Lines and A. M. Glass, *Principles and Applications of Ferroelectrics and Related Materials* Oxford Classic Text in the Physical Sciences, (2001).
- C. Pazde-Araujo, R. Ramesh and G. W. Taylor, *Science and Technology of Integrated Ferroelectrics* (Ferroelectricity and Related Phenomena), CRC Press (2001).
- K. Krakauer, *Fundamental Physics of Ferroelectrics: 11th Williamsburg Ferroelectrics Workshop*, AIP Press (2001).
- J. Yang, *Introduction to the Theory of Piezoelectricity*, Springer (2004).
- A. Amau and A. Vives, *Piezoelectric Transducers and Applications*, Springer (2004).
- A. S. Sidorkin, *Domain Structure in Ferroelectrics and Related Materials*, Cambridge International Science Publishing, Ltd. (2006).
- J. Yang, *Analysis of Piezoelectric Devices*, World Scientific Publishing Company (2006).

- K. Rabe, C. H. Ahn and J. Triscone, *Physics of Ferroelectrics: A Modern Perspective*, Springer (2007).

Bibliography

- [1] M. Budimir, *Piezoelectric Anisotropy and Free Energy Instability in Classic Perovskites*, Thesis No. 3514, Ecole Polytechnique Federal de Lausanne (2006).
- [2] J. Zelenka, *Piezoelectric Resonators and Their Applications*, Elsevier, Amsterdam (1986).
- [3] L. E. Cross and R. E. Newnham, History of Ferroelectrics, *Ceramics and Civilization, High-Technology — Past, Present, and Future*, Vol. III, The American Ceramic Society (1987).
- [4] J. Fousek, Joseph Valasek and the Discovery of Ferroelectricity, *Proceedings of the Ninth IEEE International Symposium on Applications of Ferroelectrics* (University Park, PA, 1991), pp. 1–5.
- [5] J. Valasek, The Early History of Ferroelectricity, *Ferroelectrics* **2** (1971) 239–244.
- [6] J. Valasek, Piezoelectric and Allied Phenomena in Rochelle Salt, *Physics Review* **15** (1920) 537–538.
- [7] J. Valasek, Piezo-electric and Allied Phenomena in Rochelle Salt, *Physics Review* **17** (1921) 475–481.
- [8] J. Valasek, Piezo-electric Activity of Rochelle Salt under Various Conditions, *Physics Review* **19** (1922) 478–491.
- [9] J. Valasek, Properties of Rochelle Salt related to the Piezoelectric Effect, *Physics Review* **20** (1922) 639–664.
- [10] C. A. Randall, R. E. Newnham and L. E. Cross, History of the First Ferroelectric Oxide, BaTiO₃, The Electronics Division, <http://209.115.31.62/electronics/division/> (26 Sept. 2004).
- [11] L. E. Cross and R. E. Newnham, History of Ferroelectrics, from *Ceramics and Civilization, Volume III, High-Technology Ceramics — Past, Present, and Future* (The America Ceramic Society, 1987), pp. 289–301.
- [12] H. Thurnauer and J. Deaderick, Insulating Material, U.S. Patent No. 2,429,588, Oct. 21, 1947 (Filed in 1941).
- [13] R. B. Gray, U.S. Patent No. 2,486,560, Nov. 1, 1949 (Filed in 1946).
- [14] B. Jaffe, W. R. Cook and H. Jaffe, *Piezoelectric Ceramics*, Academic Press, New York (1971).
- [15] K. Uchino, *Ferroelectric Devices*, Marcel Dekker, Inc., New York (2000).
- [16] C. Kittel, *Introduction to Solid State Physics*, 5th edn., John Wiley & Sons, New York (1976).
- [17] G. Yank, S. F. Liu, W. Ren and B. K. Mukherjee, Uniaxial Stress Dependence of the Piezoelectric Properties of Lead Zirconate Titanate Ceramics, *Proceedings of the 12th IEEE International Symposium on Applications of Ferroelectrics* **1** (2000) 85–88.

- [18] A. J. Moulson and J. M. Herbert, *Electroceramics*, 2nd Edition, John Wiley & Sons Ltd., West Sussex (2003).
- [19] M. Avdeev, J. D. Jorgensen and S. Short, Pressure-Induced Ferroelectric to Antiferroelectric Phase Transition in $\text{Pb}_{0.99}(\text{Zr}_{0.95}\text{Ti}_{0.05})_{0.98}\text{Nb}_{0.02}\text{O}_3$, *Physical Review B* **73** (2006) 064105-1–064105-14.
- [20] W. Hackenberger and E. Alberta, Private communication, TRS Technologies.
- [21] T. Haccart, D. Remiens and E. Cattan, Substitution of Nb Doping on the Structural, Microstructural, and Electrical Properties of PZT Films, *Thin Solid Films* (Elsevier Science, 2002), pp. 235–242.
- [22] R. E. Setchell, Shock Wave Compression of the Ferroelectric Ceramic $\text{Pb}_{0.99}(\text{Zr}_{0.95}\text{Ti}_{0.05})_{0.98}\text{Nb}_{0.02}\text{O}_3$: Microstructural Effects, *Journal of Applied Physics* **101** (2007) 053525-1–053525-9.
- [23] M. U. Anderson, R. E. Setchell and D. E. Cox, Effects of Initial Temperature on the Shock and Release Behavior of Filled and Unfilled Epoxies, *Shock Compression of Condensed Matter—2001*, eds. M. D. Furnish, N. N. Thadhani and Y. Horie, CP 620 (American Institute of Physics, 2002) pp. 669–672.
- [24] R. E. Setchell, M. U. Anderson and S. T. Montgomery, Compositional Effects on the Shock-Compression Response of Alumina-filled Epoxy, *Journal of Applied Physics* **101** (2007) 083527-1–083527-8.
- [25] R. E. Setchell, S. T. Montgomery, L. C. Chhabildas and M. D. Furnish, The Effects of Shock Stress and Field Strength on Shock-Induced Depoling of Normally Poled PZT 95/5, *Shock Compression of Condensed Matter — 1999*, eds. M. D. Furnish, L. C. Chhabildas and R. S. Hixson, CP505 (American Institute of Physics, 2000), pp. 979–982.
- [26] R. E. Setchell, S. T. Montgomery, D. E. Cox and M. U. Anderson, Dielectric Properties of PZT 95/5 during Shock Compression under High Electric Fields, *Shock Compression of Condensed Matter — 2005*, CP845 (American Institute of Physics, 2007), pp. 278–281.
- [27] S. L. Holt, D. J. Hemmert, J. W. Walter, J. J. Mankowski, J. C. Dickens, M. Kristiansen, L. L. Altgilbers and A. H. Stults, Characterization of Explosively Driven Ferroelectric Generator Material, *Megagauss XI*, November 2006, Santa Fe, NM. (to be Published).
- [28] S. L. Holt, D. J. Hemmert, J. T. Krile, W. S. Hackenberger, E. F. Alberta, J. W. Walter, J. C. Dickens, L. L. Altgilbers and A. H. Stults, Testing of New Ferroelectric Materials for Explosively Driven Ferroelectric Generators, *Megagauss XI*, London, UK (September 2006) (to be Published).
- [29] S. L. Holt, J. T. Krile, D. J. Hemmert, W. S. Hackenberger, E. F. Alberta, J. W. Walter, J. C. Dickens, L. L. Altgilbers and A. H. Stults, Testing of New ferroelectric Elements Custom Engineered for Explosively Driven Ferroelectric Applications, *Proceedings of the 16th IEEE International Pulsed Power Conference*, Albuquerque, NM (November 2007) (to be Published).
- [30] R. E. Setchell, J. K. Keck, S. T. Montgomery, M. U. Anderson, and D. E. Cox, Failure Mechanisms in Explosively Driven Power Supplies,

Science-Based Solutions for NNSA Mission Needs, Sandia National Laboratory (2003). See website: http://www.sandia.gov/pcnsc/research/research-briefs/2003/Failure_Mechanisms_in_Explosively_Driven_Power_Supplies_by_R.E.Setchell,_et.al..pdf.

- [31] M. D. Furnish, L. C. Chhabidas, R. E. Setchell and S. T. Montgomery, Dynamic Electromechanical Characterization of Axially Poled PZT 95/5, in *Shock Compression of Condensed Matter — 1999*, eds. M. D. Furnish, L. C. Chhabidas and R. S. Hixson, CP505 (American Institute of Physics, New York, 2000), pp. 975–978.

Chapter 10

Phase Transformations in Ferroelectric Crystals

10.1 Introduction

Ferroelectric materials with the perovskite-type crystal structure are important to a broad range of applications that utilise electromechanical coupling. Although they were initially developed for use in sonar systems, they have since found utility in applications that include fish finders, actuators for nano-positioners, ultrasonic motors, active scalpels and in numerous electro-optical devices. In most of these applications, the non-linearity and hysteresis associated with phase transformations are to be avoided. Although phase transformations involve large strain and polarisation changes that could be very useful, this is typically accompanied by significant hysteresis and cyclic degradation of the material, limiting the ability to exploit these transformations in applications requiring high frequency, such as in resonant devices. There are certain applications, however, where exploitation of the domain switching and phase transformation behavior is advantageous. Domain switching and field induced phase transformations can produce high current for a short period of time, if short-circuited, or high voltage, if open-circuited. This behavior is utilised in ferroelectric generators.

In this chapter, the material behavior will be discussed from a mechanics of materials perspective with focus on developing relationships between the macroscopically observed behavior and the underlying phenomena that occur on smaller length scales. This begins with a description of the perovskite type crystal structure and how this structure leads to ferroelectricity. It then examines how the material behavior at the length scale of the unit cell leads to the behavior of domains, single crystal grains and the ceramic. Although the effect of dopants and the associated defect structures

within the crystal lattice can be used to modify the material behavior, little will be said about this as there are many excellent books on this subject; rather, emphasis will be placed on describing the underlying phenomena that occur at multiple scales of length and time. This leads to a fundamental understanding of why the material behaves in the way it does and how it can be optimised for FEG applications.

10.2 Perovskite-Type ABO_3 Crystal Structure

The perovskite-type crystal structure is an ABO_3 oxide [2]. The high temperature cubic phase of lead titanate is shown schematically in Fig. 10.1(a), with unit cell dimensions a_0 . The unit cell is charge neutral. The A sites (corners of the unit cell) are occupied by Pb^{2+} ions, the B sites (center of the unit cell) are occupied by Ti^{4+} ions and the face centers are occupied by O^{2-} ions. The charge neutrality of the unit cell is readily shown by summing the contribution of charge from each ion to the unit cell. The center ion contributes a charge of +4, each of the eight corner ions are shared with eight neighboring unit cells, giving a contribution of one-eighth of their charge to the unit cell shown, so there is a net contribution of +2 from the corner ions, and each of the six-face centered oxygen ions is shared with one neighboring unit cell, so there is a net charge contribution of -6. These charge contributions sum to zero.

Certain perovskite type oxides undergo a phase transformation into a ferroelectric phase when cooled through their transition temperature. A detailed discussion of first-and second-order transformations is provided by Lines and Glass [3]. This characterises the transformation based on the behavior of the dielectric anomaly that occurs as the material is cooled

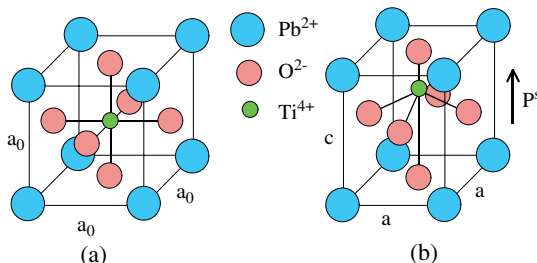


Fig. 10.1 Schematic diagrams of the crystal structure of (a) the high-temperature cubic phase of lead titanate and (b) of the lower-temperature tetragonal ferroelectric phase.

through the phase transition temperature. At this point, focus will be on the structural change rather than its description using phenomenological models. In the case of lead titanate, the cubic phase transforms to the tetragonal phase as the material is cooled through the Curie temperature. This is shown schematically in Fig. 10.1(b). The tetragonal phase has a polar axis. The unit cell is elongated in this direction to length c , and contracted transverse to this direction to length a . The source of the ferroelectric effect is described in terms of a slightly simplified schematic of the structure in which the central ion is shifted upward relative to the surrounding oxygen octahedron. This enables a discussion of the phenomenon without addressing the details of exactly how the various ions actually shift and how the oxygen octahedra tilt in some compositions.

The spontaneous polarisation and spontaneous strain can be defined in terms of the unit cell geometry. Consider the case where the central ion has shifted upward relative to the oxygen octahedron. This moves the positive charge upward relative to the negative charge resulting in a dipole moment $p = Qd$, where Q is the charge that has moved through a separation distance d . The dipole moment per unit volume is the polarisation of the unit cell. The polarisation induced by the phase transformation is referred to as the spontaneous polarisation, P_S . In the tetragonal structure there are six possible directions of spontaneous polarisation — i.e. towards the center of each face. When the structure is poled in a particular one of these directions, it will be referred to as a crystal variant, thus there are six crystal variants in the tetragonal structure. The spontaneous polarisation is accompanied by a spontaneous strain with principle directions aligned with the polarisation (elongation) and transverse to it (contraction). The spontaneous polarisation vector and strain tensor components in a Cartesian coordinate system referenced to the high temperature cubic phase are given by Eqs. (10.1) and (10.2):

$$[P_S] = \begin{bmatrix} P_S \\ 0 \\ 0 \end{bmatrix} = \begin{bmatrix} Qd/V \\ 0 \\ 0 \end{bmatrix} \quad (10.1)$$

and

$$[\varepsilon^s] = \begin{bmatrix} \varepsilon^s & 0 & 0 \\ 0 & -0.5\varepsilon^s & 0 \\ 0 & 0 & -0.5\varepsilon^s \end{bmatrix} = \begin{bmatrix} \frac{c-a_0}{a_0} & 0 & 0 \\ 0 & \frac{a-a_0}{a_0} & 0 \\ 0 & 0 & \frac{a-a_0}{a_0} \end{bmatrix}, \quad (10.2)$$

where $V = a_0^3$, $a_0 = \sqrt[3]{a^2 c}$, and the spontaneous strain is taken to have zero volume change relative to a reference state at that temperature. Note that a_0 has been used to define a reference volume and is a function of both temperature and phase.

Intrinsic piezoelectricity and ferroelectricity are associated with the spontaneous polarisation and spontaneous strain as was illustrated in Fig. 9.12. If an electric field is applied in the direction of the spontaneous polarisation, it pulls the positive ions in one direction and pushes the negative ions in the other direction. This elongates the unit cell, resulting in a positive strain change (the converse piezoelectric effect). If the electric field is applied in the opposite direction, it tends to shrink the unit cell toward the cubic state. This results in a negative strain change. If the electric field is applied perpendicular to the spontaneous polarisation, the positive charge moves in one direction and the negative charge in the other direction. This results in a shear strain (not shown). This coupling between an electric field and a mechanical field works the other way as well. If a compressive stress is applied in the polarisation direction, the unit cell is shortened and tends toward the cubic configuration. In this case, the polarisation decreases (the direct piezoelectric effect).

Polarisation switching is the term used to describe the hypothetical process of reorienting the polarisation of a single-unit cell in a step-like manner. This concept is used in Preisach type models, where the material is taken to be comprised of a large number of randomly oriented unit cells that behave as switches [4]. In the tetragonal structure, in the absence of stress or electric field, there are six stable polarisation directions corresponding to six equivalent energy minima, one for each tetragonal variant. If an applied electric field exceeds the coercive field and is applied in a direction that drives the polarisation away from its current direction and toward one of the other directions, then it is a driving force for polarisation reorientation. If that driving force exceeds a critical value, then a switch is allowed to take place. The result of step-like switching was illustrated in Fig. 9.12. This simple model gives rise to the step-like hysteresis loops shown at the right. The strain — electric field hysteresis loop shown at the top right displays linear piezoelectricity except during switching, and the electric displacement — electric field hysteresis loop at the center-right displays linear dielectric behavior except when switching.

The slope of the linear portion of the butterfly shaped loop is the piezoelectric coefficient d_{333} , and the slope of the electric displacement — electric field curve is the dielectric coefficient κ_{33} . The top two figures at the left

show the linear piezoelectric response to a negative field. This negative strain change corresponds to moving down to the left on the strain-electric field curve and simultaneously on the electric displacement — electric field curve. When a critical field level is reached, the central ion pops through the center and out the other side. This results in a polarisation reversal, which is seen on the hysteresis loops at the right. When the polarisation switches, the electric field is now aligned with the polarisation and the unit cell is being elongated by the applied field. This corresponds to the jump in the butterfly loop from a negative to a positive strain and a corresponding jump in the polarisation — electric field hysteresis loop.

Switching can also be driven by stress. When a compressive stress is applied in a direction that drives the unit cell toward a cubic shape, the polarisation is reduced. When the applied stress reaches a critical value, the *coercive stress*, the central ion will reorient itself to one of the four side sites. This results in the strain jump shown in the stress-strain hysteresis loop. A tensile stress in excess of the coercive stress will then pop the central ion back to its original position (or 180 degrees away from the initial position), resulting in a positive strain jump.

The unit cell is the smallest repeating unit in the crystal structure. Its behavior gives rise to electromechanical coupling in ferroelectric materials and is the source of the phenomena that occur at higher-length scales. Figure 10.2 is a schematic representation of some of these phenomena and the modeling approaches applicable to each of these scales.

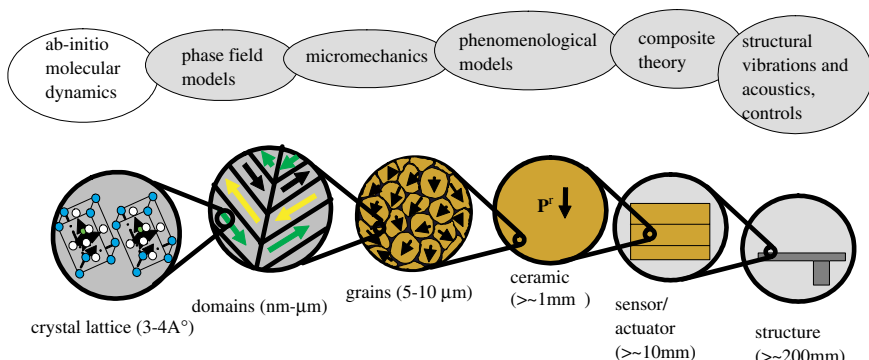


Fig. 10.2 A schematic representation of the phenomena that occur at multiple length scales in ferroelectric ceramic materials.

The smallest length scale shown in Fig. 10.2 is that of the unit cell. Material behavior at this length scale is governed by interatomic potentials, thermal energy and external fields. Current research focus is on the utilisation of ab initio calculations to determine the interatomic potentials, such that the crystal structure and phase stability can be predicted from first principles calculations [5–9]. In the future, molecular dynamics simulations may lead to the ability to simulate the formation of crystals and field driven phase transformations with sufficient accuracy that computational approaches to develop new materials will be viable. Although significant progress has been made in this area, computational material design is still a very active area of research. Domains are observed at the next length scale: they are groupings of like-oriented unit cells and are separated by domain walls. These form along crystal planes that minimise the energy of the structure. Grains are single-crystal regions within a ceramic. All of the unit cells within a grain have the same alignment, yet the grains are subdivided into domains. The ceramic is typically the working scale of the material. This is then built into a sensor or actuator used as part of a structure.

Figure 10.3 is a micrograph of a ceramic specimen. This specimen was cut and polished and then imaged using Electron Backscatter Diffraction. The larger, block-like structures are grains. These are approximately 5 microns across. The striations within the grains are domains: the black areas bordered by white are pores at the grain boundaries.

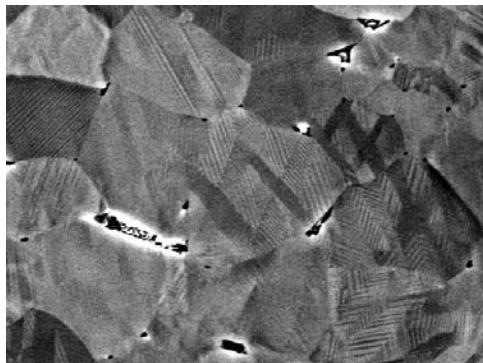


Fig. 10.3 Electron Backscatter Diffraction (EBSD) image of a polished specimen of PZT with morphotropic phase boundary composition. (Work performed in collaboration with Dr. E. Kennik at ORNL through the SHARE program.)

10.3 The Phase Diagram

The phase diagram describes the equilibrium crystal structure at zero stress and zero electric field. Figure 9.6 showed the phase diagram of PZT [2]. The PZT phase diagram displays a paraelectric cubic (P_C) phase at high temperature, a rhombohedral high temperature phase $F_{R(HT)}$ and a rhombohedral low-temperature phase $F_{R(LT)}$ in lead zirconate-rich compositions, an antiferroelectric phase (A_R) in the low temperature very high lead zirconate compositions, a tetragonal phase (F_T) in a lead titanate rich composition and a morphotropic phase boundary (MPB) separating the tetragonal and rhombohedral phases. Many commercial compositions of PZT are formulated near the MPB. These compositions tend to have enhanced piezoelectric and dielectric properties.

Each of the crystal structures can be represented as a small distortion of the high temperature cubic phase. To define the structure, a Cartesian coordinate system will be placed at the center of the cubic unit cell with a coordinate axis passing out the center of each face. Crystallographic directions are often defined using Miller indices, where h , k and l are integers, $[hkl]$ indicates a specific direction in the crystal structure, i.e. any parallel axes in this direction, and $\langle hkl \rangle$ indicates a family of such directions. The notation (hkl) represents a specific crystallographic plane, i.e. any parallel plane with this orientation, and the notation $\{hkl\}$ a family of parallel crystallographic planes. Examples are provided for each of the structures that are of interest to this discussion.

The phase diagram represents the equilibrium phase at zero stress and zero electric field. Just as stress and electric field provide driving forces for transformations from one crystal variant to another (domain switching), they also provide driving forces for phase transformations that involve strain or polarisation changes, respectively. Hydrostatic stress drives phase transformations when there is a volume decrease from the initial phase to the new phase. For example, the low-temperature rhombohedral phase just on the rhombohedral side of the $F_{R(LT)}$ boundary has a higher volume than the adjacent antiferroelectric phase. A compressive stress, therefore, provides a driving force for a ferroelectric-to-antiferroelectric phase transformation. Another example is a material in the cubic phase just above the rhombohedral or tetragonal ferroelectric phase in the equilibrium phase diagram. An electric field provides a driving force to the ferroelectric phase by inducing polarisation. Table 10.1 summarises various types of variant transformations and phase transformations that can take place in the different

Table 10.1 Examples of possible variant transformations, phase transformations and their associated driving forces.

Initial Phase	Process	New Phase	Strain Change	Polarisation Change	Driving Force
$F_{R(LT)}$	Phase Change	A_R	Volume Decrease	Decrease	Compressive Stress
A_R	Phase Change	$F_{R(LT)}$	Volume Increase	Increase	Electric Field
$F_{R(LT)}$	70.5° Switch	$F_{R(LT)}$	Strain Reorientation	Reorientation	Shear Stress, Electric Field
$F_{R(LT)}$	109.5° Switch	$F_{R(LT)}$	Strain Reorientation	Reorientation	Shear Stress, Electric Field
$F_{R(LT)}$	180° Switch	$F_{R(LT)}$	None	Reorientation	Electric Field
F_T	Phase Change	$F_{R(LT)}$	Volume Decrease and Shear Strain	Reorientation	Compressive Stress, Shear Stress, Electric Field
F_T	90° Switch	F_T	Shear Strain	Reorientation	Shear Stress, Electric Field
F_T	180° Switch	F_T	None	Reorientation	Electric Field
F_R	Phase Change	F_O	Strain Change	Change	Stress, Electric Field

compositions. The $F_{R(LT)}$ to A_R (or A_O) transformation is of particular interest in FEG design, as this transformation is from a polar to a non-polar phase and results in a complete release of all polarisation.

The geometry of the different variants and driving forces are described in terms of the cubic phase as a reference. Each of the other phases are obtained by a small distortion of the cubic phase. The tetragonal phase is an elongation along a cube edge, the orthorhombic phase an elongation along a face diagonal and the rhombohedral phase an elongation along a body diagonal.

10.3.1 Cubic

The high-temperature cubic phase is not polar, but the crystal can be cut with faces in specific orientations. The six directions from the center of the unit cell to the center of each face are given by $[001]$, $[010]$, $[100]$, $[00\bar{1}]$, $[0\bar{1}0]$ and $[\bar{1}00]$. The over bars indicate a negative. The first three are labeled in Fig. 10.4. In the cubic system, these can be interpreted to represent components of vectors pointing in the particular direction. The face of the cube intersected by a vector in the $[100]$ direction is a (100) plane. The Miller indices of a plane are found by identifying the intercept of the plane with the coordinate axes, taking the reciprocal and determining the smallest integer values. For the case of the (100) plane, this leads to an intercept with the x -axis at a constant value and no intercept with the y -axis or z -axis (intercept at infinity giving a zero index). Taking the reciprocal and finding the smallest integer value gives (100) . This identifies the plane

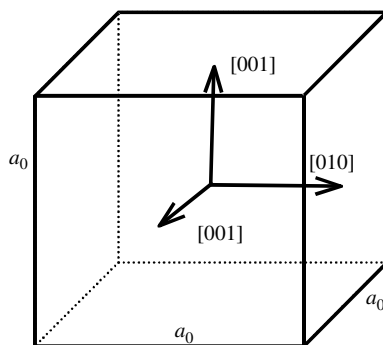


Fig. 10.4 The three crystallographic directions are identified by using this cubic structure.

in terms of the components of a vector normal to the plane. In non-cubic systems, the crystallographic directions used to describe the structure are not necessarily orthogonal. In this case the directions $[hkl]$ may not be taken as Cartesian components of vectors making up a coordinate system. In the cubic system, one can treat these as components of vectors and use the definitions of the scalar product and cross product of two vectors to easily determine if a given direction lies in a given plane. For example, $[001]$ is perpendicular to the plane (001) .

10.3.2 Tetragonal

The tetragonal structure is polar and is elongated in the polar direction. Figure 10.5 shows an example of the tetragonal structure poled in the $[001]$ direction. In this structure, the polarisation must lie in the family of directions $\langle 001 \rangle$. This notation represents each of the six possible polar directions. The spontaneous polarisation vector and spontaneous strain tensor for this structure were discussed above.

The strain and polarisation of a tetragonal crystal cut in a different orientation can be found by using orthogonal transformations. The orthogonal transformations for the spontaneous polarisation (a vector) and the spontaneous strain (a second-order tensor) are given by Eqs. (10.3)–(10.6):

$$\overline{P}_p^S = a_p^i P_i^S \quad (10.3)$$

or in matrix notation

$$[\overline{P}^S] = [A]^T [P^S] \quad (10.4)$$

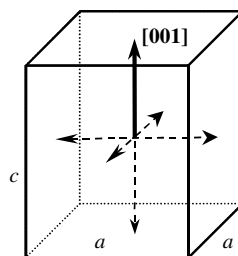


Fig. 10.5 A schematic diagram of the tetragonal structure with the polarisation shown in the z -direction.

and

$$\bar{\varepsilon}_{pq}^S = a_p^i a_q^j \varepsilon_{ij}^s \quad (10.5)$$

or in matrix notation

$$[\bar{\varepsilon}^S] = [A]^T [\varepsilon] [A], \quad (10.6)$$

where a_r^S represents the components of a direction cosine matrix that defines the rotation from the original coordinate system to the new coordinate system and, in the matrix notation, the superscript ' T ' represents the transpose of the matrix. Summation over the repeated indices is implied.

10.3.3 Rhombohedral, F

The rhombohedral structure occurs in PZT compositions that are rich in lead zirconate. The rhombohedral structure is shown in Fig. 10.6. In this structure, the polar axis lies in one of the eight $\langle 111 \rangle$ directions. The structure is elongated in the polar direction and contracted perpendicular to the polar direction. The crystal structure is again defined relative to the cubic structure. Although there are angle changes in the unit cell, the spontaneous strain is small and thus the angle changes are small.

10.3.4 Rhombohedral, AF

At room temperature there is an antiferroelectric phase in PZT. This occurs in compositions with high concentrations of lead zirconate ($> 96\%$). A phase boundary separates these two phases. The rhombohedral antiferroelectric phase has a smaller volume than the rhombohedral ferroelectric phase. There is also an alternating tilt of the oxygen octahedra that shifts the polarisation of neighboring unit cells 180 degrees out of phase. Compositions just on the antiferroelectric side of the morphotropic boundary can be

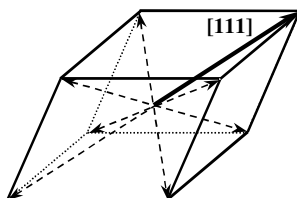


Fig. 10.6 A schematic diagram of the rhombohedral structure with the polarisation shown in the $[111]$ direction.

driven into the ferroelectric phase by application of a strong enough electric field (e.g. PLSnZT) and compositions just on the ferroelectric side of the morphotropic phase boundary may be driven into the antiferroelectric phase by application of compressive stress (e.g. PZT 95/5).

10.3.5 *Orthorhombic*

The orthorhombic structure is observed in some perovskite-type structures such as barium titanate and PMN-xPT (field induced). This structure is shown schematically in Fig. 10.7. The spontaneous polarisation lies in one of the 12 $\langle 110 \rangle$ directions.

10.3.6 *Monoclinic A, B, C*

The monoclinic phase occurs in a number of materials with the perovskite-type structure. It has been observed in morphotropic phase boundary compositions of PZT and PMN-PT. The monoclinic structures allow easy polarisation rotation along one of the edges, along one of the face diagonals or along one of the body diagonals.

10.4 Single-Crystal Behavior

Understanding the behavior of ferroelectric ceramics requires an understanding of the behavior of single crystals. Single-crystal behavior has been studied in a number of materials including barium titanate and, more recently, in PMN-xPT and PZN-xPT. Fig. 10.8 is an optical micrograph of a single crystal of PZN-4.5%PT that has been polarised in the $[110]$ direction. The electrodes have been removed by polishing and the image was taken in transmitted light using an optical microscope. Domains are clearly visible.

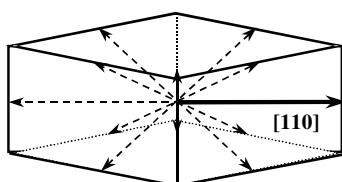


Fig. 10.7 A orthorhombic structure with the polarisation shown in the $[110]$ direction.

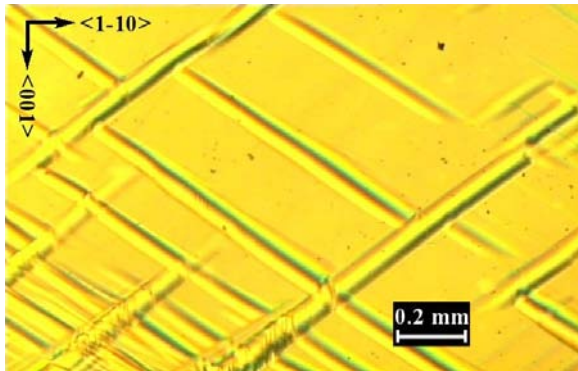


Fig. 10.8 An optical micrograph of single crystal PZN-4.5%PT shows the presence of domains.

10.4.1 Domains (*Crystal Variants*)

Domains are regions of the crystal with like polarisation. Their formation reduces the energy of the crystal by relieving local stresses and by relieving local electric fields. A tetragonal crystal, cut at an angle relative to the polar direction, would have a component of the polarisation leaving the side of the crystal. If there is an electrode on the surface, this would be terminated by a surface charge density on the electrode. If there is no electrode, the vector component would pass out the side of the crystal and give rise to a large local electric field. This high-energy state is reduced by formation of domains.

10.4.2 Domain Walls

Domain walls separate domains: they form in a manner that minimises energy. The preferred orientations can be determined from the condition that there should be no jump in the displacement components parallel to the wall and that the jump of the electric displacement component normal to the wall should be equal to the surface charge density on the wall. When these conditions are met, stress and electric field do not arise due to the presence of the wall.

In the presence of a volume charge density, the divergence of electric displacement is given by

$$\nabla \cdot \underline{D} = \rho. \quad (10.7)$$

This can be integrated over a small volume that encompasses the wall to obtain the condition that across the wall

$$\|D_n\| = Q/A, \quad (10.8)$$

which states that the jump of the normal component of electric displacement across the wall is equal to the surface charge density on the wall. In many cases, the surface charge density is zero, but probably still plays an important role in domain wall pinning in acceptor doped compositions of PZT. *Pinning* is any mechanism that hinders domain wall motion.

The condition that the jump of mechanical displacement across the wall is zero can be written as

$$\|u_t\| = 0. \quad (10.9)$$

Figure 10.11 shows examples of compatible domain walls in the tetragonal structure. The 90-degree wall lies along a (110) plane and the 180-degree wall lies along a (001) plane. The 90-degree wall is actually a little off 90 degrees. The angle can be determined by cutting the tetragonal structure along a face diagonal. One side has dimension a and the other dimension c . These are put together as shown in Fig. 10.9. Since the two diagonals are the same length, there is no stress present. Figure 10.10 shows the polarisation in three 90-degree domains: the components of the polarisation vectors are shown. It is easy to see that the normal component of electric displacement across the walls is continuous.

Each of the crystal structures discussed has its own set of compatible domain walls. In the rhombohedral structure, the domain types differ by 70.5-degree, 109.5-degree and 180-degree rotations of the polarisation

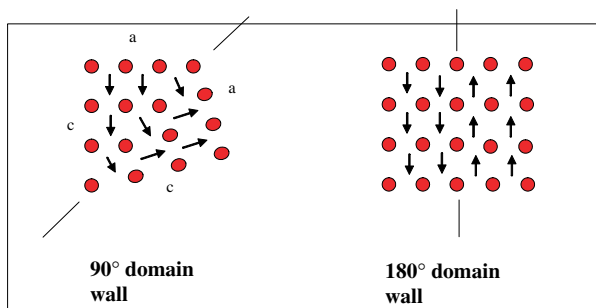


Fig. 10.9 Schematic diagrams of 90-degree and 180-degree domain walls that occur in the tetragonal structure.

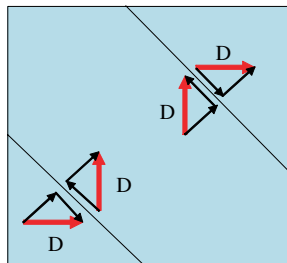


Fig. 10.10 In the absence of an electric field, the electric displacement and polarisation are equal. The normal component of the electric displacement vector across the wall is continuous in the absence of a surface charge distribution.

vector. This is the angle the vector must rotate through to change its orientation from pointing toward one corner of the unit cell to the other corners.

The equation $\nabla \cdot \underline{D} = \rho$ also leads to the boundary conditions at an electrode that enable measurement of polarisation changes. Integrating this equation over a volume V yields

$$\int_V \nabla \cdot \underline{D} dV = \int_V \rho dV. \quad (10.10)$$

Integration of the right-hand side (RHS) gives the free charge enclosed within the volume. Application of the divergence theorem to the left-hand side (LHS) gives

$$\int_S \underline{D} \cdot \hat{n} dS = Q. \quad (10.11)$$

Shrinking the volume, such that it encompasses the polarised material and a portion of the electrode, down to the point that it now consists of two large areas above and below the electrode separated by an infinitesimal distance, integrating over these areas and dividing by the area shows that the normal component of the electric displacement is equal to the charge per unit area on the electrode when there is no free charge within the dielectric.

When the boundary is an electroded surface of the crystal, the normal component of the electric displacement is equivalent to the surface charge density on the electrode. If the electric displacement is eliminated by stress induced depolarisation, the remaining surface charge density will induce a large electric field. This is how a significant portion of the electric field is generated in FEG applications.

In the case of acceptor doped PZT, the domain walls tend to be pinned. This is related to the presence of low-mobility charge defects in the crystal

lattice that, given time, will migrate to regions that terminate incompatible components of electric displacement. Should the electric displacement change in response to an applied field, the frozen-in-charge density will form a field that will pull the domain back to its original position upon removal of the field.

10.5 Driving Forces for Domain Wall Motion (Evolution of Variants, Poling and Depoling)

The driving force for domain switching will be discussed first and then extended to include phase transformations. The driving force is determined by the potential of the applied stress and electric field to do work during a switch from one polarisation state to another [10, 11]. This discussion will begin with developing expressions for the driving force. Next, models governing the polarisation reorientation process will be considered. The mechanism for evolution of volume fractions of crystal variants is domain wall motion. This process is rate dependent, non-linear and hysteretic.

10.5.1 Mechanical Work

The amount of mechanical work done during polarisation reorientation is found from the stress present and the shape change that takes place during the reorientation. Work is done by a force acting over a change of distance. Work per unit volume is done by stress (work/area) acting over a change in strain (distance/length). The driving force for a stress-driven polarisation change is found from determining the work that would be done on the material due to the strain change that accompanies a change in the crystal from one variant to another in the presence of stress. Consider the case of the tetragonal unit cell. The spontaneous strain when the polarisation is aligned with the z -axis is given by

$$[\varepsilon^S]_z = \begin{bmatrix} -0.5\varepsilon^S & 0 & 0 \\ 0 & -0.5\varepsilon^S & 0 \\ 0 & 0 & \varepsilon^S \end{bmatrix} = \begin{bmatrix} \frac{a-a_0}{a_0} & 0 & 0 \\ 0 & \frac{a-a_0}{a_0} & 0 \\ 0 & 0 & \frac{c-a_0}{a_0} \end{bmatrix}. \quad (10.12)$$

The uniaxial compressive stress applied along the z -direction is given by

$$[\sigma] = \begin{bmatrix} 0 & 0 & 0 \\ 0 & 0 & 0 \\ 0 & 0 & -\sigma_{zz} \end{bmatrix}. \quad (10.13)$$

If the polarisation were to change to the x -direction, the new spontaneous strain would be

$$[\varepsilon^S]_x = \begin{bmatrix} \varepsilon^S & 0 & 0 \\ 0 & -0.5\varepsilon^S & 0 \\ 0 & 0 & -0.5\varepsilon^S \end{bmatrix} = \begin{bmatrix} \frac{c-a_0}{a_0} & 0 & 0 \\ 0 & \frac{a-a_0}{a_0} & 0 \\ 0 & 0 & \frac{a-a_0}{a_0} \end{bmatrix} \quad (10.14)$$

If this change were to take place at a constant level of compressive stress, the mechanical work done per unit volume during this process is given by

$$W^M = \sigma_{ij} \Delta \varepsilon_{ij}^S \quad (10.15)$$

with summation on repeated indices implied. Upon substitution of the values under consideration, this gives

$$W = \sigma_{ij} \left(\varepsilon_{ij}^{S(x)} - \varepsilon_{ij}^{S(z)} \right) = -\sigma_{zz} (-3/2\varepsilon^S) = -\sigma_{zz} \left(\frac{a-c}{a_0} \right), \quad (10.16)$$

where the superscript in parenthesis indicates the polarisation direction of the variant.

Other components of stress can also do work on the change in strain that occurs during the switching process. This is readily accounted for by using Eq. (10.16). In the case of the tetragonal crystal, it is relatively easy to resolve the local stress components into a Cartesian coordinate system aligned with the polarisation directions. For other crystal structures, the spontaneous strain and the applied stress must be resolved into the same coordinate system for the calculation of work.

10.5.2 Electric Work

Work is again defined in terms of a force acting over a distance change. A charge can be moved a distance through a change of electric potential by a force. The unit of potential is the volt (1 volt = 1 Nm/C) and the unit of charge is the Coulomb (C). A force moving a charge of the Coulomb through a distance over which the potential has changed by 1 volt does work of 1 Nm or 1 Joule. An increment of work is $dW = \phi dQ$.

An applied electric field also does work on a material during polarisation reorientation. In this case, the electrical work is given by

$$W^E = E_m \Delta D_m. \quad (10.17)$$

The electrical work is computed in the same manner as the mechanical work. The applied electric field is resolved into components in a Cartesian

coordinate system aligned with the crystal structure and the possible polarisation changes are considered. Consider a material initially polarised in the positive z -direction and an electric field applied in the negative z -direction. The applied electric field is given by

$$[E] = [0 \ 0 \ -E_z]. \quad (10.18)$$

The initial polarisation is given by

$$[P^S]_{+z} = [0 \ 0 \ P^S] \quad (10.19)$$

and the final polarisation is given by

$$[P^S]_{-z} = [0 \ 0 \ -P^S]. \quad (10.20)$$

The work done during a change from positive to negative polarisation is given by

$$W^E = -E_z(-P^S - P^S) = 2E_zP^S. \quad (10.21)$$

Equation (10.17) readily includes the electric field applied in any direction relative to the polarisation direction.

10.5.3 Combined Stress and Electric Field

The work per unit volume done when both stress and electric field are present is determined by adding the electrical work to the mechanical work. This leads to

$$W^T = W^E + W^M = \sigma_{ij}\Delta\epsilon_{ij} + E_m\Delta D_m. \quad (10.22)$$

If the energy barrier to reorientation is the same for all possible reorientations, the reorientation that will take place is the one for which there is the largest driving force. If the material is known to remain within a single crystal structure (no phase changes) and it undergoes only changes in crystal variants, the largest driving force is determined by evaluating Eq. (10.22) for each possible change in polarisation direction (six in the case of tetragonal). It is entirely possible, and even likely, that the energy barrier to a 90-degree reorientation is different from the energy barrier to a 180-degree reorientation, since these two reorientations occur by a different type of domain wall motion.

10.5.4 Orientation Effects (Orthogonal Transformations)

It has already been mentioned that the applied stress and electric field must be expressed in the same coordinate system as the spontaneous strain and spontaneous polarisation in order to calculate the driving force for reorientation. For the case of the tetragonal crystal, this was particularly easy to do as the tetragonal structure is naturally aligned with a Cartesian coordinate system. This is not the case for other crystal structures, yet this does not pose too much added complexity. For the case of the rhombohedral crystal structure (and others), the calculation of work done is performed by resolving the spontaneous strain for each of the variants into a single Cartesian coordinate system. Referencing the system to the cubic unit cell is an obvious choice. The spontaneous strain in each of the eight $\langle 111 \rangle$ directions is given by a matrix of strain components that looks like

$$[\varepsilon^S]_{[111]} = \begin{bmatrix} \varepsilon^S & 0 & 0 \\ 0 & -0.5\varepsilon^S & 0 \\ 0 & 0 & -0.5\varepsilon^S \end{bmatrix}. \quad (10.23)$$

Figure 10.11 shows examples of coordinate systems with the local x_3 axis aligned with the polarisation direction and the corresponding unit vectors formed into a direction cosine matrix for three crystal structures and polarisation orientations.

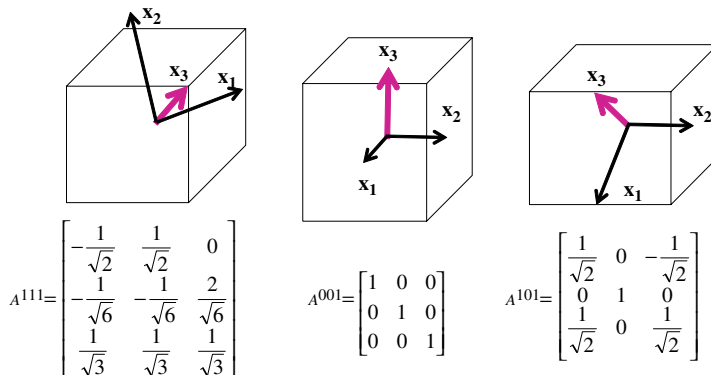


Fig. 10.11 Examples of a single-crystal variant of rhombohedral, tetragonal and orthorhombic structures. The bold arrow aligned with the local x_3 axis represents the polarisation direction. Below each is the corresponding direction cosine matrix for rotating the spontaneous strain and spontaneous polarisation to a cubic referenced Cartesian coordinate system.

A single variant single crystal has symmetry about the polar axis. This is the polarisation direction and a principle direction for the spontaneous strain tensor. It is also a principle direction for other material tensors, such as piezoelectricity, dielectric permittivity and elasticity. If all of the coefficients of a material tensor are known in one direction, they can be computed in another direction using the direction cosine matrices discussed above. The transformation equations are given by:

- Second order dielectric permittivity tensor components

$$\bar{\kappa}_{ij} = a_i^p a_j^q \kappa_{pq}. \quad (10.24)$$

- Third order piezoelectricity tensor components

$$\bar{d}_{ijk} = a_i^p a_j^q a_k^r d_{pqr}. \quad (10.25)$$

- Fourth order elasticity tensor

$$\bar{s}_{ijkl} = a_i^p a_j^q a_k^r a_l^s s_{pqrs}. \quad (10.26)$$

Although the tensors are independent of their coordinate system, their coefficients do depend on the coordinate system.

10.5.5 Stress

Computing the stress contribution to the driving force for a variant or phase transformation requires that both the stress components and the strain components be expressed in the same coordinate system. If we consider a single variant, single phase, single crystal in which the stress is applied in a global coordinate system (usually aligned with the loading mechanism), which is not aligned with the polar axes or the cubic referenced axes of the crystal structure, then both the stress and the spontaneous strain of each crystal variant will have to be resolved into the cubic referenced coordinate system for the computation of work. This leads to

$$\bar{\sigma}_{ij}^{\text{local}} = a_i^p a_j^q \sigma_{pq}^{\text{global}} \quad (10.27)$$

and

$$\bar{\varepsilon}_{ij}^{\text{local}} = a_i^p a_j^q \sigma_{pq}^{\text{global}} a_i^s a_j^t \Delta \varepsilon_{st}^S \text{ variant } A \rightarrow B. \quad (10.28)$$

Work is then calculated in the local coordinate system by using

$$W^E = a_i^p a_j^q \sigma_{pq}^{\text{global}} a_i^s a_j^t \Delta \varepsilon_{st}^S \text{ variant } A \rightarrow B. \quad (10.29)$$

10.5.6 Electric Field

A similar expression can be written for the electric field

$$W^E = a_i^p E_p^{\text{global}} a_i^s D_s^S \xrightarrow{\text{variant } A \rightarrow B}. \quad (10.30)$$

10.5.7 Kinetics of Variant Evolution

The state of a ferroelectric crystal can be defined by identifying the polarisation orientation of every unit cell and the local stress and electric field at every unit cell. This is an insurmountable task given that a crystal is microns to millimeters in length. To a good approximation, the state of the crystal can be defined by identifying a set of internal state variables. A logical choice for describing a single phase multidomain single crystal is to identify the volume fraction of each variant, f_i , where

$$f_i = \frac{V^{\text{variant } i}}{V^{\text{crystal}}}, \quad (10.31)$$

and

$$\sum_{i=1}^n f_i = 1, \quad (10.32)$$

and where n is the number of variants present. Kinetic laws can be used to describe the evolution of these volume fractions in terms of the applied loads. The expected form of the kinetic laws can be deduced from the underlying mechanisms.

Several factors affect the rate of evolution of the volume fractions of variants in response to applied loads. These include domain wall density and lattice defect structure. In the limiting case of minimal domain wall density, one domain wall must sweep across the entire crystal structure to produce a complete change from one variant to another. The distance the domain wall must travel is the full length of the crystal. If there are many domain walls present (possibly multiple nucleation sites), then the distance an individual wall must move to entirely change one variant to another is smaller. Intersecting domain walls are known to pin one another, increasing the energy threshold for domain wall motion, and defects in the crystal structure are known to hinder domain wall motion (acceptor dopants) or free up domain wall motion (donor dopants). This suggests that two additional parameters should be introduced: a length scale that must be swept to produce the transformation and a measure of domain wall mobility.

The length scale relates the time it takes a crystal to switch from one variant to another to the domain wall velocity. The simplest equation that can be introduced to describe this relation is

$$t = \frac{l}{v^{(w)}}, \quad (10.33)$$

where t is the time it takes for the transformation to take place and is equal to the characteristic length divided by the domain wall velocity.

The velocity of the wall that separates variant A from variant B is related to the driving force for this transformation. This can be described in terms of a mobility factor

$$v^{(w)A \rightarrow B} = M^{(w)A \rightarrow B} W^{A \rightarrow B}. \quad (10.34)$$

In the simplest model, the mobility is a constant and the wall velocity is linearly proportional to the driving force. This is not consistent with observed material behavior for several reasons. The length scale that must be swept is governed by a nucleation and growth-related process with a threshold for nucleation and a threshold for growth. Consider the case where the crystal is initially a single variant. The load is gradually increased until a small region of the second variant nucleates. A single domain wall then sweeps across the entire crystal converting it to the second variant. The time for the transformation to take place is the length divided by the average domain wall velocity. The wall motion itself could be at constant velocity that is a function of the driving force, could move in a stick-slip fashion, could be hindered by a frictional force or could be opposed by a viscous force proportional to the velocity.

In a ceramic, there is always a relatively large population of domain walls. These arise to accommodate intergranular stress and electric fields. Transformation behavior then becomes a matter of the motion of existing domain walls driven by the applied loads. Nucleation is not necessary. Stationary domain walls in acceptor doped PZT tend to stabilise and become pinned by a defect structure. This leads to lower piezoelectric coefficients, but also to lower losses.

These mechanisms affect the relationship between the domain wall velocity and the driving force. Consider the effects of a frictional force and a viscous force on the driving force. In the case of a frictional force, the driving force will have to overcome a threshold before motion begins. In acceptor doped PZT, the domains are stabilised by a defect structure, which can change through a diffusion process. Once the defect structure that stabilises the domain walls is in place and the domains are pinned, the

driving force to move the domain wall is increased due to the defect structure providing a driving force to return the domain walls to their original stabilised position. If the driving force is sufficient to overcome the pinning forces, then the material will undergo a change to the new variant — i.e. there will be a non-zero domain wall velocity. Not only will the defect structure apply a driving force pulling the domain wall back to its initial position, the new domain structure will provide a driving force for diffusion of the defect structure to stabilise the new domain structure. This is the reason acceptor doped PZT is poled at elevated temperature with a DC field applied for a period of time. The elevated temperature increases the mobility of the charge defects and the constant field applied over a period of time allows the defects to diffuse to locations that stabilise the poled domain structure.

This suggests that a defect mobility governing defect velocity needs to be introduced, where the driving force is provided by external loads. This gives

$$v^{(d)} = M^{(d)} W^{A \rightarrow B}, \quad (10.35)$$

where the defect mobility is likely to be a thermally activated process that can be represented by

$$M^{(d)} = M_0^{(d)} \exp(-W_0^{(d)}/kt). \quad (10.36)$$

The domain wall mobility is also quite likely a thermal activated process that can be represented by

$$M^{(w)} = M_0^{(w)} \exp(-W_0^{(w)}/kt). \quad (10.37)$$

A simple model that demonstrates the ability of low-mobility charge defects to stabilise a domain structure is illustrated in Fig. 10.12, which shows a schematic of a crystal containing a single 90-degree domain wall that is initially in a charge defect stabilised configuration with respect to the electrodes (top and bottom) and the free surfaces (left and right) by free charges that are not mobile. If the domain wall moves and the free charges do not move, a driving force is generated that pulls the domain wall back toward its initial location. The same driving force acts to drive diffusion of the defects to a new configuration. In the configuration to the left in Fig. 10.12, a layer of positive charge accumulates below the upper electrode to balance the negative charge on the electrode and a layer of negative charge forms along the right side to terminate the normal component of electric displacement. In the configuration to the right in Fig. 10.12, there

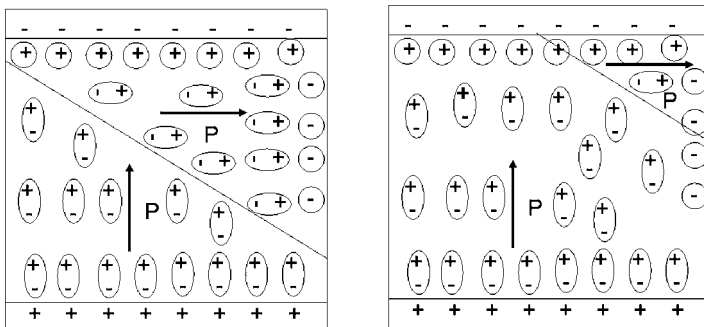


Fig. 10.12 A schematic diagram of a 90-degree domain initially stabilised by a charge distribution. When the domain wall moves and the charge distribution does not, a large local electric field results that pulls the domain wall back toward its initial location.

is a surface charge density left behind as the domain wall moves. In this region, the electric displacement is given by

$$D = \kappa_0 E + P, \quad (10.38)$$

where κ_0 is the permittivity of free space. The satisfaction of $\nabla \cdot D = \rho$ results in a large electric field produced by the charge layer. This can easily be sufficient to drive the domain wall back to its initial location upon removal of the field.

For a single crystal, various mechanisms driving and opposing domain wall motion have been discussed. The macroscopically applied driving force is provided by the applied stress and electric field. An opposing driving force is provided by a charge distribution left behind when the domain wall moves. This opposing driving force will decay over time at a rate dependent on temperature. There may also be a threshold driving force below which the domain walls will not move.

10.5.8 Volume Average Single Crystal Properties

Single crystals can contain many domains. Domain-domain interactions, such as pinning, influence material properties, but reasonable models of material behavior can be constructed based on the volume average of each variant or phase present. This is the basis for *domain engineering*, the process of selecting and controlling crystal-cut, polarisation orientation and stress orientation to obtain controlled volume fractions of crystal variants. Orthogonal transformation to obtain properties of a single variant in a cubic

referenced coordinate system were just discussed. The case where there are multiple variants present is now considered. The physical properties of the multi-variant crystal can be calculated from a weighting of the contribution of each variant by the volume fraction that is present using the following equations [12]:

- Remnant polarisation components are

$$P_i^r = \sum_{v=1}^n f_v a_i^k(v) P_k^S(v). \quad (10.39)$$

- Remnant strain components are

$$\varepsilon_{ij}^r = \sum_1^n f_v a_i^p(v) a_j^q(v) \varepsilon_{pq}^S(v). \quad (10.40)$$

- Dielectric constants are

$$\kappa_{ij}^r = \sum_1^n f_v a_i^p(v) a_j^q(v) \kappa_{pq}^S(v). \quad (10.41)$$

- Piezoelectric components are

$$d_{ijk} = \sum_1^n f_v a_i^p(v) a_j^q(v) a_k^r(v) d_{pqr}(v). \quad (10.42)$$

- Elastic components are

$$\varepsilon_{ijkl} = \sum_1^n f_v a_i^p(v) a_j^q(v) a_k^r(v) a_l^s(v) \varepsilon_{pqrs}(v). \quad (10.43)$$

These equations lead to an understanding of the measured behavior of [001] and the [011] cut and poled rhombohedral phase crystals. For the [001] crystal, the remnant strain is zero. This effect is due to the [111] strain component, when resolved into the [001] direction having a zero component. If we consider the driving force for evolution of crystal variants, the strain change in the cubic referenced ⟨001⟩ coordinate system is zero. Similarly, if the material is fully poled, four of the eight variants will not be present and there is no driving force for domain wall motion under electric field. This leads to a very low loss crystal cut, at least at low-field levels. The [011] crystal is another interesting case due to symmetry. At higher field levels, the electrical and mechanical loads induce phase transformations with associated nonlinearity and hysteresis.

10.6 Phases Transformations in Single Crystal

Developing an understanding of field induced phase transformations in single crystals is an important step toward understanding the phase transformation behavior of ceramics [13–17] and their utilisation in FEG design. The driving forces for phase transformations are computed in the same manner as the driving forces for domain wall motion. The material behavior as it passes through the transformation depends on the type of transformation, the type of phase boundary motion and the kinetics of the boundary motion. Figure 10.13 shows a schematic of a [110] poled rhombohedral crystal loaded with a uniaxial compressive stress in the [001] direction and an electric field in the [110] direction. The [110] cut and poled rhombohedral crystal tends to form equal volume fractions of two crystal variants as shown at the left.

The driving force for this phase transformation is again found from the applied stress and electric field and the resulting strain change and electric displacement change. In this case, however, the strain change is that which is associated with the transformation. Figure 10.14 shows examples of the temperature dependence of the measured behavior of the crystal cut shown in Fig. 10.13. These three-dimensional plots show the strain that is produced by simultaneous application of stress and electric field. Similar plots were generated from the measured electric displacement. The starting point of zero load is at the upper peak in the plot. The parallel curves that run down and to the left are stress-strain curves at different constant electric field values. The parallel curves that run down and to the right are strain-electric field curves at different constant stress values. The upper planar region is in the rhombohedral phase with two crystal variants

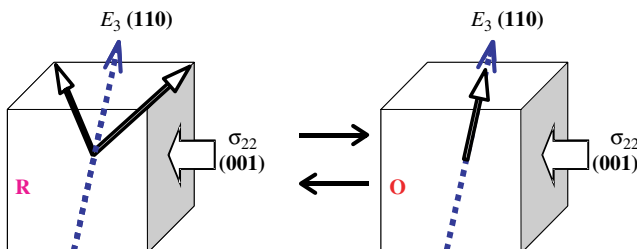


Fig. 10.13 The [110] cut and poled single crystal tend to form equal volume fractions of two rhombohedral variants. The stress [001] and electric field [110] components shown drive a phase transformation to an orthorhombic phase.

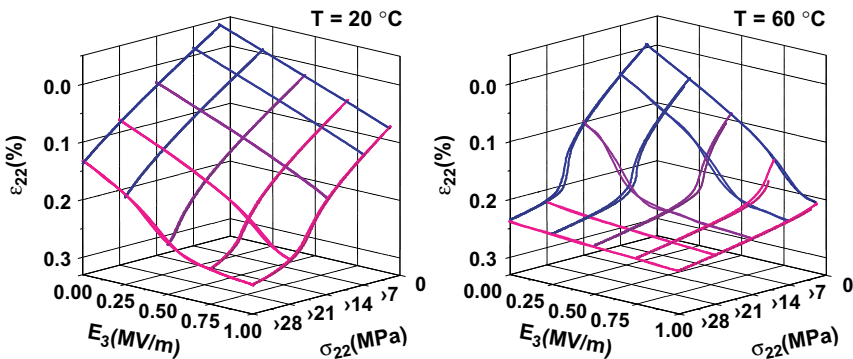


Fig. 10.14 Plots of strain as a function of applied stress and electric field at two different temperatures indicate that a phase transformation is taking place and that the driving force is a function of temperature.

present. The lower planar region is in the orthorhombic phase with one crystal variant present. The steepening of the upper planar portion of the plot with temperature increase indicates a strong temperature dependence of the elastic and piezoelectric coefficients.

As loads are applied to this material, the elastic energy is increased. As additional load is applied, the material passes through a phase transformation. The work done can be determined from the area under the stress-strain curve plus the area under the electric field-electric displacement curve. These are path integrals that must be concurrently evaluated by numerical integration of the measured material response as described in Fig. 10.15.

Field driven phase transformations in perovskite-type ferroelectrics may occur either heterogeneously or homogeneously. This depends on the material and the driving forces. Data obtained from shock loading of PZT 95-5 to drive the ferroelectric-to-antiferroelectric phase transformation [16–18] suggest that at shock compression load levels a nucleation and growth process takes place with the phase boundary motion governed by a kinetic law, and at higher load levels it is a heterogeneous process with near instantaneous response. Two different compositions of relaxor rhombohedral ferroelectric single crystals, PMN-32PT and PZN-4.5PT, illustrate that the same type of phase transformation can be of a very different nature. Figure 10.16 shows examples of these transformations. The PZN-4.5%PT composition displays a jump-type transformation with an open hysteresis loop that appears upon

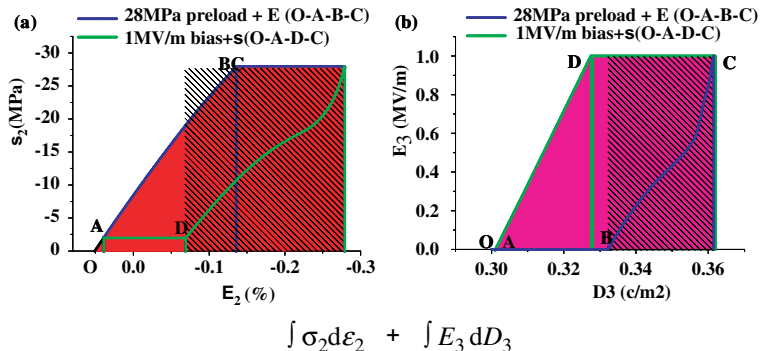


Fig. 10.15 Examples of computing the work done to drive a phase transformation along two different paths (OABC) and (OADC).

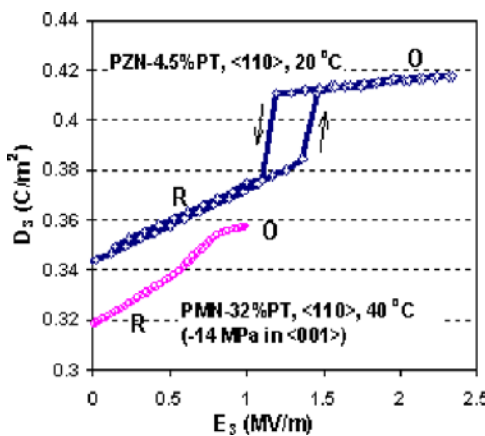


Fig. 10.16 Electric fields in the $[110]$ direction induce phase transformations in rhombohedral single crystals. Two distinctly different types of transformation are shown.

unloading. The PMN-32%PT composition displays a continuous transformation with little hysteresis upon unloading.

10.6.1 Ceramic Behavior

The behavior of ceramics is the volume average of the behavior of the materials it is made from at smaller length scales. Ceramics have more to their structure than single crystals. In addition to the crystal structure, the defect structure, the domain structure and the phase boundaries within

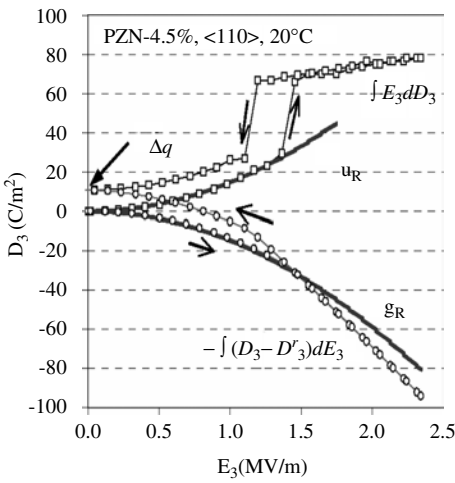


Fig. 10.17 The electrical work done during the transformation can be determined by numerical integration of the loading curves. A PZN-4.5%PT example is shown. The offset is equivalent to the heat generated by the hysteresis.

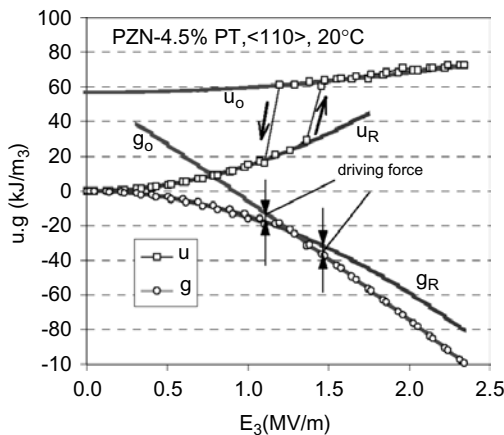


Fig. 10.18 When the heat is removed, the remaining curves can be used to determine the relative energy levels of the two phases and the forces needed to drive the phase transformations.

the crystals, ceramics have grains and grain boundaries. They also tend to have porosity at the grain boundaries and, in some cases, second phases at the grain boundaries. Each grain is a single crystal that is physically connected to its neighboring crystals. Grain boundaries can be characterised as

low-angle and high-angle tilt or twist boundaries. Domain structures may be continuous across low-angle boundaries, as was apparent in Fig. 10.3, where the striations can be clearly seen to pass from one grain to another. Texture in a ceramic is a measure of the degree of alignment of the crystallographic axes with a global coordinate system. The material can range from a completely random texture (random orientation of the grains) to a near-single crystal texture (grains well aligned). This is a property that can be controlled through processing techniques, such as templated grain growth, and may lead to a means of improving the energy density of ferroelectric generators.

The vast array of compositions of PZT, together with the effects of the many possible dopants, leads to a broad range of possible material behavior. Morphotropic phase boundary compositions that are acceptor doped are referred to as hard PZT. Hard PZT tends to have a lower resistivity due to charge mobility and mobility of oxygen vacancies. These charged defects tend to migrate to sites where they will pin domain walls. Donor doped MPB compositions tend to have a defect structure in which oxygen vacancies are charge compensated. This results in very high resistivity and relatively mobile domain walls. Compositions that lie well away from the morphotropic phase boundary still display some of these characteristics, as will be shown below with the introduction of a number of examples.

10.7 Properties of Soft, Hard and Phase Transforming PZT

10.7.1 PLZT 8/65/35 (*Soft Rhombohedral Ferroelectric*)

Hot isostatic pressed lanthanum doped PLZT 8/65/35 is a transparent ceramic (no porosity) that displays *relaxor behavior*. This means that there is not a distinct Curie point. The dielectric constant plotted as a function of temperature displays a broad peak. The properties at room temperature are representative of a soft PZT. In the sequence of measurements of the behavior of this material presented below, strain and electric displacement are measured with the strain gages affixed and Wheatstone bridges balanced and the Sawyer-Tower circuit zeroed in the unpoled configuration. The strain and electric displacement measurements give direct measures of the remnant polarisation and the remnant strain [21].

Figure 10.19 shows the strain/electric field hysteresis loops. They are symmetric and butterfly shaped. The transverse strain is roughly 0.5 times the longitudinal strain. The slope of the longitudinal strain vs. electric field

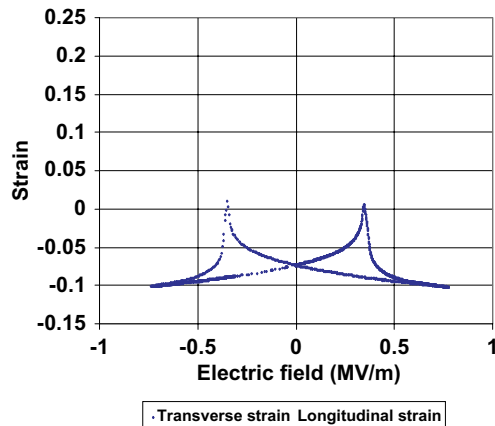


Fig. 10.19 Longitudinal and transverse strain vs. electric field in PLZT 8/65/35.

curve as it passes through zero field is the large field piezoelectric coefficient d_{333} and the slope of the transverse strain vs. electric field as it passes through zero is the large field piezoelectric coefficient d_{311} . The strain value at zero field is the remnant strain.

Figure 10.20 shows the stress vs. longitudinal and transverse strain. The nonlinearity in the stress/strain behavior is related to non-180-degree domain switching, a term that refers to large-scale stress driven polarisation reorientation through domain wall motion. In the case of rhombohedral

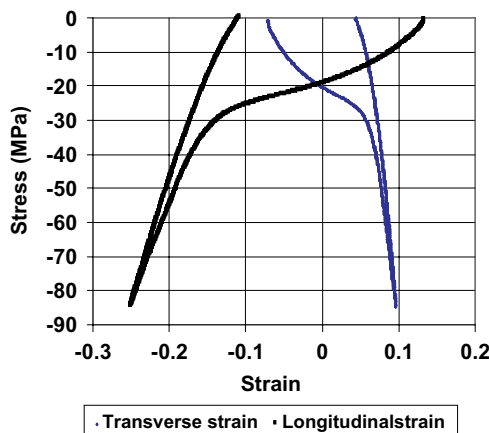


Fig. 10.20 Stress vs. longitudinal and transverse strain.

materials, this is 70.5- and 109.5-degree switching. Note that the longitudinal and transverse stress/strain curves begin at the remnant strain level. The arrows indicate the direction of loading. Stress induces a permanent strain change, as can be seen from the hysteresis present upon unloading. Note that application of an electric field to re-polarise the material will reset the strain to the remnant strain value. This is a shape memory effect. The shape of the curve corresponds to a small amount of initially elastic loading followed by polarisation reorientation (large strain change with a small stress change), followed by a much steeper slope in the regime, where the polarisation has been rotated perpendicular to the stress and additional loading is elastic.

Figure 10.21 shows a plot of the transverse vs. longitudinal strain. The arrows show the loading direction. The initial portion of the loading displays a slope of 0.5, indicating that the domain reorientation process takes place at constant volume. The loading at higher stress is elastic with a slope of around 0.38. This is the elastic Poisson's ratio perpendicular to the polarisation direction.

Figure 10.22 is a plot of the stress vs. electric displacement curve. Its shape is similar to the stress vs. strain curve. It begins at the remnant polarisation value of 0.24 C/m^2 . The initial loading is elastic. As the polarisation rotates (domain switching), there are large changes in the electric displacement. Once the loading is high enough that all the domains that can rotate have done so, the loading is elastic. Note that unloading does not

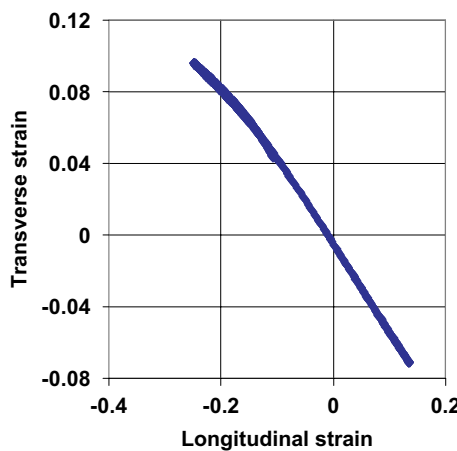


Fig. 10.21 Transverse vs. longitudinal strain under uniaxial stress loading.

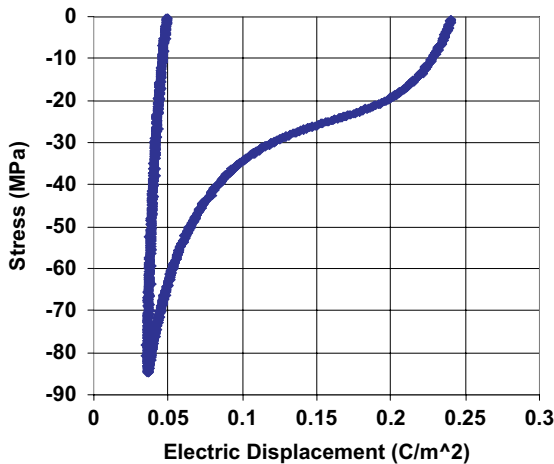


Fig. 10.22 The stress vs. electric displacement curve displays behavior similar to the stress vs. longitudinal strain curve. Not all of the polarisation can be recovered through stress loading.

return the material to a zero polarisation state. The fully-stressed depoled state still has about 20% of the polarisation of the fully-poled state. The reason is that many of the grains are oriented such that there is not a crystallographic polar direction aligned exactly perpendicular to the stress direction. The material is forced to depole with a domain switch as close to perpendicular to the stress direction as possible. This leaves a residual polarisation component that cannot be recovered by compressive loading. This is not the best choice for FEG applications.

Figure 10.23 shows the effect of generating electric displacement vs. electric field hysteresis loops at different constant compressive stress levels. At zero stress the loops are relatively square with a clearly identifiable coercive field. As the stress is increased, domains are rotated away from the stress direction. The electric field then rotates them back toward the stress direction. This results in loop flattening.

10.7.2 *PLSnZT (AF-F Double Loop)*

Figure 10.24 displays a very different type of material behavior. This is a composition that is stable in the antiferroelectric state and is pulled into the ferroelectric state by an electric field. This gives rise to a double loop

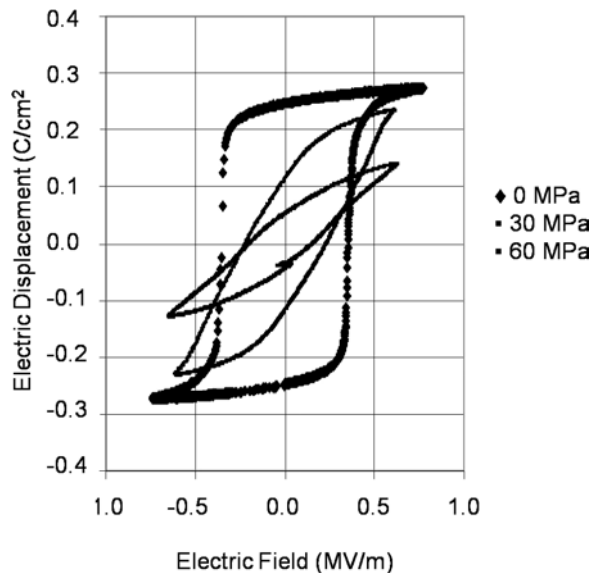


Fig. 10.23 Electric displacement vs. electric field at three stress levels.

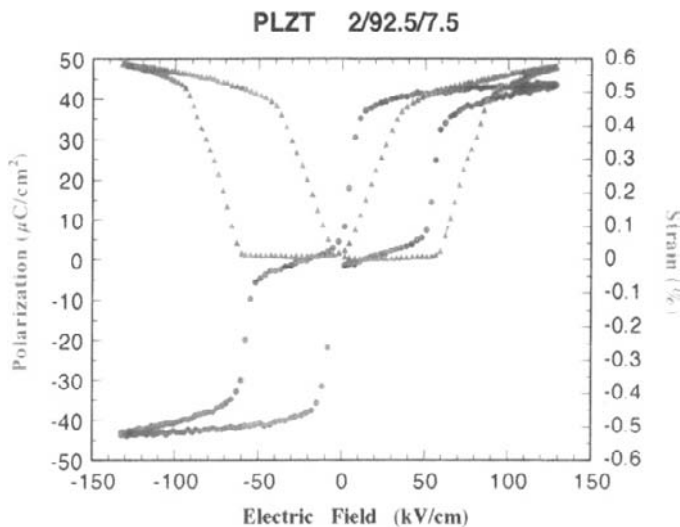


Fig. 10.24 Double loop behavior of an AF to F phase transforming material.

in the electric displacement vs. electric field curve and a butterfly shaped strain vs. electric field curve with zero remnant strain [22].

In FEG applications the material is being driven from the ferroelectric to the antiferroelectric state. The energy density achieved upon depolarisation depends on the electrical properties in the depoled state and the charge present. Some insight can be gained into the material behavior in the stress depoled state by measuring the effect of stress on the antiferroelectric-to-ferroelectric transformation. This is seen in Figure 10.25, where the double loop electric displacement vs. electric field curves have been generated at various stress levels. In this composition, the material behavior is linear dielectric up to the coercive field, at which point it switches to ferroelectric. The stress provides a driving force toward the smaller volume antiferroelectric phase and the electric field provides a driving force toward the polarisation aligned ferroelectric phase. As the stress driving force is increased, the electric field driving force must exceed the stress driving force by an amount sufficient to drive the transformation.

10.7.3 PZT 95-5

PZT 95-5 was developed specifically for FEG applications by Sandia National Laboratory in the early 1960s. This is a composition that is ferroelectric at room temperature and can be driven into the lower volume antiferroelectric state by compressive stress. The resulting polarisation change produces a high electric field.

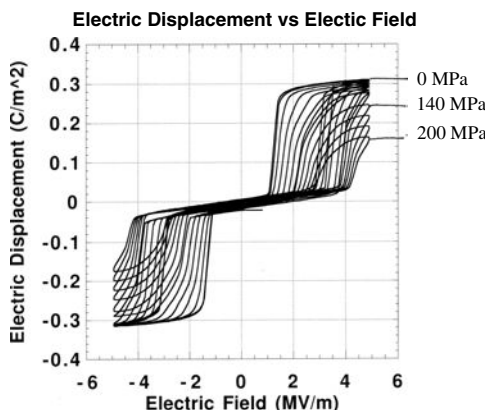


Fig. 10.25 The plot of electric displacement vs. electric field as a function of stress shows the effect of stress on the double-loop behavior associated with the AF–F transition.

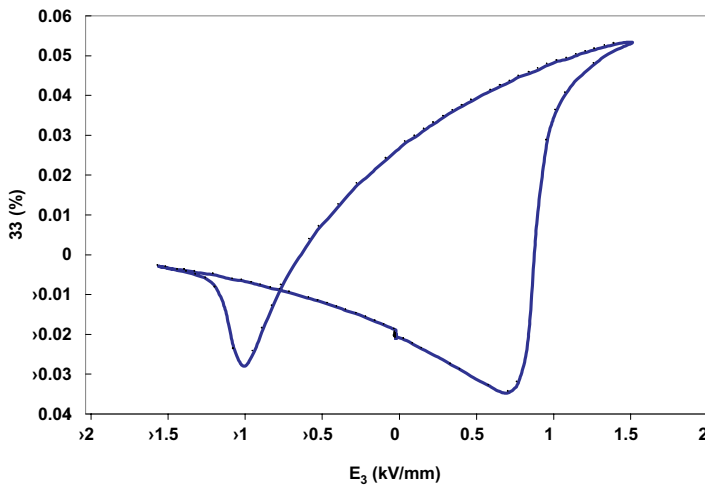


Fig. 10.26 Strain vs. electric field for PZT 95-5 doped with 2% Nb.

Figure 10.26 is a plot of the strain vs. electric field hysteresis loop at room temperature for a specimen that has been polarised in the positive direction. The lopsided butterfly hysteresis loop is similar to that observed in hard PZT. This is usually indicative of diffusion of charge defects to locations that stabilise the domain structure. There are likely oxygen vacancies slowly diffusing and possibly another charge carrier that can move through these vacancies more rapidly. This loop was run at 0.1 Hz.

Figure 10.27 shows electric displacement vs. electric field hysteresis loops for the same material. A key point is that the peak remnant polarisation magnitude is 0.303 C/m^2 . This provides direct evidence that the stress depoling experiments are driving ferroelectric switching as well as a ferroelectric-to-anti-ferroelectric phase transformation, as will be apparent from the stress-electric displacement curve presented below.

Figure 10.28 shows the stress vs. electric displacement curve generated to specimen failure. There is an initial elastic loading and a slope change (softening) associated with polarisation reorientation that transitions into a ferroelectric-to-antiferroelectric phase transformation. The evidence that there is a phase transformation taking place is that the electric displacement is trending toward complete depolarisation. Domain switching alone in a rhombohedral composition cannot eliminate the last approximately 20% of the polarisation, as was seen in Fig. 10.18 for the rhombohedral PLZT 8/65/35.

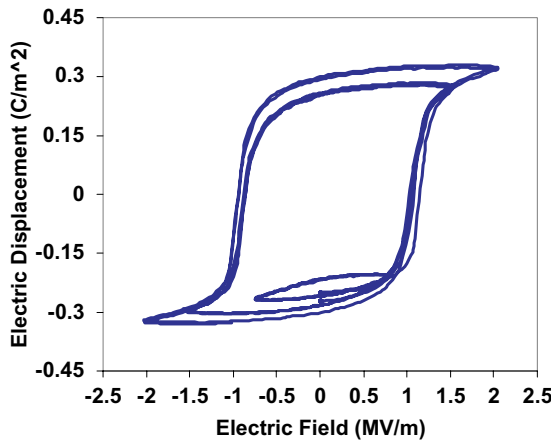


Fig. 10.27 Electric displacement vs. electric field hysteresis loops for PZT 95-5 with 2% Nb at 1, 1.5 and 2 MV/m and 1 Hz.

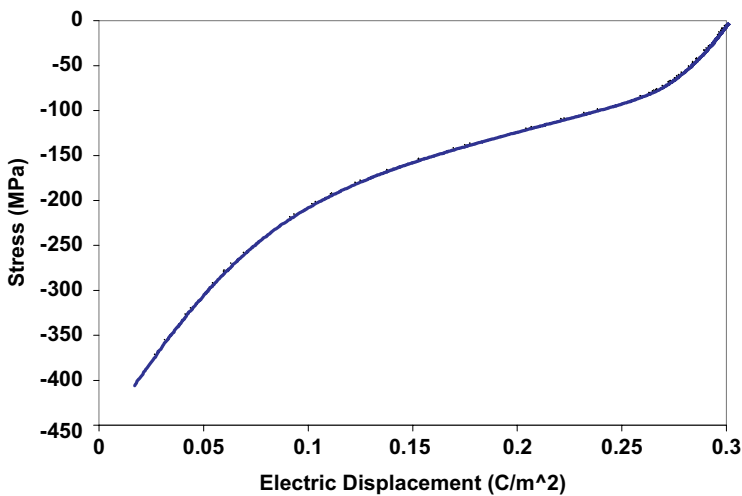


Fig. 10.28 Stress vs. electric displacement for PZT 95/5 with 2%Nb.

Figure 10.29 shows the stress vs. strain curve for the same loading as presented in Fig. 10.26. Note the non-linearity associated with a combination of domain switching and phase transformation. Although this curve starts at zero strain due to bridge balancing at this point, this should be offset to the right by the remnant strain value.

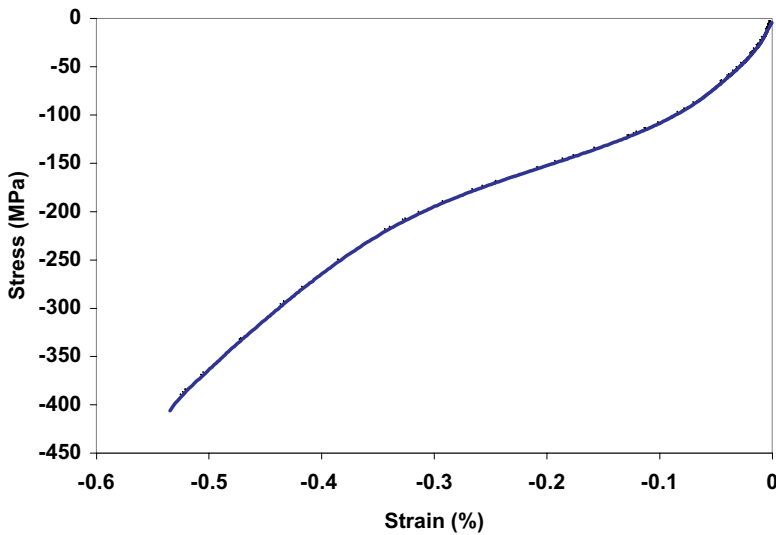


Fig. 10.29 Stress vs. strain for PZT 95/5 with 2% Nb.

10.8 Discussion of the Rh (F) to Rh (AF) Phase Transformation and FEG Design

One of the goals in FEG design is to maximise the energy density delivered by the stress depoled ferroelectric material. The ferroelectric material is generally in a parallel plate capacitor configuration. The charge density on the electrodes due to the stress depolarisation is equivalent to the initial remnant polarisation. If the material behaves as a linear dielectric in the stress depoled state, then the capacitance, C , can be calculated by using

$$C = \varepsilon \frac{A}{d}, \quad (10.44)$$

where ε is the dielectric permittivity, A is the electrode area and d is the distance between the electrodes.

The voltage generated would be given by

$$V = \frac{Q}{C} = \frac{AD}{\varepsilon A/d} = \frac{Dd}{\varepsilon}, \quad (10.45)$$

the electric field generated would be given by

$$E = \frac{D}{\varepsilon}, \quad (10.46)$$

and the stress generated energy stored in the capacitor would be given by

$$\Psi = \frac{1}{2}CV^2 = \frac{1}{2}QV. \quad (10.47)$$

There are two potential problems with doing a calculation like this. The equations are based on assumed linear dielectric properties and it is assumed that neither the stress nor the electric field will cause failure in the dielectric. If the material in the AF state behaves as the material shown in Fig. 10.22, then the linear dielectric assumption would be valid up until the coercive field is reached. In this case, a continued increase in stress would shift the coercive field for the reverse transformation to higher and higher levels until the coercive field exceeds the field generated by the stress induced depolarisation. In this special case, Eq. (10.47) can be used to compute the maximum energy and Eq. (10.46) may be used to compute the maximum field.

The slope of the linear dielectric portion of Fig. 10.22 is the dielectric permittivity, 8.33×10^{-9} F/m. The relative permittivity is thus around 940. Assuming the stress depoled PZT 95/5 material has these properties and the electric displacement is 0.3 C/m^2 , the electric field generated would be 36 MV/m. This would likely induce dielectric breakdown. Dielectric breakdown in humid air occurs at around 1 MV/m. External dielectric insulation and high dielectric breakdown strength of the ceramic are two important parameters for achieving a large-energy density in the stress depoled material.

From Fig. 10.22, each 100 MPa increase in stress induces a 0.5 MV/m increase in the AF-F coercive field. Pushing this up to 36 MV/m would require a stress on the order of 7 GPa or 70 kbar. Stress at this level in a ceramic can be achieved in plate impact tests, where the loading is purely compressive uniaxial strain. At this stress level, the material may undergo pore collapse and induced conductivity within the shock front. In addition, release waves from the edges of the specimen will result in tension, cracking and dielectric failure. It would appear that the upper limit of electric field will be difficult or impossible to achieve.

Some of these problems can be avoided through modifying the design. Dielectric breakdown may be avoided by careful design of the insulation, development of high dielectric strength ceramic and by connecting the ceramic to circuitry that removes the charge as current once a given maximum electric field level has been reached. Mechanical failure can be avoided by reducing the maximum stress, reducing the loading rate (avoids some of

the inertial effects such as unloading waves that result in tension) and by producing designs that avoid tensile stress.

10.9 Summary

- Ferroelectric generators rely on stress to produce high voltage and/or high current pulses. This is associated with field driven phase transformations.
- Field driven phase transformations occur when stress or electric field induces a transformation to a phase that is different from the equilibrium phase of the ferroelectric material at a given temperature.
- This transformation can be between variants of a given phase, a process referred to as polarisation switching, or it can be from one phase to another.
- The phase transformation typically utilised in ferroelectric generators with commercially available PZT is the stress driven ferroelectric (polar) to paraelectric (non-polar) transformation or with PZT 95/5 stress driven ferroelectric (polar) to antiferroelectric (non-polar) transformation that is accompanied by a reduction in volume. Compressive stress can reduce the volume of a ferroelectric material and drive it from a polar to a non-polar state.
- To harness the effects of this transformation, a capacitor is constructed using a polar ferroelectric material for the dielectric.
- The ferroelectric is polarised with a large external electric field. The ferroelectric stores charge. The charge per unit area on the electrodes balances the remnant polarisation of the dielectric.
- Stress induces the phase transformation to the non-polar phase.
- The capacitor becomes charged since the charge density on the electrodes is no longer balanced by the remnant polarisation.
- The voltage can be determined from the capacitance of the ferroelectric and the charge it stores. The dielectric constant of the dielectric goes from a large value to a small value during the transformation. This, together with the surface charge density, results in very high voltage levels.
- When a mechanically charged capacitor is connected to an external circuit, it does electrical work. This results in a very high current for a short period of time.

Bibliography

- [1] A. J. Moulson and J. M. Herbert, *Electroceramics: Materials, Properties, and Applications*, 2nd edn., John Wiley & Sons, Chichester (2003).

- [2] B. Jaffe, W. R. Cook, and H. Jaffe, *Piezoelectric Ceramics*, Academic Press, London (1971).
- [3] M. E. Lines and A. M. Glass, *Principles and Applications of Ferroelectrics and Related Materials*, Clarendon Press, Oxford (1977).
- [4] G. Robert, D. Damjanovic, and N. Setter, Preisach Modeling of Ferroelectric Pinched Loops, *Applied Physics Letters* **77**(26) (2000) 4413–4415.
- [5] E. B. Tadmor *et al.*, Polarization Switching in PbTiO₃: an ab initio Finite Element Simulation, *Acta Materialia* **50**(11) (2002) 2989–3002.
- [6] Y. Wei-Guo *et al.*, Molecular Dynamics Simulation of the Order-Disorder Phase Transition in solid NaNO₂, *Physical Review B: Condensed Matter and Materials Physics* **68**(17) (2003) 174106-1.
- [7] E. Heifets and R. E. Cohen (eds.), Ab initio Study of Elastic Properties of Pb(Ti,Zr)O₃, *Fundamental Physics of Ferroelectrics 2002*, CP 626 (American Institute of Physics, New York, 2002), pp. 150–159.
- [8] J. Iniguez and L. Bellaiche, Ab initio Design of Perovskite Alloys with Pre-determined Properties: The Case of Pb(Sc_{0.5}Nb_{0.5})O₃, *Physical Review Letters* **87**(9) (2001) 95503-1.
- [9] J. Iniguez, A. M. George and L. Bellaiche, Effects of Atomic Short-Range Order on the Properties of Perovskite Alloys in their Morphotropic Phase boundary, *Physical Review Letters* **91**(4) (2003) 045504-1.
- [10] S. C. Hwang, C. S. Lynch and R. M. McMeeking, Ferroelectric/Ferroelastic Interactions and a Polarization Switching Model, *Acta Metallurgica et Materialia* **43**(5) (1995) 2073–2084.
- [11] X. Chen, D. N. Fang, and K. C. Hwang, Micromechanics Simulation of Ferroelectric Polarization Switching, *Acta Materialia* **45**(8) (1997) 3181–3189.
- [12] T. Liu and C. S. Lynch, Ferroelectric Properties of [110], [001], and [111] Poled Relaxor Single Crystals: Measurements and Modeling, *Acta Materialia* **51**(2) (2003) 407–416.
- [13] L. Tieqi, C. S. Lynch, and E. A. McLaughlin, Thermodynamics of Stress and Electric Field Induced Phase Transition in Relaxor Ferroelectric Crystals, *Journal of Intelligent Material Systems and Structures* **18**(4) (2007) 409–415.
- [14] T. Liu and C. S. Lynch, Orientation Dependence of Nonlinearity and Hysteresis in PZN-4.5%PT Single Crystals I: Unipole Response, *Journal of Intelligent Material Systems and Structures* **17**(11) (2006) 953–957.
- [15] T. Liu and C. S. Lynch, Domain Engineered Relaxor Ferroelectric Single Crystals, *Continuum Mechanics and Thermodynamics* **18**(11) (2006) 119–135.
- [16] E. A. McLaughlin, T. Liu and C. S. Lynch, Relaxor Ferroelectric PMN-32%PT Crystals Under Stress, Electric Field, and Temperature Loading: 11-33-mode Measurements, *Acta Materialia* **53**(14) (2005) 4001–4008.
- [17] E. A. McLaughlin, T. Liu, and C. S. Lynch, Relaxor Ferroelectric PMN-32%PT Crystals Under Stress and Electric Field Loading: 1-32-mode Measurements, *Acta Materialia* **52**(13) (2004) 3849–3857.

- [18] R. E. Setchell, Shock Wave Compression of the Ferroelectric Ceramic $\text{Pb}_{0.99}(\text{Zr}_{0.95}\text{Ti}_{0.05})_{0.98}\text{Nb}_{0.02}\text{O}_3$: Microstructural Effects, *Journal of Applied Physics* **101**(5) (2007) 053525.
- [19] R. E. Setchell, Shock Wave Compression of the Ferroelectric Ceramic $\text{Pb}_{0.99}(\text{Zr}_{0.95}\text{Ti}_{0.05})_{0.98}\text{Nb}_{0.02}\text{O}_3$: Depoling Currents, *Journal of Applied Physics* **97**(1) (2005) 013507–1.
- [20] R. E. Setchell, Shock Wave Compression of the Ferroelectric Ceramic $\text{Pb}_{0.99}(\text{Zr}_{0.95}\text{Ti}_{0.05})_{0.98}\text{Nb}_{0.02}\text{O}_3$: Hugoniot States and Constitutive Properties, *Journal of Applied Physics* **94**(1) (2003) 573–588.
- [21] C. S. Lynch, The Effect of Uniaxial Stress on the Electromechanical Response of 8/65/35 PLZT, *Acta Materialia* **44**(10) (1996) 4137–4148.
- [22] W. Chen and C. S. Lynch, Model for Simulating Polarization Switching and AF-F Phase Changes in Ferroelectric Ceramics, *Journal of Intelligent Material Systems and Structures* **9**(6) (1998) 427–431.

Chapter 11

Ferroelectric Shock Depolarisation Studies

Since the operation of FEGs is based on the shock depoling of ferroelectric materials, a review of the vast amount of literature [1–68] on this topic is warranted. This line of research can be traced back to the 1950s, as opposed to piezoelectric compression studies that date back to the late 1800s.

Two methods are used to study the effects of stress on the electrical properties of ferroelectric materials: shock induced and non-shock induced. The first method consists of using gas guns or high explosives to generate shock waves in the ferromagnetic materials, while the second method consists of using electric presses, dropped projectiles or propellants to generate hydrostatic, quasi-static or acoustic waves. The ‘ferroelectric’ effect, which is associated with polarisation reorientation and phase transformation, can be driven by either shock compression or quasi-static loading. Shock loading of a material generally implies the ferroelectric effect, while lower amplitude stress loading implies the piezoelectric. In this chapter, attention is focused on the former method for generating stresses and the ferroelectric effect.

11.1 Early Shock Depolarisation Studies

In 1959, Berlincourt and Krueger [1] reported on the effects of mechanical and electrical stresses on lead titanate zirconate and barium titanate. They observed that poled ferroelectric ceramics exhibit linear piezoelectric effects for relatively low mechanical stresses, but under high pressure they exhibit nonlinear effects due to domain reorientation. They measured the open-circuit voltage, short-circuit charge and mechanical strains produced by ferroelectric samples that were subjected to either slowly or rapidly applied uniaxial compressive stresses ranging up to 60,000 psi, either parallel or

perpendicular to the poled axis. In summary, it was found that

- Effects in the open-circuit mode are much different to those in the short-circuit mode. In the open-circuit mode, there are no substantial nonlinearities at stresses that cause considerable nonlinearity in the short-circuit mode. This is due to charge appearing on the electrode surfaces under compression that tends to maintain a field across the ferroelectric element in the same direction as the original poling field. This field tends to prevent domain switching. If the stress is maintained, the charge will gradually bleed off and the maintaining field disappears.
- In the open-circuit mode, uniaxial compression tends to generate a field in the direction of the poling field, which tends to maintain the field across the element and prevent domain reorientation.

In 1961, Wittekindt [2] studied the shape of the current pulses generated by a shock compressed thin ferroelectric cylinder.

In 1961 and 1962, Reynolds and Seay [3, 4] reported on the observation of the formation of two-wave shock structures in explosively loaded PZT doped with Nb_2O_5 , pure barium titanate and barium titanate doped with calcium titanate. Their test setup consisted of an explosive plane wave generator, a layer consisting of a mixture of barium nitrate and TNT, an impedance matching material, Plexiglas, and the ferroelectric sample. They found that a single impinging shock wave may generate a two-wave structure as the result of material rigidity that leads to the formation of an elastic wave from a polymorphic phase transition. They also found that in order for the two-wave structure to form, the leading shock wave must have a lower pressure and a higher velocity than the follow-on shock wave. The first shock wave in the two-wave structure will have a pressure and a velocity characteristic of the material it is propagating through and independent of the strength of the supporting shock wave in most materials. Finally, they found that there is a stable shock threshold — i.e. a pressure above which the two-wave structure cannot form, since the shock wave in this case is moving with a velocity greater than the velocity of the leading shock wave in the two-wave structure.

In 1965, Graham, Nielson and Benedict [5] reported on their study of the piezoelectric current generated by shocked X-cut quartz. They found that the amplitude of the current pulse generated and how it changes in time depend on the dielectric, piezoelectric and mechanical properties of the quartz under shock loading. One of their observations was that the

electric field due to the piezoelectric field in the stressed and unstressed portions of the quartz disk was distorted by a number of mechanisms, one of which was that at the outer edge of the disk the discontinuity in the electric potential and dielectric permittivity caused electric field fringing similar to that observed in parallel-plate capacitors. They also found that the current-time waveform was distorted when the pressure exceeded 25 kbar and that this distortion was due to electrical conduction (leakage current). Another observation was that the diameter-to-thickness ratio (d/l) affected the distortion of the current pulse. When the disks were fully electrodeed, the current-time profile was

- linear when $d/l \geq 10$;
- linear for about one-half wave-transit and then becomes nonlinear when $d/l = 5$; and
- nonlinear throughout the entire transit time when $d/l < 4$.

In 1966 and 1968, Halpin [6, 7] reported on his study of the influence of the magnitude of stress on the shape of the current pulses delivered to a short-circuited load. This was accomplished by launching flat face projectiles at various velocities against ferroelectric disks coated with electrodes. The stress waves moved along the axis of the disk in a direction parallel to, but opposite to the direction of the remanent polarisation. He used three types of ferroelectric materials: normally sintered PZT 95/5, hot pressed PZT 95/5 and PSZT 68/7. The two PZT 95/5 materials were selected so that materials having the same composition, but different densities could be compared and they selected the PSZT so that he could compare materials having different compositions. Halpin noted three observations:

- The magnitude and position in time of the peak current appeared to be stress dependent. That is, for stresses less than 10 kbar, the magnitude of the peak current is relatively small and it appears late in time. As the stress is increased to 15–20 kbar, the magnitude of the peak current increased and it shifted to earlier times. As the stress continued to increase beyond 20 kbar, the magnitude of the peak current decreased and it shifted to a later time.
- The total electric charge released to a short-circuited load also appeared to be stress dependent. For the low- and high-stress regimes, the total charge released is less than the remanent charge of polarisation, while in the mid-stress regime, the total charge released has a value near to that of the remanent charge polarisation.

- Most of the current pulse lengths were greater than the time expected for the pressure wave to transit the ferroelectric element. Thus, it was believed that the stress wave front tilt also affected the overall shape of the current pulse.

Halpin concluded that the dependence of the shape of the current pulse on stress is due to the combination of stress induced changes in remanent polarisation, permittivity and conductivity in the ferroelectric sample. He also noted that similar changes in current pulse shapes were observed when quartz was used. Finally, he looked at the impact of the load on breakdown. He found that when operated in the current-mode configuration — i.e. with a finite load resistance, no electrical breakdown for shock pressures ranging up to 34 kbar was observed. When operated in the voltage-mode configuration — i.e. open-circuit, he observed breakdown at pressures as low as 10 kbar.

In 1966, Cutchin [8] reported on the effects of polarity on the charge liberated when PZT 65/35 with a short-circuited load was shocked with high explosives. The test setup consisted of a two-component explosive plane wave generator, steel spacer, PZT sample and electrodes. Two polarity orientations were examined. The positive orientation was taken to be that in which the shock wave traveled opposite to the polarisation direction and the negative orientation was taken to be that in which the shock wave traveled in the same direction as the polarisation direction. He found there was sensitivity to the orientation of the polarisation of the PZT sample. The data indicated that the PZT ceramic was more sensitive to small variations in the pressure profile and that the electric field degradation was more pronounced when the stress traveled in a direction opposite to that of the polarisation, as opposed to when it traveled in the same direction. Since the electrical load and the stress conditions were the same for both orientations, these sensitivities must arise within the ceramic itself. These results support the earlier claims of Gerson and Jaffe [9] that PZT ceramics exhibit p-type conduction. In summary, it was concluded that conduction is more pronounced if the remanent polarisation is antiparallel to the direction of shock wave propagation.

In 1967, Linde [10] reported on his investigation to determine whether permanent depolarisation occurred in microseconds or submicroseconds. Three materials were investigated: barium titanate, PZT 52/48 and PZT 95/5. In all three cases, the stress wave moved opposite or antiparallel

to the polarisation direction and the samples were connected to short-circuited loads. All three ceramic samples were significantly depolarised within the microsecond duration of the experiment. It was concluded depolarisation was the result of several mechanisms, including piezoelectric reduction of dipole moments, domain switching and dynamic phase transitions (ferroelectric-to-antiferroelectric transitions).

In 1968, Graham and Halpin [11] reported on their study of the electrical breakdown that occurs in X-cut quartz when compressed by shock waves. They looked at two different orientations: $-X$, where the shock wave traveled in a direction opposite to the polarisation, and $+X$, where the shock wave traveled in the same direction as the polarisation. They found that breakdown occurred in the $-X$ orientation, but not in the $+X$ orientation. They concluded that since an electric field is present during breakdown in the $-X$ direction, the field accelerates electrons from the shock wave front into the stressed region and initiates breakdown.

In 1968, Doran [12] reported on his study of the shock wave compression of barium titanate and PZT 95/5. He found that a two-wave structure exists in the PZT when the shock pressures exceeded 40 kbar. He also noted that the PZT compositions he was working with underwent a ferroelectric-to-antiferroelectric transition.

In 1973, Lysne [13] extended the work of Graham and Halpin by looking at dielectric breakdown in shock loaded PZT 65/35. The PZT was connected across a resistive load and the shock wave traveled antiparallel to the remanent polarisation vector. In summary, he found that

- Dielectric breakdown is not explicitly a function of stress for stress values less than 23 kbar.
- Breakdown is not instantaneous.
- For electric fields greater than the breakdown threshold ($\approx 5 \text{ kV/mm}$), the time between the introduction of the shock wave into the PZT and the onset of breakdown decreased rapidly with increasing electric field.
- Electric fields generated by PZT specimens poled to $30 \mu\text{C/cm}^2$ and shocked by pressures of 10 kbar are sufficient to cause electrical breakdown.
- Axial release waves can travel at a velocity as much as 15% faster than the initial stress wave.

Lysne points out that one important ramification of these results is that the voltage response of a partially-poled PZT sample may be greater

at higher stresses than that of a fully-poled sample shocked to the same stress values. In a follow-on paper in 1974, Lysne [14] formulated a model to predict dielectric breakdown of shock-loaded PZT 65/35. He also investigated PSZT 70/30-6 [15] and found that poling it transformed it into a metastable ferroelectric phase. This led him to suggest that shock waves could readily transform the material into a stable antiferroelectric phase without conversion to a metastable ferroelectric phase in the absence of a strong electric field. He concluded that this could lead to an effective method for using short duration stress pulses generated by high explosives to depole large pieces of ceramics in explosive-driven power supplies.

In 1973, England and Gifford [16] were granted a patent for a solid state power supply activated by a pyrotechnic chain. The intended application for this two-stage power supply was as a power supply for fuses in munitions. The power supply had two piezoelectric generators. The first piezoelectric generator was stressed or shocked when the projectile was launched. It generated an electrical pulse used to trigger a sequentially fired pyrotechnic chain of devices, each of which had a predetermined time delay and which, respectively, generated a second stress or shock wave directed against the second piezoelectric generator. The second piezoelectric generator would continue to generate power to drive other fuse circuitry until the last pyrotechnic device ceased to function.

In 1975, Lysne and Percival [17] reported on their study of the response of PZT 95/5 doped with niobium to normal and transverse shock waves. They pointed out that this poled ferroelectric ceramic has a composition that places it near an antiferroelectric phase boundary and that it is neither linear nor reversible in response to stresses on the order of a few tenths of a gigapascal.¹ They also pointed out that in the past investigators had looked at loads consisting of very low (current or short-circuit mode) and very high (voltage- or open-circuit mode) resistances. Therefore, one of the objectives of their investigation was to determine the response of PZT 95/5 to transverse shock waves as a function of load resistance. It was shown experimentally that when the load resistance is zero ($R = 0$), electric fields ahead of and behind the shock wave are zero. However, when $R \neq 0$, electric fields exist and the dielectric properties of the shocked and unshocked material are important. The electric field ahead of the shock wave influences the mechanical properties of the unshocked material, which, in turn, affects the characteristics of the shock wave. It can be concluded that the

¹1 kbar = 100 MPa

characteristics of the shock wave are a function of the electric field, since the phase transition that the shock wave causes is dependent on the electric field.

Lysne and Bartel [18] also investigated the electromechanical response of PZT 65/35 in the open-circuit mode to axially or longitudinally shock loading in a direction antiparallel to that of the polarisation vector. They found that when the pressures were below approximately 20 kbar, the wave propagation was dispersive, while between 20 and 36 kbar, the shock wave propagation was steady. For pressures greater than 36 kbar, the final stress states were reached asymptotically. Also, it was found that the electrical response of a material at pressures around 60 kbar was complicated by a ferroelectric-to-paraelectric phase transformation and the kinetics by which the polarisation changed. In summary, they observed a degradation of the electrical response of PZT 65/35 when the pressure exceeded 65 kbar. This was thought to be due to either dielectric breakdown or an increase in the electrical conductivity of the PZT material.

Lysne [19] also investigated the dielectric properties of PZT 95/5 under normal shock loading. On the one hand, he pointed out that while axial loading can be mechanically one-dimensional, the observed electrical response is complicated by electric field induced depolarisation ahead of the shock front if the specimen is connected to a low-impedance electrical load. On the other hand, normal loading is inherently two-dimensional, but has the advantage that the electrical response is a monotonic function of time. Using normal loading, he determined the charge released and the dielectric permittivity of PZT 95/5 when shocked with an initial pressure of 1.6 GPa. He found that at this pressure, the remanent polarisation had vanished and the material was in a nonferroelectric state. However, he also found that the permittivity was independent of the electric field. Also, it was noted that PZT 95/5 transforms to an antiferroelectric state at hydrostatic pressures between 0.2 and 0.3 GPa and that complete surface charge liberation occurs between 1.3 and 1.6 GPa when operating into a short-circuit. In addition, he noted that for stress states above 1.6 GPa, the permittivity is independent of both the stress and the electric field. Lysne pointed out that knowing these parameters will be useful in the design of shock wave actuated power supplies based on phase transformations in PZT 95/5.

While attempting to determine the approximate dielectric equation of state for shock compressed PZT 65/35, Lysne [20] observed that it is possible to polarise this ferroelectric ceramic with shock waves. Lysne noted that when Berlincourt and Krueger [1] measured the charge released by

quasi-statically compressed PZT 52/48 and barium titanate, they found that for pressures on the order of a few tenths of a GPa that the charge released was a nonlinear function of the pressure and that it was considerably larger than that calculated using the piezoelectric coefficients. They also found that the entire charge deposited during the poling process could be released by stresses on the order of 0.3 GPa. Since this stress was well below the stress required to cause a phase transformation, they concluded that the charge released was due to randomisation of the aligned domains created during poling. Later, Reynolds and Seay [3, 4] measured the short-circuit current generated by shock compression of specimens made of the same material and found that the charge release was a linear function of stress and about half that obtained by Berlincourt and Krueger. Reynolds and Seay concluded that the short duration of the shock waves ruled out domain randomisation and that the charge release was due to the reversible linear piezoelectric effect. Linde [10] conducted a series of shock compression studies with PZT 52/48, PZT 95/5 and barium titanate and found that ferroelectrics could be partially depoled by a shock wave and that the partial depolarisation released charge amounts near those observed by Reynolds and Seay. Halpin [6, 7] showed that there are significant differences between shock and static compression of ferroelectric ceramics. Under static compression, electric fields do not form in short-circuited ferroelectric ceramics whereas under shock compression large oppositely directed electric fields are formed either side of the shock front in short-circuited ferroelectric ceramics. If these fields exceed the coercive field of the materials, they can induce changes in the remanent polarisation and large electromechanical coupling effects that must be taken into account when comparing shock and static measurements. Lysne confirmed that irreversible domain alignment changes did occur even when the stress levels were thought to be in the regime where they were believed to be reversible. He also confirmed that shock waves can increase the remanent polarisation of ferroelectric ceramics.

Mazzie [21] proposed a simple model for generating energy by normally shock compressing ferroelectric ceramics. Unlike Lysne and Percival [17], who assumed that the permittivities of the ferroelectric were different in the stressed and unstressed states, he assumed that they did not differ over the timescale of interest. He also assumed that the PZT 95/5 sample could be modeled as a bulk capacitor with constant capacitance connected in parallel with a resistor. He found that the important design parameter was the value of the RC time constant relative to the shock transit time.

In 1978, Fritz [22] assessed the importance of phase transition and domain reorientation in stressed PZT 95/5. Up until then, it was thought that the main mechanism for shock-induced depoling was a ferroelectric-to-antiferroelectric phase transition, which was found to occur with hydrostatic pressures ranging from 0.2 to 0.5 GPa. However, Fritz found that the main mechanism for uniaxial stress depoling of PZT 95/5 in the pressure range from 0.05 to 0.3 GPa was domain switching and that there was no evidence of ferroelectric-to-antiferroelectric phase transitions.

Dick and Vorthman [23] studied the effects of the electrical state of PZT 95/5 on its mechanical and electrical response to impact loading. They considered both poled and unpoled PZT with short-circuited and resistive loads. They found that domain reorientation occurs in poled and unpoled samples, but that poling does not alter the point at which phase transition occurs nor its kinetics. They also found that domain reorientation and phase transitions cannot be separated and that domain reorientation is probably more important in unpoled materials. This result occurs because the domains in poled materials are already aligned normal to the applied strain direction. In addition, they found that when a high resistive load is connected to a poled sample, there was no dramatic change in the wave front from that observed in the short-circuit case. They did see a dramatic change in the final particle velocity. It was lower in samples with high electric fields.

Mock and Holt [24] experimentally investigated the pulse charging of a nanofarad capacitor by shock depoling PZT 56/44 and 95/5 transversely and normally. Some of their findings were:

- A decrease in charge flow from the PZT unit as the depoling stress wave passed through it. This observation is based on the decreasing amplitude of the current pulse and the concave-down shape of the voltage pulse. It was speculated that the decreasing charge flow may be due to increasing voltage on the PZT unit itself. This voltage increase may make it more difficult for the bound surface charge to be released or may cause a partial repoling of the PZT material behind the shock front. Another contributing factor may be due to stress release from the sides of the PZT unit, which was entirely encapsulated in a material having a lower shock impedance.
- An increase in charge released from identical PZT 56/44 units when the shock stress increased. This implied that the electrical conduction within the PZT unit did not increase in the stress range (4.4 to 7.8 GPa) studied.

- An increase in the load voltage as the size of the PZT unit increased. Increasing the size of the unit increased the amount of charge available for release.

Brown and Chen [25] computationally investigated the electromechanical response of axially-loaded ferroelectric ceramics. They found that the electric field reaches a peak value and then rapidly decays to a point where it gradually starts to rise. They concluded that the peak value of the field was due to the instantaneous piezoelectric response of the ceramic, the rapid decay was due to depoling and the gradual rise was due to the structure of the mechanical disturbance.

In 1979, Mock and Holt [26] reported on the shock depoling of PZT 56/44 in the longitudinal short-circuited mode. They looked at both parallel and antiparallel depoling of the PZT. For both orientations, they found that in the pressure range from 1.5 to 5.6 GPa, not all of the charge was released. In the pressure range 6.8 to 8.8 GPa, the charge released by the antiparallel orientation shots was less than that released by the parallel orientation shots.

11.2 Recent Shock Depolarisation Studies

Studies of shocked ferroelectric ceramics in the United States declined during the 1980s and early 1990s. In the late 1990s, R. Setchell and others at Sandia National Laboratory revived these studies and have published a series of papers. However, shock depolarisation studies continued in other countries such as Russia, Japan and China. Some of the more recent results, obtained mostly by Setchell and his team using modern diagnostics, will now be presented.

11.2.1 Shock Induced Stress Test Methods

Typically, the shock waves are generated by either high explosives or gas-gun launched projectiles [27, 28] in shock induced stress tests. In the case of explosives, the explosive charge can be placed in direct contact with the ferroelectric sample or in contact with a stationary material between the explosive charge and the sample. It can also be used to launch a flyer plate against the sample or a stationary material between the sample and the flyer plate.

In the case of gas guns, the shock waves are generated by either launching a projectile at a ferroelectric sample (*impact configuration*) or a ferroelectric sample at a target (*reverse-impact configuration*). The earliest shock wave studies of poled ferroelectrics used a longitudinal configuration — i.e. where the shock wave propagates along the poled axis [29]. It was found for this configuration that strong electric fields are generated and that lower than expected currents are produced in the external circuit [5]. Subsequent studies were conducted with the transverse configuration, where the shock wave propagates perpendicular to the poled axis [8, 12]. For this configuration, the electrical field generated could be either essentially zero or restricted to some value by selecting the proper load resistance. Also, the effects of different loads on generator operation were studied and included open-circuited, short-circuited, resistive, inductive and capacitive loads. A summary of the results of some of these studies will be provided in this section.

11.2.1.1 *Projectile Impact Studies*

The study of the effects of a projectile impacting with a ferroelectric sample or of a ferroelectric sample impacting with a target on the properties of the ferroelectric material has been ongoing since the early 1950s [27, 28]. The results of these as well as more recent studies were summarised in three papers by Setchell [27, 28, 62], which will serve as the basis for the brief review presented in this section. Most of the results presented here will be for PZT 95/5 modified with 2% niobium and referred to as PZT 95/5-2Nb. This material was selected since early in the study of FEGs, it was found to be the most promising material for this application. At ambient conditions, PZT 95/5-2Nb is a ferroelectric material with a rhombohedral structure that is near the boundary with an antiferroelectric phase having an orthorhombic structure. Shock compression of the ferroelectric phase of the material into an antiferroelectric phase at a pressure of about 0.3 GPa provides a rapid mechanism for depoling the material and releasing the bound charge to an external circuit.

11.2.1.2 *Hugoniot States and Mechanical Properties*

Using the reverse-impact configuration, the Hugoniot curve, Fig. 11.1, of unpoled PZT 95/5-2Nb was measured [27, 28, 62]. It was found to be a complex curve with multiple reversals in curvature resulting from the transition from an anomalous ferroelectric state to an extended mixed

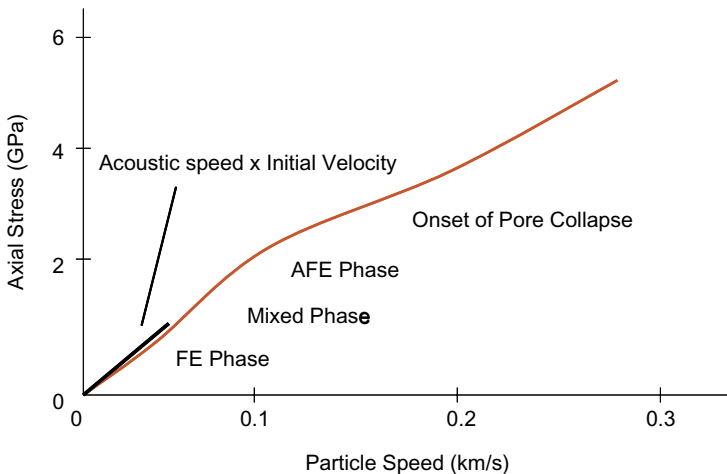


Fig. 11.1 Hugoniot curve for PZT 95/5 obtained from reverse impact experiments.

ferroelectric-antiferroelectric state, to an antiferroelectric state and finally to the onset of pore collapse as the pressure increased. Below 0.5 GPa, the curve has a negative curvature that corresponds to an anomalous compressibility. This results in the formation of an unsteady ramp at the foot of the propagating wave. The curvature reverses itself due to the onset of a ferroelectric-to-antiferroelectric phase transition, but becomes negative again above 2 GPa due to dynamic yielding. The negative curvature from 2.0 GPa to 4.0 GPa corresponds to unsteady wave motion. Above 4.0 GPa, the Hugoniot curve shows little curvature. A two-wave structure occurs at 1.8 GPa that corresponds to a phase transition. Pore collapse in the ceramic occurs at shock pressures greater than 2.5 GPa.

11.2.1.3 Shock Compression Studies

The evolution of shock wave profiles can be used to study the dynamic stress-strain behavior of materials by varying propagation distance and shock amplitude. Some of the results obtained by Setchell [27, 28] are summarised below:

- As the impact velocity of the projectile or correspondingly, the peak stress in the PZT increases, the rise time of the transmitted wave decreases. At peak stresses greater than 0.5 GPa, two distinct wave structures, which

are probably due to the onset of a ferroelectric-to-antiferroelectric transition, are observed. At peak stresses of 2.2 GPa and higher, the wave structures are insensitive to phase transitions because of the onset of a relatively slow dynamic yielding process and/or pore collapse.

- Pores are naturally present in ceramics due to the manufacturing processes used to produce them. The yield threshold of these materials appears to depend primarily on the total porosity, rather than void morphology. The Hugoniot curves for PZT are not sensitive to differences in its porous structure for materials with the same density, but does steepen rapidly with increasing initial density.
- Whether the PZT is poled or not and the orientation of the polarisation relative to the direction of the stress wave can impact the transmitted wave's profile. The recorded profiles for low amplitude stresses in unpoled, axially poled and normally poled samples show distinct features that may be partially explained in terms of a domain reorientation process. The axially poled samples show a more complex response, which could be due to the presence of strong electric fields that are unique to this case. These same features were still apparent for higher amplitude stresses and the yield thresholds appeared to be essentially the same.
- Experiments indicate that sample thickness may have an influence on the transmitted wave profile. As the thickness of the sample increases, evolution of the wave features becomes more unsteady.
- The presence of strong electric fields can affect the constitutive mechanical properties of PZT. These fields can be generated by shock depoling an axially poled material or by connecting a normally poled sample to a high resistance load. Experiments indicate that the only effect due to electric field appears to be an increase in the time required for the field within the material to reach its peak value with increasing field strength.

11.2.1.4 *Depoling Studies*

Shock wave compression of poled PZT results in the rapid depoling and release of bound charge. Early shock wave induced depolarisation studies [26] were conducted using axially poled configurations. Even though strong electric fields were generated, lower than expected currents were generated in the output circuit. This was attributed to shock induced conductivity [27]. Later work focused on normally poled configurations. It was found that the electric fields generated by this configuration can be zero or may

be controlled by the resistance in the output circuit. Using PZT 95/5-2 Nb in a normally poled configuration, Setchell [62] has conducted more recent studies, the results of which are summarised below:

- Depoling currents are independent of the peak shock pressure when the peak stresses they generate are greater than the dynamic yield threshold of the ferroelectric material. When the peak stresses generated by the shock wave are less than the dynamic yield threshold, the current pulse profiles have increasing rise times and decreasing peak values as the peak pressure of the shock wave decreases.
- Depoling currents depend on the shape of the pressure pulse. Setchell compared the depoling currents generated by a shock wave with that generated by a ramped pressure pulse. He found that when the pressures were 2.5 Pa and greater, there is a very small impact on the depoling current generated by the shock wave compared to the current generated by the ramped pulse. However, at pressures of 0.9 GPa, there was a large difference. In the case of the ramped pressure pulses, the slow rise time initially induced a piezoelectric effect, rather than a ferroelectric effect. When the pressures became high enough to start the phase transition, the ferroelectric effect became dominant.
- Depoling currents from axially poled configurations are affected by electric fields, while depoling currents from normally poled configurations are not affected and can be controlled. According to Setchell, the presence of the electric field can possibly alter the constitutive mechanical properties of the ferroelectric material, thus altering the structure of the transmitted wave; shifting the equilibrium boundary between the ferroelectric and antiferroelectric phases and modifying the kinetics of the shock-driven phase transitions.
- Depoling currents do not appear to be much affected by how the PZT is processed or the presence of pore formers, except in the high field cases where relatively small differences in transition rates and dielectric properties may be affected by the field.
- Depoling currents are strongly affected by the initial density of PZT, since its phase transition characteristics change significantly with initial density. It was found that as the sample density decreased, the pressure at which the transition begins decreased and the total change in pressure needed to complete the transition increased. It was further found that the total charge released decreased more rapidly than linearly with decreasing density.

11.3 Early FEG Studies

The first practical application of piezoelectric devices occurred during World War I, when in 1917, P. Langevin and French co-workers began to perfect an ultrasonic submarine detector. Their transducer was a mosaic of thin quartz crystals glued between two steel plates. Between 1920 and 1940, these transducers found use in a number of devices including microphones, accelerometers, ultrasonic transducers, bender element actuators, phonograph pick-ups and signal filters. During World War II, research groups in the United States, Japan and the Soviet Union, while working on improved capacitor materials, discovered that certain sintered metallic oxide powders had dielectric constants 100 times higher than those of common cut crystals. Also, methods for easily manufacturing piezoelectric ceramics were developed. These advances led to the development of a number of new devices, including sonars, ceramic phonograph cartridges, ignition systems, sonobuoys, compact microphones and relays.

The first use of piezoelectric materials in power supplies appears to have been in the summer of 1942, when the German company HASAG Hugo Schneider AG, Werk Schlieben developed and produced the first anti-tank weapon, called panzerfaust. The panzerfaust was developed by a team headed by Dr. Langweiler in Leipzig. It went into production in October 1943. The power supply for the detonator was a crush piezoelectric generator.

In 1946, Gray [69] submitted a patent, that was granted in 1949, for a transducer to convert mechanical energy into electrical energy. The transducer used barium titanate ceramic in the tetragonal crystalline state.

In 1952, Kabik and Cecil [70] submitted a patent, which was granted in 1961, for an impact responsive electric primer based on a polarised piezoelectric element composed of barium titanate ceramic to generate a voltage sufficient to initiate a high explosive charge in missiles. A plunger was abutted against one of the electrodes of the piezoelectric element. Upon impact, it was driven into the electrode, shocking the piezoelectric element and generating a voltage proportional to the rate of increase in the pressure across the element.

In 1954, Ferrara [71] submitted a patent, which was granted in 1958, for an electromechanical transducer based on the use of piezoelectric crystals or prepolarised ceramics. The transducer used a striker to activate an explosive primer or explosive charge to stress the piezoelectric or prepolarised ceramic material, generating a potential difference across it. Ferrara maintained that

the magnitude of the potential difference induced across the transducer depends upon the manner by which the stress is applied and the degree to which it is applied. The proposed application for these transducers was as a fuse for mines and/or booby traps.

In 1956, Howe [72] submitted a patent, that was granted in 1961, for an 'energy converting device' based on piezoelectric materials for converting mechanical energy into electrical energy. The device consisted of a mechanical energy source (striker or firing pin), a means for multiplying the mechanical energy (explosive primer), and a piezoelectric material for converting the mechanical energy into electrical energy. Howe pointed out that these transducers are simple, lightweight and rugged, and that they have an indefinite shelf life. It was proposed these transducers could be used in relatively small projectiles.

In 1957, Stresau [73] submitted a patent, that was granted in 1971, for a device based on piezoelectric crystals to simultaneously initiate multiple explosive charges. The device consisted of a detonator, explosive charge, stack of steel or other metals having high tensile strength that are used to flatten the shock wave generated by the explosive, piezoelectric element and steel block that holds the piezoelectric element in place when the explosive charge is detonated. The proposed application for this device was as a simple and compact detonating system for controlling the shape of a detonation shock wave to enhance the performance of shaped charges or for controlling the fragmentation of bombs or projectiles, and as a fuse that could be activated mechanically, electrically or by flame.

The first papers on using explosive driven FEGs as pulsed power sources appear to be those by Neilson [74, 75] in the mid 1950s. Neilson worked with two different ceramics: lead zirconate titanate (PZT-1) and barium titanate. With the PZT-1 sample, a peak current of 4 kA and total charge of 600 μC was delivered by a 0.3 μs pulse to a 0.1 Ω load and, with the barium titanate, a voltage pulse that ramped up to 60 kV at 3 μs was delivered to a 50 k Ω load. He also experimented with both transverse and longitudinal mode generators, as well as several different generator geometric configurations, including planar, cylindrical and spherical.

In 1966, Besancon, David and Vedel [76] reported on their theoretical and experimental studies of FEGs, which they called *ferroelectric transducers*. They developed two different types of generator. The first was a *low-impedance generator* (also referred to as a *longitudinal* or *axially poled mode generator* in the literature) (Fig. 11.2) in which the shock front moved through a thin axially polarised ferroelectric ceramic in the direction of its

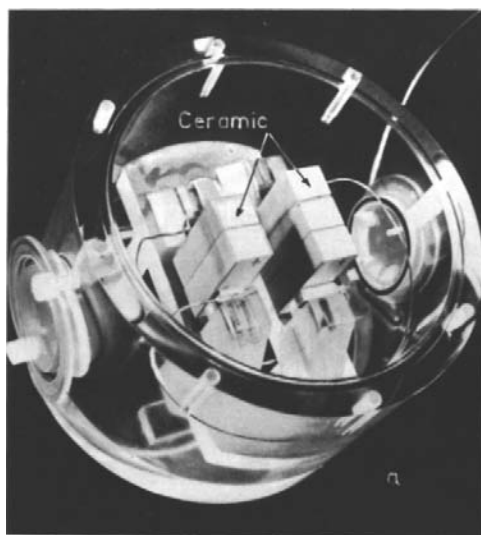


Fig. 11.2 Low-impedance FEG developed by Besancon *et al.* [76].

polarisation and the second was a *high-impedance generator* (also referred to as a *transverse* or *normally poled mode generator* in the literature) (Fig. 11.3) in which the shock front travels through a polarised ferroelectric ceramic in a direction perpendicular to its polarisation. Two types of

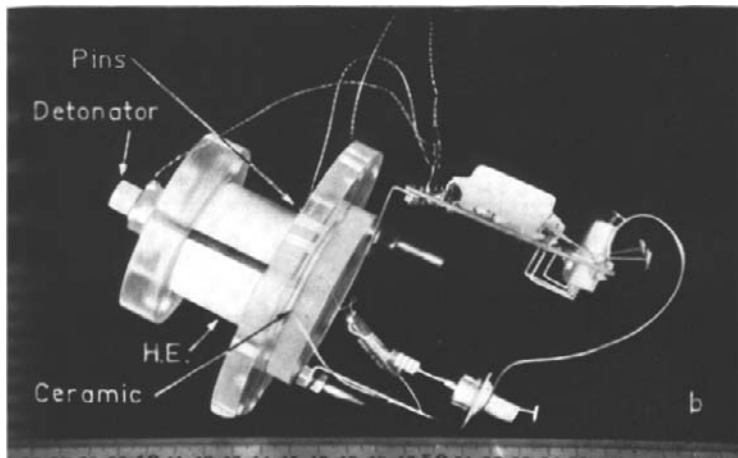


Fig. 11.3 High-impedance FEG developed by Besancon *et al.* [76].

ferroelectric were used in their experiments: barium titanate and lead zirconate titanate. They observed that the ratio of shock-released charge to polarised charge before shock action is higher for the high-impedance generators than it is for the low-impedance generators. They concluded that three phenomena accounted for the release of electric charge: (1) reorientation of molecular dipoles due to the shock wave, (2) the piezoelectric effect and (3) the pyroelectric effect.

In 1978, Rose and Mazzie [77] were granted a patent for a high-power, single-shot ferroelectric pulsed power source. The generator consisted of a pressure chamber, crystals (PZT or barium titanate) sandwiched between two electrodes and a spark gap switch. Pressure exerted on one of the electrodes, which acted as a pusher plate, induced a net voltage difference across the spark gap, which discharges when the voltage across it reaches its preset breakdown voltage. The pressure is created by igniting a combustible material with thermite pellets.

Beginning in the early 1980s, Prischepenko and Tretyakov [78], in Russia, conducted extensive testing of FEGs. They also integrated their FEGs with ferromagnetic generators to produce a very compact autonomous power supply. Demidov *et al.* [79] used a FEG to drive a cascade of FCGs. The FEG was used to seed a FCG with a diameter of 50 mm, which in turn, was used to seed an FCG with a diameter of 100 mm through a impedance matching transformer. Schoeneberg *et al.* [80] also looked at driving FCGs with FEGs. They built a FEG capable of delivering up to 1.7 J to a large inductive load. They concluded that FEGs show potential as seed sources since they are capable of driving much larger load impedances than other methods.

In 1987, Ludu, Nicolau and Novac [81] reported on their numerical and experimental study of the electrical pulses that could be generated by explosively shocked PZT 51/49. Two types of shock wave attenuator were developed. The first was based on the impedance mismatch between copper and Plexiglas, and the second was based on elasto-plastic wave separation in AISI 4340 Steel. The former consisted of two pairs of copper-plexiglass sandwiches, whose thicknesses were selected to avoid interference from reflecting shock waves while current is being generated. The highest pressure they generated in the PZT was 15 kbar. They found that if the pressure exceeded 50 kbar, there was a dramatic drop in current delivered to the load. They were able to reproducibly produce currents of 20–35 A and powers of 400–1400 W with both types of attenuator.

Wang, Dai, Sun and Chen [82] investigated possible applications for the phase transitions in PZT 95/5, one of which was explosive energy converters. They were able to deliver up to 1 kA to a short-circuit load, 15 kV to an open-circuit load and 0.5 J/cm³ to an inductive load. Wang [83, 84] tested FEGs with PZT 95/5 with two types of dopant: Nb and Sb. They found that the Nb dopant gave the best results, since the Nb increased the electrical resistivity of the material and enhanced domain orientations, both of which increase the remanent spontaneous polarisation, dielectric constant and piezoelectric constant of the PZT 95/5. They also used an FEG operating in the transverse mode to drive three types of load: short-circuit load, capacitive-resistive load and capacitive-inductive load. For the short-circuit load, they used PZT samples with dimensions of 0.5 × 28 × 1 cm and typically measured currents of about 330 A. For the capacitive-resistive load, they used PZT samples with dimensions of 4 × 4 × 1 cm and a 975 pF capacitive load with a 39 kΩ resistive load. They were able to generate 107 kV across the load. For the case of the capacitive-inductive load, they used PZT samples with dimensions of 0.5 × 7 × 1 cm and a 3.9 nF capacitive load with a 59 μH inductive load. The maximum energy density stored in the inductor was 0.243 J/cm³, which was significantly less than the energy density stored in the system prior to depoling. This result indicates that a large amount of the charge was lost inside the generator, possibly due to leakage current during the depoling process.

In 2004, Seo and Ryu [85] measured the electric current and load voltages generated by explosively shocked PZT 56/44 when connected to resistive loads. They conducted tests at with two shock strengths, 6.5 and 12 GPa, for resistive loads ranging from 10 to 1080 Ω. They concluded that the charge released by the PZT was affected by the shock pressure and load resistance. The maximum power and energy delivered to the loads used were 0.7 MW and 3.7 J respectively, when the shock pressure was 12 GPa and the load resistances were 125 and 1080 Ω.

The most recent work has been done by Texas Tech University (TTU) and Loki Incorporated in the U.S., which is the subject of the next chapter, and Diehl Munitionssysteme in Germany, which is described in Chapter 14.

11.4 Summary

It was shown in this chapter that piezoelectric and ferroelectric materials behave differently under compression. The former shows a linear response

associated with reversible processes, while the latter shows a nonlinear response associated with stress induced depolarisation or phase transitions. Setchell has shown that such parameters as porosity, particle size and density have an effect on the shock properties of a ferroelectric materials.

Explosive driven FEGs were first studied at the Sandia National Laboratory in the mid 1950s. This work continued into the early 1980s, at which time interest in FEGs waned until the late 1990s, when Sandia reinstated their FEG program and Texas Tech University started a program to investigate the physics of FEGs. In 2004, Loki Incorporated began an intense program to develop the FEG, using PZT 52/48 and PZT 95/5, and as a result they are able to produce highly reliable FEGs that provide consistent outputs.

Initially, Loki chose to work with PZT 52/48 due to the unavailability of PZT 95/5 — i.e. until TRS Technologies started to produce PZT 95/5 in 2006. Since both ceramics have been used in the most recent FEG studies, some of their properties and their advantages and disadvantages are briefly presented:

- One of the main disadvantages of PZT 52/48 is its relatively low internal breakdown strength (about 3.0–3.5 kV/mm). This property determines the open-circuit voltage produced by the FEG, which is about 3.2 kV/mm thickness of the sample. It should be noted that breakdown in both PZT 52/48 and PZT 95/5 is far from being intrinsic. Breakdown optimisation beyond 3 kV/mm is not important for commercial PZT applications. The advantages of the PZT 52/48 are its ready availability, low cost, reliability and reproducible FEG performance in the open-circuit and resistance modes.
- The primary advantages of PZT 95/5 are that it has a high remnant polarisation and can therefore store significantly more charge than PZT 52/48; it undergoes a shock induced phase transition at relative low shock pressures, which means it releases 100% of the charge stored during the poling process, unlike PZT 52/48, which tends to retain a portion of its charge; it has a high internal breakdown strength, the open-circuit voltage produced by PZT 95/5 elements is high (about 7.9 kV per mm thickness) and it has a demonstrated reliability and reproducible performance in the open-circuit mode. Since it releases its charge at relatively low shock pressures, it may be less susceptible to shock induced conductivity. This may be an issue if one tries to drive commercial PZT hard enough for complete depolarisation. However, shock induced conductivity issues are

speculative at this time. The primary disadvantage is that it has not been a commercially produced material and is therefore expensive and less mature than commercial PZT.

- The main differences between the two materials are that PZT 95/5 has a higher internal breakdown strength (6–8 kV/mm) in comparison with that of PZT 52/48; PZT 95/5 has a higher charge storage density (34–38 $\mu\text{C}/\text{cm}^2$) than PZT 52/48 (28–31 $\mu\text{C}/\text{cm}^2$); the capacitance of PZT 52/48 is about three times higher than it is for PZT 95/5; and 95/5 PZT stores more charge and releases the charge when shocked at nearly 100% efficiency (charge released/charge stored). Depending on the load, the combined effects of increased charge storage density and increased discharge efficiency result in PZT 95/5 producing up to twice the open-circuit voltage and over twice the energy per unit volume than a PZT 52/48 crystal having the same size.
- To improve the performance of PZT 95/5, a better understanding of the dielectric behavior under shock conditions is required so that designers can do a better job at achieving impedance matching to optimise energy transfer from the PZT to the load. The dielectric constant of PZT 95/5 is more complicated than suggested by small signal (*LCR* meter) measurements. When high voltages are applied to PZT 95/5, its dielectric constant changes from a small signal value of 300 to over 2000 and then slowly decreases again as the field continues to increase. Pressure induced phase transitions cause the dielectric constant to drop to at least half or more of its value before the transition. In addition, controlling the shock wave behavior is critical to improving the performance of both PZT 95/5 and PZT 52/48. For high voltage devices, the energy density of PZT 95/5 is determined by its breakdown strength, rather than its dielectric constant. Therefore, improvements in manufacturing can lead to continued increase in breakdown strength and, thus, in stored energy density for high voltage FEGs. For lower voltage FEGs, the charge delivered is the important parameter and the only way to increase this is to develop new materials that have a higher remnant polarisation.
- In general, ceramic processing is capable of providing ceramic elements with a very wide range of impedance values that can vary from relatively high impedance bulk elements, which are currently being supplied to FEG developers, to very low impedance elements that can be fabricated using ceramic capacitor technology. This provides flexibility for optimising FEG design to match a wide range of loads. To date, FEGs have been studied for resistive loads, where all the charge from the PZT 95/5

is recovered at low to moderate voltage (10 to 50 kV), and for capacitive loads, where a portion of the charge is recovered at high voltage (50 to 100 kV). Not much has been done with inductive loads. This would probably require a multilayer 95/5 element to more effectively match the low impedance. Optimisation trends for PZT 95/5 and PZT 52/48 will follow the same principals. PZT 52/48 will always have lower performance (lower voltage, lower delivered charge, lower delivered energy) than PZT 95/5 for equivalently optimised systems.

- FEGs can be used for a wide range of pulsed power applications. High voltage (>100 kV) can be generated with capacitive loads, usually at the expense of charge release efficiency, and charge release may be optimised at moderate voltage levels (<10 kV to approximately 50 kV) with resistive loads. PZT 95/5 has been well modeled as a current source when the threshold shock pressure is greater than 1–1.5 GPa. It has been found that the ‘discharge current’ is unaffected by voltage, while the ‘load current’ is affected by the voltage depending on the load type. For resistive loads, the current delivered to the load is affected by the RC time constant of the circuit. If the load resistance is high, the RC time constant increases, causing the charge delivery to the load to be slower. For capacitive loads, the FEG acts like two capacitors (the load and the PZT) being charged in parallel by a constant current source.
- To improve the performance of PZT 95/5, it needs to be determined if the voltage limitations are due to enhanced conductivity through the crystal or partial breakdown at the crystal and potting material interface.
- Improving performance also depends on the type of load. For resistive loads, improved performance will come from a high remnant polarisation to provide more charge during shock loading. Methods are being investigated to improve performance by both doping and looking at new materials with higher remnant polarisation. The first approach (PZT 95/5 doping) should retain the advantages of PZT 95/5 (complete depolarisation), but the remnant polarisation increases are expected to be modest. The second approach (new materials) has promise for more significant increases in remnant polarisation, but shock pressure for complete depolarisation may increase. For capacitive loads, more benefit can be gained by increasing dielectric breakdown strength rather than from increasing remnant polarisation. This allows the generation of higher voltages during discharge and therefore, higher energy densities for optimally matched loads. The energy density in the load increases as the square of the voltage, but only linearly with charge density. Increases

in dielectric breakdown strength are being investigated by altering a variety of process-related issues, including density, grain size, chemical stoichiometry and purity. Issues surrounding inductive loads are not known, but it is believed that this can be nearly optimised with ceramic element design — e.g. multilayer structures. Such design optimisation could also be helpful for capacitive loads by allowing one to better match the voltage generated by the PZT 95/5 with a practical capacitor design.

Bibliography

- [1] D. Berlincourt and H. A. Krueger, Domain Processes in Lead Titanate Zirconate and Barium Titanate Ceramics, *Journal of Applied Physics* **30**(11) (1959) 1804–1810.
- [2] R. H. Wittekindt, Shape of the Current Output Pulse from a Thin Ferroelectric Cylinder under Shock Compression, D. O. F. L., TR (1961), p. 922.
- [3] C. E. Reynolds and G. E. Seay, Two-Wave Shock Structures in the Ferroelectric Ceramics: Barium Titanate and Lead Zirconate Titanate, *Journal of Applied Physics* **33** (1962) 2234.
- [4] C. E. Reynolds and G. E. Seay, Multiple Shock Wave Structures in Polycrystalline Ferroelectrics, *Journal of Applied Physics* **32**(7) (1961) 1401–1402.
- [5] R. A. Graham, F. W. Nielson and W. B. Benedick, Piezoelectric Current from Shock-Loaded Quartz — A Submicrosecond Stress Gauge, *Journal of Applied Physics* **36**(5) (1965) 1775–1783.
- [6] W. J. Halpin, Current from A Shock-Loaded Short-Circuited Ferroelectric Ceramic Disk, *Journal of Applied Physics* **27**(1) (1966) 153–163.
- [7] W. J. Halpin, Resistivity Estimates for Some Shocked Ferroelectrics, *Journal of Applied Physics* **39**(8) (1968) 3821–3826.
- [8] J. T. Cutchen, Polarity Effects and Charge Liberation in Lead Zirconate Titanate Ceramics under High Dynamic Stress, *Journal of Applied Physics* **37**(13) (1966) 4745–4750.
- [9] R. Gerson and H. Jaffe, Electrical Conductivity in Lead Titanate Zirconate Ceramics, *Journal of Physics and Chemistry of Solids*, **24**(8) (1963) 979–984.
- [10] R. K. Linde, Depolarisation of Ferroelectrics at High Stress Rates, *Journal of Applied Physics* **38**(12) (1967) 4839–4842.
- [11] R. A. Graham and W. J. Halpin, Dielectric Breakdown and Recovery of X-Cut Quartz under Shock-Wave Compression, *Journal of Applied Physics* **39**(11) (1968) 5077–5082.
- [12] D. G. Doran, Shock-Wave Compression of Barium Titanate and 95/5 Lead Zirconate Titanate, *Journal of Applied Physics* **39**(1) (1968) 40–47.
- [13] P.C. Lysne, Dielectric Breakdown of Shock-Loaded PZT 95/5, *Journal of Applied Physics* **44**(2) (1973) 577–582.

- [14] P. C. Lysne, Prediction of Dielectric Breakdown in Shock-Loaded Ferroelectric Ceramics, *Journal of Applied Physics* **46**(1) (1975) 230–232.
- [15] P. C. Lysne, Kinetic Effects in the Electrical Response of a Shock-Compressed Ferroelectric Ceramics, *Journal of Applied Physics* **46**(11) (1975) 4078–4079.
- [16] F. E. England and J. H. Gifford, Solid State Power Supply Activated by a Pyrotechnic Chain, U.S. Patent 3,756,157, Granted (4 September, 1973).
- [17] P. C. Lysne and C.M. Percival, Electric Energy Generation by Shock Compression of Ferroelectric Ceramics: Normal-mode Response of PZT 95/5, *Journal of Applied Physics* **46**(4) (1975) 1519–1525.
- [18] P. C. Lysne and C. L. Bartel, Electromechanical Response of PZT 65/35 Subjected to Axial Shock Loading, *Journal of Applied Physics* **46**(1) (1975) 222–229.
- [19] P. C. Lysne, Dielectric Properties of Shock-Wave-Compressed PZT 95/5, *Journal of Applied Physics* **48**(3) (1977) 1020–1023.
- [20] P. C. Lysne, Shock-Induced polarisation of a Ferroelectric Ceramic, *Journal of Applied Physics* **48**(3) (1977) 1024–1031.
- [21] J. A. Mazzie, Simplified Model of Ferroelectric Energy Generation by Shock Compression, *Journal of Applied Physics* **48**(3) (1977) 1368–1369.
- [22] I. J. Fritz, Uniaxial-stress Effects in 95/5 Lead Zirconate Titanate Ceramic, *Journal of Applied Physics* **49**(9) (1978) 4922–4928.
- [23] J. J. Dick and J. E. Vorthman, Effect of Electrical State on Mechanical and Electrical Response of a Ferroelectric Ceramic PZT 95/5 to Impact Loading, *Journal of Applied Physics* **49**(4) 2494–2498.
- [24] W. Mock and W. H. Holt, Pulse Charging of Nanofarad Capacitors from the Shock Depoling of PZT 56/44 and PZT 95/5 Ferroelectric Ceramics, *Journal of Applied Physics* **49**(12) (1978) 5846–5854.
- [25] W. T. Brown and P. J. Chen, On the Nature of the Electric Field and the Resulting Voltage in Axially Loaded Ferroelectric Ceramics, *Journal of Applied Physics* **49**(6) (1978) 3446–3450.
- [26] W. Mock and W. H. Holt, Axial-Current-Mode Shock Depoling of PZT 56/44 Ferroelectric Ceramics, *Journal of Applied Physics* **50**(4) (1979) 2740–2748.
- [27] R. E. Setchell, Shock Wave Compression of the Ferroelectric Ceramics $Pb_{0.99}(Zr_{0.95}Ti_{0.05})_{0.98}Nb_{0.02}O_3$: Hugoniot States and Constitutive Mechanical Properties, *Journal of Applied Physics* **94**(1) (2003) 573–588.
- [28] R. E. Setchell, Shock Wave Compression of the Ferroelectric Ceramics $Pb_{0.99}(Zr_{0.95}Ti_{0.05})_{0.98}Nb_{0.02}O_3$: Depoling Currents, *Journal of Applied Physics* **97** (2005).
- [29] D. H. Edwards, L. Davies and T. T. Lawrence, The Application of a Piezoelectric Bar Gauge to Shock Tube Studies, *Review of Scientific Instruments* **41** (1964) 609–613.
- [30] P. C. Lysne, R. R. Boade, C. M. Percival and O. E. Jones, Determination of Release Adiabats and Recentered Hugoniot Curves by Shock Reverberation Techniques, *Journal of Applied Physics* **40**(9) (1969) 3786–3795.

- [31] P. C. Lysne, Determination of High-Pressure Equations of State by Shock-Loading Porous Specimens, *Communications* (1970), pp. 2152–2153.
- [32] P. C. Lysne, One-Dimensional Theory of polarisation by Shock Waves: Application to Quartz Gauges, *Journal of Applied Physics* **43**(2) (1972) 425–431.
- [33] R. A. Graham and G. E. Ingram, Piezoelectric Current from X-Cut Quartz Subjected to Short-Duration Shock-Wave Loading, *Journal of Applied Physics* **43** (3) (1972) 826–835.
- [34] P. C. Chen and L. Davison, Electrical Responses of Nonlinear Piezoelectric Materials to Plane Waves of Uniaxial Strain, *Journal of Applied Physics* **47**(11) (1976) 4759–4764.
- [35] P. C. Lysne, Shock-Induced polarisation of a Ferroelectric Ceramic, *Journal of Applied Physics* **48**(3) (1977) 1024–1031.
- [36] P. C. Lysne, Resistivity of Shock-Wave-Compressed PZT 95/5, *Journal of Applied Physics* **48**(11) (1977) 4565–4568.
- [37] M. F. McCarthy and H. F. Tiersten, Shock Waves and Acoustoelectric Domains in Piezoelectric Semiconductors, *Journal of Applied Physics* **48**(1) (1977) 159–166.
- [38] G. E. Duvall, The Shocked Piezoelectric Disk as a Maxwell Solid, *Journal of Applied Physics* **48**(10) (1977) 4415.
- [39] P. L. Stanton and R. A. Graham, The Electrical and Mechanical Response of Lithium Niobate Shock Loaded above the Hugoniot Elastic Limit, *Applied Physics Letters* **31**(11) (1977) 723–725.
- [40] P. J. Chen and S. T. Montgomery, Boundary Effects on the Normal-Mode Responses of Linear Transversely Isotropic Piezoelectric Materials, *Journal of Applied Physics* **49**(2) (1978) 900–904.
- [41] P. C. Lysne, Dielectric Properties of Shock-Wave-Compressed PMMA and an Alumina-Loaded Epoxy, *Journal of Applied Physics* **49**(7) (1978) 4186–4190.
- [42] P. C. Lysne, Electrical Response of Shock-Wave-Compressed Ferroelectrics, *High Pressure Science and Technology*, eds. K. D. Timmerhaus and M. S. Barber, Vol. 1 (Phlenum Press, New York, 1978), pp. 202–209.
- [43] P. L. Stanton and R. A. Graham, Shock-Wave Compression of Lithium Niobate 2.4 to 44 GPa, *Journal of Applied Physics* **50**(11) (1979) 6892–6901.
- [44] P. C. Lysne, Electrical Response of Relaxing Dielectrics Compressed by Arbitrary Stress Pulses, *Journal of Applied Physics* **54**(6) (1983) 3154–3159.
- [45] P. C. Lysne, Dielectric Relaxation in Insulators Slightly Damaged by Stress Pulses, *Journal of Applied Physics* **54**(6) (1983) 3160–3165.
- [46] V. Gupta and D. J. Epstein, Current from Shock-Loaded Piezoelectric Crystals, *Journal of Applied Physics* **67**(4) (1990) 2185–2188.
- [47] S. H. Chang, N. N. Rogacheva and C. C. Chou, Analysis of Methods for Determining Electromechanical Coupling Coefficients of Piezoelectric Elements, *IEEE Transactions on Ultrasonics, Ferroelectrics, and Frequency Control* **42**(4) (1995) 630–640.

- [48] D. H. Zeuch, S. T. Montgomery and D. J. Zimmerer, The Effects of Non-Hydrostatic Compression and Applied Electric Field on the Electromechanical Behavior of Poled PZT 95/5-2Nb Ceramic During $F_{R1} \rightarrow A_O$ Polymorphic Phase Transformation, Sandia Report SAND-95-1951 UC-704 (1995).
- [49] C. N. Xu, M. Akiyama, K. Nonaka, K. Shobu and T. Watanabe, Electrical Output Performance of PZT-Based Piezoelectric Ceramics, *Proceedings of the 10th IEEE International Symposium on Applications of Ferroelectrics* **2** (1996) 967–970.
- [50] C. B. Fleddermann and J. A. Nation, Ferroelectric Sources and Their Application to Pulsed Power: A Review, *IEEE Transactions on Plasma Science* **25**(2) (1997) 212–220.
- [51] C. N. Xu, M. Akiyama, K. Nonaka and T. Watanabe, Electrical Power Generation Characteristics of PZT Piezoelectric Ceramics, *IEEE Transactions on Ultrasonics, Ferroelectrics, and Frequency Control* **45**(4) (1998) 1065–1070.
- [52] R. E. Setchell, L. C. Chhabildas, M. D. Furnish, S. T. Montgomery and G. T. Holman, Dynamic Electromechanical Characterization of the Ferroelectric Ceramic PZT 95/5, *Shock Compression of Condensed Matter*, eds. S. C. Schmidt, D. P. Dandekar and J. W. Forbes, CP429 (American Institute of Physics, New York, 1998), pp. 781–784.
- [53] T. Funasaka, M. Furuhata, Y. Hashimoto and K. Nakamura, Piezoelectric Generator Using a LiNbO₃ Plate with an Inverted Domain, *Proceedings of the IEEE Ultrasonics Symposium* (1998), pp. 959–962.
- [54] D. H. Zeuch, S. T. Montgomery, D. J. Holcomb, J. M. Grazier and L. W. Carlson, Uniaxial Compression Experiments on PZT 95/5-2Nb Ceramic: Evidence for an Orientation-Dependent, Maximum Compressive Strain Criterion for Onset of the $F_{R1} \rightarrow A_O$ Polymorphic Phase Transformation, Sandia Report SAND99-0077 (1999).
- [55] L. C. Chhabildas and W. D. Reinhart, Intermediate Strain-Rate Loading Experiments — Technique and Applications to Ceramics, Sandia Report SAND-99-2116C (1999).
- [56] S. H. Zeuch, S. T. Montgomery and D. J. Holcomb, Uniaxial Compression Experiments on Lead Zirconate Titanate 95/5-2Nb Ceramic: Evidence for an Orientation-Dependent, “Maximum Compressive Stress” Criterion for Onset of the Ferroelectric \rightarrow Antiferroelectric Polymorphic Transformation, Sandia Report SAND-99-1933J (1999).
- [57] R. E. Setchell, S. T. Montgomery, L. C. Chhabildas and M. D. Furnish, The Effects of Shock Stress and Field Strength on Shock-Induced Depoling of Normally Poled PZT 95/5, *Shock Compression of Condensed Matter — 1999*, eds. M. D. Furnish, L. C. Chhabildas and R. S. Hixson, CP505 (American Institute of Physics, New York, 2000), pp. 979–982.
- [58] M. D. Furnish, L. C. Chhabildas, R. E. Setchell and S. T. Montgomery, Dynamic Electromechanical Characterization of Axially Poled PZT 95/5, *Shock Compression of Condensed Matter — 1999*, eds. M. D. Furnish, L. C. Chhabildas and R. S. Hixson, CP505 (American Institute of Physics, New York, 2000), pp. 975–978.

- [59] M. U. Anderson, R. E. Setchell and D. E. Cox, *Shock Compression of Condensed Matter — 1999*, eds. M. D. Furnish, L. C. Chhabidas and R. S. Hixson, CP505 (American Institute of Physics, New York, 2000), p. 551.
- [60] S. Sridhar, A. E. Giannakopoulos and S. Suresh, Mechanical and Electrical Response of Piezoelectric Solids to Conical Indentation, *Journal of Applied Physics* **87**(12) (2000) 8451–8456.
- [61] Yu. V. Sud'enkov, Electromagnetic Radiation Induced by the Failure of Piezoelectrics under the Action of Submicrosecond Stress Pulses, *Technical Physics* **46**(12) (2001) 1588–1590.
- [62] R. E. Setchell, Recent Progress in Understanding the Shock Response of Ferroelectric Ceramics, *Shock Compression of Condensed Matter*, eds. M. D. Furnish and N. N. Thodhani, CP620 (American Institute of Physics, New York, 2002), pp. 191–196.
- [63] S. T. Montgomery, R. M. Brannon, J. Robbins, R. E. Setchell and D. H. Zeuch, Simulation of the Effects of Shock Stress and Electrical Field Strength on Shock-Induced Depoling of Normally Poled PZT 95/5, *Shock Compression of Condensed Matter* eds. M. D. Furnish and N. N. Thodhani, CP620, (American Institute of Physics, New York, 2002), pp. 201–204.
- [64] R. E. Setchell, B. A. Tuttle, J. A. Voigt and E. L. Venturini, Effects of Initial Porosity on the Shock Response of Normally Poled PZT 95/5, *Shock Compression of Condensed Matter*, eds. M.D. Furnish and N. N. Thodhani, CP620 (American Institute of Physics, New York, 2002), pp. 209–212.
- [65] R. E. Setchell, Refractive Index of Sapphire at 532 nm Under Shock Compression and Release, *Journal of Applied Physics* **91**(5) (2002) 2833–2841.
- [66] M. Villagran-Muniz, M. Navarrete and E. V. Mejia-Uriarte, Photoacoustic Determination of Phase Transition in BaTiO₃ Induced by High Pressure at Room Temperature, *Review of Scientific Instruments* **74**(1) (2003) 732–734.
- [66] P. Yang, R. H. Moore, S. J. Lockwood, B. A. Tuttle, J. A. Voigt and T. W. Scofield, Chem-Prep PZT 95/5 for Neutron Generator Applications: The Effect of Pore Former Type and Density on the Depoling Behavior of Chemically Prepared PZT 95/5 Ceramics, Sandia Report SAND2003-3866 (2003).
- [67] A. Sani, B. Noheda, I. A. Kornev, L. Bellaiche, P. Bouvier and J. kreisel, High-Pressure Phases in Highly Piezoelectric PbZr_{0.52}Ti_{0.48}O₃, *Physical Review B* **69**(2) (2004) 020105-1–020105-4.
- [68] R. B. Gray, Transducer and Method of the Same, US Patent 2,486,560. Granted (1 November 1949).
- [69] I. Kabik and E.L. Cecil, Impact Responsive Electric Primer, U.S. Patent 2,972,306, Granted (21 Feb. 1961).
- [70] P.B. Ferrara, Energizer Assembly, U.S. Patent 2,827,851, Granted (25 March 1958).
- [71] R.C. Howe, Energy Converting Device, U.S. Patent 2,970,545, Granted (7 February, 1961).
- [72] R. H. F. Stresau, System for Multiple Point Simultaneous Initiation of Explosive Charges, U.S. Patent 3,589,294, Granted (29 June 1971).

- [73] F. W. Neilson, Ferromagnetic and Ferroelectric One-Shot Explosive Electric Transducers, Sandia Technical Report SCTM-230B-56(51) (1956).
- [74] F. W. Neilson and G. W. Anderson, *Bull. Am. Phys. Soc.* **11**(2) (1957) 302.
- [75] J. E. Besancon, J. David and J. Vedel, Ferroelectric Transducers, *Proceedings of the Conference on Megagauss Field Generation by Explosives and Related Experiments*, eds. H. Knoepfel and F. Herlach (Euroatom, Brussels, 1966), pp. 315–328.
- [76] M. F. Rose and J. A. Mazzie, Ferroelectric Pulsed Power Source, U.S. Patent 4,090,448, Submitted (29 December, 1971), Granted (23 May 1978).
- [77] A. B. Prishchepenko, D. V. Tretyakov and M. V. Shchelkachev, Energy Balance in Frequency Explosive Piezoelectric Generator during its Operation, Megagauss and Megaampere Pulse Technology and Applications, *Proceedings of the 7th International Conference on Megagauss Magnetic Field Generation and Related Topics*, eds. V. K. Chernyshev, V. D. Selemir and L. N. Plyashkevich (Sarov, VNIEF, 1997).
- [78] V. A. Demidov, V. D. Sadunov, S. A. Kazakov, L. N. Plyashkevich, T. V. Trischenko, S. N. Golosov, A. V. Blinov, I. K. Fetisov, M. V. Korotchenko and Ye. V. Shapovalov, Helical Cascade FCG Powered by Piezoelectric, *Proceedings of the 11th IEEE International Pulsed Power Conference* (1997), pp. 1476–1481 and *Proceedings of the 12th High-Power Particle Beams, Beams '98* (1998), pp. 269–272.
- [79] N. Schoeneberg, J. Walter, A. Neuber, J. Dickens and M. Kristiansen, Ferromagnetic and Ferroelectric Materials as Seed Sources for Magnetic Flux Compressors, *Proceedings of the 14th IEEE International Pulsed Power Conference* **2** (2003) 1069–1072.
- [80] A. Ludu, P. Nicolau and B. M. Novac, Shock Wave-Explosive Energy Generator of PZT Ferroelectric Ceramics, *Megagauss Technology and Pulsed Power Applications*, eds. C. M. Fowler, R. S. Caird and D. J. Erickson (Plenum Press, New York, 1987), pp. 369–375.
- [81] Y. L. Wang, X. Dai, D. Sun and H. Chen, The Applications of PZT 95/5 Ceramics by Induced Phase Transformation, *IEEE 7th International Symposium on Applications of Ferroelectrics* (1990), pp. 513–516.
- [82] Y. L. Wang, W. Z. Yuen, G. R. He, S. W. Lin, Y. H. Ling, C. F. Qu and B. G. Wang, Study on Shock Wave Explosive Energy Converter of PZT 95/5 Ferroelectric Ceramics, *Ferroelectrics* **49** (1983) 169–176.
- [83] Y. L. Wang and K. C. Kao, New Ferroelectric Ceramics for the Generation of High Energy Electric Pulses, *Conference Record of the 2000 IEEE International Symposium on Electrical Insulation* (Anaheim, CA, 2000), pp. 58–61.
- [84] M. S. Seo and J. Ryu, Explosively Driven Ferroelectric Generator for Compact Pulsed Power Systems, *Shock Compression of Condensed Matter*, eds. M. D. Furnish, Y. M. Gupta and J. W. Forbes, CP706 (American Institute of Physics, New York, 2004), pp. 1313–1316.

Chapter 12

Ferroelectric Generators

12.1 Introduction

In the previous chapter, it was noted that, beginning in the 1950s and 1960s, Sandia National Laboratory (SNL) and other laboratories studied the physical and electrical properties of piezoelectric and ferroelectric materials under shock wave compression. This work continued through the 1970s into the 1980s, at which time work in this field slowed down. It was revived in the United States in the late 1990s by Sandia National Laboratory, Texas Tech University, and a few small businesses. In this chapter, the results of the work done by Texas Tech University and Loki Incorporated will be discussed. They conducted a systematic study of compact explosive driven shock wave ferroelectric generators.

This chapter contains five main sections that give detailed descriptions of explosive driven shock wave ferroelectric generators (FEGs), results of experimental studies of the effect of shock wave depolarisation of ferroelectric materials, pulsed power generation with low and high resistance loads, and two practical applications, namely charging capacitor banks and Vector Inversion Generators (VIGs).

This chapter is unique in that all the experimental results presented herein were obtained with FEGs that had exactly the same design and contained the same type of ferroelectric energy carrying elements (lead zirconate titanate: $\text{Pb}(\text{Zr}_{0.52}\text{Ti}_{0.48})\text{O}_3$, $\text{Pb}(\text{Zr}_{52}\text{Ti}_{48})\text{O}_3$ or PZT 52/48). This makes it possible to compare the performance and efficiency of FEGs during different modes of operation. The term ‘energy carrying’ element refers to the energy stored in the ferroelectric element due to its polarisation. It is this energy that is delivered by the FEG to a load.

Some of the results described in this chapter were presented at various international conferences and workshops, as well as published in various refereed journals [1–14]. Nevertheless, some of the results herein are presented for the first time.

12.2 Gas Gun Accelerated Projectiles

In general, one can generate shock waves in piezoelectric and ferroelectric materials by the impact of an accelerated projectile. Many early studies of shock wave compression of piezoelectric and ferroelectric materials [15–20] were conducted using gas gun accelerated projectiles. Gas guns provided methods for initiating shock wave propagation along the material's polarisation vector, P , which is called longitudinal shock wave compression, and across P , which is known as normal or transverse shock wave compression. These gas gun studies provided important information about the physics of shock compressed piezoelectric and ferroelectric materials. The systems, however, are impractical for use outside the laboratory due to the large size of the gun barrel (10 m), the large mass of the system (more than 1000 kg) and their complicated control systems.

12.3 Electromagnetic Launcher Accelerated Flyer Plates

Kristiansen *et al.* [21] attempted to miniaturise FEGs by using accelerated flyer plates. An electromechanical flyer plate launcher was designed and built to induce shock loads in polarised materials. This Electromagnetic Launcher (EML) consisted of six $200\,\mu\text{F}$, 10.0 kV capacitors, which could be charged and then discharged by using an ignitron through a flat inductor on which the flyer plate rested. Copper and aluminum flyer plates of several dimensions were tested and it was found that the optimum plate for the EML was an aluminum plate with a diameter of 40 mm and a thickness of 3 mm. Using this plate and a capacitor charge voltage of 4.5 kV, the inductor current was about 100 kA and the flyer plate attained a speed of 225 m/s. This velocity was not high enough to generate a sufficiently strong shock wave in the piezoelectric or ferroelectric materials.

Kristiansen and his team [21] developed a computer code to simulate the EML and the plate motion. It was found that the EML initially accelerated the flyer plate to speeds that were two to three times greater than its final velocity. This initial acceleration was due to the first quarter period of the

current in the inductor; however, at peak current (when the rate of change in magnetic field is zero), the motion of the plate in the magnetic field became the dominant force producing mechanism and this slowed the plate. This deceleration was experimentally verified by using a high-speed camera to record the position of the plate as it left the surface of the inductor.

To make use of this reduced maximum speed, the target would have to be less than 1.0 cm from the inductor. With the target so close to the inductor and with such a large and rapidly changing magnetic field, electrical measurements at the target were impossible to make, due to induced voltages. A complete redesign of the inductor and capacitor bank would have been required in order to get the flyer plate out of the magnetic field before the current in the inductor reached its peak value. There were other limitations associated with this approach and it was eventually dropped.

12.4 Propellant Gun Accelerated Projectiles

Another approach was developed by Kristiansen *et al.* [21]. It consisted of using a .30-‘06 rifle mounted in a heavy steel tank, which could be sealed and evacuated. This propellant gun accelerated a 7.6 mm diameter, 8.4 gram copper-clad lead projectile to a speed of 840 m/s. It was shown in these experiments that evacuation of the chamber did not produce a meaningful increase in the final speed of the projectile. For this reason, most of their experiments were conducted at atmospheric pressure. This approach was capable of initiating a shock wave along the target’s polarisation vector, P , as well as across P .

Kristiansen and his team [21] conducted tests in which they generated shock waves in targets composed of poled piezoelectric cylinders by the impact of these projectiles. They chose poled cylinders of PZT 65/35 with a diameter of 2.54 cm and a length of 2.54 cm, because they had already been studied and reported on in the literature [18]. The remnant polarisation of the PZT 65/35 was $30 \mu\text{C}/\text{cm}^2$, which was the maximum charge that could be released into a load when the material was subjected to a large amplitude shock wave. The target assembly (Fig. 12.1) was mounted in a steel tank for testing. Projectile impact on the impactor plate created a stress wave in the PZT sample that generated an output voltage.

The output voltage across a $40.0 \text{ m}\Omega$ current viewing resistor was recorded with a digital oscilloscope. The impactor plates were made of brass and stainless steel with three thicknesses: 25 mm, 19 mm and 13 mm.

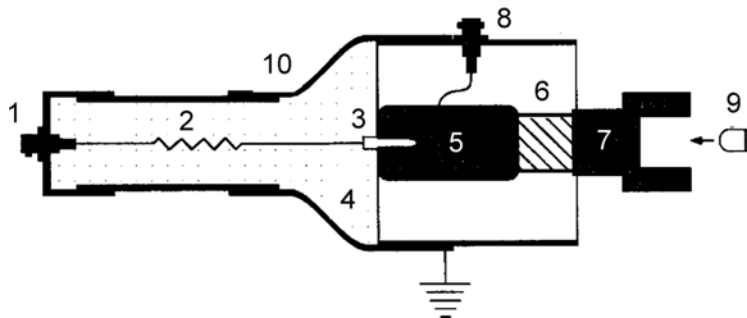


Fig. 12.1 Test setup for propellant gun-driven ferroelectric generator experiments: (1) shorted BNC, (2) $40\text{ m}\Omega$ current viewing resistor, (3) banana plug, (4) insulating potting, (5) 25 mm diameter by 50 mm long brass backing plate, (6) 22 mm diameter by 23 mm long PZT target (negative end is on the impactor plate, positive end is on the back plate), (7) impactor plate, (8) BNC for output signal, (9) incoming projectile and (10) copper tubing [23].

Tests were performed with projectiles made of different materials and having different thicknesses to optimise the shock transferred to the target.

Figure 12.2 shows a typical waveform from a propellant gun-driven longitudinal FEG. Analysis of this recorded waveform shows that a series of pulses were generated by the shock wave. Each pulse is a decaying sinusoid with a frequency that is a resonance of the target assembly.

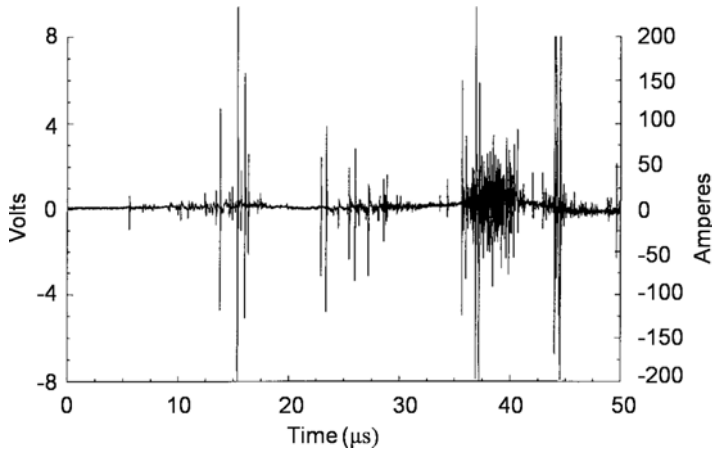


Fig. 12.2 Output voltage and current generated by a longitudinally shocked PZT 65/35 element across a $40\text{ m}\Omega$ current viewing resistor [23].

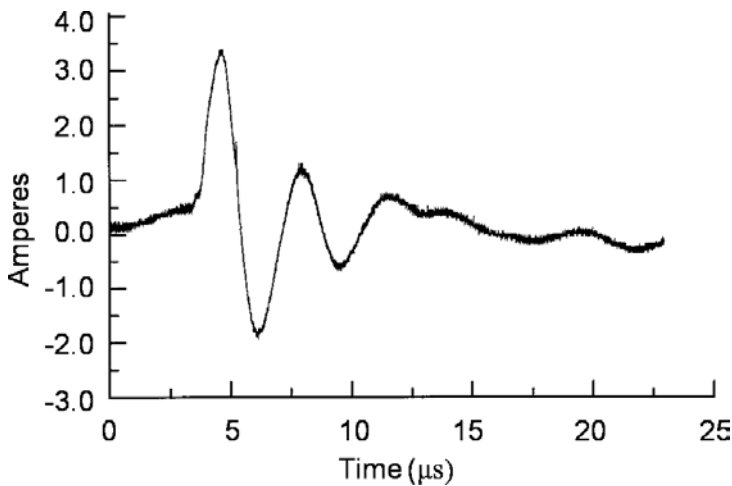


Fig. 12.3 Output current generated by a longitudinally shocked thin film of PVDF [23].

The same generator design was adapted for use with polyvinylidene fluoride (PVDF) thin films as the test material [21]. The PVDF has a higher remnant polarisation than PZT, but, as was the case in previous studies of PVDF, it was difficult to obtain pinhole-free sheets and even more difficult to polarise than PZT.

Figure 12.3 shows the current recorded for a typical shot with a PVDF disk having a diameter of 19 mm and a thickness of 0.025 mm. This voltage pulse is a decaying sinusoidal pulse. It can be seen that the PVDF did not disintegrate and that it was at least partially depolarised. The current generated in this case was only 3.75 A, because the volume of the sample was small and, thus, only a small amount of electric charge was available.

Initiation of a shock wave using the type of system described in Ref. 21 is problematic. By definition, a shock wave is an acoustic wave having an extremely short pulse length that travels in the material, at or above the material's sonic velocity. It is difficult to get a projectile to create a shock in a material that it strikes because the projectile deforms upon impact and because the transfer of kinetic energy to the target requires a finite amount of time, which is much longer than the shock pulse length. Therefore, the energy transfer must 'overdrive' the natural tendency of the material to resist being shocked in order to create an impact shock wave. It is difficult for a standard rifle projectile to overdrive a target.

12.5 Explosive Driven Ferroelectric Generators

12.5.1 Design of Explosive Driven FEGs

Significant progress in the development of autonomous compact ferroelectric generators was achieved when Shkuratov *et al.* [5] designed an explosive driven ferroelectric generator, the schematic diagram of which is shown in Fig. 12.4. This FEG design has proven to be an operationally reliable prime power source. For example, in more than 230 explosive experiments with FEGs of this design, it did not fail to generate pulsed power.

The FEG (Fig. 12.4) consists of a cylindrical body, an explosive chamber with detonator holder, a ferroelectric element holder and two leads that connect the contact plates on the ferroelectric module to its output terminals.

For the most part, the ferroelectric elements used in the FEGs described in this chapter were commercially available lead zirconate titanate [$\text{Pb}(\text{Zr}_{52}\text{Ti}_{48})\text{O}_3$ or PZT 52/48] ceramic disks supplied by EDO Corporation [22]. The polarisation direction (vector P) in the ferroelectric module is represented in Fig. 12.5 by an arrow. Metallic contact plates were deposited on both the flat surfaces of the disk. The physical properties of these PZT ceramic disks are: density $7.5 \times 10^3 \text{ kg/m}^3$, dielectric constant $\epsilon = 1300$, Curie temperature 320° C , Young's modulus $7.8 \times 10^{10} \text{ N/m}^2$,

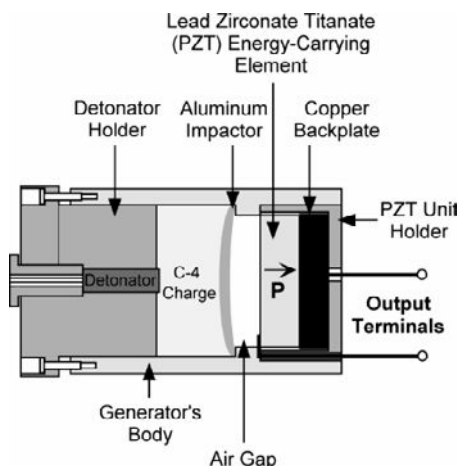


Fig. 12.4 Schematic diagram of an explosive-driven longitudinal ferroelectric generator [5].

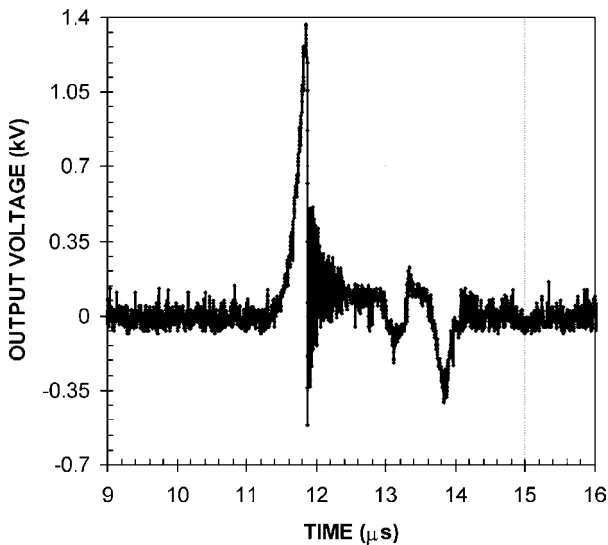


Fig. 12.5 A typical high-voltage waveform produced by an FEG containing a PZT 52/48 disk with dimensions $D = 25.0$ mm and $h = 2.5$ mm when electric breakdown has occurred inside the generator [1].

piezoelectric constant $d_{33} = 295 \times 10^{-12}$ C/N and piezoelectric constant $g_{33} = 25 \times 10^{-3}$ m²/C. While PZT 52/48 was the workhorse material for most of the testing done, other materials such as PZT 95/5 were also used in some testing. It was found that the PZT 95/5 was a superior material for use in FEGs since it generated significantly higher voltages.

Operation of the FEG is as follows. After detonation of the high explosive (HE) charge, a shock wave is generated and high-pressure gases are produced. The high-pressure gases are used to accelerate a flyer plate (labeled ‘aluminum impactor’ in Fig. 12.4). Collision of the flyer plate with the front of the ferroelectric element initiates a shock wave within the ferroelectric body. This shock wave propagates through the ferroelectric element and depolarises it. The depolarisation process releases the induced charge on the metallic end plates of the poled ferroelectric disk and a voltage pulse appears across the output terminals of the generator. The direction of shock wave propagation for the FEG in Fig. 12.4 was parallel to the polarisation vector P . This type of generator is referred to as a *longitudinal FEG*. There is a variant of the FEG in which the shock wave propagates perpendicular or normal to the polarisation vector and this type of generator is referred to as a *Transverse or normal FEG*.

The explosive portion of the FEG consisted of a plastic cylindrical detonator support that holds an RP-501 detonator, which was supplied by RISI [23], high-explosive charge and metallic impactor (flyer plate). The length of the air gap between the flyer plate and the ferroelectric element front contact plate, which is the acceleration path of the flyer plate, was 5 mm.

The metallic impactor is responsible for initiation of the shock wave in the ferroelectric element. To provide planar impact on the ferroelectric element, the impactor (Fig. 12.5) is a curved plate that deforms into a quasi-flat structure under blast loading. To derive the correct curvature and thickness of the flyer plate, the arrival times and locations of the explosive shock were estimated by applying the principles of geometric optics and impedance matching to detonation waves. Then, the shock transit time through the flyer plate material was estimated in order to calculate the arrival time of the shock wave along concentric circular loci on the target side of the flyer plate. The combination of shock arrival times and locations on the plate surface enables calculation of the plate curvature needed to produce essentially a flat flyer plate upon impact with the PZT target.

Desensitised RDX, which is essentially the same composition as Composition 4, or C-4, high explosives were used in all the FEGs described in this chapter. The detonation velocity of desensitised RDX is 8.04 mm/ μ s and the dynamic pressure at the shock front reaches 36.7 GPa. Depending on the configuration of the charge holder, the mass of the C-4 charge used varied from 12 to 17 g.

The cylindrical body of the FEG must be made from a material with good electrical insulating characteristics to avoid electrical breakdown during operation of the generator. Shkuratov *et al.* [1, 5, 12] conducted a series of experiments to determine the effects of the generator body material and its thickness on explosive and electrical operation of the FEG. Three types of plastic were used for the generator bodies: polyethylene, polyvinylchloride (PVC) and polycarbonate. The experimental results show that all of these materials work well. There was no significant difference in the generation of voltage pulses by FEGs having body-wall thicknesses ranging from 1 mm to 30 mm. From this, it can be concluded that the generator's body can be a lightweight thin plastic shell (less than a millimeter larger than the diameter of the ferroelectric element). The FEG holds together and does not disintegrate until after the explosive charge has completed detonation.

The ferroelectric disk was bonded to a copper back plate 1 mm larger in diameter than the ferroelectric element. The back plate thickness was 5 mm. A silver-loaded epoxy was used to bond the ferroelectric disk to the back

plate. The copper back plate provided mechanical impedance matching in order to minimise the reflection of stress wave when it reached the back face of the ferroelectric element. The silver-loaded epoxy also served as the electrical contact and reduced the capacitive reactance of the bond to a negligible value. The ferroelectric energy, along with the copper back plate, was centered in the cylindrical plastic holder.

The two electrical output terminals of the FEG were connected to two contact leads connected to the metallic contact plates deposited on the surface of the ferroelectric disk. One contact lead was bonded to the front plate of the ferroelectric disk, which was subjected to flyer plate impact, with silver-loaded epoxy. The other lead was bonded in the same manner to the copper back plate.

12.5.2 Electrical Breakdown Problems

One of the causes of explosive driven FEG performance degradation is electrical breakdown within the generator [14, 15, 26, 27]. A typical voltage pulse waveform produced by one of the earlier FEGs [5, 12] is shown in Fig. 12.5. The waveform had an irregular shape. The waveforms produced by similar FEGs, having ferroelectric disks of the same type and with nearly the same dimensions, varied significantly from shot to shot. It was evident that there was electrical breakdown in the system. After a series of investigations, including high-speed photography (500,000 frames per second) of an FEG in operation, it was found that electric breakdown did not take place as expected — i.e. at the high-voltage terminals, but rather on the sidewalls of the ferroelectric disk. This was not due to surface flashover as was initially suspected, since the ferroelectric disk sidewall was carefully cleaned before assembling the device. Instead, it was due to the expansion of the high-speed, high-pressure plasma generated by detonation of the HE.

In order to eliminate the effects of this detonation plasma on electrical operation of the FEG, the ferroelectric element holder was redesigned [10, 11, 16]. A schematic diagram of the redesigned ferroelectric module holder is shown in Fig. 12.6.

The gap between the ferroelectric disk sidewall and the inner wall of the module holder was increased and filled with hard insulating material (epoxy) (see Fig. 12.6). A series of experiments were performed with different types of epoxy compounds in order to find a potting material that provided the best high-voltage insulation in the FEG [10, 11, 15]. Epoxy

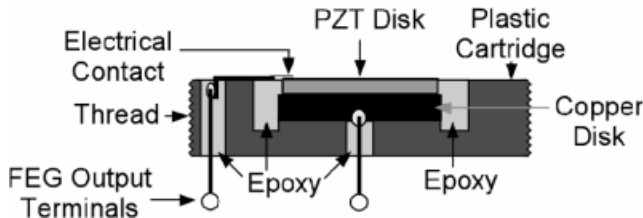


Fig. 12.6 Schematic diagram of a ferroelectric element module holder redesigned to prevent the deleterious effects caused by the detonation plasma produced during electrical operation of the FEG [4, 16].

SY-SS, which was produced by Pacer Technology LLC, possessed the highest breakdown field (4.8 kV/mm), and it proved to work well in FEGs.

Figure 12.7 demonstrates the advantage of the redesigned ferroelectric module holder. The voltage pulse amplitudes shown in Figs. 12.5 and 12.7 were generated with explosive-driven FEGs containing the same ferroelectric elements, PZT disks with $D = 25$ mm and $h = 2.5$ mm, and differed

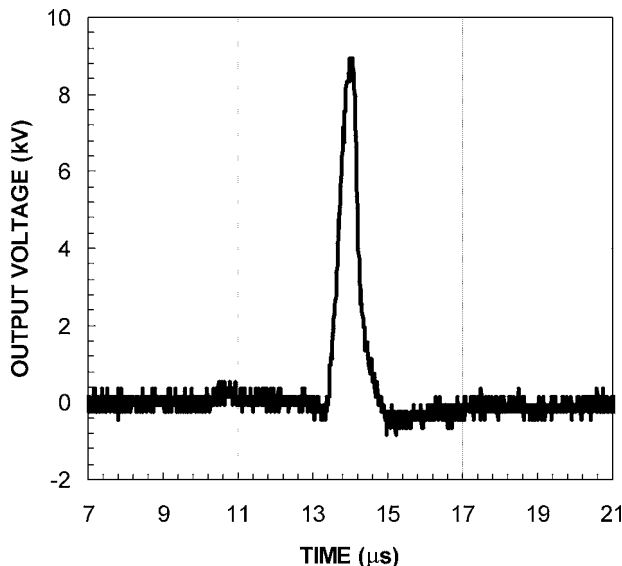


Fig. 12.7 A typical high-voltage pulse waveform produced by an FEG with a redesigned ferroelectric module holder (see Figs. 12.5 and 12.6). The ferroelectric element was a PZT 52/48 disk with dimensions of $D = 25$ mm and $h = 2.5$ mm [14].

by a factor of 6.5: $U_{\max}(t) = 9.1 \text{ kV}$ (Fig. 12.5) and $U_{\max}(t) = 1.4 \text{ kV}$ (Fig. 12.7). The waveform of the voltage pulse shown in Fig. 12.7 has a regular shape and shows no signs of electrical breakdown.

Studies [14] were performed to determine if there were any statistical deviations in the amplitudes and in the pulse durations (Full Wave at Half Maximum or FWHM) of the voltage pulses produced by FEGs with the same ferroelectric elements. The results of these studies demonstrated that the relative standard deviation of the amplitudes and FWHMs of the voltage pulses did not exceed 6–8% and 6–10%, respectively. These parameter ‘spreads’ were not considered to be critical for most practical FEG applications. Moreover, there is a high probability that these statistical variations are related to the industry standard tolerances for the initial polarisation, P , of ferroelectric cylinders (PZT 52/48), and are not related to the FEG system design.

When the output voltages produced by FEGs exceeded 20–23 kV, they were not quite reproducible and stable. It was postulated this was due to another type of electrical breakdown. To determine the location of this electrical breakdown, a series of experimental investigations was performed that included additional high-speed photography. Typical high-speed photographs for one such FEG test are shown in Fig. 12.8. The time interval between the photographs in the figure is $2 \mu\text{s}$.

Figure 12.8(a) shows detonator initiation within the FEG. Figure 12.8(c) shows complete detonation of the explosive charge. Figure 12.8(d) shows the beginning of FEG body destruction. Electrical breakdown between the output terminals of the FEG, which appears as the bright light emitted between the two upper output terminals, began at 10 microsecond (Fig. 12.8(d)). This light emission continued until $28 \mu\text{s}$ after the explosive sequence began.

Improved electrical insulation of the output terminals (heavy, insulated high-voltage cables) solved the breakdown problem in this case.

12.6 FEG Pulsed Power Generation: High Resistance Loads

High resistance loads, such as a spark gap, are quite common in different types of pulsed power systems. There are well-known difficulties associated with explosive driven pulsed power generators, including all types of FCG, magnetohydrodynamic generator, etc., delivering pulsed power to

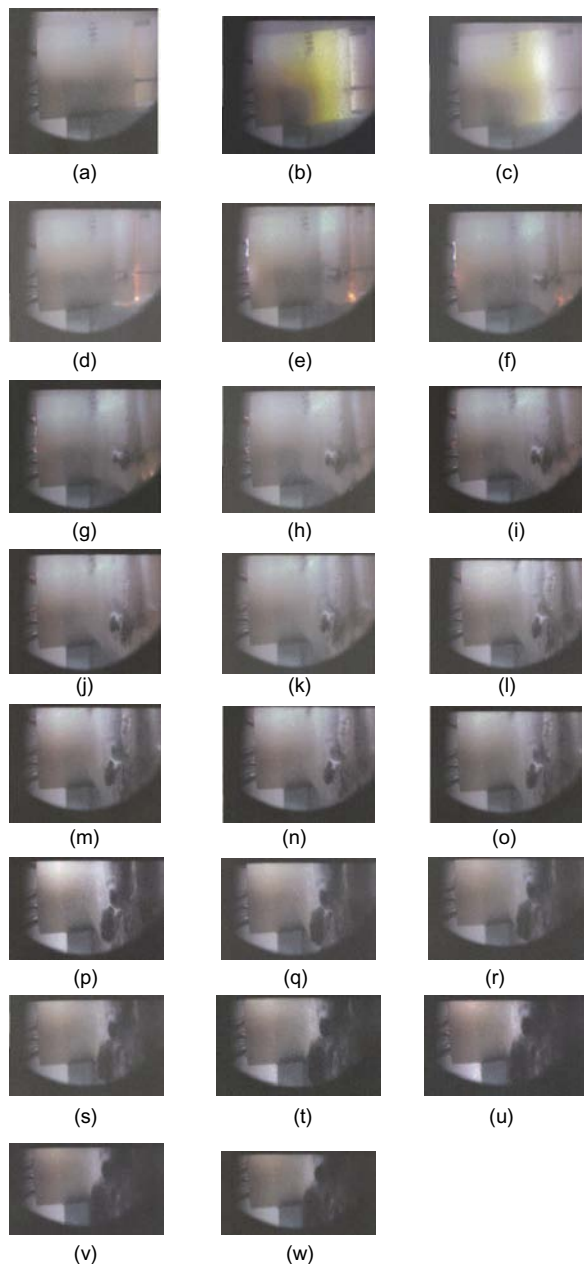


Fig. 12.8 A series of high-speed photographs taken during explosive and electrical operation of an FEG. The time interval between pictures is $2\ \mu s$.

high resistance loads. All of these generators are unable to deliver high voltages directly to high-resistance loads. In a series of systematic experimental studies conducted by Shkuratov [1, 5–7, 10, 13], it was demonstrated that longitudinal FEGs are an exception to this list. Explosive-driven FEGs are pulsed-power sources that effectively generate high voltages across high-resistance loads. It was further demonstrated that the output parameters of FEGs strongly depend on the geometric size of the ferroelectric element.

The experimental setup used to investigate the operation of the FEG in open-circuit mode is shown in Fig. 12.9. The FEG was placed inside a detonation tank. The high-voltage output terminal of the FEG, which is the positive plate of the ferroelectric element, was connected directly to the input of a Tektronix 6015A high-voltage probe (100 MΩ and 3 pF) and the negative (front) plate of the PZT disk was grounded. Note that high-voltage diodes and rectifiers were not used in these experiments.

The FEG ferroelectric elements were PZT 52/48 disks polarised along their cylindrical axis. Silver contact plates (electrodes) were deposited on both ends of the PZT disks by electron beam deposition and each disk was poled to its full remnant polarisation value of $P_0 = 30 \mu\text{C}/\text{cm}^2$. The geometrical dimensions of the PZT disks are given in Table 12.1.

The waveform of a typical voltage pulse produced by an FEG containing a PZT 52/48 ferroelectric element having dimensions of $D = 25 \text{ mm}$ and $h = 6.5 \text{ mm}$ is shown in Fig. 12.10. The voltage pulse peak amplitude was $U_g(t)_{\max} = 21.4 \text{ kV}$ and its FWHM was $1.1 \mu\text{s}$.

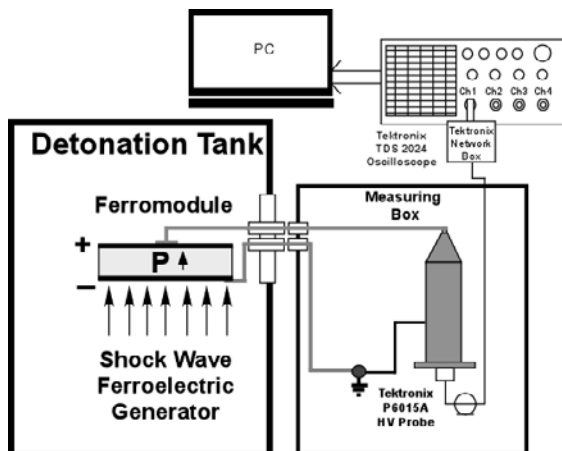


Fig. 12.9 Test setup used to investigate FEGs operating in the open-circuit mode [14].

Table 12.1 Geometrical dimensions of the PZT 52/48 ferroelectric elements used in the FEGs investigated in [4–12, 14].

Diameter, D (mm)	Thickness, h (mm)	Volume (cm ³)
26	0.65	0.35
27	2.10	1.20
25	2.50	1.23
25	5.10	2.50
25	6.50	3.20
25	10.8	5.30

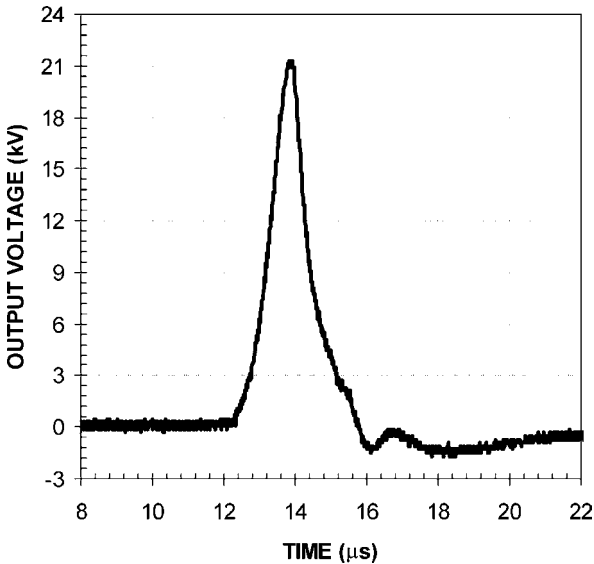


Fig. 12.10 A typical voltage pulse produced by an FEG containing a PZT 52/48 ferroelectric element having dimensions of $D = 25$ mm and $h = 6.5$ mm [14].

In Fig. 12.10, the increase in the voltage pulse from zero to its peak value is the direct result of the depolarisation of the ferroelectric element. Shock wave depolarisation caused the induced electric charge on the contact plates of the ferroelectric disk to be released to the load. Because of the high resistance and low capacitance of the load, which is the high-voltage probe, the charge released by the ferroelectric element (initially a capacitor) charges it to high voltage. The voltage pulse rise time corresponds to the shock front propagation time through the thickness of the ferroelectric disk.

Since there was no charge transfer from the ferroelectric element in this mode of FEG operation, it might be expected that the waveform of the EMF pulse produced by the FEG would be a square pulse having an amplitude of $U_g(t)_{\max}$ with a flat top that lasts several microseconds — i.e. until the mechanical destruction of the ferroelectric element has been completed. However, it follows from the experiments performed that after reaching its maximum value, the EMF pulse does not maintain its maximum value, but rather it decreases rapidly (see Fig. 12.10).

To understand this phenomenon, it is necessary to take into consideration that the shock wave propagating through the ferroelectric element has very complex characteristics [15–19, 24, 25]. The shock wave consists of the superposition of a number of elastic and inelastic acoustic and shock waves [18, 19, 25] that depolarise the ferroelectric element and significantly change its physical properties. Apparently, the rapid decrease in the voltage pulse after it reaches its peak value was the result of either a significant increase in the electrical conductivity of the shock compressed portion of the ceramic material, which is behind the shock as it traveled through the disk, and a corresponding increase in the leakage current in the element or the result of internal electrical breakdown within the ceramic disk.

Figure 12.11 summarizes the experimental results reported in Refs. 10, 11, 15 and 16 by showing the dependence of the voltage pulse amplitudes and their FWHMs on the thickness of the PZT 52/48 ferroelectric elements. It follows from the experimental data (Fig. 12.11) that the amplitude and FWHM of the voltage pulse are highly reproducible for each element of the same size, but that they increase as the thickness of the PZT ferroelectric element increases.

For a PZT 52/48 ferroelectric element with $h = 0.65$ mm, its maximum amplitude is $U_g(t)_{\max} = 3.6 \pm 0.23$ kV and its FWHM is 0.2 ± 0.04 μ s. Increasing the thickness of the ferroelectric element to 2.5 mm almost triples the amplitude of the voltage pulse to 8.9 ± 0.07 kV. The FWHM increases by more than 3 times to 0.62 ± 0.02 μ s. For a ferroelectric element having a thickness of $h = 5.1$ mm, its maximum amplitude is $U_g(t)_{\max} = 17.03 \pm 0.25$ kV and its FWHM is 0.9 ± 0.03 μ s, and for a ferroelectric element with $h = 10.8$ mm, its maximum amplitude is $U_g(t)_{\max} = 29.7 \pm 0.7$ kV and its FWHM is 1.7 ± 0.15 μ s.

It follows from the experimental data shown in Fig. 12.11 that the amplitude of the EMF pulse is directly proportional to the thickness of the PZT 52/48 element and that the coefficient of proportionality is equal to 3.4 ± 0.5 kV/mm. This dependence is practically linear. However, if there is a nonlinear component, the data will 0.012 μ s/mm.

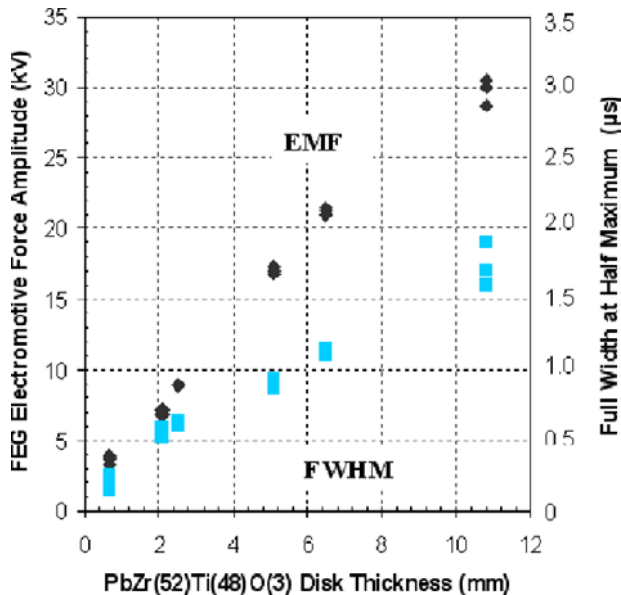


Fig. 12.11 Experimentally measured dependence of the voltage pulse amplitude (diamonds) and FWHM (squares) on the thickness of the PZT 52/48 element [1, 6, 7, 14, 16].

To find the lower boundary of the energy produced by an FEG operating in the open-circuit mode, the following relationship can be used:

$$W = C_0 \frac{U_{OC}^2}{2}, \quad (12.1)$$

where W is the energy produced by the FEG, C_0 is the initial capacitance of the ferroelectric energy-carrying element and U_{OC} is the open-circuit voltage amplitude produced by the generator.

Figure 12.12 shows the lower boundary of the energy produced by FEGs operating in the high resistance mode and the corresponding specific energy density of the PZT energy carrying elements versus the thickness of the elements. Increasing the thickness of the PZT element increases the energy produced by the FEG from $W = 47.2 \pm 7.4 \text{ mJ}$ ($h = 0.65 \text{ mm}$) to $W = 270 \pm 9 \text{ mJ}$ ($h = 10.8 \text{ mm}$). At the same time, increasing element thickness reduces the specific energy density from $136 \pm 15 \text{ mJ/cm}^3$ ($h = 0.65 \text{ mm}$) to $51.4 \pm 2.8 \text{ mJ/cm}^3$ ($h = 6.5 \text{ mm}$).

In summary, it has been experimentally determined that ultracompact explosive-driven ferroelectric generators are capable of producing voltage

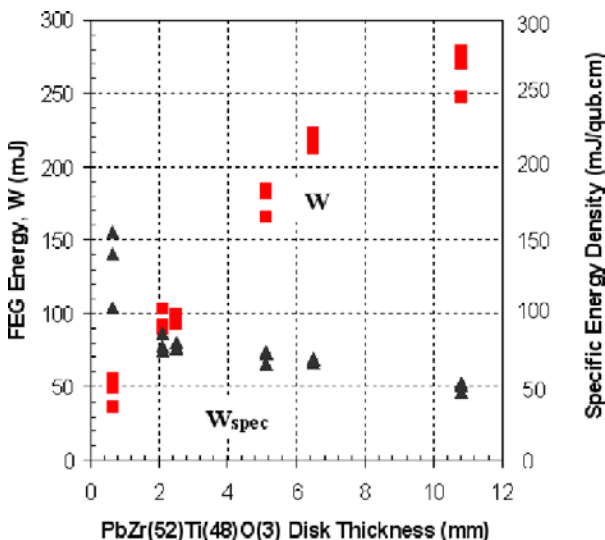


Fig. 12.12 The lower boundary of the energy (squares) and the specific energy density (triangles) produced by FEGs versus the thickness of its PZT 52/48 ferroelectric elements [1, 6, 7, 14, 16].

pulses with amplitudes of several tens of kilovolts and pulse lengths of a few microseconds in a high-resistance load.

12.7 Longitudinal Shock Wave Depolarisation of Polycrystalline PZT 54/48

As was demonstrated in the previous section, FEGs are effective autonomous high-voltage prime power sources. The physical reason for high voltage generation by FEGs is shock compression of its ferroelectric modules, which causes a ferroelectric-to-non-ferroelectric phase transition that results in the release of the electric charge stored on the surface of the ferroelectric modules to its output terminals. The electric charge is stored on the ferroelectric module end plates due to its remnant polarisation. The quantity of electric charge released and the efficiency of the FEG depend on the degree of depolarisation of the ferroelectric element. Therefore, in this section, those factors that affect the degree of shock depolarisation of PZT elements will be investigated.

In order to study the depolarisation of ferroelectric elements within the FEG, Shkuratov [6, 9] conducted a series of experiments to investigate

the longitudinal depolarisation of PZT 52/48. The test objects were ferroelectric ceramic disks supplied by EDO Corporation [22]. The longitudinal FEG used in these experiments is shown in Fig. 12.4. A description of the experimental setup can be found in Refs. 6 and 9.

12.7.1 Experimental Results

The PZT 52/48 ferroelectric disks were poled to their full remnant polarisation value. The flyer plate (Fig. 12.4) impacted the ferroelectric body and produced a shock wave that traveled in a direction parallel to its polarisation vector P_0 . Before flyer plate impact, the electric field within the ferroelectric sample was equal to zero because of compensation by surface charges due to the dipole moment, P_0 , of the sample obtained during the poling procedure. When a shock wave depolarises the ferroelectric disk, it forces a redistribution of the bound charges within the volume of the disk. This redistribution induces an electric field within the PZT 52/48, which causes an electric potential to form between the metallic contact plates attached to the ferroelectric module until a new equilibrium state can be re-established.

This pulsed electromotive force causes an electric current pulse, $I(t)$, to flow in the FEG-load electrical circuit. Integration of the $I(t)$ waveform from 0 to t gives the value of the electric charge, $\Delta Q(t)$, released to the electrical circuit up to time t during explosive operation of the FEG:

$$\Delta Q(t) = \int_0^t I(t)dt \quad (12.2)$$

A typical waveform of the depolarisation current generated by an FEG containing a PZT 52/48 disk with a diameter of 27.0 mm and a height of 2.1 mm is shown in Fig. 12.13. The amplitude of the current pulse was $I(t)_{\max} = 213 \text{ A}$, its rise time was $\tau = 0.5 \mu\text{s}$ and its FWHM was $0.5 \mu\text{s}$. Figure 12.13 also shows the evolution of the electric charge, $Q(t)$, in time during shock wave action. The maximum charge released to the circuit was $\Delta Q(13.8 \mu\text{s})_{\text{depol}} = 154 \mu\text{C}$. The average value of the electric charge released by PZT 52/48 disks having dimensions of $D = 26.0 \text{ mm}$ and $h = 0.65 \text{ mm}$ due to shock wave action in seven experiments was $\Delta Q_{\text{depol aver}} = 141 \pm 15 \mu\text{C}$.

It should be noted that in these experiments the FEGs were loaded with 12 to 18 g of high explosives. Based on these experiments, it was determined that the amount of electric charge released $Q(t)$, is a function of the amount

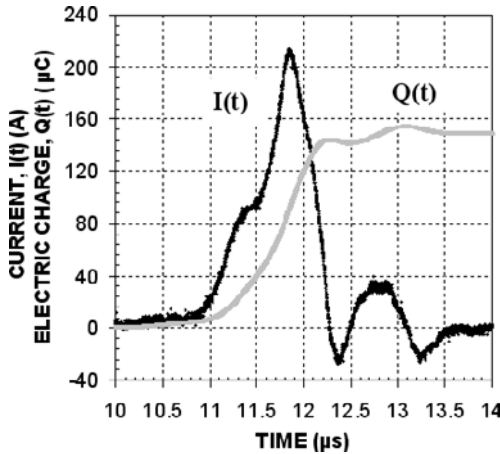


Fig. 12.13 Typical waveform of the depolarisation current, $I(t)$, generated and the corresponding time history of the electric charge, $\Delta Q(t)$, released by an FEG containing a PZT 52/48 disk with dimensions of $D = 27.0$ mm and $h=2.1$ mm due to shock wave depolarisation [12].

of high explosive used. It was found that reducing the high explosive mass to less than 12 g resulted in decreasing ΔQ_{depol} .

The initial electric charge, Q_0 , formed by the poling procedure and stored in the PZT 52/48 elements can be determined by using:

$$Q_0 = P_0 A \quad (12.3)$$

where P_0 is the remnant polarisation of the ferroelectric sample and A is the cross-sectional area of the sample. The remnant polarisation of the PZT 52/48 disks used in these experiments was $P_0 = 25 \pm 3.1 \mu\text{C}/\text{cm}^2$ [22].

It was experimentally demonstrated in Refs. 6 and 9 that a reduction in the thickness of the samples of PZT 52/48 from 2.1 mm to 0.65 mm led to a significant increase in the depolarisation current. The average amplitude of the current pulse produced by disks with thickness $h = 0.65$ mm was 332 ± 27 A. At the same time, the average value of the electric charge released by these disks was not higher than that released by disks with thickness $h = 2.1$ mm. The data from these experiments is summarised in Table 12.2.

Based on the experimental data in Table 12.2, it can be concluded that the electric charge released by the disks is almost equal to the total charge stored in the ferroelectric elements due to its remnant polarisation. This is direct evidence of the complete depolarisation of PZT 52/48 due to shock

Table 12.2 Initial electric charge stored in PZT 52/48 polycrystalline disks due to its remnant polarisation and electric charge released by the disks under shock wave action.

Diameter/Thickness of the disk (mm)	26.0/0.65	27.0/2.1
Initial Charge, Q_0 (μC)	161 ± 6.4	174.0 ± 6.9
Depolarisation Charge, $\Delta Q_{\text{depol aver}}$ (μC)	157 ± 16	169 ± 14

wave compression. Therefore, complete shock wave depolarisation of PZT 52/48 ferroelectric materials by explosive driven FEGs has been measured experimentally [6, 9].

It is important to estimate the dynamic pressure at which complete shock wave depolarisation occurs in PZT elements. The shock pressure, P_{SW} , at the front plate of the ferroelectric module was calculated by assuming that an aluminum flyer plate with infinite diameter impacted with a PZT element with infinite diameter and that the impact was perfectly elastic. Another assumption [6, 9] was that there is no plastic or fluidic behavior in either material at the moment of impact. This approach is commonly used in shock hydrodynamics, in situations where pressures cannot be directly measured.

Using these approximations, the pressure acting on the front face of the ferroelectric disk, P_{SW} , was estimated by using the following equation [26]:

$$P_{\text{SW}} = \frac{2ms}{\tau_{FP}^2 A_{FP}}, \quad (12.4)$$

where m is the mass of the aluminum flyer plate, A_{FP} is the cross-sectional area of the flyer plate, s is the length of the gap between the flyer plate and the ferroelectric element — i.e. s is the acceleration path, and τ_{FP} is the free flight time of the flyer plate preceding impact.

To determine the flight time of the flyer plate, a series of experiments were performed with generators in which the shock wave in the PZT 52/48 disk was initiated by the direct action of explosive detonation — i.e. no flyer plate was used. The flight time of the flyer plate, $\tau_{FP} = 5.1 \pm 0.2 \mu\text{s}$, was determined from the shift in the time scale of the voltage pulses generated by FEGs with a flyer plate versus those that used the direct action of a detonation shock wave.

This value of τ_{FP} was in good agreement with that obtained in another series of experiments performed with generators having thin transparent LexanTM bodies, in which the free flight of the flyer plate was recorded by using a high-speed Cordin 010-A framing camera.

Substituting the flyer plate mass, $m = 5.1\text{ g}$, acceleration gap length, $s = 0.5\text{ cm}$, flyer plate cross-sectional area, $A_{FP} = 5\text{ cm}^2$, and flight time, $\tau_{FP} = 5.1 \pm 0.2\text{ }\mu\text{s}$, into Eq (12.4) yields the pressure at impact of the flyer plate with the front face of the ferroelectric element:

$$P_{SW} = 3.8 \pm 0.3\text{ GPa.}$$

This value is an upper bound, since real impacts will produce plastic deformation in the flyer plate and since the component diameters are not infinite. Relaxation waves from the free surfaces of the plate and ferroelectric element and the energy expended in the materials while they undergo permanent deformation subtract from the pressure available at impact. In fact, experimental results show the flyer plate ‘splashes’ or deforms as if a semi-liquid on the PZT 52/48 surface, which typically shows little or no indication of deformation.

Additional pressure estimates are possible by using the basic equation for shock wave pressure in condensed matter [26]:

$$P_{SW} = \rho_0 U_S U_P. \quad (12.5)$$

This relationship can be used to estimate the pressure in a shock compressed body. Here, ρ_0 is the density of material before shock action and U_P and U_S are the particle velocity and the shock velocity, respectively, in the material.

A series of experiments were performed by Shkuratov *et al.* [6, 9] to determine the shock wave velocity, U_S , in PZT 52/48 ferroelectric elements. The voltage pulse rise time corresponded to the shock front propagation time through a PZT 52/48 disk with thickness, h . The velocity of the shock wave front could be determined by using the following relationship:

$$U_S = \frac{h}{\tau_{EMF}}, \quad (12.6)$$

where τ_{EMF} is the time it takes the EMF pulse to increase from zero to its maximum value. Accordingly, the shock wave velocity in PZT 52/48 was estimated to be

$$U_S = 3.94 \pm 0.27\text{ km/s.} \quad (12.7)$$

The particle velocity in the PZT 52/48 samples, which corresponds to the shock wave velocity determined from the experimental data, can be found from the Hugoniot for PZT 52/48:

$$U_P = 0.050 \pm 0.004\text{ km/s.} \quad (12.8)$$

The pre-shocked density of the PZT 52/48 was $7.5 \times 10^3 \text{ kg/m}^3$. Substituting the values for U_S , U_P and ρ_0 into Eq. (12.5) yields

$$P_{\text{SW}} = 1.5 \pm 0.2 \text{ GPa}. \quad (12.9)$$

Estimates of the pressure in bulk PZT 52/48 (1.5 GPa) and at the PZT 52/48 surface and flyer plate interface (3.8 GPa) are the lower and upper bounds, respectively, of the pressures generated in ferroelectric modules.

Thus, it has been experimentally determined that the pressure at which complete shock wave depolarisation of PZT 52/48 ferroelectric materials occurs due to longitudinal shock pressures lies in the pressure range of $1.5 \text{ GPa} \leq P_{\text{SW}} \leq 3.8 \text{ GPa}$.

12.8 Pulse Charging Capacitor Banks with FEGs

Many types of pulsed power generators are based on capacitive energy storage devices [30]. The Arkadiev-Marx generator is a typical example of a capacitor based pulsed power system [30, 31]. Electric energy is provided to these capacitive energy storage devices by high-voltage sources powered by conventional 110/220 V–50/60 Hz power supply lines. The operational theory of these generators and their uses are well-developed [30].

Certain modern applications, however, require that the pulsed power system be autonomous, i.e. use no external power supply line. Another important requirement is that these autonomous power supplies be compact. Based on these requirements, explosive driven ferroelectric generators are ideal sources for charging capacitor based pulsed power systems because of their ability to produce high-voltage pulses with amplitudes of several tens of kilovolts.

The feasibility of charging a capacitor bank with an explosive driven longitudinal FEG was demonstrated experimentally by Shkuratov *et al.* [11–14]. Systematic experimental and numerical simulation studies of the operation of FEG-capacitor bank systems were performed by using a variety of ferroelectric elements with different sizes [14]. It was shown that longitudinal FEGs can successfully charge capacitor banks with capacitances ranging from 1.2 to 36 nF to high voltages and can provide charging powers up to 0.3 MW [11–14]. In order to make the FEG-capacitor bank system operate in a predictable and transparent manner, a methodology for numerically simulating these devices was created. A description of the results of these studies is presented below.

12.8.1 FEG-Capacitor Bank System: Oscillatory Mode

Experimental and theoretical studies of FEG-capacitor bank systems were conducted using PZT 52/48 ferroelectric elements having the following dimensions: $D = 26.0\text{ mm}$, $h = 0.65\text{ mm}$; $D = 27.0\text{ mm}$, $h = 2.1\text{ mm}$; and $D = 25.0\text{ mm}$, $h = 5.1\text{ mm}$. The first series of experiments were conducted using ferroelectric elements with dimensions $D = 26.0\text{ mm}$, $h = 0.65\text{ mm}$ and a capacitive load of 18 nF [12, 13]. The capacitance of the capacitor bank was more than twice the initial capacitance of the FEG, which was $C_G = 7.0 \pm 0.1\text{ nF}$.

In these experiments, it was expected that the output voltage waveform generated by the FEGs across the capacitor bank would be a single pulse, similar to that shown in Fig. 12.10. In fact, the waveform was not a single pulse, but a series of oscillations with a frequency of about 1.0 MHz . Three more experiments were performed with identical FEG-capacitor bank systems [12, 13]. The results of these tests were very similar to those obtained in the first test.

Figure 12.14(a) shows a typical waveform of the voltage pulse produced by an FEG across an 18 nF capacitor bank. The peak voltage amplitude of the first pulse was $U(t = 9.1\text{ }\mu\text{s})_{\text{charge max}} = 2.16\text{ kV}$, the FWHM of this first pulse was $0.54\text{ }\mu\text{s}$ and its rise time was $\tau = 0.34\text{ }\mu\text{s}$. The peak energy delivered by the first pulse to the capacitor bank in Fig. 12.14(a) was

$$W(t)_{\text{max}} = \frac{C_0 U(t)_{\text{charge max}}^2}{2} = 42\text{ mJ}. \quad (12.10)$$

In this series of experiments, the average amplitude of the first voltage pulse produced by the FEG across the capacitor bank was $U(t)_{\text{charge max aver}} = 2.07 \pm 0.22\text{ kV}$. The average peak energy delivered to the 18 nF capacitor bank was $W_{\text{max aver}} = 39 \pm 7\text{ mJ}$.

Figure 12.14(b) shows the $I(t)_{\text{charge}}$ waveform delivered to the load by the FEG and the electric charge oscillations. The peak amplitude of the first current pulse was $I(t = 8.72\text{ }\mu\text{s})_{\text{charge max}} = 140\text{ A}$, its FWHM was $0.3\text{ }\mu\text{s}$ and its rise time was $\tau = 0.52\text{ }\mu\text{s}$. The peak amplitude of the second current pulse was higher than that of the first pulse and reached a value of 180 A , with FWHM= $0.45\text{ }\mu\text{s}$ and $\tau = 0.31\text{ }\mu\text{s}$.

The experiment (Fig. 12.14(b)) shows that the electric charge transferred, $\Delta Q_{\text{max}} = 50\text{ }\mu\text{C}$, from the PZT module during explosive operation of the FEG to the capacitor bank was 31.7% of the initial charge stored, $Q_0 = 161\text{ }\mu\text{C}$, in the ferroelectric element due to its remnant polarisation.

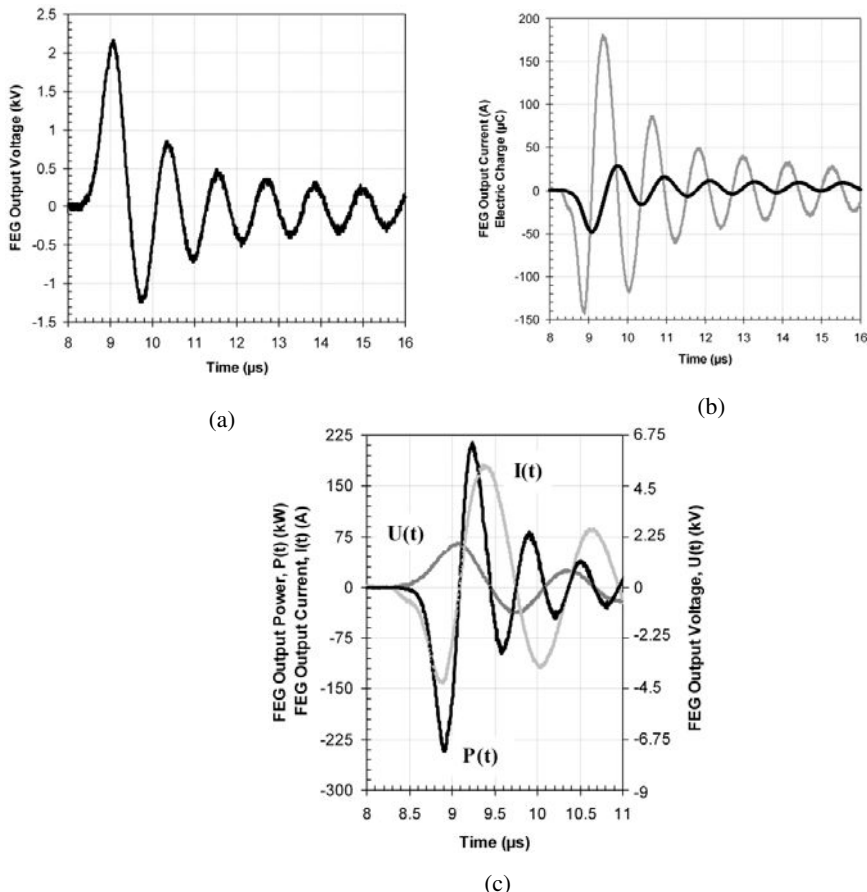


Fig. 12.14 Typical waveforms of the output voltage, $U(t)_{\text{charge}}$, current $I(t)_{\text{charge}}$, electric charge, $\Delta Q(t)$ and power, $P(t)_{\text{charge}}$ produced by an FEG, containing a PZT 52/48 disk with diameter $D = 26.0$ mm and height $h = 0.65$ mm, across an 18 nF capacitor bank: (a) waveform of $U(t)_{\text{charge}}$; (b) waveforms of $I(t)_{\text{charge}}$ and $\Delta Q(t)$; and (c) waveforms of $U(t)_{\text{charge}}$, $I(t)_{\text{charge}}$ and $P(t)_{\text{charge}}$ [16].

The waveforms of the output voltage pulse, $U(t)_{\text{charge}}$, output current pulse, $I(t)_{\text{charge}}$ and power, $P(t)_{\text{charge}}$ delivered by the FEG to an 18 nF capacitor bank are shown in Fig. 12.14(c). The power dissipated in the load was determined by taking the product of the instantaneous value of the output voltage $U(t)$ and the instantaneous value of the current in the circuit, $I(t)$: $P(t) = I(t)U(t)$. The peak output power was $P(t = 8.9 \mu\text{s})_{\text{charge max}} = 0.24 \text{ MW}$.

The next series of experiments was performed by using half as much capacitance, i.e. 9 nF. The output voltage oscillated as it did in the experiments with the 18 nF capacitor bank (Fig. 12.14). The frequency of these oscillations was slightly higher; i.e. 1.1–1.2 MHz, than that obtained with the 18 nF capacitor bank. The average amplitude of the first voltage pulse produced by the FEG across the 9 nF capacitor bank was $U(t)_{\text{charge max aver}} = 2.41 \pm 0.33$ kV. The average peak energy delivered to the 9 nF capacitor bank reached a value of $W_{\text{max aver}} = 26 \pm 5$ mJ.

An immediate conclusion from these experiments — i.e. FEGs charging 9 and 18 nF capacitor banks, is that there is an increase in the energy transferred from the FEG to the capacitor bank when the capacitance of the bank is higher. This conclusion was confirmed in a third series of FEG-capacitor bank experiments, which are described below.

The third series of experiments was performed with a 36 nF capacitor bank. Figure 12.15(a) shows a typical voltage waveform produced by an FEG across this capacitor bank. Note that the results of these experiments were different from those obtained with the 18 nF and 9 nF capacitor banks. The FEG produced a series of oscillations, but the amplitude of the first pulse is significantly higher than that of the next pulse in the train and the oscillations damp out more quickly. The amplitude of the first voltage pulse was $U(t = 9.78 \mu\text{s})_{\text{charge max}} = 1.82$ kV, its FWHM was $0.85 \mu\text{s}$ and its τ was $0.93 \mu\text{s}$.

The energy delivered to the 36 nF capacitor bank was $W(t)_{\text{max}} = 6$ mJ. The specific energy density of the PZT energy carrying element was 171 mJ/cm^3 . The average amplitude of the first voltage pulse across the 36 nF capacitor bank was $U(t)_{\text{charge max aver}} = 1.75 \pm 0.14$ kV and the average peak energy delivered to the 36 nF capacitor bank was $W_{\text{max aver}} = 55 \pm 6$ mJ.

Figure 12.15(b) shows the waveform of the $I(t)$ produced by the FEG and the electric charge oscillations. The total charge delivered by the FEG to the 36 nF capacitor bank in this experiment was $\Delta Q_{\text{max}} = 73 \mu\text{C}$, which is 55% of the initial charge.

Waveforms of the $U(t)_{\text{charge}}$, $I(t)_{\text{charge}}$ and $P(t)_{\text{charge}}$ pulses produced by an FEG across the 36 nF capacitor bank are shown in Fig. 12.15(c). The peak output power was $P(t = 9.42 \mu\text{s})_{\text{charge max}} = 0.29$ MW.

It follows from these experimental results that it is fundamentally possible to pulse charge a capacitor bank with a miniature explosive-driven longitudinal FEG [11–13]. The electric charge transfer from the longitudinal FEG to the capacitor bank can reach 55% of the remnant polarisation

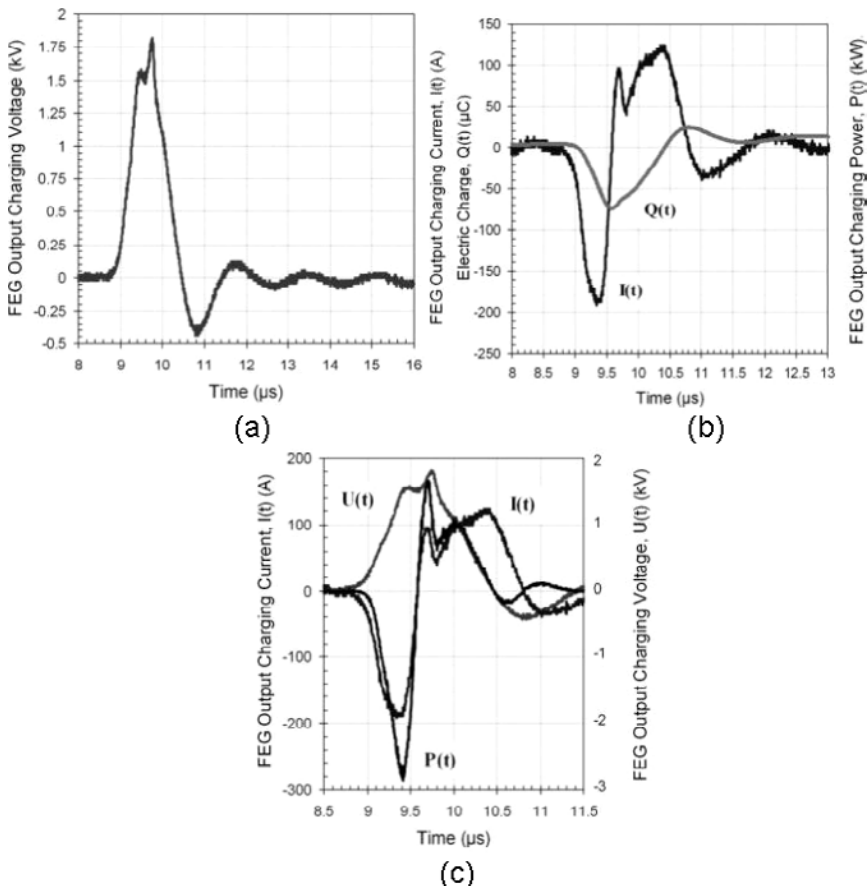


Fig. 12.15 Typical waveforms of the output voltage, $U(t)_{\text{charge}}$, current $I(t)_{\text{charge}}$, electric charge, $\Delta Q(t)$, and power, $P(t)_{\text{charge}}$ produced by an FEG, containing a PZT 52/48 disk with dimensions $D = 26.0$ mm and $h = 0.65$ mm, across a 36 nF capacitor bank: (a) waveform of $U(t)_{\text{charge}}$; (b) waveforms of $I(t)_{\text{charge}}$ and $\Delta Q(t)$; and (c) waveforms of $U(t)_{\text{charge}}$, $I(t)_{\text{charge}}$ and $P(t)_{\text{charge}}$ [16].

charge. The peak power delivered by the longitudinal FEG to the capacitor bank can reach a value of 0.3 MW. The specific energy density transferred to the capacitive load by the FEG was 170 mJ/cm³.

It follows from the experimental results presented in Refs. 11–13 that the capacitance of the capacitor bank has a significant effect on the processes that occur in the FEG-capacitor bank circuit. The correct choice of capacitor bank capacitance provides maximum output power and maximum

Table 12.3 Amplitude of the maximum output voltage generated in an FEG-Capacitor bank system and energy transferred from the FEG module to the capacitor bank as a function of the capacitance of the bank.

Capacitance (nF)	Voltage Amplitude (kV)	Energy Transferred (mJ)
9	2.41 ± 0.33	26 ± 5
18	2.07 ± 0.22	39 ± 7
36	1.75 ± 0.14	55 ± 6

energy transfer from the FEG to the external circuit. Table 12.3 summarises the results of the FEG-capacitor bank experiments for all three capacitances considered.

12.8.2 *Theoretical Description of FEG-Capacitor Bank Systems*

As mentioned above, the oscillatory behavior of FEG-capacitor bank systems was not expected and, at this time, the cause of these oscillations is not completely understood. In order to understand the physical nature of these oscillations, a theoretical model that describes the basic physical mechanisms that cause these oscillations of the FEG-capacitor bank system was developed by Shkuratov *et al.* [12, 13]. The approach used in this model was that used earlier to model FMGs [39–41]. The innovation in this approach was to use the voltage produced by the FEG as the basic parameter for determining the voltage and current delivered to the loads. It was demonstrated that the predicted FEG output current and voltage amplitudes and rise times are in good agreement with the experimental data obtained for a variety of loads and generator types.

A schematic diagram illustrating longitudinal depolarisation of a ferroelectric module is shown in Fig. 12.16.

When a longitudinal shock wave passes through the polarised ferroelectric element, its volume is divided into two regions or zones; the shock compressed zone, which is the portion of module through which the shock wave has already passed, and the uncompresssed zone, which is the portion of the module through which the shock wave has not passed. The differences between these two zones depend on the degree of polarisation (the compressed zone is depolarised) and other physical properties, such as conductivity and permittivity.

The equivalent circuit diagram employed in the simulation of the FEG-capacitor bank system is shown in Fig. 12.17. The capacitance of the

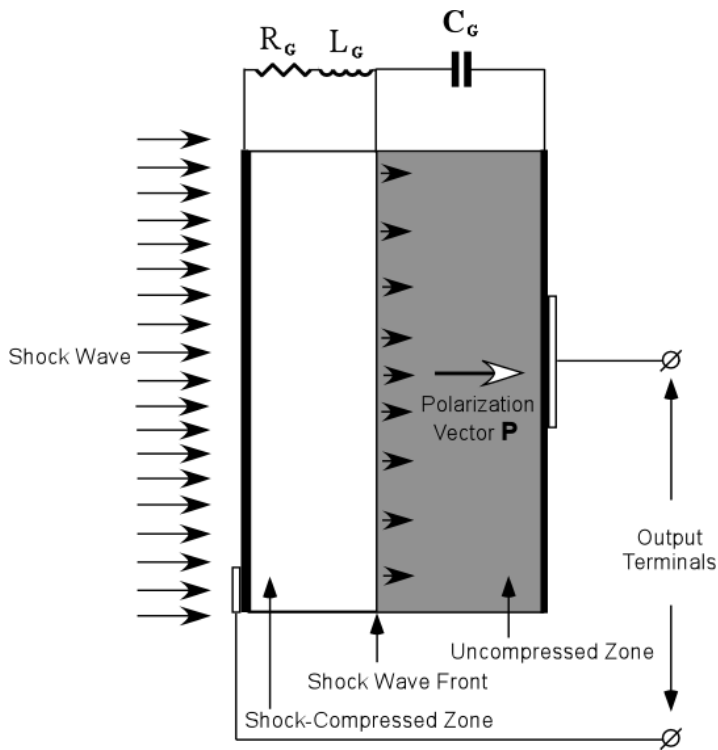


Fig. 12.16 A schematic diagram illustrating the longitudinal depolarisation of a PZT element.

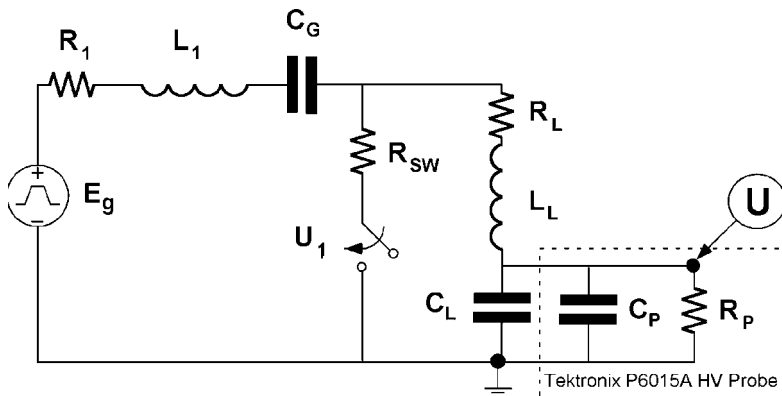


Fig. 12.17 The equivalent circuit diagram employed in the numerical simulation of a FEG-capacitor bank system [16].

ferroelectric module is represented by C_G . The shock compressed portion of the ferroelectric element can have a higher electrical conductivity than the uncompressed portion. The inductance and resistance of the shock compressed portion of the ferroelectric module are represented by L_1 and R_1 , respectively (Fig. 12.17). The inductance, resistance and capacitance of the load (capacitor bank) and the connecting cables are represented in the equivalent circuit diagram as L_{Load} , R_{Load} and C_{Load} , respectively.

Internal electrical breakdown in the PZT element is simulated by switch U_1 , which has a resistance of R_{SW} . It closes when the voltage across the capacitor bank reaches its maximum value.

The results of the simulation of an FEG-charged 18 nF capacitor bank are presented in Fig. 12.18. The voltage across the bank oscillates, as it did in the experiment (Fig. 12.14). The system parameter values used in the simulation were: $C_G = 7 \text{ nF}$, $L_1 = 5 \mu\text{H}$, $R_1 = 0.2 \Omega$, $C_{\text{Load}} = 18 \text{ nF}$, $L_{\text{Load}} = 2 \mu\text{H}$, $R_{\text{Load}} = 2 \Omega$ and $R_{\text{SW}} = 0.3 \Omega$.

The results of the simulation for the 36 nF capacitor bank are shown in Fig. 12.19. The parameters of the system — i.e. C_G , L_1 , R_1 , L_L and R_L were equal to those used for the case with the 18 nF capacitor bank, except for C_{Load} being 36 nF and R_{SW} being 4.3Ω . The output voltage of the FEG was 20% lower than in the case of the 18 nF bank (Fig. 12.18). These results are similar to those obtained in the experiments (Table 12.3). The waveform of the simulated charging voltage (Fig. 12.19) is practically a single pulse, as it was in the experiment (Fig. 12.15).

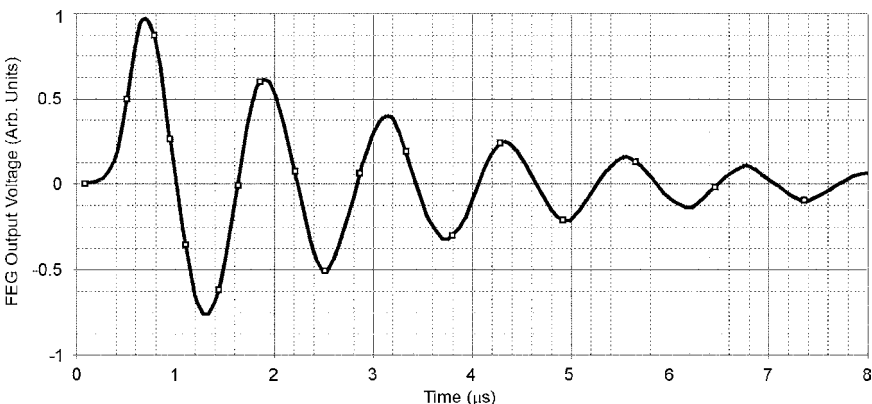


Fig. 12.18 Results of the numerical simulation of the operation of a FEG-capacitor system in which the PZ 52/48 element had the dimensions of $D = 26 \text{ mm}$ and $h = 0.65 \text{ mm}$ and the capacitor had a capacitance of 18 nF [16].

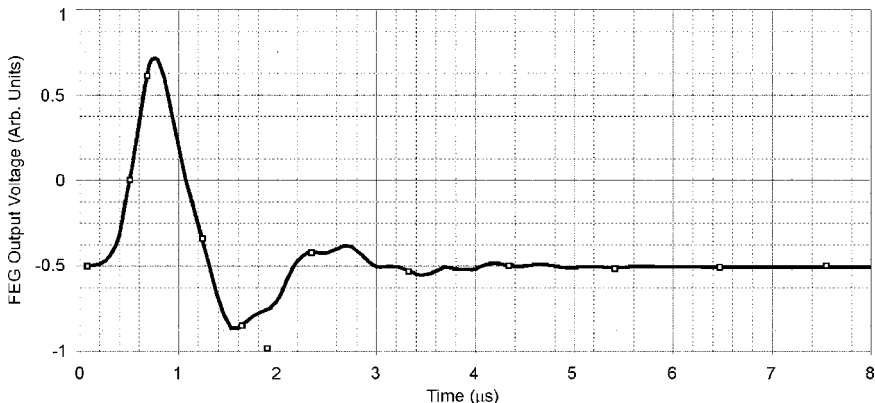


Fig. 12.19 Results of the numerical simulation of the operation of a FEG-capacitor bank system in which the PZT 52/48 element had dimensions of $D = 26$ mm and $h = 0.65$ mm and the capacitor had a capacitance of 36 nF [16].

Based on the results of these numerical simulations, it can be concluded that a key parameter responsible for the oscillatory mode of operation of the FEG-capacitor bank system is the resistance of the PZT element after shock compression. This means that electrical conductivity and the intensity of internal electrical breakdown in the shock compressed portion of the PZT module have a significant effect on the processes that occur in the FEG-capacitor bank system.

In the experiments described above, increasing the capacitance of the capacitor bank lead to a decrease in the voltage produced by the FEG across the capacitor bank and, correspondingly, a decrease in the voltage applied across the shock compressed portion of the ceramic disk. Increased capacitance also had a significant effect on the intensity of the electrical breakdown in the PZT. Decreasing the voltage across the capacitor bank below a certain threshold level results in lower impedances in the conductive channels formed in the ceramics due to electrical breakdown and correspondingly causes the aperiodic behavior of the signals in the FEG-capacitor bank system.

12.8.3 FEG-Capacitor Bank Energy Transfer

FEG-capacitor bank experiments [11–14] were conducted with load capacitances that varied from $C_L = 2.25$ nF to $C_L = 36.0$ nF. Figure 12.20 shows the results of a typical experiment in which a 4.5 nF capacitor bank

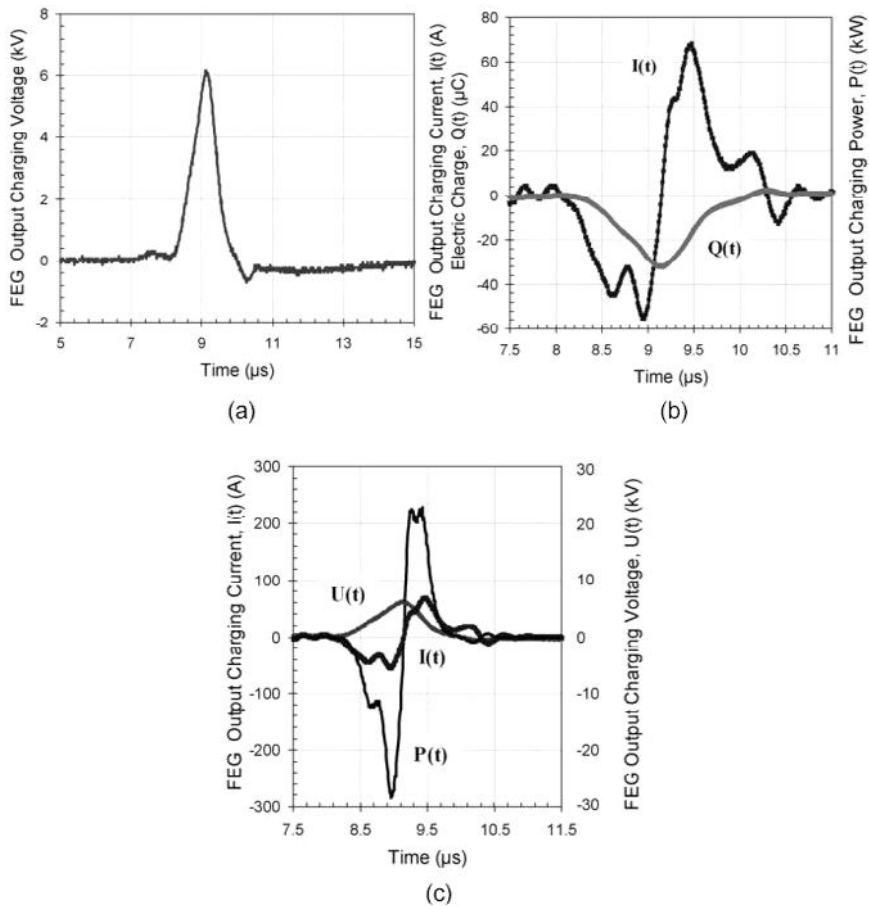


Fig. 12.20 Typical waveforms of the output charging voltage, $U(t)$, current, $I(t)$, electric charge transfer, $\Delta Q(t)$, and power, $P(t)$, delivered by an FEG, containing a PZT 52/48 element having dimensions of $D = 27$ mm and $h = 2.1$ mm, to a 4.5 nF capacitor bank.
 (a) Waveform of the charging high-voltage pulse, $U(t)$; (b) waveform of the charging current, $I(t)$, and electric charge in the circuit, $\Delta Q(t)$ and (c) waveforms of a high-voltage pulse, $U(t)$, charging current, $I(t)$, and power, $P(t)$ delivered to the capacitor bank [10].

was pulse charged by an FEG containing PZT 52/48 with dimensions $D = 27$ mm and $h = 2.1$ mm. The peak voltage amplitude (Fig. 12.20(a)) of the charging pulse was $U(t = 9.05\text{ }\mu\text{s})_{\text{charge max}} = 6.16\text{ kV}$, the FWHM of the pulse was $0.7\text{ }\mu\text{s}$, and the rise time of the pulse was $\tau = 0.87\text{ }\mu\text{s}$. The slope of the $U(t)$ curve at the moment when depolarisation began

was $\Delta U_{\text{charge}}/\Delta t = 7.1 \text{ kV}/\mu\text{s}$. It is almost two times less than the same quantity measured when the FEG was operated in the open-circuit mode ($\Delta U_g/\Delta t = 13.4 \text{ kV}/\mu\text{s}$).

The rapid decrease in the right edge of the voltage pulse $U(t)_{\text{charge}}$ in Fig. 12.20(a) is direct evidence of electrical breakdown in the shock compressed portion of the ferroelectric module. The electrical breakdown field, $E_{\text{break}} = U(t = 9.05 \mu\text{s})_{\text{charge max}} = 2.9 \text{ kV/mm}$, did not change significantly from that obtained for the open-circuit mode ($E_{\text{max}} = 3.33 \pm 0.11 \text{ kV/mm}$).

The peak energy delivered to the capacitor bank reached a value of $W(t)_{\text{charge max}} = C_0 U(t)_{\text{charge max}}^2 / 2 = 85 \text{ mJ}$. The average amplitude of the charging voltage pulse was $U(t)_{\text{charge max ave}} = 5.6 \pm 0.4 \text{ kV}$. The average peak energy delivered to the 4.5 nF capacitor bank was $W(t)_{\text{charge max ave}} = 71 \pm 10 \text{ mJ}$.

Figure 12.20(b) shows the waveforms of the charging current, $I(t)$, in the circuit and the electric charge oscillations. The peak amplitude of the negative (charging) current pulse was $I_1(t)_{\text{charge max}} = -55.5 \text{ A}$, its FWHM was $0.7 \mu\text{s}$ and its rise time was $\tau = 0.8 \mu\text{s}$. It was experimentally (Fig. 12.20(b)) shown that the electric charge transferred from the PZT module during explosive operation of the FEG to the capacitor bank was $\Delta Q_{\text{max}} = 32 \mu\text{C}$, which is 22% of the initial charge.

Waveforms of the output voltage pulse, $U(t)_{\text{charge}}$, current pulse, $I(t)_{\text{charge}}$, and power, $P(t)_{\text{charge}}$, produced by an FEG across the 4.5 nF capacitor bank are shown in Fig. 12.20(c). The peak output charging power was $P(t)_{\text{charge max}} = 0.28 \text{ MW}$.

Figure 12.21 summarises the voltage amplitudes produced by three types of FEG across capacitive loads having different capacitances. It follows from these experimental results that increasing the capacitance of the capacitor bank leads to a gradual decrease in the voltage produced by FEGs containing PZT 52/48 elements having dimensions of $D = 26.0 \text{ mm}$, $h = 0.65 \text{ mm}$; $D = 27.0 \text{ mm}$, $h = 2.1 \text{ mm}$ and $D = 25.0 \text{ mm}$, $h = 5.1 \text{ mm}$. The highest voltage, $U_{\text{charge max}} = 13.7 \text{ kV}$, was obtained from the FEG with elements having dimensions of $D = 25.0 \text{ mm}$ and $h = 5.1 \text{ mm}$ across the capacitor bank with capacitance of 2.25 nF. The lowest voltage, $U_{\text{charge max}} = 1.2 \text{ kV}$, was obtained from the same FEG across the capacitor bank with a capacitance of 36 nF.

Figure 12.22 summarises the electric charge transferred from the three types of FEG described earlier in this subsection to capacitor banks having different capacitances. Electric charge transfer strongly depends on the

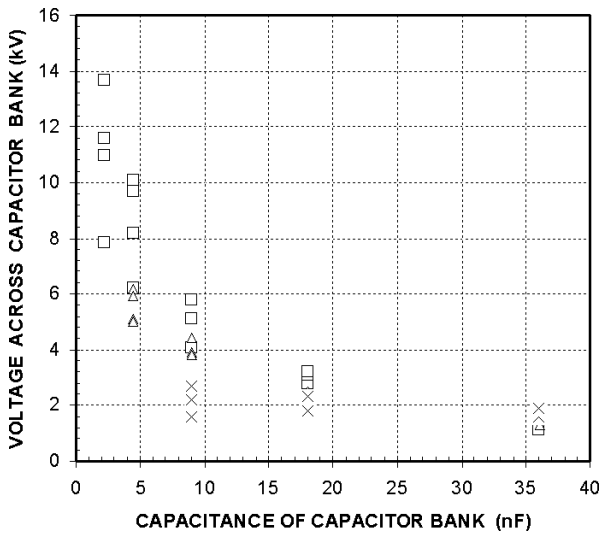


Fig. 12.21 Amplitude of the voltage pulsed delivered by FEGs, containing PZT 52/48 elements with dimensions of $D = 26.0\text{ mm}$, $h = 0.65\text{ mm}$ (diamonds); $D = 27.0\text{ mm}$, $h = 2.1\text{ mm}$ (triangles); and $D = 25.0\text{ mm}$, $h = 5.1\text{ mm}$ (squares), to capacitor banks with different capacitances [6, 7, 10, 11, 16].

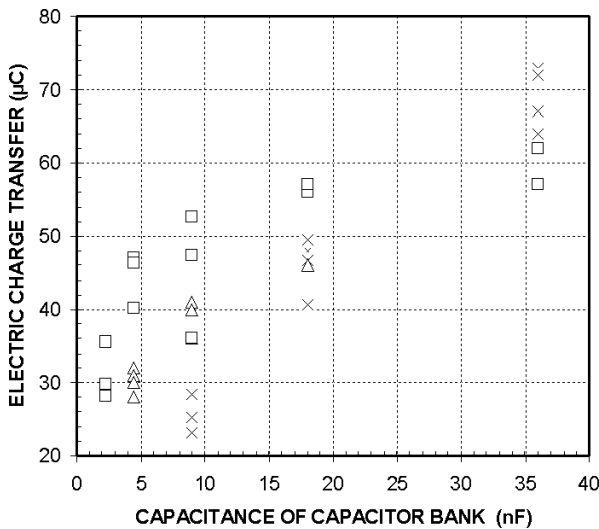


Fig. 12.22 Electric charge transferred from FEGs, containing PZT 52/48 elements with dimensions of $D = 26.0\text{ mm}$, $h = 0.65\text{ mm}$ (diamonds); $D = 27.0\text{ mm}$, $h = 2.1\text{ mm}$ (triangles); and $D = 25.0\text{ mm}$, $h = 5.1\text{ mm}$ (squares), to capacitor banks having different capacitances [6, 7, 10, 11, 16].

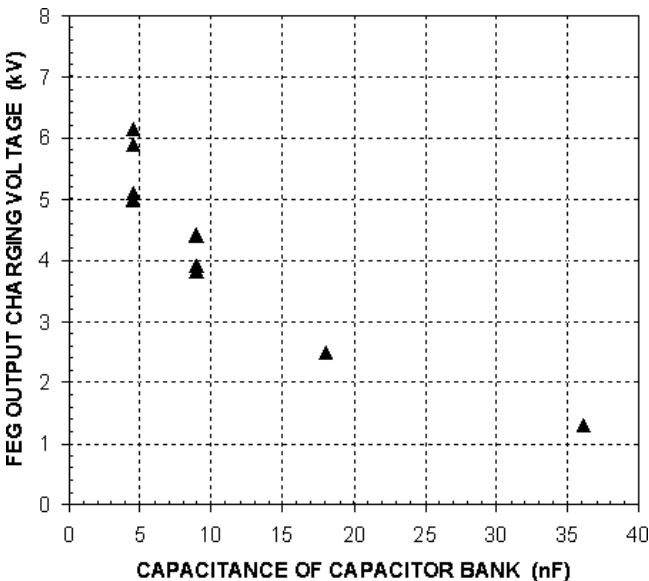


Fig. 12.23 Amplitude of the voltage pulse delivered by FEGs, containing PZT 52/48 elements having dimensions $D = 27$ mm and $h = 2.1$ mm, to capacitor banks having different capacitances [11].

capacitance of the capacitor bank. Increasing the capacitance of the bank from 2.25 nF to 36.0 nF results in a significant increase in the amount of electric charge transferred by all three types of FEG.

A summary of the energy delivered by the three types of FEG described earlier in this subsection to loads having different capacitances is presented in Fig. 12.23. It can be clearly seen that maximum energy is transferred by the FEGs having PZT 52/48 elements with dimensions of $D = 25.0$ mm and $h = 5.1$ mm to the capacitor bank with a capacitance of 4.5 nF. Increasing the capacitance of the capacitor bank from 2.5 nF to 36 nF results in a significant decrease in the energy transferred — i.e. the energy transferred decreases from 177 ± 27 mJ to 47 ± 12 mJ. Decreasing the capacitance from 4.5 nF to 2.25 nF decreases the amount of energy transferred to 156 ± 25 mJ.

Similar results (Fig. 12.24) were obtained for FEGs containing PZT 52/48 elements with dimensions of $D = 27.0$ mm and $h = 2.1$ mm with the exception that maximum energy transfer occurred when the capacitor bank had a capacitance of 9 nF. It should be noted that the initial capacitance of the FEG with PZT elements having dimensions of $D = 25.0$ mm and

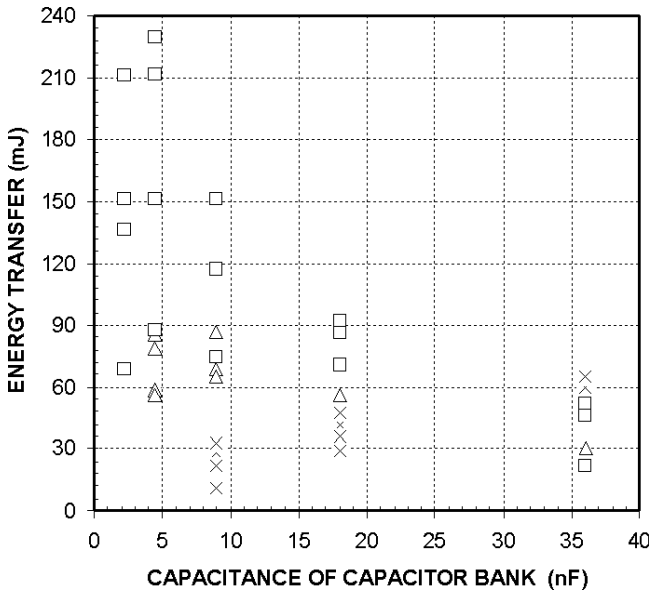


Fig. 12.24 Energy delivered by FEGs, containing PZT 52/48 elements with dimensions of $D = 26.0$ mm, $h = 0.65$ mm (diamonds); $D = 27.0$ mm, $h = 2.1$ mm (triangles) and $D = 25.0$ mm, $h = 5.1$ mm (squares), to capacitor banks having different capacitances [6, 7, 10, 11, 16].

$h = 5.1$ mm was $C_G = 0.98 \pm 0.09$ nF, which is about 2.3 times lower than the initial capacitance ($C_G = 2.27 \pm 0.14$ nF) of the FEG with PZT elements having dimensions of $D = 27.0$ mm and $h = 2.1$ mm

Similar effects were observed for FEGs containing PZT 52/48 elements having dimensions of $D = 27$ mm and $h = 5.1$ mm. But in this case, the maximum energy transfer took place when the capacitance of the bank was 9 nF. It should be noted that the initial capacitance of the PZT 52/48 elements having dimensions of $D = 25$ mm and $h = 5.1$ mm was $C_G = 0.98 \pm 0.09$ nF. This is about 2.3 times lower than the initial capacitance of PZT 52/48 elements having dimensions of $D = 27$ mm and $h = 2.1$ mm, which was $C_G = 2.27 \pm 0.14$ nF.

12.9 Operation of FEGs with Resistive Loads

Information about the operation of explosive-driven ferroelectric generators with resistive loads is important for certain applications. One of the

unique features of ferroelectric generators is that the ferroelectric elements can be directly connected to the load. The ferroelectric element is always a part of the load circuit during explosive and electrical operation of the FEG. The electrical parameters of the ferroelectric element change significantly under shock wave loading and this affects the electrical parameters of the FEG-load system. It follows from systematic experimental investigations by Shkuratov *et al.* [37] of the operation of explosive-driven FEGs with resistive loads that the output voltage, current and power produced by the FEG depends on both the electrical parameters of the load and the geometrical dimensions of the ferroelectric element in the FEG. It was experimentally demonstrated that FEGs are capable of delivering powers with peak amplitudes of 0.35 MW to active loads. A detailed theoretical treatment of the operation of FEGs with resistive loads was performed by Tkach *et al.* [38]. The results of these experimental and theoretical studies are presented below.

12.9.1 Experimental Results

Experimental studies of the operation of longitudinal FEGs with resistive loads, referred to as the *resistive mode*, were performed by using PZT 52/48 elements having the following dimensions: $D = 25.0\text{ mm}$, $h = 5.1\text{ mm}$; $D = 25.0\text{ mm}$, $h = 2.5\text{ mm}$ and $D = 26.0\text{ mm}$, $h = 0.65\text{ mm}$. The FEG loads were made by using low-inductance 2-Watt bulk carbon composition resistors. From three to five resistors were connected in series to avoid electrical breakdown along the surface. The inductance of loads did not exceed 230 nH. Pearson Electronics current monitors (models 411 and 110) were used to measure the pulsed current. A Tektronix P6015A high-voltage probe was used to monitor the FEG output voltage. The explosive-driven FEGs were placed in the detonation tank. The load, measuring circuits, and pulse recording equipment were placed outside the detonation tank.

Figure 12.25(a) shows a typical waveform of the voltage pulse produced by an FEG, containing a PZT 52/48 element having dimensions of $D = 25\text{ mm}$ and $h = 5.1\text{ mm}$, across a 300Ω load. The amplitude of the voltage pulse was $U(t = 8.7\mu\text{s})_{\max} = 6.82\text{kV}$, its FWHM was $1.52\mu\text{s}$ and its rise time τ was $1.5\mu\text{s}$. The maximum electric field strength attained in the ferroelectric element in this experiment was 1.34kV/mm . The voltage pulse amplitude averaged over three experiments conducted in this series of tests was $U(t)_{\text{aver}} = 6.77 \pm 0.71\text{kV}$.

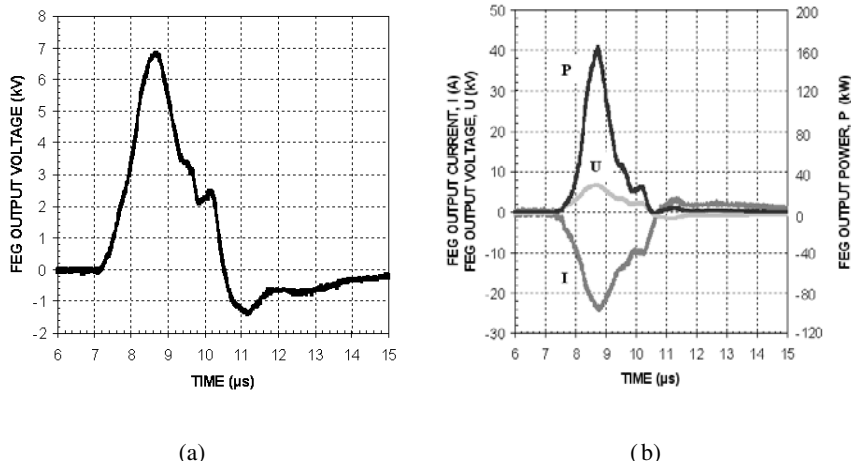


Fig. 12.25 (a) A typical waveform of the voltage pulse produced by an FEG, containing a PZT 52/48 element with dimensions of $D = 25$ mm and $h = 5.1$ mm, across a 300Ω load. (b) Corresponding waveforms of the output current, $I(t)$, voltage, $U(t)$, and power, $P(t)$, are also shown [1].

The corresponding waveforms for the output current, $I(t)$, voltage, $U(t)$, and power, $P(t)$, pulses produced by an FEG with a 300Ω load are shown in Fig. 12.25(b). The peak output current was $I(t = 8.83\mu s)_{\max} = 24.0$ A.

The power dissipated in the load was found by taking the product of the instantaneous value of the output voltage $U(t)$ and the instantaneous value of the current in the circuit, $I(t)$: $P(t) = I(t) \bullet U(t)$. The peak output power was $P(t = 8.74\mu s)_{\max} = 164$ kW. The average peak power delivered to the load in this series of experiments was $P_{\text{aver}} = 158 \pm 11$ kW.

Integration of the $P(t)$ waveform from 0 to t yields the energy, $W(t)$, delivered to the resistive load during explosive operation of the FEG: $W(t) = \int_0^t P(t) \cdot dt$. The maximum energy delivered to the 300Ω load in this experiment was $W_{\max} = 186$ mJ. The energy averaged over three experiments conducted during this series of tests was $W_{\text{aver}} = 181.4 \pm 12.7$ mJ. The specific energy density of the PZT 52/48 elements in these experiments was $W_{\text{spec aver}} = 72.4 \pm 5.1$ mJ/cm³.

A typical waveform of voltage pulse produced by an FEG, containing a PZT 52/48 element with dimensions of $D = 26.0$ mm and $h = 0.65$ mm, across a 0.7Ω load is shown in Fig. 12.26(a). There are oscillations in the voltage waveform, but the main voltage peak is distinctly visible. The

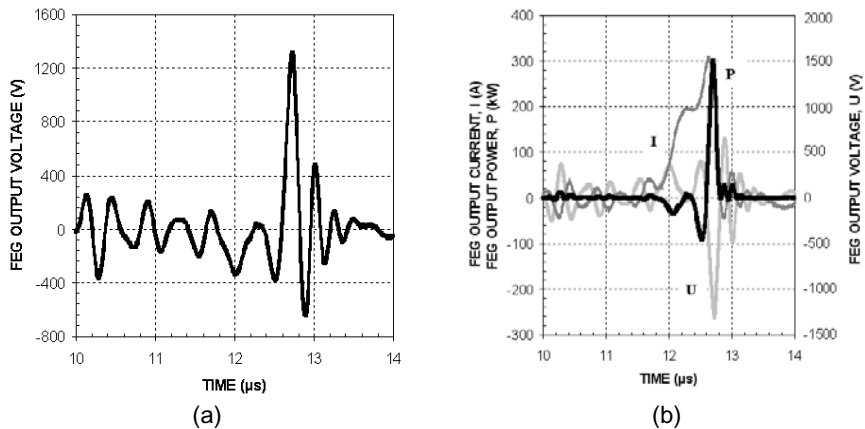


Fig. 12.26 (a) A typical waveform of the voltage pulse produced by a FEG, containing a PZT 52/48 element having dimensions of $D = 26.0\text{ mm}$ and $h = 0.65\text{ mm}$ across 0.7Ω load. (b) Corresponding waveforms of the output current, $I(t)$, voltage, $U(t)$, and power, $P(t)$, [4].

peak amplitude of the voltage pulse was $U(t = 12.7\mu\text{s})_{\max} = 1.31\text{ kV}$ with $\text{FWHM} = 0.1\mu\text{s}$ and risetime $\tau = 0.1\mu\text{s}$.

Corresponding waveforms of the output current, $I(t)$, voltage, $U(t)$ and power, $P(t)$, pulses produced by an FEG across a 0.7Ω load are shown in Fig. 12.26(b). The peak output current was $I(t = 12.6\mu\text{s})_{\max} = 308\text{ A}$. It is more than twelve times higher than that produced by the FEG, containing an PZT 52/48 element with dimensions of $D = 25\text{ mm}$ and $h = 5.1\text{ mm}$, across the 300Ω load (Fig. 12.25). The peak power delivered from the FEG to the 0.7Ω load was $P(t = 12.7\mu\text{s})_{\max} = 301\text{ kW}$. The average peak power delivered to the load in this series of experiments was $P_{\text{aver}} = 328 \pm 24\text{ kW}$. The energy delivered from the FEG in the 0.7Ω load was 41 mJ . The average energy delivered in the load in this series of experiments was $W_{\text{aver}} = 42 \pm 5\text{ mJ}$.

Figure 12.27 shows the amplitudes of the voltage pulses produced by FEGs, containing PZT 52/48 elements with dimensions of $D = 26.0\text{ mm}$ and $h = 0.65\text{ mm}$, $D = 25.0\text{ mm}$ and $h = 2.5\text{ mm}$, and $D = 25.0\text{ mm}$ and $h = 5.1\text{ mm}$, across active loads with different resistances. Because of the wide range of load resistances, the X -axis (Load Resistance) of the graph is a logarithmic scale. As it follows from the experimental results, increasing the load resistance leads to an increase in the voltage produced by the FEG. The voltage vs. resistance plot is practically linear on the logarithmic

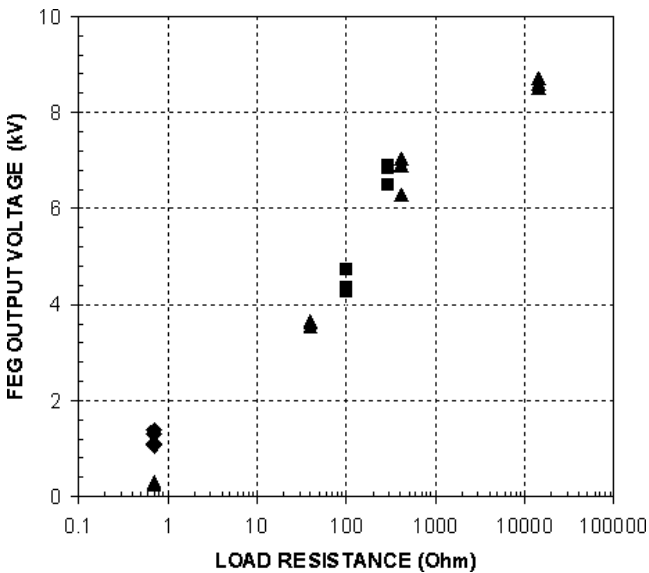


Fig. 12.27 Amplitude of the voltage pulses delivered by FEGs, containing PZT 52/48 elements with dimensions of $D = 26.0\text{ mm}$, $h = 0.65\text{ mm}$ (diamonds); $D = 25.0\text{ mm}$, $h = 2.5\text{ mm}$ (triangles), and $D = 25.0\text{ mm}$, $h = 5.1\text{ mm}$ (squares), to active loads having different resistances [1, 4, 12, 14].

scale (Fig. 12.27). This is direct evidence that there is an exponential relationship between the FEG output voltage amplitude and the resistance of the load.

Figure 12.28 shows the amplitudes of the current pulses delivered by FEGs containing all three types of PZT 52/48 elements described in the preceding paragraph to active loads with different resistances. It follows from these experimental results that decreasing the resistance of the load leads to an increase in the amplitude of the current delivered to the load.

Comparing the results obtained for FEGs, containing PZT 52/48 elements with dimensions of $D = 25.0\text{ mm}$ and $h = 2.5\text{ mm}$ and $D = 26.0\text{ mm}$ and $h = 0.65\text{ mm}$, driving low-resistance loads (Fig. 10.28), it can be concluded that the FEGs containing PZT elements with thickness $h = 0.65$ are capable of producing almost double the current than FEGs containing PZTs element with thickness $h = 2.5\text{ mm}$. This means that the output current produced by the FEG depends on both the resistance of the load and the geometrical and, correspondingly, electrical parameters of the ferroelectric

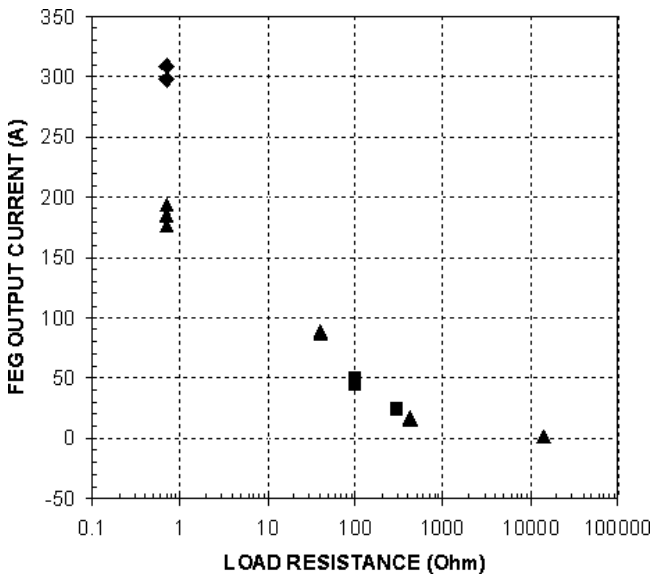


Fig. 12.28 Amplitude of the current pulses delivered by FEGs, containing PZT 52/48 elements with dimensions of $D = 26.0\text{ mm}$, $h = 0.65\text{ mm}$ (diamonds); $D = 25.0\text{ mm}$, $h = 2.5\text{ mm}$ (triangles); and $D = 25.0\text{ mm}$, $h = 5.1\text{ mm}$ (squares), to active loads with different resistances [1, 4, 12, 14].

element. The thickness of the PZT element is one of the parameters that determines the output current delivered by the FEG to an active load.

It follows from the experimental results presented in Fig. 12.28 that FEGs of these particular types can be considered to be effective prime current sources for active loads having resistances ranging up to a few tens of ohms. The highest currents ($317 \pm 29\text{ A}$) were obtained with the thinnest PZT 52/48 elements ($D = 26.0\text{ mm}$ and $h = 0.65\text{ mm}$).

Figure 12.29 shows the energy delivered by FEGs to active loads with different resistances. It follows from the experimental results presented in Fig. 12.29 that there is an optimum load resistance at which the FEGs containing all three types of PZT element provide maximum output power and energy. For PZT elements with thickness $h = 2.5\text{ mm}$, the optimum load lies at several tens of ohms. The PZT elements with thickness $h = 0.65\text{ mm}$ provide significantly higher output energy across low-resistance loads than do the PZT elements with thickness $h = 2.5\text{ mm}$. The thickness of the PZT element is one of the important parameters of the FEG that can be adjusted to maximise the output energy delivered by the FEG to resistive loads.

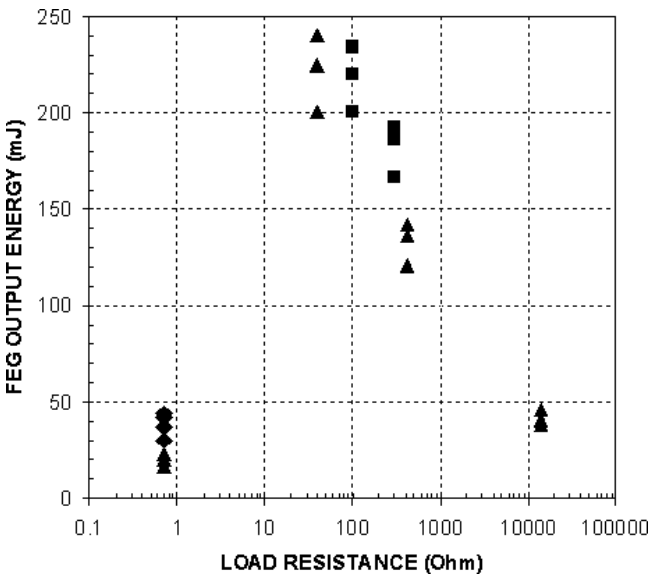


Fig. 12.29 Energy delivered by FEGs, containing PZT 52/48 elements with dimensions of $D = 26.0$ mm, $h = 0.65$ mm (diamonds); $D = 25.0$ mm, $h = 2.5$ mm (triangles) and $D = 25.0$ mm, $h = 5.1$ mm (squares), to active loads with different resistances [1, 4, 12, 14].

12.10 Theoretical Models for FEGs

12.10.1 Single Element FEGs

In order to understand the experimental results obtained by Shkuratov *et al.* [1, 2] for longitudinal FEGs operating in the resistance mode, a simulation model for the longitudinal FEG was developed by Tkach *et al.* [3, 4]. Figure 12.30 shows a diagram illustrating the propagation of a shock wave through a ferroelectric element and the field distributions in the element. The compressed portion of the ferroelectric element is hatched. The uncompressed portion of the element is clear. These two zones are different, since their parameters, such as the bulk polarisation, P , permittivity, ϵ , and conductance, λ , are different. The charge $Q_1(t)$ is that released at the contact plates of the ferroelectric element. The bulk polarisation and permittivity in the uncompressed portion are denoted by P_1 and ϵ_1 , respectively. The bulk polarisation, permittivity and conductance in the compressed portion of the element are denoted by P_2 , ϵ_2 and λ_2 , respectively. The velocity of the shock wave front moving in the ferroelectric element is denoted by V_S .

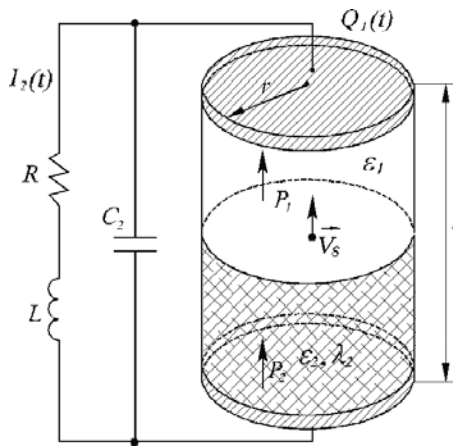


Fig. 12.30 Diagram illustrating the propagation of a shock wave through a ferroelectric element connected to a resistive load and the field distributions within the element.

In building the model, the following assumptions were made:

- Bulk compression of the ferroelectric material was not taken into account, since experimental results indicate that this value does not exceed 0.05.
- Shock polarisation inherently bears an inertial characteristic — i.e. domain rearrangement is a kinetic process.
- The ferroelectric material is a linear dielectric in both the compressed and uncompressed zones.

Taking these assumptions into consideration, the general set of ordinary differential equations and initial conditions for a FEG connected to a resistive load are:

$$\begin{aligned} \frac{dQ_1}{dt} + \frac{dQ_2}{dt} &= I_0(t) - I_2 - I_{\text{leak}}(Q_1), \quad Q_1|_{t=0} = 0; \\ L \frac{dI_2}{dt} &= Q_2 C_L^{-1} - RI_2, \quad I_2|_{t=0} = 0; \end{aligned} \quad (12.11)$$

$$\frac{dQ_1}{dt} C^{-1}(t) - \frac{dQ_2}{dt} C_L^{-1}(t) = C^{-2}(t) Q_1 \frac{dC(t)}{dt}, \quad Q_2|_{t=0} = 0;$$

where R with units of ohms, L with units of Henries, and C_L with units of farads are the resistance, inductance and capacitance of the load respectively and $I_2(t)$ is the current flowing through the resistive part of the load circuit.

In longitudinal shock wave FEGs, the ferroelectric element polarisation vector, P_1 , is parallel to the shock wave velocity vector, V_S (Fig. 12.30). The capacitance of the ferroelectric element, $C(t)$, is described by using the standard model for a layered parallel plate capacitor, where one layer is the compressed portion and the other is the uncompressed portion of the ferroelectric element. For this type of capacitor, it is a requirement that the distance between the plates, l , be less than the radius of the plates, $S^{1/2}\pi^{-1/2}$. When calculating the capacitance for geometries other than parallel plate capacitors, errors are introduced. However, taking into account the specific geometry of the element and the distribution of the electric fields, this does not pose a problem when solving the set of equations in Eq. (12.6). Therefore, the capacitance of the ferroelectric element shown in Fig. 12.30 becomes:

$$C(t) = \begin{cases} \varepsilon_0 \varepsilon_1 [l + (\varepsilon_1 \varepsilon_2^{-1}(p) - 1) V_S t]^{-1}, & l \geq V_S t; \\ \varepsilon_0 \varepsilon_2(p) S l^{-1}, & l < V_S t; \end{cases} \quad (12.12)$$

where S has the units of m^2 and is the area of the contact plates on the ferroelectric element, ε_1 is the permittivity of the uncompressed region, $\varepsilon_2(p)$ is the permittivity of the compressed region, ε_0 is the permittivity of free space, l is the total length of the ferroelectric element r is the radius of the element and V_S is the velocity of the shock wave in the ferroelectric material, which is approximately equal to the velocity of sound in the material. The permittivity of the shock compressed ferroelectric material is a complex function of the pressure in the shock wave.

The total electric charge released by the end plates of the ferroelectric element during the time it takes for the shock wave to travel through the element is $Q_{\text{tot}} = \sigma(p)S$. Since the free surface charge density, $\sigma(p)$, released at the end plates is equal to the difference in the specific bulk polarisation in the compressed and uncompressed regions of the material, $\sigma = P_1 - P_2$, the amount of charge released at any given moment in time, $Q_0(t)$, is proportional to the depolarised volume of the element and is described by the expression:

$$Q_0(t) = \sigma(p)V_S t l^{-1}. \quad (12.13)$$

Taking the derivative with respect to time yields the depolarisation current:

$$I_0(t) = \theta(t) \frac{d\sigma(p)V_S t l^{-1}}{dt}, \quad (12.14)$$

where $\theta(t)$ takes into account the ‘switching on’ of the polarisation current at the origin, which corresponds to the moment in time at which the shock wave enters the ferroelectric element, and the ‘switching off’ which is the moment in time at which the shock wave exits the ferroelectric element ($t_f = lV_S^{-1}$). Shock depolarisation is assumed to be an inertial process due to the substantial time required for the dipole moments to rotate in solid dielectrics and the motion of the domain boundaries. Thus, the *relaxation time* is the period from the moment in time at which the shock wave enters the element to the moment when charge is first released from the end plates. Ferroelectric materials require this amount of time to change polarisation.

According to Shkuratov *et al.* [33, 34], when a shock wave enters or leaves a ferroelectric element, the current increases or decreases, respectively, linearly with respect to time, t_{rel} . This linear behavior cannot be accounted for in the expressions for the capacitance of the element or the resistance of the load. Therefore, it seems reasonable to introduce a similar increase or decrease in the current in the simulation by means of a hyperbolic tangent function, $\theta(t)$, which behaves linearly at the transient points. Since the rise time and the fall time of the current are assumed to be the same [33], they are chosen to be equal to t_{rel} . Taking these assumptions into account, $\theta(t)$ is represented by the semi-empirical expression:

$$\theta(t) = \frac{1}{4}(1 - \tanh[4t_{\text{rel}}^{-1}(p)(t - lV_S^{-1}) - 2])(1 + \tanh[2t_{\text{rel}}^{-1}(p)t - 2]), \quad (12.15)$$

which is convenient for numerical calculations, since it is a smooth function. Since the calculation of $t_{\text{rel}}(p)$ using kinetic theory is relatively complex, experimentally measured values of $0.05\text{--}2.0\,\mu\text{s}$ are used. These values decrease significantly as the pressure in the shock wave increases.

The electrical conductance of the ferroelectric materials sharply increases under shock compression and part of the charge released at the end plates leaks through the compressed region of the element forming a leakage current, $I_{\text{leak}}(p)$. In the case of a longitudinal driving force, the leakage takes place over the entire surface of the element and, consequently, does not depend on time. The leakage current can be found from the field strength in the shock compressed region of the element by using Ohm’s law:

$$\begin{aligned} j_{\text{leak}}(Q_1) &= \lambda_2(p)E_2, \\ I_{\text{leak}}(Q_1) &= j_{\text{leak}}(Q_1)S = \lambda_2(p)Q_1 [\varepsilon_2\varepsilon_0]^{-1}, \end{aligned} \quad (12.16)$$

where λ_2 ($\Omega \cdot \text{m}$) is the specific conductance of the compressed ferroelectric material. This conductance increases as the pressure in the shock wave

increases due to the increase in the number of free-charge carriers because of electron tunneling, ionisation and other phenomena.

The set of equations in Eq. (12.6) describes the operation of a longitudinally driven ferroelectric element before the onset of bulk breakdown in the compressed region of the element. Generally speaking, breakdown can occur in both the compressed and uncompressed regions, but it first starts in the compressed region because the electric field breakdown strength of the ferroelectric material in the compressed region is less than it is in the uncompressed region. This is related to the formation of local breakdowns in the compressed zone due to the impact of the shock wave with powder grain boundaries, defects, dislocations and air-filled cavities generated during the baking process. Thus, Eq. (12.6) is restricted to the time domain prior to the start of bulk breakdown in the compressed zone. The electrical breakdown condition can be expressed in terms of the following equation:

$$E_{\text{br}} > Q_1(t)[S\varepsilon_2(p)\varepsilon_0]^{-1}, \quad (12.17)$$

where E_{br} [kV/m] is the electric field breakdown strength of the compressed ferroelectric material.

Since the set of equations in Eq. (12.6) is stiff and cannot be efficiently solved with the required precision, they must be normalised by introducing the following normalised variables:

$$\tau = t/\tilde{t}, \quad q = Q/\tilde{Q}, \quad \text{and} \quad i = I\tilde{t}/\tilde{Q}, \quad (12.18)$$

where $\tilde{t} = lV_S^{-1}$ and $\tilde{Q} = \sigma(p)S$. After making the appropriate substitutions, Eq. (12.6) becomes:

$$\begin{aligned} \frac{dq_1}{d\tau} &= \frac{1}{C(\tau) + C_L} \left[q_1 \frac{C_L}{C(\tau)} \frac{dC(\tau)}{dt} + C(\tau)(i_0(\tau) - i_2 - i_{\text{leak}}(q_1)) \right], \\ &\quad \text{where } q_{1\tau=0} = 0; \\ \frac{dq_2}{d\tau} &= \frac{1}{C(\tau) + C_L} \left[q_1 \frac{C_L}{C(\tau)} \frac{dC(\tau)}{dt} + C_L(i_0(\tau) - i_2 - i_{\text{leak}}(q_1)) \right], \\ &\quad \text{where } q_{2\tau=0} = 0; \\ \frac{di_2}{d\tau} &= \tilde{t}^2 \frac{q_2}{LC_L} - \tilde{t}Ri_2; \quad \text{where } i_{2\tau=0} = 0; \end{aligned} \quad (12.19)$$

where

$$\begin{aligned} i_0(\tau) &= \frac{1}{4}(1 - \tanh[4\tilde{t}\tilde{t}_{\text{rel}}^{-1}(p)(\tau - 1) - 2])(1 + \tanh[4\tilde{t}\tilde{t}_{\text{rel}}^{-1}(p)t - 2]); \\ C(\tau) &= \begin{cases} \varepsilon_1\varepsilon_0[1 + (\varepsilon_1\varepsilon_2^{-1}(p) - 1)/\tau]^{-1}, & \tau \leq 1; \\ \varepsilon_2\varepsilon_0(p)Sl^{-1}, & \tau > 1; \end{cases} \end{aligned}$$

$$\begin{aligned} \frac{dC(\tau)}{d\tau} &= \begin{cases} \varepsilon_1 \varepsilon_2(p) \varepsilon_0 S l^{-1} (\varepsilon_2(p) - \varepsilon_1)[\varepsilon_2(p) + (\varepsilon_1 - \varepsilon_2(p))\tau]^{-2}, & \tau \leq 1; \\ 0, & \tau > 1; \end{cases} \\ I_{\text{leak}}(q_1) &= (\varepsilon_2(p) \varepsilon_0)^{-1} \lambda_2(p) \tilde{t} q_1. \end{aligned} \quad (12.20)$$

The normalised bulk breakdown condition for the longitudinal FEG is:

$$E_{\text{br}} > \sigma(p) q_1(\tau) [\varepsilon_2(p) \varepsilon_0]^{-1}. \quad (12.21)$$

This set of equations was solved numerically using the Gear method with a relative error less than 10^{-5} for all variables.

12.10.1.1 *Simulation Results and Discussions*

The theoretical model described in the previous section was employed to calculate the output of the FEG. The results of these calculations are compared to experimental results presented in Refs. 1 and 2. These calculations were conducted by substituting the known parameters for the FEG into the equations in the previous section. Since some of the parameters, such as τ_{rel} , σ , ε_2 and λ_2 , are not known at shock pressures, they were calculated by using data collected in earlier shots and used in calculations for later shots. Figure 12.31 presents the experimental and calculated outputs of the FEG. The calculated waveform is in good agreement with the experimental waveform.

The load resistance is one of the parameters of the FEG-load system that can be adjusted. The experimental study of this parameter was described in previous sections. Theoretical investigations of this parameter were conducted by using the phenomenological computer code for the FEG described in the previous section.

A numerically generated parametric plot of the amplitude of the current in an active load is presented in Fig. 12.32. There is good agreement between the simulations (Fig. 12.32) and the experimental results (Fig. 12.28). The current in the active load decreases as the load resistance increases. It follows from the simulation results that the reason for this is the increase in the losses in the shock-compressed portion of the PZT element due to bulk leakage stimulated by the shock wave. Both the theoretical and experimental results suggest the FEG can be effectively treated as a current source until the load resistance begins to approach the shunt resistance of the shock-compressed portion of the PZT element.

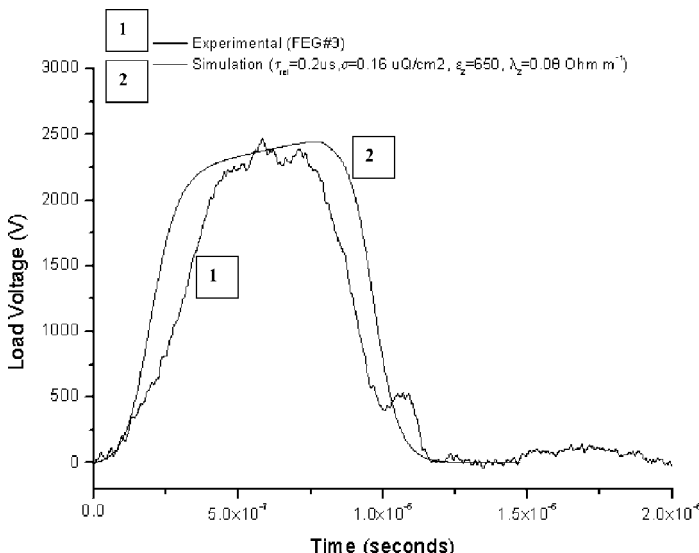


Fig. 12.31 Comparison of the experimental (curve 1) with the simulated (curve 2) output voltage waveforms produced by a FEG [38].

A numerically simulated plot of the specific energy density of the PZT module versus load resistance is presented in Fig. 12.33. Both experimental (Fig. 12.29) and calculated (Fig. 12.33) plots indicate the specific energy density passes through a maximum at a certain resistance. It follows from the simulation results that this maximum corresponds to an optimal balance between the output current and the leakage current.

The second important adjustable parameter of the FEG-load system is the geometric size and shape of the ferroelectric modules. Plots of the amplitude of the current and energy density delivered to a 10Ω load as a function of the length of the PZT module with a diameter of 25 mm are presented in Fig. 12.34. As can be seen, the short modules tend to deliver higher currents and energy densities to the load. These results are physically sound, since the surface-charge density depends only on the bulk density of polarisation dipoles, not the volume of the PZT module. It confirms the experimental results obtained using PZT elements having different sizes.

12.10.2 Multi-Element FEG Model

So far, only FEGs with single elements have been considered. However, it is possible to use more than one PZT element connected in series, in parallel,

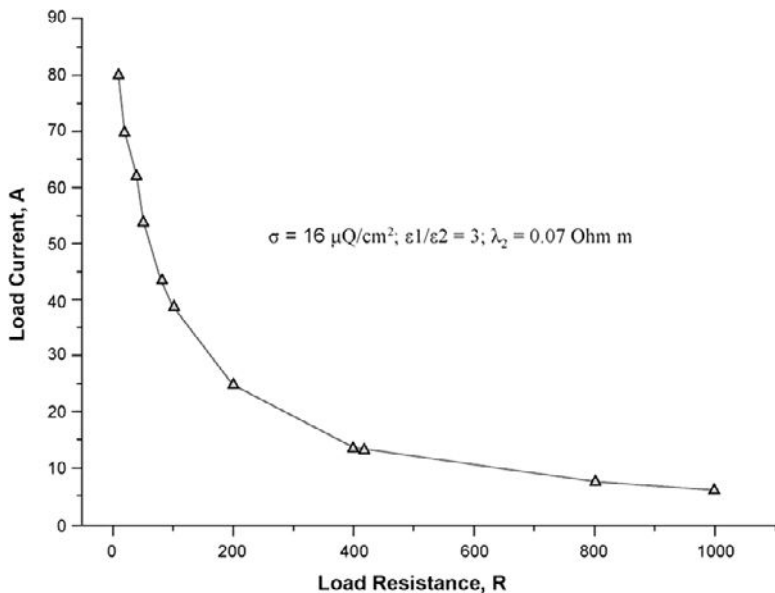


Fig. 12.32 The calculated current amplitudes delivered by a FEG to an active load versus the load resistance. The PZT 52/48 element had dimensions of $D = 25 \text{ mm}$ and $h = 2.5 \text{ mm}$ [38].

or some combination thereof, and that can be longitudinally or transversely depoled. In this section, techniques for modeling these more complicated structures will be briefly outlined.

In addition to the longitudinal model for the FEG discussed earlier, Ya. Tkach [39] has developed an FEG model that takes into consideration these more complicated FEG modules, FEGs with different types of load and the effects of breakdown within the FEG elements. Tkach's model for the transverse mode is presented in Refs. 3 and 13. His model for multi-element FEGs will now be presented, along with a semi-empirical model for the breakdown that occurs in the PZT elements.

12.10.2.1 Transverse Shocked Parallel Element FEG with an RLC Load

When multiple PZT elements are connected in parallel, there will be an increase in both the depolarisation and leakage currents, and a decrease in the internal capacitance of the multi-element working body. Solving the

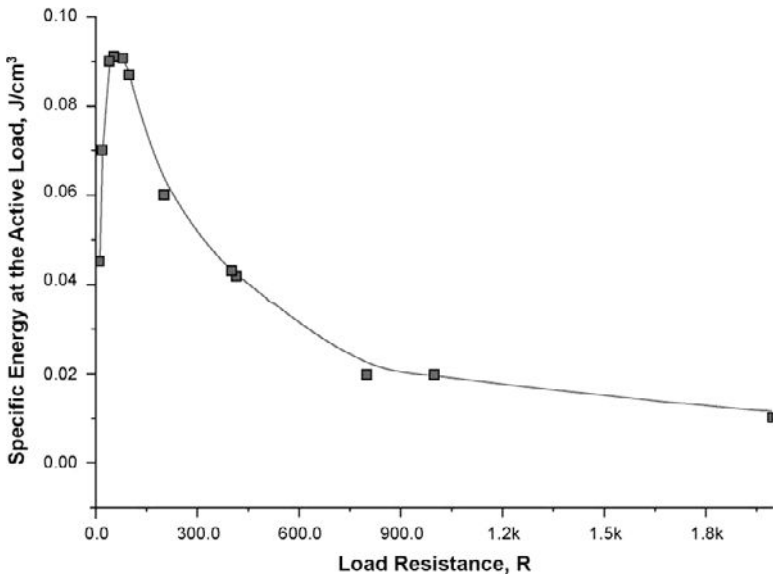


Fig. 12.33 The calculated specific energy density of a PZT element in a FEG versus the resistance of the load. The PZT 52/48 element had dimensions of $D = 25\text{ mm}$ and $h = 2.5\text{ mm}$ [38].

basic Kirchhoff's equations, Eq. (12.15), the depolarisation current is

$$I_M(\tau_i) = \frac{n}{4} (1 - \tanh[4t_{\text{rel}}^{-1}(p)(t_i - lV_S^{-1}) - 2]) (1 + \tanh[4t_{\text{rel}}^{-1}(p)t - 2]) h V_S \sigma; \quad (12.22)$$

where n is the number of elements connected in parallel, σ is the remanent polarisation in $\mu\text{C}/\text{cm}^2$ and h is the thickness of the PZT element. The internal capacitance of this array decreases due to several PZT elements being connected in parallel and is described by the equation:

$$C(t) = \begin{cases} n\varepsilon_0 h d^{-1} [\varepsilon_1 l + (\varepsilon_2 - \varepsilon_1) V_{St}], & l \geq V_{St}; \\ n\varepsilon_0 \varepsilon_2 h l d^{-1}, & l < V_{St}; \end{cases} \quad (12.23)$$

The leakage current increases proportionally to the depolarisation current, since the number of simultaneously depolarised elements also increases, and is given by the following equation:

$$I_{\text{leak}}(Q_1, t) = \begin{cases} n\lambda_2 Q_1 V_{St} [\varepsilon_0 (\varepsilon_1 l + (\varepsilon_2 - \varepsilon_1) V_{St})]^{-1}, & l \geq V_{St}; \\ n\lambda_2 Q_1 [\varepsilon_2 \varepsilon_0]^{-1}, & l < V_{St}, \end{cases} \quad (12.24)$$

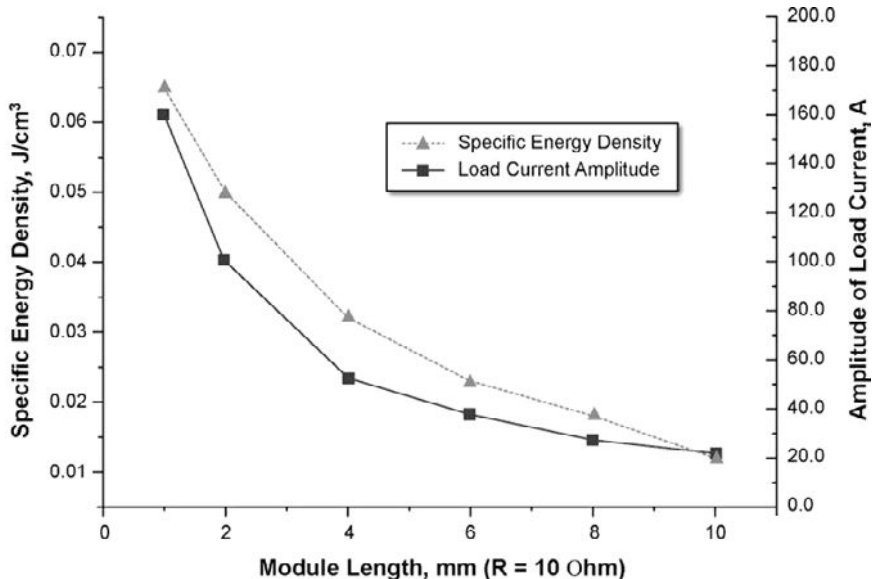


Fig. 12.34 The calculated current amplitude and specific energy delivered to an active 10Ω load as a function of PZT module length. The PZT module had a diameter of 25 mm [38].

12.10.2.2 Transverse Shocked Series Element FEG with an Open-Circuit Load

Assuming all the PZT elements are shocked at the same moment in time and that all the elements have identical material properties, the voltage generated by a chain of transversely-shocked ferroelectric elements connected in series is

$$U_s(t_{i+1}) = \frac{n}{C_M(t)} \int_0^{t_i} [I_m(\tau) - I_{\text{leak}}(\tau) - I_{\text{load}}(\tau)] d\tau, \quad (12.25)$$

where $t_{i+1} = t_i + \Delta t$ and $U(t_0 = 0) = 0$ and the capacitance of each element is

$$C_M(t_i) = \begin{cases} n\varepsilon_0 hd^{-1}[\varepsilon_1 l + (\varepsilon_2 - \varepsilon_1)V_{St}], & l \geq V_{St}; \\ n\varepsilon_0 \varepsilon_2 h l d^{-1}, & l < V_{St}; \end{cases} \quad (12.26)$$

Since the electric field strength of each ferroelectric element is

$$E_i = U(t_i)d^{-1}n^{-1}, \quad (12.27)$$

the leakage current through the element is

$$I_{\text{leak}} = \begin{cases} \lambda U(t_i) d^{-1} n^{-1} V_S t_i, & l \geq V_S t_i; \\ \lambda U(t_i) l d^{-1} n^{-1}, & l < V_S t_i, \end{cases} \quad (12.28)$$

Since the load is an open circuit, the load current can be neglected and the voltage generated by the element array is

$$U_s(t_{i+1}) = \frac{n}{C_M(t)} \int_0^{t_i} [I_m(\tau) - I_{\text{leak}}(\tau)] d\tau. \quad (12.29)$$

Thus, the depolarisation current is

$$I_M(t_i) = \frac{n}{4} (1 - \tanh[4t_{\text{rel}}^{-1}(p)(t_i - lV_S^{-1}) - 2]) (1 + \tanh[4t_{\text{rel}}^{-1}(p)t - 2]) h V_S \sigma. \quad (12.30)$$

12.10.3 Semi-Empirical Model for PZT Breakdown

This semi-empirical model for the electrical breakdown of PZT is based on the following three observations:

- Breakdown is characterised by a sharp exponential increase in the leakage current inside the PZT element;
- Breakdown, at least initially, recovers after a certain finite time although the breakdown recovery time may turn out to be long compared to the time it takes for the explosive processes to occur;
- Breakdown strength of ferroelectric materials never recovers to the initial pre-breakdown level.

Based on these assumptions, the equation for the leakage current becomes:

$$I_{\text{leak}}(t_i) = \begin{cases} \lambda U(t_i) d^{-1} n^{-1} V_S t_i, & l > t_{\text{br}} + t_{\text{rec}} \text{ or } t < t_{\text{br}}; \\ \lambda U(t_i) d^{-1} n^{-1} V_S t_i \left[g_{\text{leak}} \tanh \left(4 \frac{t - t_{\text{br}}}{t_{\text{rec}}} \right) \right], & t_{\text{br}} \leq t \leq t_{\text{br}} + t_{\text{rec}}, \end{cases} \quad (12.31)$$

where t_{br} is the time at which breakdown occurs, t_{rec} is the breakdown recovery time and g_{leak} is the leakage current gain due to breakdown. Since breakdown reduces the dielectric strength of the PZT, this is accounted for by using the expression

$$U_{\text{br},i} = C_F U_{\text{br},i-1}, \quad (12.32)$$

where C_F is an empirically determined correction factor that depends on the type of material used.

12.11 High-Voltage Nanosecond FEG-VIG Pulsed Power System

As was shown in the previous sections, ultracompact explosive driven ferroelectric generators are capable of producing high-voltage pulses with amplitudes of several tens of kilovolts and pulse lengths of microseconds. There are three possible applications for FEGs.

The first is as an autonomous high-voltage pulsed power source. An FEG or an array of FEGs can be used to power a variety of loads, including spark gaps, resistive loads and capacitive loads.

The second application of FEGs is as a prime power source (seed source) for explosive-driven pulsed power amplifiers (in particular, magnetic flux compression generators). This type of pulsed power system is generally referred to as a ‘completely autonomous explosive pulsed power system’. Completely autonomous explosive FEG-FCG systems were first developed by Demidov *et al.* [30].

A third possible way to utilise shock wave ferroelectric prime power sources is in combination with conventional pulsed power devices. A novel type of explosive-driven pulsed power system was recently developed by Shkuratov *et al.* [40]. This system uses the FEG as a prime power source and a spiral vector inversion generator (VIG) as the power conditioning stage. In this system, the amplitude of the microsecond long-voltage pulses produced by the FEG can be amplified by up to 20 times and the pulse width compressed to nanoseconds.

12.11.1 General Design of a FEG-VIG Pulsed Power System

The Vector Inversion Generator (VIG) is a capacitive-type electric device invented by Fitch and Howell [41], which, as a single unit, can store an electric charge at one voltage and discharge it as a voltage pulse, having a peak value higher than that of the stored voltage. A schematic diagram of the spiral VIG is shown in Fig. 12.35.

The VIG contains two sheets of conductive material and two sheets of electrically insulting material. These sheets are alternatively layered and

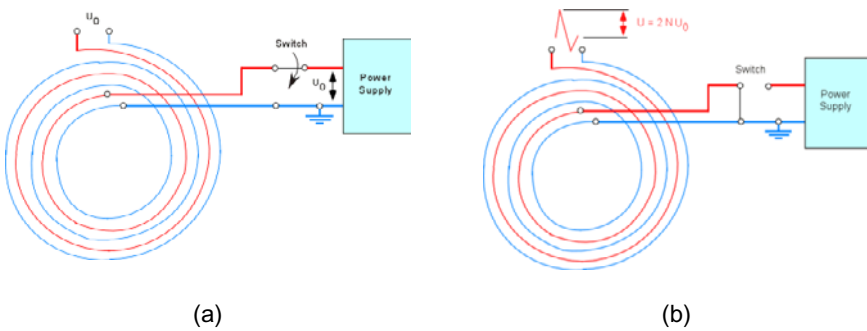


Fig. 12.35 Schematic diagram of the spiral-vector inversion generator (VIG). The red and blue lines are metal sheets. The intermediate spaces are sheets of insulating materials. The VIG in its (a) charging and (b) pulse-generating states.

wound together into a roll, forming an open-ended transmission line. If this rolled foil capacitor is charged to a voltage of U_0 (Fig. 12.35(a)) and then the switch in Fig. 12.35(b) is closed, the discharge generates an electromagnetic wave that originates from the switch and travels along the transmission line. As the wave travels, it converts the electrostatic field into an electromagnetic field, and when it retraces its path after reflection at the end of the transmission line, it converts the electromagnetic field back into an electrostatic field. An output pulse of amplitude

$$U_{\text{out}} = 2nU_0 \quad (12.33)$$

and a rise time equal to double the electrical length of the transmission line is produced at the output contacts of the VIG, where U_{out} is the output voltage of the VIG, U_0 is the charging voltage and n is a number of turns in the roll. The advantages of this system are its simplicity, ease to manufacture, low cost, adaptability to fit various form factors and short (nanosecond) rise time.

The voltage multiplication factor of the VIG can be calculated by using the following equation:

$$U_{\text{out}} = 2n\beta U_0, \quad (12.34)$$

where β is the efficiency coefficient, which depends on the design of the VIG and ranges in value from 0.8 to 0.9.

The VIG is a capacitive-type device and it can be characterised by two electrical parameters: its input and output capacitances. The input

capacitance of the VIG, C_{VIG} , can be calculated by using

$$C_{\text{VIG}} = \frac{2\epsilon\epsilon_0 A}{d}, \quad (12.35)$$

where ϵ is the dielectric constant of the insulating material used in the VIG, A is the area of the foil used in the device and d is the thickness of the dielectric material used between the metallic foils.

The output capacitance of the VIG, C_{out} , can be calculated by using

$$C_{\text{out}} = \frac{C_{\text{VIG}}}{4n^2}. \quad (12.36)$$

The test setup used to test explosive-driven FEG-VIG systems is shown in Fig. 12.36. The FEG was placed inside a detonation tank. The output terminals of the FEG were connected to the input of the VIG. The negative terminal of the FEG was grounded. When fired, the FEG produced a positive voltage pulse that was applied to the input of the VIG.

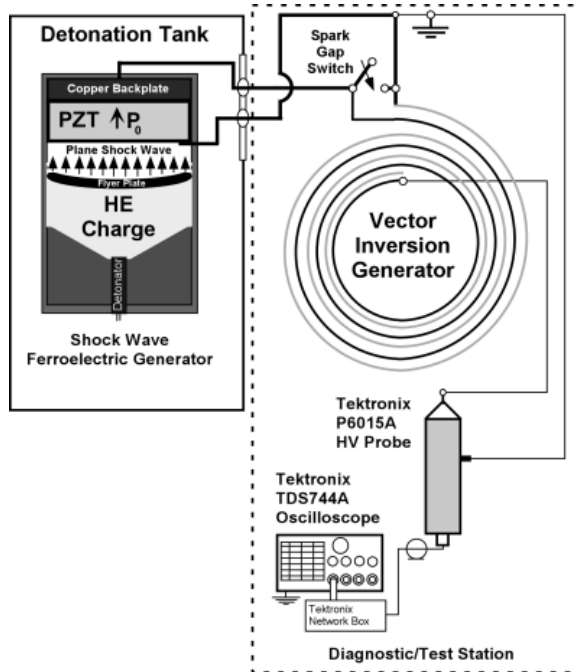


Fig. 12.36 Test setup used to test the explosive-driven FEG-VIG systems [15].

The output voltage of the explosive driven FEG-VIG system was monitored with a Tektronix P6015A high-voltage probe (rise time 4 ns, resistance $100\text{ M}\Omega$, capacitance 3 pF) connected directly to the output of the VIG. All pulsed signals were recorded with Tektronix TDS744A (bandwidth 500 MHz, sampling rate 2 GS/s) and Tektronix TDS2024 (bandwidth 200 MHz, sampling rate 2 GS/s) oscilloscopes.

12.11.2 FEG-VIG System Performance

The first series of experiments was performed with FEGs containing PZT 52/48 ferroelectric ceramic disks having diameter $D = 27\text{ mm}$ and thickness $h = 2.1\text{ mm}$. The waveform of a typical voltage pulse produced by an FEG operating in the open-circuit mode is shown in Fig. 12.37. The EMF pulse amplitude was $U_g(t)_{\max} = 6.88\text{ kV}$, its FWHM was $0.68\text{ }\mu\text{s}$ and its rise time was $\tau = 0.81\text{ }\mu\text{s}$.

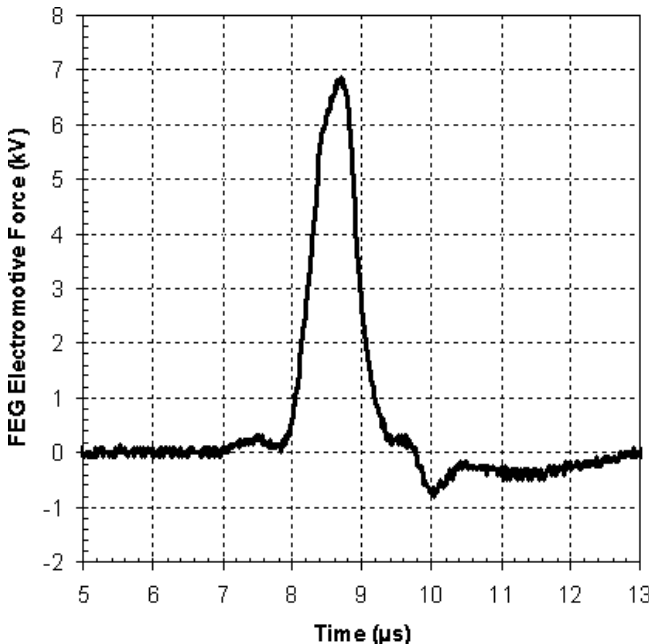


Fig. 12.37 The open-circuit voltage waveform produced by the FEG used in FEG-VIG tests. The FEG contained a PZT 54/48 element having dimensions of $D = 27\text{ mm}$ and $h = 2.1\text{ mm}$ [15].

It follows from experimental work with VIGs of different types that the design and implementation of the VIG-spark gap system is mostly determined by employing trial-and-error experiments. A standard paper punch was used as the switch since it is possible to make repeatable holes in dielectric films, which could be stacked to lengthen the gap. In this way, the switch inductance was kept at a minimum and the breakdown voltage could be somewhat controlled. To get some idea of the impulse behavior of the gap, a simple test fixture was developed to allow an impulse to be applied to the switch ensemble [40].

The VIG chosen for the first experiments was an 8-turn unit made with 0.1 mm thick capacitor grade Teflon as the dielectric that had a width of 50.8 mm and with 0.05 mm-thick copper shims as the capacitor conducting plates. These VIGs were wound on ferrimagnetic mandrels (ferrite 2535) with a width of 25.4 mm. The VIG had a ‘rectangular cross section’, which did not affect its efficiency. The voltage efficiency, which was measured by voltage multiplication, of these devices was in the 80–90% range. The calculated capacitance of these devices was approximately 8.9 nF. A photograph of a typical VIG is shown in Fig. 12.38.

Operation of the FEG-VIG system is as follows. The explosive driven FEG produces a microsecond pulse that impulse charges the VIG. When



Fig. 12.38 Photograph of the VIGs used in the FEG-VIG experiments [15].

the charge voltage exceeds the VIG spark gap voltage hold-off threshold, the VIG erects in a time equal to two wave transit times around the device (~ 6 ns), producing a transient voltage several times greater than the breakdown voltage of the VIG spark gap switch. Preliminary characterisation of the VIG spark gap was done in the laboratory in real time. The gap was tuned using a high-voltage D.C. power supply and was set to breakdown at approximately 3 kV.

The waveform of a typical voltage pulse produced by an FEG-VIG system is shown in Fig. 12.39. The generated pulse consisted of two peaks having different amplitudes with the highest peak amplitude being $U(t)_{\max} = 28.8$ kV and having a FWHM = 20 ns and a rise time $\tau = 6.75$ ns.

The actual VIG charge voltage at the gap trigger point can be calculated from the spiral efficiency, $U_{\text{out}} = 2nU_0$ (Eq. (12.26)), and the output voltage. The unit triggered at about 2.6 kV. Even at voltages of only 28.8 kV, the effects of corona in the VIG were appreciable and reduced the efficiency of the system to approximately 75%.

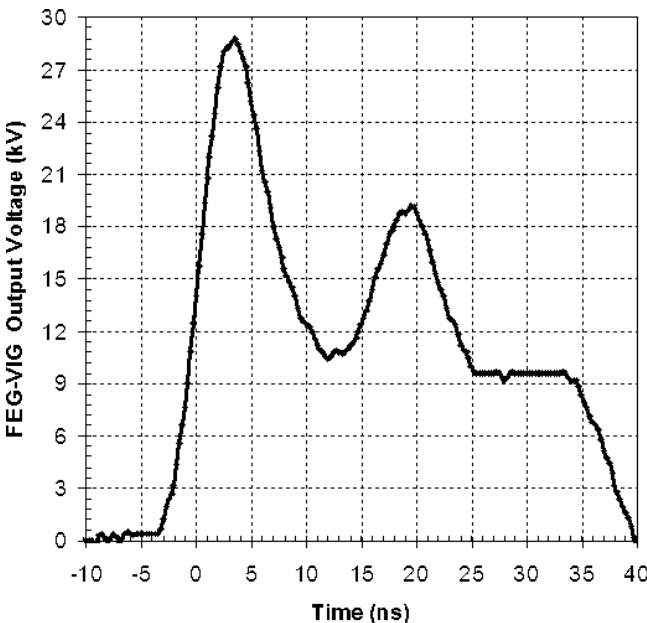


Fig. 12.39 Typical waveform of the voltage pulse produced by an explosive-driven FEG-VIG system. The FEG contained a PZT 52/48 disk having dimensions of $D = 27$ mm and $h = 2.1$ mm. The VIG contained 8 turns. The spark gap breakdown voltage was 2.6 kV [15].

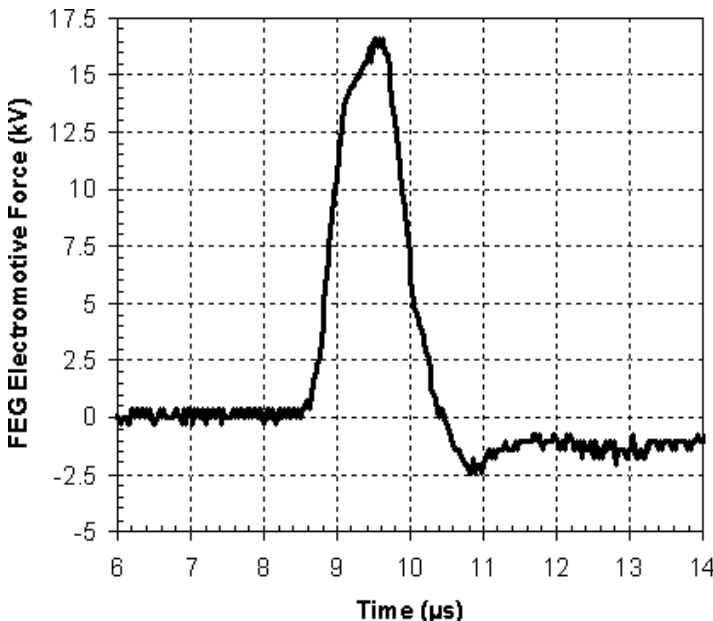


Fig. 12.40 The open-circuit voltage pulse produced by a FEG used in FEG-VIG tests. The FEG contained a PZT 52/48 element with dimensions of $D = 25$ mm and $h = 5.1$ mm [15].

The next series of experiments were performed with FEGs containing PZT 52/48 disks having dimensions of $D = 25$ mm and $h = 5.1$ mm. The pulsed EMF waveform produced by an FEG operating in the open-circuit mode is shown in Fig. 12.40. The EMF pulse amplitude was $U_g(t)_{\max} = 16.7$ kV, its FWHM was $0.99 \mu\text{s}$ and its τ was $1.02 \mu\text{s}$.

In this series of experiments, a 5-turn VIG was used [39]. The device was prepared similarly to the 8-turn unit described above, but this time, it was oil impregnated to eliminate corona effects and was capable of producing output voltages in excess of 100 kV. The input capacitance of the VIG was $C_{\text{VIG}} = 5.6 \text{ nF}$.

The breakdown voltage of the VIG spark gap was once again tuned to trigger at a set voltage using a high-voltage D.C. power supply to ensure the unit would discharge at the appropriate time. The spark gap spacing was set to DC discharge at approximately 6.0 kV, expecting that it would probably be more than that under impulse conditions. The experimental setup for this series of tests was similar to that used in the previous series. The only

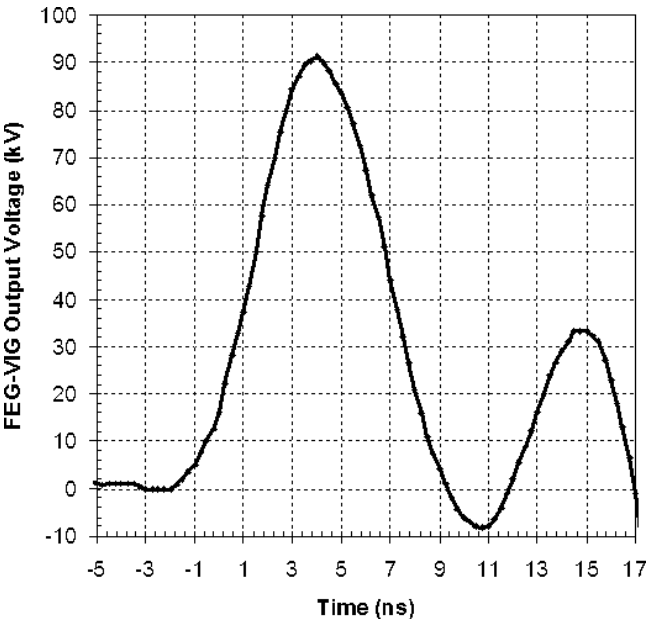


Fig. 12.41 Waveform of a typical voltage pulse produced by an explosive-driven FEG-VIG system. The FEG contained a PZT 52/48 disk having dimensions of $D = 25$ mm and $h = 5.1$ mm. The VIG contained 5 turns. The VIG spark gap breakdown voltage was 11.1 kV [15].

difference was that a custom-made voltage divider with a coefficient of 5.02 was connected to the Tektronix P6015A high-voltage probe.

The waveform of a typical voltage pulse produced by this FEG-VIG system is shown in Fig. 12.41. The waveform consisted of two peaks and had a peak voltage amplitude of $U(t)_{\max} = 91.4$ kV with a FWHM of 6.5 ns and τ of 5.25 ns.

It should be mentioned that the rise time of the generated electric pulse approached the resolution limit of the Tektronix P6015A high-voltage probe. Probe resolution, as well as stray capacitive effects, may distort the rise time of the FEG-VIG system and introduce considerable rise time error. The calculated rise time for this system was on the order of 4 ns. The unit triggered at approximately 11.1 kilovolts, which was almost twice the voltage at which the spark gap switch was set to breakdown under D.C. conditions.

Thus, the world's first autonomous explosive driven high-voltage pulsed power system based on a shock wave FEG as the prime power source and a

VIG as a power conditioning stage was successfully designed, constructed and tested. Adding the VIG stage increases the voltage output of the FEG by a multiplication factor that depends on the parameters of VIG, while simultaneously compressing the pulse width to a few nanoseconds.

12.12 Other Factors That Affect FEG Design

There are several other factors that affect FEG performance and include:

- New ferroelectric materials with higher-energy storage densities and higher electric breakdown thresholds that significantly increase the output voltage of the FEG.
- Ferroelectric element size and shape.
- New potting materials that yield good electrical, mechanical and shock properties.
- Improved power conditioning techniques that yield optimal output voltages and provide better impedance matching with a variety of loads.

12.12.1 *Ferroelectric Material and Geometry*

So far in this chapter, attention has been focused on FEGs using the ferroelectric material PZT 52/48. However, Sandia National Laboratory [45] and the Naval Surface Weapons Center [46] have looked at several different formulations of PZT, including PZT 52/48 and PZT 95/5, since the 1970s. The main difference in these two materials is that the PZT 52/48 undergoes stress-induced depolarisation, while the PZT 95/5 undergoes a ferroelectric-to-antiferroelectric transition. The PZT 95/5 offers several advantages over other ferroelectric materials, including higher-stored energy density ($\sim 2\text{--}4 \text{ J/cm}^3$), complete instantaneous low-loss depolarisation, and higher breakdown voltages. Poled ferroelectric PZT 95/5 lies near the phase boundary between the ferroelectric state and the nonpolarised antiferroelectric state, and shock waves can easily force the phase change.

Recently, S. Shkuratov and J. Baird [47] demonstrated that FEGs using rectangular PZT 95/5 elements with dimensions $0.5 \times 0.5 \times 2.0 \text{ in}^3$ generated voltages in excess of 80 kV, which is twice that generated by EC-64 — i.e. between 37 and 39 kV. In addition, they [48] have demonstrated that cylindrical PZT 95/5 samples with dimensions of $d = 0.75$ inches and $h = 1.0$ inches generated even higher voltages — i.e. 128 and 139 kV. These results are summarised in Fig. 12.42. As can be seen, both

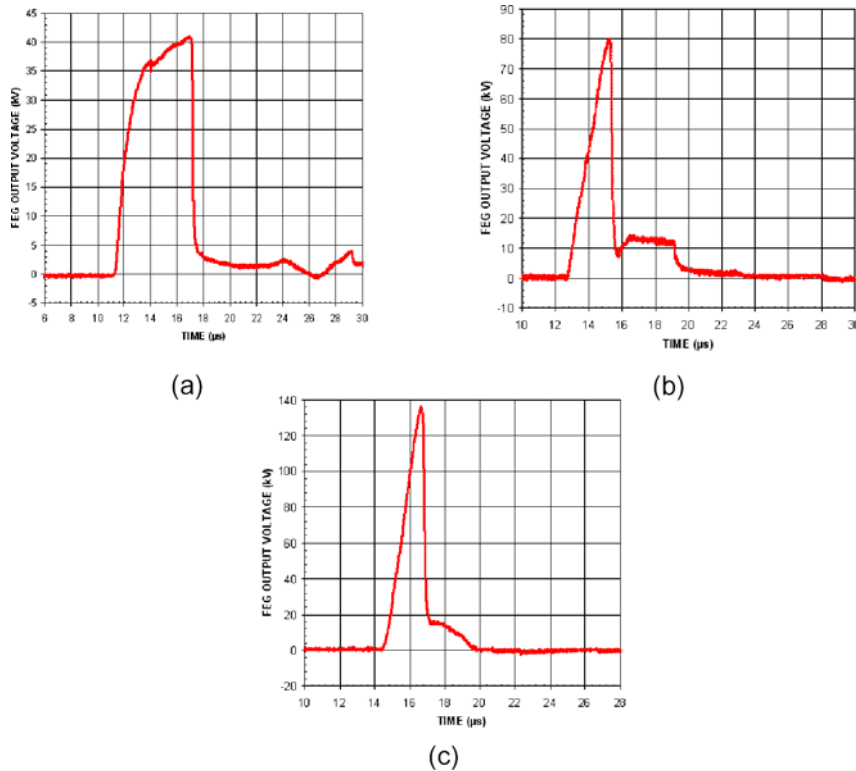


Fig. 12.42 Open-circuit voltage generated by FEGs with (a) rectangular PZT 52/48 element having dimensions of $12.7 \times 12.7 \times 50.8$ mm, (b) rectangular PZT 95/5 element having dimensions of $12.7 \times 13.4 \times 49$ mm and (c) cylindrical PZT 95/5 element having a diameter of 19.2 mm and a length of 25.4 mm [47, 48].

the type of material and its geometrical shape have an impact on FEG output.

At this moment in time, it appears that PZT 95/5 is the preferred material for use in FEGs. However, the search continues for new materials with higher-stored energy densities and higher electric breakdown strengths. Work at Penn State University and TRS Technologies indicates that single-crystal ferroelectrics may be the next preferred material for FEGs.

12.12.2 Potting Materials

Several different potting materials have been investigated. The potting material needs to have good electrical, mechanical and shock properties.

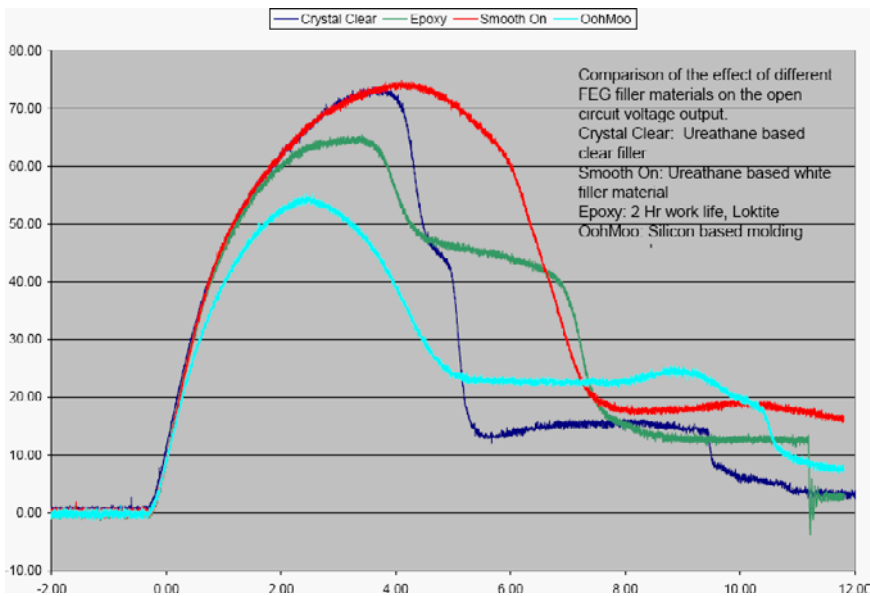


Fig. 12.43 Comparison of different potting compounds used in FEGs (courtesy of Dr. M. Rader, Naval Research Laboratory).

A comparison of the effects of various potting compounds on the output of FEGs is presented in Fig. 12.43. Sandia National Laboratory prefers a material called ALOX, which is alumina dispersed in an epoxy matrix. They have found there is good mechanical coupling between this potting material and PZT 95/5 [49] and that it has good electrical properties [50].

12.12.3 Shock Wave Profile

Due to their small size, the shock waves generated in explosive-driven FEGs are not perfectly planar. This results in a much more complex electrical response by the shock-compressed ferroelectric modules in miniature FEGs in comparison with that obtained in those experiments in which planar shock compression was generated by gas-gun projectiles. The shock profile must be considered in FEG design since the wrong profiles can lead to fracturing and/or voltage breakdown. Numerical codes, such as Lawrence Livermore National laboratory's ALE3D code, can be used to model FEGs. The profile of the shock wave significantly affects the amplitude of the output voltage and current pulses produced by both longitudinal and transverse

FEGs. Changing the shock wave profile leads to an increase (or decrease) in the amplitude of the output voltage pulses by a factor as high as 2.4 times for both types of FEG with the same PZT elements.

12.13 Summary

In summary, significant progress has been made since the early 2000s in the development of FEGs. Some of the achievements include the following:

- Both longitudinal and transverse FEGs have undergone intense experimental and theoretical investigations.
- Multiple FEG designs with both single and multiple ferroelectric elements have been successfully designed, built and tested.
- As a result, reliable compact FEGs that provide consistent outputs have been developed. Longitudinal FEGs with a total volume of 50 cm^3 are capable of generating output voltages as high as 30 kV and output powers as high as 0.35 MW.
- Longitudinal FEGs have been experimentally investigated with several different loads, including open-circuit, capacitive, resistive loads, VIGs, spark gap switches and antennae, the latter of which will be discussed in Chapter 14.
- It has been experimentally shown that the output voltage from a longitudinal FEG depends on the resistance of the load. In addition, it has been shown that the amplitude of the voltage pulse generated across a high-resistance load is directly proportional to the thickness of the longitudinal FEG ferroelectric element. The amplitude and FWHM of the voltage pulse produced by FEGs are highly reproducible and increase as the thickness of the PZT element increases. In addition, increasing PZT thickness increases the energy produced by the FEG, but reduces the specific energy-density stored in the PZT. The amplitude of the output voltage increases exponentially as the resistance increases. However, the amplitude of the current pulse decreases as the resistance increases. The power and energy transferred to the load increase up to a certain load resistance, after which they decrease.
- It has been experimentally demonstrated that the voltage produced by a longitudinal FEG across a capacitor bank is inversely proportional to the capacitance of the capacitor bank. The amplitude of the voltage pulse decreases as the capacitance increases. However, the electric charge

transferred to the load increases as the capacitance increases. The energy transferred to the load increases up to a certain load capacitance, after which it decreases.

- The maximum energy delivered by a longitudinal FEG to a capacitor bank depends on both the geometrical dimensions of the FEG ferroelectric element and on the capacitance of the capacitor bank. For each type of longitudinal FEG, there is an optimal load capacitance for delivering maximum energy to the capacitor bank.
- It has been experimentally demonstrated that longitudinal FEG-VIG systems are capable of compressing the microsecond voltage pulses produced by longitudinal FEGs to nanoseconds and are capable of multiplying the voltage pulse amplitude by several times.
- The main limitation of longitudinal FEGs is its dimensions. In order for the FEG to generate voltages greater than 50 kV, it is necessary to increase the diameter of the FEG and to significantly increase the amount of explosive charge. It is almost not possible to design miniature ultra high-voltage longitudinal FEGs.
- It has been demonstrated that transverse FEGs are miniature high-efficiency, high-voltage sources. Transverse FEGs with a diameter as small as 38 mm have been successfully built and tested. Transverse FEGs are capable of producing output voltages with amplitudes as high as 140 kV.
- The profile of the shock wave significantly affects the amplitude of the output voltage and current pulses produced by both longitudinal and transverse FEGs. Changing the shock wave profile leads to an increase (or decrease) in the amplitude of the output voltage pulses by a factor as high as 2.4 times for both types of FEG with the same PZT elements.
- Certain ferroelectric and potting materials and certain ferroelectric element shapes are better than others for yielding high output voltages. As an example, single-element generators with rectangular shaped EC-64 and PZT 95/5 elements and one with a cylindrically shaped PZT 95/5 element were tested and it was found that the latter provided significantly higher voltages.

Bibliography

- [1] S. I. Shkuratov, M. Kristiansen, J. Dickens, A. Neuber, L. L. Altgilbers, P. T. Tracy and Ya. Tkach, Experimental Study of Compact Explosive

- Driven Shock Wave Ferroelectric Generators, *Proceedings of 13th International Pulsed Power Conference*, Las Vegas, USA, IEEE Catalog Number: 01CH37251, ISBN: 0-7803-7120-8, Vol. II (2001), pp. 959–962.
- [2] Ya. Tkach, S. I. Shkuratov, J. Dickens, M. Kristiansen, L. L. Altgilbers and P. T. Tracy, Explosive Driven Ferroelectric Generators, *Proceedings of 13th International Pulsed Power Conference*, Las Vegas, USA, IEEE Catalog Number: 01CH37251, ISBN: 0-7803-7120-8, Vol. II (2001) pp. 986–989.
- [3] Ya. Tkach, S. I. Shkuratov, J. Dickens, M. Kristiansen, L. L. Altgilbers and P. T. Tracy, *Parametric and Experimental Investigation of EDFEG*, *Proceedings of 13th International Pulsed Power Conference*, Las Vegas, USA, IEEE Catalog Number: 01CH37251, ISBN: 0-7803-7120-8, Vol. II (2001), pp. 990–993.
- [4] S. I. Shkuratov, E. F. Talantsev, J. Baird, H. Temkin, Y. Tkach, L. L. Altgilbers and A. H. Stults, depolarisation of a Pb(Zr₅₂Ti₄₈)O₃ Polycrystalline Piezoelectric Energy-Carrying Element of Compact Pulsed Power Generator by a Longitudinal Shock Wave, *Proceedings of 15th International Pulsed Power Conference* (Monterrey, USA, 2005), pp. 529–532.
- [5] S. I. Shkuratov, J. Baird, E. F. Talantsev, M. F. Rose, Z. Shotts, L. L. Altgilbers, A. H. Stults and S. V. Kollossenok, Completely Explosive Ultra-compact High-Voltage Pulse Generating System, *Proceedings of 15th International Pulsed Power Conference* (Monterrey, USA, 2005), pp. 445–448.
- [6] S. I. Shkuratov, E. F. Talantsev, J. Baird, Y. Tkach, L. L. Altgilbers, A. H. Stults and S. V. Kollossenok, Pulsed Charging of Capacitor Bank by Compact Explosive-Driven High-Voltage Primary Power Source Based on Longitudinal Shock Wave depolarisation of Ferroelectric Ceramics, *Proceedings of 15th International Pulsed Power Conference*, Monterrey, USA (2005), pp. 537–540.
- [7] S. I. Shkuratov, E. F. Talantsev, J. Baird, A. V. Ponomarev, L. L. Altgilbers and A. H. Stults, Operation of the Longitudinal Shock wave Ferroelectric Generator Charging a Capacitor Bank: Experiments and Digital Model, *Proceedings of 16th International Pulsed Power Conference*, Albuquerque, USA (2007).
- [8] S. I. Shkuratov, E. F. Talantsev, J. C. Dickens, and M. Kristiansen, Novel Type of Explosive Driven High-Current and High-Voltage Source of Primary Power Based on Longitudinal Shock Wave Demagnetization of Nd₂Fe₁₄B High-Energy Hard Ferromagnets, *Proceedings of Ninth International Conference on Megagauss Magnetic Field Generation and Related Topics* (Megagauss-IX), Moscow-St. Petersburg, Russia, eds. V.D. Selemir and L.N. Plyashkevich, Sarov, VHIEF 2004, 5-9515-0036-2 (2002), pp. 279–285.
- [9] M. Kristiansen, A. Neuber, J. C. Dickens, M. Giesselmann and S. Shkuratov, Compact Pulsed Power, *Proceedings of the Tenth International Conference on Megagauss Magnetic Field Generation and Related Topics* (Megagauss-X), ed. M. von Ortenberg, ISBN 3-00-015743-3 (Berlin, Germany, Sarov, VHIEF, 2005), pp. 169–175.

- [10] S. I. Shkuratov, E. F. Talantsev, J. Baird, L. L. Altgilbers and A.H. Stults, Pulse Charging of Capacitor Bank by Explosive-driven Shock Wave Ferroelectric Generator, *Proceedings of the 2006 International Conference on Megagauss Magnetic Field Generators and Related Topics and the International Workshop on High Energy Liners and High Energy Density Applications*, eds. G. F. Kiutti, R. E. Reinovsky and P. J. Turchi, Institute of Electrical and Electronics Engineers (Inc., Santa Fe, NM, 2007).
- [11] S. I. Shkuratov, E. F. Talantsev, J. Baird, L. L. Altgilbers and A. H. Stults, Operation of Explosive-Driven Longitudinal Shock Wave Ferroelectric Generator Charging a Capacitor Bank, *Proceedings of Megagauss XI International Conference* (Ultrahigh magnetic Fields: their science, technology and application), eds. I. Smith and B. Novac, London, U.K. (2006).
- [12] S. I. Shkuratov, E. F. Talantsev, J. Baird, H. Temkin, L. L. Altgilbers and A. H. Stults, Longitudinal Shock Wave depolarisation of Pb(Zr₅₂Ti₄₈)O₃ Polycrystalline Ferroelectric materials and Their Utilization in Explosive Pulsed Power, Shock Compression of Condensed Matter, eds. M. D. Furnish, M. Elert, T. P. Russel, and C. T. White, *American Institute of Physics Publishing*, ISBN: 0-7354-0341-4, Vol. II, **845** (2006), pp. 1169–1172.
- [13] Y. Tkach, S. I. Shkuratov, E. F. Talantsev, M. Kristiansen, J. Dickens, L. L. Altgilbers and P. T. Tracy, Theoretical Treatment of Explosive Driven Ferroelectric Generators, *IEEE Transactions on Plasma Science* **30**(5) (2002) 1665–1673.
- [14] S. I. Shkuratov, E. F. Talantsev, L. Menon, H. Temkin, J. Baird and L. L. Altgilbers, Compact High-Voltage Generator of Primary Power Based on Shock Wave depolarisation of Lead Zirconate Titanate Piezoelectric Ceramics, *Review of Scientific Instruments* **75**(8) (2004) 2766–2769.
- [15] S. I. Shkuratov, E. F. Talantsev, J. Baird, M. F. Rose, Z. Shotts, L. L. Altgilbers and A. H. Stults, Completely explosive ultracompact high-voltage nanosecond pulse generating system, *Review of Scientific Instruments* **77** (2006) No.: 043904.
- [16] S. I. Shkuratov, E. F. Talantsev, J. Baird, A. V. Ponomarev, L. L. Altgilbers and A. H. Stults, High-Voltage Charging of a Capacitor Bank by an Ultra-compact Explosive-Driven Ferroelectric Generator, *IEEE Transactions on Plasma Science*, Accepted for publication (2007).
- [17] C. E. Reynolds and G. E. Seya, Two-Wave Shock Structures in the Ferroelectric Ceramics Barium Titanate and Lead Zirconate Titanate, *Journal of Applied Physics* **33** (1962) 2234–2241.
- [18] W. J. Halpin, Current from a Shock-Loaded Short-Circuited Ferroelectric Ceramic Disks, *Journal of Applied Physics* **37** (1966) 153–163.
- [19] D. G. Doran, Shock-Wave Compression of Barium Titanate and 95/5 Lead Zirconate Titanate, *Journal of Applied Physics* **39** (1968) 40–47.
- [20] P. C. Lysne, Kinetic Effects In the Electrical Response of a Shock-Compressed Ferroelectric Ceramic, *Journal of Applied Physics* **46** (1975) 4078–4079.

- [21] E. Z. Novitskii, V. D. Sadunov and G. Ya. Karpenko, Behavior of Ferroelectric materials in Shock Waves, Combustion, Explosion, and Shock Waves, **14**(4) (1978) 505–516.
- [22] R. E. Setchell, Shock wave compression of the ferroelectric ceramic $\text{Pb}_{0.99}(\text{Zr}_{0.95}\text{Ti}_{0.05})_{0.98}\text{Nb}_{0.02}\text{O}_3$: Hugoniot states and constitutive mechanical properties, *Journal of Applied Physics* **94** (2003) 573–588.
- [23] M. Kristiansen and B. McQuistion, *New World Vista 2000 Annual Report, Air Force Office of Scientific Research* (Washington DC, USA, 2000) unpublished.
- [24] EDO Electro-Ceramic Products Inc., 2645 South 300 West, Salt Lake City, Utah 84115, www.edoceramic.com.
- [25] Reynolds Industries Systems Incorporated, 3420 Fostoria Way, San Ramon, CA 94583, www.risi-usa.com.
- [26] E. Z. Novitskii and V. D. Sadunov, Development of Breakdown in a Shock-Compressed Ferroelectric, Combustion, Explosion, and Shock Waves, **20**(4) (1984) 439–441.
- [27] P. C. Lysne, Dielectric Breakdown of Shock-Loaded PZT 65/35, *Journal of Applied Physics* **44** (1973) 577–582.
- [28] R. F. Trunin, *Shock Compression of Condensed Materials*, Cambridge: University Press (1998).
- [29] C. E. Reynolds and G. E. Seya, Two-Wave Shock Structures in the Ferroelectric Ceramics Barium Titanate and Lead Zirconate Titanate, *J. Appl. Phys.* **33** (1962) 2234–2241.
- [30] L. L. Altgilbers, M. D. J. Brown, I. Grishnaev, B. M. Novac, I. R. Smith, I. Tkach and Yu. Tkach, *Magnetocumulative Generators*, Springer-Verlag, New York (2000).
- [31] *Megagauss Magnetic Field Generation and Pulsed Power Application*, eds. M. Cowan and R. B. Spielman, Nova Science, New York, 1994.
- [32] Proceedings of 9th International Conference on Megagauss Magnetic Field Generation and Related Topics (Megagauss-IX), eds. V. D. Selemir and L. N. Plyashkevich, VNIIEF, Sarov, Russia (2004).
- [33] S. I. Shkuratov, E. F. Talantsev, J. C. Dickens and M. Kristiansen, Transverse Shock Wave Demagnetization of $\text{Nd}_2\text{Fe}_{14}\text{B}$ High-Energy Hard Ferromagnetics, *J. Appl. Phys.* **92** (2002) 159–162.
- [34] S. I. Shkuratov, E. F. Talantsev, J. C. Dickens and M. Kristiansen, Ultra-compact Explosive-Driven High-Current Source of Primary Power Based on Shock Wave Demagnetization of $\text{Nd}_2\text{Fe}_{14}\text{B}$ Hard Ferromagnetics, *Rev. Sci. Instrum.* **73** (2002) 2738–2742.
- [35] S. I. Shkuratov, E. F. Talantsev, J. C. Dickens and M. Kristiansen, Compact Explosive-Driven Generator of Primary Power Based on a Longitudinal Shock Wave Demagnetization of Hard Ferri- and Ferromagnets, *IEEE Transaction on Plasma Science* **30**(5) (2002) 1681–1691.
- [36] S. I. Shkuratov, E. F. Talantsev, J. C. Dickens, M. Kristiansen and J. Baird, Longitudinal-Shock-Wave Compression of $\text{Nd}_2\text{Fe}_{14}\text{B}$ Hard Ferromagnet: The Pressure Induced Magnetic Phase Transition, *Appl. Phys. Letters* **82** (2003) 1248–1251.

- [37] S. I. Shkuratov, E. F. Talantsev, L. Menon, H. Temkin, J. Baird and L. L. Altgilbers, Compact High-Voltage Generator of Primary Power Based on Shock Wave Depolarisation of Lead Zirconate Titanate Piezoelectric Ceramics, *Rev. Sci. Instrum.* **75** (2004) 2766–2769.
- [38] Y. Tkach, S. I. Shkuratov, E. F. Talantsev, M. Kristiansen, J. Dickens, L. L. Altgilbers and P. T. Tracy, Theoretical Treatment of Explosive Driven Ferroelectric Generators, *IEEE Transaction on Plasma Science* **30**(5) (2002) 1665–1673.
- [39] Private communication with Ya. Tkach, May (2008).
- [40] S. I. Shkuratov, J. Baird, E. F. Talantsev, M. F. Rose, Z. Shotts, L. L. Altgilbers, A. H. Stults and S. V. Kollossenkok, Completely Explosive Ultra-compact High-Voltage Pulse Generating System, *2005 IEEE Pulsed Power Conference* (2005), pp. 445–448.
- [41] Z. Shotts, Z. Roberts and M. F. Rose, Design Principles for Vector Inversion Generators, *Abstracts of the 2007 Pulsed Power Plasma Science Conference* (2007), p. 423.
- [42] W. J. Halpin, Current from a Shock-Loaded Short-Circuited Ferroelectric Ceramic Disk, *J. Appl. Phys.* **37**(1) (1966) 153–163.
- [43] W. Mock and W. H. Holt, Pulse Charging of Nanofarad Capacitors from the Shock Depoling of PZT 56/44 and PZT 95/5 Ferroelectric Ceramics, *J. Appl. Phys.* **49**(12) (1978) 5846–5854.
- [44] S. L. Holt, D. J. Hemmert, J. T. Krile, W. S. Hackenberger, E. F. Alberta, J. W. Walter, J. C. Dickens, L. L. Altgilbers and A. H. Stults, Testing of New Ferroelectric Materials for Explosive Driven Ferroelectric Generators, *Proceedings of Megagauss XI*, London (2006), to be published.
- [45] R. E. Setchell, Recent Progress in Understanding the Shock Response of Ferroelectric Ceramics, *Shock Compression of Condensed Matter*, eds. M. D. Furnish and N. N. Thodhani, CP620 (American Institute of Physics, New York, 2002), pp. 191–196.
- [46] W. Mock and W. H. Holt, Pulse Charging of Nanofarad Capacitors from the Shock Depoling of PZT 56/44 and PZT 95/5 Ferroelectric Ceramics, *Journal of Applied Physics* **49**(12) (1978) 5846–5854.
- [47] S. I. Shkuratov and J. Baird, Loki Inc. SBIR Progress Report, January (2006).
- [48] S. I. Shkuratov and J. Baird, Loki Inc. SBIR Progress Report, January (2008).
- [49] M. D. Furnish, J. Robbins, W. M. Trott, L. C. Chhabildas, R. J. Lawrence and S. T. Montgomery, Multi-Dimensional Validation Impact Tests of PZT 95/5 and ALOX, Shock Compression of Condensed Matter-2001 eds. M. D. Furnish, N. N. Thadhani and Y. Horie, American Institute of Physics, CP620 (2002), pp. 205–208.
- [50] R. A. Anderson, R. R. Lagasse, J. L. Schroeder, D. H. Zeuch and S. T. Montgomery, *Pulsed Breakdown of Aluminum Oxide (ALOX): Effects of Formulation and Electric Stress Concentration*, Sandia Report SAND2001-2897 (2001).

Chapter 13

Moving Magnet Generators

Moving Magnet Generators (MMGs) are pulsed power devices that convert the magnetic and mechanical energy of ferromagnetic projectiles into electrical energy. The idea of using the linear motion of permanent magnets to produce electrical power was first patented 1888 [1–26]. This idea is based on Faraday’s law.

Significant progress in the development of various types of MMG was made by Shkuratov *et al.* [27–38] at Texas Tech University between 1998 and 2003. They designed, constructed and experimentally and theoretically studied different types of MMG. In fact, pulsed power systems based on the rectilinear motion of ferromagnetic projectiles were first named Moving Magnet Generators by Shkuratov *et al.* in 1999 [27]. It was experimentally demonstrated that compact MMGs are capable of producing voltage pulses with amplitudes up to 52 kV and current pulses with amplitudes up to 7 kA [27–38]. These experimental results established that moving magnet generators are a new type of pulsed power system.

13.1 Principles of Operation

The electrical operation of MMGs is based on the generation of a pulsed electromotive force (EMF) by the rectilinear motion of a ferromagnetic projectile through a pulse generating coil. A schematic diagram that illustrates the operation of MMGs [36] is shown in Fig. 13.1. In Fig. 13.1(a), the ferromagnet is approaching the coil. The magnetic flux inside the pulse generating coil is close to zero at this moment in time. In Fig. 13.1(b), the ferromagnet enters the coil. The magnetic flux inside the coil changes from zero to its maximum value. During this stage of the operation, the MMG produces the first EMF pulse in accordance with Faraday’s law. In

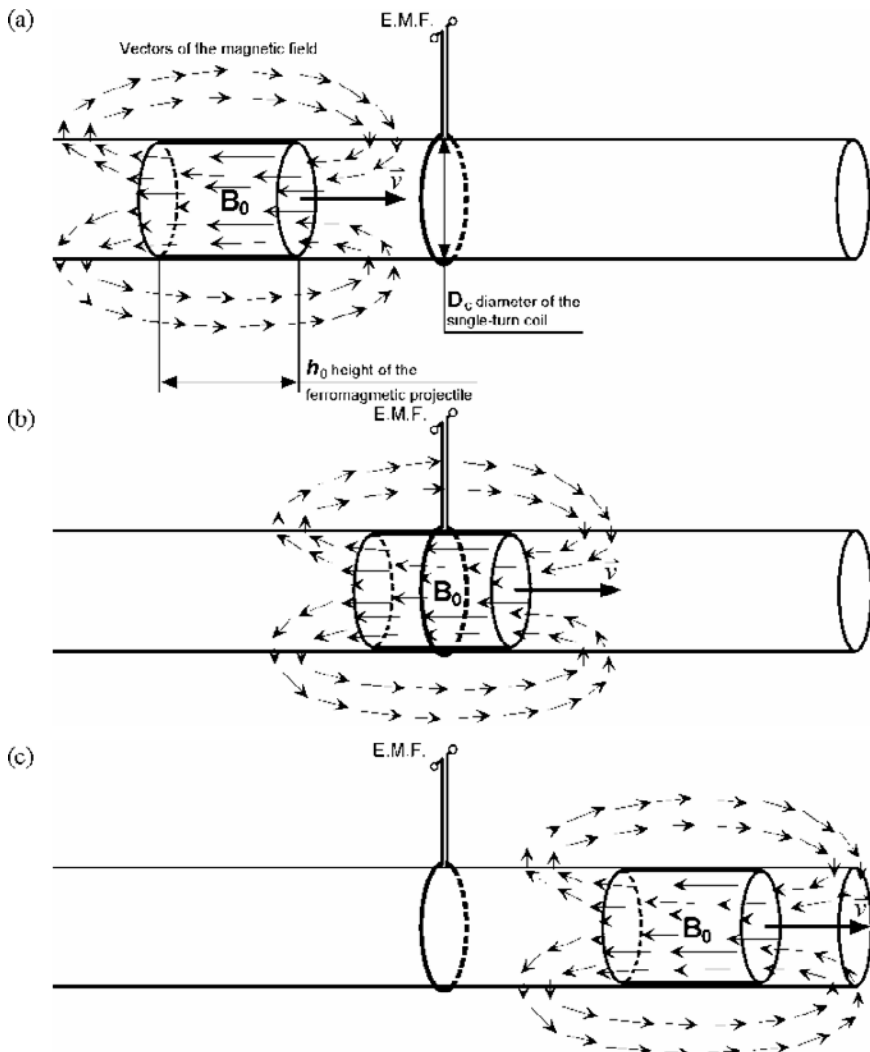


Fig. 13.1 Schematic diagram illustrating the operation of moving magnet generators [36]. (a) The ferromagnet approaches the coil. The magnetic flux inside the pulse generating coil is close to zero at this moment in time. (b) The ferromagnet enters the coil. The flux inside the coil changes from zero to its maximum value. During this stage of operation, the MMG produces the first EMF pulse. (c) The magnet departs from the coil. The magnetic flux inside the coil changes from its maximum value to almost zero and the second EMF pulse (having a polarity opposite to that of the first pulse) is induced at the output terminals of the coil.

Fig. 13.1(c), the magnet departs from the coil. The magnetic flux inside the coil changes from its maximum value to almost zero and a second EMF pulse (having a polarity opposite to that of the first pulse) is induced at the output terminals of the coil.

Consider a cylindrically shaped ferromagnet that has a diameter of D_{ferro} and has been magnetised along its axis. This ferromagnetic projectile is moving through a coil with inner diameter D_c and consisting of N turns. Assuming

- that the ferromagnet has a length of h and that the length of the coil is equal to the length of the ferromagnet,
- that the ferromagnetic projectile is moving with a velocity of v and that its velocity is constant over the time the ferromagnet is moving through the coil,
- that the inner diameter of the coil D_c is equal to the diameter of the ferromagnet D_{ferro} ,
- that prior to the ferromagnetic projectile entering the coil that the total magnetic flux Φ_0 in the coil is zero,

then when the ferromagnet enters the coil, the total magnetic flux in the coil is

$$\Phi_0 = \pi B_0 \frac{D_c^2}{4}, \quad (13.1)$$

where B_0 is the average magnetic flux density in the cross section of the coil. The magnetic flux reaches its peak value when the center of the ferromagnetic projectile is at the center of the coil. Since it was assumed that the velocity v of the ferromagnet is constant during the time it takes to move through the coil, the electromotive force generated in the coil forms a sine wave and, to the first approximation, can be estimated by using the following expression:

$$\text{EMF} = -N \frac{\Delta \Phi}{\Delta t} = -N \frac{\Delta(\pi B_0 D_c^2 / 4)}{\Delta t} = -N \pi D_c^2 B_0 \frac{v}{2h}. \quad (13.2)$$

The time it takes for the magnetic flux to increase from zero to its peak value at the center of the coil is $\Delta t = (h/2)/v$. Since the flux is increasing as the center of the ferromagnetic projectile approaches the center of the coil, the integrated voltage generated in the coil is $N\pi D_c^2 B_0 v / 2h$. When the projectile departs from the coil, the magnetic flux decreases from its maximum value to zero and the second electromotive force pulse having a polarity opposite to that of the first pulse is formed. Based on system

symmetry, it could be assumed that the amplitude of the second EMF pulse is equal to that of the first pulse, but this was not confirmed in the experiments described in [31]. Thus, the peak-to-peak voltage of the EMF pulse generated in the coil was

$$\text{EMF} = -2N \frac{\Delta\Phi}{\Delta t} = -N \frac{\Delta(\pi B_0 D_c^2 / 2)}{\Delta t} = -N\pi D_c^2 B_0 \frac{v}{h}. \quad (13.3)$$

It follows from Eqs. (13.2) and (13.3) that the amplitude of the EMF pulses is proportional to the number of turns in the coil, the diameter of the ferromagnet, the magnetic flux density in the ferromagnet and the velocity of the projectile. The duration of the voltage pulse is inversely proportional to the velocity of the ferromagnetic projectile.

13.2 Moving Magnet Pulsed Power Generators

An expression for the specific EMF produced by MMGs can be obtained by dividing Eq. (13.3) by the number of turns N in the pulse generating coil:

$$\text{EMF} = -\frac{d\Phi}{dt} = -\frac{d(B_r \cdot A)}{dt}. \quad (13.4)$$

Equation (13.4) can be used to define those conditions necessary for the MMG to be used as a pulsed power source. In order for the MMG to produce high-power pulses, it is necessary that the magnetic flux in the pulse generating coil undergo a rapid rate of change in time. In other words, it is necessary that the magnetic projectile move at a high velocity and that the projectile have a high magnetic flux.

An explosive driven MMG can accelerate a magnetic projectile with $D = 25.4$ mm and $h = 19.0$ mm to several hundred meters per second with a relatively small amount of high explosive or propellant. It should be noted that the magnetic projectile is an expendable part of the system because it is not possible to decelerate and re-use a magnet with a mass of about 100 g moving at a velocity of several hundred meters per second in a small size system. The expendability of some parts of explosive pulsed power systems is a typical requirement for all types of explosive driven pulsed power devices.

Another requirement for producing pulsed power with compact MMGs is to use a magnetic projectile with high magnetic flux. Table 13.1 summarizes the calculated amplitudes of the specific EMF pulses produced

Table 13.1 Summary of the calculated amplitudes of the specific EMF pulses produced by MMGs with projectiles having dimensions of $D = 25.4$ mm and $h = 19.0$ mm. The projectiles were made from magnetic materials that were available at different times over the past 120 years. The velocity of the projectiles was 300 m/s.

Years	Available Magnetic Materials [15–16]	Average B in Cross Section of Projectile (T)	Calculated Amplitude of EMF_{spec} (V/turn)	Experimental Data
1888–1930s	Mechanically deformed iron and carbon steels	0.005	0.04	None
1930s–late 1950s	ALNICO	0.02	0.15	None
1960s–1980s	Hard ferrites	0.2	1.5	1998 [27–29]
1980s–1990s	Sm-Co magnets	0.4	3.0	None
1990s–Present	Nd-Fe-B magnets	1.3	10.2	1998–2002 [27–38]

by MMGs using magnetic projectiles made from ferromagnetic and ferrimagnetic materials that have been available since 1888, when the first patent for the idea of using the linear motion of permanent magnets to produce electrical power was granted, to the present time. The dimensions of these magnetic projectiles were assumed to be $D = 25.4$ mm and length $h = 19.0$ mm. The velocity of these projectiles was assumed to be 300 m/s. The average value of the magnetic flux density of these different magnetic materials were calculated by using the Maxwell 3D code [31, 36, 39].

In order to produce an output voltage of $U = 10$ kV with the MMG described in the first fuze patent (Lt. E.L. Zalinski, 1888 [1]), the number of turns, N , in the pulse generating coil would have to be equal to

$$N = (10,000 V) / (0.04 \text{ V/turn}) = 250,000 \text{ turns.} \quad (13.5)$$

Even with copper wire having a diameter of 0.1 mm, the outer diameter of this coil [Eq. (13.5)] would have to have been 25.0 m, and its inductance and resistance would have been enormous. It is absolutely not possible to produce pulsed power with this type of MMG. The results with ALNICO and hard ferrite projectiles, which were the only commercially available hard ferromagnetic materials until the 1980s, would not have been much better. The other hard ferromagnetic materials that were developed between the 1960s and the 1980s were not considered. These materials (Pt(50%)-Co(50%), Pt(75%)-Co(25%), etc.) could not be used in single shot expendable pulsed

power systems because of their extremely high cost since platinum was the main component of these alloys.

Based on data presented in Table 13.1, it can be concluded that before the beginning of the 1990s, it was practically impossible to design an explosive driven MMG. It should be noted that all patents granted since 1988 [1] were not aimed at the development of MMG pulsed power systems, but rather to the development of prime power sources that were competitive to electrochemical cells.

A new approach for using the rectilinear motion of magnetic projectiles to generate pulsed power was developed by Shkuratov *et al.* in 1998 [27–38]. The basis of this approach was the idea that in order to produce pulsed power with an MMG, it was necessary that the magnetic projectile have both high kinetic energy and high magnetostatic energy. The magnetostatic energy of a ferromagnet depends on its residual magnetisation, B , and its coercive force, H_c . The energy stored in the ferromagnet is determined by its maximum energy product $(B \cdot H)_{\max}$.

The first pulsed power generators based on the rectilinear motion of ferromagnetic projectiles were designed, constructed and experimentally investigated by Shkuratov *et al.* in 1998 at Texas Tech University [27–29]. It was experimentally demonstrated that MMGs using Nd₂Fe₁₄B ferromagnetic projectiles with its maximum energy product of $(B \cdot H)_{\max} = 11.2 \text{ MG} \cdot \text{Oe}$ and that were accelerated to 320 m/s produced specific EMF pulses with amplitudes of EMF = 8.2 V [27–29]. Voltage pulses with amplitudes up to 35 kV were produced by MMGs equipped with compact pulse generating coils having an outer diameter of 57 mm. High-current MMGs were capable of producing output currents exceeding 1 kA. These MMGs can be considered to be a new class of compact pulsed power generators. In the next few years, detailed studies of the operation of pulsed power MMGs were performed by Shkuratov *et al.* [27–38] and the results of this research are described below.

13.3 Principle MMG Designs

13.3.1 Open Magnetic Circuit MMGs

A magnetic circuit is a combination of ferromagnetic cores and the windings used to link these cores. The cores can be made from soft or hard ferrimagnetic or ferromagnetic materials. The windings may be either single- or multiple-turn coils and placed in various arrangements with respect to other windings and cores. Each magnetic circuit is designed and built for

a specific function. Some of the most common functions of magnetic circuits are to transform voltage, current and/or impedance. Other possible functions include providing force or torque.

In the MMG pulsed power system, the function of the magnetic circuit is to generate high power electrical pulses. It was demonstrated by Shkuratov *et al.* [27–38] that MMGs can be either open magnetic circuit or closed magnetic circuit designs.

Open magnetic circuits are based on open magnetic paths. The most frequently used open magnetic circuit MMGs are those in which cylindrical or rectangular magnets, magnetised along their axes, are accelerated along a barrel about which a pulse generating coil is wound. Only a small portion of the magnetic flux lines lie within the barrel. The majority of the magnetic flux lines lie outside the confines of the barrel.

Schematic diagrams of an MMG [28] utilizing an open magnetic circuit is shown in Fig. 13.1 and 13.2. The system contains a ferromagnetic cylinder magnetised along its axis, which serves as the projectile, and one or more pulse generating coils wound on a dielectric cylindrical barrel. In this system, a significant portion of the magnetic flux lines is situated in the air around the MMG (see Fig. 13.1). When the ferromagnetic projectile moves through the coils, there is a time rate of change in the magnetic flux, which induces an electromotive force pulse in the coils. A typical waveform of the EMF pulse produced by an open magnetic circuit MMG equipped with a multi-turn pulse generating coil is shown in Fig. 13.3. The Nd₂Fe₁₄B ferromagnetic projectile, with dimensions of $D = 25.4$ mm and $h = 19.0$ mm,

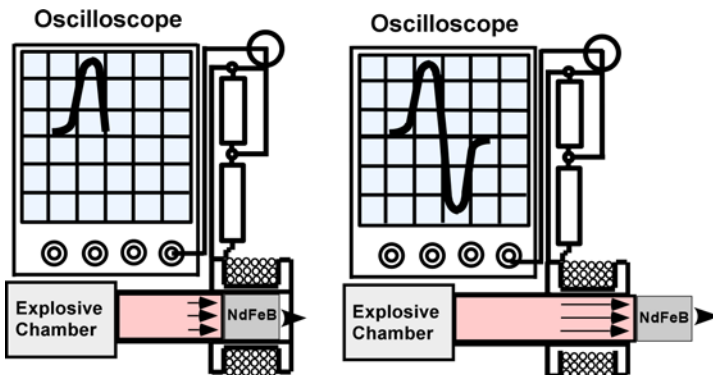


Fig. 13.2 Schematic diagram of an open magnetic circuit MMG [28]. The two figures show that (a) when the magnet enters the coil, a positive voltage pulse is produced and (b) when the magnet departs the coil, a voltage pulse having opposite polarity is produced.

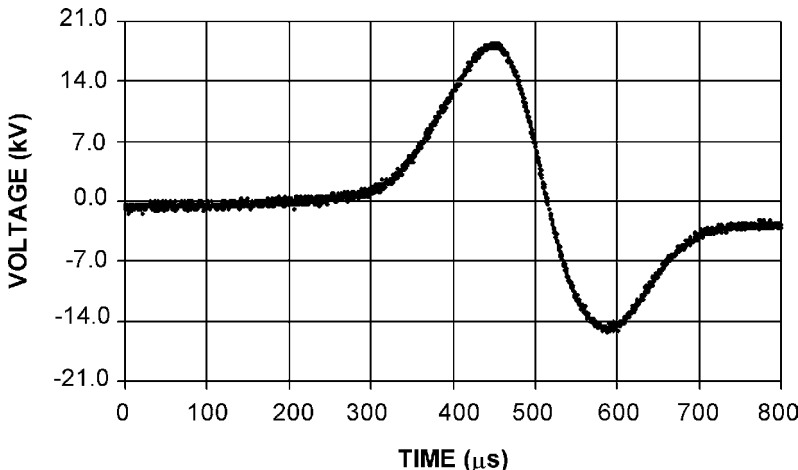


Fig. 13.3 A typical waveform of the voltage pulse produced by an open magnetic circuit MMG [28].

moving with a velocity of 317 m/s produced an EMF pulse with a peak-to-peak amplitude of 33.4 kV.

Open magnetic circuit MMGs were experimentally studied in detail by Shkuratov *et al.* [27–38]. To calculate the output signals produced by these MMGs, Shkuratov *et al.* [32, 34–36] also developed a theoretical model. The signals calculated with this model are in good agreement with their experimental results.

13.3.2 Closed Magnetic Circuit MMGs

Closed magnetic circuits are based on closed magnetic paths. Closed magnetic paths are designed to retain all the ferromagnetic projectiles' magnetic flux within the MMG. The most commonly used closed magnetic path geometries are toroidal cores, E-cores and pot cores. Theoretically, flux leakage outside these structures is zero. If the closed magnetic path is disrupted by an air gap, there is flux leakage into the MMGs environment. Still, such a system can be considered as a closed magnetic circuit provided the largest portion of the flux lines is still concentrated within the core.

A schematic diagram of a closed magnetic circuit MMG developed by Shkuratov *et al.* [27–29] is shown in Fig. 13.4. It contains a ferromagnetic cylinder, which serves as the projectile, a soft ferrite toroidal core with an air gap and a pulse generating coil wound on the ferrite core. A key

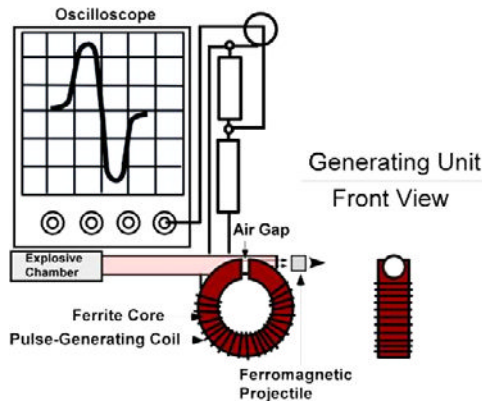


Fig. 13.4 Schematic diagram illustrating the operation of a closed magnetic circuit MMG [28].

component of the closed magnetic circuit MMG [27–29] is its soft ferrite toroidal core with a coil wound on it.

Figure 13.4 illustrates the operation of a closed magnetic circuit MMG [27–29]. Initially, the magnetic circuit of the ferrite core was partly an open circuit and the flux inside the pulse generating coil was low. When the hard ferromagnetic projectile entered the air gap in the ferrite core, the magnetic circuit of the core was closed and the magnetic flux inside the pulse generating coil reached its peak value. The MMG produced the first EMF pulse. When the projectile departed the ferrite core, the magnetic circuit of the core was partly opened. This resulted in an abrupt decrease in the magnetic flux inside the coil. The second EMF pulse, having a polarity opposite to that of the first pulse, was induced across the output terminals of the coil.

Successful operation of a closed circuit MMG was experimentally demonstrated by Shkuratov *et al.* [27–29]. A typical waveform of the voltage pulse produced by a closed circuit MMG is shown in Fig. 13.5. The peak-to-peak amplitude of the voltage pulse was 4.3 kV. The shape of the second high-voltage pulse was not the same as that of the first pulse. The difference was due to the hysteretic behavior of the ferrite core.

The advantage of closed magnetic circuit MMGs is that it is possible to place several pulse generating coils on a single ferrimagnetic or ferromagnetic core. Each coil generates high-voltage or high-current pulses. A single ferromagnetic core with several coils wound on it can produce a series of pulses at the same moment in time. These pulses can be used to simultaneously drive multiple circuits. This is not possible with the open

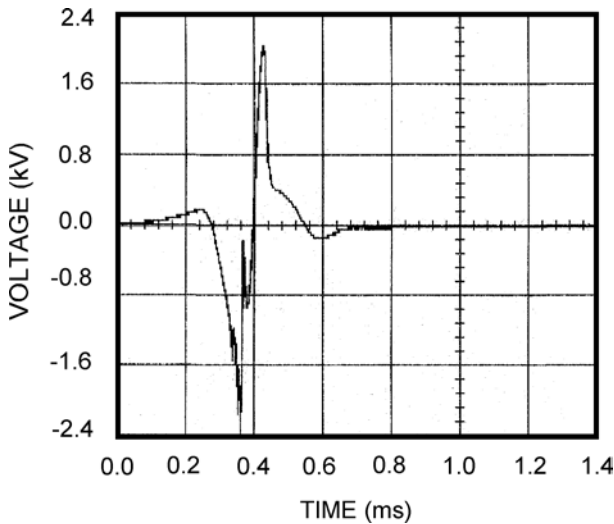


Fig. 13.5 A typical waveform of the voltage pulse produced by a closed magnetic circuit MMG [28].

magnetic circuit MMGs (Fig. 13.2), where each coil generates high-voltage or high-current pulses at different moments in time because of the way the ferromagnetic projectile moves through the coils. It was experimentally demonstrated by Shkuratov *et al.* in Refs. 27–29 that another advantage of closed magnetic circuit MMGs is its ability to generate sinusoidal signals, which is described in the next subsection.

13.3.3 MMG Ferromagnetic Projectiles

There are two types of ferromagnetic projectile used in MMGs [27–29]. The first type is shown in Figs. 13.1, 13.2 and 13.4. It is solid ferromagnetic cylinder magnetised along its axis. Waveforms of the pulses produced by this type of projectile are shown in Figs. 13.3 and 13.5.

A new type of ferromagnetic projectile was developed by Shkuratov *et al.* [27–29] to specifically generate multiple sinusoidal signals using a closed magnetic circuit MMG. A schematic diagram of this new type of ferromagnetic projectile is shown in Fig. 13.6. It is a multi-component projectile consisting of magnetic disks alternating with dielectric layers. The ferromagnetic disks are magnetised along their axis. The magnetisation

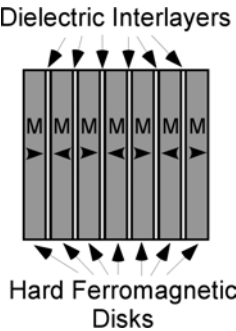


Fig. 13.6 Multi-component ferromagnetic projectile [27–29] to produce sinusoidal signals. The magnetisation vectors of the ferromagnetic disks are represented by the arrows.

vector of each disk is oriented in a direction opposite to that of the previous disk and the disk following it (Fig. 13.6).

The method by which repetitive sinusoidal signals are generated by multi-component ferromagnetic projectiles is as follows. The multi-component ferromagnetic projectile moves at high speeds through the soft ferrite toroidal core of a closed magnetic circuit MMG. The instant the air gap in the core is closed by the projectile entering the air gap, a positive pulse is produced, and the instant the air gap is opened by the projectile leaving the air gap, a negative pulse is produced. This process generates a full period sine wave (Fig. 13.5). A short time after the first magnetic disk passes into and out of the air gap, the second magnetic disk enters and leaves the coil and generates another full period sine wave, and so on. The interval between the two sine waves is determined by the thickness of the dielectric layer between the magnetic disks and by the speed of the ferromagnetic projectile. The number of periods is determined by the number of magnetic disks in the multi-component ferromagnetic projectile.

A series of experiments were performed by Shkuratov *et al.* [27–29] to investigate the generation of multiple signals by multi-component ferromagnetic projectile with different numbers of magnetic disks. A typical waveform of the voltage produced by a closed magnetic circuit MMG using a multi-component projectile containing seven ferromagnetic disks, having dimensions of $D = 12.7\text{ mm}$ and $h = 5.0\text{ mm}$, is shown in Fig. 13.7. Seven sinusoid signals, having nearly the same amplitude, were sequentially formed. The generated repetitive signals were perfect waveforms with no breaks or distortions. There was no attenuation of the signals. This output voltage can be applied directly to a transmitting antenna.

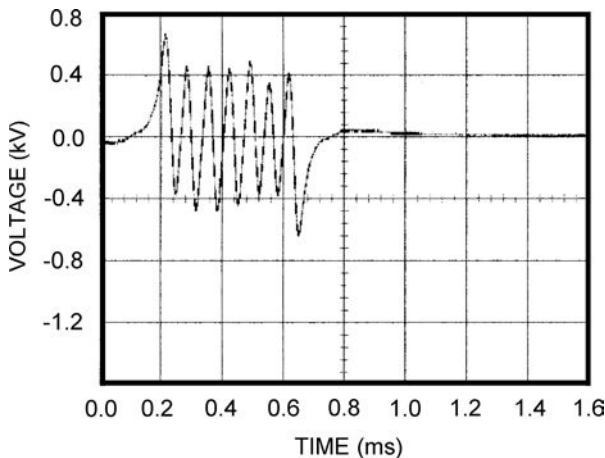


Fig. 13.7 A typical voltage waveform produced by a closed magnetic circuit MMG [28] with a multi-component ferromagnetic module projectile containing seven ferromagnetic disks (Fig. 13.6).

Analysis of closed ferromagnetic circuit MMGs has shown that in order to generate high-power periodic signals, it is preferable to harness the motion of the multi-component ferromagnetic projectile not along, but across the magnetic flux lines in the soft ferromagnetic core. A schematic diagram of an explosive-driven closed magnetic circuit MMG, designed to produce high power microwave pulses, is shown in Fig. 13.8. A hole, through which the ferromagnetic projectile passes, is drilled in the core. The hole is drilled in such a way that it also makes a short air gap in the core. When the projectile is in the air gap, the magnetic circuit is momentarily closed. The motion of the projectile through the air gap generates an electrical signal in the coil wound on the core.

A diagram of the ferromagnetic projectile used in the MMG depicted in Fig. 13.8 is shown in Fig. 13.9. The ferromagnetic disks are separated by dielectric disks. The ferromagnetic disks are magnetised normal to their axis. The N-S poles of neighboring ferromagnetic disks are oriented in opposite directions. Prior to a shot, the ferromagnetic projectile is oriented in such a way that the direction of the N-S poles of the ferromagnetic disks coincide precisely with the direction that will cause optimal magnetisation of the magnetic core.

As the multi-component ferromagnetic projectile moves through the air gap of the magnetic core, the core is sequentially magnetised by the

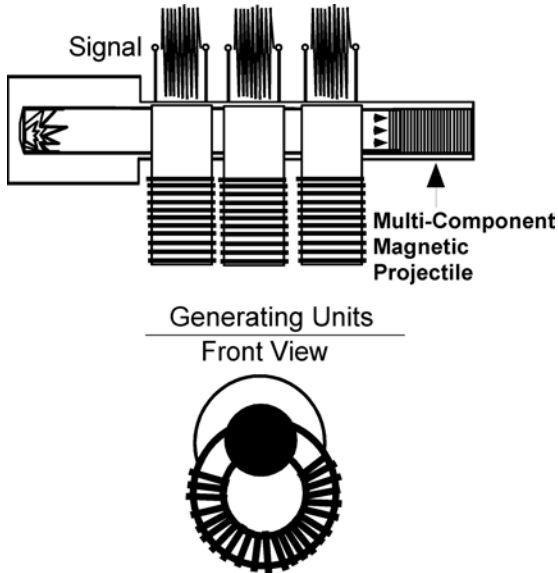


Fig. 13.8 Schematic drawing of an explosive-driven closed magnetic circuit MMG [28, 29] to produce high-power microwave pulses.

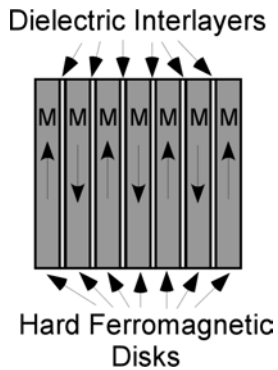


Fig. 13.9 Diagram of the multi-component ferromagnetic projectile used in the sinusoidal MMG shown in Fig. 13.8. The magnetisation vectors of the ferromagnetic disks are represented by the arrows.

magnetic disks in alternating directions. The variations in the magnetic flux generate high-frequency repetitive oscillations in the coil. One multi-component ferromagnetic projectile could contain up to a few hundred thin magnetic disks. When this projectile completely passes through the air gap

of the magnetic core, hundreds of periods of high-voltage oscillation will be generated in the series connected pulse generating coils. These high-voltage signals can be applied directly to a transmitting antenna to generate high-power microwaves.

13.4 High-Current Explosive-Driven MMGs

13.4.1 Experimental Systems

Ferromagnetic projectiles can be accelerated through a MMG by high-pressure gases generated by explosive charges or by previously compressed high-pressure gases. Several series of both types of MMG were designed, constructed and investigated by Shkuratov *et al.* [27–38].

A schematic diagram of a compact explosive-driven MMG [32–38] is presented in Fig. 13.10. It consists of an explosive chamber loaded with an explosive charge, an aluminum disk, an acceleration barrel, a plastic protection disk, a hard ferromagnetic projectile magnetised along its axis and a series of pulse-generating coils connected to loads. The total length of the explosive-driven MMG with a ferromagnetic projectile, having dimensions of $D = 25.4$ mm and $h = 19.0$ mm, does not exceed 400 mm. A photograph of this explosive-driven MMG is shown in Fig. 13.11.

Operation of the explosive-driven MMG is as follows. After initiation of the explosive charge, high-pressure gases are generated in the explosive chamber. The aluminum disk installed at the front of the acceleration barrel (Fig. 13.10) serves as a rupture valve. When the required pressure is reached in the explosive chamber, the aluminum disk ruptures, high pressure gases

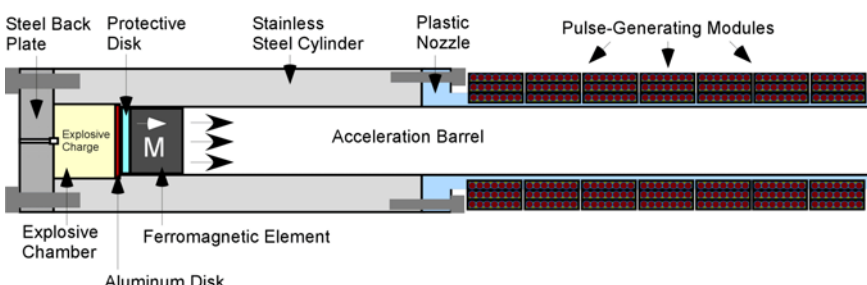


Fig. 13.10 Schematic diagram of an explosive-driven high current MMG [37, 38]. The direction of the magnetisation vector of the ferromagnetic elements is represented by arrows.

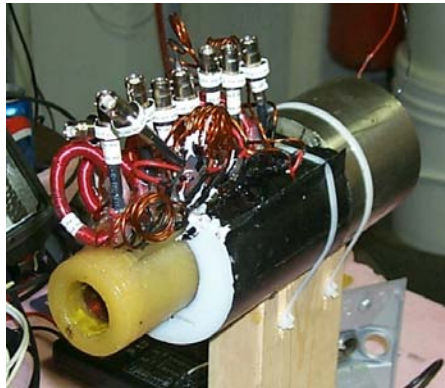


Fig. 13.11 Photograph of an explosive-driven high current MMG [32].

enter the acceleration barrel and the ferromagnetic projectile is accelerated along the barrel. In order to protect the ferromagnetic element from overheating by the explosive-generated gases, a plastic disk was installed on its back side (Fig. 13.10). The sharp edges of the ferromagnetic projectile were rounded to reduce friction. In addition, the inside surface of the barrel was coated with gun lubricant.

The ferromagnetic projectile was subjected to an initial acceleration in the metallic part of the acceleration barrel, where the pressure of the gases is at its highest value. When the ferromagnetic element enters into the plastic part of the barrel, it has already been accelerated to high velocity and is capable of generating high-power signals in the pulse-generating coils. Shkuratov *et al.* [32–38] performed systematic experimental investigations of the operation of explosive-driven MMGs utilising high explosives, low explosives and propellant charges. The experimental data indicated that the MMGs yielded the best output parameters when military propellants were used. A typical waveform of the current pulse produced by an MMG utilising a propellant charge is shown in Fig. 13.12. The velocity of a ferromagnetic projectile with $D = 25.4$ mm and $h = 19.0$ mm was $V = 198$ m/s. The inductance of the pulse generating system in this experiment was $L(10\text{ KHz}) = 1.1\ \mu\text{H}$ and its serial resistance was $R(10\text{ KHz}) = 72\ \text{m}\Omega$. The amplitude of the positive current pulse was $I_{\max}(t) = 907\ \text{A}$ with an FWHM of $103\ \mu\text{s}$.

The barrels of MMG that use previously compressed high-pressure gases [27–31, 33, 34] are significantly longer than those that use high explosives [32, 35–38]. The main reason for this is that the gas pressures are significantly lower in gas-gun systems (not higher than 4 MPa) than in propellant

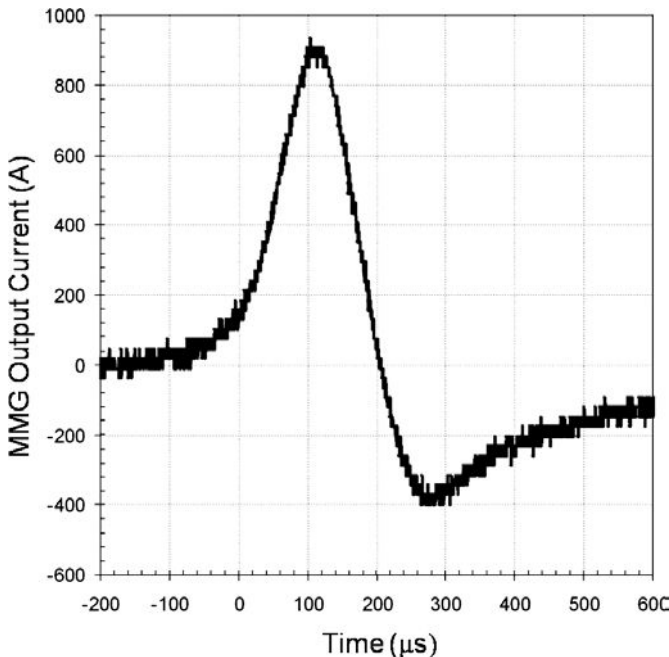


Fig. 13.12 A typical waveform of the current pulse produced by an explosive-driven MMG [38].

driven MMGs. A typical waveform of the current pulse produced by gas-gun MMGs that use compressed gases in bottles is shown in Fig. 13.13. The parameters of the pulse-generating coil in this experiment were identical to those used in the explosive-driven experiment (Fig. 13.12). The velocity of the ferromagnetic projectile, which had dimensions of $D = 25.4$ mm and $h = 19.0$ mm, was $V = 200$ m/s. The amplitude of the positive current pulse was $I_{\max}(t) = 910$ A, with FWHM of $103\ \mu\text{s}$. Comparing the waveforms shown in Figs. 13.12 and 13.13, it can be concluded that there is no difference in the amplitude of the positive current pulse and the FWHM for explosive-driven MMGs and gas-gun MMGs. The outputs of these two pulsed power systems were practically identical.

13.4.2 Principles of High Current Generation

One of the possible applications for explosive-driven MMGs is as a seed source for magnetic flux compression generators. Systematic studies of the

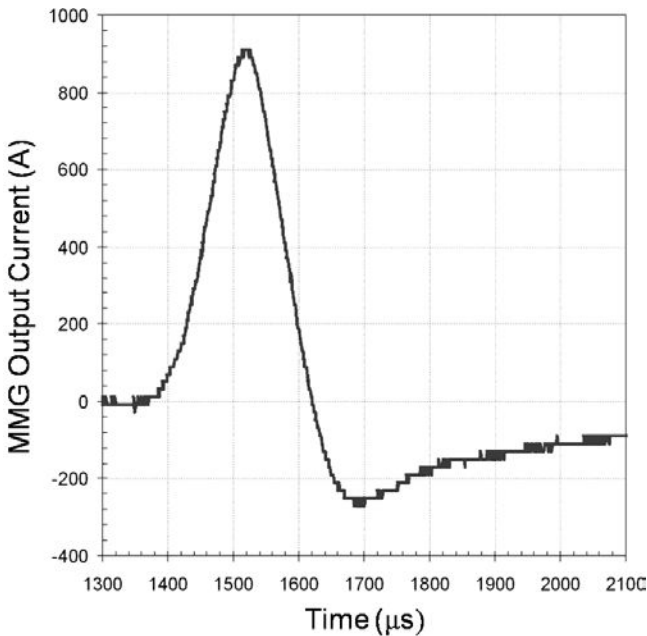


Fig. 13.13 A typical waveform of the current pulse produced by an MMG utilising bottled high-pressure gases [34].

operation of explosive-driven MMGs operating in the high current mode were performed by Shkuratov *et al.* [32–38].

Let's consider the generation of high current by a pulsed power system based on rectilinear motion of a ferromagnet. The basic cause of current generation by MMGs is the EMF induced in their pulse generating coils due to changes in the magnetic flux in the coils caused by the rectilinear motion of the ferromagnetic projectile as it passes through the coils. The EMF induced in a single turn of the pulse generating coil of a high current MMG is determined by using the following equation:

$$EMF = -\frac{d\Phi}{dt} = -\frac{d(B_r \cdot A)}{dt}, \quad (13.6)$$

where B_r is the average magnetic field density of the ferromagnetic projectile and A is the cross-sectional area of the ferromagnetic element. The amplitude of the EMF is directly proportional to the remnant magnetisation of the ferromagnetic projectile.

The current produced in the pulse generating system of the MMG is a Faraday-Lenz current, whose magnitude and direction are self induced

so that the magnetic flux induced by this current, $\Delta\Phi_{\text{current}}$, compensates for the change in the magnetic flux in the MMG pulse-generating coil, $\Delta\Phi_{\text{ferro-motion}}$, produced by the rectilinear motion of the ferromagnetic element through the coil. The direction of the magnetic field induced in the pulse-generating coil is exactly opposite to the direction of the magnetic field of the ferromagnetic projectile moving through the coil. Therefore, the magnetic field generated by the pulsed current in the coil demagnetises the ferromagnetic projectile.

It was first postulated by Shkuratov *et al.* [27–38] that in order for MMGs to produce high amplitude current pulses and high amplitude power pulses that it was a necessary condition that the ferromagnetic projectiles possess both high residual magnetisation, B_r , and high coercive force, H_c . The coercive force of the ferromagnetic projectiles is not part of Eq. (13.5), which governs the electrical operation of MMGs, but in accordance with the principles formulated by Shkuratov *et al.* [27–38], the H_c and the corresponding magnetostatic energy of the ferromagnetic projectile, W , which is a function of the maximum energy product $W = (B \cdot H)_{\max}/2$, are the main parameters that determine pulsed power generation by MMGs. This principle was experimentally verified [27–38]. It was also experimentally demonstrated that MMGs utilising high-energy Nd₂Fe₁₄B projectiles provide the highest amplitude current and power pulses [27–38].

13.4.3 High Current MMG Seed Sources

A schematic diagram of an explosive-driven high current MMG [32–36] is shown in Fig. 13.14. It contains three pulse-generating coils. Three strip transmission lines connected the MMG pulse-generating coils to the three single-turn FCG seed coils that were equipped with current transformers.

High-energy Nd₂Fe₁₄B solid cylinders, with $D = 25.4$ mm and $h = 19.0$ mm and magnetised along their axis, were used as ferromagnetic projectiles in experiments conducted by Shkuratov *et al.* [32–38]. The parameters of the Nd₂Fe₁₄B ferromagnets were: residual flux density $B_r = 1.23$ T, coercive force $H_c = 8.99 \cdot 10^5$ A/m and maximum energy product $BH_{\max} = 0.279$ J/cm³, where the industry tolerances are: $B_r \pm 5\%$, $H_c \pm 8\%$ and $BH_{\max} \pm 10\%$, respectively. The speed of the ferromagnetic projectile was measured with a trigger coil system installed in front of each of the pulse generating coils.

The pulsed power circuit of the MMG seed source consisted of a current generating system, with an impedance of Z_G , and a load, with an impedance

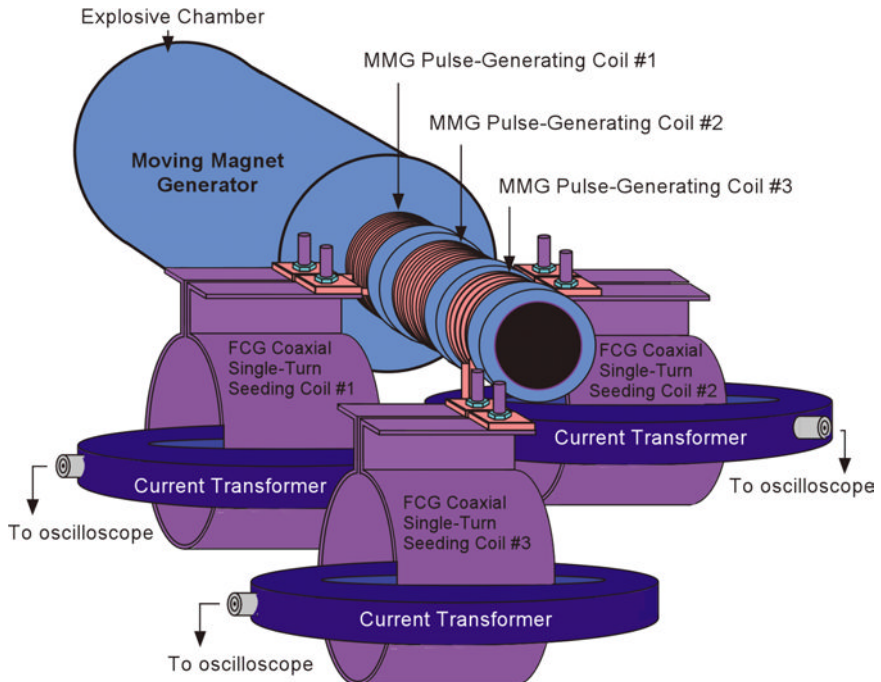


Fig. 13.14 Schematic diagram of an explosive-driven MMG powering three seed coils of a magnetic flux compression generator [38].

of Z_L . The load included a transmission line and a single-turn coaxial coil, which created the initial magnetic field in the helical flux compression generator [42]. Since both the pulse-generating coil and the load were inductive coils, the equivalent circuit of the system included the inductance L_G and the resistance R_G of the pulse-generating unit and the inductance L_L and the resistance R_L of the load, all of which were connected in series. The circuit diagram of the test setup is shown in Fig. 13.15. The output voltage and current were monitored with Tektronix voltage probes and current transformers.

For some applications, MMGs need to be very compact devices, which was one of the main objectives in the design and development of explosive-driven MMGs [32–38]. Because of these dimension restrictions, a series of pulse-generating coils [32–38] were placed on the acceleration barrel and separated by a small distance (Figs. 13.10, 13.11 and 13.14). It was obvious that the magnetic fields induced in the adjacent pulse generating coils would interfere with each other and with the magnetic field of the ferromagnetic

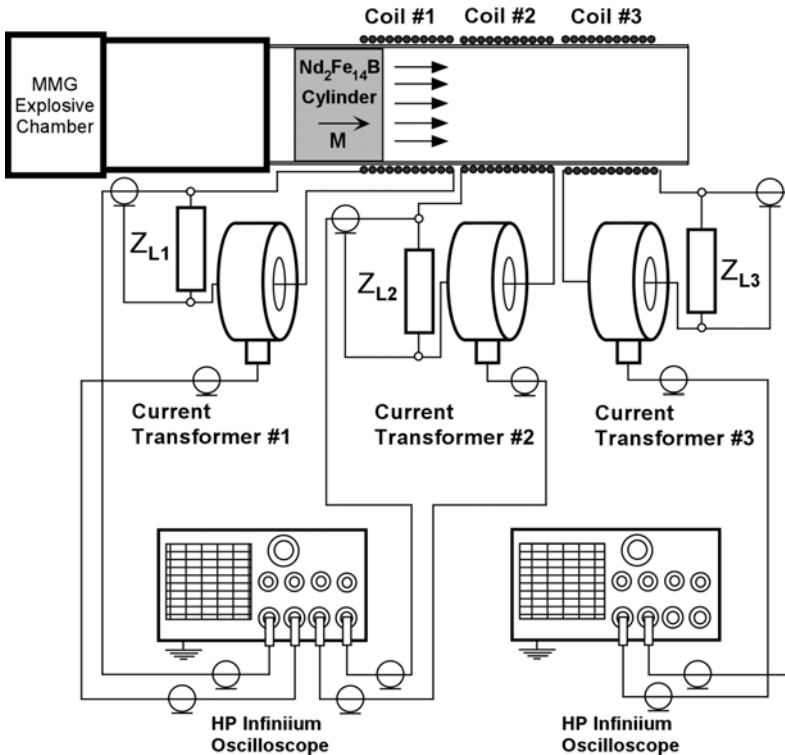


Fig. 13.15 Circuit diagram of the test setup used to study the operation of explosive-driven MMGs [38].

projectile. Therefore, an important question that had to be answered was whether or not it would be possible to produce high amplitude current pulses with a series of pulse-generating units placed close together.

The answer to this question was provided by a series of systematic investigations performed with explosive-driven MMGs containing three identical pulse-generating coils placed 1 mm apart [37]. A schematic diagram of this MMG is shown in Fig. 13.14. The length of each coil was $h_c = 19.0$ mm and its inner diameter was $D_c = 28.0$ mm. The electrical parameters of the coils and the loads were: inductance $L(10\text{ KHz}) = 1.2\ \mu\text{H}$ and serial resistance $R(10\text{ KHz}) = 87\text{ m}\Omega$.

Figure 13.16 shows typical waveforms of the output current pulses delivered by all three pulse-generating coils to the seed coil of an FCG. All three coils delivered high amplitude current pulses to the load. It follows

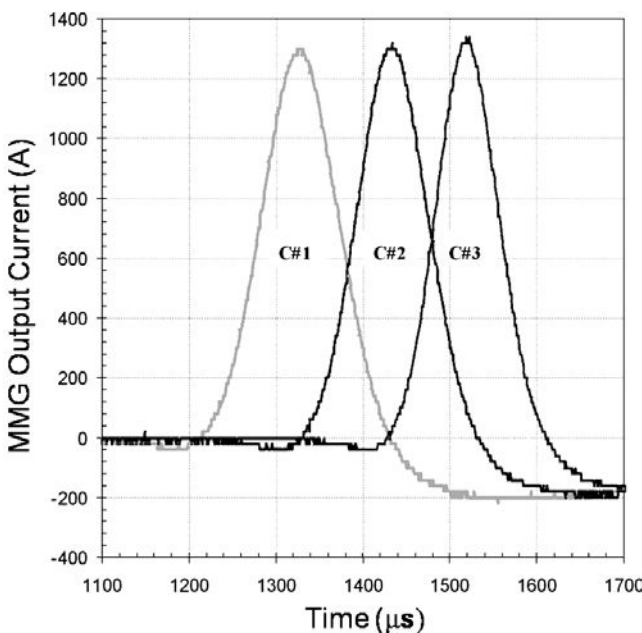


Fig. 13.16 Typical waveforms of the current pulses produced by three pulse-generating coils placed on the barrel of an explosive-driven MMG and separated by a distance of 1 mm [37].

from these experimental results that it is fundamentally possible to generate a series of high-current pulses with compact explosive-driven multi-coil MMGs.

The amplitude and the FWHM of the positive current pulse produced by each coil were $I_{\text{Coil}\#1}(t) = 1260 \text{ A}$ and $\text{FWHM} = 119 \mu\text{s}$, $I_{\text{Coil}\#2}(t) = 1300 \text{ A}$ and $\text{FWHM} = 91 \mu\text{s}$ and $I_{\text{Coil}\#3}(t) = 1340 \text{ A}$ and $\text{FWHM} = 83 \mu\text{s}$, respectively. The amplitude of the current pulse produced by each succeeding coil is higher than that of the previous coil. This increase in the amplitude of the current pulses was caused by the acceleration of the ferromagnetic projectile as it moved through the coils due to the action of the high-pressure explosive gases. The measured velocity of the ferromagnetic projectile in Coil #1 was $V_1 = 199 \text{ m/s}$, in Coil #2 was $V_2 = 245 \text{ m/s}$ and in Coil #3 was $V_3 = 288 \text{ m/s}$. The energy in the high-pressure explosive gases was much higher than the energy losses of the ferromagnetic element due to pulsed power generation. Based on these results, it can be concluded that placing more pulse-generating coils along the acceleration barrel of

the explosive-driven MMG leads to an increase in the total output energy from the system unless the energy of the explosive gases is reduced due to decreases in their pressure and/or the ferromagnetic projectile decelerates due to energy losses.

The amplitudes of the negative current pulses produced by all three coils (Fig. 13.16) were significantly lower than those of the positive pulses. The rise times of the negative pulses were much longer than those of the positive pulses. This is probably the result of the interference of the magnetic field of the ferromagnetic projectile with the magnetic fields induced by the pulse-generating coils.

The amplitude of the current pulses produced by an explosive-driven MMG versus the velocity of its ferromagnetic projectile is shown in Fig. 13.17 [38]. It follows from these experimental results that the amplitude of the current pulse is proportional to the velocity of the ferromagnetic element. The highest current pulse amplitude was $I_{\max} = 1400 \text{ A}$ and was reached when the velocity of the ferromagnetic projectile was $V = 319 \text{ m/s}$.

There is a significant non-linear dependence of the current pulse amplitude on the velocity of the ferromagnetic projectile (Fig. 13.17). Increasing the velocity of the ferromagnet projectile from $V = 25 \text{ m/s}$ to $V = 100 \text{ m/s}$ increases the amplitude of output current pulse by almost seven times. Based on these results, it can be concluded that in order to produce

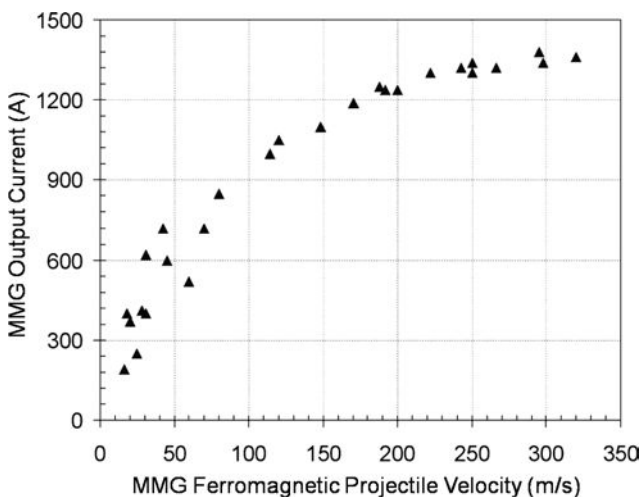


Fig. 13.17 Amplitude of the current pulses produced by explosive-driven MMGs versus the velocity of its ferromagnetic projectile [38].

high-amplitude current pulses, it is necessary to accelerate the ferromagnetic projectile to velocities greater than 200 m/s.

The output current, voltage and power waveforms produced by an explosive-driven MMG in which the velocity of the ferromagnetic projectile was $V = 319$ m/s are presented in Fig. 13.18. The amplitude of the positive current pulse was $I_{\max}(1010 \mu\text{s}) = 1400$ A and its FWHM was $72 \mu\text{s}$. The amplitude of the positive voltage pulse was $U_{\max \text{ pos}}(t = 986 \mu\text{s}) = 2.97$ V and its FWHM was $63 \mu\text{s}$. The amplitude of the negative voltage pulse was significantly lower than that of the positive pulse — i.e. $U_{\max \text{ neg}}(1050 \mu\text{s}) = -1.27$ V and its FWHM was $71 \mu\text{s}$. The amplitude of the positive power pulse was $P_{\max \text{ pos}}(995 \mu\text{s}) = 3200$ W and its FWHM was $49 \mu\text{s}$. The amplitude of the negative power pulse was more than two times lower than that of the positive pulse — i.e. $P_{\max \text{ neg}}(1040 \mu\text{s}) = 1140$ W — and its FWHM was $49 \mu\text{s}$.

Figure 13.19 shows the amplitude of the positive power pulse delivered by an MMG to a load versus the velocity of its ferromagnetic projectile [38].

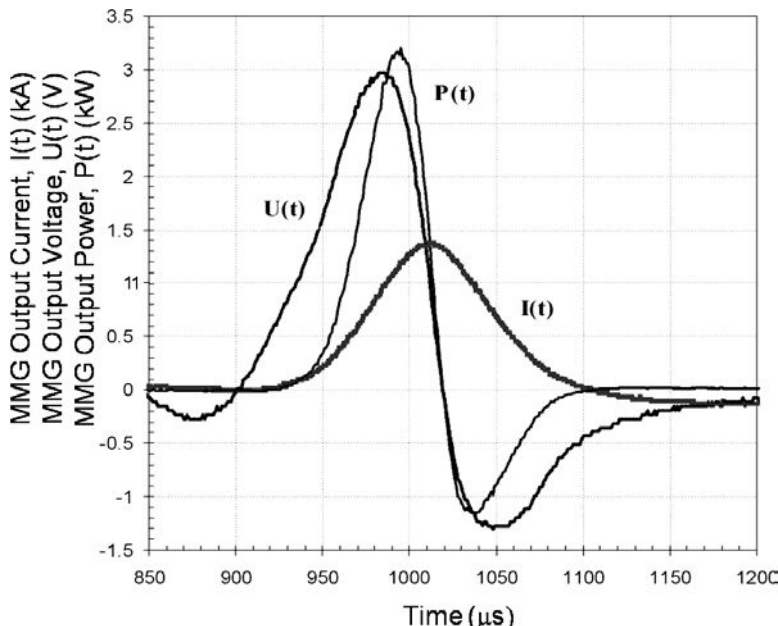


Fig. 13.18 Waveforms of the current, voltage and power pulses produced by an explosive-driven MMG. The velocity of the Nd₂Fe₁₄B ferromagnetic projectile was $V = 319$ m/s [38].

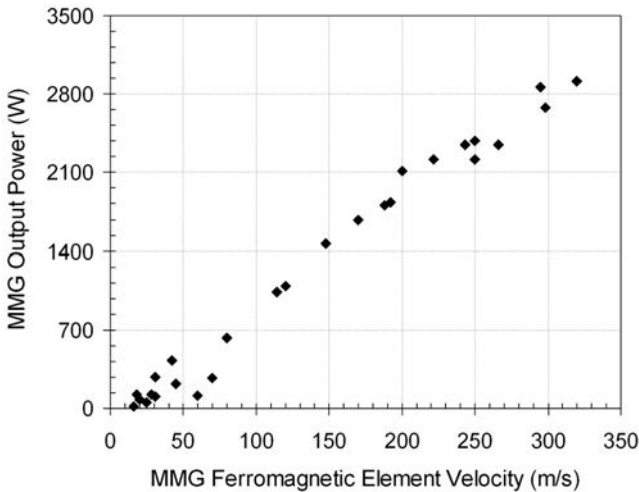


Fig. 13.19 Amplitude of the positive power pulse delivered to a load by an explosive driven MMG versus the velocity of its ferromagnetic projectile [38].

It follows from this data that the power delivered to the load is directly proportional to the velocity of the ferromagnetic projectile.

13.5 High-Voltage Explosive-Driven MMGs

Detailed studies of the operation of high-voltage MMGs were conducted by Shkuratov *et al.* [27–29, 37, 38]. It was experimentally demonstrated that explosive-driven MMGs are capable of producing voltage pulses with amplitudes up to 50 kV [28, 37].

A new type of multi-stage high voltage MMG was developed by Shkuratov *et al.* [27–29, 37, 38]. In this system, each stage multiplies the voltage and power produced by the previous stage in turn. The output voltage produced by the pulse-generating system of the MMG is proportional to the number of stages and to the voltage generated in each stage. In this system, there are no inter-stage switches or other components that are necessary in Marx and other types of conventional pulsed power generator.

One of the advantages of the explosive-driven MMG (Fig. 13.10) is the possibility of increasing the number of high-power pulses generated by a single-shot device by simply serially extending the pulse generating system. This does not require an increase in the dimensions and mass of the ferromagnetic projectile and/or in the amount of explosives used. It is not

possible with other types of explosive-pulsed power systems, i.e. shock wave ferromagnetic generators, shock wave ferroelectric generators and magnetic flux compression generators. Extending the pulse-generating systems in FMGs, FEGs and FCGs leads to an increase in both the dimensions and mass of the ferromagnetic and ferroelectric elements in the FMG and the FEG, respectively, and the dimensions of the stator and the armature in the FCG, as well as a corresponding increase in the amount of explosives used in all these systems.

Operation of the MMG is based on the conversion of the magneto-static energy and kinetic energy of ferromagnetic projectiles into pulses of electromagnetic energy. The kinetic energy of an Nd₂Fe₁₄B ferromagnetic projectile with dimensions of $D_{\text{ferro}} = 25.4$ mm and $h_{\text{ferro}} = 19.0$ mm, mass of $m_{\text{ferro}} = 90$ g and moving at a velocity of $V = 300$ m/s is:

$$W_{\text{kinetic}} = \frac{m_{\text{ferro}} \cdot V^2}{2} = 4.50 \text{ kJ.} \quad (13.7)$$

It follows from the experimental results obtained by Shkuratov *et al.* [35, 37, 38] that the energy induced in the pulse-generating module of a MMG by a Nd₂Fe₁₄B projectile moving at a velocity of $V = 300$ m/s does not exceed $W_{\text{Pulsed Power}} = 2$ J, which is less than 0.1% of the kinetic energy of the ferromagnet projectile Eq. (13.7). Serial extension of the pulse generating system of the MMG from one to a few tens of pulse-generating modules increases the output energy in direct proportion to the number of modules [35, 37, 38]. Moreover, the extension of the pulse-generating system can provide an increase in the operating velocity of the ferromagnetic projectile in multi-module MMGs using the same amount of explosive charge because they possess longer acceleration paths in comparison with single-module systems.

One more advantage of explosive-driven MMGs is that it is possible to design two different devices: completely expendable single-shot systems and multi-shot systems with an expandable cartridge containing a propellant charge and ferromagnetic element. This is not possible for FMGs, FEGs and FCGs because they are strictly expendable single-shot systems. Multi-shot MMGs can be designed with more complicated (and correspondingly more expensive) power conditioning stages because of their longer operational life.

13.5.1 High-Voltage Generation

The basis for the production of high voltage at the output terminals of MMGs is Faraday's law, which is related to the change in the magnetic

flux in the pulse-generating coil of an MMG due to the rectilinear motion of a ferromagnetic projectile through the coil. For a multi-turn coil, the electromotive force generated is the sum of the EMFs produced by each of the turns

$$EMF_{m\text{-turns}}(t) = \sum_N \left[-\frac{d\Phi_n(t)}{dt} \right], \quad (13.8)$$

where dt is the time it takes for the magnetic flux in a turn to change, $d\Phi_n(t)$ is the magnetic flux captured by the n th turn and N is the number of turns in the coils.

A schematic diagram of the explosive-driven MMG used in high-voltage experiments is shown in Fig. 13.10. The Nd₂Fe₁₄B projectiles used in the experiments had dimensions of $D = 25.4$ mm and $h = 19.0$ mm and were magnetised along their axis. The multi-turn pulse generating coils of the MMG were prepared with heavy-build magnet wire of different gauges. The length of each coil was $h_{\text{coil}} = 19.0$ mm.

A typical waveform of the high-voltage pulse produced by an MMG equipped with a 7721-turn pulse generating coil is shown in Fig. 13.20. The coil was wound with AWG 36 magnet wire with a diameter of $d = 0.16$ mm. The outer diameter of the coil was $OD_{\text{coil}} = 51.7$ mm. The inductance and resistance of the coil were $L_c(10\text{ KHz}) = 1.27\text{ H}$ and $R_c(10\text{ KHz}) = 1697\text{ }\Omega$, respectively. The velocity of the ferromagnetic projectile was $V = 292\text{ m/s}$. The peak-to-peak amplitude of the output voltage pulse was $U(t)_{\text{max}} = 50.3\text{ kV}$. The specific peak-to-peak voltage in this experiment was $U_{\text{spec}} = 6.5\text{ V/turn}$.

The amplitude of the voltage pulse produced by an explosive-driven MMG equipped with a 7721-turn pulse generating coil versus the velocity of the ferromagnetic projectile [37, 38] is shown in Fig. 13.21. It follows from these experimental results that the amplitude of the output voltage pulse is directly proportional to the velocity of the ferromagnetic projectile. The amplitude of the output voltage pulse varied from $U(t)_{\text{max}} = 28.6\text{ kV}$ for a projectile moving at a velocity of $V = 147\text{ m/s}$ to $U(t) = 50.3\text{ kV}$ for a projectile moving at a velocity of $V = 292\text{ m/s}$.

13.5.2 Multi-Stage High-Voltage MMGs

Marx generators and Tesla transformers are widely used in conventional pulsed power systems for producing high-voltage pulses with amplitudes

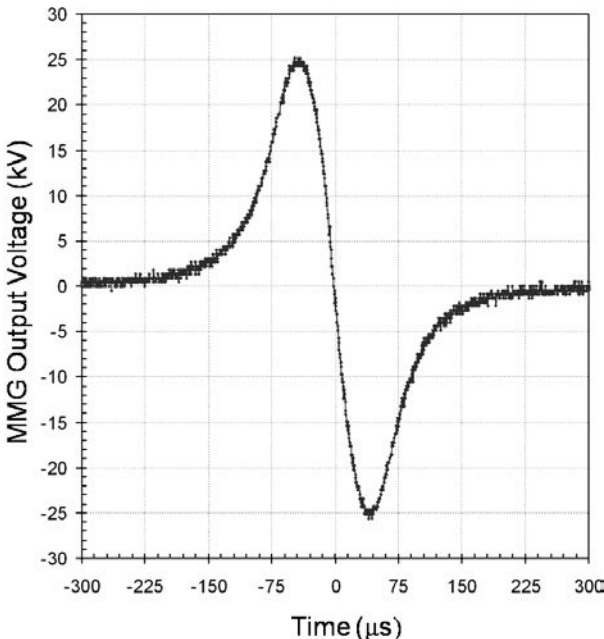


Fig. 13.20 A typical waveform of the voltage pulse produced by an explosive-driven MMG equipped with a 7721-turn pulse-generating coil. The velocity of the ferromagnetic projectile was $V = 292$ m/s [37].

ranging up to several hundreds of kilovolts [18]. The Marx generator contains a number of stages, where each stage consists of a capacitor bank and a high-voltage switch and where the stages are charged in parallel, and a high-voltage DC power supply. During discharge, all the high voltage switches close at the same time and the configuration of the capacitor banks changes from parallel to series connection. Thus, the Marx generator multiplies the voltage.

A Tesla transformer contains less components than the Marx generator. It contains two inductively coupled oscillatory circuits and a high-voltage switch. The Tesla transformer requires a high-current power supply to power the primary winding. The voltage multiplication coefficient of Tesla transformers can reach thousands.

A new type of multi-stage high-voltage pulsed power system based on MMGs was developed by Shkuratov *et al.* [27–29, 37, 38]. Operation of this system is completely different from that of the Marx generator and the Tesla transformer.

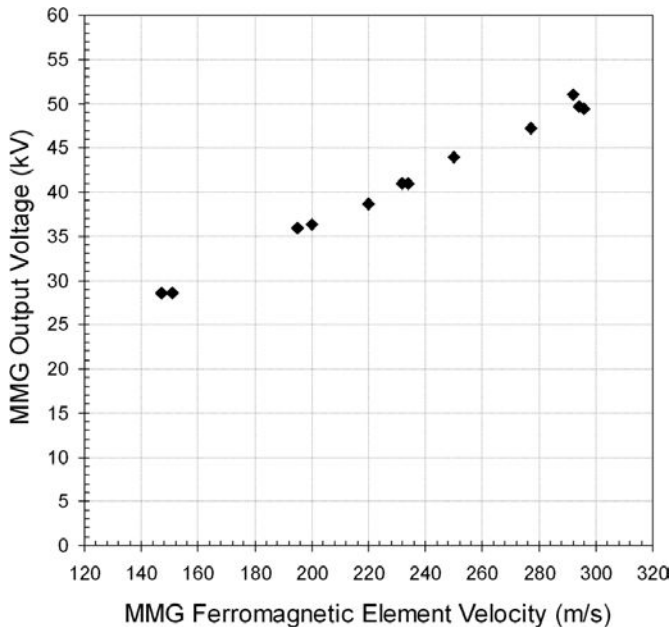


Fig. 13.21 Amplitude of the peak-to-peak voltage pulse produced by an explosive-driven MMG equipped with a 7721-turn pulse-generating coil versus the velocity of the ferromagnetic projectile [37, 38].

A schematic diagram of this system is shown in Fig. 13.22. The system contains a series of pulse-generating modules. Each module consists of multi-turn pulse-generating coils, a capacitor bank and a high-voltage rectifier, which is used to ensure that both polarities of the high-voltage pulses produced by the MMG pulse generating coil are used. The output of each module is connected to the input of the next module in line.

Operation of the multi-stage system shown in Fig. 13.22 is as follows. When the ferromagnetic projectile approaches the first pulse-generating module, an EMF pulse is induced in the coil. This EMF pulse charges the capacitor bank as the ferromagnet projectile moves through the coil. The input terminal of the first pulse-generating module is grounded. The output terminal of the first module is connected to the input terminal of the next module.

When the ferromagnetic projectile moves through the first pulse generating coil, the capacitor bank of the first module is charged to a high-voltage $U_{\text{mod}1}$ by the EMF pulse produced in the first coil. The output voltage of

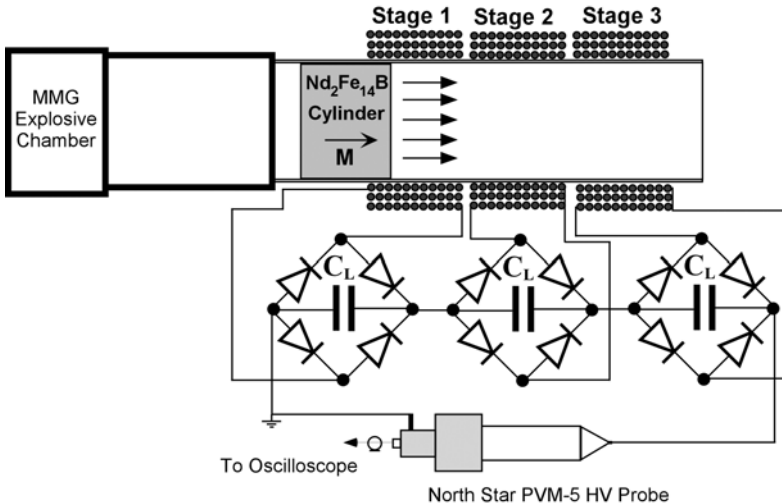


Fig. 13.22 Schematic diagram of a multi-stage high-voltage pulsed power system [28, 37].

the first module is $U_{\text{Out mod } 1} = U_{\text{mod } 1}$. The input to the second module is connected to the output of the first module (Fig. 13.22). During the motion of ferromagnet through the first coil, the electric potential of the second module equals the output potential of the first module, $U_{\text{mod } 1}$.

When the ferromagnetic element enters the second pulse-generating coil, the capacitor bank of the second module is charged by the EMF pulse produced in the second coil to the voltage $U_{\text{mod } 2}$. The output voltage produced at the output terminal of the second module is equal to the output voltage produced by the first module plus the output voltage produced by the second module, $U_{\text{Out mod } 2} = U_{\text{mod } 1} + U_{\text{mod } 2}$. The output voltage produced by a multi-stage MMG containing N modules is:

$$U_{\text{Out mod } N} = \sum_{n=1}^N U_{\text{mod } n}, \quad (13.9)$$

where $U_{\text{mod } n}$ is the output voltage produced by the n th module of the multi-stage MMG system and N is the total number of stages.

The initial electric potential in the third module is equal to the sum of electric potentials produced by the first and second modules. As a result of the motion of the ferromagnetic projectile through the third stage of the system, a high-voltage pulse appears at its output terminals. This voltage is the sum of the voltages across the previous three modules. Addition of

more modules to the pulse generating system of the MMG provides further multiplication of the voltage produced by the system.

There are no high-voltage switches between the stages (Fig. 13.22), like there are in Marx generators. The capacitors are connected in series with no switches between them. There is no primary winding in the system (Fig. 13.22) that requires a high-current power supply, like in Tesla transformers.

The key element of this multi-stage system is the high-energy ferromagnetic projectile that moves with high velocity through the pulse generating modules. The operation of this system is based on the conversion of the magnetostatic energy and the kinetic energy of the ferromagnet projectiles into pulsed power.

Figure 13.23 shows a typical waveform of the voltage pulse produced by a three-stage MMG pulsed power system [37]. Each of the three MMG modules contained a 3424-turn pulse generating coil and a capacitor bank with a capacitance of $C = 2 \text{ nF}$. The velocity of the ferromagnetic projectile, which was measured at the beginning of the first module, was $V = 202 \text{ m/s}$.

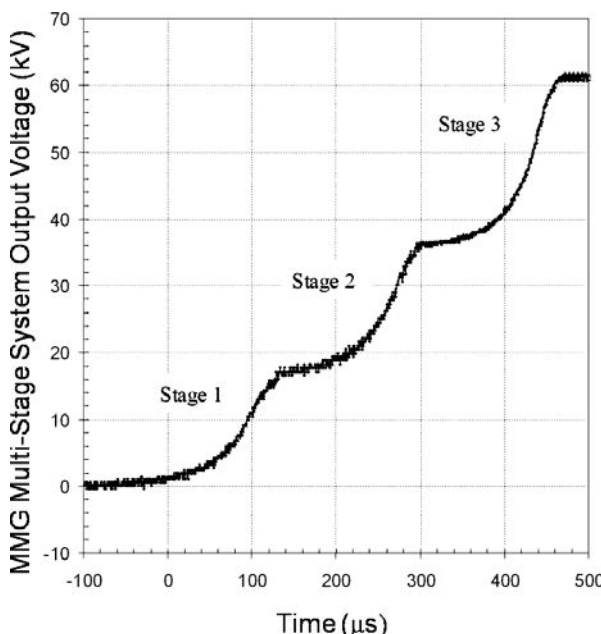


Fig. 13.23 A typical waveform of the high-voltage pulse produced by an explosive-driven multi-stage MMG [37].

The first stage produced a voltage pulse with an amplitude of $U_{\text{stage}1} = 16.7 \text{ kV}$. The second stage produced a voltage pulse with an amplitude of $U_{\text{stage}2} = 19.7 \text{ kV}$. The third stage produced a voltage pulse with an amplitude of $U_{\text{stage}3} = 25.3 \text{ kV}$. Apparently, the increase in the voltage amplitude produced by the individual stages is due to the acceleration of the ferromagnetic projectile to higher velocities during its motion through the barrel of the MMG. The output voltage produced by the system as a whole was the sum of voltages produced by the individual stages — i.e. $U_{\text{Output}} = 61.7 \text{ kV}$. The energy stored in the capacitor banks of this multi-stage system (Fig. 13.23) was

$$W = \frac{C_L}{N_{\text{stage}}} \cdot \frac{U_{\text{Output}}^2}{2} = 1.27 \text{ J}, \quad (13.10)$$

where C_L is the capacitance of each stage and N_{stage} is the number of stages in the system.

It follows from the results of investigations conducted by Shkuratov *et al.* [27–29, 37] that the energy produced by the multi-stage system shown in Fig. 13.22 is directly proportional to the velocity of the ferromagnetic projectile. Another factor that determines the output energy produced by this system is the number of turns in the pulse-generating coils. Increasing the number of turns in the coils results in higher flux linkage and higher output energy, when produced by a system using the same ferromagnetic projectile. At the same time, increasing the number of turns results in higher inductance and resistance in the coils and higher flux losses due to the larger diameter of the coils. As was shown in Ref. 37, there is an optimum number of turns for each configuration of these multi-stage systems that provides the maximum energy output.

A compact ten-stage system with a total length of 200 mm and a diameter of 50 mm (Fig. 13.22) is capable of producing voltage pulses with amplitudes ranging up to 250 kV and output energies ranging up to 10 J. One of the advantages of these systems is that the ferromagnetic projectile does not have direct electrical connection to any part of the system. The electric potential of the ferromagnetic projectile is floating. When the ferromagnetic projectile approaches the last modules of this multi-stage system, which can hold off hundreds of kilovolts, there is no risk of electric breakdown through the relatively thin wall of the plastic acceleration barrel between the high-voltage module and the ferromagnet because of the ferroelectric projectile's floating electric potential.

13.6 Summary

After years of intense research by one of the authors of this book (SIS), a new type of explosive pulsed power system — i.e. the MMG, was developed, built and tested. Based on this research, many new results not previously published have been included in this chapter and are summarised below:

- The experimental basis for and the operational principles of Moving Magnet Generators have been developed [27, 28]. These systems convert the magnetostatic high energy of hard ferromagnets and the chemical energy of explosive materials, which is converted into the kinetic energy of the ferromagnetic projectiles, into electrical energy. The first pulsed power generators based on the rectilinear motion of high-energy hard ferromagnetic projectiles have been designed, constructed and experimentally investigated.
- It has been experimentally demonstrated that it is possible to produce a series of electrical pulses with compact explosively-driven open and closed magnetic circuit MMGs [27–38].
- It has been shown that it is possible to increase the number of high-power pulses produced by single-shot MMGs by serially extending the pulse generating system with no increase in the dimensions and mass of the ferromagnetic projectile and with no increase in the mass of the explosive charge [32–38]. This is not possible with the other types of explosive pulsed power systems described in this book. Extending the pulse generating system of FMGs, FEGs and FCGs leads to an increase in the dimensions of the ferromagnetic and ferroelectric elements in the FMGs and FEGs, respectively, and in the dimensions of the stators and the armatures in the FCGs. There will also be a corresponding increase in the amount of explosive charge used.
- It was experimentally demonstrated that compact, explosive-driven high-current MMGs using Nd₂Fe₁₄B ferromagnetic projectiles are capable of producing a series of current pulses with amplitudes exceeding 6 kA and output energies of 1.5 J [29–38].
- It was determined that in order for MMGs to effectively produce high-current pulses, the velocity of the ferromagnetic projectiles has to be greater than 150 m/s [30–38].
- It was experimentally demonstrated that compact high-voltage MMGs are capable of producing a series of voltage pulses with amplitudes exceeding 50 kV [27–29, 33, 35–38].

- It follows from experimental studies that the amplitude of the voltage pulses produced by a single-module MMG is directly proportional to the velocity of the ferromagnetic projectile and to the number of turns in the pulse generating coil [27–29, 35–38].
- A new type of high-voltage multi-stage MMG was developed [27–29, 37, 38]. This system contains a series of pulse generating stages (modules). Each stage multiplies the voltage and power produced by the previous stage.
- In multi-stage MMGs, there is no need for inter-stage high-voltage switches or other components, which are necessary in Marx generators or other similar types of conventional pulsed power generators, and there is no need for high-current power supplies as required by Tesla transformers.
- It was experimentally demonstrated that the output voltage produced by multi-stage MMGs is proportional to the number of stages and to the voltage generated in each stage [27–29, 37, 38]. Compact, explosive-driven multi-stage MMGs are capable of producing voltage pulses with amplitudes exceeding 250 kV.
- Two types of pulsed power MMG were designed, constructed and investigated. The first type is an expendable single-shot system and the second is a multi-shot generator with the only expandable part being a cartridge containing the propellant charge and the ferromagnetic projectile [32, 33, 35, 37, 38]. Because of the long service life of multi-shot MMGs, it can be considered not only to be a new type of explosive-driven pulsed power system, but also as a new class of conventional autonomous compact pulsed power system.

Bibliography

- [1] E. L. Zalinski, Magneto-Electric Fuse, U.S. Patent 384,662, Granted June (1888).
- [2] J. W. Graydon, Electrical Fuse for Ordnance-Shells, U.S. Patent 399,879, March (1889).
- [3] H. Ruhleman, Electric Fuse for Projectiles, U.S. Patent 1,711,693, May (1929).
- [4] W. Summerbell, Percussion Fuse, U.S. Patent 1,774,043, August (1930).
- [5] H. Ruhleman, Electric Fuse for Projectiles, U.S. Patent 1,858,969, May (1932).
- [6] C. B. Gardner, Projectile-Actuated Surge Generator, U.S. Patent 2,544,077, March (1951).
- [7] J. D. Jordan, Fuze, U.S. Patent 2,655,867, October (1953).
- [8] H. J. Plumley and R. O. Wynn, Fuze for a Bomb, U.S. Patent 2,719,486, October (1955).

- [9] F. E. McGee, Point Detonating Fuse, U.S. Patent 2,703,530, March (1955).
- [10] H. J. Plumley, Magnetic Inertia Controlled Fuze, U.S. Patent 2,775,941, January (1957).
- [11] W. J. Kroeger and G. E. Hirt, Combined Electromagnetic Fuze and Electronic Detonator, U.S. Patent 2,800,081, July (1957).
- [12] P. W. Griffin, Mechanically Activated Source of Electrical Energy, U.S. Patent 2,813,988, November (1957).
- [13] R. O. Wynn and G. F. Hyde, Fuze for Special Shaped Charge Bomb, U.S. Patent 2,911,914, November (1959).
- [14] D. Schermer and F. W. Petit, Magnetomotive Generator Fuze, U.S. Patent 3,034,437, May (1962).
- [15] W. G. Blodgett, F. M. Cummings and W. H. Fleming, Force Responsive Electrical Impulse Generator, U.S. Patent 3,116,428, December (1963).
- [16] W. Giulio, Projectiles Fitted with an Electric Generator of the Inertia Type, U.S. Patent 3,120,187 (1964).
- [17] S. D. Weisman and G. Drucker, Firearm Activated Generator, U.S. Patent 3,257,905, June (1966).
- [18] J. J. Allport, Electrical Power Generator, U.S. Patent 3,337,760, August (1967).
- [19] J. J. Furlani, Fuze Arming System, U.S. Patent 3,417,700 (1968).
- [20] C. O. Leiber and G. Heimke, Magnetic-Electric Switch Element, U.S. Patent 3,569,876, March (1971).
- [21] B. E. Stauder and W. O. Christianson, Explosive Pulsed Generator, U.S. Patent 3,636,390, January (1972).
- [22] J. J. Furlani, H. J. Davis and P. Ingersoll, Electronic Device Applicable to Ordnance Safety and Arming Systems, U.S. Patent 3,653,324, April (1972).
- [23] P. Karayannis and K. Munzel, Apparatus for Generating an Electrical Ignition Current in a Fuze of a Projectile, U.S. Patent 4,080,869, March (1978).
- [24] R. L. Schlischer, Repeatable Explosive-Driven Pulse Generator System and Method, U.S. Patent 4,594,521, June (1986).
- [25] C. C. DeLerno, Electric Current Generation Apparatus, U.S. Patent 5,650,681, July (1997).
- [26] W. M. Schmidt, J. A. Hewlett, P. W. McGregor, E. S. Walker and D. R. Helton, High Precision Fuze for a Munition, U.S. Patent 6,727,995 B1, August (2001).
- [27] S. I. Shkuratov, M. Kristiansen, J. C. Dickens, L. L. Hatfield and R. Martin, Pulsed power Generation Using Ferromagnetic Circuits, *12th IEEE International Pulsed Power Conference, Digest of Technical Papers*, Vol. II (1999) pp. 716–719.
- [28] S. I. Shkuratov, M. Kristiansen, J. C. Dickens, L. L. Hatfield and R. Martin, Pulsed Power Generation Using Open and Closed Ferromagnetic Circuits, *IEEE Transactions on Plasma Science*, **28**(5), (2000) 1347–1352.
- [29] S. I. Shkuratov, Progress Report for the New World Vistas Project (2000). Unpublished.
- [30] S. I. Shkuratov, M. Kristiansen, J. C. Dickens and J. C. Hernandez, The current mode of pulsed power generation in moving magnet systems, *13th*

- International Pulsed Power Conference, Las Vegas, Digest of Technical Papers*, IEEE Catalog Number: 01CH37251, ISBN: 0-7803-7120-8, Vol. II (2001) pp. 967–970.
- [31] S. I. Shkuratov, M. Kristiansen, J. C. Dickens, J. C. Hernandez, The charging and integrating modes of pulsed power generation in moving magnet systems, *Abstracts of the 13th International Pulsed Power Conference, Las Vegas, USA*, ISBN: 0-7803-7141-0 (2001) p. 624.
 - [32] S. I. Shkuratov, M. Kristiansen, J. C. Dickens, Explosive-Driven Moving Magnet Generators, *13th International Pulsed Power Conference, Las Vegas, Digest of Technical Papers, IEEE Catalog Number: 01CH37251*, ISBN: 0-7803-7120-8, Vol. II (2001) pp. 963–966.
 - [33] S. I. Shkuratov, Progress Report for the New World Vistas Project (2001). Unpublished.
 - [34] S. I. Shkuratov, E. F. Talantsev, J. C. Dickens, M. Kristiansen and J. C. Hernandez, The Current Mode of Pulsed Power Generation in a Moving Magnet System, *IEEE Transactions on Plasma Science*, **30**(5) (2002) 1674–1680.
 - [35] S. I. Shkuratov, Progress Report for the New World Vistas Project (2002). Unpublished.
 - [36] S. I. Shkuratov, E. F. Talantsev, J. C. Dickens and M. Kristiansen, A New Type of Two-Stage Autonomous Pulsed Power System Using a Moving Magnet Generator as a Source of Primary Power, in V. D. Selemir and L. N. Plyashkevich, *Proceedings of Ninth International Conference on Megagauss Magnetic Field Generation and Related Topics* (Megagauss-9), Moscow-St. Petersburg, Russia, July 7–14, 2002, Sarov, VNIEF 2004, 5-9515-0036-2, pp. 274–278.
 - [37] S. I. Shkuratov, E. F. Talantsev, J. Baird, L. L. Altgilbers, Explosively Driven Moving Magnet Pulsed Power Generator, *Review of Scientific Instruments*. Will be submitted for publication (2009).
 - [38] S. I. Shkuratov, E. F. Talantsev, J. Baird, L. L. Altgilbers, Generation of Primary Pulsed Power Utilizing Rectilinear Motion of Hard Ferromagnets, *Journal of Applied Physics*. Will be submitted for publication (2009).
 - [39] Ansoft Corporation, Four Station Sq., Suite 660, Pittsburgh, PA 15219, U.S.A.; www.ansoft.com.
 - [40] R. M. Bozorth, *Ferromagnetism*, Piscataway, NJ: IEEE (1993).
 - [41] P. Campbell, *Permanent Magnet Materials and Their Application*, Cambridge, U.K.: Cambridge University Press (1994).
 - [42] S. I. Shkuratov, E. F. Talantsev, J. Baird, L. L. Altgilbers and A. H. Stults, Transformer-Type Seeding System of a Helical FCG Based on a Transverse Shock Wave Ferromagnetic Generator. J. F. Kiutu, R. E. Reinovsky and P. J. Turchi (eds). IEEE Proceedings of the 2006 International Conference on Megagauss Magnetic Field Generation and Related Topics (2007) pp. 313–318.
 - [43] G. A. Mesyats, *Pulsed Power*, Kluwer Academic/Plenum Publishers, New York (2005).

This page intentionally left blank

Chapter 14

Case Studies

14.1 Introduction

In this chapter, four examples of how explosive pulsed power devices have been used will be briefly discussed. The first is a high-voltage generator based on FEGs developed by Diehl BGT Defence GmbH and Company in Germany. Diehl approached the development of this generator in a very systematic way, which is described in detail in [1] and [2]. Second is the results of a study in which FEGs were used to direct-drive antenna. The third is a FCG-driven microwave test bed developed by Texas Tech University. The fourth is Project Birdseed, where Los Alamos National Laboratory and Sandia National Laboratory incorporated two FCGs into a rocket as a power supply for a plasma gun.

14.2 Case Study 1: Piezoelectric High Voltage Generator

Staines *et al.* [1, 2] developed a prototype of a propellant-driven High Voltage Generator (HVG) using PZT-5A ferroelectric elements that had a diameter of 15 mm and a length of 20 mm and a pyrotechnic gas generator that drives a piston. A photograph of the HVG is shown in Fig. 14.1. The diameter of the generator shown in Fig. 14.16 is 65 mm and its length is 275 mm, not including the electrical connector for the gas generator.

A small pyrotechnic gas generator, a modified DM82 cartridge, which has been produced in large quantities by Diehl BGT Defence GmbH and Company for many years, at one end of the generator produces a pressure pulse that increases linearly over a 10 ms period to 200 bars in a small gas volume in front of the piston. During this time, the piston transmits a force



Fig. 14.1 Photograph of a prototype piezoelectric High Voltage Generator (HVG) developed by Diehl BGT Defence GmbH and Company in Germany.

of up to 40 kN to the ferroelectric elements, thus compressing them. The force is contained by a robust fiberglass housing.

The generator can contain either 4 or 6 ferroelectric elements split into two groups or modules. The limitation on the voltage that can be generated by this generator is not the ferroelectric elements, but rather the voltage that can be sustained both inside the generator and across the exterior of its housing without electrical breakdown. The generator can be filled with either oil or SF₆ gas to inhibit breakdown, but outside the breakdown voltage is limited by the atmosphere. When the electric field on the housing reaches 3 MV/m, a discharge can form, which can short-circuit the load. Since the charging current provided by the ferroelectric elements is small, on the order of 1 mA, even a highly resistive path will be sufficient to discharge the load. If the exterior of the source housing is wet or if the air humidity is greater than 60%, the problem will be even more serious. This is especially critical for small sources, where even modest voltages of 100 kV can produce electric fields of more than 1 MV/m.

The simplest technique for pulse charging is to arrange two groups or modules containing multiple ferroelectric elements so that their polarisations are in opposite directions. This means that when pressure is applied, the total voltage across the load will remain at approximately 0 V. A metal connecting rod in the center of the generator between the ferroelectric modules will be charged to two or three times the voltage on each ferroelectric element, depending on the number of elements used. A voltage of at least 200–300 kV should be achievable in this manner.

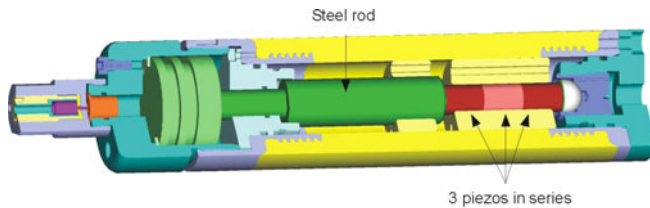


Fig. 14.2 Diehl HVG with three piezoelectric elements in series.

14.2.1 *Three Ferroelectric Element Module Voltage Tests*

In order to demonstrate that higher voltages could be obtained through simple series cascading of ferroelectric elements, a test configuration for a generator with multiple ferroelectric elements, shown in Fig. 14.2, was developed. This configuration represents only half of the system shown in Fig. 14.1. In Fig. 14.1, two groups of three ferroelectric elements in series were used. The polarisation of each group is opposite, so that the total voltage across the generator only appears when the spark gap in the load fires and is zero during the long charging time. This is essential to avoid breakdown along the exterior of the generator. For the tests discussed in this section, it was necessary that the voltage be measured during ferroelectric element compression. Therefore, the generator was placed into a bucket containing transformer oil to prevent breakdown during the measurements. This exterior insulation is only necessary for test purposes. The complete ferroelectric generator was explicitly designed to avoid the requirement for any exterior insulation.

The maximum voltage measured with the three-element module was 240 kV using a modified DM82 gas generator with 310 mg of K525 powder (Fig. 14.3). Note that this was limited by external breakdown in the voltage probe and is not the maximum voltage attainable by this generator. Since the voltage obtained with the three-element module is clearly three times the voltage from a single element, it can be reliably inferred that the maximum voltage that would have been obtained with three elements and 390 mg of K525 powder would have been about 390 kV.

A final point for demonstration was that this generator with three elements could be used to charge a capacitive load. The capacitance of the module with three elements in series should be about 42 pF. A voltage of 390 kV corresponds to a maximum energy of about 3 J. To confirm this, a short length of high-voltage coaxial cable was connected across the output

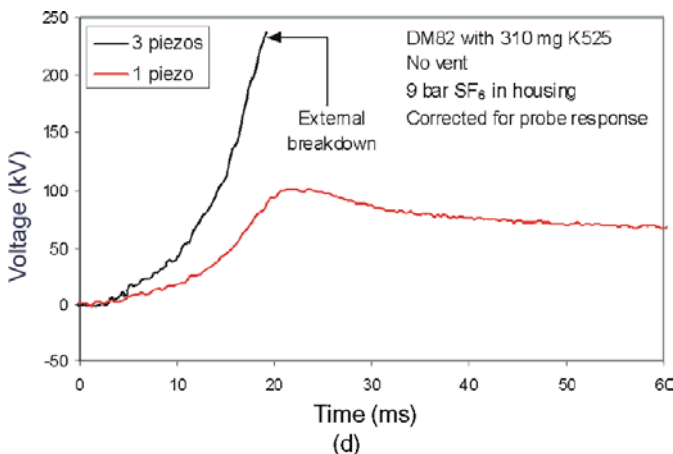


Fig. 14.3 Output voltage from a Diehl HVG with three piezoelectric elements using a K525 powder gas generator.

of the generator. The capacitance of the open-circuit cable was 80 pF. Figure 14.4 shows the voltage measured across the output of the generator with and without the cable (open-circuit or no load) case. The maximum voltage with the capacitive load was about 80 kV. Breakdown occurred close to this value, probably across the end of the coaxial cable; however, it was clear that the maximum voltage was almost attained at this point.

With no load, the measured output voltage was about 200 kV. Ideally, the open-circuit voltage should be about three times the voltage that would be obtained with an 80 pF load. The measured result agrees reasonably well with this prediction, with the voltage across the capacitive load being

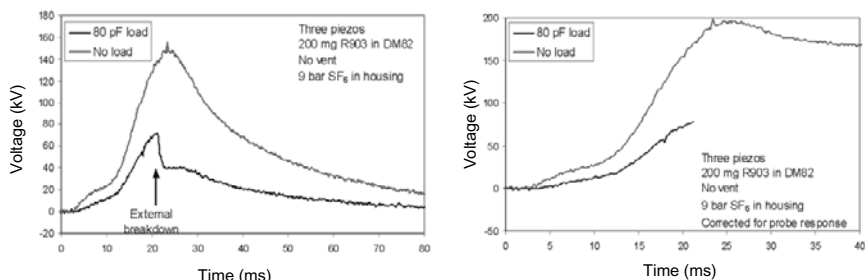


Fig. 14.4 (a) Output voltage and (b) corrected output voltage from a Diehl HVG with three piezoelectric elements and a capacitive load.

slightly higher than the expected value of 66 kV. This discrepancy could be accounted for by variations in the pressure from shot to shot. This test showed that the ferroelectric generator was producing both high voltage and significant amounts of energy, with about 250 mJ stored in the coaxial cable.

14.2.2 *Summary*

The results presented here show that a compact high-voltage generator (HVG) based on ferroelectric compression is feasible and that it can generate voltage and energy outputs consistent with realistic loads. The tests described have shown that simple quasi-static compression of the ferroelectric elements is adequate to charge a low-capacitance load to a voltage of about 400 kV. The charging voltage can be increased by cascading more ferroelectric elements in series. Alternatively, to increase the energy in the generator for a given voltage, more ferroelectric elements could be cascaded in parallel. This effectively increases the capacitance of the generator and the amount of charge generated.

One of the goals of this study was to show that a small fiberglass housing can withstand the large force required for quasi-static ferroelectric compression. Over 50 kN was repeatedly applied to the housing used in the tests. In principle, even larger forces can be considered with such housings, especially if the diameter of the generator increases.

The main limitation on the achievable output voltage from a compact ferroelectric generator will be electrical breakdown inside or outside the generator, rather than a limitation of the ferroelectric materials themselves. For this reason, more complicated schemes, such as shock depolarisation or dynamic compression of the ferroelectric elements, are not warranted. In principle, a voltage as high as 1 MV could be attained in a reasonably compact system and an energy as high as 100 J might be attained by cascading up to 100 ferroelectric elements in series and parallel. To achieve these specifications, the volume of the high-voltage generator would be about 100 mm in diameter and 250 mm long. Even higher energy could be attained in a larger system, but the number of ferroelectric elements may become impractically high. The ferroelectric generator could then be used to charge a high-energy antenna, which, in turn, produces an RF pulse. Alternatively, there may be sufficient energy to drive a microwave source. Such a ferroelectric generator could also be used as a general purpose single-shot charging system for general pulsed-power applications. The advantages

of this type of system are its compact size, direct high-voltage output and virtually unlimited maintenance-free storage time.

14.3 Case Study 2: FEG-Driven Antenna

In 2005, the Naval Research Laboratory [3] conducted a series of tests in which they used an FEG to drive a simple dipole antenna through a simple pulse forming network. They conducted three test shots using the same dipole antenna and pulse forming network and using FEGs with identical or similar physical configurations. A similar receiving dipole antenna was placed approximately 3 m from the transmitting antenna. The received waveforms were recorded along with the voltage pulse (Fig. 14.5) delivered by the FEG to the pulse-forming network.

The FEG contained a $2 \times \frac{1}{2} \times \frac{1}{2}$ EC-64 PZT element. The FEG used 25 g of RDX high explosives. This generator produced peak voltages that were as high as 40 kV into an open-circuit load. The pulse-forming network was constructed by using approximately 280 mm of RG-58 coaxial cable. The cable length may be used to control the frequency spectrum of the output signal. Since the cable was a quarter wavelength impedance matching circuit, the expected radiated frequency was 21.67 MHz.

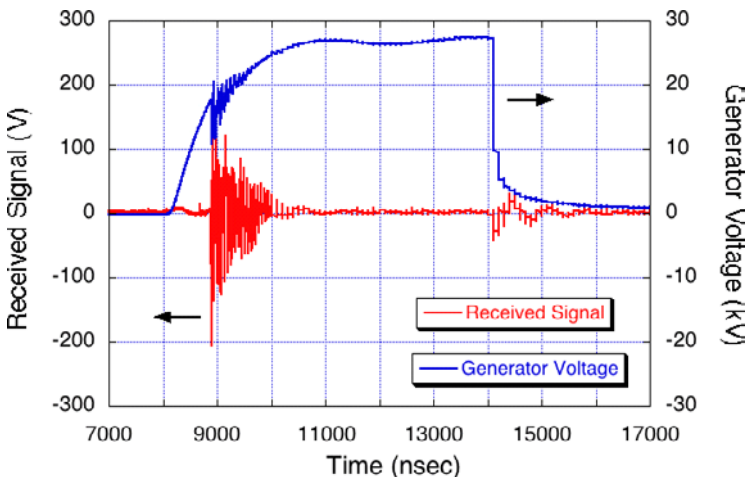


Fig. 14.5 Voltage generated by a FEG and radiated signal produced when this FEG was used to drive a dipole antenna [3]. The signal was detected by a receive antenna at 3 m.

A spark gap was placed between the inner conductor of the coaxial cable and the antenna. The antenna was V-shaped and each leg had a length of 1 m. The resonant frequency of the antenna was estimated to be about 75 MHz. The receiving antenna was similarly constructed.

Each shot produced what appeared to be two RF bursts that coincided with rapid changes in the source voltage. The first RF burst produced a pulse with a peak-to-peak voltage amplitude of -30 V and lasted for $1\text{ }\mu\text{s}$. The second burst produced a pulse with an estimated peak-to-peak voltage amplitude of 50 V that also lasted for $1\text{ }\mu\text{s}$. The true peak voltage of the second burst could not be determined accurately since the second burst saturated the input of the oscilloscope.

Using the peak voltages picked up by the receive antenna, the peak power density at the receive antenna was calculated to be 1.64 W/cm^2 and the Effective Radiated Power (ERP) at the source antenna was calculated to be 2 MW , assuming the receiving antenna had a gain near unity. The FEG generated about 2.4 MW of electrical power.

A Fast Fourier Transform (FFT) (Fig. 14.6) revealed that the spectrum of the RF bursts was concentrated between 18 and 26 MHz, with the largest signal being at 21.4 MHz, which is in good agreement with the predicted value of 21.67 MHz.

Utilising two independent field diagnostic techniques, it was demonstrated in other experiments that an FEG-dipole antenna setup similar to the one described above exhibited similar behavior with a radiated frequency of around 100 MHz [3]. One field probe was an electric field sensor

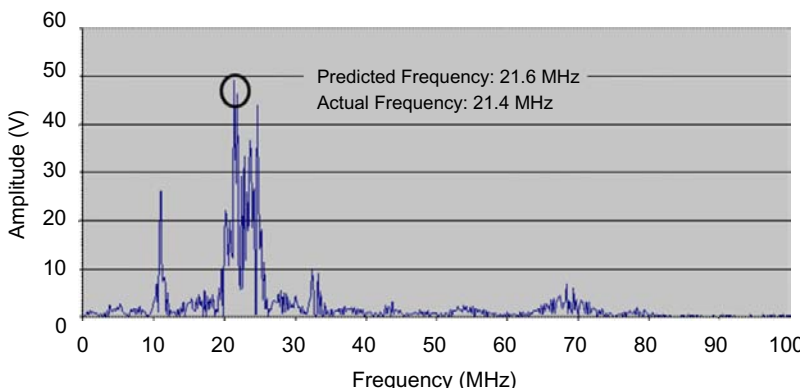


Fig. 14.6 FFT of the signal generated by the FEG driven dipole antenna in Fig. 14.5 [3].

that transmitted the detected signal back to the diagnostics screen room over a fiber optic cable and the other sensor was a D-dot probe matched with a wideband balun. Both probes recorded a maximum peak-to-peak electric field of around 850 V/m at a distance of 5 m, giving a field-range product of about 4.2 kV.

14.4 Case Study 3: FCG-Driven Microwave Test Bed

Texas Tech University has developed a compact, explosive-driven high-power microwave (HPM) test bed. The major design constraints on Texas Tech [3, 5] were that the system had to

- Be completely self-contained — i.e., no external power source.
- Fit into a volume with a diameter no greater than 15 cm and a length no greater than 1.5 m.
- Radiate energy.

The primary objectives of this effort were to

- Develop and optimise the various components of the system.
- Study the issues associated with system integration.
- Train students in the fields of explosive pulsed power, high-voltage engineering and high-power microwaves.

The major components of the test bed are shown in Fig. 14.7. As can be seen, it consists of a prime power or seed source for the flux compression

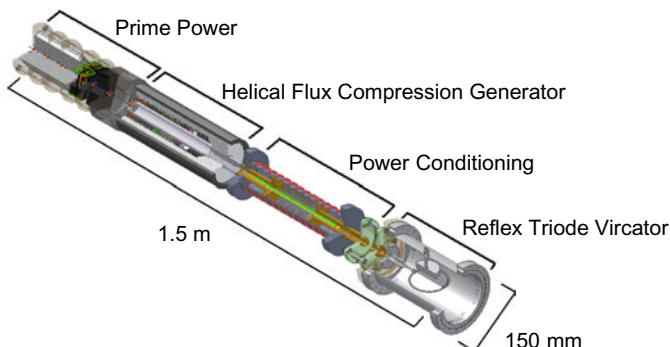


Fig. 14.7 Explosive-driven HPM test bed at Texas Tech University.

generator, helical FCG, power conditioning module, microwave source and antenna. Since the focus of this book is on explosive pulsed power, attention will be primarily focused on the helical FCG and its power conditioning module.

14.4.1 *Fire Set*

Texas Tech developed a fire set for the RP-501 Exploding Bridgewire (EBW) detonators they use in their FCGs. It consisted of a single $1\ \mu\text{F}$ capacitor, high-voltage DC-DC converter, battery and circuit board. A single NPN BJT transistor was used as a closing switch in a common emitter configuration. This fire set was designed for integration into their Compact Seed Source.

14.4.2 *Compact Seed Source*

The *Compact Seed Source* (CSS) (Fig. 14.8) consisted of a 12 V lead-acid battery, charge limiter circuit, solid state high-voltage switching circuit, four step-up DC-DC converters and a single-energy storage capacitor. The seed source had a volume of $0.005\ \text{m}^3$ (diameter less than 6 inches and length of 12 inches) and a weight of 8.6 lb. This source was capable of delivering 360 J and 10 kA to a $6\ \mu\text{H}$ load. The charge time was < 30 seconds. A newly designed switching scheme used off-the-shelf high-voltage semiconductor components that minimised system cost and, more importantly, size [6].

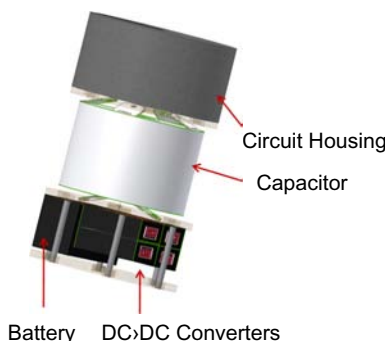


Fig. 14.8 Compact Seed Source (CSS) for FCGs: diameter — 6 inches, height — 12 inches, weight — 8.6 lb, volume — 340 cubic inches and energy density — roughly $100\ \text{mJ/cm}^3$. (Courtesy of Moe Elsayed, Texas Tech University.)

The prime energy source was a rechargeable 12 V lead-acid battery, which is labeled V2 in Fig. 14.9. It was rated at 1.2 amp-hours. Four HV DC-DC converters, which are labeled DC1–DC4 in Fig. 14.39, were utilised to charge a single $50\ \mu\text{F}$ capacitor, which is labeled C1, to the desired voltage. A charge limiter was placed between the battery and DC-to-DC converters to limit the capacitor to a preset voltage. The maximum charge voltage of the capacitor was 5 kV.

To discharge the capacitor into an inductive load, Texas Tech developed a solid state switch (Fig. 14.9). The switch made use of a low-current, high-voltage NPN Bipolar Junction Transistor (BJT) and a high-voltage diode. The BJT-only configuration combined one NPN BJT transistor with a second transistor that used just one P-N junction as the high-voltage diode. However, due to the large switching current (kAs), the BJT, which had a mA rating, operated conventionally for less than roughly 200 ns. After that, the BJT was destroyed. It is believed that after a few hundred nanoseconds, the NPN junctions were destroyed and the internal bond wires connecting the junctions to the external leads were vaporised. This process briefly caused a reduction of the current in the seed circuit, which generated a voltage pulse higher than the initial charging voltage across the collector and emitter junctions. It has been shown experimentally that this high

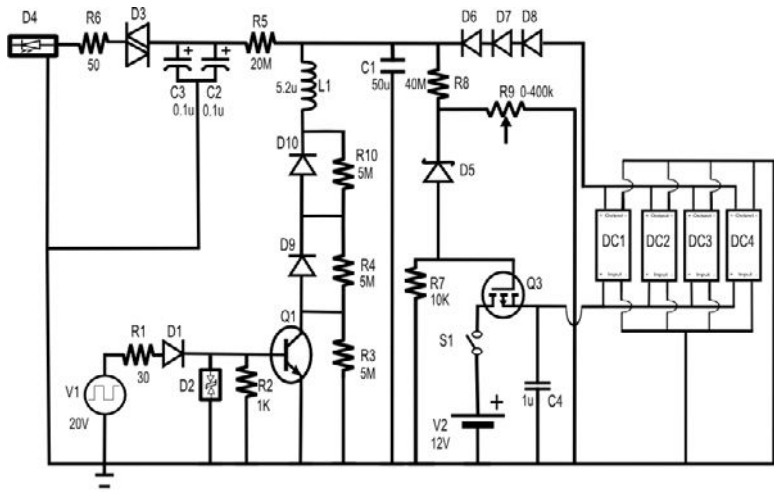


Fig. 14.9 Stand-alone Compact Seed Source circuit diagram. C1 is the energy storage capacitor and L1 is the FCG seed inductance. (Courtesy of Moe Elsayed, Texas Tech University.)

potential leads to the formation of a discharge arc along the external leads that re-establishes a path for the current to flow (similar to a spark gap). It should be noted that the above process limits the BJT to single use, which is acceptable for explosive pulsed power systems.

14.4.3 Helical Flux Compression Generator

14.4.3.1 Helical FCG Overview

The TTU helical FCG (Fig. 14.10) consisted of two stages that used *flux trapping* (also called a *dynamic transformer*) between each stage [7]. The first stage, referred to as the *booster stage*, was coupled to the seed source through the first dynamic transformer. The booster stage was responsible for energy gain. The load for the first stage was the primary in the second dynamic transformer for the second stage, with the coil of the secondary cascade; i.e., the second-stage stator, serving as the secondary of this second transformer. The second stage served as a *peaking stage*; i.e., it served to shorten the length of the current pulse and to increase the output impedance and voltage of the generator.

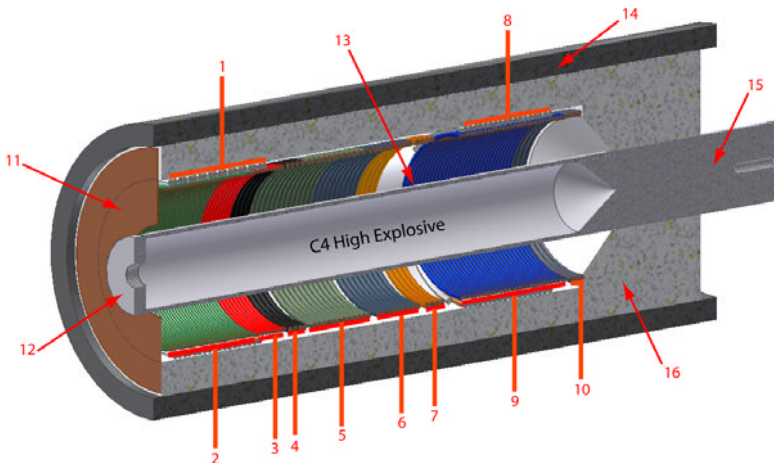


Fig. 14.10 Diagram of the Texas Tech helical FCG: 1 — Booster Stage Seed Coil, 2 — Booster Stage Section 1, 3 — Booster Stage Section 2, 4 — Booster Stage Section 3, 5 — Booster Stage Section 4, 6 — Booster Stage Section 5, 7 — Booster Stage Section 6, 8 — Peaking Stage Seed Coil, 9 — Peaking Stage Section 1, 10 — Peaking Stage Section 2, 11 — Copper Crowbar Disc, 12 — Detonator Centering Cap, 13 — Annealed Aluminum Armature, 14 — PVC Shell, 15 — Aluminum End Plug and 16 — Filler Epoxy. (Courtesy of Thomas Holt and Andrew Young, Texas Tech University.)

The overall diameter of the generator was ~ 150 mm and its total length was ~ 430 mm. The stator and armature had an inner diameter of 76 mm and 38 mm, respectively. Thus, the expansion ratio of the armature was 2:1.

The armature was a seamless annealed aluminum pipe with a wall thickness of 2.135 mm and a length of 305 mm. The explosive charge was Compositions C-4 and it had a weight of 410 g. It was connected to a 38-mm diameter aluminum end plug, which connected the armature to the load and held the armature concentric with the stator in the generator volume.

The stator had a total length of 254 mm. The booster stage had a length of ~ 172 mm and was composed of six different sections. Each section was comprised of wires having different conductor cross-sectional areas and pitches and, with a decreasing number of turns of stranded Teflon insulated, silver-coated copper wire in each succeeding section. The conductor cross-sectional area and pitch were increased for each successive section to compensate for the increasing current density. The wires were also bifurcated (paralleling wires in a section to increase the overall cross-sectional area) in the last three sections, again, to handle the higher current density.

The peaking stage consisted of only two sections. The objective of this stage was to step down the magnitude of the current generated in the booster stage. This had the effect of shortening the length of the current pulse and increasing the output impedance and voltage of the generator.

The primary of the first dynamic transformer was made from magnet wire with a thin coating of polyamide insulation. This insulation was adequate, since the booster stage seed-coil voltages did not reach voltage breakdown levels between turns. This dynamic transformer was an air core unit, which meant it had a significantly lower coupling coefficient than magnetic core transformers. The second-stage seed coil was insulated with PVC jacketing to hold off the high voltages that developed between this seed coil and the second stage before the second stage had crowbarred and that developed during second-stage operation. The windings in the peaking stage were insulated with Teflon.

To switch the booster stage into the circuit and to trap the flux to be compressed, a copper crowbar disk was used. The crowbar was designed so that the generator volume is closed before there is any appreciable loss of flux. Most FCGs have a glide plane for the armature as it expands outward so that contact with the disk is never lost and the current conduction is continuous. Previous research at Texas Tech showed that the crowbar disk performed, at significantly reduced fabrication cost, as well as the glide planes used in medium-size generators [8]. They introduced a radial

cut through one edge to prevent eddy currents. In addition, a thin insulator was placed on the edge of the crowbar disk closest to the armature to prevent premature electrical breakdown between the armature and the crowbar disk. Initially, the crowbar for the peaking stage of their FCG was a Teflon coated pin, but it was removed and crowbarring accomplished by the expansion of the armature onto the windings of this stage.

14.4.3.2 *Fabrication Procedure*

The power conditioning systems for helical FCGs require that their output be well-known and reproducible in order to minimise the power conditioning requirements and to efficiently drive a load [4, 5]. If a reliability, which is quantified in terms of the deviation of the helical FCG energy gain from shot-to-shot, on the order of 10% can be achieved, this would relax the requirements placed on the power conditioning system. This can be accomplished by minimising all physical variations, such as alignment of the armature relative to the stator and maintaining the proper pitch, introduced during manufacturing. Thus, Texas Tech developed new techniques for manufacturing helical FCGs [4, 5]. These techniques included using a collapsible threaded mandrel for manufacturing the stator and an unthreaded centering mandrel to align the armature and stator, and to facilitate helical FCG casting.

Collapsible Mandrel and Stator Construction The collapsible mandrel consists of five independent pieces (Fig. 14.11(a)): one support piece made from Polyvinylidene Fluoride (PVDF), two aluminum key pieces and two aluminum side pieces [4, 5]. The five pieces were held together by two bolts and temperature sensitive adhesive as shown in Fig. 14.11(b). The assembly was then turned down on a lathe to a diameter slightly greater than the desired inner diameter for the stator, as shown in Fig. 14.11(c). Finally, a CNC lathe was used to thread the desired grooves (Fig. 14.11(d)) on the surface of the mandrel at a depth equal to the desired inner diameter of the stator. The groove pitch was controlled by introducing the proper input parameters into the threading routine. Upon completion, the bolts were removed and the adhesive released by heating. A photograph of the completed mandrel held together by two hose clamps is shown in Fig. 14.41(d).

The collapsible mandrel was placed on a lathe or winding machine (Fig. 14.12(a)) to facilitate winding the stator. The stator was divided into sections, where the pitch and wire size changed from section to section.

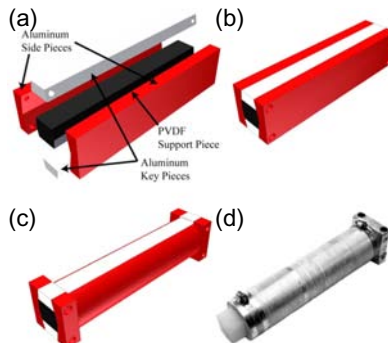


Fig. 14.11 The procedure used to fabricate the collapsible mandrel and its components. (a) An exploded view of the individual pieces of the collapsible mandrel. (b) The assembled mandrel held together with bolts and adhesive. (c) A view of the mandrel after being machined on a lathe. (d) The final collapsible mandrel. (Courtesy of Thomas Holt and Andrew Young, Texas Tech University.)

When the winding of the stator transitions from one section to another, either the wire diameter was increased or the number of parallel conductors was increased (a process called *bifurcation*) to increase the overall diameter of the conductor in that section to account for the increased current density downstream. The transition from one section to another was accomplished by bending the end of the wire (or wires) in a previous section and by bending the beginning of the wire (or wires) in a successive section perpendicular to the mandrel, and soldering and electrically taping them together (see Figs. 14.12(b) and 14.12(c)). The places where the wires from two sections were joined together are called *transition points*. After the stator was wound around the surface of the mandrel and all sections were joined, a thin layer of epoxy was applied to the exposed surface of the stator and mandrel, as shown in Fig. 14.12(d). This epoxy maintained the form of the coil after the mandrel was removed.

The PVDF support piece kept the mandrel from collapsing while the stator was being wound. This material was selected as the support material due to its relative high melting point, which is required when the mandrel is heated to release the adhesive used during fabrication of the mandrel. Since the PVDF was dissimilar from the other materials used to make the mandrel, this facilitated the removal of the support piece after the epoxy cures on the stator. Removal of the support piece permits easy removal of the remaining pieces that make up the mandrel.



Fig. 14.12 Step-by-step illustration of the fabrication of a dual-stage HFCG stator using the collapsible mandrel. (Courtesy of Thomas Holt and Andrew Young, Texas Tech University.)

Seed Coil Construction The seed coils were hand wound around the working coils (stator) of each stage without using any method to control the pitch [4, 5]. The thickness of the epoxy between the seed coil and the stator was thick enough to prevent breakdown through the wire insulation. The seed coil of the first stage was constructed by using both solid-core

polyimide coated magnet wire and AWG 12 Litz wire and the seed coil of the second stage constructed by using stranded core PVC insulated AWG 12-copper wire.

Both seed coils were constructed using the same procedure. First, an epoxy coating was applied around the working coil; i.e., the stator, as shown in Fig. 14.12(d). The thickness of this layer was controlled by using a putty knife to scrape off excess epoxy, as shown in Fig. 14.12(e). This step ensured that the voids between adjacent wires of the coil were filled with degassed epoxy and no air was inadvertently trapped between the seed and working coils when the seed coil was wound in place. The resulting epoxy coating is shown in Figs. 14.12(e) and 14.12(h). Additional layers of epoxy were added as needed over the length of the working coil. The first stage seed coil was wound in place after the layers of epoxy were cured, as shown in Fig. 14.12(f). The pitch of this seed coil was typically wide enough so that air pockets did not form between adjacent wires when more epoxy was applied to hold it in place. Conversely, the pitch of the seed coil of the second stage was such that the adjacent wires had no space between them. The pitch of this coil was simply the wire diameter multiplied by the number of wires in parallel, as shown in Fig. 14.12(j), and could trap air, if wound in the same fashion as it was done in the first stage. Thus, a thin layer of epoxy was applied, as shown in Fig. 14.12(i), and the seed coil was wound in place while the recently applied epoxy was still in a workable state, as shown in Fig. 14.12(j). This ensured that the fluid epoxy filled the voids between adjacent wires in the seed coil. A final coating of epoxy was applied over the two seed coils to complete fabrication of the dual-stage stator (see Fig. 14.12(l)).

Armature Alignment Mandrel After construction of the stator was complete (see Fig. 14.13(a)), it was placed on a centering mandrel [4, 5]. The centering mandrel, shown in Fig. 14.13(a), had an outer diameter equal to the inner diameter of the stator. A center bore with a diameter equal to the outer diameter of the armature was provided to ensure coaxial alignment of the armature with the stator. Excess epoxy was removed from both ends of the armature, as shown in Fig. 14.13(b), to ensure that the stator seated properly on the centering mandrel. The wires that were soldered together at the transition point were trimmed down (see Figs. 14.13(c) and 14.13(e)) to ensure the stator would fit into the PVC shell that it was inserted into. The epoxy was removed from the transition points so that the stator could be checked for continuity and then re-soldered to ensure good



Fig. 14.13 The remaining steps in HFCG fabrication following the completion of the stator. (Courtesy of Thomas Holt and Andrew, Texas Tech University.)

electrical contact. The stator was placed on the centering mandrel, as shown in Fig. 14.13(d). Three parallel coupled 15 kV rated high-voltage wires were then spliced onto the end of the PTFE coated second-stage output wire, as shown in Fig. 14.13(f). Once the continuity of the stator was verified, a coat of release agent was applied to the centering mandrel and the pre-assembled annealed armature inserted to a predetermined depth into the center bore of the centering mandrel. The output wires of the load coil of the first stage were soldered together and then fastened to the end plug of the armature with a loose clamp. A 45° flared transition beginning from the end of the stator, which flared up to the center bore of the centering mandrel, ensured that the filler epoxy aligned the armature with the stator and did not shear off the armature during its expansion. The flared transition also helped

to fix the position of the output wires of the load coil of the first stage (see Fig. 14.13(f)). The stator once again underwent a continuity check.

The PVC outer shell was set in place, along with a refrigeration line that was used to flow SF₆ through the generator volume to help control internal breakdown. The refrigeration line was fitted into a small hole drilled normal to the flared transition region of the centering mandrel and fastened with electrical tape to the outer shell, as shown in Fig. 14.13(g). Second smaller PVC armature shells were also propped in place, as shown in Fig. 14.13(g). The purpose of these shells was to prevent the field enhancements from the knurled surface of the armature from breaking down electrically to the high-voltage output wires of the second stage. With both PVC shells in place, the filler epoxy was mixed and degassed, and then poured into the void between the outer shell and the stator to the level shown in Fig. 14.13(h). After the filler epoxy cured, the centering mandrel was extracted by using a gear puller (pulling on the edges of the mandrel and pressing on the armature). All junctions (such as the output wire of the second stage and the parallel coupled high-voltage wires) were safely encapsulated in a cured filler epoxy.

To prevent damage occurring to the armature during storage and transportation, a plastic storage end plug (simply a much smaller version of the centering mandrel and shown in Fig. 14.13(j)) was inserted between the armature and the stator, as shown in Fig. 14.13(k). The void between PVC armature shell and the armature shown in Fig. 14.13(g) can be filled with epoxy as long as an electrical connection to the armature is established (copper braid in Fig. 14.13(g)). The HFCGs shown in Fig. 14.14 were manufactured using this method.

14.4.3.3 *Dual-Stage Helical FCG Design*

As noted earlier, the first stage is called the booster stage and is designed for maximum energy gain, which means it needs to be maintained at a constant high-voltage throughout its run time. A detailed cross-sectional view of the first-stage stator and its seed coil is shown in Fig. 14.15 and labeled Detail View A. The distinct wire colors along the length of the first stage distinguish one section from another and serve no other purpose. The specific construction details of the first-stage stator and seed coil are presented in Table 14.1. The second stage of the helical FCG is called the peaking stage and its construction details are also presented in Table 14.1. A detailed cross-sectional view of the second-stage stator and its seed coil is shown in Fig. 14.15 and labeled Detail View B.

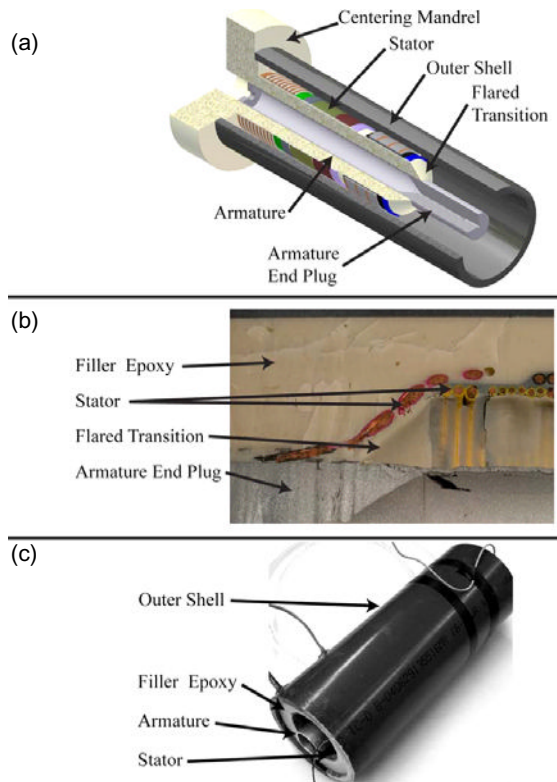


Fig. 14.14 (a) HFCG components ready for casting with filler epoxy. (b) Cross-sectional view of assembled HFCG detailing the flared transition region. (c) Completed HFCG. (Courtesy of Thomas Holt and Andrew Young, Texas Tech University.)

A three-quarter sectional view of the helical FCG is shown in Fig. 14.16. This design uses a simple 8-mil thick copper crowbar disk in the first stage. The annealed aluminum armature is packed with 430 g of Composition C-4 explosives. The conical portion of the end plug is designed to slow the expansion of the armature beyond the final turn of the stator and to prevent the armature from shearing off at any point prior to the end of the helical FCG run time, which could interrupt current flow.

14.4.4 Power Conditioning System

The *Power Conditioning System* (PCS) consists of an *Inductive Energy Store* (IES), peaking gap and electroexplosive opening switch [4, 5, 9]. The

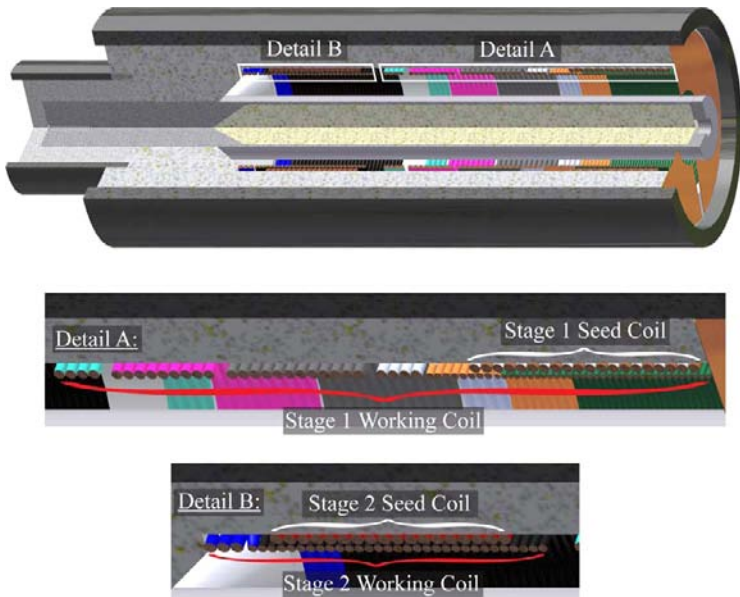


Fig. 14.15 Cross-section of a dual-stage HFCG detailing the seed and working coils of both stages. (Courtesy of Thomas Holt and Andrew Young, Texas Tech University.)

IES (Fig. 14.17) is simply an intermediate energy storage device that accumulates the output energy from the FCG and transfers it to the HPM source. The limiting design factor for the IES is its cross-sectional area. Since the FCG delivers tens of kiloamps, the conductor cross-sectional area must be sufficiently large to minimise resistance, while at the same time meet the diameter constraints of the system. The IES was made by winding PVC-insulated copper wires in parallel onto a cylindrical mandrel with a diameter of 76 mm and coating it with a thick layer of epoxy to keep the turn spacing fixed and to provide insulation between windings.

The *Electroexplosive Opening Switch* (EEOS) was basically a fuse composed of wires. Since the overall diameter of the system could not exceed 15 cm, the electroexplosive opening switch (Fig. 14.18) was placed inside the IES. To minimise the length of the fuse and to make the power conditioning system as compact as possible, 18 gold wires were used in the switch in place of silver wires. Brass gears were used to space the wires equidistant from each other. Field shaping rings were used to suppress fuse re-strike by distributing the fields more homogeneously across the gear surface. The

Table 14.1 Section details for Texas Tech helical FCG [16, 17].

Stage Number	Section Number	Number of Conductors	Number of Turns	Pitch (inches)	Wire Gage	Wire Type
Seed Source for Stage 1						
1	1	2	8–15	~ 0.303	12	Litz Magnet PVC
Stator for Stage 1						
1	1	1	32	0.072	20	Teflon
1	2	1	8	0.091	16	Teflon
1	3	1	4	0.126	12	Teflon
1	4	2	6	0.252	12	Teflon
1	5	3	3	0.387	12	Teflon
1	6	4	1	0.504	12	Teflon
Seed Source for Stage 2						
2	1	7	2.5	~ 0.882	12	PVC
Stator for Stage 2						
2	1	1	30	0.091	16	Teflon
2	2	1	3	0.126	12	Teflon

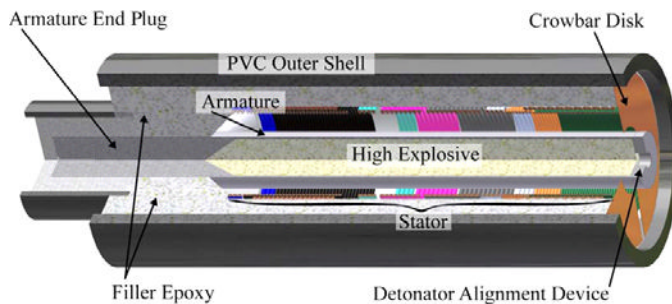


Fig. 14.16 Three-quarter-sectional view of the dual-stage HFCG detailing each component of the device. (Courtesy of Thomas Holt, Texas Tech University.)

switch was charged with SF₆ to quench re-strokes. Both the IES and EEOS were placed inside a stainless steel housing.

The EEOS can be treated as a variable resistor that starts with low-impedance and increases to very high impedance in a short period of time. The 10 μ s rise time of the current pulse from the FCG causes the fuse to operate in two stages. Before the fuse reaches its *action limit*,¹ the current

¹In physics and engineering, the action is a quantity that describes the operation of a physical system. Action only requires that the initial and final states of a physical variable be specified. The action is typically an integral over time and is an alternative

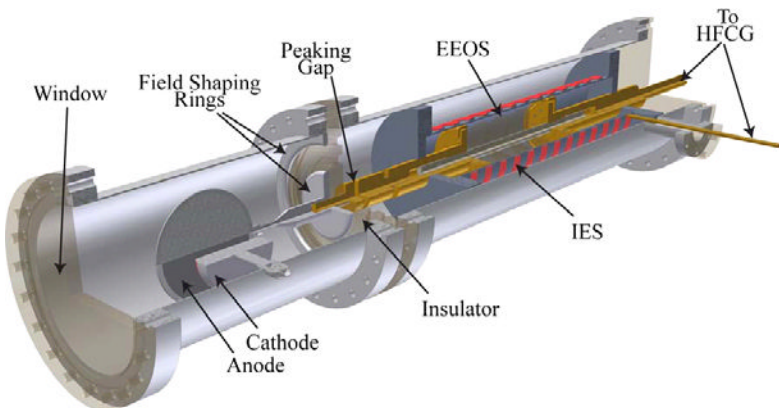


Fig. 14.17 Three-quarter-sectional view of the PCS components housed within a 6-in. diameter stainless steel tubing. (Courtesy of Thomas Holt and Andrew Young, Texas Tech University.)

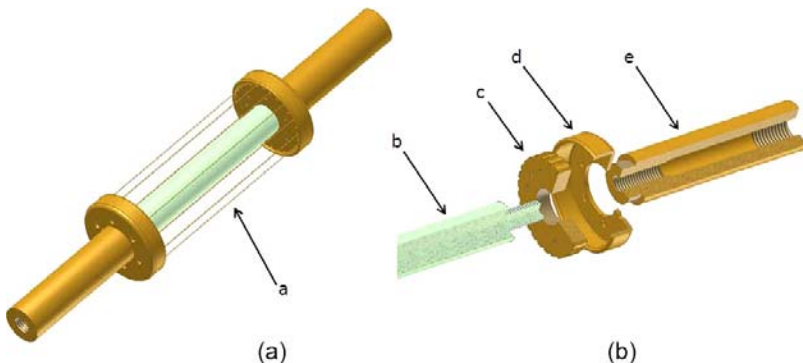


Fig. 14.18 (A) Photograph and (B) diagram of a complete fuse and (C) exploded view of fuse components: (a) gold wire, (b) G-10 rod insulator, (c) fuse gear, (d) electric field distribution ring and (e) brass connection inserts. (Courtesy of Thomas Holt and Andrew Young, Texas Tech University.)

flowing through the fuse and the finite resistance of the fuse generates a voltage in accordance with Ohm's law. This voltage increases slowly and somewhat linearly as the current increases until the action limit of the switch is reached. As the action limit is approached, the fusing process begins to take

to differential equations. In the case of exploding wires, the action is the integral of the electric current squared over the time from the start of current until the wire bursts.

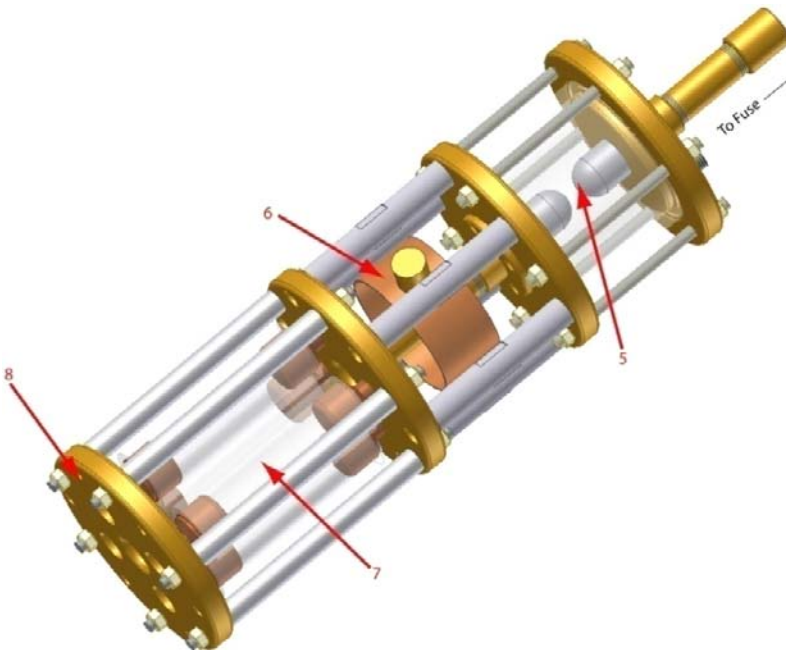


Fig. 14.19 Diagram of the spherical electrode peaking gap in the inductive energy store. 1 — Peaking gap, 2 — capacitive voltage divider, 3–4 parallel 80 W water resistors and 4 — Ground plate. (Courtesy of Thomas Holt and Andrew Young, Texas Tech University.)

place and the impedance increases exponentially. To prevent plasma formation on the surface of the cathode of the HPM source and premature closure of the anode-cathode gap, a *peaking gap switch* (Fig. 14.19) was introduced between the power conditioning system and the HPM source. The peaking gap is a simple self-breakdown spark gap that closes on over voltage. The peaking gap switch was designed to operate in SF₆ at a pressure of 100 psig.

14.4.5 Loads

The FCG and PCS described above were tested with several different loads: inductive dummy load (the IES), resistive dummy load filled with CuSO₄ solution, transformer and EEOS, dipole antenna and reflex virtual cathode oscillator [4, 5]. The diagnostics included a Rogowski coil that measures the derivative of the current, a Pearson current monitor that measures the

current directly, a capacitive voltage divider to measure high voltages and antennae to measure radiated microwaves.

The main objective of the Texas Tech program was to use a helical FCG to drive a HPM source. The HPM source selected for their experiments was the reflex virtual cathode oscillator, since it is one of only two HPM sources that are compatible with FCGs. The other HPM source that is compatible with FCGs is the Magnetically Insulated Line Oscillator (MILO). In order to observe the behavior of the FCG while it is driving a reflex virtual cathode oscillator, a resistive dummy load was used to characterise the output voltages and rise times of the FCG. The magnitude, rise time and shape of the electrical pulse delivered to the HPM source affects HPM generation. Therefore, the water resistor was designed to have impedance characteristics similar to that of a reflex virtual cathode oscillator. Since the impedance of a reflex triode Vircator is characteristically tens of ohms, the water resistor was designed to have a resistance of 20Ω .

Experiments were also performed with the dual-stage helical FCG driving an inductive load to determine the operating point for the exploding wire fuses used in the power conditioning circuit. During these tests, several problems were observed and corrected [4].

Since the power conditioning circuit may include pulse transformers, an inductive load was developed to see how the primary of the pulsed transformer and a series connected EEOS will affect operation of the dual-stage helical FCG. Whenever a transformer is used in a power conditioning system, care must be taken to ensure that the stray inductance is kept to a minimum, since the magnetic flux in the stray inductances does not couple to the secondary of the transformer.

Two sets of experiments were conducted looking at antennae as the load. The first set was with a power conditioning system and a 370Ω load. The impedance of the dummy load was chosen to approximate the impedance of an antenna. It was observed that the run time of the helical FCG was limited by the opening of the EEOS and that the load imposed no limitations on the performance of the helical FCG. A second set of tests were conducted in which the dummy load was replaced by a dipole antenna designed to operate at 60 MHz. The system did radiate energy with strong frequency components at 60 MHz and its first harmonic of 120 MHz.

The main distinction between power conditioning systems consisting of a transformer and EEOS and of the ILS is how the energy flows after each system's EEOS opens. The position of the EEOS in the transformer based power conditioning circuit requires elimination of stray inductances,

because the majority of the magnetic flux in the primary circuit loop does not efficiently couple to the secondary side of the transformer. The ILS-based power conditioning circuit does not suffer from this limitation since the flux stored in the stray inductances is efficiently coupled into the load.

Tests were also conducted in which the helical FCG was used to drive a reflex virtual cathode oscillator through a IES and PCS (Fig. 14.20). The virtual cathode oscillator was designed to operate at ~ 3.8 GHz. The output of the IES was coupled to the anode of the Vircator via a peaking gap electrode. It was demonstrated that the helical FCG could drive the Vircator and generate radiated RF energy.

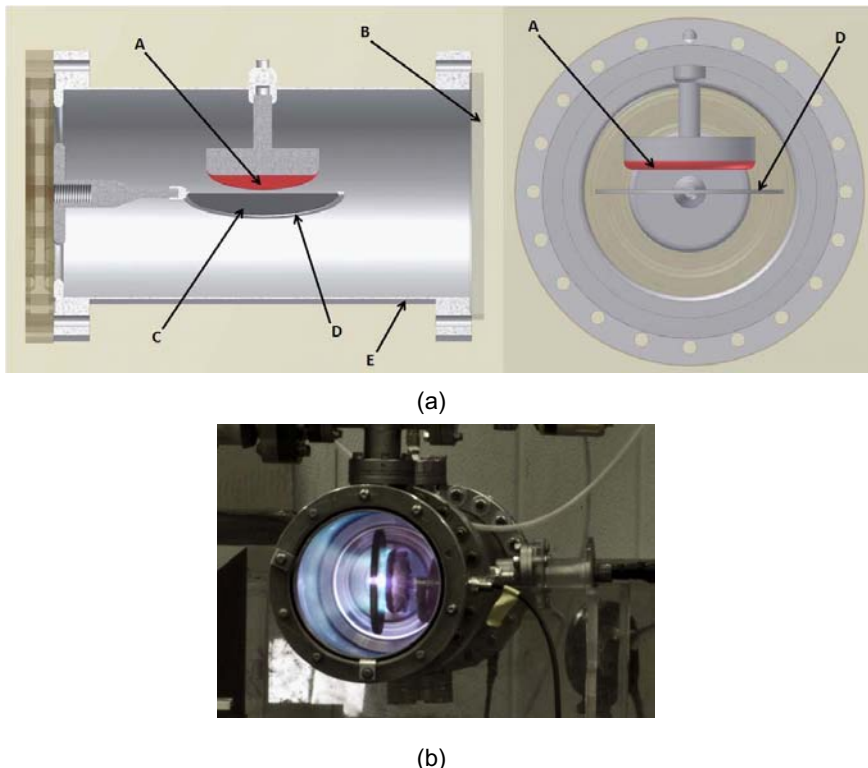


Fig. 14.20 (a) Cross-sectional view (rotated off axis) and end-section view of reflex-triode vircator. (A) Cloth velvet cathode, (B) optical glass, (C) mesh anode, (D) anode ring and (E) stainless steel housing. (b) Time-integrated picture of reflex-triode vircator during operation with field shapers in place. (Courtesy of Thomas Holt and Andrew Young, Texas Tech University.)

14.5 Case Study 4: Birdseed Program

The Birdseed program [10–12] was conducted in the late 1960s and early 1970s. The objective was to inject optically traceable amounts of neon plasma into the ionosphere to investigate the interaction of high-energy plasmas with the upper atmosphere and the earth's geomagnetic field. The experimental objective was to deliver 100kJ of plasma so that the average plasma velocity would be at least 10^7 cm/s and the quantity of particles would be sufficient to ensure that 'collective effects' could be observed. These conditions were achieved by using a pair of helical FCGs to drive a neon-loaded, coaxial plasma gun. These experimental objectives were achieved by Los Alamos National Laboratory (LANL) and Sandia National Laboratory (SNL), when three Birdseed payloads were successfully launched to altitudes of between 220 and 240 km in STRYPI rockets (Fig. 14.21). The Strypi rocket carried a payload of 500 kg, of which 200 kg was available for the power supply.

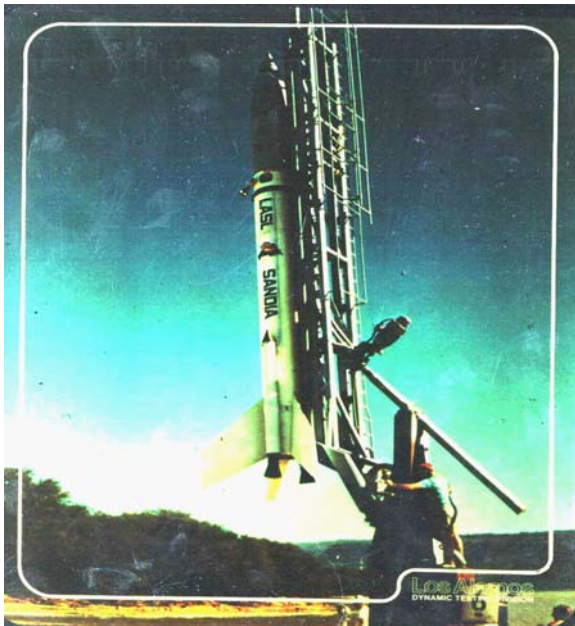


Fig. 14.21 Photograph of the Strypi Rocket with Birdseed Payload on the launch pad. (Courtesy of C. M. Fowler, Los Alamos National Laboratory.)

The design of the power supply was driven by several requirements including:

- Delivering a minimum energy of 250 kJ to the plasma gun.
- Meeting a maximum mass allowance of < 250 kg.
- Delivering an initial voltage of 5 kV to start the plasma gun.
- Delivering a current waveform that peaks in a few tens of microseconds and remains crowbarred for several tens of microseconds.

Because of the lower energy-to-weight ratio of capacitors (< 220 J/kg) at the time, the only way to meet all these requirements within the allocated mass was to use FCGs. The explosive pulsed power system used two helical FCGs; i.e., the Mark V generator developed by LANL and the Model 169 generator developed by SNL. The Mark V was a traditional end-fired helical FCG, while the Model 169 generator was a helical FCG that is initiated at both ends, its output located at the center of the stator.

The seed source for the Mark V generator was a 1360 μF capacitor bank that was electrically rated at 6 kV and 15 kJ, with a mass of 110 kg. The capacitor bank was charged during flight by a battery powered DC-DC converter. It delivered 8 kA of seed current to the Mark V generator. The Mark V served as the seed source for the Model 169 generator, as shown in Fig. 14.22. The Mark V delivered between 60 to 75 kJ of energy to the Model 169 generator. Tests at LANL showed that this power supply delivered 300–350 kJ to the Marshall plasma gun.

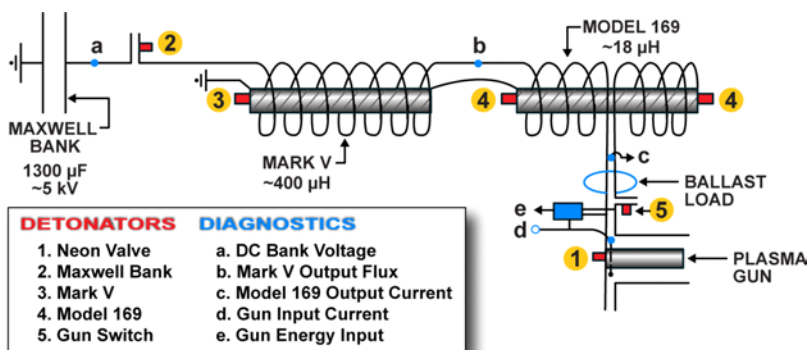


Fig. 14.22 Birdseed flux compression generators: the Marx generator seeds the Mark V booster generator, which, in turn, seeds the Model 169 generator. (Courtesy of C. M. Fowler, Los Alamos National Laboratory.)

Two closing switches were used. The first connected the Mark V to the capacitor bank and the second connected the plasma gun to the output of the Model 169 generator. All switching was accomplished by using detonator-activated solid dielectric switches. The switches consisted of two metal plates separated by polyethylene sheets. Small holes were drilled into one of the plates under the detonators. Closure of the switch was achieved when jets formed by the detonators penetrated the polyethylene. Due to high transient voltages produced by the detonator fire sets (also called X-units at LANL), the signals to the detonators were fired through isolation transformers built by SNL for use in rockets. A ballast load at the output of the Model 169 generator was used to complete the circuit prior to driving the switch to the plasma gun. After switch closure, the ballast shares the output current from the Model 169 generator. The inductance of the ballast load and the switching time determined the initial voltage applied to the plasma gun. Because the ballast load has a greater impedance than the plasma gun, most of the energy is delivered to the gun.

All components of the power supply were chosen to withstand the stabilising spin and the launch acceleration forces of the rocket. The program concluded with three successful shots at the Barking Sands Facility in Kauai, Hawaii.

14.6 Summary

In this chapter, we have looked at four case studies. The first test case was a High Voltage Generator based on ferroelectric materials. The second reported on the results of FEG-driven dipole antenna tests. The third test case was a detailed look at the components of an FCG-driven HPM test bed and how these components were manufactured. The fourth test case was a look at the design of a rocket-borne FCG-driven plasma gun for conducting experiments in the ionosphere. There are, of course, other examples that could have been discussed, but we will refer the reader to the proceedings of the various Megagauss and Pulsed Power Conferences that have been conducted since the 1960s.

In this book, we have looked at four different types of EPP device, their capabilities and limitations, and how they can be used in practical systems. Basically, the three practical generators are the FCG, FEG and FMG, where the FCG is a high-energy source, the FEG is a high-voltage source and the FMG is a high-current source. The operation of these generators is affected

by the power conditioning circuit and the nature of the load to be driven. Therefore, the selection of an explosive pulsed power generator will require a complete system analysis. That is, one needs to start with the load and work back through the power conditioning system to determine the parameters that the generator should have, which will, in turn, determine which type of generator is best for this application.

Bibliography

- [1] G. Staines, H. Hofman, J. Dommer, L. L. Altgilbers and Ya. Tkach, Compact Piezo-Based High Voltage Generator — Part I: Quasi-Static measurements, *Journal of Electromagnetic Phenomenon* **11**(3) (2003) 373–383.
- [2] G. Staines, H. Hofman, J. Dommer, L. L. Altgilbers and Ya. Tkach, Compact Piezo-Based High Voltage Generator — Part II: Prototype Generator, *Journal of Electromagnetic Phenomenon* **4**(6) (2004) 477–489.
- [3] M. S. Rader, C. Sullivan and T. D. Andreadis, Experimental Observation of RF Radiation Generated by an Explosively Driven Voltage Generator, Naval Research Laboratory Report NRL/FR/5745-05-10,122 (2005).
- [4] A. Young, *Explosively Driven Pulsed Power for High Power Microwave Generation*, Masters Thesis, Texas Tech University (2008).
- [5] T. A. Holt, *Design of a Dual-Stage Helical Flux Compression Generator*, PhD Dissertation, Texas Tech University (2008).
- [6] M. Elsayed, T. Holt, A. Young, A. Neuber, J. Dickens, M. Kristiansen, L. L. Altgilbers and A. H. Stults, High-Current Compact FCG Seed Source Implementing Solid State Switching, *Proceedings of the 2008 IEEE International Power Modulator Conference*, Las Vegas, Nevada, USA (May 27–31, 2008).
- [7] T. A. Holt, A. J. Young, A. A. Neuber and M. Kristiansen, A Fabrication Method for a Mid-Sized, High Energy-Density, Flux Compression Generator, *Proceedings of the 2006 International Conference on Megagauss Magnetic Field Generators and Related Topics and the International Workshop on High Energy Liners and High Energy Density Applications*, eds. G. F. Kiutu, R. E. Reinovsky and P. J. Turchi, Institute of Electrical and Electronics Engineers, Inc., (2008), pp. 281–286.
- [8] P. Worsey, J. Baird and J. Rasty, Mechanical Aspects of Helical Flux Compression Generators in Explosively Driven Pulsed Power, *Helical Magnetic Flux Compression Generators*, ed. A. Neuber, Springer Verlag (2005) (ISBN 3-540-26051-X).
- [9] P. Worsey, J. Baird and J. Rasty, Mechanical Aspects of Helical Flux Compression Generators in Explosively Driven Pulsed Power, *Helical Magnetic Flux Compression Generators*, ed. A. Neuber, Springer Verlag (2005) (ISBN 3-540-26051-X).
- [10] A. J. Young, T. A. Holt, M. A. Elsayed, A. A. Neuber, M. Kristiansen, L. L. Altgilbers and A. H. Stults, Fuse and Load Testing with Mid-Sized,

- High Energy Density Flux Compression Generators, *Proceedings of the 2007 IEEE Pulsed Power and Plasma Science Conference*, Albuquerque, NM (2007), pp. 1165–1168.
- [11] R. S. Caird, C. M. Fowler, W. B. Garn, I. Henins, J. C. Ingraham, R. A. Jeffries, D. M. Kerr, J. Marshall and D. B. Thomson, Payload Development for a High Altitude Plasma Injection Experiment, Los Alamos Report LA-4302-MS (1970).
 - [12] C. M. Fowler, D. B. Thomson, W. B. Garn and R. S. Caird, LASL Group M-6 Summary Report: The Birdseed Program, Los Alamos Report LA-5141-MS (1973).
 - [13] C. M. Fowler, D. B. Thomson and W. B. Garn, Explosive Flux Compression: 50 Years of Los Alamos Activities, Los Alamos Report LA-UR-98-4180 (1998).

Index

- acoustic impedance, 342
- action, 175
- activation energy, 66
- active elements, 17
- active integrating Rogowski sensor, 104
- air-core transformer, 20
- Ampere's Law, 14
- antiferromagnetic materials, 263
- armature, 6
 - liners, 130
- Arrhenius parameter
 - collision factor, 67
- Arrhenius's Equation, 67
- bellows generator, 149
- bifurcation, 220
- Birdseed program, 568
- booster generator, 196
- booster stage, 553
- boosting, 220
- boundary conditions, 16
- breakdown field strength
 - dielectric strength, 26
- burn time, 187
- burnout time, 139
- burst action, 77
- burst action coefficient, 77
- cameras
 - image converter
 - charge-coupled device (CCD), 126
- rotating-mirror
 - rotating-drum, 124
- capacitive discharge unit
 - CDU, 80
- capacitive voltage divider, 97
- capacitors, 19
- cavity current monitor, 108
- Chapman-Jouguet (C-J) plane, 53
- Chapman-Jouguet pressure and velocity, 53
- chemical kinetics, 66
- chemical reaction, 62
- CHNO explosives, 59
- CJ theory, 56
- closing switches, 22, 172
- coaxial cable transformer, 194
- coaxial flux compression generator
 - coaxial generator, 151
- coercive force
 - coercivity, 266
- compact seed source
 - CSS, 551
- compliance, 341
- compound transients, 30
- compressive strain, 47
- conductance, 18
- constitutive parameters, 14
- contact point resistance model, 229
- converse piezoelectric effect
 - inverse piezoelectric effect, 334
- coupling coefficient, 20
- coupling coefficient, transformers, 177

- crowbar, 131
crystalline phase diagrams, 375
Curie temperature, 263
Curie temperature, ferroelectrics, 336
current generators
 Type II, Mark II, MC-II, MK-II
 generators, 130
current viewing resistor, 107
cutter switch, 176
cylindrical flux compression generator
 cylindrical generator, 151
cylindrical implosion generator, 149
- decompression wave
 rarefaction wave
 release wave, 51
- deflagration, 52
- detonation, 52
detonation velocity, 53
detonation wave, 52
detonators, 73
diamagnetic materials, 262
dielectric constant, 14, 27
 relative permittivity, 339
- disk flux compression generator
 disk generator
 DFCG, 153
- displacement interferometry, 120
- dissipative circuits, 30
- domain switching, 384
- dynamic transformer, 197
- eddy current loss, 274
- effective coupling coefficient,
 transformers, 178
- efficiency, ferroelectrics, 342
- elastic limit
 yield point, 47
- elastic stiffness
 modulus of elasticity
 Young's modulus, 341
- electric displacement
 electric flux density, 13
- electric field strength
 electric intensity, 13
- electrical breakdown in FEGs, 447
- electrical conductivity, 14
electrical networks
 lumped element
 distributed element, 27
- Electroexplosive opening switch
 EEOS, 562
- electromechanical coupling factor, 342
- endothermic reaction, 63
- energy gain, 137
- energy transmission coefficient, 342
- enthalpy, 64
- equivalent characteristic velocity of
 nonexplosives, 69
- Eulerian coordinate system, 49
- exothermic reaction, 63
- expansion ratio, 225
- exploding bridgewire detonators
 EBWs, 74
- exploding wire switch
 exploding foil switch, 173
- explosive delay lines, 73
- explosive formed fuse
 EFF, 176
- explosive lenses, 73
- explosive magnetohydrodynamic
 generator, 7
- explosive power
 power index, 72
- explosive train, 73
- explosively driven pulsed power
 explosive pulsed power, 3
- Faraday effect, 98
- Faraday's Law, 15
- FCG battery, 245
- FEG and high resitant loads, 449
- FEG driven antenna, 548
- ferrimagnetic materials, 263
- ferroelectric crystal, 335
- ferroelectric generator
 FEGs, 439
 piezoelectric generator, 9
- ferroelectric transducer, 426
- ferroelectricity, 332
- ferromagnetic generator, 10
- ferromagnetic materials, 263

- field enhancement factor, 39
field generators
 Type I, Mark I, MC-I, or MK-I
 generators, 129
field interaction generators, 6
figure of merit, 137
 perfectness factor, 224
fire set, 80
flux capture, 197
flux compression generator
 FCG, 6
flux loss coefficient, 137
flux multiplication, 179
flux trapping, 197
 flux pocketing, 231
flux trapping or pocketing, 168
fuses, 173
- gas guns, 440
 reverse-impact configuration, 421
Gauss's Law, 15
geometrical compression ratio, 137
glide plane, 7
Gurney energy, 84
Gurney equation, 86
Gurney Model, 83
Gurney velocity, 86
- hard magnets, 263
heat of detonation, 65
heat of formation, 64
heat of reaction, 64
helical flux compression generators
 helical or spiral generators
 HMCG, 159, 217
helical-wound transformers, 191
HFCG computer models, 254
HFCG current gain, 225
HFCG energy gain, 225
high power microwave test bed
 HPM test bed, 550
HMX, 59
Hugoniot, 50
hysteresis loop, 265
hysteresis loss, 274
- ideal detonation velocity, 71
inductance
 self-inductance
 mutual inductance, 19
Inductive Energy Store, 561
Inductors, 18
intrinsic flux loss parameter
 figure of merit, 223
intrinsic loss factor, 229
intrinsic losses, 229
- Kerr effect, 98
Kirchhoff's laws, 28
Kiuttu critical point, 229
- Lagrangian coordinate system, 49
LANL (Los Alamos National
 Laboratory), 132
lead zirconate titanate
 PZT, 346
linear current density, 228
linear magnetic diffusion, 227
liner, 6
longitudinal FEG
 low impedance FEG
 axially poled FEG, 426
longitudinal ferroelectric generator,
 445
longitudinal fracturing, 232
loop flux compression generator
 loop generator
 LFCG, 155
Lorentz force, 33
- magnetic analog of Kirchhoff's laws,
 272
magnetic circuit, 261, 267
magnetic conductance, 269
magnetic diffusion equation, 32
magnetic diffusivity, 32
magnetic dipole moment, 264
Magnetic Domain
 Weiss Domain, 263
magnetic field strength
 magnetic intensity, 13
magnetic flux, 15

- flux compression generator
- magnetocumulative generator
 - magnetic compression
 - generators, 129
- magnetic flux density
 - magnetic induction, 13
- magnetic permeability, 14, 265
- magnetic potential gradient, 269
- magnetic pressure, 35
- magnetic reluctance, 268
- magnetic Reynolds number, 230
- magnetic saturation, 265
- magnetic stress, 33
- magnetic susceptibility, 264
- magnetization, 264
- magnetization curve, 265
- magneto-optical current sensor, 109
- magnetomotive force
 - mmf, 267
- Maxwell's equations, 13
- mild-detonating fuses, 73
- minimum burst current
 - Threshold burst current, 79
- moving magnet generator, 8
- multi-element FEGs, 486
- non-explosive pulsed power, 2
- nonlinear magnetic diffusion, 227
- Ohm's law, 14
- open circuit, 18
- opening switches, 22, 173
- optical voltage monitor, 98
- oxidation reaction, 60
- paraelectric, 336
- paramagnetic materials, 263
- passive differentiating Rogowski coil
 - I-dot probe
 - L/R Rogowski coil, 103
 - passive elements, 17
 - Passive Integrating RC Rogowski coil,
 - 103
 - peaking gap switch, 565
 - peaking stage, 553
 - Pearson current monitor, 106
 - perovskite crystal structure, 370
- phase transformations in single crystals, 394
- phase transition generators, 6
- piezoelectric charge constant, 341
- piezoelectric effect, 332
- piezoelectric gages, 123
- piezoelectric generators, 9
- piezoelectric high voltage generator
 - HVG, 543
- piezoelectric voltage constant, 341
- piezoelectricity, 332
- piezoresistive gages, 122
- plastic deformation, 47
- plate flux compression generators
 - plate generators
 - PMCG, 146
- Pockels effect, 98
- polymer bonded explosives, 60
- post flux compression generator
 - post generator, 155
- Power Conditioning System, 561
- primary explosives, 58
- Pro-FLUX generator, 9
- propellant guns, 441
- pulse charging capacitors with FEGs, 460
- pulse compression, 2
- pulse forming line, 25
- Pulsed Power, 2
- quasistationary fields, 14
- Rankine-Hugoniot jump equations, 49
- rate constant, 67
- RDX, 59
- reaction zone, 53
- reluctance, 268
 - reluctance drop, 269
- remanence
- retentivity, 265
- remnant polarization, 336
- resistive voltage divider, 92
- resistors
 - linear
 - nonlinear, 17
- Rogowski coil, 100

- secondary high explosives, 58
seed source, 194
self-integrating Rogowski coil, 102
Semtex, 60
shear strain, 47
shock impedance, 82
shock wave, 48
shock wave flux compression generator
 semiconductor generator
 SWFCG, 162
shock wave source
 SWS, 6
short circuit, 18
simultaneous axial initiation, 242
skin depth, 31
skin layer, 31
skin time, 33
small HFCG, 252
soft magnets, 263
staging, 196
stator, 6
stator transition point, 556
stators, 130
steady state circuit, 30
Stoke's theorem, 14
strain, 45
streamer breakdown, 37
stress, 45
strip flux compression generators
 strip generators
 SF CG, 147
switches, 21
switching transients, 30

tamping in fuses, 173
tamping of explosives, 171
tape-wound transformers, 193

Taylor angle approximation, 87
tensile strain, 46
tertiary explosives, 58
theoretical maximum density, 68
thermodynamic standard state, 64
time of arrival detectors, 118
TNT, 59
Townsend breakdown, 37
transformers, 19
transient circuits, 30
transient transients, 30
transmission line, 24
transverse FEG
 high impedance FEG
 normally poled FEG, 427
transverse ferroelectric generator
 transverse FEG
 normal FEG, 445
turn-around radius, 150

universal gas constant, 67

velocity interferometry, 120
virtual spallation, 233
VISAR, Velocity Interferometer
 System for Any Reflector, 120
VNIIEF (All Soviet Scientific
 Institute of Experimental Physics)
 All Russian Scientific Institute of
 Experimental Physics, 132
volume fraction, 69
volume strain, 47

wave equation, 32

X-ray radiography, 126